Farkhondeh Jabari
Behnam Mohammadi-Ivatloo
Mousa Mohammadpourfard *Editors*

Integration of Clean and Sustainable Energy Resources and Storage in Multi-Generation Systems

Design, Modeling and Robust Optimization

Springer

Integration of Clean and Sustainable Energy Resources and Storage in Multi-Generation Systems

Farkhondeh Jabari • Behnam Mohammadi-Ivatloo
Mousa Mohammadpourfard
Editors

Integration of Clean and Sustainable Energy Resources and Storage in Multi-Generation Systems

Design, Modeling and Robust Optimization

Springer

Editors
Farkhondeh Jabari
Department of Power System Operation and Planning
Niroo Research Institute (NRI)
Tehran, Iran

Mousa Mohammadpourfard
Faculty of Chemical and Petroleum Engineering
University of Tabriz
Tabriz, Iran

Behnam Mohammadi-Ivatloo
Faculty of Electrical and Computer Engineering
University of Tabriz
Tabriz, Iran

Department of Energy Technology
Aalborg University
Aalborg, Denmark

ISBN 978-3-030-42419-0 ISBN 978-3-030-42420-6 (eBook)
https://doi.org/10.1007/978-3-030-42420-6

This Springer imprint is published by the registered company Springer Nature Switzerland AG
The registered company address is: Gewerbestrasse 11, 6330 Cham, Switzerland

Preface

Recently, the application of clean and sustainable energy resources and storage technologies in poly-generation systems has increased due to huge value of energy utilization and interdependency between power, water, heat, cool, hydrogen, etc. production facilities. Meanwhile, robust co-optimization of multi-output systems under various operating conditions is vital to ensure techno-economic and environmental benefits of renewable- and storage-based hub networks.

This book provides design principles, performance assessment, and optimization of multi-production systems for transition from traditional oil- and gas-fired energy supply to green near zero energy microgrids.

Chapter 1 reviews the concept of renewable energy-based multi-generation systems for producing a number of outputs, such as power, heat, hot water, cooling, hydrogen, and freshwater and discusses its economic and environmental benefits.

Chapter 2 reviews the selection of the storages from cost-efficiency and energy-efficiency viewpoints. Furthermore, updated approaches for selecting the storages with high performance in order to cover the stochastic behavior of the power system's components are introduced. Moreover, different applications of the storages are analyzed, and this concept's practical objective functions, constraints, and useful technologies are considered. In addition, a comprehensive comparison of the diverse kinds of storages which are applied for improving the level of the power system's operation is performed. Ultimately, a general deduction about the storage selection and the future trend of this issue are presented regarding the efficiency of the storages and uncertainty of the power system.

Chapter 3 categorizes various kinds of fluctuations and uncertainties of renewable energy resources in different time scales with intensities. In addition, different ESS technologies and their characteristics, which are important in selecting them, are surveyed. Each of these technologies could be used for different applications in power systems. Finally, according to the type of fluctuations and uncertainties, the appropriate options of ESSs are selected based on the techno-economic aspects.

Chapter 4 pays more attention to the solar-driven reliable energy-converting systems equipped with auxiliary equipment for energy storage.

Chapter 5 devises an innovative multi-generation system operated by a solar tower power (STP) plant to produce cooling, power, freshwater, heating, and hot water simultaneously. For this aim, a supercritical CO_2 (S-CO_2) power cycle (for power, heating, and hot water generation), a transcritical CO_2 (T-CO_2) refrigeration cycle (for cooling production), and a humidification-dehumidification (HDH) unit (for desalinating seawater) are used in a more efficient configuration. Due to cumbersome task of the mathematical modeling of the unit, energy analysis of the devised integrated system is performed in this chapter, and exergy and exergoeconomic evaluation are postponed to the Chap. 6.

Chapter 7 proposes a multi-generation system for the Sabalan geothermal energy source to produce power, heating, hydrogen, purified water, and NG supply. In this novel system, absorption power cycle using ammonia water as working fluid is used to produce power, vapor compression cycle to generate heating, hydrogen extraction via proton exchange membrane (PEM) electrolyzer, and freshwater via reversed osmosis (RO) unit using power extracted through pressurizing of the liquefied natural gas. An exhaustive thermodynamic modeling of the proposed system is presented from first and second laws of thermodynamics vantage point.

Chapter 8 presents a heat sink of liquefied natural gas (LNG) and an absorption power cycle (APC) that are used to capture thermal energy of the Sabalan geothermal source in Iran. The main purpose is stockpiling of simultaneous electricity and natural gas (NG) to the Sabalan district users. Extension of the exergoeconomic relations for the devised combined APC/LNG plant is inspected in order to figure out the working concept of the devised setup. Furthermore, using genetic algorithm (GA) method, single- and multi-objective optimization procedures of the devised setup are outlined by delineating turbine inlet pressures, generator hot pinch point temperature difference, absorber temperature, heat exchanger minimum temperature difference, and basic LiBr fraction as decision variables.

Chapter 9 presents a mathematical robust model for an MG (micro-grid) to obtain the BESS charge/discharge scheduling and the exchange of power with upstream network considering the uncertainties of electricity market price, demand, and water flow. In this regard, a min-max problem, which is modeled as a bi-level optimization problem is developed and is solved in two iterative steps. In the first step, GA is applied to obtain the worst case wherein uncertain parameters are determined such that MG energy procurement cost is maximized. Then in the second step, a mixed-integer linear problem is solved to minimize the energy procurement cost over MG decision variables considering the values determined in the first step. The steps are iterated to converge to the best solution.

Chapter 10 first studies different game theory models and their applications in power system. Then, an appropriate model is selected to formulate the optimization problem for finding the optimal operating point of the multi-production system. The study considers fluctuations of renewable energy resources, various load levels, and the market environment. Two game models based on deterministic and stochastic approaches are proposed, formulated, and investigated.

Chapter 11 presents a detailed energy, exergy, and economic and environmental analysis of a double-stage subcooled-compressed air energy storage (CAES) system.

The subcooled-CAES is a new mechanical energy storage technology that offers the trigeneration of cold, heat, and electricity at a pretty high overall efficiency and can facilitate the integration of three energy sectors. For carrying out the analyses, the system is assumed to be employed in the energy system of Denmark with its certain energy pricing and supply specifications.

Waste-driven combined heat and power (CHP) plants are extremely popular in many countries, especially in northern Europe. Waste CHP is mainly employed for baseload demand supply of heat and power grids. Chapter 12 proposes the hybridization of such power plants with solar parabolic trough collectors to open the gate for reliable growth of the share of solar power plants into the existing energy matrices via a 100% dispatchable energy output. The hybrid power plant is proposed to have a flue gas condensation unit to maximize the net efficiency.

Chapter 13 introduces a probabilistic optimal power flow (P-OPF) for modeling the uncertainties associated with the correlated input random variables. Moreover, the point estimate method (PEM) is used for generating $2m + 1$ stochastic scenarios in a way that the correlated wind speeds with Weibull and loads with normal distribution functions are transformed into the independent normal distribution using the Nataf transformation.

Concerns in energy shortage and the impact of greenhouse gas emissions motivate the production of transportation fuel via a biomass gasification (BG) and Fischer-Tropsch (FT) process. Chapter 14 explains the basic background of the BG-FT process, including the gasification, gas cleaning, and FT processes. Numerous aspects of this process, such as the influence of the feedstock type and characteristics and the processing conditions, efficient process design, and FT catalyst performance improvement, are reviewed based on laboratory-scale research.

Chapter 15 presents the energetic, exergetic, and economic analyses of solar-powered integrated energy system for multi-generation. The proposed solar plant is integrated with a thermal energy storage sub-plant in order to overcome intermittency of solar energy. Integrated energy system for multi-generation consists of the solar tower with thermal energy storage (TES), Rankine cycle, organic Rankine cycle (ORC), cooling sub-plant with single-effect absorption cycle with ejector (SEACE), hydrogen production and liquidation subsystem, freshwater production subsystem, hot water production, and drying process for power, hydrogen, methanol, cooling, heating, hot water, freshwater, and drying production.

Tehran, Iran — Farkhondeh Jabari
Tabriz, Iran — Behnam Mohammadi-Ivatloo
Tabriz, Iran — Mousa Mohammadpourfard

Contents

Chapter 1
Economic and Environmental Benefits of Renewable Energy Sources in Multi-generation Systems

Amir Farahmand-Zahed, Sayyad Nojavan, Kazem Zare, and Behnam Mohammadi-Ivatloo

1.1 Introduction

World energy demand is increasing constantly, as the population of the world and the standards of living grows. Responding to the growth of energy demand, while maintaining its safety and environmental aspects is an important challenge. The mentioned increase in energy needs has critical effects on the environment as the generation processes of energy emit harmful pollutants (i.e. greenhouse gases, particularly carbon dioxide) to the environment. On the other hand, fossil fuel reserves are limited. Renewable energies are the best alternative energy sources. Some of the renewable energy sources (RES) are available in nature such as solar, biomass, hydro, wind, wave, tidal, ocean current, ocean thermal, and geothermal. Also, some human activities can be used as renewable energy sources. These activities are waste material recovery and heat recovery.

In recent decades, new technologies for increasing the efficiency of energy systems and relieving global warming have been proposed and tested in many countries. One of these technologies is multi-generation processes which have the

A. Farahmand-Zahed (✉) · K. Zare
Faculty of Electrical and Computer Engineering, University of Tabriz, Tabriz, Iran
e-mail: amir.farahmand96@ms.tabrizu.ac.ir; kazem.zare@tabrizu.ac.ir

S. Nojavan
Department of Electrical Engineering, University of Bonab, Bonab, Iran
e-mail: sayyad.nojavan@bonabu.ac.ir

B. Mohammadi-Ivatloo
Faculty of Electrical and Computer Engineering, University of Tabriz, Tabriz, Iran

Department of Energy Technology, Aalborg University, Aalborg, Denmark
e-mail: bmohammadi@tabrizu.ac.ir

F. Jabari et al. (eds.), *Integration of Clean and Sustainable Energy Resources and Storage in Multi-Generation Systems*,
https://doi.org/10.1007/978-3-030-42420-6_1

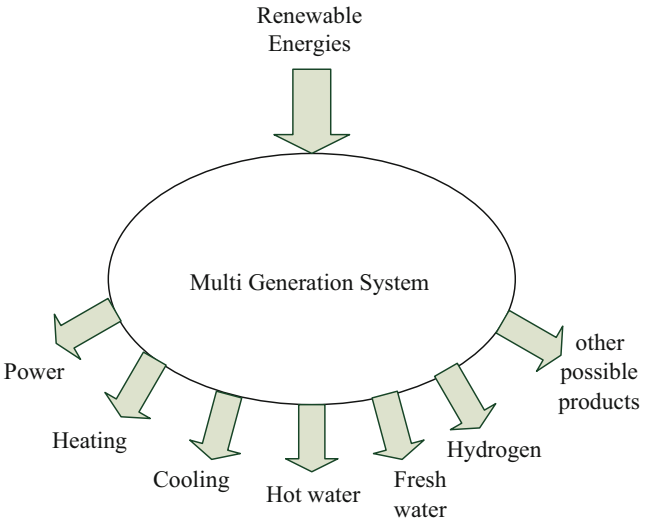

Fig. 1.1 Schematic of a renewable-energy-based multi-generation system

potential for high efficiencies, low pollution emissions, and low operating costs. Reducing cost and environmental impact as well as increasing the efficiency and sustainability are among the main objectives of using multi-generation technologies. A multi-generation system can have products like electricity, heating, cooling, hot water, fresh water, and hydrogen. In recent years, the popularity of multi-generation systems has been increasing due to their potential in supplying energy demands in a better economic and environmental condition. Some of the advantages of multi-generation systems over single-generation systems can be summarized as increasing efficiency, minimizing losses, and reducing CO_2 emissions and fuel usage [1]. The flexibility of the system will be increased by multi-generation systems. For example, the storage characteristics of thermal loads can be used to participate in reserve and frequency response to contribute in balancing power system [2].

In recent years, there is increased attention to the concept of multi-generation systems. Many researches were conducted on the different aspects of multi-generation systems, such as thermodynamic, operation optimization, economic, and environmental analysis [3–7]. The combination of multi-generation and renewable energy systems can provide significant benefits. The schematic of a renewable-energy-based multi-generation system is illustrated in Fig. 1.1. A review of the achieved progress in clean power generation, including the high-temperature solid oxide and molten carbonate fuel cells, conducted by U.S. Department of Energy, as well as the hybrid system that combines these two fuel cells with gas turbines, is studied in [8]. In another review study, the optimization problem of a combined cooling, heat, and power (CCHP) system powered by geothermal and solar energies is investigated in [9]. And a review of small-scale applications of CCHP systems powered by biomass is studied in [10].

In this chapter, the concept of renewable-energy-based multi-generation systems for producing a number of outputs, such as power, heat, hot water, cooling, hydrogen, and fresh water from the economic and environmental viewpoints is reviewed, and its benefits are discussed.

In the remaining of the chapter, at first, different types of energy demands are explained briefly in Sect. 1.2. Then the different types of multi-generation systems according to the number of their outputs are reviewed in Sect. 1.3, and the conclusion of the chapter is presented in Sect. 1.4.

1.2 Different Energy Demands

In this section, energy demands are briefly introduced. These energy demands are electricity, heating and cooling, hydrogen, potable water, and so on.

1.2.1 Power

In the beginning, electricity was generated by burning fossil fuels in central areas or by the hydroelectric dams that were located in remote areas. The electricity and heat produced from combusting fossil fuels were used to supply the nearby buildings. The demand for electricity was increased as a result of the growth of the city's population. But generating enough electricity to supply the demand inside the cities was not possible due to the environmental effects of combusting fossil fuels such as coal and their harmful emissions. So, the power plants were moved out of cities and urban areas, and as a result, the transmission of waste heat was not possible. Also, the transmission losses of electricity increased by 10–15% [11]. Then, the system components were developed so the efficiency of transmitting electricity improved. At that time, it was believed that the efficiency of centralized generation was more than a decentralized generation. Nowadays, there is an increasing interest in the economic, clean, and more efficient electricity generation in both centralized and decentralized generation systems. One of the clean energy sources is renewable energies. The main advantages of them can be summarized in being non-pollutant, producing minimum or zero waste, and not contributing to global warming [12].

Some of the renewable resources are biomass, geothermal, hydropower, ocean, solar, and wind. Different aspects of these technologies are summarized in Table 1.1, including their current share of generation, generation cost, CO_2 emission, and mitigation potential. Also, in order to compare these resources with fossil fuels, the same data is provided for gas and coal. The decrease of CO_2 emissions due to the reduction of using fossil fuels is defined as mitigation potential [1]. According to Table 1.1 [1, 13], gas and coal have the lowest generation cost and the biggest share of annual electricity generation, but their disadvantage is their high CO_2 emissions compared to renewable energies. The wind has the highest mitigation potential, while biomass has the lowest. The CO_2 emissions of solar are higher than other

Table 1.1 Comparison of fossil-fueled and renewable energy resources

	Current share of generation (TWh/year)	Mitigation potential	CO_2 emissions (g/kWh)	Generation cost ($/kWh)
Gas	3807	N/A	450–900	4–6
Coal	7755	N/A	900–1200	3–6
Wind	260	450–500	65–80	3–7
Biomass	240	100	35–85	3–9
Geothermal	60	25–500	20–140	6–8
Solar	12	25–200	40–200	10–20
Hydro	3121	200–300	45–200	4–10

technologies, and the lowest is caused by hydro. The generation cost of biomass and wind is lower than solar and hydro technologies.

1.2.2 Heating and Cooling

One of the important parts of worldwide energy demand growth is cooling and heating demands. In cold regions, heating demand is high, mostly during winters, and the cooling demand is increasing, resulting in the growth of the usage of refrigeration and air conditioning systems. These demands are mostly being supplied by fossil fuels, but a better alternative source to provide heating and cooling is renewable energies. The decentralized generation does not have the distribution and transmission losses, which is a problem of centralized generation, and renewable energy resources capture this feature of decentralized generation. One of the problems of renewable energies is their fluctuating nature that would lead to supply and demand imbalance. This problem can be relieved by thermal energy storage. District heating and cooling, thermal energy storage, cool thermal energy storage, heat pumps, and hybrid systems are some of the practical systems that store or combine the geothermal, biomass, and solar resources. The advantage of hybrid systems is that in the absence of one of the renewable resources, other renewable resources are able to provide sufficient energy to meet the demand. If the temperatures of the demand and source are not the same, heat pumps are used [1]. Another solution is to utilize the waste heat of power generation and industry to supply the heating and cooling demands.

1.2.3 Hydrogen

A sustainable renewable-energy-based system requires sufficient energy storage systems, to provide enough supply when the renewable source is not available. The mechanism of these storages can be different, and the energy can be stored in

different forms, such as chemical or electrical. One of the chemical mechanisms to store and carry energy is hydrogen. In order to achieve economic, sustainable, and clean development, it is necessary that the generation of energy and its carriers be done from clean and efficient sources.

Hydrogen has some advantages over electricity; for example, hydrogen can be stored and transferred through the existing transportation system, hydrogen can be stored for a longer period of time, hydrogen does not have transmission losses and can be transported for a long distance, no emissions are released during the production of hydrogen from water, and if renewable energies were used for its production, its storage and production will not have environmental effects, hydrogen can be stored in the forms of liquid or gas, and its efficiency of energy conversion is high. However, the costs of producing hydrogen are high, and the efficiency of its existing processes is low, which is because these methods are not mature, and future studies should address these issues [14]. Supply, energy security, air quality concerns, and environmental problems are some of the factors that can help the economic support of hydrogen. Fossil fuel dependence, logistic investments, fuel cell cost, and enhancements of the combustion engine are among these problems [15].

1.2.4 Potable Water

One of the methods of providing clean water is through desalination technologies. But these technologies are energy-intensive. One solution to supply the energy need of desalination units is through integrating the multi-generation systems, so the waste heat would be used to supply the energy demand of desalination units. A summary of the possible output that can be produced from different types of renewable energies is listed in Table 1.2.

1.3 Multi-generation Systems

In recent years, the popularity of multi-generation systems has been increasing due to their potential in supplying energy demands in a better economic and environmental conditions. Some of the advantages of multi-generation systems over single-generation systems can be summarized as increasing efficiency, minimizing losses, and reducing CO_2 emissions and fuel usage [1]. The flexibility of the system will be

Table 1.2 Possible outputs from different types of renewable energies

	Solar	Geothermal	Wind	Biomass	Hydro
Power	✓	✓	✓		✓
Hydrogen	✓	✓		✓	
Heating or cooling	✓	✓		✓	

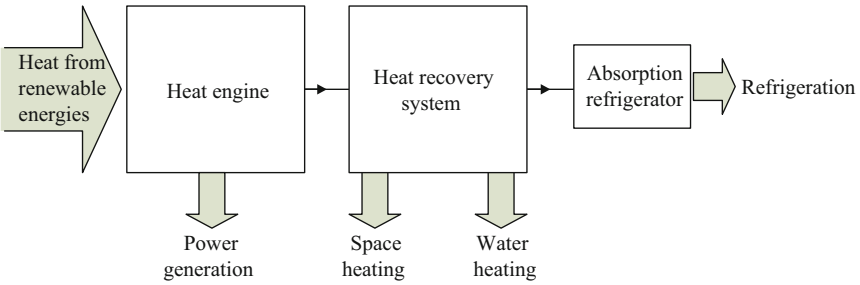

Fig. 1.2 A system based on renewable energies that produce heat to generate power, water heating, space heating, and refrigeration

increased by multi-generation systems. For example, the storage characteristics of thermal loads can be used to participate in reserve and frequency response to contribute in balancing power system [2]. The direct production of some of the renewable energy sources such as industrial heat recovery, geothermal heat, combustion of biomass-derived products, and concentrated solar radiation is heat. A schematic of a multi-generation system based on renewable energies that produce heat to generate power is illustrated in Fig. 1.2.

Decentralized multi-generation systems, also referred to as distributed multi-generation (DMG) systems, are small-scale multi-generation systems that provide several types of energy, such as electricity, heating, cooling, potable water, hydrogen, and gas in the output from the same energy resource. Small scale means less than 50 MW^e [16].

Multi-generation systems can be classified based on their number of outputs into cogeneration, trigeneration, and so on.

1.3.1 Cogeneration

Cogeneration (also referred to as combined heat and power (CHP)) systems utilize the produced heat in the power generation process to provide both electrical and thermal energy. The cogeneration system is able to recover the heat that power plants release during the process of electricity generation. So CHP provides a solution for the economic and environmental problems related to the energy generation by increasing its efficiency. Some of the benefits of cogeneration are increasing energy security, reducing costs, efficiency improvements, and decreasing CO_2 emissions. Cogeneration is the simplest form of multi-generation systems and is analyzed from the energy/exergy point of views in [17]. Also, the advantages and disadvantages of decentralized cogeneration systems are analyzed in [18]. Power plants that use fossil fuels have an average efficiency of 37%, which is 58% for the cogeneration system. The efficiency of state-of-the-art CHP systems can reach 85% and more [19].

Combining CHP systems with renewable energies is a good solution to achieve a clean and economical energy generation system. Some of the studies that address renewable-energy-based CHP systems are presented below.

1.3.1.1 Solar-Energy-Based Cogeneration Technologies

A concentrating photovoltaic/thermal system with single-effect absorption cooling is comprehensively analyzed from the economic and performance aspects in [20]. The results indicate that solar-energy-based combined cooling and power generation system has a better economic performance than the conventional systems. A comprehensive analysis of desiccant cooling systems (DEC) which are combined with both single glazed standard air and hybrid photovoltaic/thermal (PV/t) collectors is studied in [21]. In this study, the economic and energy performance of the system is investigated, and the system is considered to be used in humid and hot climate conditions. A simple model of the buildings with renewable-energy-based systems, such as photovoltaic arrays, absorption chiller, and thermal collectors, is studied in [22], to analyze energy savings, environmental and economic benefits, and CO_2 emission reduction.

1.3.1.2 Fuel Cells Based on Cogeneration Technologies

A comparative and detailed analysis of the solid oxide fuel cell system and electricity-, oil-, and gas-based heating systems was investigated in [23]. In this study, a simplified model that contains a single family was used, and the HOT2000 building simulation program was used for the estimation of the energy consumption of the house. Also, they investigated the economic analysis considering energy price, the electricity buyback strategy of an energy utility, acceptable payback period, and system sizing and reported the results including the sensitivity of the maximum allowable capital cost.

A review of the achieved progress in clean power generation, including the high-temperature solid oxide and molten carbonate fuel cells, conducted by the US Department of Energy, as well as the hybrid system that combines these two fuel cells with gas turbines, is studied in [8].

1.3.2 Trigeneration

Trigeneration or combined cooling, heat, and power (CCHP) is the complete form of CHP. This technology has been used large-scale centralized power plants for almost a century, and its reliability is proven. Trigeneration is the "natural" extension of cogeneration. In CHP systems, heat and power are produced at the same time. A CCHP system in addition to heat and power uses the available mechanical or

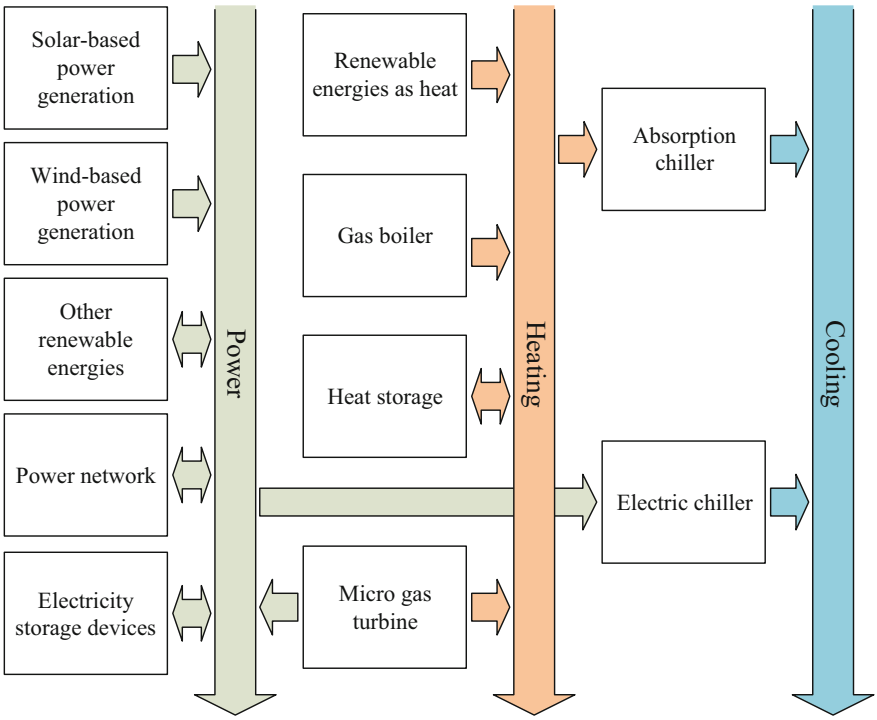

Fig. 1.3 Schematic of the energy flow in a CCHP system

electrical energy to provide cooling for process or space cooling purposes. A "classical" trigeneration is made by combining a CHP plant with absorption chillers to enable it to produce cooling. In this case, in the summer hot weather conditions that there is no need for heating, cooling can be produced. The cooling demands during winter are near to zero, so the CCHP system would not provide cooling, and this is why CCHP systems might be considered to be "seasonal operation." A schematic of the flow of energy in a CCHP system is illustrated in Fig. 1.3. According to Fig. 1.3, power demand can be supplied through renewable energies, power grid, electricity storages, and micro gas turbine. Possible sources for heating are gas boiler, micro gas turbine, heat storage, and renewable energy sources such as industrial heat recovery, geothermal heat, combustion of biomass-derived products, and concentrated solar radiation. And the cooling demand can be supplied from heat energy through an absorption chiller or from electricity through electric chiller. Regular applications of trigeneration systems are reviewed in [24]. CCHPs are investigated in details from the environmental and energy points of view in [25].

In addition to large-scale applications, CCHP technologies can also be combined with decentralized (distributed) energy sources to supply different energy demands of end users with high efficiency. CCHP systems are able to improve the fuel energy utilization efficiency and bring to 70–90%. The efficiency of conventional systems is

around 30–45%. So in order to generate the same amount of energy, they need the fewer amount of input which would decrease the costs and possible environmental effects, such as emissions. They also reduce transmission losses. The CCHP systems' reliability is more than that of large-scale centralized generation systems [24]. Also, they are able to continue their work during electricity blackouts because they are not dependent on the grid. The comparison of the reliability of centralized and distributed energy systems was studied in [26].

A power generation unit (electricity generator and prime mover) and HVAC components (air handling units, cooling towers, and absorption chillers) are the main components of a CCHP system. Different prime movers of the CCHP are investigated in [27]. Collecting the heat generated by the prime mover is an important part of CCHP operation which is done by a heat recovery unit.

1.3.2.1 Solar-Energy-Based Trigeneration Technologies

Different combinations of renewable energies and trigeneration system are studied in various researches. One of the common renewable energy resources that are used in trigeneration systems is solar energy [28]. A solar-energy-based CCHP system has some advantages over independent solar-energy-based power, heating, and cooling systems, which would lead the researches to this system. In this system, the same pipes, storage system, solar collection, and auxiliary equipment are used, and that can reduce the total cost in comparison to the three independent systems.

A solar-energy-powered CCHP system that consists of the combination of a transcritical CO_2 refrigeration cycle and a Brayton cycle is studied in [29]. In another framework, a CCHP system powered by solar energy based on organic working fluid is tested for a special building [30]. In order to analyze its economic and thermodynamic performance and the effect of different parameters, a parametric analysis was studied. The economic, environmental, and energetic investigation of a CCHP system powered by solar energy and including a heat storage tank is analyzed in [31].

A multi-objective optimization of a trigeneration system driven by solar energy and fossil fuels using nonlinear programming formulation with the objective of minimizing total annual cost is presented in [32]. In this study, it was considered that the continued supply of demand is possible through the installed thermal storage unit when solar energy is not available. Their system provides cooling and electricity using the combination of an ejector refrigeration cycle and an organic Rankine cycle.

1.3.2.2 Solar- and Wind-Energy-Based Trigeneration

A CCHP system powered by solar and wind energies is shown in Fig. 1.4. The combination of renewable energy sources with multi-energy systems with the aim of enhancing the sustainability of urban areas is studied in [33]. The results show that in a midsized city with cold climate conditions, by deploying the potential synergies

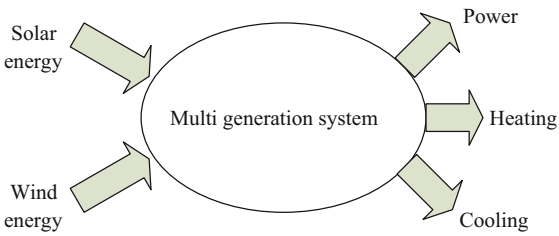

Fig. 1.4 Solar- and wind-energy-based CCHP system

between wind and district heating, the allowable wind capacity could rise by 40–200% over the non-heat case. And in a megacity with high cooling demand, photovoltaic-powered trigeneration was able to supply 30% of all energy demand, which has the potential to highly decrease the carbon emissions. Detailed reviews of different urban energy system models are presented in [34, 35].

1.3.3 More Products

1.3.3.1 Cooling, Heat, Power, and Hydrogen (CCHP-H_2)

Combined cooling, heat, power, and hydrogen systems are novel technologies that are attracting more attention due to the worldwide tendency for meeting the global energy demand in a cleaner way. Producing hydrogen by CHP or CCHP systems improves the operation of the combined system and decreases the emissions and losses. The advantages of both hydrogen and the multi-generation system are combined in CCHP-H2 system to achieve a more sustainable, economic, efficient, and clean system. Several studies have analyzed the thermodynamic behavior of renewable-energy-based multi-generation systems that can produce electricity, hydrogen, cooling, and heat and have proved that these systems have benefits, such as decreasing cost, decreasing environmental effects, better sustainability, and better efficiency [36–39]. Hydrogen production by a solar-energy-powered CO_2 Rankine cycle was developed and examined in [40].

1.3.3.2 Cooling, Heat, Power, and Potable Water (CCHP-HO_2)

Population growth, industry development, and increasing living standards are the reasons for the rapid and dramatic growth in energy and freshwater demands. The supplies of fresh water are not distributed homogeneously everywhere. According to the United Nations World Water Assessment Program, 85% of the population of the world lives in regions that are considered to be “dry.” This means that 783 million people do not have clean water availability, and 2.5 billion people do not have enough sufficient sanitation, and this results in the death of 6–8 million people each year [31].

One of the solutions for providing clean water is through desalination technologies. But these technologies are energy-intensive. One solution to supply the energy need of desalination units is through integrating multi-generation systems, so the waste heat would be used to supply the energy demand of desalination units. A complete way to meet the energy demand of desalination units is through renewable-energy-based multi-generation systems, which would be developed by innovative technologies to get more efficient, lower energy needs and lower costs.

The existing renewable-energy-based desalination technologies and their costs are investigated in [41]. And the sustainable, economic, and efficient solutions of meeting worldwide water and energy demands were analyzed, and the results indicated that recovering waste and the renewable-energy-based combined systems are the best way.

A combined system for the production of power, cooling, heat, and freshwater powered by wind, geothermal, and solar energies was studied in [42]. The result was the production of 3500 kW power, 200 kW cooling water, 2300 kW heat, 87.3 kg/s fresh water, and 2.8 kg/s product drying. And 37% and 25% were the energy and exergy efficiencies, respectively. These results indicate that the efficiencies of the combined system are higher than single-generation units. They mentioned that the problem of this system is to find a suitable location that has access to solar energy, high wind speed, and geothermal water. In the absence of one or two of the renewable sources, the other available source can be used to supply the potable water demand.

1.3.3.3 More than Four Products

A linear programming model for the planning of a multi-energy system considering the environmental constraints and the existence of renewables, with the objective of finding an optimal solution for the usage of waste, biomasses, and productions, was presented in [43]. A detailed model of a regional multi-energy system including the transportation is studied in [44]. The products of this system were electricity, heat, biogas, and ethanol (to be used in transportation). The results indicate that producing ethanol (for transportation) by CHP systems is able to make a 30% reduction in the costs of transportation.

1.4 Conclusion

In this chapter, a review of the available researches in the concept of renewable-energy-based multi-generation systems for producing a number of outputs, such as power, heat, hot water, cooling, hydrogen, and fresh water, from the economic and environmental viewpoints was presented. Reviewed articles were classified according to the number of their outputs into cogeneration, trigeneration, quadgeneration, and more products. The renewable-energy-based multi-generation

systems are able to improve the sustainably, efficiency, economic, and environmental aspects and reduce the emissions of energy generation. So, these systems can play a key role in meeting the global energy demand in a clean, economical, and efficient way, which is important and necessary due to the worldwide rapidly growing energy demands.

References

1. Dincer, I., & Acar, C. (2015). A review on clean energy solutions for better sustainability. *International Journal of Energy Research, 39*(5), 585–606.
2. Mancarella, P. (2014). MES (multi-energy systems): An overview of concepts and evaluation models. *Energy, 65*, 1–17.
3. Cho, H., Smith, A. D., & Mago, P. (2014). Combined cooling, heating and power: A review of performance improvement and optimization. *Applied Energy, 136*, 168–185.
4. Ahmadi, P., Dincer, I., & Rosen, M. A. (2013). Thermodynamic modeling and multi-objective evolutionary-based optimization of a new multigeneration energy system. *Energy Conversion and Management, 76*, 282–300.
5. Modi, A., Bühler, F., Andreasen, J. G., & Haglind, F. (2017). A review of solar energy based heat and power generation systems. *Renewable and Sustainable Energy Reviews, 67*, 1047–1064.
6. Malik, M., Dincer, I., & Rosen, M. A. (2015). Development and analysis of a new renewable energy-based multi-generation system. *Energy, 79*(C), 90–99.
7. Khalid, F., Dincer, I., & Rosen, M. A. (2015). Energy and exergy analyses of a solar-biomass integrated cycle for multigeneration. *Solar Energy, 112*, 290–299.
8. Williams, M. C., Strakey, J. P., & Singhal, S. C. (2004). U.S. distributed generation fuel cell program. *Journal of Power Sources, 131*(1–2), 79–85.
9. Asadi, R., Assareh, E., Moltames, R., Olazar, M., Nedaei, M., & Parvaz, F. (2019). Optimisation of combined cooling, heating and power (CCHP) systems incorporating the solar and geothermal energy: A review study. *International Journal of Ambient Energy*, 1–19.
10. Wegener, M., Malmquist, A., Isalgué, A., & Martin, A. (2018). Biomass-fired combined cooling, heating and power for small scale applications – A review. *Renewable and Sustainable Energy Reviews, 96*, 392–410.
11. Högselius, P. (2009). Spent nuclear fuel policies in historical perspective: An international comparison. *Energy Policy, 37*(1), 254–263.
12. Twidell, J., & Weir, T. (2015). *Renewable energy resources*. New York: Routledge.
13. Lenzen, M. (2010). Current state of development of electricity-generating technologies: A literature review. *Energies, 3*(3), 462–591.
14. Dincer, I. (2002). Technical, environmental and exergetic aspects of hydrogen energy systems. *International Journal of Hydrogen Energy, 27*(3), 265–285.
15. Midilli, A., Ay, M., Dincer, I., & Rosen, M. A. (2005). On hydrogen and hydrogen energy strategies I: Current status and needs. *Renewable and Sustainable Energy Reviews, 9*(3), 255–271.
16. Chicco, G., & Mancarella, P. (2009). Distributed multi-generation: A comprehensive view. *Renewable and Sustainable Energy Reviews, 13*(3), 535–551.
17. Horlock, J. H. (1997). *Cogeneration--combined heat and power (CHP): Thermodynamics and economics*. Malabar: Krieger Pub.
18. Pehnt, M. (2008). Environmental impacts of distributed energy systems – The case of micro cogeneration. *Environmental Science & Policy, 11*(1), 25–37.
19. IEA. (2014). International Energy Agency, 2014 Key World Energy Statistics.

20. Mittelman, G., Kribus, A., & Dayan, A. (2007). Solar cooling with concentrating photovoltaic/thermal (CPVT) systems. *Energy Conversion and Management, 48*(9), 2481–2490.
21. Beccali, M., Finocchiaro, P., & Nocke, B. (2009). Energy and economic assessment of desiccant cooling systems coupled with single glazed air and hybrid PV/thermal solar collectors for applications in hot and humid climate. *Solar Energy, 83*(10), 1828–1846.
22. Medrano, M., Castell, A., Fontanals, G., Castellón, C., & Cabeza, L. F. (2008). Economics and climate change emissions analysis of a bioclimatic institutional building with trigeneration and solar support. *Applied Thermal Engineering, 28*(17–18), 2227–2235.
23. Alanne, K., Saari, A., Ugursal, V. I., & Good, J. (2006). The financial viability of an SOFC cogeneration system in single-family dwellings. *Journal of Power Sources, 158*(1), 403–416.
24. Wu, D. W., & Wang, R. Z. (2006). Combined cooling, heating and power: A review. *Progress in Energy and Combustion Science, 32*(5–6), 459–495.
25. Mancarella, P., & Chicco, G. (2009). *Distributed multi-generation systems: Energy models and analyses*. New York: Nova Science Publishers.
26. Alanne, K., & Saari, A. (2006). Distributed energy generation and sustainable development. *Renewable and Sustainable Energy Reviews, 10*(6), 539–558.
27. Al-Sulaiman, F. A., Hamdullahpur, F., & Dincer, I. (2011). Trigeneration: A comprehensive review based on prime movers. *International Journal of Energy Research, 35*(3), 233–258.
28. Bai, W., & Xu, X. (2018). Comparative analyses of two improved CO2 CCHP systems driven by solar energy. *Thermal Science, 22*, 54.
29. Wang, J., Zhao, P., Niu, X., & Dai, Y. (2012). Parametric analysis of a new combined cooling, heating and power system with transcritical CO2 driven by solar energy. *Applied Energy, 94*, 58–64.
30. Wang, J., Yan, Z., Wang, M., Song, Y., & Dai, Y. (2013). Parametric analysis and optimization of a building cooling heating power system driven by solar energy based on organic working fluid. *International Journal of Energy Research, 37*(12), 1465–1474.
31. United Nations. (2014). United Nations World Water Assessment Programme.
32. Wang, M., Wang, J., Zhao, P., & Dai, Y. (2015). Multi-objective optimization of a combined cooling, heating and power system driven by solar energy. *Energy Conversion and Management, 89*, 289–297.
33. Niemi, R., Mikkola, J., & Lund, P. D. (2012). Urban energy systems with smart multi-carrier energy networks and renewable energy generation. *Renewable Energy, 48*, 524–536.
34. Keirstead, J., Jennings, M., & Sivakumar, A. (2012). A review of urban energy system models: Approaches, challenges and opportunities. *Renewable and Sustainable Energy Reviews, 16*(6), 3847–3866.
35. Keirstead, J., & Shah, N. (2013). *Urban energy systems: An integrated approach*. New York: Routledge.
36. Ahmadi, P., Dincer, I., & Rosen, M. A. (2013). Development and assessment of an integrated biomass-based multi-generation energy system. *Energy, 56*, 155–166.
37. Ratlamwala, T. A. H., Dincer, I., & Gadalla, M. A. (2012). Thermodynamic analysis of an integrated geothermal based quadruple effect absorption system for multigenerational purposes. *Thermochimica Acta, 535*, 27–35.
38. Ratlamwala, T. A. H., Dincer, I., & Gadalla, M. A. (2012). Performance analysis of a novel integrated geothermal-based system for multi-generation applications. *Applied Thermal Engineering, 40*, 71–79.
39. Dincer, I., & Zamfirescu, C. (2012). Renewable-energy-based multigeneration systems. *International Journal of Energy Research, 36*(15), 1403–1415.
40. Zhang, X. R., Yamaguchi, H., & Cao, Y. (2010). Hydrogen production from solar energy powered supercritical cycle using carbon dioxide. *International Journal of Hydrogen Energy, 35*(10), 4925–4932.
41. Gude, V. G., Nirmalakhandan, N., & Deng, S. (2010). Renewable and sustainable approaches for desalination. *Renewable and Sustainable Energy Reviews, 14*(9), 2641–2654.

42. Ghosh, S., & Dincer, I. (2014). Development and analysis of a new integrated solar-wind-geothermal energy system. *Solar Energy, 107*, 728–745.
43. Cormio, C., Dicorato, M., Minoia, A., & Trovato, M. (2003). A regional energy planning methodology including renewable energy sources and environmental constraints. *Renewable and Sustainable Energy Reviews, 7*(2), 99–130.
44. Daianova, L., Dotzauer, E., Thorin, E., & Yan, J. (2012). Evaluation of a regional bioenergy system with local production of biofuel for transportation, integrated with a CHP plant. *Applied Energy, 92*, 739–749.

Chapter 2
Selection of Cost-Effective and Energy-Efficient Storages with Respect to Uncertain Nature of Renewable Energy Sources and Variations of Demands

Tohid Khalili, Ali Bidram, Sayyad Nojavan, and Kittisak Jermsittiparsert

2.1 Introduction to Storages

There are several techniques for improving the efficiency of the systems, such as storage deployment, implementation of the demand response program, and installation of renewable energy sources (RESs). Storages as one of the best technologies have excessive advantages for the entire systems. Recently, different kinds of storages are utilized more and more in order to reduce the operation costs [1, 2], improve efficiency, and increase the profit of the systems. Storages' usage for storing different kinds of energy, e.g., electricity, heat, and cool, is impressively proliferated. Each type of storages has its specific characteristics, and their cost, application, and efficiency [3] are different [4]. Moreover, the control and energy management procedure of these storages play an important role in operating the systems [5–8]. In [9], an updated review about new controlling methods of storages in the small-scale power systems is performed. Also, in order to optimally use the storages, it is significant to locate the proper place of the storages and select a suitable capacity for each of storages [10].

T. Khalili · A. Bidram
Department of Electrical and Computer Engineering, University of New Mexico, Albuquerque, NM, USA
e-mail: khalili@unm.edu; bidram@unm.edu

S. Nojavan
Department of Electrical Engineering, University of Bonab, Bonab, Iran
e-mail: sayyad.nojavan@bonabu.ac.ir

K. Jermsittiparsert (✉)
Social Research Institute, Chulalongkorn University, Bangkok, Thailand
e-mail: kittisak.j@chula.ac.th

F. Jabari et al. (eds.), *Integration of Clean and Sustainable Energy Resources and Storage in Multi-Generation Systems*,
https://doi.org/10.1007/978-3-030-42420-6_2

Additionally, due to the uncertain nature of the RESs, the rapid growth of them causes several problems for operators which could be mended by applying the storages [11]. In [12], a general review regarding the storages in the systems which have RESs is performed. In several papers, the effect of the uncertain output of RESs is analyzed, and some useful methods are proposed [13]. In another paper, upcoming power systems which definitely will have a high number of installation of storages and high penetration of RESs are investigated [14]. For instance, various approaches for modeling the uncertainties of the distribution systems are reviewed in [15]. In [16], probabilistic optimization of an energy hub is considered. In another approach, a hybrid system consists of photovoltaic cells, and energy storages are presented which improve the energy efficiency of the whole system [17]. Besides, the specific storage technologies for utilizing in the systems which use wind turbines are comprehensively represented in [18]. Likewise, [19] presents a new strategy for optimally scheduling and sizing of the energy storage systems for improving the efficiency of a solar–wind hybrid system and increasing the benefit of the whole system.

The efficiency of storages has an undeniable influence on the overall outcome of that system and the level of satisfaction of its customers. The pros and cons of energy efficiency are fundamentally surveyed and reviewed in [20]. The effects of storages on the environmental issues and a comparison among the different storages are studied in [21]. Also, optimization of the storages for minimizing the cost of a system is executed, and the benefits of the storages are demonstrated in [22]. In the other hand, RESs could potentially increase the energy efficiency level of the systems [23]. In [24], the impact of the storages on the procurement of the energy is analyzed when RESs provide the power of the system and demand response program is implemented. Additionally, inordinate advanced technologies of energy storage systems for improving the operation and service quality of power systems are generally introduced and reviewed in [25].

On the other hand, the power system has faced excessive hardships for responding to the instant variations of demands. Meanwhile, storages could resolve the negative aspects of the demand variation. In [26], a novel model for simultaneously managing the storages and RESs to supply the loads is proposed.

In addition to the electrical energy, storages can store other types of energy, e.g., thermal energy, chemical energy, and mechanical energy. Reference [27] reviews thermal energy storage systems with hot-water tanks which are heated by solar energy. Also, the application of thermal energy storage for transferring the heat is discussed in [28]. Moreover, an integrated system combined of energy storages and fuel cells which forms a hybrid heat and power system is proposed in [29]. In another approach, an advanced method is proposed for cooling hot atmospheres by thermal energy storage systems in [30]. Additionally, a novel dispatch model is presented for combined heat and power systems with thermal energy storage systems in [31]. In [32], a multi-energy system is planned and proposed consisting of heating system and thermal energy storage systems.

In this chapter, the selection of the storages is reviewed from cost efficiency and energy efficiency viewpoints. Furthermore, updated approaches for selecting the

storages with high performance in order to cover the stochastic behavior of the power system's components are introduced. Moreover, different applications of the storages are analyzed, and this concept's practical objective functions, constraints, and useful technologies are considered. Also, a comprehensive comparison of the diverse kinds of storages which are applied for improving the level of the power system's operation is performed, and a general deduction about the storage selection and the future trend of this issue are presented regarding the efficiency of the storages and uncertainty of the power system.

The remainder of this chapter has been organized as follows: Section 2.2 presents different types and technologies of the storages. Furthermore, applications of the storages are expressed in Sect. 2.3. Section 2.4 provides a comprehensive comparison of the efficiency of storages regarding the cost of the real-world systems. In addition, storages are analyzed from the energy efficiency point of view in Sect. 2.4. Also, management of the stochastic generation of RESs by storages is discussed in Sect. 2.5. Additionally, papers which have proposed the optimal methods for managing the load's variation by storages are reviewed in Sect. 2.5. Eventually, the relevant conclusions and the future trend of the storages with respect to the uncertainty of RESs and the demands variations are declared in Sect. 2.6.

2.2 Storage Types and Technologies

In recent years, several types and technologies of storages are released which increase the rate of the storages' usage regarding their diverse performances and characteristics. Figure 2.1 illustrates the current and forecasted future global

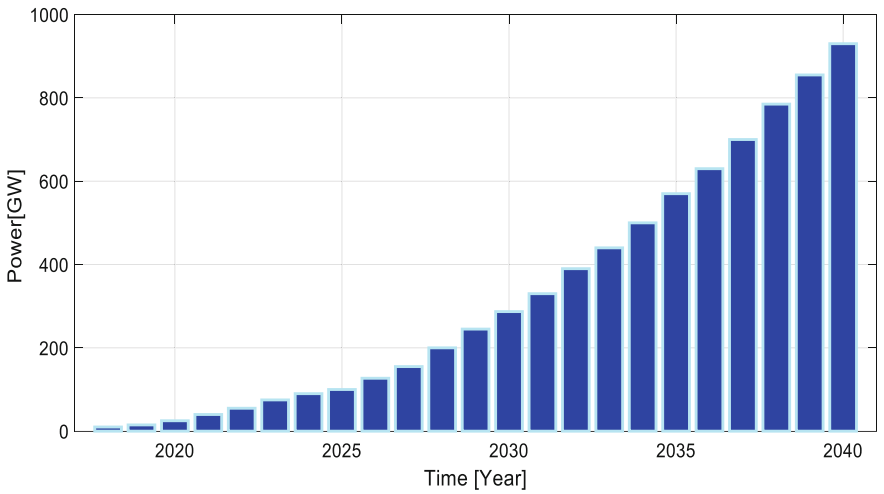

Fig. 2.1 Global cumulative storage deployments

cumulative storage installations [33]. According to Fig. 2.1, deployment of the energy storage systems will be significantly increased in the upcoming years. In addition, storage types and technologies are mentioned in the following sections.

2.2.1 Storage Types

Energy has various forms in which they could be converted to each other. As a result, several storages are designed, and they could stock different types of energy. The most practical and common types of energy storages are as follows [12]:

- Fossil fuel storage
- Electrochemical storage
- Mechanical storage
- Thermal storage
- Electrical storage
- Electromagnetic storage
- Chemical storage

2.2.2 Storage Technologies

During the past years, scholars and inventors proposed diverse technologies which are gradually improved and advanced [25]. As a consequence, the storage technologies are divided into six sections, i.e., mature, commercial, demonstration, pilot, laboratory, and idea. In addition, the mature storages have a lower risk, higher energy efficiency, and better financial status than the immature technologies which are proved in Sect. 2.4. In this section, the most famous and practical technologies of the storages are introduced. Figure 2.2 demonstrates the main common storage technologies. These 15 technologies contain the majority of the current technologies of the storages [21, 34]. Each of these technologies has numerous subsections. As shown in this figure, storages could stock all kinds of energy. Also, these technologies could be combined with each other and create a new type of storage which are so-called hybrid systems.

Energy storages could be installed aboveground or underground [35]. Current technologies of the energy storages which could be deployed underground are gas storage, hydrogen storage, compressed air energy storage, pumped hydro energy storage, thermal energy storage, etc. Furthermore, it is notable that batteries and thermal energy storages face a significant advance among other types of batteries [36], and they have remarkable popularity in the real-world systems due to their performance and variety. Additionally, Table 2.1 illustrates the batteries and thermal energy storage technologies. As it can be observed, 14 kinds of batteries are presented. These rechargeable batteries are obtained by properly connecting the

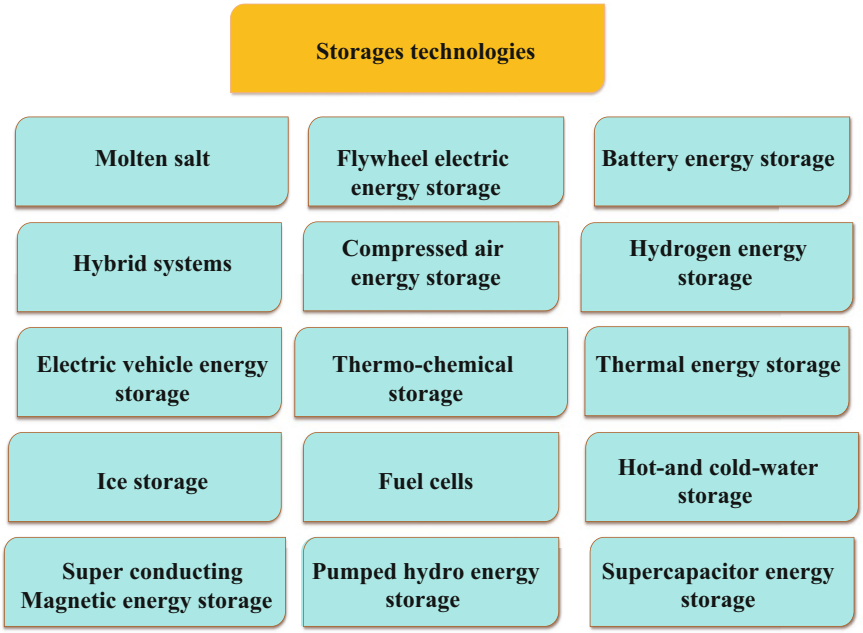

Fig. 2.2 Overview of the storage technologies

Table 2.1 Technologies of the batteries and thermal energy storages

Batteries	Lead–acid	Thermal energy storages	Sensible heat storage
	Zinc–bromine (Zn–Br)		Borehole thermal energy storage
	Lithium–ion (Li–Ion)		Tank thermal energy storage
	Vanadium redox (VR)		Pit thermal energy storage
	Sodium–sulfur (Na–S)		Cryogenic energy storage
	Polysulfide–bromide		Ice-based
	Aluminum–air		Pumped-heat electricity storage
	Nickel–hydrogen (Ni–H_2)		Aquifer thermal energy storage
	Nickel–metal hydride (Ni–MH)		Latent-heat storage
	Nickel–zinc (Ni–Zn)		Hot silicon technology
	Nickel–cadmium (Ni–Cd)		
	Sodium–nickel chloride (Na–$NiCl_2$)		
	Sodium–ion (Na–Ion)		
	Zinc–air (Zn-air)		

required number of the cells. Also, 10 technologies of thermal energy storages are demonstrated in this table [27]. These thermal energy storages use water, ice, molten salt, silicon, or other materials, and by cooling or heating these materials, energy

could be stored and utilized when the systems require. The main characteristics of the thermal energy storages which should be considered in selecting the appropriate technology are as follows:

- Thermal loss
- Thermal insulation
- Location limitation
- Thermal capacity
- Construction cost
- Freedom of design
- Extendibility
- Maintenance and repair

2.3 Application of Storages

In this section, the goals of the storage utilization and the practical limitations of the storages' usage are determined. Generally, storages are selected regarding the economic limitations, overall power generation of the system, demanded load of the system, requested application, considered objective functions, practical constraints, individual characteristics of the storages, etc. In order to demonstrate the applications of the storages, Fig. 2.3 indicates an overview of the storages' benefits in the end user, distribution, transmission, system, independent system operator (ISO), and other parts of a complete system [37–39]. Also, each part's specific advantages are comprehensively declared. According to this figure, storages could be deployed in the systems regarding various objective functions which consider economic, reliability, security, protection, stability, flexibility, customers' satisfaction, and other technical subjects.

Additionally, general constraints which should be observed in the energy storages' problems are presented by (2.1), (2.2), (2.3), (2.4), (2.5), (2.6), (2.7), (2.8), (2.9), and (2.10):

$$\text{cost}^{\text{inv}} = C^{\text{cap}}\text{cap} + C^{\text{P}}P \tag{2.1}$$

$$\text{cost}^{\text{inv}} \leq \text{UB} \tag{2.2}$$

In (2.1), total investment cost of storage is represented with respect to its capacity and power rating. As expressed by (2.2), affordability of the investment cost should be ensured. Also, cost^{inv}, C^{cap}, C^{P}, cap, P, and UB are the total investment cost, investment cost rate regarding the energy, investment cost rate regarding the power, capacity of the storage, power of the storage, and the utility's budget, respectively:

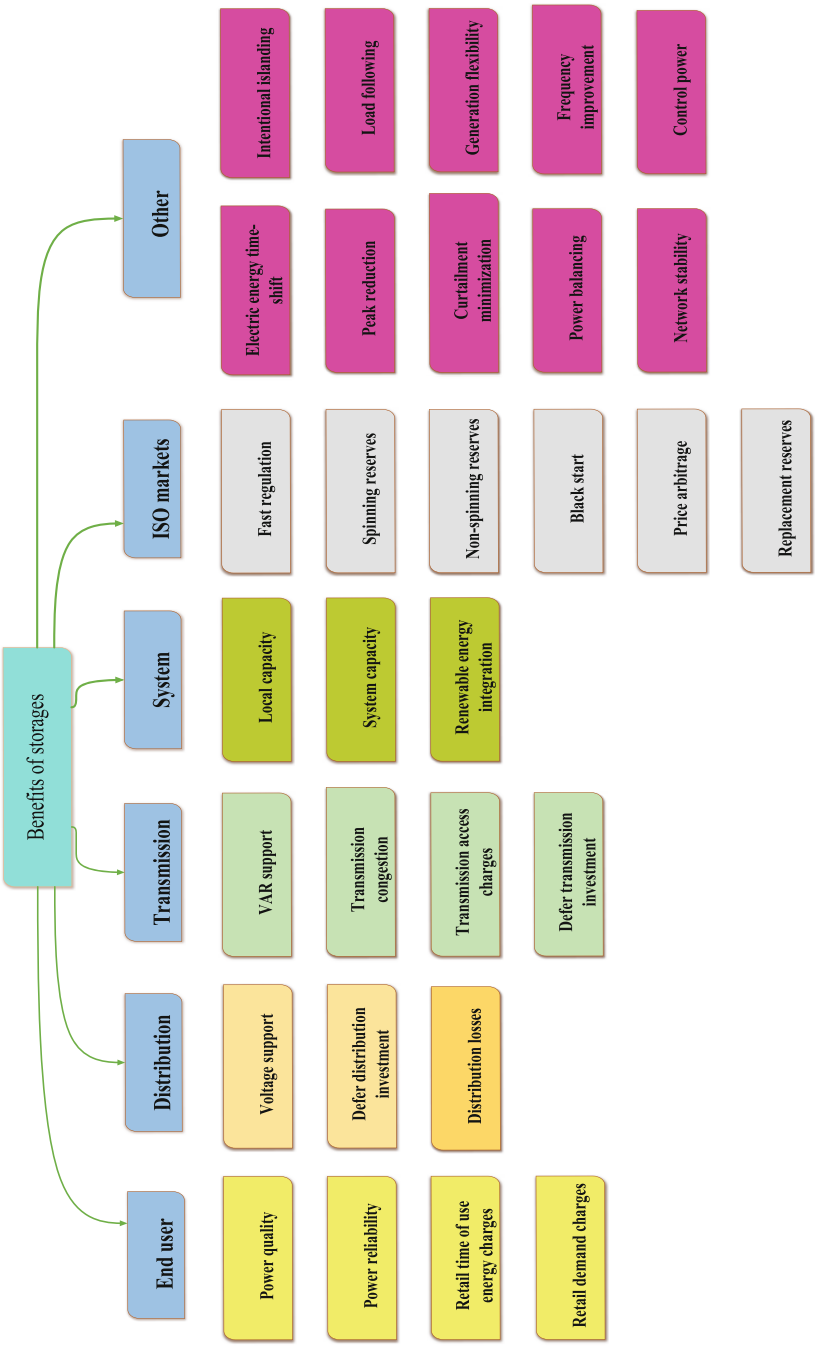

Fig. 2.3 Diagram of the advantages and applications of the storages

$$\text{cap}_{\min} \leq \text{cap} \leq \text{cap}_{\max} \tag{2.3}$$

$$P_{\min} \leq P \leq P_{\max} \tag{2.4}$$

$$P^{\text{ch}}_{\min} \leq P^{\text{ch}} \leq P^{\text{ch}}_{\max} \tag{2.5}$$

$$P^{\text{disch}}_{\min} \leq P^{\text{disch}} \leq P^{\text{disch}}_{\max} \tag{2.6}$$

Constraints (2.3), (2.4), (2.5), and (2.6) are the limitations of the storage capacity, power rating, charged power, and discharged power, respectively. Accordingly, $\text{cap}_{\min}$ and $\text{cap}_{\max}$ are the minimum and maximum capacity of the storages, respectively. Also, P^{ch}, P^{disch}, $P_{\max}$, $P^{\text{ch}}_{\max}$, $P^{\text{disch}}_{\max}$, $P_{\min}$, $P^{\text{ch}}_{\min}$, and $P^{\text{disch}}_{\min}$ are the charged power, discharged power, maximum power rating, maximum charged power, maximum discharged power, minimum power rating, minimum charged power, and minimum discharged power of the storages, respectively:

$$\text{SOC}_{\min} \leq \text{SOC} \leq \text{SOC}_{\max} \tag{2.7}$$

$$\text{SOC}_{\min} = 1 - \text{DOD} \tag{2.8}$$

$$\text{SOC}_{\text{h}} = \text{SOC}_{(\text{h}-1)} + \eta^{\text{ch}} P^{\text{ch}}_{\text{h}} - \frac{P^{\text{disch}}_{\text{h}}}{\eta^{\text{disch}}} \tag{2.9}$$

$$0 \leq \text{LL} \leq \text{LL}_{\max} \tag{2.10}$$

According to the (2.7), state of charge (SOC) of the storages should be within a specific range. Regarding the (2.8), state of charge of a storage is obtained by using the depth of discharge (DOD) of that storage. Also, (2.9) expresses how SOC of a storage is calculated by using the previous operation periods SOC, charging efficiency (η^{ch}), discharging efficiency (η^{disch}), etc. As expressed by (2.10), the life length (LL) of the storages should be less than their maximum possible life length ($\text{LL}_{\max}$). In addition, $\text{SOC}_{\min}$ and $\text{SOC}_{\max}$ are the minimum and maximum SOC of the storages, respectively.

2.4 Cost Efficiency and Energy Efficiency of Storages

In the systems, storages should be selected and applied by considering the financial and performance points of view. As a result, utilization of the cost-effective and energy-efficient storages is highly regarded with respect to their specific applications.

In order to show characteristics of the storages, Tables 2.2 and 2.3 are provided [40]. As shown in Table 2.2, various kinds of storages are presented which could stock energy in distinguished ways [17]. In addition, these storages' cost efficiencies are represented by expressing their investment power cost and investment energy cost [21]. Furthermore, the energy efficiency of the presented storages is compared

Table 2.2 Cost, efficiency, and other specifications of the storages

Technology	Power rating (MW)	Investment power cost ($/kW)	Investment energy cost ($/kWh)	Lifetime (year)	Efficiency (%)
Cryogenic energy storage	0.1–300	200–300	3–30	20–40	40–50
Superconducting magnetic energy storage	0.1–10	200–300	1000–10,000	>20	95–98
Hydrogen energy storage (fuel cell)	5–50	550–4500	10–20	5–15	20–66
Thermal energy storage	0–60	100–400	20–50	10–20	30–60
Supercapacitor	0–0.3	100–300	300–2000	10–30	84–97
Compressed air energy storage	5–300	400–800	2–50	20–60	50–89
Chemical batteries	0.1–100	–	–	–	70–95
Flywheel energy storage	0–0.25	250–350	1000–5000	15	85–95
Pumped hydro energy storage	100–5000	600–2000	5–100	40–60	65–87

Table 2.3 Cost, efficiency, and other specifications of the batteries

Type of battery	Power rating (MW)	Investment power cost ($/kW)	Investment energy cost ($/kWh)	Lifetime (year)	Efficiency (%)
Lead–acid	0–20	300–600	200–400	5–15	63–90
Li–ion	0–0.1	1200–4000	600–2500	5–15	75–97
Ni–Cd	0–40	400–600	400–2400	13–16	60–90
Zn–Br	0.05–2	700–2500	150–1000	5–10	65–85
Na–S	0.05–8	1000–3000	300–500	10–15	75–90
Metal–air	0–0.01	100–250	10–60	–	50–55
VR	0.03–3	600–1500	150–1000	5–10	65–90
Polysulfide–bromide	0.1–15	–	400–1100	15	60–65
Zn–Br	0.1–1	1450–1750	290–350	8–10	65–85

and evaluated, and the mentioned storages' power rating and lifetime are also declared. Superconducting magnetic energy storage has the best energy efficiency situation, and the compressed air energy storage and the pumped hydro energy storage have the most lifetime. The power rating of the pumped hydro energy storage is the highest value among other types of storages.

Table 2.3 indicates the specifications and efficiencies of the current common batteries [5, 36]. As it is presented, lead–acid battery is one of the best batteries, and its power rating, lifetime, and efficiency are among the top technologies, and its costs are not so expensive which made it as the most popular battery [25]. Also, Ni–Cd has

the highest power rating among these practical batteries. Also, metal–air batteries have the least investment costs. Each system's operator could select the preferred technology for its required application by knowing the characteristics and capabilities of the batteries [12].

2.5 Uncertainty Management of Load and RESs' Output by Storages

Managing and solving the uncertainty of the systems form a huge part of investigations. Although distributed generators have several advantages [41], they have some unfavorable consequences which should be compensated by legislating regulations [42], performing demand response program [43], installing the storages, etc. As a result, deployment of the storages could basically assist the system's operator to reduce the negative effect of the RESs' stochastic output. As mentioned in Sect. 2.3, storages could smooth the load profile of the consumers which are utilized in several articles [10]. Moreover, simultaneously using the storages and implementing the demand response program in the systems with the high penetration of the RESs could significantly improve the efficiency of the RESs from environmental and economic aspects [44]. As presented in [45], energy storages could be applied for optimally robust operating in the systems and overcoming the system's uncertainties. In addition, storages' utilization could improve the energy management of the systems and increase the overall profit and benefit of the systems regarding the RESs' uncertain outputs [46].

In [47], a hybrid energy storage system accompanied by implementing the demand response program is presented which could amend the disadvantages of the RESs' uncertainties, reduce the CO_2 emission, and decrease the overall costs of the system. Also, the effects of the uncertain outputs of the RESs and load's probabilistic nature on the energy storages are analyzed in [48]. In another research, benefits of the storages are surveyed with respect to the RESs' uncertainty, unpredicted demanded load, and investment costs of the energy storages [49]. As presented in [50, 51], integration of the storages, RESs, implementation of the demand response program, and uncertainties consideration will cause significant improvements in the operational condition of the systems.

2.6 Conclusion and Future Trend

In the present chapter, a general explanation of the storages and their rapid installation growth are represented. Furthermore, various types of storages are reviewed regarding the uncertain output of the RESs and the variations of the demands. Additionally, the advantages and disadvantages of the presented technologies of

the storages are explained from cost efficiency and energy efficiency viewpoints. By utilizing recent papers, novel methods for choosing suitable storages for the specific tasks are comprehensively declared. Moreover, different applications of each kind of storages are introduced. Also, a detailed comparison among the currently applied storages is reported, and the main objective functions and constraints of the storages are determined. The presented material of this chapter exhibits the approaches for managing and solving the systems' malfunctions and problems by using the proper type of storages. As the future trends, storages will be applied increasingly in the diverse parts of systems which will dramatically increase the cost efficiency and energy efficiency of the systems. Considering the remarkable privileges of the storages, the negative influences of the probabilistic nature of the RESs and oscillation of the demand will be significantly decreased. In addition, all of the newly proposed methods can be used for improving the performance of the storages.

References

1. Banshwar, A., Sharma, N. K., Sood, Y. R., & Shrivastava, R. (2019). Market-based participation of energy storage scheme to support renewable energy sources for the procurement of energy and spinning reserve. *Renewable Energy, 135*, 326.
2. Nojavan, S., Majidi, M., Najafi-Ghalelou, A., Ghahramani, M., & Zare, K. (2017). A cost-emission model for fuel cell/PV/battery hybrid energy system in the presence of demand response program: ε-constraint method and fuzzy satisfying approach. *Energy Conversion and Management, 138*, 383–392.
3. Zarębski, T. (2018). Analysis of the efficiency of energy storage systems. In *2018 Innovative materials and technologies in electrical engineering (i-MITEL)* (pp. 1–4). *IEEE.*
4. Xu, Y., & Shen, X. (2018). Optimal control based energy management of multiple energy storage systems in a microgrid. *IEEE Access, 6*, 32925–32934.
5. Khalili, T., Jafari, A., Abapour, M., & Mohammadi-Ivatloo, B. (2019). Optimal battery technology selection and incentive-based demand response program utilization for reliability improvement of an insular microgrid. *Energy, 169*, 92.
6. Bidram, A., Lewis, F. L., & Davoudi, A. (2014). Distributed control systems for small-scale power networks: Using multiagent cooperative control theory. *IEEE Control Systems, 34*, 56.
7. Bidram, A., Davoudi, A., & Lewis, F. L. (2014). A multiobjective distributed control framework for islanded AC microgrids. *IEEE Transactions on Industrial Informatics, 10*, 1785.
8. Bidram, A., Davoudi, A., Lewis, F. L., & Qu, Z. (2013). Secondary control of microgrids based on distributed cooperative control of multi-agent systems. *IET Generation, Transmission and Distribution, 7*(8), 822–831.
9. Arani, A. A. K., Gharehpetian, G. B., & Abedi, M. (2019). Review on energy storage systems control methods in microgrids. *International Journal of Electrical Power & Energy Systems, 107*, 745–757.
10. Khalili, T., Jafari, A., & Babaei, E. (2018). *Scheduling and siting of storages considering power peak shaving and loss reduction by exchange market algorithm.* In IEEE proceedings 2017 smart grid conference, SGC 2017.
11. Dostál, Z., & Ladányi, L. (2018). Demands on energy storage for renewable power sources. *Journal of Energy Storage, 18*, 250–255.
12. Amrouche, S. O., Rekioua, D., Rekioua, T., & Bacha, S. (2016). Overview of energy storage in renewable energy systems. *International Journal of Hydrogen Energy, 41*(45), 20914–20927.

13. Vahid-Pakdel, M. J., Nojavan, S., Mohammadi-ivatloo, B., & Zare, K. (2017). Stochastic optimization of energy hub operation with consideration of thermal energy market and demand response. *Energy Conversion and Management, 145*, 117.
14. Gaete-Morales, C., Gallego-Schmid, A., Stamford, L., & Azapagic, A. (2019). A novel framework for development and optimisation of future electricity scenarios with high penetration of renewables and storage. *Applied Energy, 250*, 1657–1672.
15. Ehsan, A., & Yang, Q. (2019). State-of-the-art techniques for modelling of uncertainties in active distribution network planning: A review. *Applied Energy, 239*, 1509.
16. Nojavan, S., Zare, K., & Mohammadi-Ivatloo, B. (2017). Optimal stochastic energy management of retailer based on selling price determination under smart grid environment in the presence of demand response program. *Applied Energy, 187*, 449.
17. Liu, J., Chen, X., Cao, S., & Yang, H. (2019). Overview on hybrid solar photovoltaic-electrical energy storage technologies for power supply to buildings. *Energy Conversion and Management, 187*, 103–121.
18. Díaz-González, F., Sumper, A., Gomis-Bellmunt, O., & Villafáfila-Robles, R. (2012). A review of energy storage technologies for wind power applications. *Renewable and Sustainable Energy Reviews, 16*(4), 2154–2171.
19. Berrada, A., & Loudiyi, K. (2016). Operation, sizing, and economic evaluation of storage for solar and wind power plants. *Renewable and Sustainable Energy Reviews, 59*, 1117–1129.
20. Kamal, A., Al-Ghamdi, S. G., & Koc, M. (2019). Revaluing the costs and benefits of energy efficiency: A systematic review. *Energy Research & Social Science, 54*, 68.
21. Dehghani-Sanij, A. R., Tharumalingam, E., Dusseault, M. B., & Fraser, R. (2019). Study of energy storage systems and environmental challenges of batteries. *Renewable and Sustainable Energy Reviews, 104*, 192.
22. Vatu, R., Ceaki, O., Porumb, R., & Seritan, G. (2018). *Storage optimization: Benefits brought by storage itself, with an energy price minimization*. In Proceedings – 2018 53rd International Universities Power Engineering Conference, UPEC 2018.
23. Zicmane, I., Berzina, K., Lomane, T., & Kasperjuks, K. (2018). Improving the energy efficiency of an autonomous power system with renewable sources. In *2018 International conference on intelligent and innovative computing applications (ICONIC)* (pp. 1–6). IEEE.
24. Aalami, H. A., & Nojavan, S. (2016). Energy storage system and demand response program effects on stochastic energy procurement of large consumers considering renewable generation. *IET Generation, Transmission and Distribution, 10*(1), 107–114.
25. Akinyele, D. O., & Rayudu, R. K. (2014). Review of energy storage technologies for sustainable power networks. *Sustainable Energy Technologies and Assessments, 8*, 74–91.
26. Yan, J., Menghwar, M., Asghar, E., Panjwani, M. K., & Liu, Y. (2019). Real-time energy management for a smart-community microgrid with battery swapping and renewables. *Applied Energy, 238*, 180–194.
27. Dahash, A., Ochs, F., Janetti, M. B., & Streicher, W. (2019). Advances in seasonal thermal energy storage for solar district heating applications: A critical review on large-scale hot-water tank and pit thermal energy storage systems. *Applied Energy, 239*, 396.
28. Mahdi, J. M., Lohrasbi, S., & Nsofor, E. C. (2019). Hybrid heat transfer enhancement for latent-heat thermal energy storage systems: A review. *International Journal of Heat and Mass Transfer, 137*, 630–649.
29. Arsalis, A. (2019). A comprehensive review of fuel cell-based micro-combined-heat-and-power systems. *Renewable and Sustainable Energy Reviews, 105*, 391–414.
30. Berger, M., & Waser, R. (2019). Advanced latent thermal energy storage for space cooling in the tropics. In *2019 IEEE PES GTD Grand international conference and exposition Asia (GTD Asia)* (pp. 842–847). IEEE.
31. Dai, Y., Chen, L., Min, Y., et al. (2018). Integrated dispatch model for combined heat and power plant with phase-change thermal energy storage considering heat transfer process. *IEEE Transactions on Sustainable Energy, 9*, 1234.
32. Cheng, H., Wu, J., Luo, Z., Zhou, F., Liu, X., & Lu, T. (2019). Optimal planning of multi-energy system considering thermal storage capacity of heating network and heat load. *IEEE Access, 7*, 13364–13372.

33. https://about.bnef.com/blog/energy-storage-620-billion-investment-opportunity-2040/
34. Landry, M., & Gagnon, Y. (2015). Energy storage: Technology applications and policy options. *Energy Procedia, 79*, 315.
35. Matos, C. R., Carneiro, J. F., & Silva, P. P. (2019). Overview of large-scale underground energy storage technologies for integration of renewable energies and criteria for reservoir identification. *Journal of Energy Storage, 21*, 241.
36. Sasikala, S. P., Jeong, G. H., Yun, T. Y., & Kim, S. O. (2019). A perspective on R&D status of energy storage systems in South Korea. *Energy Storage Materials, 23*, 154.
37. EPRI. (2010). *Electricity energy storage technology options-A white paper primer on applications, costs and benefits*. Report.
38. Eyer, J. M., & Corey, G. P. (2010). *Energy storage for the electricity grid: Benefits and market potential assessment guide: A study for the DOE Energy Storage Systems Program*. Albuquerque: Sandia National Laboratories.
39. Zucker, A., Hinchliffe, T., & Spisto, A. (2013). *Assessing storage value in electricity markets: A literature review*. JRC Science Policy reports.
40. Wong, L. A., Ramachandaramurthy, V. K., Taylor, P., Ekanayake, J. B., Walker, S. L., & Padmanaban, S. (2019). Review on the optimal placement, sizing and control of an energy storage system in the distribution network. *Journal of Energy Storage, 21*, 489–504.
41. Khalili, T., Hagh, M. T., Zadeh, S. G., & Maleki, S. (2019). Optimal reliable and resilient construction of dynamic self-adequate multi-microgrids under large-scale events. *IET Renewable Power Generation, 13*(10), 1750–1760.
42. Tarafdar Hagh, M., & Khalili, T. (2019). A review of fault ride through of PV and wind renewable energies in grid codes. *International Journal of Energy Research, 43*(4), 1342–1356.
43. Khalili, T., Nojavan, S., & Zare, K. (2019). Optimal performance of microgrid in the presence of demand response exchange: A stochastic multi-objective model. *Computers & Electrical Engineering, 74*, 429–450.
44. Seyyedeh-Barhagh, S., Majidi, M., Nojavan, S., & Zare, K. (2019). Optimal scheduling of hydrogen storage under economic and environmental priorities in the presence of renewable units and demand response. *Sustainable Cities and Society, 46*, 101406.
45. Nojavan, S., Najafi-Ghalelou, A., Majidi, M., & Zare, K. (2018). Optimal bidding and offering strategies of merchant compressed air energy storage in deregulated electricity market using robust optimization approach. *Energy, 142*, 250.
46. Nojavan, S., Zare, K., & Mohammadi-Ivatloo, B. (2017). Application of fuel cell and electrolyzer as hydrogen energy storage system in energy management of electricity energy retailer in the presence of the renewable energy sources and plug-in electric vehicles. *Energy Conversion and Management, 136*, 404.
47. Majidi, M., Nojavan, S., Nourani Esfetanaj, N., Najafi-Ghalelou, A., & Zare, K. (2017). A multi-objective model for optimal operation of a battery/PV/fuel cell/grid hybrid energy system using weighted sum technique and fuzzy satisfying approach considering responsible load management. *Solar Energy, 144*, 79–89.
48. Biyya, I., Aniba, G., & Maaroufi, M. (2017). Impact of load and renewable energy uncertainties on single and multiple energy storage systems sizing. In *2017 IEEE power & energy society innovative smart grid technologies conference (ISGT)* (pp. 1–5). IEEE.
49. Bucciarelli, M., Giannitrapani, A., Paoletti, S., Vicino, A., & Zarrilli, D. (2017). Sizing of energy storage systems considering uncertainty on demand and generation. *IFAC-PapersOnLine, 50*(1), 8861–8866.
50. Nojavan, S., & Aalami, H. A. (2015). Stochastic energy procurement of large electricity consumer considering photovoltaic, wind-turbine, micro-turbines, energy storage system in the presence of demand response program. *Energy Conversion and Management, 103*, 1008–1018.
51. Ghalelou, A. N., Fakhri, A. P., Nojavan, S., Majidi, M., & Hatami, H. (2016). A stochastic self-scheduling program for compressed air energy storage (CAES) of renewable energy sources (RESs) based on a demand response mechanism. *Energy Conversion and Management, 120*, 388.

Chapter 3
Determining the Type and Size of Energy Storage Systems to Smooth the Power of Renewable Energy Resources

Mehrdad Gholami, Hadi Tarimoradi, Navid Rezaei, Abdollah Ahmadi, and Seyed Ehsan Ahmadi

3.1 Introduction

Due to environmental reasons and increased demand for electrical energy, the presence of renewable energy resources in the grid has grown enormously, as these resources account for a significant share of the total generation.

In spite of the many advantages of renewable resources, due to the random and fluctuated nature of environmental phenomena (wind, radiation, etc.), the power of these resources is intermittent and uncertain, and unlike traditional units, these systems do not have the ability to produce fixed and predetermined power. Therefore, power systems are faced with many challenges, such as frequency and voltage instability and power imbalance [1]. In traditional power systems, the dominant portion of network uncertainty is due to network loads and the failure or loss of generating units. While in modern power systems and micro grids, along with network loads, renewable energy sources are also the source of uncertainty, which causes a loss of balance of the generation and consumption and can lead to frequency instability in networks with high penetrations of renewable resources [2]. In conventional networks, various methods are used to maintain the power balance, such as load shedding and using the spinning reserve.

M. Gholami (✉) · H. Tarimoradi · N. Rezaei · S. E. Ahmadi
Faculty of Engineering, Department of Electrical Engineering, University of Kurdistan, Sanandaj, Iran
e-mail: m.gholami@uok.ac.ir; Tarimoradi@uok.ac.ir; n.rezaei@uok.ac.ir; ehsan.ahmadi@eng.uok.ac.ir

A. Ahmadi
Australian Energy Research Institute and the School of Electrical Engineering and Telecommunications, University of New South Wales, Sydney, NSW, Australia
e-mail: a.ahmadi@student.unsw.edu.au

F. Jabari et al. (eds.), *Integration of Clean and Sustainable Energy Resources and Storage in Multi-Generation Systems*,
https://doi.org/10.1007/978-3-030-42420-6_3

However, in micro grids, fluctuations in various short-, medium-, and long-term ranges may occur, due to the slow response of the spinning reserve method, this method can be only suitable for compensating long-term fluctuations. Therefore, in order to compensate for fluctuations in micro grids, it is proposed to use energy storage systems (ESSs) that can compensate a wide range of oscillations [3].

There are different technologies for ESSs such as battery, supercapacitor, compressed air system, flywheel, superconducting magnetic energy storage, pumped storage hydroelectricity, thermal storage, and electrolysis of water [4]. Also, there are some characteristics which are more important in the selection of the ESSs: cost, lifetime, maintenance, energy efficiency, response time, and storage capacity including power and energy capacity. Each of these technologies could be used for different applications in power systems. For example, the pumped storage hydroelectricity is suitable for peak shaving application because of high energy capacity. On the other hand, the batteries could be better solution for short fluctuations due to renewable resources because of suitable power and energy capacity as well as fast response time. A comprehensive comparison and classification of the various ESS technologies is provided through which the power system operator can make an appropriate decision of storage selection in the next section.

One of the impressive factors in the selection of the cost-effective and imperative ESS technology is power system uncertainty management. Evidently, according to the intermittent and variable nature of the power system elements, uncertainties are inevitable part in system planning and operation. The resource of the uncertainties can be dominantly originated from demand deviations, renewable energy intermittent outputs, and contingencies. Principally, the more developed prediction tools result in more precise uncertainty modeling.

On the other hand, renewable fluctuations due to environmental conditions could be categorized in different timescales with different intensities. For example, wind power fluctuations could be stated in three groups. The first group is short-term fluctuations due to turbulence which are stochastic and with rapid variations. The second one is medium-term fluctuations due to temperature difference such as diurnal variations of wind which has slower variations. Also, the third one is long-term fluctuations such as seasonal variations of the wind. Compensation of these fluctuations need different characteristics of ESSs; for example, short-term fluctuations need the high power capacity and fast response, so batteries and supercapacitors or a combination of them could be a suitable solution for compensating these fluctuations. On the other hand, for compensating diurnal fluctuations, high energy capacity is needed, so the pumped storage or compressed air system or using power system spinning reserve could be better solutions [5].

Also, given the randomness of the generation of renewable sources, it is necessary to use predictive methods for declaring the amount of power to participate in dispatching programs and unit commitment, in which the presence of errors in these methods is inevitable. Therefore, ESSs can be used to compensate for the forecast error [6].

In fact, ESSs can be used to smooth the output power of renewable resources, save power at low demand, and deliver power to the grid in the high demand time intervals.

In general, the purpose of combining renewable energy sources with ESSs is to provide a behavior similar to the behavior of the traditional generation units, so that they can control their generation, participate in power dispatching and unit commitment programs, and maintain the grid frequency and voltage stability. However, due to the uncertain and intermittent nature of the renewable resources, they cannot play these roles alone [7].

Here are the requirements for a generation unit that actually includes a set of capabilities for different operating conditions that are necessary to maintain the power system stability in different conditions and to participate in power market [8].

3.1.1 Fluctuation Smoothing

Fluctuations in natural phenomena, such as wind and solar irradiation, consequently fluctuation in the generation of renewable resources, can be in the range of minutes, hours, and days. The slow fluctuations of these resources can be offset by spinning reserve, while their rapid fluctuations can confront the grid with the challenge of frequency and voltage instability and affect the power quality.

The problem of volatility of these resources will increase with the capacity of these resources in the grid, because even compensating for long-term fluctuations will increase the need for network spinning reserve, which will increase its dependence on traditional units. One of the solutions to compensate for these fluctuations is the use of energy storage systems. Due to different types of fluctuations with different time periods and different levels of power and energy needed to compensate for them, it will naturally need different ESSs to compensate for any fluctuations that will be examined in the Sect. 3.3 with their specifications. Then, in the final section, suitable ESSs will be introduced to compensate for the different items.

3.1.2 Compensation of Forecasting Error

Regarding the randomness of natural phenomena, the amount of the generation of renewable resources is uncertain; therefore, in order to declare generation capacity to participate in dispatching programs and unit commitment, it is necessary to use prediction methods to estimate the amount of production. Since the presence of the error in the prediction models is inevitable, the predicted value is not always the same as the generation value. On the other hand, the generation deviation from the pre-applied amount leads to the fining of the units, so the amount of forecast error should be compensated. One of the ways to compensate for this is to use ESSs, which can provide the ability to announce previous generating power for these resources.

3.1.3 Inertia Emulation

Inertia of rotors in synchronous generators plays important roles in grid frequency stability, so that it can absorb or inject the instantaneous power to the grid at time of turbulence and thus prevent the frequency collapse of the grid. However, renewable energy resources are mostly based on power electronics that are lacking inertia. Therefore, as one of the network requirements, this should be provided as virtual inertia for these resources. One of the ways in which virtual inertia is created is to use energy storage systems, especially those ESSs that have high response speeds and can provide high power density for a short time.

3.1.4 Load Following

In power systems, to maintain the synchronism, the balance of generation and consumption is usually achieved by following the pattern of the load by the generation units. However, the level of generation and volatility of renewable energy resources are independent of the pattern of load. To accomplish this, energy storage systems can be used so that at low consumption, the energy produced by resources is stored and at high consumption, this energy is injected into the network.

3.1.5 Spinning Reserve

In traditional power systems, in order to carry out frequency control and respond to sudden load changes, some of the network power is in standby mode, so that it can be used to maintain power system synchronism. Therefore, by increasing the amount of penetration of renewable resources in the network, these resources should also have the same capabilities as the spinning reserve, so that if necessary, they can inject additional power into the network. One of the solutions is to make it possible to use ESSs. The spinning reserve is usually activated with a response time of about 10 minutes. Therefore, energy storage systems with a moderate time response can be a good option for this case.

In addition to the above, the combination of energy storage systems and renewable energy resources can be used for other applications such as voltage support, low voltage ride through, and peak shaving that are beyond the scope of this book.

In addition to technical issues that affect the choice of the type of energy storage system, the cost of them is another factor that should be considered in the design stage. Due to the relatively high cost of storage systems, the optimal choice of type and size of the storage system is very important.

In this chapter, firstly, we discuss about different energy storage technologies in detail. Then, the uncertainty modeling and resources of intermittent renewable

energy resources such as wind turbines (WTs) and photovoltaics (PVs) will be surveyed. In the next subsection, the demand uncertainties will be investigated. Finally, the procedure of the optimal selection of energy storage systems (ESSs) will be performed considering the cost and efficiency indices. Moreover, it is aimed to allocate the appropriate ESS technologies subject to uncertainty management topic.

3.2 Statistics Related to the Documents

The section presents the statistics related to the documents. "Renewable energy" and "energy storage" keywords have been searched in the Scopus database, and the VOSviewer software has been used.

Figure 3.1 depicts the number of documents by year; the number of documents increased significantly over the period.

Figure 3.2 shows the number of documents by source; Energy Procedia published the highest number of documents.

Figure 3.3 illustrates the number of documents by the author; J. M. Guerrero has published the highest number of documents.

Figure 3.4 shows collaboration between authors based on the years.

Figure 3.5 shows the number of documents based on affiliation; Ministry of Education of the People's Republic of China has published the highest number of documents.

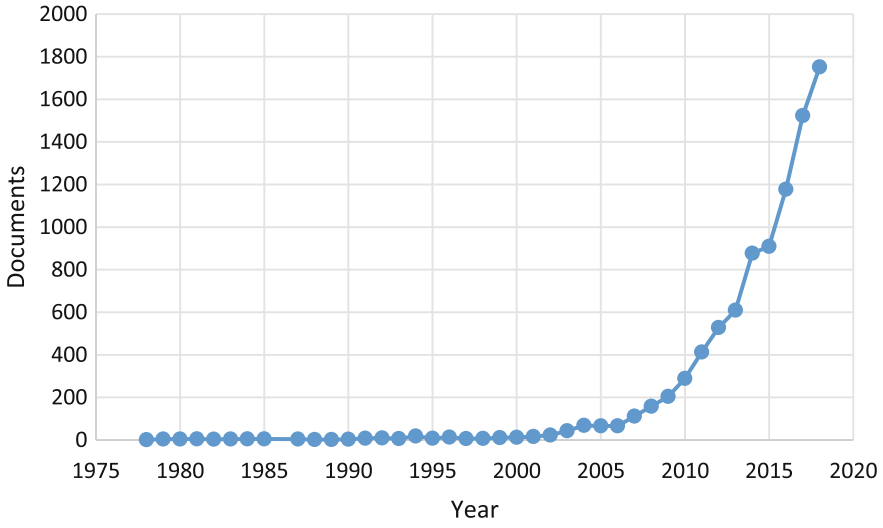

Fig. 3.1 Documents by year

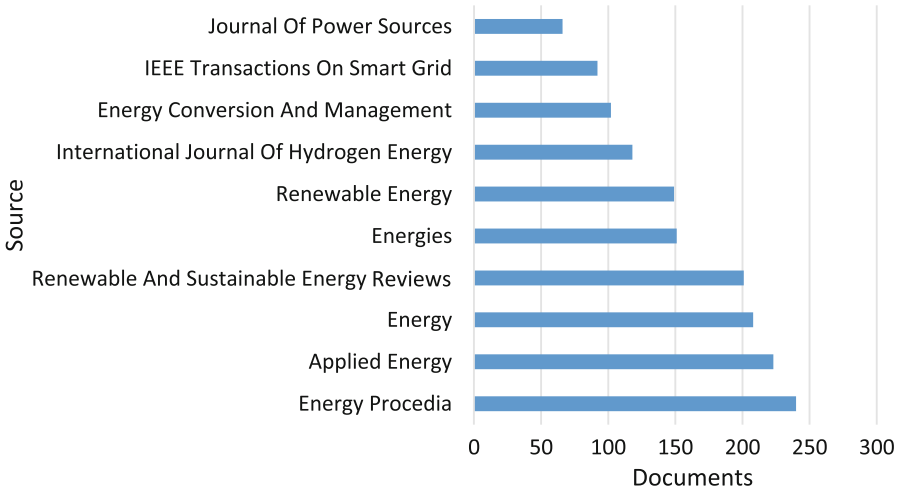

Fig. 3.2 Documents by source

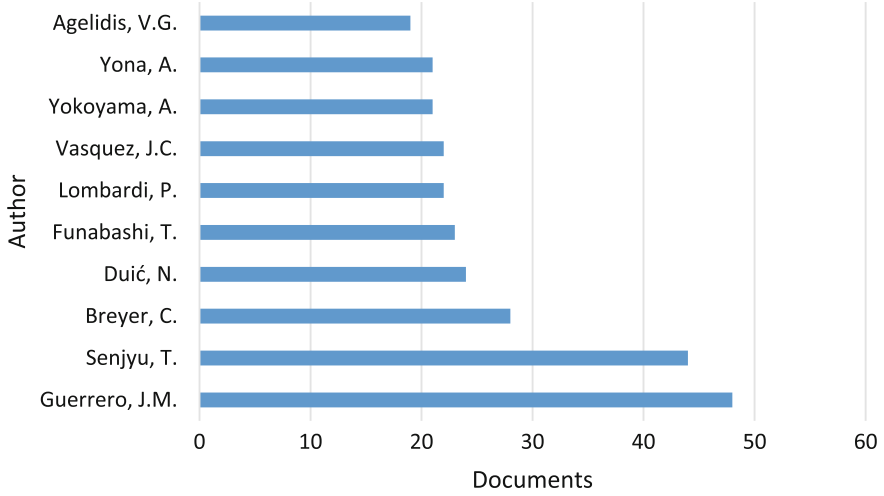

Fig. 3.3 Documents by author

Table 3.1 shows the number of documents by the top 10 countries. Researchers from the United States published 1753 documents with 62,721 citations.

Figure 3.6 shows the number of documents by subject area; most documents were published in the energy and engineering fields.

Figure 3.7 shows the number of documents by type; most documents were published conference papers and articles.

Figure 3.8 depicts the popular keywords by year. For instance, the yellow color shows popular keywords in 2016.

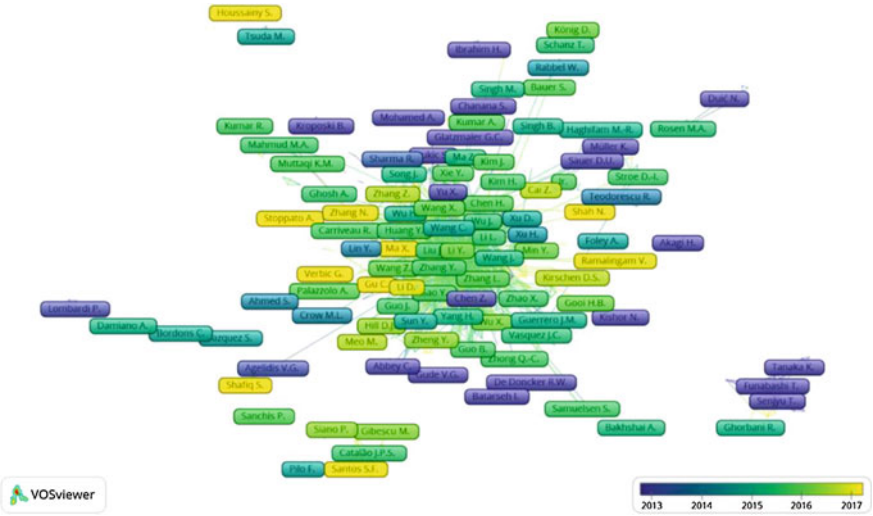

Fig. 3.4 Collaboration between authors

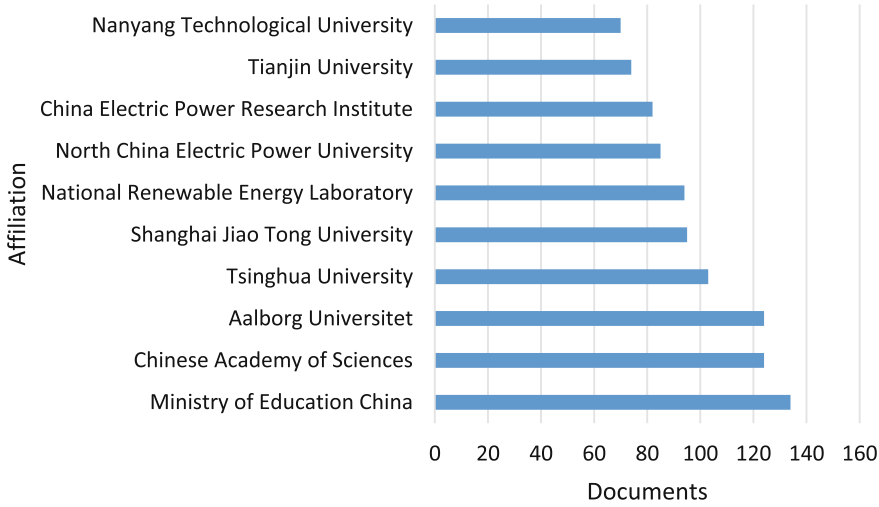

Fig. 3.5 Documents by affiliation

Table 3.1 Documents by country

Number	Country	Documents	Citations
1	The United States	1753	62,721
2	China	1424	33,521
3	Germany	657	9670
4	India	577	7542
5	The United Kingdom	515	11,547
6	Italy	496	6925
7	Australia	374	7673
8	Japan	365	7076
9	Canada	362	8800
10	Spain	352	11,862

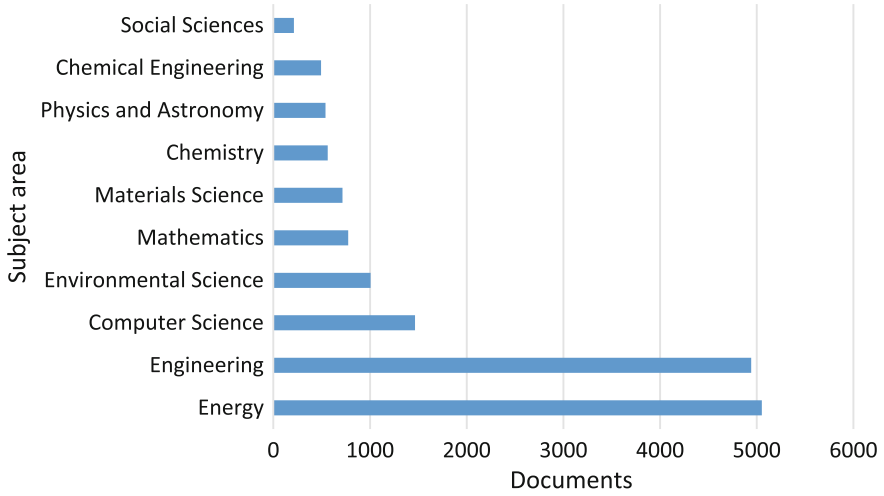

Fig. 3.6 Documents by subject area

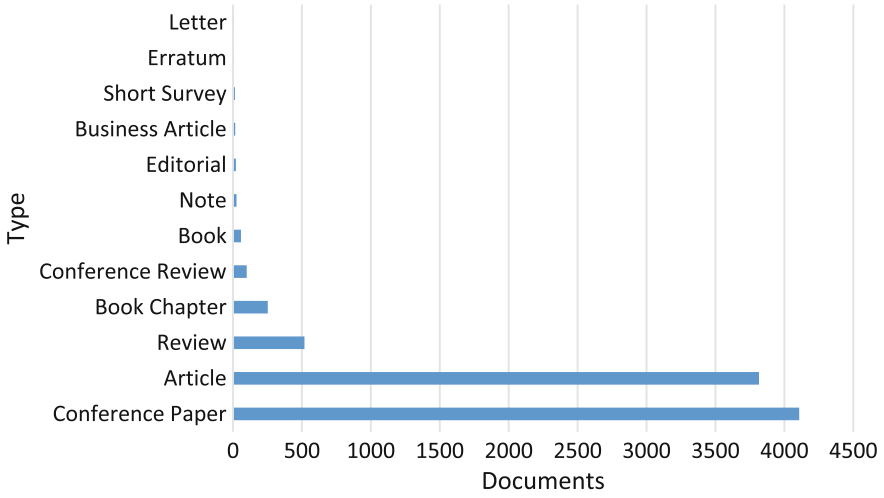

Fig. 3.7 Documents by type

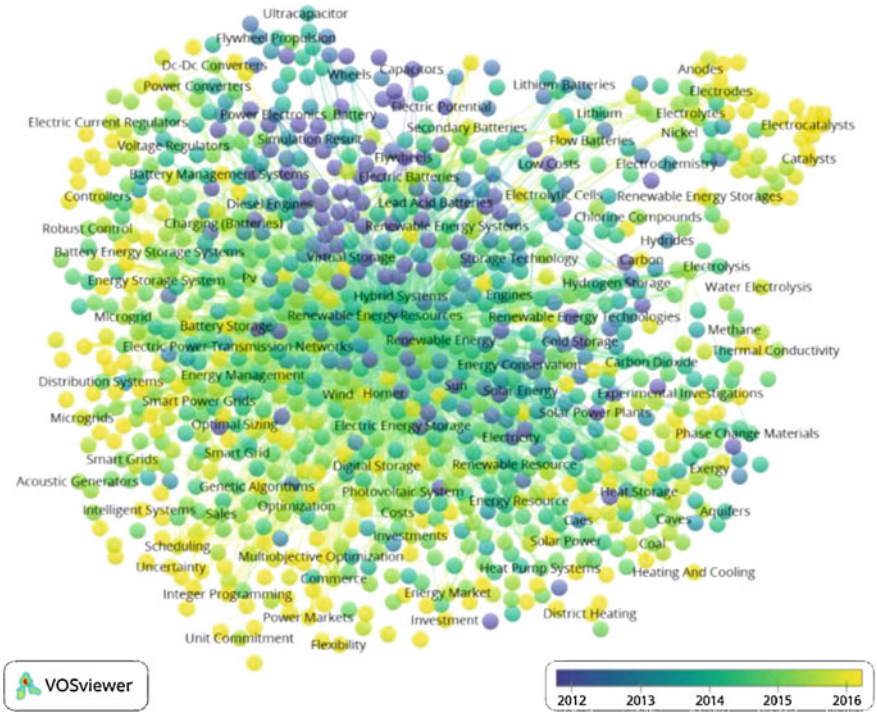

Fig. 3.8 The popular keywords by year

Table 3.2 shows the top 20 popular keywords; renewable energy resources with 4330 times occurrence is the most popular keyword.

Table 3.3 shows the top 10 sources with highest citations; Renewable and Sustainable Energy Reviews with 201 documents and 17,781 citations is the most popular source.

Table 3.4 shows the top 10 published documents with the highest citations.

3.3 Energy Storage Technologies

From the configuration point of view, there are two types of ESS: distributed and aggregated. In a network with many renewable resources, in terms of number and capacity, in order to assuage the power flow fluctuations, the ESS capacity should increase in an aggregated system. In a large-scale ESS, in addition to increasing costs, manufacturing and controlling will also be complicated. Distributed systems are a good solution to this problem, although they are also challenged with power flow controlling.

Table 3.2 The most popular keywords

Number	Keyword	Occurrences
1	Renewable energy resources	4330
2	Energy storage	4326
3	Renewable energies	2219
4	Renewable energy source	1950
5	Electric energy storage	1794
6	Renewable energy	1455
7	Wind energy	1411
8	Energy storage systems	1336
9	Electric power transmission networks	1261
10	Solar energy	1011
11	Optimization	897
12	Electric batteries	895
13	Micro grid	851
14	Smart power grids	746
15	Costs	740
16	Energy efficiency	740
17	Digital storage	667
18	Heat storage	657
19	Photovoltaic cells	649
20	Renewable resources	639

Table 3.3 The top 10 sources with highest citations

Number	Source	Documents	Citations
1	Renewable and Sustainable Energy Reviews	201	17,781
2	Applied Energy	223	8463
3	Chemical Reviews	6	8152
4	Science	6	8085
5	Energy and Environmental Science	30	6110
6	Energy	208	6096
7	Renewable Energy	149	5007
8	IEEE Transactions on Industrial Electronics	32	4685
9	IEEE Transactions on Smart Grid	92	4626
10	Energy Conversion and Management	102	4323

The most common criteria used to compare different technologies of ESSs are as follows:

- Power capacity (kW or MW)
- Energy storage capacity (kWh or MWh)
- Energy density or specific energy (Wh/kg or Wh/dm^3)
- Efficiency
- Charge time (mS)

Table 3.4 The top 10 documents with highest citations

Reference	Authors	Source	Citation	Year
[9]	Günes et al.	Chemical Reviews	5125	2007
[10]	Dunn et al.	Science	5016	2011
[11]	Liu et al.	Advanced Materials	2810	2010
[12]	Carrasco et al.	IEEE Transactions on Industrial Electronics	2449	2006
[13]	Sharma et al.	Renewable and Sustainable Energy Reviews	2363	2009
[14]	Larcher and Tarascon	Nature Chemistry	1753	2014
[15]	Liu et al.	Science	1669	2015
[16]	Manwell et al.	John Wiley & Sons	1582	2010
[17]	Pan et al.	Energy & Environmental Science	1564	2013
[18]	Cook et al.	Chemical Reviews	1563	2010

- Response time (mS)
- Self-discharge rate (percent per day)
- Lifetime (years) or life cycle (number of times)
- Capital cost ($/kWh)

The electrical energy for storage can be converted to a variety of other energies. Some of these types of energy that are more commonly used in ESSs are depicted in Fig. 3.9.

3.3.1 Mechanical Energy Storage Systems

3.3.1.1 Compressed Air Energy Storage

Compressed air energy storage (CAES) is actually saving power generated by compressing air at a time, for use at another time. The advantage of this type of storage is that the energy generated during low energy demand periods (out of peak) can be used to meet demand at peak. This is especially important for renewable energy sources such as wind and solar energy, which are considered as the most important sources of clean energy supplies. The small scale of this energy storage system has been used for a long time in applications such as locomotive engines, but in large-scale applications, very high thermal energy from compressed air should be controlled. The topology of this system is shown in Fig. 3.10.

When the stored energy is required to be injected into the grid, the compressed air is transmitted from the storage cavern, heated, and then expanded in a set of high- and low-pressure turbines which convert most of the stored energy of the

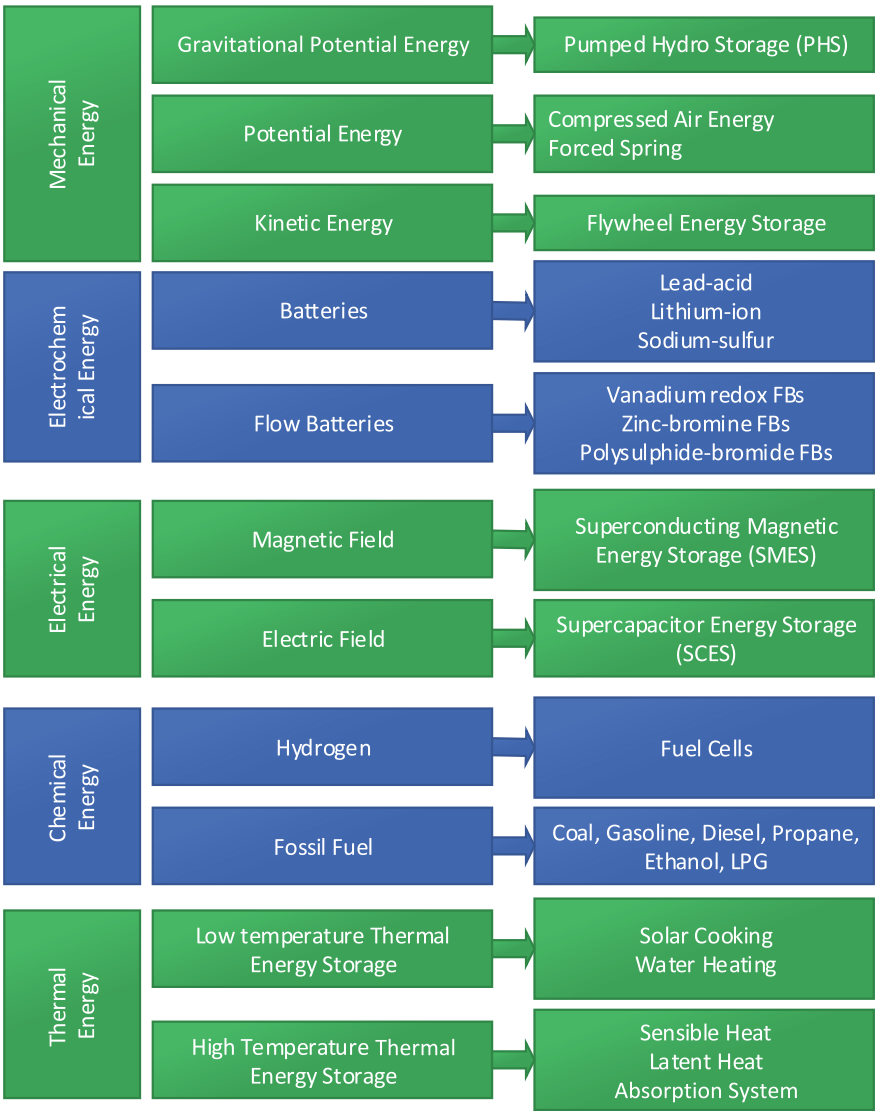

Fig. 3.9 Energy storage technologies

compressed air into the rotational kinetic energy. The turbine output air is additionally mixed with natural gas and combusted. Generally, the output of turbine exhaust is used to heat the cavern air. The topology of the whole system is shown in Fig. 3.10.

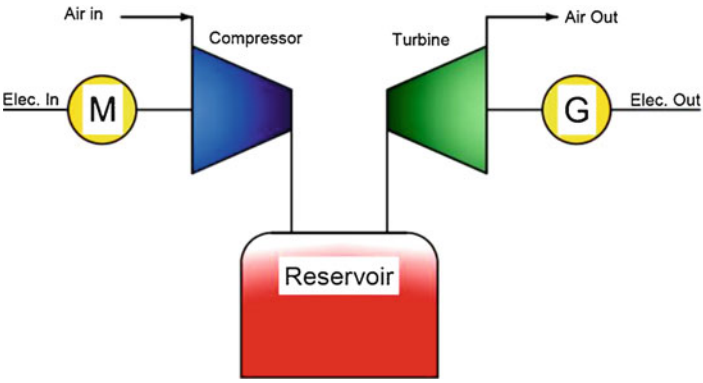

Fig. 3.10 Compressed air energy storage

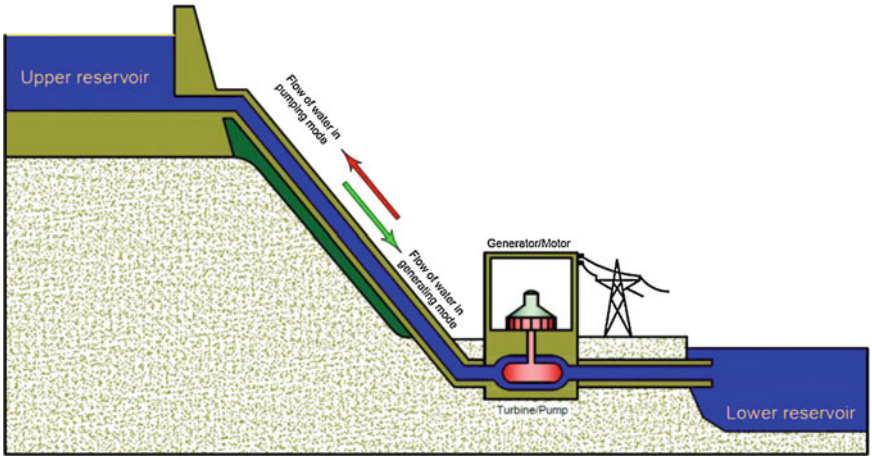

Fig. 3.11 Pumped hydro energy storage diagram

3.3.1.2 Pumped Hydro Energy Storage (PHES)

The pump hydro energy storage system is consisting of a downstream reservoir, a high stream reservoir, a channel or a tube that connects these two reservoirs, and a pump/turbine motor/generator set. At times, when electricity consumption is low (off-peak period) or there is extra generated electricity, the water is pumped from the lower reservoir to the upper reservoir. During the peak period of electricity consumption or loss of electricity production, water flows from the upper reservoir to the lower reservoir, activating the turbines to generate electricity. As indicated in Eq. (3.1)), the energy stored is proportional to the water volume in the upper reservoir and the height difference between the two reservoirs. This energy storage technology is most used for large-scale applications. An illustrative example of a pumped hydro storage is shown in Fig. 3.11. The lifetime of PHS is around

30–50 years. The efficiency of this technology is around 65–70%, and the capital cost is about (500–1500) €/kW and 10–20 €/kW. The response time is less than 1 minute.

$$E = mgh \overset{\rho=1\ \mathrm{l/kg}}{\Longrightarrow} E = Vgh \tag{3.1}$$

3.3.1.3 Flywheel

Advanced functional electrical stimulation (FES) systems have rotors that are made of very tight carbon fiber compounds that are suspended with magnetic bearings and rotate in a vacuum chamber at speeds ranging from 20 to 50,000 rpm. The structure of the energy storage system in the flywheel is depicted in Fig. 3.12. Such flywheels can quickly reach to their rated speed (less than 15 minutes) and store energy very fast. Compared to other energy storage systems, this system has longer lifetimes, high power density, and high output power. The FES's efficiency is about 90%. The characteristic energy of the rotor flywheel depends on two basic factors: rotor geometry and material properties.

The stored energy in the flywheel is in accordance with Eq. (3.2)):

$$\begin{aligned} E &= \frac{1}{2} J\omega^2 \\ J &= \frac{1}{2} mr^2 \end{aligned} \overset{m=\pi r^2 h\rho}{\Longrightarrow} E = \frac{1}{4}\pi\rho h r^4 \omega^2 \tag{3.2}$$

where m, r, h, ρ, and ω are the mass, ratios, height, density, and angular velocity of the flywheel, respectively.

The advantages and disadvantages of the flywheel energy storage system (FESS) are listed in Table 3.5.

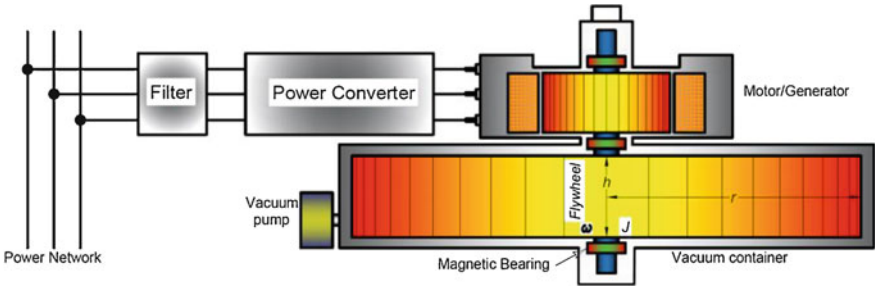

Fig. 3.12 Flywheel energy storage system structure

Table 3.5 Advantages and disadvantages of the flywheel energy storage system

Advantages	Disadvantages
High power density	High capital cost (5000 $/kWh)
High efficiency	High rate of self-discharge (3–20% per hour)
Low maintenance cost (19 $/kW per year)	Low energy density
Long cycle period	

3.3.2 Electrochemical Storage Systems

In an electrochemical storage system, the chemical energy in the active material is converted into electrical energy [19]. Conventional rechargeable batteries and flow batteries (FBs) are two techniques that store energy in electrochemical form. However, chemical reaction reduces the life expectancy and energy of battery although minimal maintenance is needed for these batteries [5]. Electrochemical storage devices are available in different sizes, which is the main advantage of this technology. Lead-acid, lithium-ion, sodium-sulfur (NaS), nickel-cadmium (NiCd), nickel-metal hydride (NiMH), and FBs are examples of this storage system.

Batteries are one of the most used power storage technologies. Energy is stored in an electrochemical form and in a set of cells that are connected in series, in parallel, or in combination. The number of cells connected in serial and parallel is to reach the desired voltage and capacity. Each cell consists of two conductive electrodes and an electrolyte, which are placed together in a special container. In general terms, the battery operation is based on reduction and oxidation reactions (commonly called redox reactions). An electrochemical reduction reaction is one that allows the component involved to gain electrons, while an oxidation reaction allows the component to lose electrons. A battery cell is just a device that provides the conditions for redox reactions to happen, thus generating a flow of ions and electrons between the areas in which these occur. The flow of electrons and ions exists as long as there is an energy difference between the electrochemically active substances involved in the reduction and oxidation reactions. To enable this flow of ions and electrons, the battery cell has two circuits: one external and the other internal. The internal circuit comprises the battery cell itself and provides the path through which the resultant ions flow.

A number of key battery factors for storage applications include high energy density, efficiency, charging and discharge capability, lifetime, and initial cost. Advances in battery technology have dramatically increased energy density, longer lifetime, greater reliability, and lower costs. The principal specificities of each technology are presented in the following sections.

3.3.2.1 Lead-Acid (PbA) Battery

Lead-acid batteries are the oldest type (it was first introduced in 1859) of rechargeable battery that is widely used and available in different sizes and designs. The

positive electrode of these batteries is made up of lead dioxide (PbO_2) and negative electrode from lead (Pb), and sulfuric acid (H_2SO_4) is also used as electrolyte. During the discharging period, both electrodes will be converted to lead sulfate ($PbSO_4$) and will return to the initial state during charging period. Traditional lead-acid batteries have some problems and limitations, such as short lifetime, periodic water maintenance, and low special energy. To overcome these problems, advanced lead-acid batteries have been developed, with advantages such as excellent charge retention, high energy density, fast response, low self-discharge rate (<3% per month), and high lifetime (5–15 years).

3.3.2.2 Lithium-ion (Li-ion) Battery

This type of battery was first commercially developed in 1990 and has grown well in recent years. The cathode of these batteries is made up of lithium oxide and anode from a graphite carbon cell; the electrolyte used here can be formed using an organic solvent with dissolved lithium salt or solid polymer. During the charging period, Li-ion passes from the cathode to the anode, and the process reverses in the discharge period. The most important feature of this technology is increasing the level of energy storage capacity, which can store energy at the megawatt scale. Other advantages of this technology include high efficiency (>90%), high energy density (75–200 Wh/kg), fast response time (millisecond), long lifetime (About 20 years), low self-discharge rate (<5% per month), and wide temperature range (−20 to 55 °C). Because of these, this technology is very popular.

The main disadvantage of this battery is its high capital cost due to the particular type of packaging and internal protection overcharge circuits.

3.3.2.3 Sodium-Sulphur (NaS) Battery

NaS battery comprises molten electrodes (sodium for negative electrode and sulfur for positive electrode), and ceramic Beta-Al_2O_3 acts as both the electrolyte and the separator simultaneously. The main limitation of this technology is that it should work at high temperatures to ensure that sodium and sulfur turn into liquid and maintain high reactivity. In this technology, the energy density is very high, and its charge/discharge efficiency is about 90%. This type of battery is usually suitable for large-scale and nonmoving applications such as power network storage. At present, up to 34 MW, 245 MWh units of this battery are built for wind farms in Japan.

3.3.2.4 Flow Battery (FB)

This type of battery allows its active materials to be stored outside the battery, and these materials flow to the amount required by the pump among the battery cells,

which is why this type of battery is called flow battery. The advantages of this battery can be put in several categories:

- The main characteristic of this battery that separates it from other batteries is the power and energy independence of the battery, due to the separation of battery cells and electrolyte reservoirs. The involvement of more battery cells increases the power capacity, and the size of the electrolyte reservoir leads to an increase in battery power capacity.
- Long battery lifecycle (over 10,000 cycles).
- High efficiency.
- More depth of discharge (DoD) (a wide range of 20–100%).
- Low charge-to-discharge ratio.
- High energy density and power density (increasing).
- Low costs, less per kWh/$, due to long lifetime.
- Due to the lack of lead and cadmium in soluble materials and unlimited lifetime, the environmental effects of this type of battery are much lower than other batteries.

Until now, up to a capacity of 500 kW, 3.6 MWh of this type of battery has been installed. The two leading types of these batteries are zinc bromine (ZnBr) and vanadium redox batteries (VRB).

3.3.3 Electrical Storage Systems

3.3.3.1 Supercapacitor Energy Storage Systems

Supercapacitors (SCs), also called ultracapacitors (UCs) and electric double-layer capacitors (EDLCs), are much more capacitive than conventional capacitors, but their breakdown voltage is lower. Since the energy stored in the capacitor is proportional to their capacity in accordance with Eq. (3.2)), the supercapacitors are capable of storing much more energy. Supercapacitors can be an alternative for conventional capacitors and general batteries. Although supercapacitors are a kind of electrochemical device, they do not use any chemical reaction to store electrical energy.

$$E = \frac{1}{2}CV^2$$

The structure and working principles of a charged supercapacitor are shown in Fig. 3.13. To increase the capacitance as well as the breakdown voltage of the capacitor, a number of cells are connected in series and parallel.

The most important advantages of supercapacitors include high power density, high peak power output, long lifetime cycle, and fast response time, and the high self-discharge rate and high capital cost are also its disadvantages.

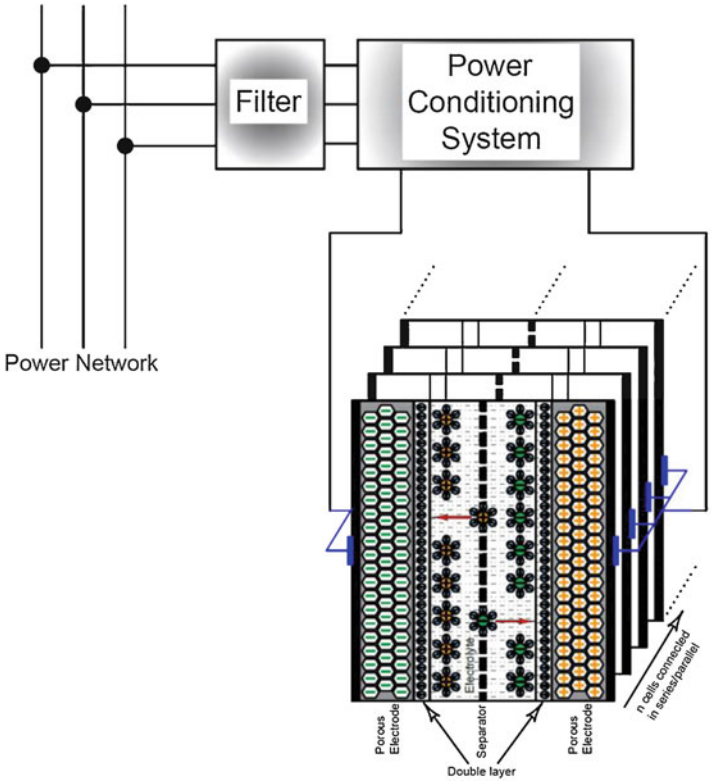

Fig. 3.13 Structure and working principles of a charged supercapacitor

3.3.3.2 Superconducting Magnetic Energy Storage (SMES) Systems

In a supercapacitor energy storage system, the energy is stored in a magnetic field. The magnetic field is created by passing a DC current from a large superconducting coil located in a chamber with a temperature below the superconducting critical temperature. The conductivity of the superconductors is extremely high in superconducting state, but unfortunately, these temperatures are so low that they can only be reached with the aid of cooling with liquid helium. There is a superconducting phenomenon for a wide range of materials such as tin and aluminum. Also, some of the alloys and semiconductors are superconducting, but metals such as gold and silver do not show this phenomenon, nor does the phenomenon of superconductivity occur in ferromagnetic metals. In 1986, high-temperature superconductors (HTSCs) (known as type II superconductors) were discovered. The critical temperature of these superconductors is more than 90 Kelvin. Technically, HTSCs have far more applications, because they have superconducting temperatures

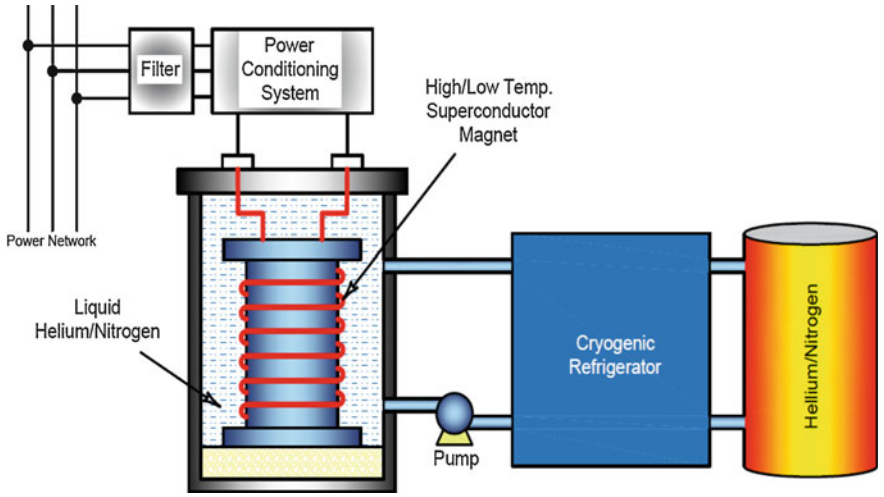

Fig. 3.14 The general principle of a SMES system

that are easier to create. The research continues to find materials whose critical temperatures are still higher, as well as to find a theory to explain high-temperature superconductivity.

The general principles of the energy storage system based on the SMES system are illustrated in Fig. 3.14. As it is seen, a SMES system consists of three parts in general:

- Superconducting coil
- Power consolidation system
- Cryogenically cooled refrigerator

When the superconducting coil is charged, due to the coil zero resistance, the current is flow without any power losses or decays. By discharging the coil, the stored energy can return back to the grid. The power conditioning system consists of a bidirectional AC/DC, with 2–3% energy loss in each direction. Energy losses in SMES are the least among all energy storage technologies, and its efficiency is greater than 95%.

Due to the high cost of superconducting wire and the energy requirement of refrigeration, SMES is now used for short-term energy storage, such as power quality improvement systems. SMES has other advantages over other energy storage technologies: low charge and discharge time delay, the ability to release stored energy instantaneously at high power (for short time period), and high reliability due to motionless parts.

The characteristics of different types of energy storage system technologies are compared in Table 3.6.

Table 3.6 Characteristics of ESS technologies [5]

	Mechanical energy storage		Electrochemical energy storage					Chemical energy storage	Electrical energy storage	
	PHES	CAES	FESS	Lead-acid	Lit-ion	NaS	FBs	Fuel cells	SMES	SCES
Capital cost ($/kWh)	10–70	3–70	400–800	50–270	900–1300	200–400	600	2–15		6800–20,000
Lifetime (year)	30–50	30–40	20	5–15	15	12–20	15–20	15	20	8–10
Efficiency	70–80	70	85	75–80	80–85	80–85	65–75	35–40	90	75–85
Energy density (Wh/kg)		100–150	20–100	30–50	10–200	100–175	20–35	100–1000	10–75	2–30
Power density (W/kg)			11,900	180–200	245–2000	115–230	166		800–23,600	
Power rating (MW)	10–1000	110–300	0.1–20	0.05–10	0.015–50	0.05–34	0.25–12	0.1–50	1–100	0.05–0.25
Energy rating (MWh)	500–8000	580–2860	0.0052–5	0.01–40	0.0015–50	0.05–34	2–120	120	0.001–0.015	0.01
Cycling capability	$<5 \times 10^4$	$<3 \times 10^4$	$<10^7$	<3500	<3500	<2500	<13,000	$<10^4$	$<10^5$	$<10^6$

3.4 Uncertainty and Fluctuation

Renewable energy sources are faced with two fundamental challenges of oscillation and uncertainty, so for the vast presence of these resources in the power system, these two challenges must be solved, and these resources should behave in the same way as conventional generation units as they have specific and smooth output power. In this way, these resources can participate in grid scheduling and not create instability problems.

As mentioned earlier, one of the ways to offset volatility and uncertainty is to use ESSs. In connection with ESSs, two issues should be considered: one is the selection of the type of the ESS technology that is being carried out in the first stage, and the other is determining the size and capacity of ESSs.

To implement the first stage, the characteristics of volatility and uncertainties in the system should be reviewed to determine the type and capacity required for the ESSs. This section deals with fluctuations and uncertainties. Basically, the main sources of fluctuations and uncertainties are renewable energy resources and network loads. In this section, two renewable energy resources, wind and photovoltaic generation system, which have the highest presence in the network, are reviewed along with the specifications of the grid loads.

3.4.1 Wind Generation Systems

The basic challenges of wind systems are oscillating and indeterminable power generation, which, in view of the network's requirements, must be addressed. In this section, the characteristics of fluctuations and uncertainties for wind power systems are investigated.

3.4.1.1 Fluctuations

Wind fluctuations are caused by several factors, turbulence and daily and seasonal variations in temperature. Fluctuations caused by turbulence are rapid fluctuations and other fluctuations in the range of hourly, daily, and seasonal variations. Some oscillations (fluctuations of less than 1 minute) are taken in turbine inertia, but a major part of these oscillations are transmitted to the turbine output. According to the ratio of the output power to the wind speed (cubic equation), the intensity of the oscillations in the output power is very high. These volatilities can put the power system in a challenge of frequency and voltage instability. By creating a wind farm consisting of several turbines, the farm output fluctuations will be greatly reduced relative to single turbines, but there are also some fluctuations at the output of the wind farm.

Table 3.7 Classification of renewable fluctuations

Timescale	Power rating	Energy rating	Frequency
Short-term (<1 h)	High	Low	High
Mid-term (1 h–1 D)	Medium	Medium	Medium
Long-term (>1 D)	Low	High	Low

One of the solutions to compensate for fluctuations is the use of energy storage systems. Capacity and type of storage system are determined based on the type of output power volatility. As it is said, the fluctuations in the wind farm's output power are in different range of minutes, hours, days, and seasons. Each of the fluctuations can be discussed separately. Fluctuations caused by turbulence are of high-frequency variation. These fluctuations around an average value can be investigated, which usually have a relatively high standard deviation. Therefore, to compensate for these fluctuations, a storage system with high power density and a large number of charging and discharging cycles should be used. As it is said, the fluctuations due to turbulence can be reduced by forming wind farm. Therefore, in order to have the lowest required capacity, it is better to consider a storage system for the entire wind farm. This mode requires a much lower storage capacity compared to single-turbine compensation.

Mid-term fluctuations caused by daily temperature variations are usually in the range of hours. The compensation of this category of oscillations requires average power and energy density and average response speed. Therefore, the appropriate storage system should be chosen for these fluctuations. Finally, long-term fluctuations due to seasonal variations in the climate are slowly fluctuating, which requires high energy to compensate for them. Therefore, the energy storage systems with a low time response and high energy capacity for this category of fluctuations are appropriate. Table 3.7 shows the classification of fluctuations with their characteristics.

For each time interval, an average value is defined as the output power of wind power system [20]:

$$P_{\mathrm{d}} = \frac{1}{T} \int P_{\mathrm{w}}(t)dt \tag{3.3}$$

And the maximum difference between real power and the mean value is defined as power capacity:

$$P_{\mathrm{ess}} = \max_T \{P_{\mathrm{ess}i} = (P_{\mathrm{w}} - P_{\mathrm{d}i}), i = 1 : N\}. \tag{3.4}$$

in which T is a long time interval, for example, 2 years, which divided into N intervals. For a typical wind power profile, the dispatched power and power requirements of the ESS are shown in Fig. 3.15 [20].

Also, the highest amount of positive or negative energy to be injected is determined as energy capacity:

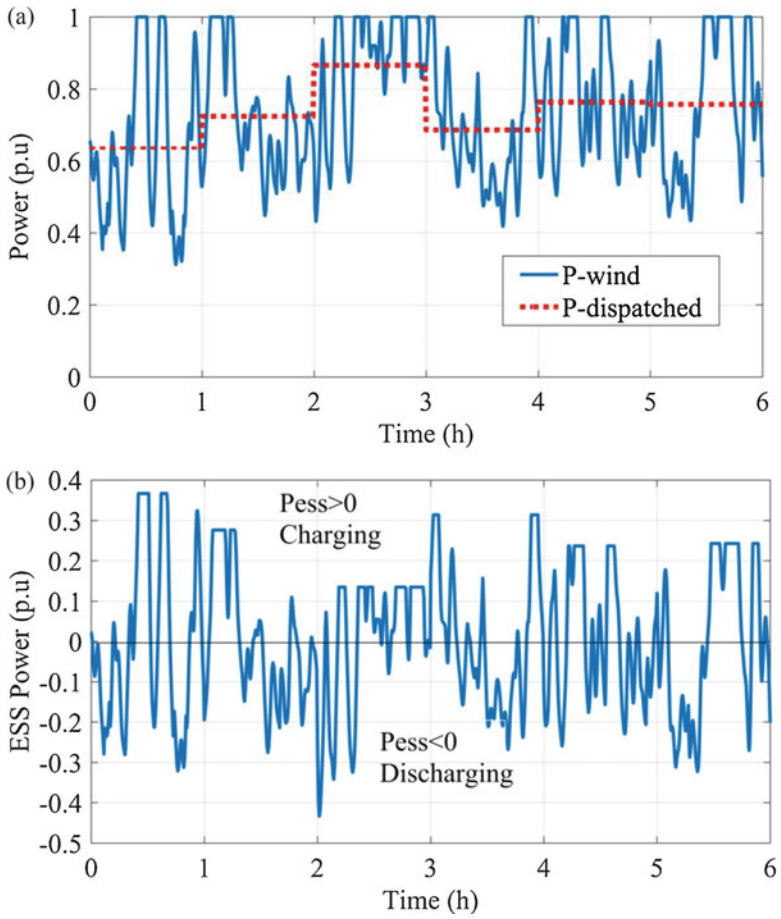

Fig. 3.15 A typical wind power profile; (**a**) dispatched power, (**b**) ESS power

$$E_{\text{ess}} = \max_T \left\{ E_{\text{e}}(t) = \int_0^t P_{\text{ess}}(\tau) d\tau \right\}. \tag{3.5}$$

And the frequency actually represents the frequency power variation around the mean value. This option actually determines the required number of charge/discharge cycles for energy storage system.

3.4.1.2 Uncertainties

Wind speed and hence wind power are random phenomena. Therefore, prediction models are needed to estimate the amount of power generated at different time intervals. On the other hand, the presence of error in prediction methods is

Table 3.8 Classification of prediction error

Timescale	Prediction range	Prediction method	Error rate
Short-term	One to several hours ahead	Statistical and persistence method	Low
Mid-term	One day to a weak ahead	Hybrid method	Medium
Long-term	Several weeks to a year ahead	Physical method	High

inevitable, so that the predicted value is not the same as the actual value. Estimated time intervals can be hourly, daily, and long term.

Several methods have been proposed for the prediction of wind power, which are classified into four general categories: persistence methods, physical methods, statistical methods, and hybrid methods. Usually, statistical methods based on probability density functions are suitable for short-term forecasting and have less error than other methods, physical models based on meteorological data are more suitable for long-term forecasting, and hybrid methods are based on physical data and statistical models, which makes it more optimal methods. In prediction methods, the average wind speed (wind power) is usually predicted at a time interval (e.g., 1 h). The predicted error value varies depending on the model used and the forecast period. For example, in smaller intervals (hourly), the error rate is less than the long-term (daily) intervals.

In Table 3.8, a variety of forecasting scales and appropriate approaches for each interval are presented with error rates. Of course, it should be noted that the error rate is approximate and depends on the type of method used, because each approach can be done in several ways. For example, the statistical approach is applicable to methods such as the use of probability density functions, neural networks, etc., which have different results and errors.

A wind farm as a generation unit must declare its production in advance in order to participate in the unit commitment and dispatching programs. If the amount of power generated differs from the declared value, the unit will be fined. Therefore, in order to avoid penalties, it is necessary to offset the forecast error. One of the ways to compensate for this is to use energy storage systems.

The amount of storage capacity required depends on the amount of error. Therefore, in order to compensate for the short-term forecast error, a smaller capacity is required for the storage system, while larger-capacity storage system is required to offset long-term forecasts.

Usually, for each method, the error rate of that method is presented in different time intervals as a percentage of the nominal value. Therefore, in order to determine the amount of capacity required for the storage system, the type of forecasting method and the time interval of prediction should be known.

3.4.2 Photovoltaic

Due to the oscillatory and random behavior of the irradiance and temperature, in photovoltaic systems, like wind turbine systems, output power will be oscillatory

and random, and it is necessary to compensate for power fluctuations and forecast errors. Like wind systems, there are also short-term, mid-term, and long-term fluctuations, each with the same characteristics as previously discussed. As short-term fluctuations require higher power capacity and more cycles of charge-discharge, long-term fluctuations require a large energy capacity and a lower number of charge-discharge cycles.

Another problem with solar cells is that during the night, the production of a solar cell stops, so for the same behavior of a production unit, it must be combined with other energy sources or energy storage systems. When using a photovoltaic system with an energy storage system, a large capacity of the storage system is required so that its capacity is approximately as large as the capacity of the photovoltaic system.

In addition to the daily and annual apparent movements of the sun, the amount of solar radiation that reaches the surface of the earth depends on the geographical position (length, width, and height) and weather conditions (e.g., cloud cover). Many studies have shown that cloud cover is a major contributor to the difference between measured solar radiation outside the atmosphere and on the surface of the earth. Therefore, the output power of PV depends on the amount of solar radiation.

In PV systems, like wind power systems, we face the challenges of power fluctuations and uncertainty of production, so we can use energy storage systems to compensate for fluctuations and forecast errors.

3.4.3 Load

Power loads, especially residential loads, are variable, and their data is almost unclear. For example, the variable consumption of a residential customer generally depends on the presence of family members at the time of using several power units with a relatively short longevity throughout the day, and due to the high uncertainty, probabilistic approach and fuzzy theory can be used to analyze the uncertainty parameters.

Ideally, with regard to predictive errors, loads should not be considered as definite parameters in planning and operation of a power system. Stochastic energy demand is modeled as a normal Gaussian PDF, where the mean is equal to the predicted value. In most cases, the forecasted load value is considered as the standard deviation of PDF. The description of the normal Gaussian PDF is as

$$f\left(x|m,\vartheta^2\right)=\frac{1}{\sqrt{2\pi\vartheta^2}}\exp\left(-\frac{(x-m)^2}{2\vartheta^2}\right)\quad -\infty<x<+\infty$$

where m is the mean of the input variable, ϑ^2 is the variance, and ϑ is the standard deviation of the input variable [21].

3.5 Optimum Selection

Energy storage systems can be combined in several ways alongside renewable energy resources and network loads. These systems can be combined with only one resource, for example, PV-battery systems or wind-battery systems, or combined with several resources, for example, PV-wind-battery systems. Optimum energy storage system selection is a two-step process: determining the type of technology used and determining the capacity of the storage system. Initially, in the first stage, the type of the storage system should be determined, and then, in the next stage, the required capacity is determined. In this section, these two stages are examined individually.

3.5.1 ESS Type Selection

As mentioned in Sect. 3.2, there are different types of energy storage technologies with different specifications which are classified in Table 3.1. On the other hand, in Sect. 3.3, the characteristics of the volatility and uncertainty of the power of renewable energy resources were investigated, and various characteristics of power capacity, energy, and frequency of variations for different types of fluctuations and uncertainties are shown in Tables 3.2 and 3.3.

Now, according to Tables 3.6, 3.7, and 3.8, we can select the appropriate options for energy storage systems for different types of fluctuations and forecast errors. The results are presented in Table 3.9 for different modes. As it can be seen, for any type of oscillation or error, more than one type of storage technology may be appropriate. The final selection is based on the expense, including the initial investment cost, maintenance cost, and lifetime.

Table 3.9 Suitable technologies for different modes

Fluctuation/ uncertainty	Technical selection	Techno-economic selection
Short-term fluctuation	Supercapacitors, batteries, hybrid supercapacitors and batteries, SMES	Hybrid supercapacitors and batteries
Mid-term fluctuation	Batteries, fuel cells	Fuel cells
Long-term fluctuation	CAES, PSH	CAES, PSH
Short-term uncertainty	Supercapacitors, batteries, SMES, FESS	Batteries
Mid-term uncertainty	Batteries, fuel cells	Fuel cells
Long-term uncertainty	CAES, PSH	CAES, PSH

3.5.2 Optimum Sizing

After selecting the type of energy storage system, the capacity of the system should also be determined. In fact, the required capacity is dependent on the magnitude of the oscillation compensation and the forecast error.

Usually, long-term data, such as wind speed or sunlight, are used to determine the capacity of the ESS. Thus, the long-term period is divided into a number of subintervals, and at each subinterval, the required capacity power and energy are determined according to relations (3.2)) and (3.3)), and then the maximum value over the long-term period is chosen as the nominal required capacity of the ESS. Given the high cost of energy storage systems, determining the optimal capacity is of great importance so that technical requirements are met and at the lowest cost.

Several steps can be taken to reduce the required capacity. The first step is to reduce the volatility of the output power of renewable energy resources. The second step is to establish coordination between the network load fluctuations and the volatility of renewable energy resources, and finally, the third step is a compromise between the amount of fines due to volatility and error of prediction and the cost of the ESS.

3.5.2.1 Spatial Smoothing

Due to the phase difference of natural phenomena, wind and solar radiation, and the reduction of the similarity of wind speed and solar radiation profiles in different locations, wind farms and PV farms can reduce the level of output power fluctuations relative to individual units to a large extent, which is known as spatial smoothing.

In this case, an ESS for the whole wind or PV farm is used, with the capacity required to be much less than that of a single turbine or PV. Two hybrid battery-wind farm and battery-PV farm systems are shown in Figs. 3.16 and 3.17.

3.5.2.2 Load Following

Another solution to reduce the capacity of the ESS is to coordinate the fluctuations of renewable energy resources and network load so that the consumption pattern is consistent with the generation pattern of renewable resources, in which case all the fluctuations of the renewable resources need not be compensated. Therefore, the storage capacity required will be greatly reduced [22].

In this case, in order to manage the volatility of renewable resources, it is possible to predict the generation of these resources to match the demand response with them.

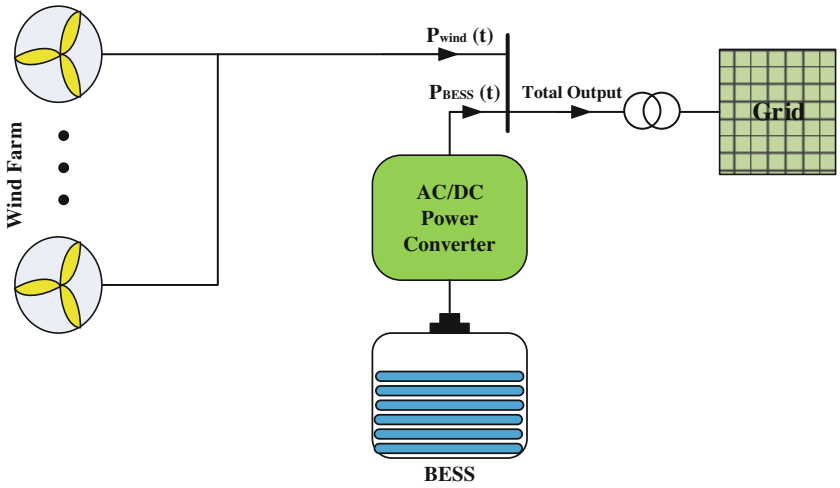

Fig. 3.16 Wind farm-battery hybrid system

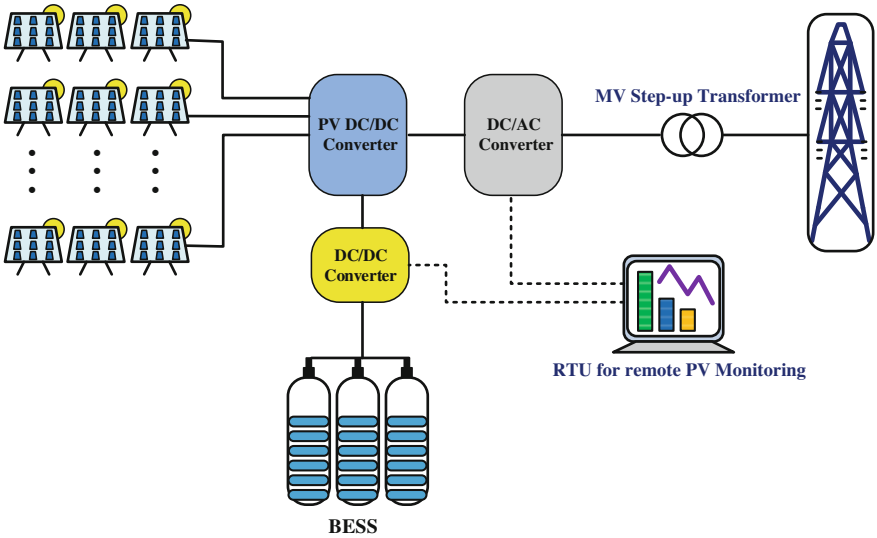

Fig. 3.17 PV farm-battery hybrid system

3.5.3 Optimum Sizing and Operation

Ultimately, in addition to spatial smoothing and coordinated generation and demand management, which reduce the capacity required for the ESS, other factors such as the penalty rate and the allowable amount of injectable fluctuations in the network can also be considered. In this way, it may not be necessary to compensate for any

fluctuations in the power of renewable energy resources, or to compensate for the full forecast error. In this case, a tradeoff between the cost of the ESS and the fine resulting from the lack of full compensation must be done.

To select the best ESS technology optimally coping with a techno-economic design of a renewable-energy-based power system, the main factors can be assessed through a comprehensive objective function. The quantified technical and economical indices are transformed into the following objective function:

$$J = \omega_1.\lambda_f.\boldsymbol{f}\left(\mu_{PLT}^{UnV}, \sigma_{PLT}^{UnV}\right) + \omega_2.\lambda_g.\boldsymbol{g}\left(P_{PLT}^{FLV}, \rho_{PLT}^{FLV}\right) + \omega_3.\boldsymbol{C_{INV}}(\alpha, \beta, \delta, PLT) + \omega_4.\boldsymbol{C_{MTC}}(n, P_{ESS}, PLT) + \omega_5.\boldsymbol{C_{LFT}}(PLT) + \omega_6.\boldsymbol{C_{OP}}(\pi_{EN}, P_{ESS}, ST). \quad (3.6)$$

μ_{PLT}^{UnV} and σ_{PLT}^{UnV} are the mean and variance of the forecasting values of the uncertain variables in each planning time horizon, respectively. UnV is the set of energy system uncertain variables which can be defined as UnV = {Load, Wind Turbine, Photovoltaic}. PLT describes the set of energy system planning horizon which can be defined as PLT = {Short − Term (ST), Mid − Term (MT), Long − Term (LT)}. P_{PLT}^{FLV} and ρ_{PLT}^{FLV} stand for fluctuation mitigation behavior of the ESS which is stem from the intermittent nature of the particularly renewable-energy-based resources, i.e., WT and PV, respectively. In other words, P_{PLT}^{FLV} is the dispatched active power of the renewable sources, and ρ_{PLT}^{FLV} represents the active power fluctuated around the dispatched points. FLV is the set of energy system fluctuation variables which can be defined as FLV = { Wind Turbine, Photovoltaic}. λ_f and λ_g are two coefficients which convert the technical assessment factors to cost-based objectives. C_{INV}, C_{MTC}, C_{LFT}, and C_{OP} representing the costs associated with investment, repair-maintenance, lifetime functions, and costs of charge/discharge in the operational scheduling horizon, respectively. α, β, and δ are the inflation, interest, and invest return rates, respectively. n and P_{ESS} show the number of charge/discharge of the ESSs and the amount of active power of the ESSs. π_{EN} indicates the price of energy in the wholesale/retail market. ω_1, ω_2, ω_3, ω_4, ω_5, and ω_6 are weight coefficients of the techno-economic objectives which are showing the importance of each term from the decision-maker's viewpoint. Obviously, technical experience and insight economical view can have great impact on decision-making procedures. In the case where all the weight coefficients are equal, the techno-economic characteristics of each ESS technology make the objective function be biased toward to one or two factors. For example, for ST planning horizon, supercapacitors are near-optimal candidates which can also satisfy other factors in that horizon.

In the present chapter, a cost-based unit commitment problem was comprehensively presented to determine the best operating schedule of the conventional generation stations. The start-up cost, shut-down cost, and the fuel cost of the fossil-fuel-based power plants was introduced as the single objective function and minimized in two case studies: "Without demand response program" and "With demand response program". It was found that optimal generation curve of each thermal unit was flatten by shifting a part of peak electrical demand to off-peak load periods. Therefore, daily fuel cost and start-up cost of thermal power plants were

decreased, considerably. But shut-down cost in two cases was obtained to be equal to zero, which reveals the capability of the generalized mathematical algebraic modeling system software in finding the least operation cost. As the future trends, the value of the incentives, which should be paid to participants in demand-side management strategies, will be considered in load procurement process. In addition, the uncertainties of electrical load and renewable energy resources in cost-based unit commitment problem can be modeled using the risk-constrained short-term scheduling methods such as information gap decision theory, game theory, and robust optimization approach.

3.6 Conclusion

Due to the high penetration of renewable energy resources in the power grid, it is necessary that the volatile and randomized power challenges of these resources be solved in such a way that the stability of the power system is not compromised and that these resources can participate in the dispatching program and also the electricity market.

One of the solutions to offset the power fluctuations and prediction errors is the use of ESSs along with these resources. In this regard, due to the wide variety of technologies of ESSs, determining the appropriate type of ESSs based on technical and economic issues is of great importance. Also, due to the high cost of the storage system, the capacity required for these systems should be optimized to meet both technical and economic needs. Finally, different technologies must be considered in order to compensate for various types of fluctuations and forecast errors. Also, due to economic issues, it may not be necessary to compensate for any fluctuations or errors so that the optimum capacity of ESS can be determined on the basis of the minimum final cost.

References

1. Aigner, T., Jaehnert, S., Doorman, G. L., & Gjengedal, T. (2012). The effect of large-scale wind power on system balancing in Northern Europe. *IEEE Transactions on Sustainable Energy, 3* (4), 751–759.
2. Nguyen, N., & Mitra, J. (2016). An analysis of the effects and dependency of wind power penetration on system frequency regulation. *IEEE Transactions on Sustainable Energy, 7*(1), 354–363.
3. Barton, J. P., & Infield, D. G. (2004). Energy storage and its use with intermittent renewable energy. *IEEE Transactions on Energy Conversion, 19*(2), 441–448.
4. Ibrahim, H., Ilinca, A., & Perron, J. (2008). Energy storage systems—Characteristics and comparisons. *Renewable and Sustainable Energy Reviews, 12*(5), 1221–1250.
5. Díaz-González, F., Sumper, A., Gomis-Bellmunt, O., & Villafáfila-Robles, R. (2012). A review of energy storage technologies for wind power applications. *Renewable and Sustainable Energy Reviews, 16*(4), 2154–2171.

6. Lange, M. (2005). On the uncertainty of wind power predictions—Analysis of the forecast accuracy and statistical distribution of errors. *Journal of Solar Energy Engineering, 127*(2), 177.
7. Bevrani, H., Ghosh, A., & Ledwich, G. (2010). Renewable energy sources and frequency regulation: Survey and new perspectives. *IET Renewable Power Generation, 4*(5), 438.
8. Erlich, I., & Bachmann, U. (2005). *Grid code requirements concerning connection and operation of wind turbines in Germany*. In IEEE Power Engineering Society General Meeting (pp. 2230–2234).
9. Günes, S., Neugebauer, H., & Sariciftci, N. S. (2007). Conjugated polymer-based organic solar cells. *Chemical Reviews, 107*(4), 1324–1338.
10. Dunn, B., Kamath, H., & Tarascon, J.-M. (2011). Electrical energy storage for the grid: A battery of choices. *Science, 334*(6058), 928–935.
11. Liu, C., Li, F., Ma, L.-P., & Cheng, H.-M. (2010). Advanced materials for energy storage. *Advanced Materials, 22*(8), E28–E62.
12. Carrasco, J. M., et al. (2006). Power-electronic systems for the grid integration of renewable energy sources: A survey. *IEEE Transactions on Industrial Electronics, 53*(4), 1002–1016.
13. Sharma, A., Tyagi, V. V., Chen, C. R., & Buddhi, D. (2009). Review on thermal energy storage with phase change materials and applications. *Renewable and Sustainable Energy Reviews, 13*(2), 318–345.
14. Larcher, D., & Tarascon, J.-M. (2015). Towards greener and more sustainable batteries for electrical energy storage. *Nature Chemistry, 7*(1), 19–29.
15. Liu, J., et al. (2015). Metal-free efficient photocatalyst for stable visible water splitting via a two-electron pathway. *Science, 347*(6225), 970–974.
16. Manwell, J. F., McGowan, J. G., & Rogers, A. L. (2009). *Wind energy explained*. Wiley: Chichester.
17. Pan, H., Hu, Y.-S., & Chen, L. (2013). Room-temperature stationary sodium-ion batteries for large-scale electric energy storage. *Energy & Environmental Science, 6*(8), 2338.
18. Cook, T. R., Dogutan, D. K., Reece, S. Y., Surendranath, Y., Teets, T. S., & Nocera, D. G. (2010). Solar energy supply and storage for the legacy and nonlegacy worlds. *Chemical Reviews, 110*(11), 6474–6502.
19. Faisal, M., Hannan, M. A., Ker, P. J., Hussain, A., Bin Mansor, M., & Blaabjerg, F. (2018). Review of energy storage system technologies in microgrid applications: Issues and challenges. *IEEE Access, 6*, 35143–35164.
20. Gholami, M., Fathi, S. H., Milimonfared, J., Chen, Z., & Deng, F. (2018). A new strategy based on hybrid battery–wind power system for wind power dispatching. *IET Generation Transmission and Distribution, 12*(1), 160–169.
21. Tabar, V. S., Jirdehi, M. A., & Hemmati, R. (2017). Energy management in microgrid based on the multi objective stochastic programming incorporating portable renewable energy resource as demand response option. *Energy, 118*, 827–839.
22. Wu, H., Shahidehpour, M., Alabdulwahab, A., & Abusorrah, A. (2015). Demand response exchange in the stochastic day-ahead scheduling with variable renewable generation. *IEEE Transactions on Sustainable Energy, 6*(2), 516–525.

Chapter 4
Solar-Powered Energy Systems for Water Desalination, Power, Cooling, Heating, and Hydrogen Production: Exergy and Exergoeconomic Analysis

Hossein Nami, Sahand Saeidi, and Amjad Anvari-Moghaddam

Nomenclature

Sets

i The streams in the cycle

Variables

C Cost
c Cost per unit of exergy
E Energy
K Kinetic energy
P Potential energy
Q Heat
T Temperature
U Internal energy
W Work

H. Nami (✉)
Department of Mechanical Engineering, Faculty of Engineering, University of Maragheh, Maragheh, Iran
e-mail: h.nami@maragheh.ac.ir

S. Saeidi
Faculty of Engineering and Natural Sciences, Sabanci University, Istanbul, Turkey

A. Anvari-Moghaddam
Department of Energy Technology, Aalborg University, Aalborg, Denmark

F. Jabari et al. (eds.), *Integration of Clean and Sustainable Energy Resources and Storage in Multi-Generation Systems*,
https://doi.org/10.1007/978-3-030-42420-6_4

Greek letters

Ψ Exergy efficiency
φ Exergy
η Energy efficiency

4.1 Introduction

Industrialization and population growth lead to a worldwide growing energy demand, and fossil fuels are the main and primary resource that satisfies it. The increasing application of renewable energy resources in different industries and sectors can and will change this trend into a sustainable and clean future. Renewable energy sources, including solar energy, are considered as clean, free, and more importantly, inexhaustible resources which are able to provide sustainability. Also, their other objective is to reduce the application of fossil fuels in modern society, whose price has increased dramatically in the past and most probably will again.

Solar radiation which is collected by the Earth's surface is the most basic form of renewable energy which is available in nature. Solar energy, along with wind and geothermal energy, performs an important role in human kind's future. The average global solar radiation on a daily basis is the most crucial factor for different applications of solar energy, e.g., concentrating collectors, solar furnaces, thermo-electricity, and interior illumination of buildings. Figure 4.1 presents the global map of total annual and daily direct normal irradiation (DNI) based on long-term data. As it is illustrated, there are many areas which benefit from significant DNI potential, in

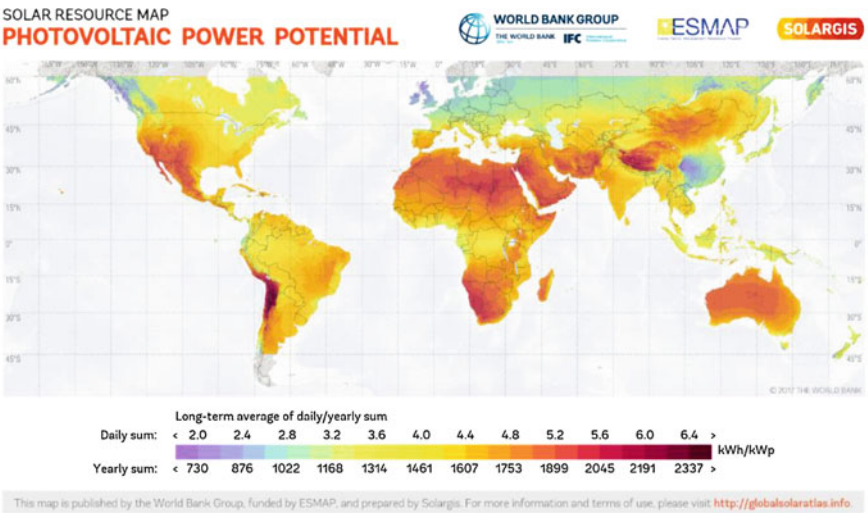

Fig. 4.1 Map for direct normal irradiation on daily and annual bases

a range between 2000 kWh/m^2 and about 3000 kWh/m^2. These regions are the US Southwest, Chile, Spain, South Africa, the Middle East, North Africa, India, southwestern China, and Australia, which are mostly covered by desert and semidesert areas that lack humidity, clouds, dust, and fumes.

Solar energy is widely available at zero cost and is able to be utilized in a wide range of applications. The sun provides for almost all forms of life on this planet, supports agriculture, and affects the climate conditions. Solar energy is an essential source of renewable energy and helps to significantly decrease our dependency on fossil fuels, in future. Therefore, the abundance of solar radiation in a region is advantageous since solar-based technologies can be easily developed.

Solar energy is a solution to reduce the environmental impact of the growing energy demand. But since it is not continuous and evenly distributed in every region, configurations that employ solar energy can always be coupled with ones running by fossil fuels. This is also known as system hybridization which can guaranty a consistent performance during any time period. The idea of solar integrated thermal systems has been proposed and developed for many years. Solar energy can be transformed into other forms of energy by employing photovoltaic (PV) panels and solar heat collectors. The solar heat collectors, including concentrating and non-concentrating (also known as stationary), are applied for absorbing the solar irradiance and heating fluids to different temperatures. On the other hand, the PV module can directly produce electricity from solar energy. The solar-driven district energy systems (DES), solar cooling system, PV-coupled combined heat and power (CHP) systems, solar-driven (thermal and/or PV) combined cooling, heating, and power (CCHP) systems, organic Rankine cycle (ORC) coupled with solar heat collectors, solar desalination layouts, and hydrogen production by using solar power are just a few examples for application of solar energy in thermal systems.

Unfortunately, the current rate of solar radiation application in generating mechanical, electrical, and thermal energy does not include a significant portion of the energy budget in most countries. However, due to its positive environmental impacts, solar and other renewable sources will and should be more favorable, in the near future. Therefore, it is crucial to have the necessary thermodynamic tools prepared in order to be ready when the demand increases. Furthermore, similar to any other emerging technology, solar energy systems will eventually have to be optimized. Thermodynamic analyses, i.e., the first and the second law efficiency, which are known as energy and exergy efficiency analyses, respectively, are powerful tools to study the performance of a thermal system. However, the exergy analysis, as the maximum possible obtained work, gives a better perspective over the overall system and each component individually, as well. Economic investigation of the system based on the results from thermodynamic, especially exergy, analysis could also reveal valuable information. All these data will be employed to modify and improve the studied system, financially and technically.

In this chapter, it is tried to introduce and explain a few applications of solar energy and show how it can be employed in current technologies and help to develop a sustainable and clean future. After a brief introduction about solar energy and radiation, two thermal systems that can be coupled with solar collection fields are

introduced and discussed. Combined cooling, heating, and power systems and desalination plants are two perfect examples that show how solar power can be integrated into current technologies. Afterward, hydrogen production by using solar irradiation is introduced and discussed. Hydrogen as a byproduct of a thermal system can increase its efficiency, significantly. Moreover, hydrogen production can be considered as an energy storage method. By generation hydrogen, a clean and efficient fuel, energy can be delivered constantly, over time. Finally, energy, exergy, and exergoeconomic analyses of solar-driven systems are discussed to present an overall view over beneficial aspects of this clean and free energy source.

4.2 Solar Radiation

Solar radiation is included among the electromagnetic energies and transmits through space with speed of light. The annual average radiation from outside of the atmosphere, known as extraterrestrial radiation, is about 1367 W/m^2 of which an estimated amount of 1000 W/m^2 reaches the Earth's surface [1]. This value attributes to a collective surface which is perpendicular to the sun's radiation, clear sky, and the sun at the zenith. From the radiation which crosses the atmosphere, a portion is absorbed, reflected, and scattered before contacting the surface. The scattered part is known as diffuse radiation, while the part of the solar irradiation that is able to touch directly the Earth's surface is called beam radiation. Moreover, a percentage of the radiation which is reflected from the surfaces at the surrounding is called reflected radiation.

Therefore, solar radiation on an arbitrarily oriented surface is composed of three components of diffuse, beam, and reflected radiations. In the case of horizontal exteriors, the reflected section is not possible to absorb and vanishes; ergo, the global radiation only consisted of diffuse and beam parts. Figure 4.2 illustrates the components of solar radiation, which travels from the sun to the Earth's surface.

4.2.1 Solar Exergy

Exergy is defined as the maximum available work from a system in a specific environment. Based on the fundamental thermodynamic laws, energy is neither destroyed nor created. However, every process reduces the capacity of the input energy in performing work, due to entropy generation which is caused by irreversibility. Therefore, the energy analysis of a system cannot result in useful data. Exergy efficiency, on the other hand, represents the ratio of the maximum obtained mechanical work to the energy input and takes irreversibility into account.

There have been numerous investigations about the exergy analyses of solar radiation and solar thermal power [3]. One of the earliest and the most well-known studies belongs to Petela [4]. According to his reports, the entering solar radiation

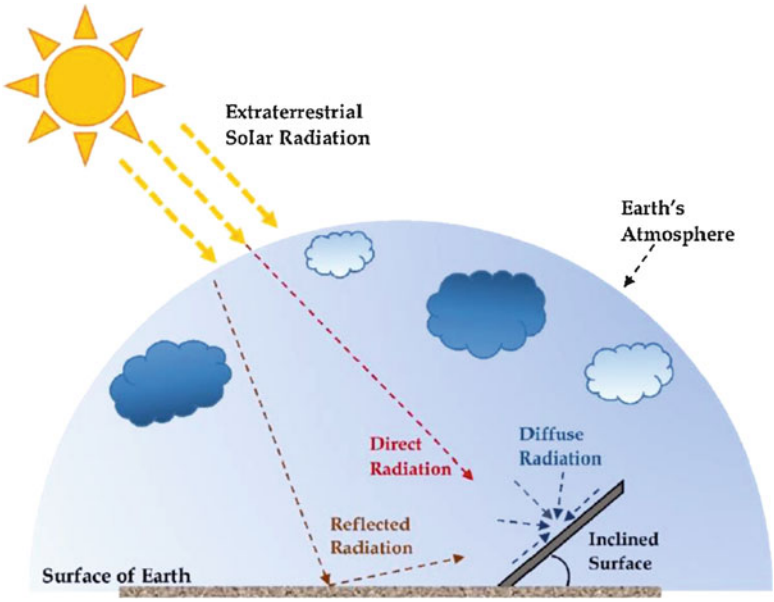

Fig. 4.2 Different components of solar radiation [2]

into the Earth's atmosphere is attenuated by the presence of different substances in the atmosphere, e.g., ozone, water vapor, and carbon dioxide. The spectral distribution of this radiation is also dependent on different factors such as solar orientation upon the investigated surface and chemical composition of the atmosphere at the studied location [2].

Petela assumed the maximum obtained work from an ideal (reversible) process as the exergy of radiation and considered the radiation energy as the input:

$$W_{\max} = \varphi. \tag{4.1}$$

These assumptions express the maximum energy efficiency or exergy efficiency as below [5]:

$$\eta_{\max} = \Psi = \frac{W_{\max}}{E_{\text{rad}}}. \tag{4.2}$$

By utilizing the Stefan-Boltzmann law formula for radiation energy, it is clear that the radiation energy depends only on the sun's surface temperature, T_s:

$$E_{\text{rad}} = \sigma T_s^4. \tag{4.3}$$

where σ represents Stefan-Boltzmann constant. Further, Petela's work concludes that the exergy efficiency of solar radiation is only dependent on T_s and temperature

Table 4.1 Radiation exergy efficiency, proposed by different studies [6, 7]

	Ψ	Input	Output
Petela	$1+\frac{1}{3}\left(\frac{T_0}{T_s}\right)^4-\frac{4}{3}\frac{T_0}{T_s}$	Radiation energy	Radiation exergy
Spanner	$1-\frac{4}{3}\frac{T_0}{T_s}$	Radiation energy	Absolute work
Jeter	$1-\frac{T_0}{T_s}$	Heat	Net work of a heat engine

of the collecting surface, T_0, as long as $T_s > T_0$. His expression of the exergy efficiency is brought in Table 4.1, along with the results of other studies. All investigations are agreed on temperature dependency of exergy efficiency.

4.2.2 Modeling

There are many proposed empirical models for predicting the solar irradiation on a horizontal surface. These models try to predict the solar exergy of receiving radiation at different times of the year. In that order, various factors should be taken into account, e.g., sunshine duration, mean temperature, and relative humidity for 1 year.

Chu et al. [3] utilized the Simple Model of the Atmospheric Radiative Transfer of Sunshine (SMARTS) to predicts beam, diffuse, and global radiation irradiance. Moreover, they studied the impact of tilted angle and air mass on exergy of the terrestrial solar radiation. They have concluded that by increasing the tilted angle, the exergy of terrestrial solar radiation increases initially and decreases afterward. Furthermore, an increase of air mass results in a reduction of the total energy quality factors of the direct, the diffuse, and the global terrestrial solar radiation.

Arslanoglu [5], by using the meteorological data, developed three empirical models in order to forecast the exergy of monthly average global radiation on a horizontal surface in different regions of Turkey. The statistical results of these studies indicated that all regression models are valid in Turkey. He also investigated the effect of ambient temperature variation and concluded that the mean conversion coefficient of exergy to energy is to be around 93% at the studied districts, by applying Petela's model.

More empirical and analytical models are required to have an accurate prediction of the incoming exergy from solar radiation. This data is of high importance for the application of solar-driven equipment and facilities.

4.3 Solar-Driven Combined Cooling, Heating, and Power (CCHP)

Multi-energy systems have always been more efficient than the thermal systems which focus only on power or heat generations [8]. Taking into account lateral productions that could be obtained in a system increases the output and subsequently

the energy and exergy values for the overall production. Moreover, this method avoids a sizable amount of waste heat due to repurposing and recycling the exhaust heat. This factor makes these kinds of systems environmentally beneficial. Combined cooling, heating, and power (CCHP) system is among one of the most well-known and efficient of multi-generation systems. Having three productions as the system's output increases its efficiency to the highest and decreases its waste to the lowest level possible.

The most significant application of CCHP systems is in the building sector. CCHP systems are mostly known as economic small to medium power systems with power generation in a range of less than 10 MW. This characteristic makes them a good fit for building. The building sector is responsible for a significant portion of overall energy consumption in the world. It consumes over 40% of the energy consumption and emits about 36% of total greenhouse gas emissions in Europe [9]. Although dual integrated systems of combined heat and power (CHP) systems are able to improve the energy efficiency of a building and lower their need for energy storage, they cannot compete with triple-generation systems of CCHP. CCHP systems, unlike CHPs, can satisfy most of the energy demands of a building. Furthermore, the overall energy consumption of a CCHP system can easily be optimized in a way that no separate energy system is able to [10].

Unfortunately, most of the current CCHP systems are running with fossil fuels, mainly natural gas, as their source of energy. In order to lower this harmful environmental impact, there have been efforts to integrate these systems with renewable energy resources or even with municipal waste sources as studied by Nami et al. [11] CCHP systems with hybrid renewable/fossil fuel energy sources are at the center of interest, especially from perspective of distributed energy systems, since they use locally available energy sources and reduce the consumption of fossil fuel and consequently greenhouse gas emissions. Geothermal and biomass energy resources are being engaged in a few cases and have shown promising results, but abundance and availability of solar power make it a perfect and viable alternative. Of course, the lack of consistency and its dependency on meteorological conditions can be considered as setbacks, but these can be resolved with energy storage units. Moreover, as discussed before, solar power is an economical option that is highly beneficial for modern urban areas.

4.3.1 Solar Radiation Collector

Integrating solar energy with CCHP systems happens by harvesting solar heat at different temperatures utilizing concentrating or non-concentrating solar heat collectors. This also can happen with or only by photovoltaic (PV) panels. In comparison to the systems which use PV panels and heat collectors separately, the flat photovoltaic thermal (PVT) solar units and concentrating parabolic PVT (CPVT) units, Fig. 4.3, which combines PV cells with solar heat collectors, can simultaneously transform solar radiation into heat and electricity by a higher efficiency, at the same aperture area. The two products of these CPVT units can be easily

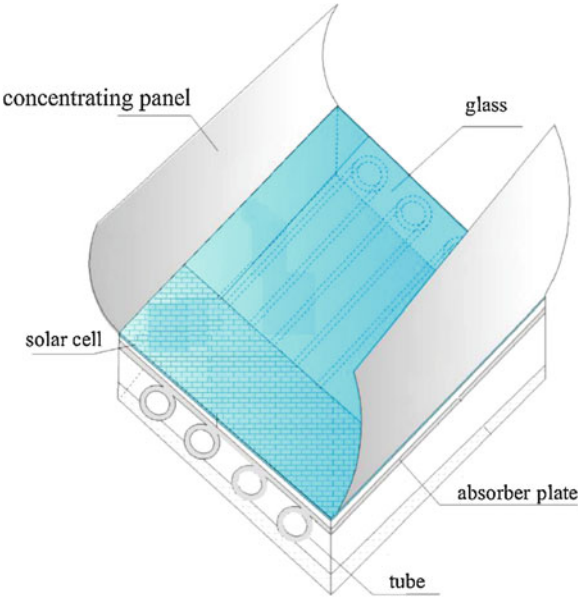

Fig. 4.3 Structure of a concentrating parabolic PVT unit [13]

integrated into CCHP systems and increase the ratio of electricity to heat production of these system. This advantage solves the fixed ratio limitation of conventional CCHP systems in following electrical or thermal load modes that often lead into the excess or shortage of the system production when the consumers' requests vary [12].

4.3.2 System Layout

A typical CCHP system integrated with CPVT panels, Fig. 4.4, includes a solar collector, two pumps, a storage tank for hot water, and an auxiliary heater. The auxiliary heater produces the extra required heat for the system to function properly, especially when the collector, due to instabilities in solar radiation, cannot supply enough heat.

For more specification, Fig. 4.5 illustrates a detailed configuration of a solar-driven CCHP system. It consists of a CPVT solar collector field, internal combustion engine (ICE), thermal energy storage (TES), absorption heat pump (AHP) and its cooling tower, and heat exchanger (HX). The detailed energy and thermodynamic properties of each stream can be found in the literature [13]. Natural gas is fed to ICE in order to generate electricity and next its hot exhaust gas stream and jacket water flow to AHP for chilled water production in cooling purposes or hot water production in heating and domestic hot water demands. The CPVT collects solar radiation to harvest solar heat which is as the second heat source with the waste heat of jacket water to be utilized. The electricity produced by PV modules with the produced electricity from the ICE is sent to users.

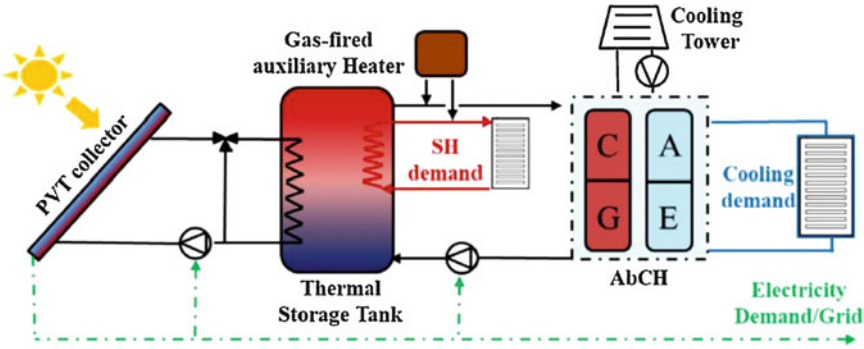

Fig. 4.4 General schematic diagram of solar-driven CCHP system [9]

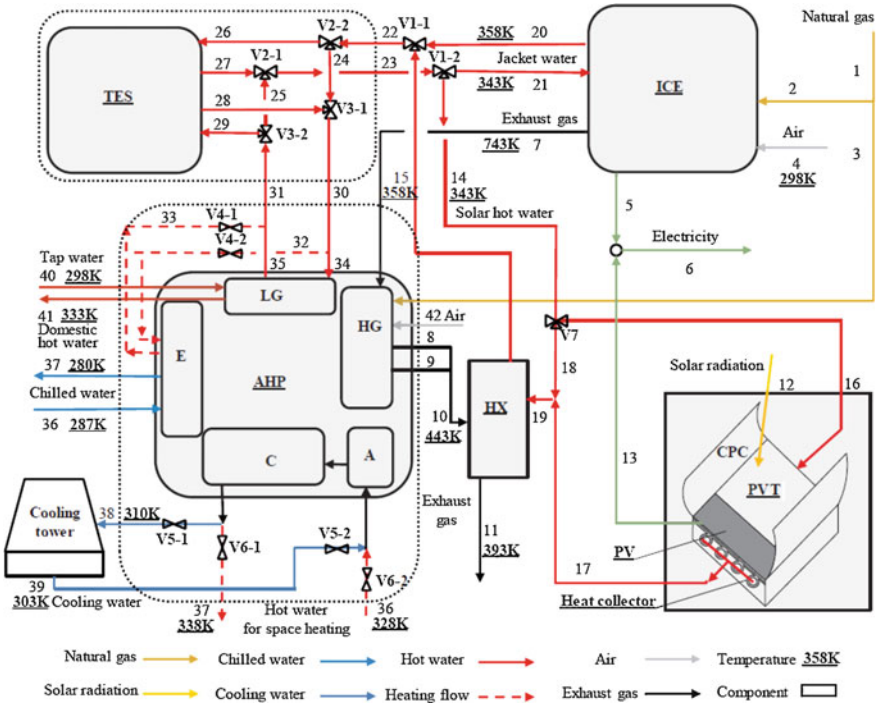

Fig. 4.5 Detailed configuration of solar-integrated CCHP system [14]

The AHP is employed to waste heat recovery purposes. The high-temperature exhaust gas is sent to the high-pressure generator (HG) of the AHP, and then the exhaust gas is cooled in the HX. The recovered heat is utilized to heat the hot water provided by solar energy. The hot water provided by solar power is mixed with the jacket water and will be fed to the low-pressure generator (LG) of AHP. After using waste heat by AHP, the hot water flows back into ICE and CPVT to complete the cycle.

Figure 4.5 is just one of the many possible configurations for solar-driven CCHP systems. Different layouts have been presented and studied in the literature [15–17]. Solar heat can be utilized at a biomass gasifier to generate syngas for driving the system [14]. Additionally, organic Rankine cycles (ORC) can be applied for concentrating solar heat energy, especially when the received temperature is at a lower temperature. ORC is also a reliable option for recovering the waste heat in different parts of the system. Additional research and experiments are required in order to come up with the most effective configuration. Of course, each section and industry has its own specific requirement which should be considered. Energy and most importantly exergy analyses are reliable equipment for this purpose.

4.4 Solar-Driven Desalination Systems

Shortage of drinking water resources has impacted millions of people in most regions of the world, and the World Health Organization's forecasts assess the situation as a threat in the coming future. The nearly constant quantity of Earth's drinking water, the rapid growth in population, and increasing demand for food have put tremendous pressure on the available sources of drinking water. Seawater desalination in many regions of the world is and will be a critical method for solving freshwater shortages.

Numerous scientists have tried to tackle this issue of severe water scarcity by suggesting different methods of desalination in order to turn seawater into freshwater. The suggested approaches, however, require significant amounts of energy, and criteria such as high energy costs and following environmental issues have adversely affected their technical and economic viability [18]. While recent adjustments and developments have concentrated on economizing, improving quality, increasing the product reliability, and improving the sustainability of desalination processes, meeting the energy demand of these systems is most important. Fossil fuels are the main source of energy to drive desalinating processes. Depending on such fuels has brought many problems and, most importantly, greenhouse gas emission. Fortunately, various renewable energy sources are available at the regions where desalination is mostly required. Alternative solutions, e.g., wind, solar, and geothermal, are good options to replace fossil fuels in freshwater production technologies. This has been a great inspiration for scientists to use solar energy in desalination techniques as a safe and sustainable source of energy.

Concentrated solar power (CSP) systems such as solar heliostat fields utilize various mirrors to concentrate the solar irradiation to drive integrated systems. These systems are able to supply enough thermal energy for heating large thermochemical courses [19]. Applying CSP is considered as one of the most interesting and viable options for a sustainable supply of the demanding energy for desalination systems. CSP systems can easily be joint with thermal energy storage systems and are perfect to be combined with renewable or fossil fuel energy sources. These characteristics make CSP an intriguing alternative in large-scale desalination for the production of

freshwater during the year, especially in dry districts with an abundant amount of yearly solar radiation and access to seawater.

Desalination technology is categorized into two main sections: thermal and membrane. Membrane processes employ membranes and consist of three major techniques: electrodialysis (ED), reverse osmosis (RO), and membrane distillation (MD) [20]. The membrane desalination functions with a penetrable body which makes two zones with different concentrations by moving either salt or water. Among three major methods of membrane desalination, RO and ED are electrically driven technologies. On the other hand, MD is driven by thermal energy and therefore has attracted significant attention.

Thermal desalination relies on processes including phase change and contains multistage flash distillation (MSF), multi-effect distillation (MED), humidification-dehumidification (HDH), and thermal vapor compression (TVC) [21]. Solar radiation collectors, including CSP, can be easily integrated with thermal desalination processes. Furthermore, one of the most significant factors to assess the performance of a desalination system is gain output ratio (GOR), which is defined as the amount of produced distilled water to the consumed steam [22]. Due to their high scale of production capacity, RO, MSF, and MED are the most dominant methods, currently.

There have been various proposed configurations for integrated solar energy desalination systems, in the literature. Figure 4.6 illustrates a concept of solar-driven freshwater plant by Tellez et al. [23]. They combined a linear Fresnel solar field with nine-effect MED plants.

The study conducted by Sharaf et al. [24] is another example to show the diversity of available system layouts. They developed two different CSP desalination configurations, presented at Fig. 4.7, and analyzed them from thermodynamic and economic points of view. In configuration (a), the solar heat energy is directly transmitted to the MED unit, while in configuration (b), it utilizes an ORC unit to generate electricity from solar thermal power and uses the produced electricity to drive the MED system. This study concluded that configuration (a), despite of its

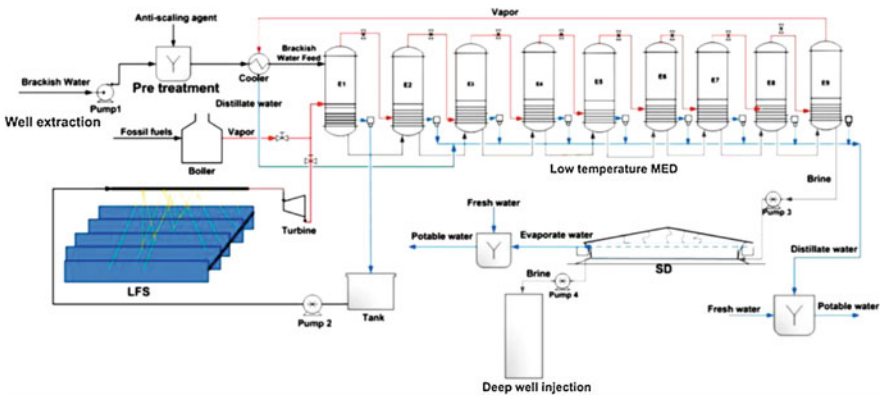

Fig. 4.6 A proposed solar desalination concept [23]

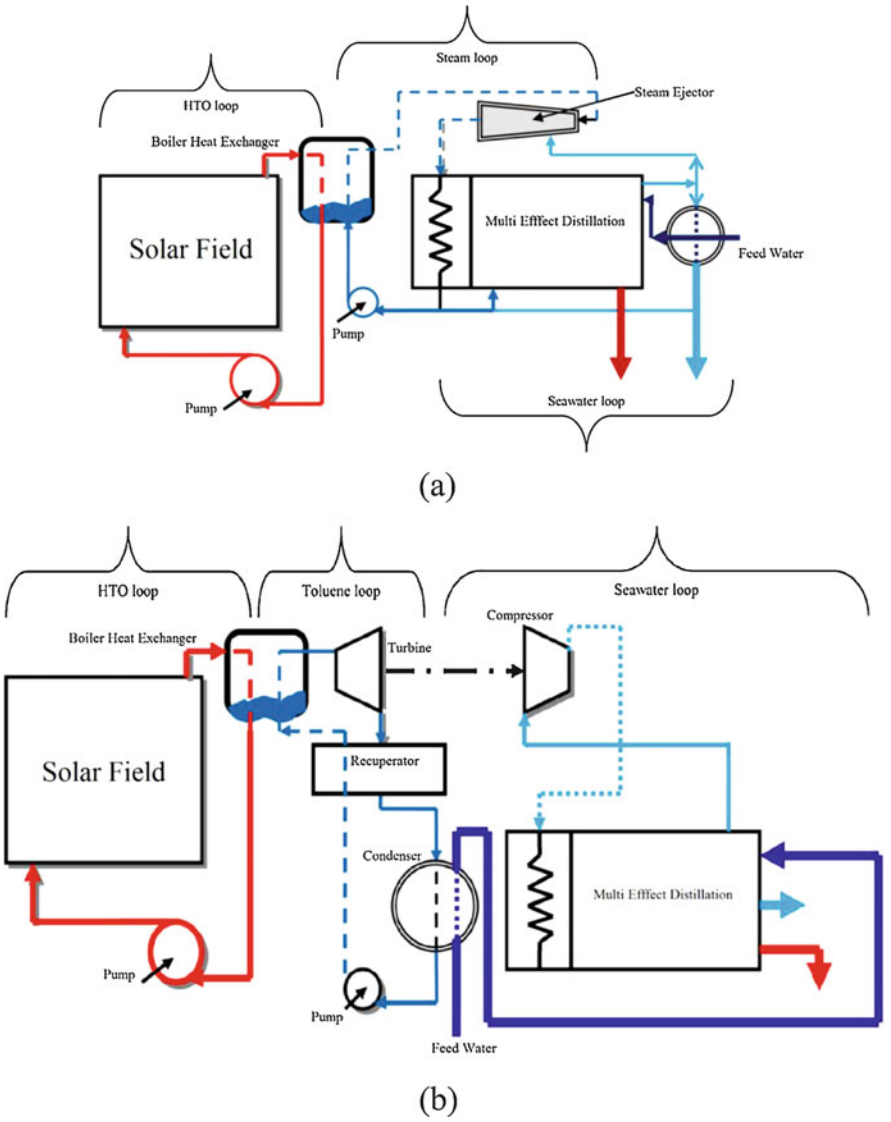

Fig. 4.7 Schematics of proposed configurations by Sharaf et al. [24]

need for larger solar radiation collecting field, is more appealing layout, because of its higher GOR factor and lower production costs.

These few examples and many others [25–27] show that solar radiation can be integrated to desalination systems in numerous ways. All the proposed configurations are efficient, since they reduce the fossil fuel consumption for freshwater production and subsequently lower the final product cost and more importantly the carbon dioxide emission into the atmosphere. A necessary factor for a modern and

sustainable development is to avoid any ecological footprints on the environment. Solar irradiation can also be integrated with other technologies and renewable energy sources, e.g., ORC, heat pumps, geothermal, and biomass. As explained in previous sections, a thorough thermodynamic and economic analysis is required in order to develop the most efficient desalination system.

4.5 Solar-Powered Hydrogen Generation

Increasing the life standards resulted in paying more attention to find and utilize the best available fuels. Starting from coal, to oil, and then finally to natural gas, fossil fuel is one of the base fuels in the industry. On the other hand, we have to find a way to fulfill the ever-increasing energy demand by societies. Therefore, there is a push toward finding new environmentally friendly fuels. It seems that hydrogen is one of the most promising solutions so far. Hydrogen is considered not only as a green fuel but also as an energy career. In addition, hydrogen is the required substance for methanol synthesis in the carbon hydrogenation process [28]. However, it should be highlighted that, to produce hydrogen in a sustainable and economical way, it has to be generated from renewable and clean sources of energy, that is, solar energy. Among all, photocatalytic water splitting can be claimed as the most promising method for this purpose. Solar-driven hydrogen production can be sorted into four main categories: (1) photovoltaic, (2) thermal energy, (3) photo-electrolysis, and (4) bio-photolysis. A simple case of photovoltaic hydrogen production system is shown in Fig. 4.8.

To produce hydrogen via renewable sources, thermal energy and electricity are required, and in fact, the electricity demand by the hydrogen producer system will be supplied through solar energy [29]. In fact, the application of solar energy has not been limited to power, heating, and cooling production, and hydrogen generation with solar energy is one of the most recently developed scenarios to energy storage. To put in a nut shell, electricity is produced by solar energy, and the generated electricity is then utilized in electrolysis for hydrogen production.

These days, employing electrolysis to produce hydrogen is a mature and well-established technology, which grows and develops day by day [30]. In electrolysis,

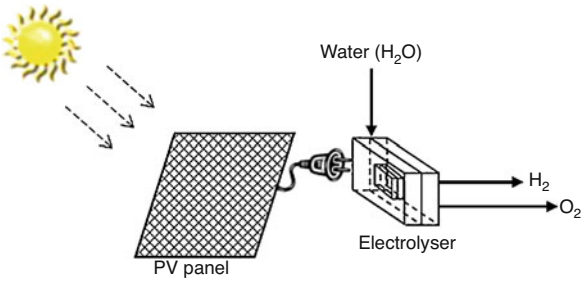

Fig. 4.8 Schematic diagram of a photovoltaic hydrogen production system [29]

H_2O breaks into O_2 (collected at the anode) and H_2 (collected at the cathode) when a DC (direct current) line is passed through it with the aid of electrolyte. Generally, water electrolysis is classified into two main types, namely, proton exchange membrane (PEM) electrolysis and alkaline water electrolysis (AWE) [31]. Both the mentioned electrolyses have their own advantages and disadvantages. For example, AWE is a relatively mature technology compared with PEM, as it operates in lower ranges of DC (200–600 mA/cm^2) and lower efficiency, while PEM operates in higher ranges of DC (1000–2000 mA/cm^2) and higher efficiency [32].

Most of the studies in the field of solar-powered hydrogen production are the thermodynamic and economic analysis of complex energy-converting systems including electrolysis which are fed by the electricity generated by solar energy. Akrami et al. [7] have studied a combination of CPVTs with PEM electrolysis to produce hydrogen, which is shown in Fig. 4.9. They used energy- and exergy-based cost analyses to obtain the unit cost of exergy rate associated with the produced hydrogen. It is worthy of mentioning that the cost of the produced hydrogen is a direct function of the electricity generated from renewables. Then, to provide a cost-effective hydrogen, the economic performance of power systems operating with renewables should be taken into account.

In another study, Moharramian et al. [34] studied a biomass-based power system coupled with a solar-driven hydrogen-producing system. Figure 4.10 illustrates the simplified system considered in this study. As can be seen, they have employed solar panels to produce electricity and run the electrolysis. In this study, advanced exergy analysis is adopted, and exergy destruction is divided into endogenous, exogenous, avoidable, and unavoidable parts. The authors have also considered the environmental impact of injecting the produced hydrogen in the combustion chamber.

4.6 Energy, Exergy, and Exergoeconomic Analysis of Energy-Converting Systems

4.6.1 Energy and Exergy (Thermodynamic) Analysis

In the thermodynamic analysis, the system is a specific region that is separated from everything else through a system boundary or control surface, and this system will be considered as a control volume [35]. The thermodynamic analysis normally consists of energy (the first law) and exergy (the second law) principles. Energy analysis is known as a fundamental concept of thermodynamics. For a closed system, energy can be transferred by heat rate or work, while the total value of energy is conserved in all transfers. Energy different between two points can be stated in terms of the work and heat transfer:

$$(K_2 - K_1) + (P_2 - P_1) + (U_2 - U_1) = \dot{Q}_{CV} - \dot{W}_{CV} \tag{4.4}$$

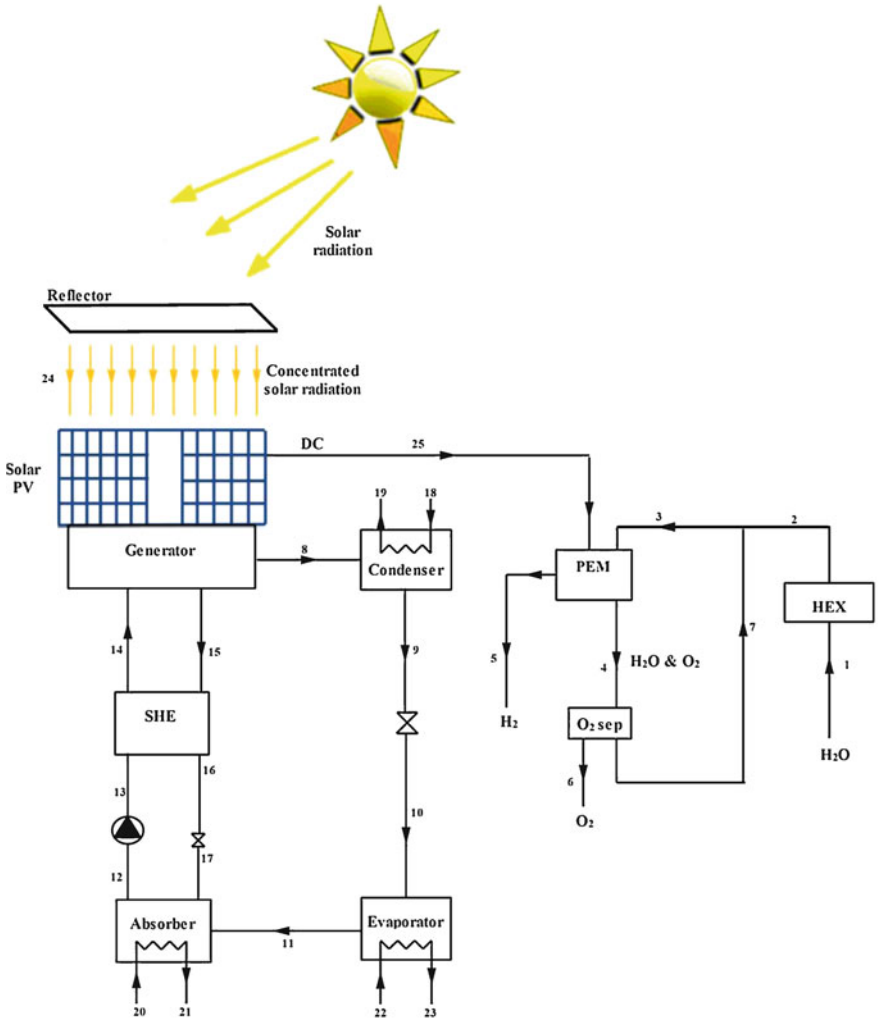

Fig. 4.9 Schematic diagram of the proposed system by Akrami et al. [33]

here, K, P, U, $\dot{Q}$, and $\dot{W}$ refer to kinetic energy, potential energy, internal energy, heat transfer, and work, respectively, while 1 and 2 denote the initial and final points. In most of the energy analysis related to the thermodynamic systems like the energy analysis of a cogeneration system, the kinetic and potential energies are ignored. For example, considering the heat recovery steam generator (HRSG) in Fig. 4.10 as an adiabatic control volume without any power production/consumption, the energy conservation equation can be written as follows:

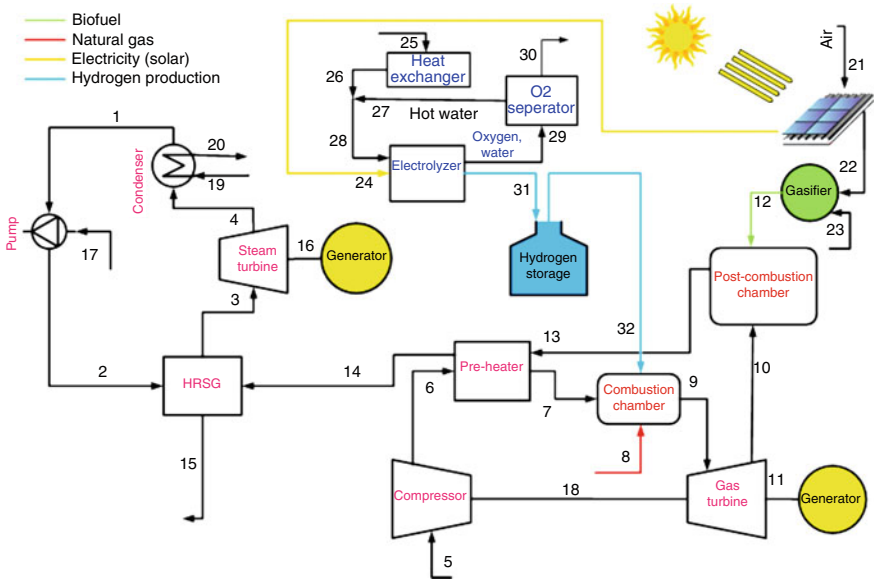

Fig. 4.10 Solar-aided biomass-based energy system presented by Moharramian et al. [34]

$$\dot{m}_2 h_2 + \dot{m}_{14} h_{14} = \dot{m}_3 h_3 + \dot{m}_{15} h_{15}. \tag{4.5}$$

To give a clear understanding of energy or thermal efficiency, the solar-driven system presented in Fig. 4.9 can be considered as an instance. Products of the system in terms of the energy is the generated cooling ($\dot{m}_{22}(h_{22} - h_{23})$) as well the heating value of the produced hydrogen. Meanwhile, the input energy of the system is the absorbed energy by the solar panels. Then, energy rates associated with the products divided by the input energy can be defined as thermal or the first law efficiency. A comprehensive list of energy conservation equations, which can be adopted for different equipment or components can be found in the literature [8, 30, 36–45].

Unlike the energy, exergy is not conserved and may destroy during real thermodynamic processes due to irreversibilities. A thermodynamic process is irreversible if there is no way to completely undo it. In fact, exergy analysis is a powerful tool to determine the exact location and magnitude of irreversibilities (both internal and external) in each energy-converting system. As an example, the system shown in Fig. 4.9, exergy analysis has revealed that the biggest part of irreversibility refers to the PVT unit. To define the exergy in its simplest way, it can be stated that the exergy is a quantity of the departure of each state of the considered system from that of the environment [35].

For the case of power-producing/power-consuming components like turbine/pump, exergy is the maximum theoretical obtainable work (shaft work or electrical work) as the considered systems move toward equilibrium, while heat transfer only occurs with the ambient. On the other hand, exergy is the minimum theoretical

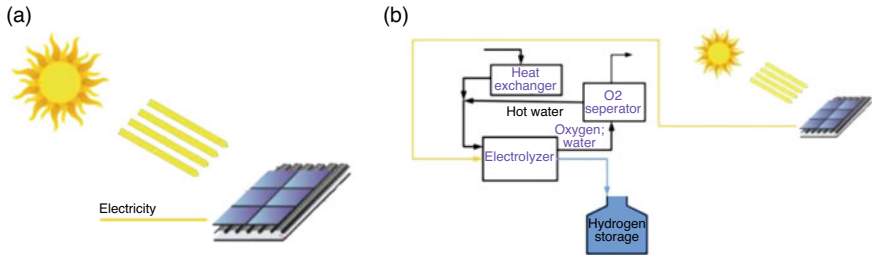

Fig. 4.11 Schematic diagram of a solar-driven (**a**) electricity generation and (**b**) hydrogen generation

required work to form a quantity of matter from materials present in the ambient and while bringing it to a specified state.

Neglecting magnetic nuclear, electrical, and surface tension effects, exergy can be mainly considered in four parts: physical, chemical, kinetic, and potential. The latter two parts have been ignored in most of the solar-driven hydrogen-producing systems. To illustrate a clear view of exergy destruction and exergy (or second law) efficiency of each component employed in the solar-driven energy systems, defining fuel (F) and product (P) exergy streams is of importance. In fact, fuel is the consumed exergy rate to generate the product, while the anticipated output from a component, in terms of exergy, is the product. If one consider Fig. 4.11a as the control volume, fuel exergy is the exergy rate associated with the solar radiation, while the product exergy is the output electricity produced by panels.

Now, suppose that the system shown in Fig. 4.11b (the entire solar-driven hydrogen-producing system) is the considered control volume. In this condition, again, fuel exergy is the exergy rate associated with the solar radiation, but the product exergy is the exergy rate associated with the produced hydrogen.

4.6.2 Exergoeconomic (Thermoeconomic) Analysis

Exergoeconomics is one of the engineering branches that combines conventional exergy analysis with economic principles providing useful information not achievable but exergy or economic principles, separately [46]. In most cases, this information is crucial to the design and operation of a cost-effective system. This method was developed by Tsatsaronis et al. [47] for the first time. Generally, exergoeconomic analysis can be considered as the exergy-aided cost minimization method. Obtaining the unit cost of products in terms of USD per each GJ is the main aim of the exergoeconomic evaluation of energy-converting systems. For example, calculating the unit cost of produced electricity in Fig. 4.11a and the unit cost of produced hydrogen in Fig. 4.11b (as a function of electricity cost) can be claimed as the main target of exergoeconomic analysis. Adopting the cost balance equation can be supposed to be the first step of the exergoeconomic analysis:

$$\dot{C}_{\mathrm{P}} = \dot{C}_{\mathrm{F}} + \dot{Z}_{\mathrm{CI}} + \dot{Z}_{\mathrm{OM}}. \tag{4.6}$$

The cost balance equation states that the cost rate related to the product of each system ($\dot{C}_{\mathrm{P}}$) equals the total cost rates associated with the expenditures made to supply the product, namely, the fuel cost rate ($\dot{C}_{\mathrm{F}}$) and the cost rates in conjunction with capital investment ($\dot{Z}_{\mathrm{CI}}$) and operating and maintenance ($\dot{Z}_{\mathrm{OM}}$). In the equation above,

$$\dot{C}_i = c_i \dot{\varphi}_i \tag{4.7}$$

where c_i is the average cost per unit of exergy in dollars per gigajoule ($/GJ).

In fact, the exergoeconomic analysis formulation of the cost balance equation consists of cost balance equations usually formulated for the employed components in the system, separately. Each of the adopted cost balance equations reveals that the sum of cost rates associated with all entering exergy streams plus the associate charges related to the capital investment, operating, and maintenance cost equals the sum of cost rates associated with all exiting exergy streams.

$$\sum \dot{C}_e + \dot{C}_w = \dot{C}_q + \sum \dot{C}_i + \dot{Z}. \tag{4.8}$$

Considering the simple power-producing system in Fig. 4.11a, the cost balance equation can be written as follows:

$$\dot{C}_{\mathrm{electricity}} = \dot{C}_{\dot{Q}_{\mathrm{sun}}} + \dot{Z} \tag{4.9}$$

This equation states that the cost rate of the produced power is the combination of cost rate related to the solar radiation (which is zero) and the cost rate of the panel's capital investment cost.

4.7 Conclusion

In this chapter, recently developed solar-driven energy systems are introduced, including solar-powered (or solar-aided), cooling, heating, and hydrogen production systems and water desalination systems as well. Naturally, solar energy has known as the most available renewable energy source. However, it suffers from the irregular profiles of availability since providing an accurate long-term estimate of its fluctuations is almost impossible. To solve this problem, energy storage technologies can be combined with solar-driven energy system, and that is why the hydrogen generation systems were introduced in the present chapter. On the other hand, to design an energy-converting system, not only thermodynamic principles but also economic concerns should be addressed. Therefore, exergoeconomic methodology (an exergy-based cost analysis) is proposed in this chapter.

References

1. Neri, M., Luscietti, D., & Pilotelli, M. (2017). Computing the exergy of solar radiation from real radiation data. *Journal of Energy Resources Technology, 139*(6), 1–7.
2. Jamil, B., & Bellos, E. (2019). Development of empirical models for estimation of global solar radiation exergy in India. *Journal of Cleaner Production, 207*, 1–16.
3. Chu, S. X., & Liu, L. H. (2009). Analysis of terrestrial solar radiation exergy. *Solar Energy, 83* (8), 1390–1404.
4. Petela, R. (2003). Exergy of undiluted thermal radiations. *Solar Energy, 74*(6), 469–488.
5. Arslanoglu, N. (2016). Empirical modeling of solar radiation exergy for Turkey. *Applied Thermal Engineering, 108*, 1033–1040.
6. Edalati, S., Ameri, M., Iranmanesh, M., & Tarmahi, H. (2016). Modelling and drawing energy and exergy of solar radiation. *International Journal of Exergy, 19*(4), 544–568.
7. Akrami, E., Nemati, A., Nami, H., & Ranjbar, F. (2018). Exergy and exergoeconomic assessment of hydrogen and cooling production from concentrated PVT equipped with PEM electrolyzer and LiBr-H2O absorption chiller. *International Journal of Hydrogen Energy, 43* (2), 622–633.
8. Nami, H., Ertesvåg, I. S., Agromayor, R., Riboldi, L., & Nord, L. O. (2018). Gas turbine exhaust gas heat recovery by organic Rankine cycles (ORC) for offshore combined heat and power applications - energy and exergy analysis. *Energy, 165*, 1060–1071.
9. Herrando, M., Pantaleo, A. M., Wang, K., & Markides, C. N. (2019). Solar combined cooling, heating and power systems based on hybrid PVT, PV or solar-thermal collectors for building applications. *Renewable Energy, 143*, 637–647.
10. Jafari Mosleh, H., Hakkaki-Fard, A., & DaqiqShirazi, M. (2019). A year-round dynamic simulation of a solar combined, ejector cooling, heating and power generation system. *Applied Thermal Engineering, 153*, 1–14.
11. Nami, H., Arabkoohsar, A., & Anvari-Moghaddam, A. (2019). Thermodynamic and sustainability analysis of a municipal waste-driven combined cooling, heating and power (CCHP) plant. *Energy Conversion and Management, 201*, 112158.
12. Wang, J., Chen, Y., Lior, N., & Li, W. (2019). Energy, exergy and environmental analysis of a hybrid combined cooling heating and power system integrated with compound parabolic concentrated-photovoltaic thermal solar collectors. *Energy, 185*, 463–476.
13. Wang, J., Chen, Y., & Lior, N. (2019, August). Exergo-economic analysis method and optimization of a novel photovoltaic/thermal solar-assisted hybrid combined cooling, heating and power system. *Energy Conversion and Management, 199*, 111945.
14. Wang, J., Ma, C., & Wu, J. (2019, December). Thermodynamic analysis of a combined cooling, heating and power system based on solar thermal biomass gasification☆. *Applied Energy, 247*, 102–115.
15. Abdollahi Haghghi, M., Mehdi Pesteei, S., Chitsaz, A., & Hosseinpour, J. (2019, March). Thermodynamic investigation of a new combined cooling, heating, and power (CCHP) system driven by parabolic trough solar collectors (PTSCs): A case study. *Applied Thermal Engineering, 163*, 114329.
16. Ahn, H., Rim, D., Pavlak, G. S., & Freihaut, J. D. (2019, May). Uncertainty analysis of energy and economic performances of hybrid solar photovoltaic and combined cooling, heating, and power (CCHP + PV) systems using a Monte-Carlo method. *Applied Energy, 255*, 113753.
17. Chang, H., Duan, C., Xu, X., Pei, H., Shu, S., & Tu, Z. (2018). Technical performance analysis of a micro-combined cooling, heating and power system based on solar energy and high temperature PEMFC. *International Journal of Hydrogen Energy, 44*(38), 21080–21089.
18. Rafiei, A., Alsagri, A. S., Mahadzir, S., Loni, R., Najafi, G., & Kasaeian, A. (2019, August). Thermal analysis of a hybrid solar desalination system using various shapes of cavity receiver: Cubical, cylindrical, and hemispherical. *Energy Conversion and Management, 198*, 111861.
19. Abbasi, H. R., Pourrahmani, H., Yavarinasab, A., Emadi, M. A., & Hoorfar, M. (2019, September). Exergoeconomic optimization of a solar driven system with reverse osmosis

desalination unit and phase change material thermal energy storages. *Energy Conversion and Management, 199*, 112042.
20. Mito, M. T., Ma, X., Albuflasa, H., & Davies, P. A. (2019, May). Reverse osmosis (RO) membrane desalination driven by wind and solar photovoltaic (PV) energy: State of the art and challenges for large-scale implementation. *Renewable and Sustainable Energy Reviews, 112*, 669–685.
21. Filippini, G., Al-Obaidi, M. A., Manenti, F., & Mujtaba, I. M. (2019, March). Design and economic evaluation of solar-powered hybrid multi effect and reverse osmosis system for seawater desalination. *Desalination, 465*, 114–125.
22. Mohammadi, K., Saghafifar, M., Ellingwood, K., & Powell, K. (2019, August). Hybrid concentrated solar power (CSP)-desalination systems: A review. *Desalination, 468*, 114083.
23. Téllez, D., et al. (2009). Evaluation of technologies for a desalination operation and disposal in the Tularosa Basin, New Mexico. *Desalination, 249*(3), 983–990.
24. Sharaf, M. A., Nafey, A. S., & García-Rodríguez, L. (2011). Thermo-economic analysis of solar thermal power cycles assisted MED-VC (multi effect distillation-vapor compression) desalination processes. *Energy, 36*(5), 2753–2764.
25. Shafieian, A., & Khiadani, M. (2019, November). A novel solar-driven direct contact membrane-based water desalination system. *Energy Conversion and Management, 199,* 112055.
26. Shaaban, S. (2019, April). Performance optimization of an integrated solar combined cycle power plant equipped with a brine circulation MSF desalination unit. *Energy Conversion and Management, 198*, 111794.
27. Abdelgaied, M., Kabeel, A. E., & Zakaria, Y. (2019, July). Performance improvement of desiccant air conditioner coupled with humidification-dehumidification desalination unit using solar reheating of regeneration air. *Energy Conversion and Management, 198*, 111808.
28. Nami, H., Ranjbar, F., & Yari, M. (2019). Methanol synthesis from renewable H2 and captured CO2 from S-Graz cycle – Energy, exergy, exergoeconomic and exergoenvironmental (4E) analysis. *International Journal of Hydrogen Energy, 44*(48), 26128–26147.
29. Dincer, I., & Joshi, A. S. (2013). *Solar based hydrogen production systems*. New York: Springer.
30. Nami, H., Ranjbar, F., & Yari, M. (2018). Thermodynamic assessment of zero-emission power, hydrogen and methanol production using captured CO 2 from S-Graz oxy-fuel cycle and renewable hydrogen. *Energy Conversion and Management, 161*, 53–65.
31. Asif, M., Gao, X., Lv, H., Xi, X., & Dong, P. (2018). Catalytic hydrogenation of CO2 from 600 MW supercritical coal power plant to produce methanol: A techno-economic analysis. *International Journal of Hydrogen Energy, 43*(5), 2726–2741.
32. Stojić, D. L., Grozdić, T. D., Umićević, B., & Maksić, A. D. (2008). A comparison of alkaline and proton exchange membrane electrolyzers. *Russian Journal of Physical Chemistry A, 82* (11), 1958–1960.
33. Akrami, E., Nemati, A., Nami, H., & Ranjbar, F. (2018). Exergy and exergoeconomic assessment of hydrogen and cooling production from concentrated PVT equipped with PEM electrolyzer and LiBr-H 2 O absorption chiller. *International Journal of Hydrogen Energy, 43*(2), 1–12.
34. Moharramian, A., Soltani, S., Rosen, M. A., Mahmoudi, S. M. S., & Bhattacharya, T. (2019). Modified exergy and modified exergoeconomic analyses of a solar based biomass co-fired cycle with hydrogen production. *Energy, 167*, 715–729.
35. Bejan, A., & Tsatsaronis, G. (1996). *Thermal design and optimization*. New York: John Wiley & Sons.
36. Akrami, E., Chitsaz, A., Nami, H., & Mahmoudi, S. M. S. (2017). Energetic and exergoeconomic assessment of a multi-generation energy system based on indirect use of geothermal energy. *Energy, 124*, 625–639.

37. Nami, H., & Akrami, E. (2017). Analysis of a gas turbine based hybrid system by utilizing energy, exergy and exergoeconomic methodologies for steam, power and hydrogen production. *Energy Conversion and Management, 143*, 326–337.
38. Nami, H., & Arabkoohsar, A. (2019). Improving the power share of waste-driven CHP plants via parallelization with a small-scale Rankine cycle, a thermodynamic analysis. *Energy, 171*, 27–36.
39. Nami, H., Ranjbar, F., Yari, M., & Saeidi, S. (2016). Thermodynamic analysis of a modified oxy-fuel cycle, high steam content Graz cycle with a dual-pressure heat recovery steam generator. *International Journal of Exergy, 21*(3), 331–346.
40. Nemati, A., Nami, H., & Yari, M. (2018). Assessment of different configurations of solar energy driven organic flash cycles (OFCs) via exergy and exergoeconomic methodologies. *Renewable Energy, 115*, 1231–1248.
41. Nami, H., Mahmoudi, S. M. S., & Nemati, A. (2017). Exergy, economic and environmental impact assessment and optimization of a novel cogeneration system including a gas turbine, a supercritical CO2 and an organic Rankine cycle (GT-HRSG/SCO2). *Applied Thermal Engineering, 110*, 1315–1330.
42. Saeidi, S., Mahmoudi, S. M. S., Nami, H., & Yari, M. (2016). Energy and exergy analyses of a novel near zero emission plant: Combination of MATIANT cycle with gasification unit. *Applied Thermal Engineering, 108*, 893–904.
43. Nami, H., Akrami, E., & Ranjbar, F. (2017). Hydrogen production using the waste heat of benchmark pressurized molten carbonate fuel cell system via combination of organic Rankine cycle and proton exchange membrane (PEM) electrolysis. *Applied Thermal Engineering, 114*, 631–638.
44. Nemati, A., Nami, H., Ranjbar, F., & Yari, M. (2017). A comparative thermodynamic analysis of ORC and Kalina cycles for waste heat recovery: A case study for CGAM cogeneration system. *Case Studies in Thermal Engineering, 9*, 1–13.
45. Nami, H., Mohammadkhani, F., & Ranjbar, F. (2016). Utilization of waste heat from GTMHR for hydrogen generation via combination of organic Rankine cycles and PEM electrolysis. *Energy Conversion and Management, 127*, 589–598.
46. Aali, A., Pourmahmoud, N., & Zare, V. (2017). Exergoeconomic analysis and multi-objective optimization of a novel combined flash-binary cycle for Sabalan geothermal power plant in Iran. *Energy Conversion and Management, 143*, 377–390.
47. Tsatsaronis, G., Lin, L., & Pisa, J. (1993). Exergy costing in exergoeconomics. *Journal of Energy Resources Technology, 115*(1), 9–16.

Chapter 5
Design and Evaluation of a New Solar Tower-Based Multi-generation System: Part I, Thermal Modeling

Hamed Ghiasirad, Hadi Rostamzadeh, and Sajjad Nasri

Nomenclature

Symbols

C	Concentration ratio
h	Enthalpy (kJ. kg^{-1}), convection coefficient (W/m^2K)
K	Conductivity (W/m.K)
L	Length of tube (m)
S	Supercritical
T	Temperature (K), transcritical
V	Wind velocity (m/s)
X	Salinity (g. kg^{-1})

Abbreviations

F_r	View factor
HTR	High-temperature recuperator
HU	Heating unit
LTR	Low-temperature recuperator
MC	Main compressor
MFR	Mass flow ratio
PPTD	Pinch point temperature difference (K)
RC	Recompression compressor
STP	Solar tower power

H. Ghiasirad (✉) · S. Nasri
Department of Mechanical Engineering, Faculty of Engineering, Sahand University of Technology, Tabriz, Iran

H. Rostamzadeh
Energy and Environment Research Center, Niroo Research Institute (NRI), Shahrak Ghods, Tehran, Iran

F. Jabari et al. (eds.), *Integration of Clean and Sustainable Energy Resources and Storage in Multi-Generation Systems*,
https://doi.org/10.1007/978-3-030-42420-6_5

Greek Letters

δ Thickness (m)
ε Effectiveness, emissivity
η Efficiency (%)
λ Conductivity (W/m.K)
μ Viscosity (Pa.s)
ω Humidity
ρ Reflectivity, density (kg/m^3)

Subscripts and Superscripts

Ape	Aperture
em	Emissive
Dhum	Dehumidifier
fc	Forced convection
Gen	Generator
Hum	Humidifier
H, Hel	Heliostat
Insi	Inner side of receiver
Insu	Insulation
is	Isentropic
ms	Molten salt
nc	Natural convection
ref	Reflection
Sur	Surface
sw	Seawater
TC	Transcritical compressor
W	Wall

5.1 Introduction

Galloping consumption of energy around the world has captivated attention of many scholars to design more efficacious energy conversion systems. While many sectors in industry convert the available energy from one form to another more useful form, the conversion of energy in power plants is highly crucial in the developed civilization today. Numerous schemes are devised to further increase power plant efficiency with considering cost aspect of the procedure, where among all using renewable energy has received a well agreement benefit [1, 2].

Among disparate renewable sources, solar energy has widespread applications in high-tech energy conversion systems. Recently, burgeoning growth in development of the concentrating solar power (CSP) technologies have decreased the initial capital costs associated with the installation at wide areas. Among different tools developed to further extend applicability of CSP technologies, thermal, exergy, and cost analysis are highly commendable tools for performance evaluation of the solar

systems. As the major topic of this chapter covers thermal modeling of an innovative solar-based energy systems and the next chapter covers the exergy and exergy-based cost evaluation of the devised system, thermal modeling part of the solar-based systems is spotlighted.

Multi-generation or poly-generation energy conversion systems preeminently refer to the integrated or combined energy systems which produce several useful forms of energy from the same heat source by managing energy losses associated with different sectors of the plant. The term "combined" or "integrated" should be used more carefully in this regard since each has different meaning in energy systems; nonetheless, they may have been used exchangeably in literature. The term "combined energy system" refers to a proper combination of basic energy units in a way to decrease external waste of energy associated with external flow directing into or out of each subunit. The design procedure associated with this arrangement can be fulfilled by applying pinch technology methods or similar concepts in design of a heat exchanger since heat exchangers are the main part of this combination. In this configuration, any mismatching between cold and hot streams may lead to an evenly huge waste thermal heat and hence the meaning of the combination may be lost. Of course, power generation elements such as turbine and power user components such as compressors/pumps can be externally combined by directing a specific generated power of turbine into a compressor which is mainly more meaningful in pure mechanical-driven energy systems such as mechanical compression cooling (MCC) systems. Referring to the second part of the category, the integrated energy systems deal with the internal misarrangements which lead to low energy conversion performance. Special care must be taken in terms of dealing with such integral energy systems since the configuration is real novel, and inspecting the first law of thermodynamics is indeed a matter of concern. The design procedure related to this type of energy systems can be complex in some scenarios, and hence a proper and practical numerical solution should be performed. In this chapter, we have deliberately used both terms in their proper way in order to prevent any vague understanding. Based upon the discussed terms, a new definition can be proposed for multi-generation systems. Broadly speaking, a multi-generation system refers to an integrated or a combined energy system which is composed of at least two subsystems joined to each other internally or externally to produce two or several different useful forms of energy from a unit heat source.

Based upon the above definition, a combined multi-generation system driven by a solar tower power (STP) setup is devised in this chapter to support the arrangement of the main system in terms of energy or thermal modeling as well as exergy and economic. Thermal modeling of the devised multi-generation system is presented in this chapter and its exergy and economic modeling is delivered in the next chapter. Before we proceed further, it is imperious to elaborate on thermal modeling of the solar-based multi-generation systems carried out in recent years.

Yilmaz [3] devised a new multi-generation system for electricity, cooling/heating, hydrogen, and freshwater production using solar energy absorbed via a solar heliostat. The devised system was composed of a Brayton cycle (BC), an organic Rankine cycle (ORC), a Rankine cycle (RC), a flash desalination unit, an absorption cooling/heating unit, and proton exchange membrane (PEM)

electrolyzer. Based upon the thermal modeling presented, the author has reported thermal efficiency of 78.93% with freshwater production of 0.8862 kg/s and with total power capacity of 18,992 kW. They recommended more study should be performed on the solar field from exergy viewpoint.

Yuksel et al. [4] used absorbed heat of a STP plant as a prime mover of a new multi-generation system to produce hydrogen, liquefaction, hot water, freshwater water, cooling, and heating. They reported a thermal performance of 65.1% and concluded that the solar intensity is the most influential parameter in their designed system.

Yilmaz et al. [5] designed a new multi-generation system driven by a STP plant for multiproductions of electricity, cooling, heating, hydrogen, drying products, and liquefaction. They used a gas turbine (GT) cycle as the top cycle operated with the solar energy instead of the conventional combustion firing. They reported thermal performance of 60.14% and pinpointed that the solar intensity and pinch point temperature difference (PPTD) of the heat recovery steam generator (HRSG) have a dominant effect.

Wu et al. [6] designed a new multi-generation system by using a STP plant to supply the required load of the biomass gasification. Despite high thermal efficiency of 44.26%, they found that the intermittency of solar energy can be serious problem in their devised system due to the presence of the chemical energy storage module.

El-Emam and Dincer [7] used heliostat solar system for power generation via a steam turbine, freshwater production via a reverse osmosis (RO) unit, cooling via an absorption chiller cycle (ACC), and hydrogen via water electrolysis. They supplied water production of 90 kg/s and hydrogen generation of 1.25 kg/h for the related users.

In the light of reviewed literature, it is evident that capturing solar energy for electricity, cooling, heating, and freshwater generation is an urgent solution, especially in arid and semiarid regions. Regarding this requirement, several studies have considered this idea and have proposed new multi-generation system to produce such products. The devised multi-generation is composed of a STP plant, a supercritical CO_2 (S-CO_2) power cycle, a transcritical CO_2 (T- CO_2) refrigeration cycle, and a humidification-dehumidification (HDH) unit. The current devised multi-generation system has revealed a promising outcome in terms of thermal efficiency which is competitive from different perspectives. It should be noted that using some portion of the generated electricity instead of thermal energy of S-CO_2 refrigeration cycle is another alternative resolution in the combined energy system which is investigated in this chapter. This deliberation prevents further complexity of the multi-generation systems and increases reliability and availability of the setup since the required electricity can be replaced by the network electricity in the case of shutdown. The rest of this chapter is arranged in the following order. In Sect. 5.5.2, a brief description of the layout is presented. In Sect. 5.5.3, all employed thermal mathematical relations and presumptions are displayed. In Sect. 5.4, results are presented and discussed extensively. Finally, some concluding comments are listed in Sect. 5.5.

5.2 Setup Description

The overall layout of the devised solar-based multi-generation system is displayed in Fig. 5.1. The setup encompasses from four subsets of a STP plant, a supercritical CO_2 power cycle, a T-CO_2 refrigeration cycle, and a HDH unit. Molten salt is used as circulating refrigerant through the STP plant without considering a thermal storage tank due to the steady characteristics of the problem.

STP plant includes two subcomponents of a heliostat field and a central receiver. Heliostats receive solar irradiances and reflect them into the aperture region of the central receiver at the top of a tower, using a tracking unit for each heliostat. The receiver becomes hotter as the solar rays are concentrated on its center. Molten salt is used as refrigerant flowing through the pipes inside the receiver. The heated molten

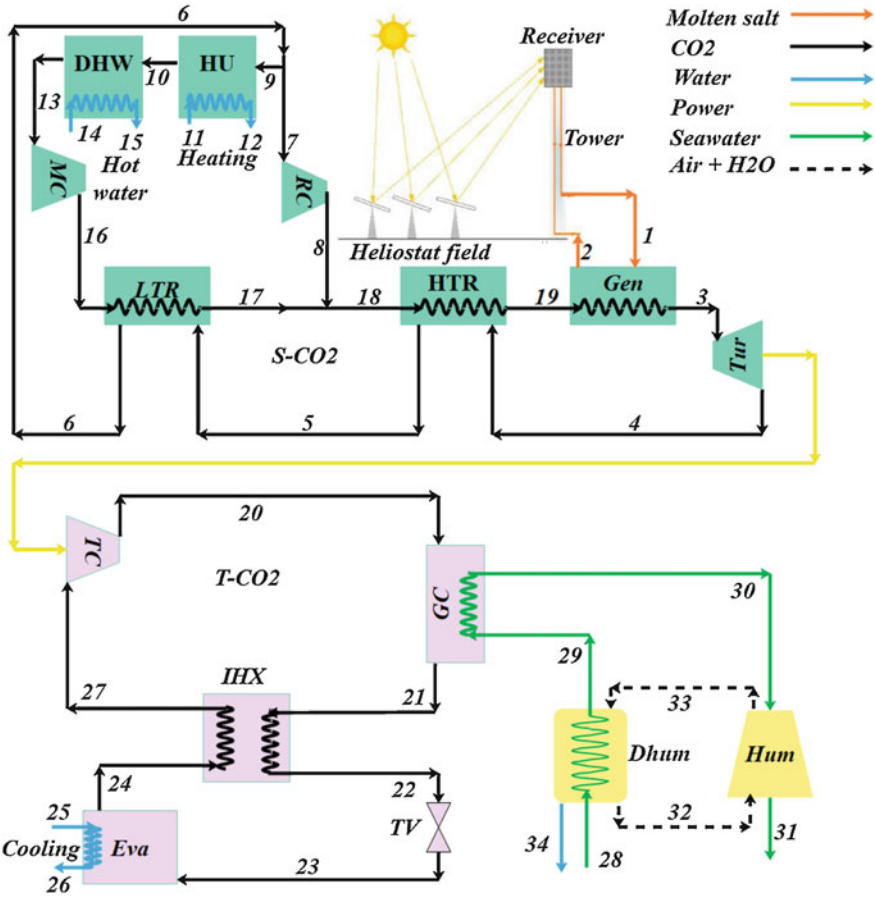

Fig. 5.1 Layout of the devised combined multi-generation system driven by a STP plant

salt is directed to the generator (Gen) and provides required heating load of the S-CO_2 power cycle. Then, the flow is directed back to the receiver.

In S-CO_2 power cycle, the system encompasses a generator, a turbine, a low-temperature recuperator (LTR), a high-temperature recuperator (HTR), a main compressor (MC), an auxiliary compressor or a recompression (RC), a heating unit (HU), and a DHW unit. As the generator receives high-temperature thermal load from the STP plant, the supercritical CO_2 rotates through the turbine to generate electricity and is cooled through two processes by the HTR and LTR to heat the two compressed flows. The cooled stream is split into two flows. One stream flows into the HU to produce the required heating load of the user and then is precooled via a DHW unit prior to the compression process. The flow is compressed through the MC and is heated up through the LTR and is mixed with the rest of the split stream (compressed by RC). The mixed stream is heated up through the HTR and is fed into the generator.

In T-CO_2 refrigeration cycle, a compressor, a gas cooler (GC), an internal heat exchanger (IHX), an evaporator, and a throttling valve (TV) are employed. The supercritical CO_2 is directed to the compressor to boost fluid pressure by consuming some external power supplied by the turbine and then chilled through the gas cooler (GC) at the same pressure. The discarded heating load from the gas cooler is used to provide heating demand of a simple HDH unit. The refrigerant at the outlet of the GC is further cooled via an IHX and then is expanded through a TV. The expanded two-phase stream is vaporized through the evaporator to provide required refrigeration load of the users. The chilled stream is flowed back to the IHX and is directed into the compressor again.

As T-CO_2 refrigeration cycle exchanges its waste heating capacity via a gas cooler with seawater at the HDH side, HDH unit begins its working process. In this study, a basic closed-air open-water (CAOW) HDH unit is used since it has higher efficiency in comparison with its basic closed-water open-air (CWOA) counterpart [8]. As saline water is dehumidified through stage 28→29, it is heated up to the maximum accessible of desalination temperature and is sprayed in a humidifier while leaving it. At the same time, air experiences a successive humidification and dehumidification processes through a closed loop in order to provide evaporation and condensation processes of the seawater. Ultimately, freshwater can be distillated through this integral process via a natural process.

5.3 Materials and Methods

Overall, in this section, simulation procedure, presumptions, and relations based on energy/thermal concept are presented. In the first subsection, all relations required for simulation of a STP plant are presented. In the second subsection, thermal presumptions are expressed on the basis of the first law of thermodynamics. Ultimately, the main thermal performance relations are extended.

5.3.1 Solar Tower Formulae

Steady mathematical modeling of the solar tower power plant is presented in this section. To better understand the modeling, the structure of the receiver is shown in Fig. 5.2. The receiver absorbs $\dot{Q}_{\text{rec}}$ from the heliostat field and transfers part of it to the molting salt fluid, while the rest is lost to the ambient by emission, reflection, convection, and conduction, all are expressed as $\dot{Q}_{\text{rec,totloss}}$ [9].

5.3.1.1 Heliostat

Heliostat field receives solar radiation as [11]:

$$\dot{Q}_{\text{Hel}} = A_h.\text{DNI} \tag{5.1}$$

where A_h is the total heliostat aperture area and DNI stands for the direct normal irradiation. The total energy that the receiver absorbs from the heliostat is given in terms of the heat absorbed by the receiver ($\dot{Q}_{\text{rec,abs}}$) and total lost heat ($\dot{Q}_{\text{rec,totloss}}$) as [10]:

$$\dot{Q}_{\text{rec}} = \dot{Q}_{\text{rec,abs}} + \dot{Q}_{\text{rec,totloss}} \tag{5.2}$$

where

$$\dot{Q}_{\text{rec,abs}} = \dot{m}_{\text{ms}} c_{\text{p,ms}} (T_{\text{ms,out}} - T_{\text{ms,in}}) \tag{5.3}$$

where subscript ms stands for the molten salt. The total heat loss includes emissive (em), reflective (ref), convective (conv), and conductive (con) heat loss as follows [10]:

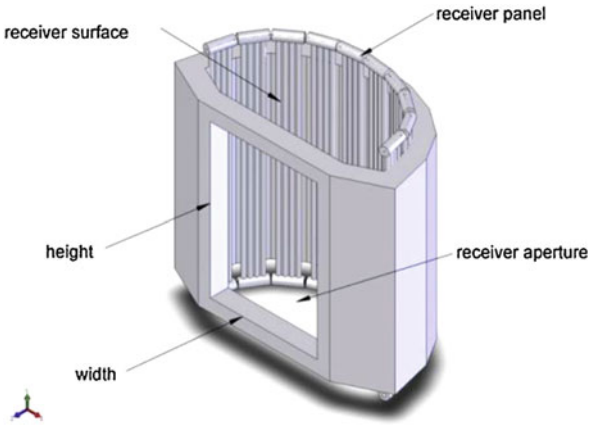

Fig. 5.2 Schematic of the receiver [10]

$$\dot{Q}_{\text{rec,totloss}} = \dot{Q}_{\text{rec,em}} + \dot{Q}_{\text{rec,ref}} + \dot{Q}_{\text{rec,conv}} + \dot{Q}_{\text{rec,con}} \tag{5.4}$$

The total energy efficiency of the central receiver can be articulated as:

$$\eta_{\text{rec}} = 1 - \frac{\dot{Q}_{\text{rec,totloss}}}{\dot{Q}_{\text{rec}}} = \frac{\dot{Q}_{\text{rec,abs}}}{\dot{Q}_{\text{rec}}} \tag{5.5}$$

5.3.1.2 Receiver Surface Temperature

Before we calculate total losses associated with the receiver, it is imperious to calculate the receiver surface temperature as [10]:

$$T_{\text{rec,sur}} = \frac{\dot{Q}_{\text{rec}}}{\frac{A}{F_r \cdot C}} \left[\frac{d_{\text{out}}}{d_{\text{in}} h_{\text{ms}}} + \frac{d_{\text{out}}}{2k_{\text{tube}}} \ln \frac{d_{\text{out}}}{d_{\text{in}}} \right] + T_{\text{ms}} \tag{5.6}$$

where T_{ms} is the characteristic temperature and $T_{\text{ms}} = (T_{\text{ms, in}} + T_{\text{ms, out}})/2$. d_{in} is the characteristic length. h_{ms} is the convective heat transfer coefficient of the molten salt in the absorber tube and is defined as [9]:

$$h_{\text{ms}} = 0.023 \frac{k_{\text{ms}}}{d_{\text{in}}} Re_{\text{ms}}^{0.8} Pr_{\text{ms}}^{0.4} \tag{5.7}$$

where k_{ms} is the thermal conductivity of the molten salt and can be found as [11]:

$$k_{\text{ms}} \left[\frac{W}{m.K} \right] = 0.443 + 1.9 \times 10^{-4} \times T_{\text{ms}} \left[^{\circ}\text{C} \right] \tag{5.8}$$

Density, specific heat, and absolute viscosity of the molten salt are also required to obtain Prandtl number (Pr) and Reynolds number (Re), which are calculated, respectively, as follows [9, 11]:

$$\rho_{\text{ms}} \left[\frac{\text{kg}}{\text{m}^3} \right] = 2090 - 0.636 \times T_{\text{ms}} \left[^{\circ}\text{C} \right] \tag{5.9}$$

$$c_{\text{p,ms}} \left[\frac{\text{J}}{\text{kg.K}} \right] = 1443 + 0.172 \times T_{\text{ms}} \left[^{\circ}\text{C} \right] \tag{5.10}$$

$$\begin{aligned} \mu_{\text{ms}} \left[\frac{\text{J}}{\text{kg.K}} \right] = \big(& 22.714 - 0.12 \times T_{\text{ms}} \left[^{\circ}\text{C} \right] + 2.281 \times 10^{-4} \times T_{\text{ms}}^2 \left[^{\circ}\text{C} \right] \\ & - 1.474 \times 10^{-7} \times T_{\text{ms}}^3 \left[^{\circ}\text{C} \right] \big) \times 10^{-6} \end{aligned} \tag{5.11}$$

5.3.1.3 Emissive Heat Loss

Only the heat transfer between the aperture and receiver surface is accounted as follows [11]:

$$\dot{Q}_{\mathrm{rec,em}} = \frac{\varepsilon_{\mathrm{avg}}\sigma\left(T_{\mathrm{rec,sur}}^4 - T_{\mathrm{air}}^4\right)A_{\mathrm{field}}}{C} \tag{5.12}$$

where C is the concentration ratio and $\sigma = 5.67 \times 10^{-8}$ W. m^{-2}K^{-4} is the Stefan-Boltzmann constant. $\varepsilon_{\mathrm{avg}}$ and F_{r} are the average emissivity and view factor given, respectively, by [9]:

$$\varepsilon_{\mathrm{avg}} = \frac{\varepsilon_{\mathrm{w}}}{\varepsilon_{\mathrm{w}} + (1 - \varepsilon_{\mathrm{w}})F_{\mathrm{r}}} \tag{5.13}$$

$$F_{\mathrm{r}} = \frac{A_{\mathrm{ape}}}{A_{\mathrm{field}}} \tag{5.14}$$

In Eq. (5.14), A_{ape} is the aperture area.

5.3.1.4 Reflective Heat Loss

Reflective heat loss due to the surface reflectivity and view factor without considering the receiver surface reflectivity with the receiver surface temperature can be expressed as [10]:

$$\dot{Q}_{\mathrm{rec,ref}} = \dot{Q}_{\mathrm{rec}}.F_{\mathrm{r}}.\rho \tag{5.15}$$

where ρ is the surface reflectivity.

5.3.1.5 Convective Heat Loss

Convective heat loss includes both forced and natural convection heat transfer as [9, 10]:

$$\dot{Q}_{\mathrm{rec,conv}} = \dot{Q}_{\mathrm{rec,conv,fc}} + \dot{Q}_{\mathrm{rec,conv,nc}} \tag{5.16}$$

where

$$\dot{Q}_{\mathrm{rec,conv,fc}} = h_{\mathrm{air,fc,insi}}\left(T_{\mathrm{rec,sur}} - T_0\right)\frac{A_{\mathrm{field}}}{C} \tag{5.17}$$

$$\dot{Q}_{\mathrm{rec,conv,nc}} = h_{\mathrm{air,nc,insi}}(T_{\mathrm{rec,sur}} - T_0)\frac{A_{\mathrm{field}}}{F_{\mathrm{r}}C} \tag{5.18}$$

$$h_{\mathrm{air,fc,insi}} = 0.0287\frac{k_{\mathrm{air}}}{L}\,Re^{0.8}_{\mathrm{air,insi}}Pr^{1/3}_{\mathrm{air,insi}} \tag{5.19}$$

$$h_{\mathrm{air,nc,insi}} = 0.81 \times (T_{\mathrm{rec,sur}} - T_0)^{0.426} \tag{5.20}$$

In Eq. (5.19), L is the characteristic length and $h_{\mathrm{air,\ fc,\ insi}}$ and $h_{\mathrm{air,\ nc,\ insi}}$ are the forced and natural convective heat transfer coefficients, respectively.

5.3.1.6 Conductive Heat Loss

Only conductive heat loss associated with the insulation layer is accounted as follows:

$$\dot{Q}_{\mathrm{rec,con}} = (T_{\mathrm{insu,w}} - T_0)\frac{A_{\mathrm{field}}h_{\mathrm{air,out}}}{F_{\mathrm{r}}C} \tag{5.21}$$

where ($n = 1$) [10]:

$$h_{\mathrm{air,out}} = \left(h^n_{\mathrm{air,nc,out}} + h^n_{\mathrm{air,fc,out}}\right)^{1/n} \tag{5.22}$$

$$h^n_{\mathrm{air,nc,out}} = 1.24 \times (T_{\mathrm{insu,w}} - T_0)^{1/3} \tag{5.23}$$

$$h_{\mathrm{air,fc,out}} = 0.0239\frac{k_{\mathrm{air}}}{L}\,Re^{0.805}_{\mathrm{air,out}} \times \left(0.785 \times \frac{T_{\mathrm{insu,w}}}{T_0}\right)^{0.2} \times 1.167 \times Pr^{0.45}_{\mathrm{air,out}} \tag{5.24}$$

For the calculation of outlet air specifications, consider $T_{\mathrm{air,\ out}} = T_0$ [10]. $T_{\mathrm{insu,\ w}}$ could be fined from Eq. (5.25) [9]:

$$(T_{\mathrm{insu,w}} - T_0)h_{\mathrm{air,out}} = \frac{\lambda_{\mathrm{insu}}}{\delta_{\mathrm{insu}}}(T_{\mathrm{Rec,Sur}} - T_{\mathrm{insu,w}}) \tag{5.25}$$

5.3.2 *Thermal Presumptions and Evaluation*

Subsequent presumptions are made through the analysis:

- Steady-state condition is governed.
- Compressors and turbine operate with an isentropic efficiency.
- Isenthalpic condition prior and after the expansion valve is assumed.

- Temperature of the distilled water is presumed as the average of the exit air dry-bulb temperature and the inlet air dew-point temperature in the dehumidifier [8, 12, 13].
- The exiting and entering air relative humidity is set at 90% [8].
- Around 11.6% of turbine output power is supplied to the compressor of T-CO_2 refrigeration cycle to achieve around 200 kW cooling load [14].
- Pressure drops in HTR, LTR, generator, DHW, and HU are deliberated 3%, 2%, 2%, 1%, and 1%, respectively [15].
- Evaporator outlet is assumed as saturated vapor.
- Water entering the HU, DHW, and evaporator, and the seawater entering the dehumidifier are at ambient pressure and temperature.
- HTR, LTR, humidifier, and dehumidifier work with specific effectiveness of 86% [15].
- Molten salt pressure is equal to ambient pressure [16].
- Molten salt weight percent is 60% $NaNO_3$ and 40% KNO_3 [16].

Additionally, some other presumptions in terms of input data are listed in Table 5.1.

In terms of mass and energy conservation relations, thermal analysis of a setup may be articulated as:

- Mass balance equation:

$$\sum \dot{m}_{\text{in}} - \sum \dot{m}_{\text{out}} = 0 \tag{5.26}$$

- Energy balance equation:

$$\dot{Q}_{\text{c.v.}} - \dot{W}_{\text{c.v.}} = \sum (\dot{m}h)_{\text{out}} - \sum (\dot{m}h)_{\text{in}} \tag{5.27}$$

Based upon the above-defined relations, the energy balance equations for different constituents of the suggested setup are presented in Table 5.2.

5.3.3 Main Thermal Criteria

The first law of thermodynamics for the devised unit is expressed as follows:

$$\eta_{\text{en}} = \frac{\dot{W}_{\text{net}} + \dot{Q}_{\text{HU}} + \dot{Q}_{\text{DHW}} + \dot{Q}_{\text{eva}} + \dot{m}_{34}.h_{\text{fg@}T_{34}}}{\dot{Q}_{\text{Hel}}} \tag{5.28}$$

where $\dot{W}_{\text{net}}$, $\dot{Q}_{\text{HU}}$, $\dot{Q}_{\text{DHW}}$, and $\dot{Q}_{\text{eva}}$ are the produced net electricity, heating load, DHW heat transfer rate, and refrigeration load, respectively. The net electricity can be expressed as:

Table 5.1 Input data of poly-generation system

Parameter	Value	Ref.
Ambient temperature, T_0 (K)	298.15	[17]
Ambient pressure, P_0 (bar)	1	[17]
Direct normal irradiance, DNI (kW/m^2)	0.8	[11]
Heliostat area, A_h (m^2)	10,000	[11]
Heliostat efficiency, η_h	0.75	[11]
Sun temperature, T_{sun} (K)	4500	[11]
Molten salt high temperature, T_1 (K)	838.15	[11]
Generator PPTD, (K)	10	—
Tube diameter, d_i (m)	0.019	[11]
Tube thickness, $(d_o - d_i)$ (m)	0.00165	[11]
Tube conductivity, λ_{tube} (W/m. K)	23.9	[10]
Emissivity, ε	0.8	[11]
Concentration ratio, C	1200	[18]
Aperture area of receiver, A_{ape} (m^2)	12.5	[11]
View factor, F_r	0.8	[11]
Reflectivity, ρ	0.04	[11]
Wind velocity, V (m/s)	5	[11]
High of receiver, L (m)	6	[10]
Insulation layer thickness, δ_{insu} (m)	0.07	[10]
Insulation conductivity, λ_{insu} (m)	40	[9]
MC and RC pressure ratio, $PR_{MC,\ RC}$	3	[15]
Maximum temperature of S-CO_2, $T_3(K)$	823.15	[15]
Turbine isentropic efficiency, $\eta_{is,\ Tur}$	0.9	[15]
MC and RC isentropic efficiencies, $\eta_{is,\ MC,\ RC}$	0.85	[15]
Heating unit PPTD, (K)	30	—
Domestic hot water unit PPTD, (K)	15	—
Turbine outlet pressure, P_4 (bar)	74	[15]
Mass flow ratio of S-CO_2, $\dot{m}_7/\dot{m}_6$	0.25	[15]
HU outlet water temperature, T_{12} (K)	353.15	[19]
DHW outlet water temperature, T_{15} (K)	323.15	[20]
Evaporator temperature, T_{24} (K)	273	[21]
Internal heat exchanger PPTD, (K)	5	—
Maximum pressure of T-CO_2, P_{20} (bar)	90	[21]
T-CO_2 compressor isentropic efficiencies, $\eta_{is,\ TC}$	0.7	[21]
Evaporator temperature difference, (K)	10	[21]
Gas cooler PPTD, (K)	25	—
Mass flow ratio of HDH, $\dot{m}_{28}/\dot{m}_{32}$	2.5	[22]
Desalination top temperature, T_{30} (K)	353.15	[22]
Seawater salinity, X_{28} (g/kg)	35	[22]

Table 5.2 Required energy balances for system analysis

Constituent	Mass and energy balance equations
Heliostat field	$\dot{Q}_{\text{Loss,Hel}} = \dot{Q}_{\text{Hel}} - \dot{Q}_{\text{Rec}}$
Cavity receiver	$\dot{Q}_{\text{Rec}} = \eta_{\text{h}}\dot{Q}_{\text{Hel}}$ $T_2 = T_{19} + \text{PPTD}_{\text{Gen}}$ $T_{\text{Air}} = (T_0 + T_{\text{Rec, Sur}})/2$
Generator	$\dot{m}_{19}(h_{19} - h_{18}) = \dot{m}_4(h_4 - h_5)$
HTR	$\varepsilon = \frac{T_4 - T_5}{T_4 - T_{18}}$ $P_{17} = P_{18} = P_8$ $\dot{m}_{17}h_{17} + \dot{m}_8h_8 = \dot{m}_{18}h_{18}$
LTR	$\varepsilon = \frac{T_5 - T_6}{T_5 - T_{16}}$ $\dot{m}_5(h_5 - h_6) = \dot{m}_{17}(h_{17} - h_{16})$
Heating unit	$\dot{m}_{12}(h_{12} - h_{11}) = \dot{m}_9(h_9 - h_{10})$ $T_{10} = T_{11} + \text{PPTD}_{\text{HU}}$
DHW	$\dot{m}_{15}(h_{15} - h_{14}) = \dot{m}_{10}(h_{10} - h_{13})$ $T_{13} = T_{14} + \text{PPTD}_{\text{DHW}}$
T-CO_2 compressor	$\dot{W}_{TC} = \dot{m}_{20}(h_{20} - h_{27})$ $\text{ER} = \dot{W}_{\text{TC}}/\dot{W}_{\text{Tur}}$
IHX	$T_{27} = T_{21} - \text{PPTD}_{\text{IHX}}$ $h_{21} - h_{22} = h_{27} - h_{24}$
Evaporator	$T_{26} = T_{25} - \text{TD}_{\text{Eva}}$
Hum	$\dot{m}_{28}X_{28} = \dot{m}_{31}X_{31}$ $\dot{m}_{33}(h_{33} - h_{32}) = \dot{m}_{30}h_{30} - \dot{m}_{31}h_{31}$ $\dot{m}_{31} = \dot{m}_{28} - \dot{m}_{34}$ $\varepsilon = \max\left(\frac{h_{33} - h_{32}}{h_{33,\text{ideal}} - h_{32}}, \frac{h_{30} - h_{31}}{h_{30} - h_{31,\text{ideal}}}\right)$ $h_{33,\text{ ideal}}$ @ T_{30} & $h_{31,\text{ ideal}}$ @ T_{32}
Dhum	$\dot{m}_{33}(h_{33} - h_{32}) = \dot{m}_{29}(h_{29} - h_{28}) + \dot{m}_{34}h_{34}$ $\dot{m}_{34} = \dot{m}_{32}(\omega_{33} - \omega_{32})$ $\varepsilon = \max\left(\frac{h_{29} - h_{28}}{h_{29,\text{ideal}} - h_{28}}, \frac{h_{33} - h_{32}}{h_{33} - h_{32,\text{ideal}}}\right)$ $h_{32,\text{ ideal}}$ @ T_{28} & $h_{29,\text{ ideal}}$ @ T_{33}

$$\dot{W}_{\text{net}} = \dot{W}_{\text{tur}} - \dot{W}_{\text{MC}} - \dot{W}_{\text{RC}} - \dot{W}_{\text{TC}} \tag{5.29}$$

5.4 Results and Discussion

Table 5.3 exhibits the results of thermal modeling of the devised multi-generation system in terms of chief performance criteria. According to Table 5.3, the devised configuration can produce net electricity of 1335 kW, desalinated water of 34.79 m^3/day, refrigeration load of 200 kW, heating load of 2870 kW, and hot water of 633 kW. Under such design circumstance, energy efficiency is calculated 74.81% which can further be increased by manipulating some input data which is discussed in parametric study section.

Table 5.3 Important thermal modeling analysis of multi-generation system

Parameter	Value
Receiver energy efficiency (%)	87.91
Heliostat heat input (kW)	8000
Receiver input energy (kW)	6000
Receiver total energy loss (kW)	725.2
DHW heating load (kW)	633
HU heating load (kW)	2870
Turbine power output	3766
MC power consumption (kW)	1207
RC power consumption (kW)	787.9
Refrigeration load (kW)	200
COP of T-CO_2 refrigeration	0.4589
TC power consumption (kW)	436.9
Freshwater production (m^3/day)	34.79
Gained output ratio (GOR) of HDH	1.484
Net power output (kW)	1335
Energy efficiency (%)	74.81

5.5 Parametric Study

In this section, the most important parameters were studied in order to obtain their impacts on energy efficiency.

5.5.1 Effect of Direct Normal Irradiance

The first effect of direct normal irradiance (DNI) can be seen in Fig. 5.3, in which with increasing DNI, energy efficiency decreases. The decrease of thermal efficiency with increasing DNI is because of high increase in solar heat transfer rate. Although net power output, heating and DHW values have a small increase and cooling and desalination values are constant, solar energy input has a big increment and for this reason efficiency will be decreased. So, it is suitable selection to have a minimum DNI to maximize the first law efficiency.

5.5.2 Effect of Receiver Concentration Ratio

Receiver concentration ratio is an important parameter because it affects the receiver surface temperature, conduction, convection, and radiation heat losses. Its effect can be seen in Fig. 5.4 that its increase causes higher energy efficiency. With increasing receiver concentration ratio, the receiver surface temperature and aperture area will be increased and decreased, respectively. Increasing the receiver temperature causes

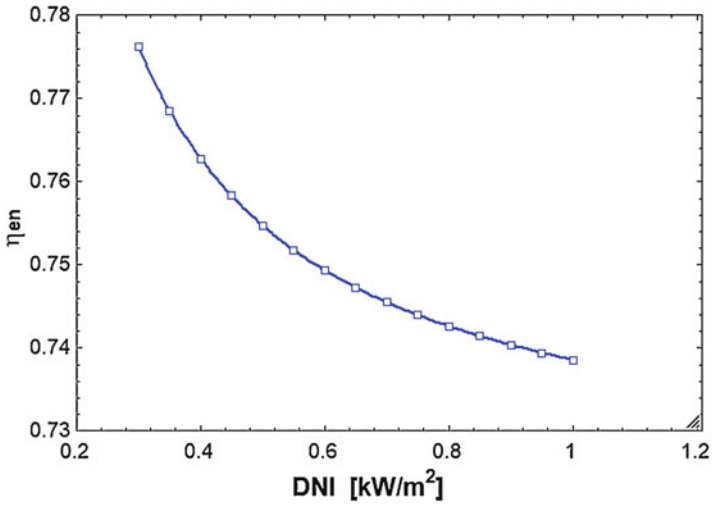

Fig. 5.3 Effect of DNI on thermal efficiency of the system

small increase of heat losses, but decreasing the aperture area causes high decrease of heat losses. So, the overall decrease of heat losses is good reason of increasing the first law efficiency and it is good selection for concentration ratio to be as high as possible for obtaining higher energy efficiency (Fig. 5.4).

5.5.3 Effect of Generator Pinch Point Temperature Difference

Considering Fig. 5.5, with increasing generator pinch point temperature difference, energy efficiency will be decreased. The reason of this effect is the decreasing net power, heating, and DHW values, while cooling, desalination, and solar energies are constant.

5.5.4 Effect of MC and RC Pressure Ratio

Considering Fig. 5.6, there is an increase in energy efficiency with increasing pressure ratio. With this increment, cooling, desalination, and solar heat transfer rates are constant, but the net power and DHW values have decreased and heating heat transfer rate has a higher increase. So, the heating energy increase causes an increase in thermal efficiency. So, in higher pressure ratios, energy efficiency will be higher.

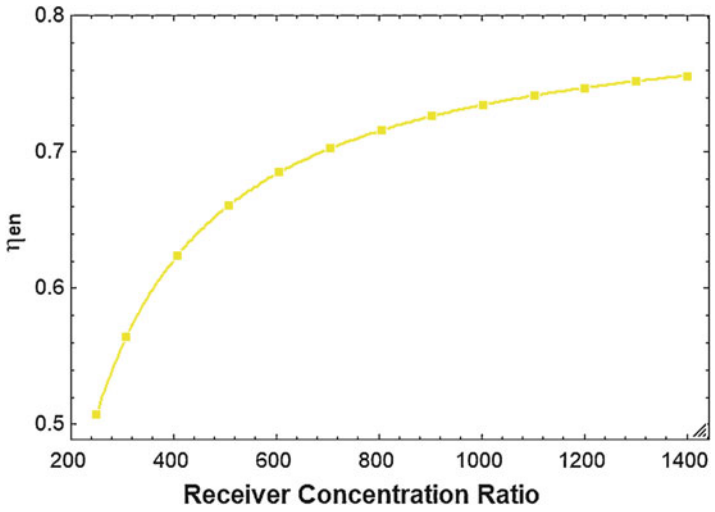

Fig. 5.4 Effect of receiver concentration ratio on thermal efficiency of the system

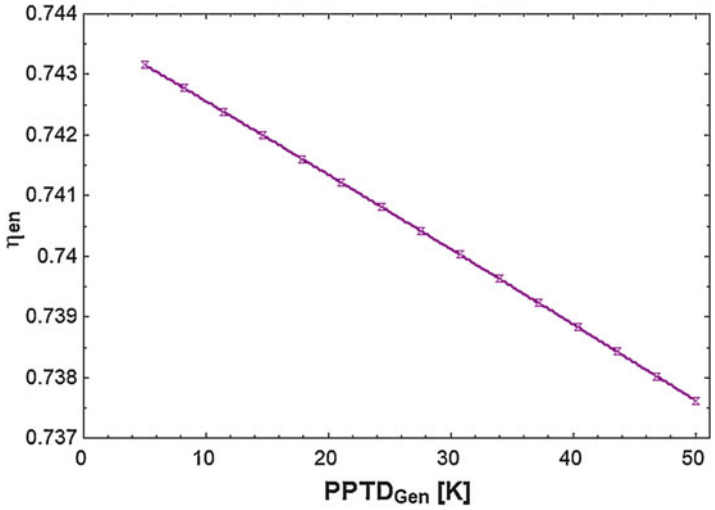

Fig. 5.5 Effect of generator PPTD on thermal efficiency of the system

5.5.5 Effect of HTR, LTR, Hum, and Dhum Effectiveness

Effectiveness is one of the main parameters that has high effect on objectives because it has the same value for HTR, LTR, Hum, and Dhum. It is clear that high effectiveness values result to high performance of heat exchangers and better energy efficiency (Fig. 5.7).

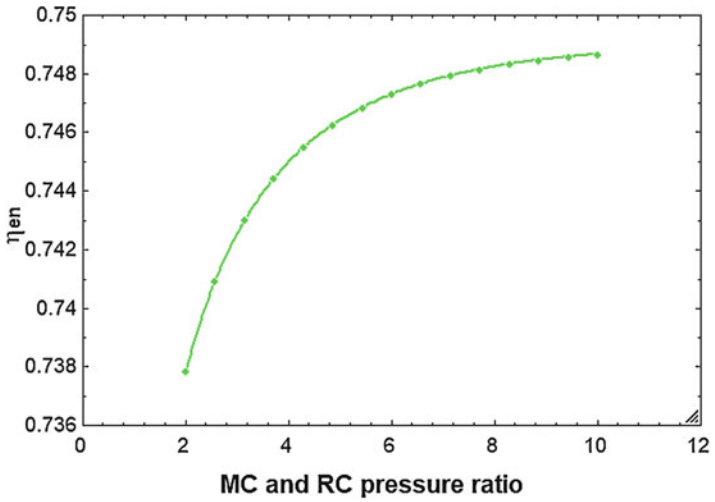

Fig. 5.6 Effect of MC and RC pressure ratio on thermal efficiency of the system

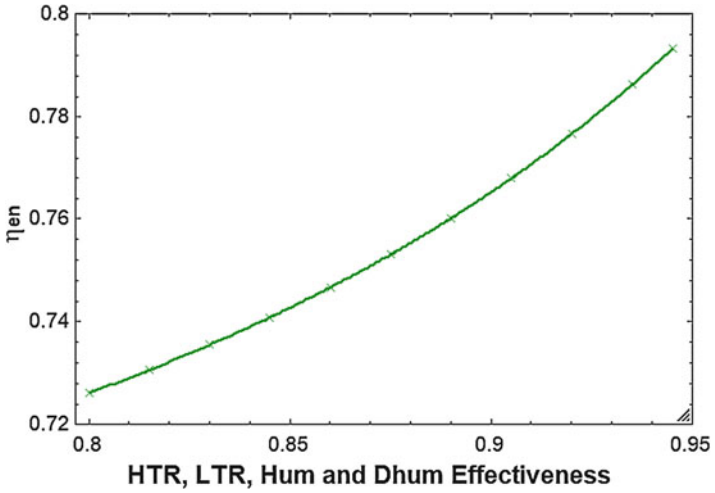

Fig. 5.7 Effect of HTR, LTR, Hum, and Dhum effectiveness on thermal efficiency of the system

5.5.6 *Effect of Ambient, Water, and Seawater Inlet Temperatures*

According to Fig. 5.8, ambient temperature is one of the most important parameters that plays a significant role in energy efficiency. Also, the ambient temperature is the same value of DHW and HU inlet water temperatures and seawater inlet temperature

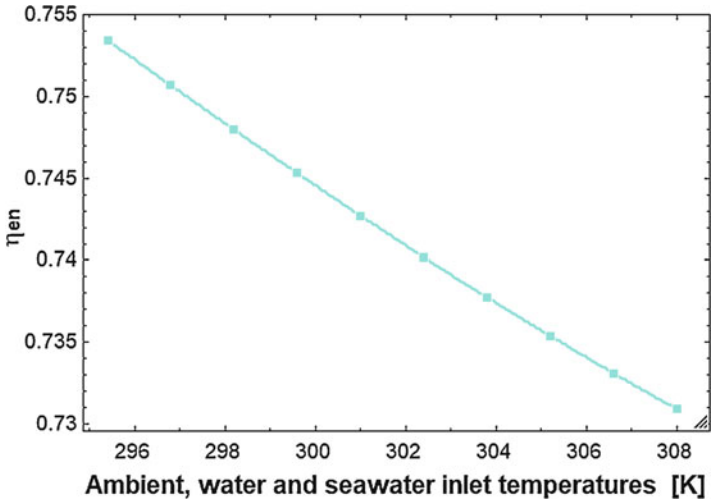

Fig. 5.8 Effect of ambient, water, and seawater inlet temperatures on thermal efficiency of the system

to the HDH system. When ambient temperature increases, net power, DHW, and desalination heat transfer rates decrease more than the increase in heating and cooling values. So, the overall energy efficiency will be decreased and it is good idea to use proposed system in cold regions to maximize the first law efficiency.

5.5.7 Effect of T-CO_2 Compressor to Turbine Electricity Ratio

Power consumption of T-CO_2 compressor is one of the most important parameters that affects energy efficiency. With increasing electricity ratio, solar, heating, and DHW energies are constant, but net power output will be decreased slowly and cooling and desalination products will be increased rapidly. So, conforming to Fig. 5.9, the enhancement of electricity ratio causes the growth of energy efficiency and it is appropriate option to raise T-CO_2 power consumption.

5.6 Concluding Comments

An innovative MGS integrated with a STP plant was devised in this chapter to produce cooling, power, freshwater, heating, and hot water simultaneously. For this aim, a S-CO_2 power cycle, a T-CO_2 refrigeration cycle, and a HDH unit were used in a more efficient configuration. The results of simulation indicated a promising outcome of the proposed arrangement. It was found that the devised multi-

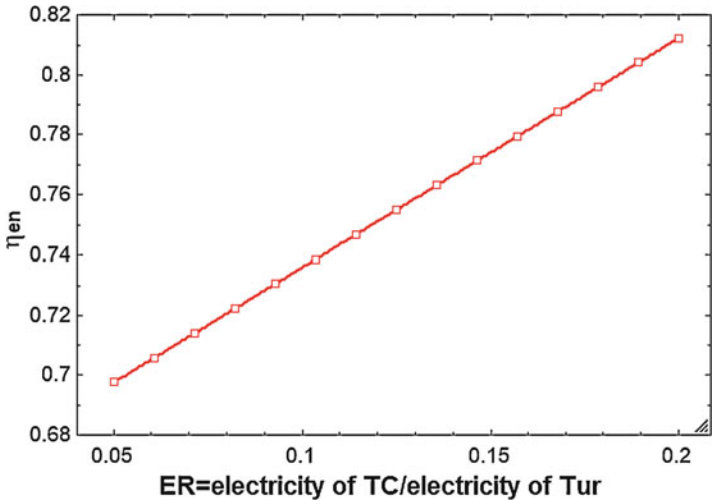

Fig. 5.9 Effect of T-CO_2 compressor to turbine electricity ratio on thermal efficiency of the system

generation system has energy efficiency of 74.81% and can produce net electricity of 1335 kW, desalinated water of 34.79 m^3/day, refrigeration load of 200 kW, heating load of 2870 kW, and hot water of 633 kW. Under such design circumstance, it was discerned that the energy efficiency can further be increased by increasing the receiver concentration ratio, compressor ratios, effectiveness of heat exchangers, and supplying more power from the power cycle to the mechanical T-CO_2-driven refrigeration cycle or by decreasing ambient temperature, generator pinch point temperature, and direct normal irradiance.

References

1. Dincer, I., & Rosen, M. A. (2012). *Exergy: Energy, environment and sustainable development*. Newnes. London: Elsevier
2. Kalogirou, S. A. (2013). *Solar energy engineering: Processes and systems*. Burlington: Academic.
3. Yilmaz, F. (2018). Thermodynamic performance evaluation of a novel solar energy based multigeneration system. *Applied Thermal Engineering, 143*, 429–437.
4. Yuksel, Y. E., Ozturk, M., & Dincer, I. (2019). Energetic and exergetic assessments of a novel solar power tower based multigeneration system with hydrogen production and liquefaction. *International Journal of Hydrogen Energy, 44*(26), 13071–13084.
5. Yilmaz, F., Ozturk, M., & Selbas, R. (2020). Development and performance analysis of a new solar tower and high temperature steam electrolyzer hybrid integrated plant. *International Journal of Hydrogen Energy, 45*, 5668.
6. Wu, H., et al. (2019). Performance investigation of a novel multi-functional system for power, heating and hydrogen with solar energy and biomass. *Energy Conversion and Management, 196*, 768–778.

7. El-Emam, R. S., & Dincer, I. (2018). Development and assessment of a novel solar heliostat-based multigeneration system. *International Journal of Hydrogen Energy, 43*(5), 2610–2620.
8. Narayan, G. P., et al. (2010). Thermodynamic analysis of humidification dehumidification desalination cycles. *Desalination and Water Treatment, 16*(1–3), 339–353.
9. Jamel, M., Abd Rahman, A., & Shamsuddin, A. (2013). Performance evaluation of molten salt cavity tubular solar central receiver for future integration with existing power plants in Iraq. *Australian Journal of Basic and Applied Sciences, 7*(8), 399–410.
10. Li, X., et al. (2010). Thermal model and thermodynamic performance of molten salt cavity receiver. *Renewable Energy, 35*(5), 981–988.
11. Xu, C., et al. (2011). Energy and exergy analysis of solar power tower plants. *Applied Thermal Engineering, 31*(17–18), 3904–3913.
12. Narayan, G. P., McGovern, R. K., & Zubair, S. M. (2012). High-temperature-steam-driven, varied-pressure, humidification-dehumidification system coupled with reverse osmosis for energy-efficient seawater desalination. *Energy, 37*(1), 482–493.
13. Narayan, G. P., John, M. G. S., & Zubair, S. M. (2013). Thermal design of the humidification dehumidification desalination system: An experimental investigation. *International Journal of Heat and Mass Transfer, 58*(1–2), 740–748.
14. Farsi, A., Ameri, M., & Mohammadi, S. (2018). Application of transcritical CO2 in multi-effect desalination system: Energetic and exergetic assessment and performance optimization. *Desalination and Water Treatment, 135*, 108–123.
15. Mohammadi, Z., Fallah, M., & Mahmoudi, S. S. (2019). Advanced exergy analysis of recompression supercritical CO2 cycle. *Energy, 178*, 631–643.
16. Ma, Y., et al. (2019). Optimal integration of recompression supercritical CO2 Brayton cycle with main compression intercooling in solar power tower system based on exergoeconomic approach. *Applied Energy, 242*, 1134–1154.
17. Dincer, I., Midilli, A., & Kucuk, H. (2014). *Progress in exergy, energy, and the environment*. Cham: Springer.
18. Sachdeva, J., & Singh, O. (2019). Thermodynamic analysis of solar powered triple combined Brayton, Rankine and organic Rankine cycle for carbon free power. *Renewable Energy, 139*, 765–780.
19. Parikhani, T., et al. (2020). Thermodynamic and thermoeconomic analysis of a novel ammonia-water mixture combined cooling, heating, and power (CCHP) cycle. *Renewable Energy, 145*, 1158–1175.
20. Ahmadi, P., Dincer, I., & Rosen, M. A. (2013). Thermodynamic modeling and multi-objective evolutionary-based optimization of a new multigeneration energy system. *Energy Conversion and Management, 76*, 282–300.
21. Pérez-García, V., et al. (2016). Comparative analysis of energy improvements in single transcritical cycle in refrigeration mode. *Applied Thermal Engineering, 99*, 866–872.
22. Rostamzadeh, H., et al. (2018). Performance assessment and optimization of a humidification dehumidification (HDH) system driven by absorption-compression heat pump cycle. *Desalination, 447*, 84–101.

Chapter 6
Design and Evaluation of a New Solar Tower-Based Multi-generation System: Part II, Exergy and Exergoeconomic Modeling

Hamed Ghiasirad, Hadi Rostamzadeh, and Sajjad Nasri

Nomenclature

Symbols

C	Concentration ratio
h	Enthalpy (kJ. kg^{-1}), convection coefficient (W/m^2K)
K	Conductivity (W/m.K)
L	Length of tube (m)
S	Supercritical
T	Temperature (K), transcritical
V	Wind velocity (m/s)
X	Salinity (g. kg^{-1})

Abbreviations

F_r	View factor
HTR	High-temperature recuperator
HU	Heating unit
LTR	Low-temperature recuperator
MC	Main compressor
MFR	Mass flow ratio
PPTD	Pinch point temperature difference (K)

H. Ghiasirad (✉) · S. Nasri
Department of Mechanical Engineering, Faculty of Engineering, Sahand University of Technology, Tabriz, Iran

H. Rostamzadeh
Energy and Environment Research Center, Niroo Research Institute (NRI), Tehran, Iran

F. Jabari et al. (eds.), *Integration of Clean and Sustainable Energy Resources and Storage in Multi-Generation Systems*,
https://doi.org/10.1007/978-3-030-42420-6_6

RC Recompression compressor
STP Solar tower power

Greek Letters

δ Thickness (m)
ε Effectiveness, emissivity
η Efficiency (%)
λ Conductivity (W/m.K)
μ Viscosity (Pa.s)
ω Humidity
ρ Reflectivity, density (kg/m^3)

Subscripts and Superscripts

Ape Aperture
em Emissive
Dhum Dehumidifier
fc Forced convection
Gen Generator
Hum Humidifier
H, Hel Heliostat
Insi Inner side of receiver
Insu Insulation
is Isentropic
ms Molten salt
nc Natural convection
ref Reflection
Sur Surface
sw Sea water
TC Transcritical compressor
W Wall

6.1 Introduction

Exergy has been introduced as a conceptual tool in the design of more efficacious energy systems when the performance of the system should be judged by evaluating it relative to a reference state. Broadly speaking, exergy is defined as a maximum available work that a unit can do while interacting with the ambient [1]. Therefore, thermodynamic properties of the ambient can be inferred as the reference state through the exergy analysis. An intensive and accurate exergy analysis based on practical assumptions will lead to recognition of the main source of the losses occurring through the operation of the system both qualitatively and quantitatively. This is the main distinctive feature of exergy analysis, which is wanted in energy

analysis. The quantitative feature of exergy analysis refers to avoidance of thermodynamic imperfection in different elements of a system by spotlighting the causes and locations of these imperfections for redesign purposes [2].

Exergoeconomic is the combination of exergy analysis and cost estimation based on exergy values at each state. Application of exergoeconomic in energy systems mainly aims at designing more sustainable units in terms of waste handling by considering cost and the source of irreversibility. Basically, the main aim of exergoeconomic analysis can be categorized as follows [3] :

- The source, location, and magnitude of the cost destructed or lost in an energy system can be determined.
- To assess the overall cost of a multi-generation system or individual cost associated with each product.
- To make a multi-objective optimization of a complex system more feasible since an overall unit cost can be defined for the entire system.
- To expand the decision-making procedures into more viable analysis such as reliability and risk evaluation based upon the obtained cost index.
- To justify the initial design process of the devised setup evaluated based on the energy and exergy concepts by comparing it to similar systems where their cost index is more encouraging.

Application of exergoeconomic analysis in multi-generation systems (the conceptual definition of a multi-generation system is presented in Chap. 5) can be satisfactory based upon the above-categorized reasons. In multi-generation systems, each state experiences a series of complex thermodynamic processes, where determination of thermodynamic properties at each state can provide favorable information for designers. The same merit can be found in exergy and exergoeconomic analysis since exergy rate and cost rate associated with each state can be determined. This detail evaluation in terms of cost can be much more than an asset since present modern marketing in energy management profusely emphasizes on more viable ideas that are based on more accurate and detail cost data. Future plans on ameliorating performance and cost of the current combined power plants will more intensively be centralized on developing multi-generation systems that are more efficient and economical in their different utility sectors. As pinpointed in Chap. 5, a multi-generation system can be constructed in two forms: combined or integrated. Depending on which classification the designed multi-generation system is set on, the cost rate manipulation in terms of decreasing overall cost of the unit can be more or less complex. This is partly because of minor constructive development in exergoeconomic analysis of multi-generation systems. The objective is even highly imperative when the design layout includes a competitive heat source, especially a reliable renewable source such as solar energy. Even though the intermittency of solar irradiance through the nights or low-temperature periods of a year is questionable (which makes the cost-benefit of the proposal at stake), recent advances in development of high-tech storage energy devices and materials have proved the cost profitability of the solar-based multi-generation systems from mathematical-based cost models like exergoeconomic. Therefore, it is crucial to further discuss economic

perspectives of the devised new solar-based multi-generation system elaborated in previous chapter from energy viewpoint. Before we proceed further in the construction of a robust exergoeconomic model for the designed multi-generation system, it is important to look around the most recent constructed integrated/combined energy systems from exergoeconomic viewpoint. The only study in exergoeconomic of multi-generation systems in solar-based multi-generation system is the study of Leiva-Illanes et al. [4]. According to Ref. [4], authors carried out exergoeconomic analysis of a new solar-based multi-generation system and suggested the best configuration in terms of unit exergy cost. They found that the high portion of cost associated to the system (in order) is the solar collectors, evaporator, and reheater. They also deduced that the devised solar-based multi-generation system is more economical than the stand-alone setup. With their devised layout, the unit exergy cost associated with electricity, cooling, water, and heating were declined by 6.8%, 45.6%, 59.2%, and 32.2%, respectively.

In the light of reviewed literature and based on the results of previous chapter, it can be figured out that no study has been carried out to study exergoeconomic analysis of a high-efficient multi-generation system operated by a solar tower power (STP) plant up to yet. The only study was Leiva-Illanes et al. [4] in which they used solar collectors applicable for low-temperature combined plants. To cover this shortcoming of the existing literature works, exergoeconomic analysis of the devised solar-based multi-generation system in the first part of this study is investigated in this chapter. The rest of this chapter is arranged in the following order. In Sect. 6.2, all employed mathematical relations and presumptions related to exergy and exergoeconomic analysis are displayed. In the third sub-section, results are presented and discussed extensively. Finally, some concluding comments from economic vantage point are listed in the last part.

6.2 Materials and Methods

In this part, exergy and exergoeconomic presumptions and relations are intensively presented. In the first subsection, exergy concept and the relations associated with it are presented. In the second subsection, exergoeconomic analysis is elaborated in detail. Ultimately, the main cost parameters are extended.

6.2.1 Exergy Analysis

In this study, only physical and chemical exergies are considered through exergy assessment [1]. The exergy-based balance relation for individual constituent of a system may be articulated in the sense of the all exiting and entering exergy rates of the constituents as follows:

$$\dot{\mathrm{E}}\mathrm{x}_{\mathrm{D},k} = \dot{\mathrm{E}}\mathrm{x}_{\mathrm{F},k} - \dot{\mathrm{E}}\mathrm{x}_{\mathrm{P},k} - \dot{\mathrm{E}}\mathrm{x}_{\mathrm{L},k} \tag{6.1}$$

Disregarding the inconsequential impact of the potential and kinetic exergies of all flows, the total exergy of the kth fluid stream is articulated as follows [5] :

$$\dot{\mathrm{E}}\mathrm{x}_{k} = \dot{\mathrm{E}}\mathrm{x}_{\mathrm{ph},k} + \dot{\mathrm{E}}\mathrm{x}_{\mathrm{ch},k} \tag{6.2}$$

where:

$$\dot{\mathrm{E}}\mathrm{x}_{\mathrm{ph},k} = \dot{m}(h - h_0 - T_0(s - s_0))_k \tag{6.3}$$

$$\dot{\mathrm{E}}\mathrm{x}_{\mathrm{ch,MS}} = \dot{m}\left(0.6\left[\frac{\mathrm{ex}^0_{\mathrm{ch,NaNO_3}}}{M_{\mathrm{NaNO_3}}}\right] + 0.4\left[\frac{\mathrm{ex}^0_{\mathrm{ch,KNO_3}}}{M_{\mathrm{KNO_3}}}\right]\right) \tag{6.4}$$

$$\dot{\mathrm{E}}\mathrm{x}_{\mathrm{ch,Water,CO_2}} = \dot{m}\left(\left[\frac{\mathrm{ex}^0_{\mathrm{ch,Water,CO_2}}}{M_{\mathrm{Water,CO_2}}}\right]\right) \tag{6.5}$$

in which, 0 refers to the environment condition. To compute saline water exergy, pressure-based correlations accessible in EES software are used [6, 7]. Exergy of humid air is computed from Eq. (6.6) [8]:

$$\begin{aligned}\mathrm{ex}_{\mathrm{da}} = {} & \left(c_{\mathrm{p,a}} + \omega c_{\mathrm{p,v}}\right)T_0\left(\frac{T}{T_0} - 1 - \ln\frac{T}{T_0}\right) + (1 + 1.608\omega)R_{\mathrm{a}}T_0\ln\frac{P}{P_0} \\ & + R_{\mathrm{a}}T_0(1 + 1.608\omega)\ln\frac{1 + 1.608\omega_0}{1 + 1.608\omega} + 1.608\omega\ln\frac{\omega}{\omega_0}\end{aligned} \tag{6.6}$$

where, $R_{\mathrm{a}} = 0.287$ (kJ/kg. K) and ω is the humidity ratio:

$$\omega = \frac{\dot{m}_{\mathrm{v}}}{\dot{m}_{\mathrm{a}}} \tag{6.7}$$

The exergetic efficiency for each constituent of a system may be articulated as follows:

$$\eta_{\mathrm{ex},k} = \frac{\text{Exergy of product}}{\text{Total supplied exegy}} = \frac{\dot{\mathrm{E}}\mathrm{x}_{\mathrm{out}}}{\dot{\mathrm{E}}\mathrm{x}_{\mathrm{in}}} = \frac{\dot{\mathrm{E}}\mathrm{x}_{\mathrm{P},k}}{\dot{\mathrm{E}}\mathrm{x}_{\mathrm{F},k}} \tag{6.8}$$

Based upon the above-defined relations, the exergy balance equations for different constituents of the suggested multi-generation system are presented in Table 6.1.

Table 6.1 The exergy balance equations for different constituents of the suggested multi-generation system

Constituents	Fuel	Product	Loss
Hel	$\dot{Q}_{\text{Hel}}\left(1-\frac{T_0}{T_{\text{sun}}}\right)$	$\dot{Q}_{\text{Rec}}\left(1-\frac{T_0}{T_{\text{sun}}}\right)$	–
Rec	$\dot{Q}_{\text{Rec}}\left(1-\frac{T_0}{T_{\text{sun}}}\right)$	$\dot{\text{E}}\text{x}_1-\dot{\text{E}}\text{x}_2$	$\dot{Q}_{\text{Rec,Loss}}\left(1-\frac{T_0}{T_{\text{Rec}}}\right)$
Gen	$\dot{\text{E}}\text{x}_1-\dot{\text{E}}\text{x}_2$	$\dot{\text{E}}\text{x}_3-\dot{\text{E}}\text{x}_{19}$	–
Tur	$\dot{\text{E}}\text{x}_3$	$\dot{\text{E}}\text{x}_4+\dot{\text{W}}_{\text{Tur}}$	–
HTR	$\dot{\text{E}}\text{x}_4-\dot{\text{E}}\text{x}_5$	$\dot{\text{E}}\text{x}_{19}-\dot{\text{E}}\text{x}_{18}$	–
LTR	$\dot{\text{E}}\text{x}_5-\dot{\text{E}}\text{x}_6$	$\dot{\text{E}}\text{x}_{17}-\dot{\text{E}}\text{x}_{16}$	–
HU	$\dot{\text{E}}\text{x}_9-\dot{\text{E}}\text{x}_{10}$	$\dot{\text{E}}\text{x}_{12}-\dot{\text{E}}\text{x}_{11}$	–
DHW	$\dot{\text{E}}\text{x}_{10}-\dot{\text{E}}\text{x}_{13}$	$\dot{\text{E}}\text{x}_{15}-\dot{\text{E}}\text{x}_{14}$	–
MC	$\dot{\text{E}}\text{x}_{13}+\dot{\text{W}}_{\text{MC}}$	$\dot{\text{E}}\text{x}_{16}$	–
RC	$\dot{\text{E}}\text{x}_7+\dot{\text{W}}_{\text{RC}}$	$\dot{\text{E}}\text{x}_8$	–
TC	$\dot{\text{E}}\text{x}_{27}+\dot{\text{W}}_{\text{TC}}$	$\dot{\text{E}}\text{x}_{20}$	–
GC	$\dot{\text{E}}\text{x}_{20}-\dot{\text{E}}\text{x}_{21}$	$\dot{\text{E}}\text{x}_{30}-\dot{\text{E}}\text{x}_{29}$	–
IHX	$\dot{\text{E}}\text{x}_{21}-\dot{\text{E}}\text{x}_{22}$	$\dot{\text{E}}\text{x}_{27}-\dot{\text{E}}\text{x}_{24}$	–
TV	$\dot{\text{E}}\text{x}_{22}$	$\dot{\text{E}}\text{x}_{23}$	–
Eva	$\dot{\text{E}}\text{x}_{23}-\dot{\text{E}}\text{x}_{24}$	$\dot{\text{E}}\text{x}_{26}-\dot{\text{E}}\text{x}_{25}$	–
Hum	$\dot{\text{E}}\text{x}_{30}$	$\dot{\text{E}}\text{x}_{33}-\dot{\text{E}}\text{x}_{32}$	$\dot{\text{E}}\text{x}_{31}$
Dhum	$\dot{\text{E}}\text{x}_{33}-\dot{\text{E}}\text{x}_{32}$	$\dot{\text{E}}\text{x}_{29}-\dot{\text{E}}\text{x}_{28}+\dot{\text{E}}\text{x}_{34}$	–

6.2.2 Exergoeconomic Analysis

The balance equation based on the cost of the *k*th constituent of a system is articulated as follows [1]:

$$\dot{C}_{\text{q},k}+\sum\dot{C}_{\text{in},k}+\dot{Z}_k=\dot{C}_{\text{w},k}+\sum\dot{C}_{\text{out},k} \tag{6.9}$$

where, the utilized parameters are:

$\dot{C}_{\text{in},k}$: stands for the cost rate of the incoming stream of the *k*th constituent.
$\dot{C}_{\text{out},k}$: stands for the cost rate of the outcoming stream of the *k*th constituent.
$\dot{C}_{\text{w},k}$: stands for the cost rate of work.
$\dot{C}_{\text{q},k}$: stands for the cost rate of heat transfer.

Exergy and cost rate are related as follows [1]:

$$\dot{C}_k=c_k\dot{\text{E}}\text{x}_k \tag{6.10}$$

The overall cost rate of the *k*th constituent of a system is articulated as follows [1]:

$$\dot{Z}_k = \dot{Z}_k^{\mathrm{CI}} + \dot{Z}_k^{\mathrm{OM}} = \frac{\mathrm{PEC}_k \times \phi_{\mathrm{c}} \times \mathrm{CRF}}{\tau} \tag{6.11}$$

where:

$\dot{Z}_k^{\mathrm{CI}}$: stands for the capital investment cost of the kth constituent.
$\dot{Z}_k^{\mathrm{OM}}$: stands for the operating and maintenance cost of the kth constituent.
τ: stands for the annual operating hours.
ϕ_{c}: stands for the maintenance factor.
PEC_k: stands for the purchase cost of the kth constituent.
CRF: stands for the capital recovery factor.

CRF is attained from Eq. (6.12) [1]:

$$\mathrm{CRF} = \frac{i(1+i)^{n_{\mathrm{r}}}}{(1+i)^{n_{\mathrm{r}}} - 1} \tag{6.12}$$

where:

i: stands for the interest rate.
n_{r}: stands for the total operating years of the system.

The cost rate of exergy destruction of the kth constituent is articulate as follows [1]:

$$\dot{C}_{\mathrm{D},k} = c_{\mathrm{F},k}\dot{\mathrm{E}}\mathrm{x}_{\mathrm{D},k}\left(\mathrm{If}\ \ \dot{\mathrm{E}}\mathrm{x}_{\mathrm{P},k} = \mathrm{constant}\right) \tag{6.13}$$

The relative cost difference (r_k) and exergoeconomic factor (f_k) for the kth component of a system may be expressed, respectively, as [1] follows:

$$r_k = (c_{\mathrm{P},k} - c_{\mathrm{F},k})/c_{\mathrm{F},k} \tag{6.14}$$

$$f_k = \dot{Z}_k/\left(\dot{Z}_k + \dot{C}_{\mathrm{D},k}\right) \tag{6.15}$$

The detail cost balance relations and purchase equipment cost (PEC) for each constituent of the devised multi-generation system are presented in Tables 6.2 and 6.3.

Some central exergy and economic parameters required for analysis are presented in Table 6.4.

Assuming the logarithmic mean temperature difference (LMTD) and the total heat transfer coefficient, the total heat exchanger area might be attained from the equation below:

$$A_k = \frac{\dot{Q}_k}{U_k \Delta T_{\mathrm{LMTD}}} \tag{6.16}$$

Table 6.2 Purchase equipment cost (PEC) for each constituent of the devised multi-generation system

Constituents	PEC_{2018} [9]	Ref.
Hel	$PEC_{2009\rightarrow2018} = \left(\frac{638.1}{521.9}\right) \times 216\, A_h$	[10]
Rec	$PEC_{2009\rightarrow2018} = \left(\frac{638.1}{521.9}\right) \times 3.52 \times 10^6 \times \left(\frac{\dot{Q}_{Rec,Abs}}{1000}\right)^{0.44}$	[10]
Tower	$PEC_{2009\rightarrow2018} = \left(\frac{638.1}{521.9}\right) \times 30.5\dot{Q}_{Rec,Abs} + 961000$	[10]
Gen HTR LTR HU DHW GC IHX Eva	$P_{Gen}[bar] = P_{19} - 1$, $P_{HTR} = P_{18} - 1$, $P_{LTR} = P_{17} - 1$, $P_{HU} = P_9 - 1$ $P_{DHW} = P_{10} - 1$, $P_{GC} = P_{20} - 1$, $P_{IHX} = P_{21} - 1$, $P_{Eva} = P_{24} - 1$ $PEC_{1996\rightarrow2018} = \left(\frac{638.1}{381.7}\right) \times Z_0(1.63 + 1.66F_P)$ $\log_{10}(Z_0) = 4.3247 - 0.303\log_{10}(A) + 0.1634(\log_{10}(A))^2$ $\log_{10}(F_P) = 0.03881 - 0.1127\log_{10}(P_K) + 0.0818(\log_{10}(P_K))^2$	[11]
Tur	$PEC_{1996\rightarrow2018} = \left(\frac{638.1}{381.7}\right) \times Z_0 3.5\, Z_{0.Tur}$ $\log_{10}(Z_{0.Tur}) = 2.7051 - 1.4398 \log_{10}(\dot{W}_{Tur}) - 0.1776(\log_{10}(\dot{W}_{Tur}))^2$	[11]
MC RC TC	$PEC_{1996\rightarrow2018} = \left(\frac{638.1}{381.7}\right) \times 3.8\, Z_{0.Com}$ $\log_{10}(Z_{0.Com}) = 2.2897 - 1.3604 \log_{10}(\dot{W}_{Com}) - 0.1027(\log_{10}(\dot{W}_{Com}))^2$	[11]
TV	$PEC_{2000\rightarrow2018} = \left(\frac{638.1}{394.1}\right) \times 114.5\, \dot{m}_{22}$	[12]
Hum	$PEC_{2012\rightarrow2018} = \left(\frac{638.1}{584.6}\right) \times 133\left(\frac{\dot{m}_{FW}}{0.0015}\right)^{0.6}$	[13]
Dhum	$PEC_{2012\rightarrow2018} = \left(\frac{638.1}{584.6}\right) \times 70\left(\frac{\dot{m}_{FW}}{0.0015}\right)^{0.6}$	[13]

Table 6.3 Cost balances and auxiliary equations for each constituent of the devised multi-generation system

Constituents	Cost balance	Auxiliary equation
Hel	$\dot{C}_{\text{in,Hel}} + \dot{Z}_{\text{Hel}} = \dot{C}_{\text{in,Rec}}$	$c_{\text{in, Hel}} = 0$
Rec	$\dot{C}_2 + \dot{C}_{\text{in,Rec}} + \dot{Z}_{\text{Tower}} + \dot{Z}_{\text{Rec}} = \dot{C}_1$	–
Gen	$\dot{C}_1 + \dot{C}_{19} + \dot{Z}_{\text{Gen}} = \dot{C}_2 + \dot{C}_3$	$c_2 = c_1$
Tur	$\dot{C}_3 + \dot{Z}_{\text{Tur}} = \dot{C}_4 + \dot{C}_{\text{W,Tur}}$	$c_4 = c_3$
HTR	$\dot{C}_{18} + \dot{C}_4 + \dot{Z}_{\text{HTR}} = \dot{C}_{19} + \dot{C}_5$	$c_5 = c_4$
LTR	$\dot{C}_{16} + \dot{C}_5 + \dot{Z}_{\text{LTR}} = \dot{C}_{17} + \dot{C}_6$	$c_6 = c_5$
Division point	$\dot{C}_6 = \dot{C}_9 + \dot{C}_7$	$c_9 = c_7$
HU	$\dot{C}_{11} + \dot{C}_9 + \dot{Z}_{\text{HU}} = \dot{C}_{10} + \dot{C}_{12}$	$c_{10} = c_9$ $c_{11} = 0$
DHW	$\dot{C}_{10} + \dot{C}_{14} + \dot{Z}_{\text{DHW}} = \dot{C}_{15} + \dot{C}_{13}$	$c_{13} = c_{10}$ $c_{14} = 0$
MC	$\dot{C}_{\text{W,MC}} + \dot{C}_{13} + \dot{Z}_{\text{MC}} = \dot{C}_{16}$	$c_{\text{W, MC}} = c_{\text{W, Tur}}$
RC	$\dot{C}_{\text{W,RC}} + \dot{C}_7 + \dot{Z}_{\text{RC}} = \dot{C}_8$	$c_{\text{W, RC}} = c_{\text{W, Tur}}$
TC	$\dot{C}_{\text{W,TC}} + \dot{C}_{27} + \dot{Z}_{\text{TC}} = \dot{C}_{20}$	$c_{\text{W, TC}} = c_{\text{W, Tur}}$
GC	$\dot{C}_{20} + \dot{C}_{29} + \dot{Z}_{\text{GC}} = \dot{C}_{21} + \dot{C}_{30}$	$c_{21} = c_{20}$
IHX	$\dot{C}_{21} + \dot{C}_{24} + \dot{Z}_{\text{IHX}} = \dot{C}_{22} + \dot{C}_{27}$	$c_{22} = c_{21}$
TV	$\dot{C}_{22} + \dot{Z}_{\text{TV}} = \dot{C}_{23}$	–
Eva	$\dot{C}_{23} + \dot{C}_{25} + \dot{Z}_{\text{Eva}} = \dot{C}_{24} + \dot{C}_{26}$	$c_{23} = c_{24}$ $c_{25} = 0$
Hum	$\dot{C}_{30} + \dot{C}_{32} + \dot{Z}_{\text{Hum}} = \dot{C}_{31} + \dot{C}_{33}$	$c_{30} = c_{31}$ $c_{32} = c_{33}$
Dhum	$\dot{C}_{28} + \dot{C}_{33} + \dot{Z}_{\text{Dhum}} = \dot{C}_{34} + \dot{C}_{32} + \dot{C}_{29}$ $\frac{\dot{C}_{32} - \dot{C}_{28}}{\dot{E}x_{32} - \dot{E}x_{28}} = \frac{\dot{C}_{29} - \dot{C}_{28}}{\dot{E}x_{29} - \dot{E}x_{28}}$	$c_{28} = 0$

Table 6.4 Some required exergy and economic parameters for exergoeconomic evaluation of the proposed multi-generation system [14]

Parameters	Value	Ref.
Annual number of hours, τ (hr)	4800	[5]
Components' expected life, n_r (years)	30	[5]
Maintenance factor, $\varnothing_c$	1.02	[5]
Interest rate, i	0.08	[5]
ex^0_{ch,KNO_3}, (kJ/kmol)	−15,290	[15]
$ex^0_{ch,NaNO_3}$, (kJ/kmol)	−15,745	[15]
ex^0_{ch,CO_2}, (kJ/kmol)	14,176	[15]
$ex^0_{ch,water}$, (kJ/kmol)	45	[15]

Table 6.5 The overall heat transfer coefficient for heat exchangers

Component	U (kW/m^{2}K)	Ref.
Gen and HTR	3	[16]
LTR	1.6	[16]
HU	1.6	[16]
DHW	2	[16]
GC	0.3	[11]
Eva	1.5	[11]
IHX	1	[11]

The total heat transfer coefficients for each heat exchanger are tabulated in Table 6.5. The updated cost rates for each individual component would be updated as follows:

$$\text{Original cost} = \text{Cost at reference year} \times \frac{\text{Cost index for the original year}}{\text{Cost index for the reference year}} \tag{6.17}$$

6.2.3 Main Exergy and Cost Parameters

The second-law efficiency of the proposed poly-generation system can be written as follows:

$$\eta_{ex} = \frac{\dot{W}_{net} + \dot{E}x_{P,HU} + \dot{E}x_{P,DHW} + \dot{E}x_{P,Eva} + \dot{E}x_{Desal}}{\dot{E}x_{F,Hel}} \tag{6.18}$$

where, fuel and product exergy rates are listed in Table 6.1 and desalination exergy rate is given by Eq. (6.19):

$$\dot{E}x_{Desal} = \dot{E}x_{FW} - \dot{E}x_{SW} \tag{6.19}$$

System total cost rate ($\dot{C}_{sys}$) for the devised multi-generation system can be expressed as follows:

$$\dot{C}_{sys} = \dot{C}_1 + \dot{Z}_{tot} \tag{6.20}$$

where, $\dot{Z}_{tot}$ is the total investment and operating cost rate and $\dot{C}_1$ is the high-temperature molten salt cost.

6.3 Results and Discussion

Table 6.6 presents results of exergy and exergoeconomic analysis of the devised multi-generation system described in Chap. 5. According to Table 6.6, exergy efficiency of the proposed MGS is computed 21.45%. Also, among all subsystems, heliostat field has the exergy of fuel of 7470 kW. The total investment cost of the whole system is estimated 433.2 $/h. Moreover, the overall cost rate of the setup was calculated 743.2 $/h. Figure 6.1 indicates results of exergy destruction for all elements available in the system. Accordingly, the receiver has a pivotal role in the overall exergy destruction by exergy destruction of 2006 kW, followed by heliostat by 1867 kW.

Table 6.6 The significant results of exergy and economic analysis

Parameter	Value
$\dot{E}x_{F,Hel}$ (kW)	7470
$\dot{E}x_{P,HU}$ (kW)	236.1
$\dot{E}x_{P,DHW}$ (kW)	25.13
$\dot{E}x_{Desal}$ (kW)	2.8
η_{ex} (%)	21.45
$\dot{Z}_{tot}$ (/h)	433.2
$c_{W,\ Tur}$ ($/GJ)	43.06
$\dot{C}_{sys}$ (/h)	743.2

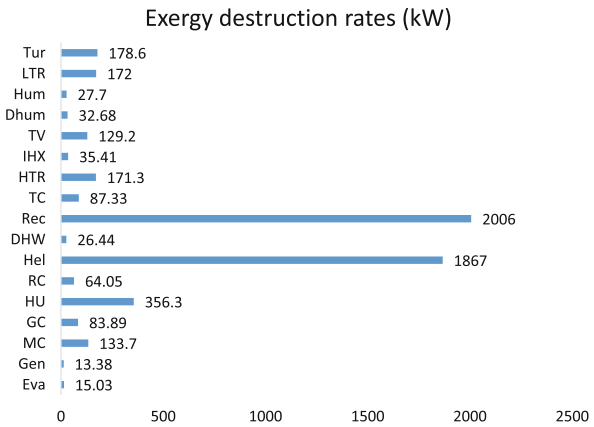

Fig. 6.1 Exergy destruction rates of each component of multi-generation system

6.4 Parametric Study

6.4.1 Effect of Direct Normal Irradiance

In this sub-section, some parameters are studied to obtain their effect on exergy efficiency and total cost rate of the system. In the beginning, effect of direct normal irradiance (DNI) can be seen in Fig. 6.2, in which, with increasing DNI, exergy efficiency and total cost rate increase. With increasing DNI, cooling and desalination product exergies are constant, but product exergy of heating, DHW, and net electricity have higher increase than solar exergy input, and for this reason, the second-law efficiency will be increased. On the other hand, the total investment cost rate and cost rate of stream 1 have linear increase. So, there is a linear increase in the total cost rate. Hence, DNI should be optimized for simultaneous high exergy efficiency and low total cost rate.

6.4.2 Effect of Receiver Concentration Ratio

Receiver concentration ratio is a critical parameter because of its impacts on receiver surface temperature, conduction, convection, and radiation energy losses. Its impact is shown in Fig. 6.3, wherein its enhancement creates higher energy efficiency. With growing receiver concentration ratio, receiver surface temperature and aperture area get larger and fall off, respectively. Enhancement of the receiver temperature causes a few increases of heat losses. On the other hand, decrease of aperture area causes high decrease of heat losses. So, decrease of heat losses is a suitable reason in

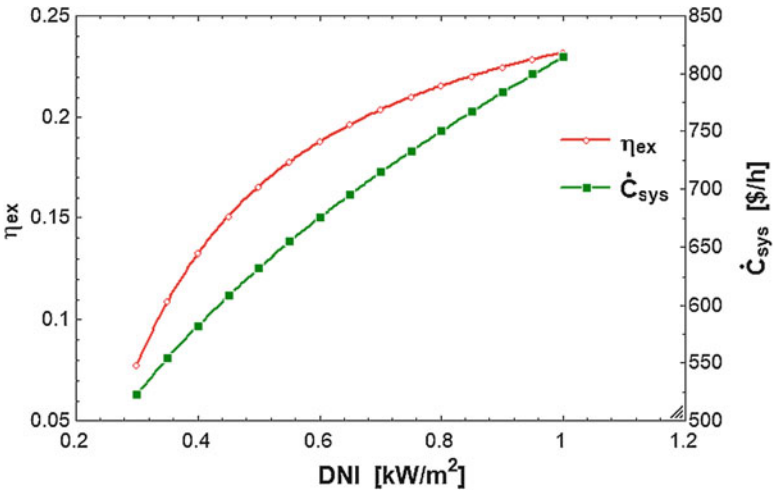

Fig. 6.2 Effect of DNI on exergy efficiency and total cost rate of the system

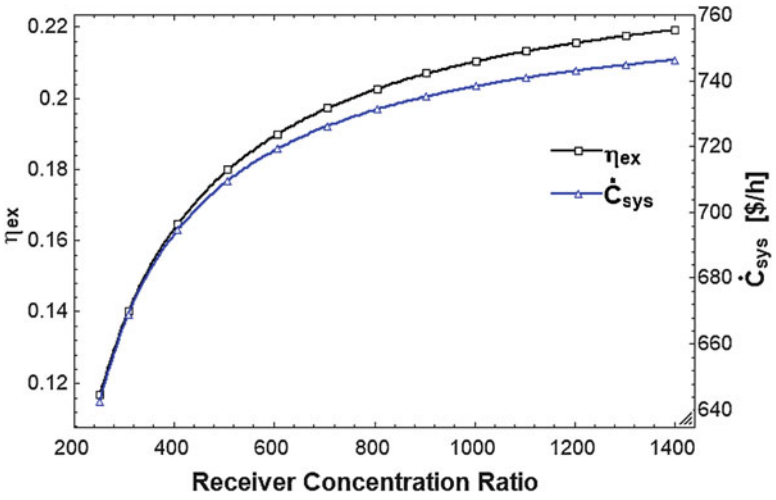

Fig. 6.3 Effect of receiver concentration ratio on exergy efficiency and total cost rate of the system

increasing exergy efficiency. Also, investment cost and fuel cost rates of stream 1 have an enhancement with increment of concentration ratio. Decrease of this effect is heat loss reduction and absorbed heat transfer of receiver, investment cost of receiver and tower, and mass flow of stream 1 enhancement. So, it is a good idea to optimize concentration ratio for two objective functions.

6.4.3 Effect of Generator Pinch Point Temperature Difference

According to Fig. 6.4, with increasing generator PPTD, exergy efficiency and total cost rate will be decreased and increased, respectively. Because cooling, desalination and solar exergy values are constant and heating, DHW and net electricity product exergy rates have a slight decrease. So, there is a few decreases in the second-law efficiency. With increasing generator PPTD, the total capital cost is almost constant, but $\dot{C}_1$ has a high increase, and for this reason, the total cost rate will be increased.

6.4.4 Effect of MC and RC Pressure Ratio

Pressure ratio of compressors is an important parameter because its increment has a considerable effect on power consumption and investment cost. Figure 6.5 shows its effect on main objectives. According to the figure, pressure ratio around 4 is the best

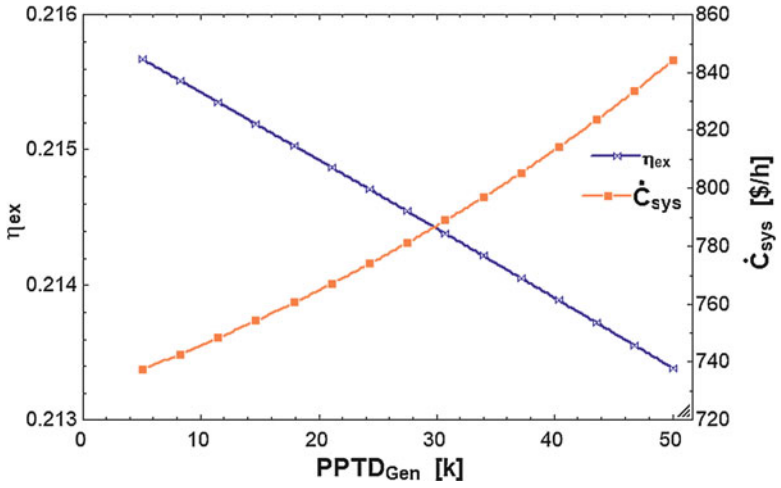

Fig. 6.4 Effect of generator PPTD on exergy efficiency and total cost rate of the system

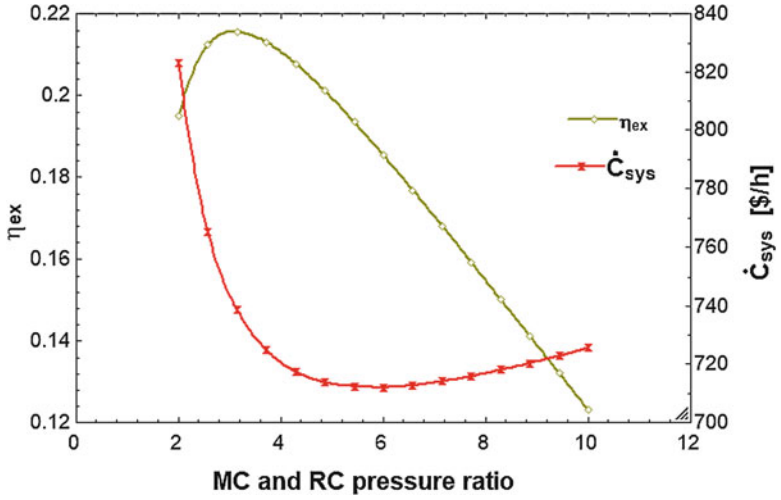

Fig. 6.5 Effect of MC and RC pressure ratio on exergy efficiency and total cost rate of the system

option to maximize exergy efficiency and minimize total cost rate. With increasing pressure ratio, cooling, desalination, and solar exergy rates are constant, and net electricity and DHW exergy rates have decreased, but heating exergy rate will be increased. Also, there is a high decrease in $\dot{C}_1$ and small increase in the total capital costs. These decrease and increase of various values cause to have an optimal point in Fig. 6.5.

6.4.5 *Effect of HTR, LTR, Hum, and Dhum Effectiveness*

Effectiveness is one of significant parameters that has more effect on main products because it has the same value for HTR, LTR, Hum, and Dhum. It is obvious that high effectiveness values cause high proficiency of heat exchangers, superior exergy efficiency, and further total cost rate. So, effectiveness should be optimized in order to obtain good objective functions simultaneously (Fig. 6.6).

6.4.6 *Effect of Ambient, Water, and Seawater Inlet Temperatures*

According to Fig. 6.7, ambient temperature is one of most important parameters that plays a significant role in main objectives. Also, ambient temperature has the same value as DHW and HU inlet water temperatures and seawater inlet temperature to the HDH system. Because of the existing environment temperature in negative part of exergy formulas, all streams' exergy rates will be decreased with the enhancement of ambient temperature, and for this reason, exergy efficiency decreases. On the other hand, $\dot{C}_1$ has small reduction, but $\dot{Z}_{tot}$ has high enhancement, and these behaviors cause to increase the total cost rate. So, in this result, it can be obtained that the proposed system should be created in cold regions.

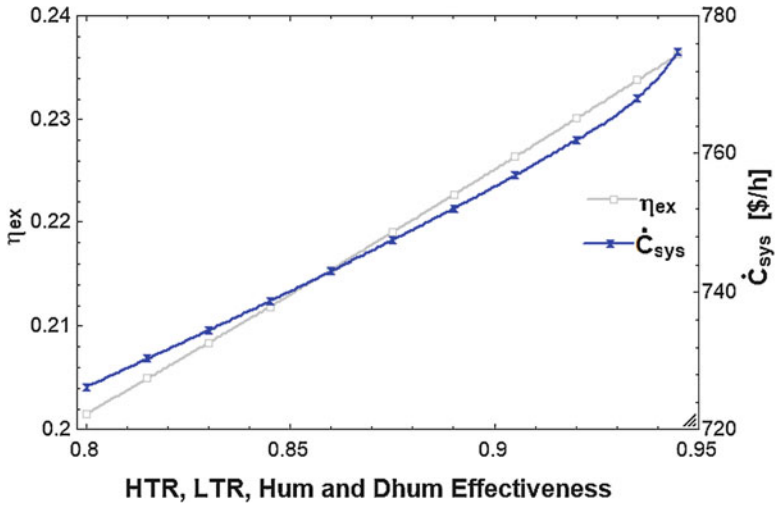

Fig. 6.6 Effect of HTR, LTR, Hum, and Dhum effectiveness on exergy efficiency and total cost rate of the system

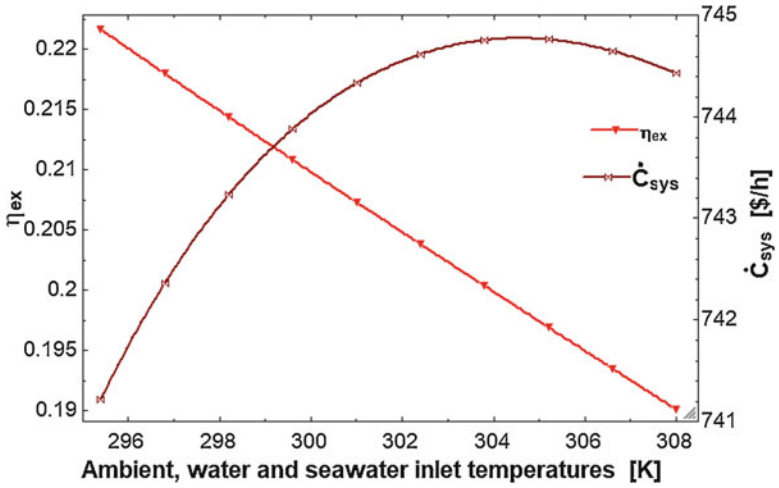

Fig. 6.7 Effect of ambient, water, and seawater inlet temperatures on exergy efficiency and total cost rate of the system

6.4.7 Effect of T-CO2 Compressor to Turbine Electricity Ratio

Electricity consumption of T-CO2 compressor is one of the principal parameters that impacts on exergy efficiency and total cost rate. By enhancement of work ratio, solar, heating and DHW exergy rates are not changed, but net power output has large reduction than cooling and desalination exergy rate enhancement. So, according Fig. 6.8, increment of electricity ratio causes reduction of the second-law efficiency. On the other hand, $\dot{C}_1$ is invariant, and total investment costs have enhancement due to increasing of power consumption of T-CO2 compressor and mass flow rates of cooling and desalination units. So, in small electricity ratios, the proposed system has suitable performance.

6.5 Concluding Comments

Exergy and exergoeconomic analysis of a multi-generation system operating with a solar tower power (STP) plant was carried out in this chapter. It was found that using STP plant as a prime mover of a multi-generation system leads to encouraging results, notwithstanding less attention is paid in this regard in comparison with direct capturing of solar irradiance via solar collectors. The following major results are extracted through the study:

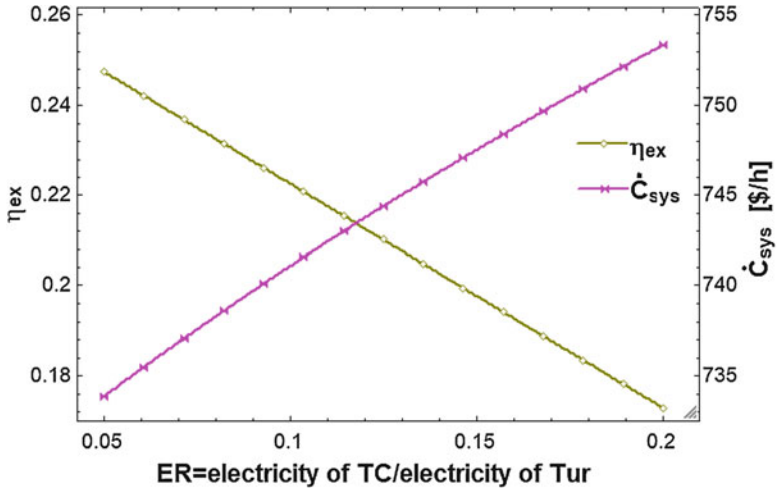

Fig. 6.8 Effect of T-CO2 compressor to turbine electricity ratio on exergy efficiency and total cost rate of the system

- The receiver had a pivotal role in the overall exergy destruction by exergy destruction of 2006 kW, followed by heliostat with exergy destruction of 1867 kW.
- The overall exergy efficiency and cost of the system were computed 21.45% and 743.2 $/h, respectively.
- It was discerned that exergy efficiency can be raised up from the base value with the rise of direct normal irradiance (DNI), receiver concentration ratio, and heat exchangers effectiveness or with the decrease of the generator pinch point temperature, ambient temperature, and amount of electricity supplied to the transcritical CO_2 refrigeration cycle.
- The overall cost rate parameter can be decreased by decreasing the amount of electricity supplied to the transcritical CO_2 refrigeration cycle, heat exchangers effectiveness, generator pinch point temperature, DNI, and receiver concentration ratio.

References

1. Bejan, A., & Tsatsaronis, G. (1996). *Thermal design and optimization*. John Wiley & Sons, USA.
2. Bejan, A. (2016). *Advanced engineering thermodynamics*. John Wiley & Sons, USA.
3. Tsatsaronis, G. (1993). Thermoeconomic analysis and optimization of energy systems. *Progress in Energy and Combustion Science, 19*(3), 227–257.

4. Leiva-Illanes, R., et al. (2019). Exergy cost assessment of CSP driven multi-generation schemes: Integrating seawater desalination, refrigeration, and process heat plants. *Energy Conversion and Management, 179*, 249–269.
5. Ma, Y., et al. (2019). Optimal integration of recompression supercritical CO2 Brayton cycle with main compression intercooling in solar power tower system based on exergoeconomic approach. *Applied Energy, 242*, 1134–1154.
6. Nayar, K. G., Sharqawy, M. H., & Banchik, L. D. (2016). Thermophysical properties of seawater: A review and new correlations that include pressure dependence. *Desalination, 390*, 1–24.
7. Sharqawy, M. H., Lienhard, J. H., & Zubair, S. M. (2010). Thermophysical properties of seawater: A review of existing correlations and data. *Desalination and Water Treatment, 16* (1–3), 354–380.
8. Wepfer, W., Gaggioli, R., & Obert, E. (1979). Proper evaluation of available energy for HVAC. *ASHRAE Transactions, 85*(1), 214–230.
9. CEPCI. (2016). Chemical engineering plant cost index. *Chemical Engineer*. www.chemengonline.com.
10. Nathan, G., Battye, D., & Ashman, P. (2014). Economic evaluation of a novel fuel-saver hybrid combining a solar receiver with a combustor for a solar power tower. *Applied Energy, 113*, 1235–1243.
11. Ipakchi, O., Mosaffa, A., & Farshi, L. G. (2019). Ejector based CO2 transcritical combined cooling and power system utilizing waste heat recovery: A thermoeconomic assessment. *Energy Conversion and Management, 186*, 462–472.
12. Rostamzadeh, H., et al. (2018). Exergoeconomic optimisation of basic and regenerative triple-evaporator combined power and refrigeration cycles. *International Journal of Exergy, 26*(1–2), 186–225.
13. Sayyaadi, H., & Ghorbani, G. (2018). Conceptual design and optimization of a small-scale dual power-desalination system based on the Stirling prime-mover. *Applied Energy, 223*, 457–471.
14. Gholizadeh, T., Vajdi, M., & Mohammadkhani, F. (2019). Thermodynamic and thermoeconomic analysis of basic and modified power generation systems fueled by biogas. *Energy Conversion and Management, 181*, 463–475.
15. Kotas, T. J. (2013). *The exergy method of thermal plant analysis*. John Wiley & Sons, USA.
16. Wang, X., & Dai, Y. (2016). Exergoeconomic analysis of utilizing the transcritical CO2 cycle and the ORC for a recompression supercritical CO2 cycle waste heat recovery: A comparative study. *Applied Energy, 170*, 193–207.

Chapter 7
Energy and Exergy Analysis of a Geothermal-Based Multi-generation System

Mohammad Ebadollahi, Pourya Seyedmati, Hadi Rostamzadeh, Hadi Ghaebi, and Majid Amidpour

Nomenclature

Symbols

A	Area (m^2)
c_p	Specific heat at constant pressure (kJ. kg^{-1})
D	Membrane thickness (μm)
E	Electricity
$\dot{E}$	Exergy rate (kW)
e	Exergy per mass (kW. kg^{-1})
F	Faraday constant (C. mol^{-1})

M. Ebadollahi
Faculty of Mechanical Engineering, Department of Energy System Engineering, K.N. Toosi University of Technology, Tehran, Iran

P. Seyedmati
Department of Mechanical Engineering, Faculty of Aerospace Engineering, Tarbiat Modares University, Tehran, Iran

H. Rostamzadeh
Energy & Environment Research Center, Niroo Research Institute (NRI), Tehran, Iran

H. Ghaebi (✉)
Department of Mechanical Engineering, Faculty of Engineering, Mohaghegh Ardabili University, Ardabil, Iran
e-mail: hghaebi@uma.ac.ir

M. Amidpour
Faculty of Mechanical Engineering, Department of Energy System Engineering, K.N. Toosi University of Technology, Tehran, Iran

Energy & Environment Research Center, Niroo Research Institute (NRI), Tehran, Iran
e-mail: amidpour@kntu.ac.ir

F. Jabari et al. (eds.), *Integration of Clean and Sustainable Energy Resources and Storage in Multi-Generation Systems*,
https://doi.org/10.1007/978-3-030-42420-6_7

Gth	Geothermal
h	Enthalpy (kJ. kg^{-1})
J	Current density (A. m^{-2})
$\dot{m}$	Mass flow rate (kg. s^{-1})
M	Molar mass (kg. $kmol^{-1}$)
P	Pressure (bar)
RR	Recovery ratio
$\dot{Q}$	Heat transfer rate (kW)
R	Ohmic resistance
s	Entropy (kJ. $kg^{-1}K^{-1}$)
S	Salinity (g. kg^{-1})
T	Temperature (K)
TTD	Thermal temperature difference (K)
U	Overall heat transfer coefficient (W. $m^{-2}K^{-1}$)
V	Electric potential (V)
X	Concentration (kg. m^{-3})
YB	Basic ammonia concentration

Abbreviations

FF	Fouling factor
HP	High pressure
KS	Kalina system
PEM	Proton Exchange Membrane
PR	Pump ratio
RHE	Recovery heat exchanger
RO	Reverse osmosis
SHE	Solution heat exchanger
SPC	Specific power consumption
TER	Turbine expansion ratio
TCF	Temperature correction factor

Greek Letters

E	Effectiveness
η	Efficiency (%)
ρ	Density (kg. m^{-3})
σ	Ionic conductivity (s. m^{-1})
λ	Membrane surface water (Ω^{-1})
$\prod$	Osmic pressure

Subscripts and Superscripts

abs	Absorber
act	Activation
B	Brine
CH	Chemical

comp	Compressor
D	Distillate
D	Destruction
e	Element
E.V	Expansion valve
f	Feed
F	Fuel
G	Generator
H	Heater
in	Inlet
int	Intercooler
Is	Isentropic
KN	Kinetic
mem	Membrane
net	Net value
out	Outlet
p	Pure
pu	Pump
P	Product
PH	Physical
PT	Potential
sw	Sea water
T	Turbine
tri	Trigeneration

7.1 Introduction

Geothermal energy is considered as more sustainable heat source, in many regions of the globe, than other available renewable energies such as solar, biogas, and wind. Underground rocks and fluids of the earth mainly store the geothermal energy in shape of heat. This energy not only can be utilized for heating but also can be transferred to different appropriate systems to be converted to other useful forms of energy [1]. The geothermal sources are generally classified into three categories based on the temperature [2, 3]:

- Low-temperature geothermal sources (below 90 °C)
- Moderate-temperature geothermal sources (between 90 °C and 150 °C)
- High-temperature geothermal sources (above 150 °C)

The applications of these heat sources are various, which is determined by their temperature. The low-temperature heat sources are used for directly heating. The medium-temperature heat sources is introduced as the most practical for small-scale system due to its ability to be used for production of many different commodities

such as power production and cooling and heating production. Accordingly, large-scale energy-supplying systems need high-temperature geothermal heat sources [3]. Moreover, cogeneration systems driven by renewable energy sources are recommended as energy systems of the future. In this matter, geothermal heat source, as one of the most sustainable sources of renewable energies, has key role in next-generation energy plants due to its high potential of providing energy in different scales and various applications. Multi-generation systems are alluded to produce various useful forms of energy from the same heat source. Several research works have studied the usage of geothermal heat sources for multi-generation purposes. Ghaebi et al. [1] devised a new multi-generation system driven by geothermal source to produce cooling via a absorption refrigeration system (ARS), heating via a domestic hot water (DHW), freshwater via a humidification-dehumidification (HDH) unit, and electricity via a KS. They executed exergoeconomic optimization of the reckoned setup and reported optimum thermal and exergy efficiencies of 94.84% and 47.89%. Also, Ghaebi et al. [4] devised a multi-generation system for heat production via a heat pump system (HPS), cooling via an ARS, and electricity via liquefied natural gas cold exergy. They introduced the first heat exchanger (HE) used for recovery of cold energy of LNG as the most destructive element. In another study, Rostamzadeh et al. devised a new multi-generation system and investigated the efficiency of the setup from thermodynamic [5] and thermoeconomic vantage points [6]. They highly recommended the use of geothermal in a hybrid way with biogas energy to further increase reliability and availability of the devised multi-generation system from thermoeconomic vantage point. Ebadollahi et al. [7] used geothermal source and LNG heat sink to drive a novel multi-generation system by using an integral trigeneration system and a PEM electrolyzer. They computed exergy and energy efficiencies of 28.91% and 38.33%, respectively.

Nowadays, extracting energy from geothermal-based power systems utilizing low-temperature heat sources and LNG cold energy as heat sink is presented strongly by researchers. For instance, Ghaebi et al. [8] used LNG to recover cold energy from a new geothermal-based cogeneration cycle. They analyzed the performance of the proposed system based on the energy, exergy, and exergoeconomic viewpoints, and obtained the energy and exergy efficiencies of 43.25% and 22.51%, respectively. Also, they showed that increment of LNG-turbine inlet pressure leads to an increase in the net output power, thermal efficiency, and exergy efficiency, while sum unit cost of product (SUCP) decreases. In another study conducted by this group [4], LNG cold energy as a heat sink and geothermal heat source are used to drive a novel system based on the absorption refrigeration system (ARS) and heat pump system (HPS). They used high concentrated ammonia at condenser outlet of ARS to produce heat production, while power production is supplied by ARS condenser latent heat of the basic solution. Conducting exergoeconomic assessment of the trigeneration system, the results showed that the suggested system can produce 405.1 kW net power. Ebadollahi et al. [9] used LNG in the mountainous district of the Meshkin Shahr city to supply natural gas required by the resident of the area. Their devised system used geothermal energy of the Sabalan source in the region.

They used KC and ORC as the topping cycles of the devised cogeneration system and recommended ORC for such purpose.

According to the researchers' studies, using geothermal energy for multi-generation systems leads to a promising results. Hence, a novel multi-generation system conducted by a low-temperature Sabalan geothermal source, including an absorption power cycle (APC), a reverse osmosis (RO) unit, a HPS, a PEM electrolyzer, and a LNG, is devised in this research. In Sect. 7.2, an extensive description of the system is presented. In Sect. 7.3, methods, presumptions, equations used for simulation, input parameters, first and second laws of thermodynamic, and economic equations are presented. In the subsequent section, results are displayed, and the conclusion is presented comprehensively.

7.2 Cycle Description

In this study, a multi-generation system of power, heating, hydrogen, NG (natural gas), and pure water production from geothermal heat sources has been presented. A schematic picture of proposed system is shown in Fig. 7.1. The generated vapor enters to the turbine 1 (state 1) to produce power in which the needed heat is supplied by a geothermal heat source. Dense solution of ammonia water leaves the generator (state 7). The high temperature and pressure solution is cooled down through solution heat exchanger (SHE) and is expanded by expansion valve 1 (E.V1) and then goes to the absorber (state 9). The outlet of turbine 1 goes through recovery heat exchanger (RHE) to heat the working fluid in vapor compression (VC) sub-cycle before entering to the absorber. Dilute solution of ammonia water is pumped into generator (state 6), but before that, it is preheated through SHE (process 5–6). In VC sub-cycle, the heated working fluid is compressed by comp1 (process 12–13). The high-temperature outlet of compressor 1 is cooled down through an intercooler (process 13–14) to raise the NG temperature to the temperature needed for consumption (process 21–22). The cooled working fluid is again compressed through comp2 (process 14–15) before entering to heater (state 15) to supply heating needs. Eventually, the high-pressure working fluid is expanded through E.V2 and flows to the RHE to complete the VC sub-cycle (17). The proposed system has three main subsystems in which the waste heat of the absorber is used to heat up the pumped LNG (state 19) to generate the NG, and high-pressure NG is expanded through turbine 2 to produce power. A portion of the produced power in turbine 2 drives two other more subsystems of producing H2 and pure water. The PEM electrolyzer receives electric power to produce H2 by separating water, which has been preheated by a heat exchanger (HE) (process 23–24) to reach the PEM working temperature, to H2 and O2. The produced H2 and O2 is stored in specific tanks, respectively. The seawater is pumped into RO unit (process 29–30) by a high-pressure pump (HPP) in which the RO unit does the duty of purifying the seawater. The high-pressure brine in RO is used to produce power through turbine 3 (process 32–33).

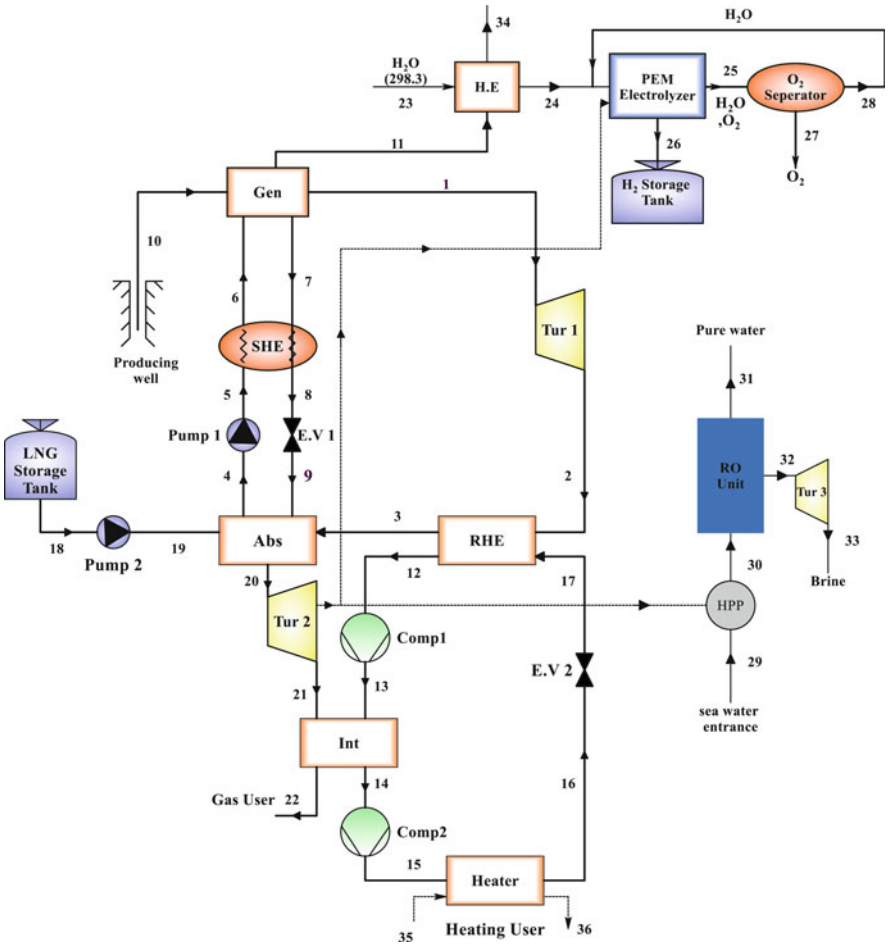

Fig. 7.1 Schematic diagram of proposed multi-generation system

7.3 Presumption and Methodology

7.3.1 Presumption

The following presumptions are made through this modeling [10–12].

- Mathematical models are developed at steady-state condition.
- Specific heat is considered constant.
- There are no pressure losses through pipelines and connections.
- In turbines, there is no heat transfer losses.
- The reference pressure and temperature are considered 0.101 MPa and 298 K, respectively.

- Water enters the PEM electrolyzer at ambient condition.
- The produced H_2 and O_2 are cooled to ambient temperature.
- There is no energy loss during the electrolyzing process.

7.3.2 PEM Electrolyzer Mathematical Modeling

An illustrative configuration of the PEM electrolyzer is depicted in Fig. 7.1. An electrochemical modeling is required to assess the PEM from thermodynamic prospects. The PEM equations are derived from [7].

When the needed thermal energy ($T\Delta S$) and ΔG (Gibb's free energy) of the chemical reaction are summed, the overall energy is as follows:

$$\Delta H = \Delta G + \Delta T \tag{7.1}$$

The H2 molar mass flow rate is estimated by the following:

$$\dot{N}_{H_2} = \frac{J}{2F} \tag{7.2}$$

F is the Faraday constant and J is called the current density. The electrical power entrance rate to the electrolyzer is derived as follows:

$$E_{\text{electric}} = JV \tag{7.3}$$

The voltage potential (V) is given as follows:

$$V = V_0 + V_{\text{act,a}} + V_{\text{act,c}} + V_{\text{Ohm}} \tag{7.4}$$

where V_0 is the reversible potential and is extracted by the Nernst equation as follows:

$$V_0 = 1.229 - 8.5 \times 10^{-4}(T_{\text{PEM}} - 298) \tag{7.5}$$

Here, $V_{\text{act, a}}$, $V_{\text{act, c}}$ and V_{ohm} are the anode activation overpotential, cathode activation overpotential, and the ohmic overpotential of the electrolyte, respectively. The ionic conductivity at each region of the PEM membrane $\lambda(x)$ is calculated as follows:

$$\sigma_{\text{PEM}}[\lambda(x)] = [0.5139\lambda(x) - 0.326] \exp\left[1268\left(\frac{1}{303} - \frac{1}{T}\right)\right] \tag{7.6}$$

where x is the distance calculated from the cathode side and $\lambda(x)$ is calculated as follows:

$$\lambda(x) = \frac{\lambda_a - \lambda_c}{D} x + \lambda_c \tag{7.7}$$

λ_a and λ_c represent the water quantity of anode and cathode membranes at their own surfaces, respectively. D is the thickness of the used membrane. The PEM ohmic resistance is estimated as follows:

$$R_{PEM} = \int_0^D \frac{dx}{\sigma_{PEM}[\lambda(x)]} \tag{7.8}$$

The ohmic overpotential equation based on the Ohm's potential law is defined as follows:

$$V_{ohm,PEM} = JR_{PEM} \tag{7.9}$$

The activation overpotential ($V_{act,\ i}$) is obtained by the following:

$$V_{act,i} = \frac{RT}{F} \sin h^{-1}\left(\frac{J}{2J_{a,i}}\right), i = a, c \tag{7.10}$$

Here, J_0 is the exchange current density of the electrolyzer obtained as follows:

$$J_{0,i} = J_i^{ref} \exp\left(-\frac{E_{act,i}}{RT}\right), i = a, c \tag{7.11}$$

$E_{act,\ i}$ is the activation electricity of PEM (for both anode and cathode sides) and J_i^{ref} is called the pre-exponential factor of function.

7.3.3 RO Mathematical Modeling

The distillate mass flow rate M_d is division of feed mass flow rate M_f on recovery ratio RR as follow [13]:

$$M_d = \frac{M_f}{RR} \tag{7.12}$$

The rejected brine is calculated as follows:

$$M_b = M_f + M_d \tag{7.13}$$

The distilled water concentration (X_d) is computed as follows:

$$X_{\mathrm{d}} = X_{\mathrm{f}}(1 - \mathrm{SRP}) \tag{7.14}$$

X_{f} is the feed flow rate salt concentration and SRP is salt rejection percentage. The rejected salt concentration X_{b} in kg/m^3 can be obtained by the following:

$$X_{\mathrm{b}} = \frac{M_{\mathrm{f}} \times X_{\mathrm{f}} - M_{\mathrm{d}} \times X_{\mathrm{d}}}{M_{\mathrm{b}}} \tag{7.15}$$

The average salt concentration X_{av} in kg/m^3 can be obtained by the following:

$$X_{\mathrm{av}} = \frac{M_{\mathrm{f}} \times X_{\mathrm{f}} - M_{\mathrm{b}} \times X_{\mathrm{b}}}{M_{\mathrm{b}}} \tag{7.16}$$

The temperature correction factor TCF is estimated as follows:

$$\mathrm{TCF} = \exp\left(2700 \times \left(\frac{1}{273 + t} - \frac{1}{298}\right)\right) \tag{7.17}$$

The membrane salt permeability k_{s} is calculated as follows:

$$k_{\mathrm{s}} = \mathrm{FF} \times \mathrm{TCF} \times 4.72 \times 10^{-5} \times \left(0.06201 - \left(5.31 \times 10^{-5} \times (t + 273)\right)\right) \tag{7.18}$$

where, FF is the fouling factor. The water permeability k_{w} is as follows:

$$k_{\mathrm{w}} = 6.84 \times 10^{-8} \times (18.6863 - (0.177 \times X_{\mathrm{b}}))/(t + 273) \tag{7.19}$$

The osmic pressure for feed side, distillate product side, and brine side are obtained as follows:

$$\prod_{\mathrm{f}} = 75.84 \times X_{\mathrm{f}} \tag{7.20}$$

$$\prod_{\mathrm{d}} = 75.84 \times X_{\mathrm{d}} \tag{7.21}$$

$$\prod_{\mathrm{b}} = 75.84 \times X_{\mathrm{b}} \tag{7.22}$$

Moreover, on the feed side, the average osmic pressure is found as follows:

$$\prod_{\mathrm{av}} = 0.5 \times \left(\prod_{\mathrm{f}} + \prod_{\mathrm{b}}\right) \tag{7.23}$$

The net osmotic pressure across the membrane is calculated as follows:

$$\Delta \prod = \prod_{\text{av}} - \prod_{\text{d}} \tag{7.25}$$

Thus, the net pressure difference across the membrane is as follows:

$$\Delta P = \left(\frac{M_{\text{d}}}{3600 \times \text{TCF} \times \text{FF} \times A_{\text{e}} \times n_{\text{e}} \times n_{\text{v}} \times k_{\text{w}}} \right) + \Delta \prod \tag{7.26}$$

In which A_{e} is the area of the element, n_{e} is the number of elements, and n_{v} is the number of used pressure vessels.

RO is driven by a high-pressure pump. The amount of required input power for RO pump is calculated by the following relation:

$$\text{HP} = \left(\frac{1000 \times M_{\text{f}} \times \Delta P}{3600 \times \rho_{\text{f}} \times \eta_{\text{p}}} \right) \tag{7.27}$$

ρ_{f} is feed flow density and η_{p} is driving pump efficiency. Accordingly, the specific power consumption in kW/m^3 is obtained as follows:

$$\text{SPC} = \frac{HP}{M_{\text{d}}} \tag{7.28}$$

7.4 Thermodynamic Analysis

In this section, thermodynamic modeling and some other mathematical relations of the proposed system are explained in details. Each part of the proposed system is regarded as a control volume. The general form of energy and mass balance equations for a control volume at steady state can be expressed as follows [14]:

$$\sum \dot{m}_{\text{in}} = \sum \dot{m}_{\text{out}} \tag{7.29}$$

$$\dot{Q} - \dot{W} = \sum \dot{m}_{\text{out}} h_{\text{out}} - \sum \dot{m}_{\text{in}} h_{\text{in}} \tag{7.30}$$

The rate of total exergy of a flow ($\dot{E}_{\text{total}}$) consists of four main components: physical exergy rate ($\dot{E}_{\text{PH}}$), kinetic exergy rate ($\dot{E}_{\text{KN}}$), potential exergy rate ($\dot{E}_{\text{PT}}$), and chemical exergy rate ($\dot{E}_{\text{CH}}$) [15]:

$$\dot{E}_{\text{total}} = \dot{E}_{\text{PH}} + \dot{E}_{\text{KN}} + \dot{E}_{\text{PT}} + \dot{E}_{\text{CH}} \tag{7.31}$$

Among these four components, kinetic and potential exergies are usually negligible due to their small value. The rate of physical exergy of a closed system is given as below:

$$\dot{E}_{\mathrm{PH}} = \dot{m}(h - h_0 - T_0(s - s_0)) \tag{7.32}$$

Also, for chemical exergy rate, we have the following:

$$\dot{E}_{\mathrm{CH}} = \dot{m}\left[\sum_{i=1}^{n} y_i e_{\mathrm{CH},i} + RT_0 \sum_{i=1}^{n} y_i \ln y_i\right] \tag{7.33}$$

In which y_i is the molar concentration and $e_{\mathrm{CH},\ i}$ shows the specific chemical exergy of the material.

The exergy balance equation for the ith component of a system can be stated as follows:

$$\dot{E}_{\mathrm{F}}^{i} = \dot{E}_{\mathrm{P}}^{i} + \dot{E}_{\mathrm{D}}^{i} \tag{7.34}$$

In the above formula, $\dot{E}_{\mathrm{D}}^{i}$ is the rate of exergy destruction and $\dot{E}_{\mathrm{F}}^{i}$ and $\dot{E}_{\mathrm{P}}^{i}$ are exergy rates of fuel and product of the ith component, respectively.

In the same way, the balance equation for the overall system can be considered as follows:

$$\dot{E}_{\mathrm{F}}^{\mathrm{total}} = \dot{E}_{\mathrm{P}}^{\mathrm{total}} + \dot{E}_{\mathrm{D}}^{\mathrm{total}} \tag{7.35}$$

Exergetic efficiency of element $i(\eta_{\mathrm{ex}}^{i})$ is expressed as follows:

$$\eta_{\mathrm{ex}}^{i} = \dot{E}_{\mathrm{P}}^{i} / \dot{E}_{\mathrm{F}}^{i} \tag{7.36}$$

To compare the exergetic destruction of each component of the system with other components, the exergy destruction ratio is defined as follows [16]:

$$y_{\mathrm{D},i} = \dot{E}_{\mathrm{D},i} / \dot{E}_{\mathrm{D,total}} \tag{7.37}$$

The total system exergy efficiency is considered as the same as Eq. (7.36):

$$\eta_{\mathrm{ex}}^{\mathrm{total}} = \dot{\mathrm{E}}\mathrm{x}_{\mathrm{P}}^{\mathrm{total}} / \dot{\mathrm{E}}\mathrm{x}_{\mathrm{F}}^{\mathrm{total}} \tag{7.38}$$

Table 7.1 provides some of the important energy- and exergy-based balance equations of the introduced setup.

The amount of net power and other relations for the whole system have been reported at the last row of Table 7.1. These equations show that turbines 1 and

Table 7.1 Energy and exergy balance of components

Component	Energy balance equations	Exergy balance equations
Generator	$\dot{Q}_{\mathrm{g}} = \dot{m}_{10}(h_{10} - h_{11})$ $\dot{Q}_{\mathrm{g}} = \dot{m}_1 h_1 + \dot{m}_7 h_7 - \dot{m}_6 h_6$	$\dot{E}_{\mathrm{D}}^{\mathrm{g}} = (\dot{E}_{10} - \dot{E}_{11}) - (\dot{E}_1 + \dot{E}_7 - \dot{E}_6)$
Absorber	$\dot{Q}_{\mathrm{abs}} = \dot{m}_3 h_3 + \dot{m}_9 h_9 - \dot{m}_4 h_4$ $\dot{Q}_{\mathrm{abs}} = \dot{m}_{19}(h_{20} - h_{19})$	$\dot{E}_{\mathrm{D}}^{\mathrm{abs}} = (\dot{E}_3 + \dot{E}_9 - \dot{E}_4) - (\dot{E}_{20} - \dot{E}_{19})$
SHE	$\dot{Q}_{\mathrm{SHE}} = \dot{m}_7(h_7 - h_8)$ $\dot{Q}_{\mathrm{SHE}} = \dot{m}_5(h_6 - h_5)$	$\dot{E}_{\mathrm{D}}^{\mathrm{SHE}} = (\dot{E}_7 - \dot{E}_8) - (\dot{E}_6 - \dot{E}_5)$
RHE	$\dot{Q}_{\mathrm{RHE}} = \dot{m}_2(h_2 - h_3)$ $\dot{Q}_{\mathrm{RHE}} = \dot{m}_{12}(h_{12} - h_{17})$	$\dot{E}_{\mathrm{D}}^{\mathrm{RHE}} = (\dot{E}_2 - \dot{E}_3) - (\dot{E}_{12} - \dot{E}_{17})$
Heater	$\dot{Q}_h = \dot{m}_{15}(h_{15} - h_{16})$ $\dot{Q}_h = \dot{m}_{35}(h_{36} - h_{35})$	$\dot{E}_{\mathrm{D}}^{h} = (\dot{E}_{15} - \dot{E}_{16}) - (\dot{E}_{36} - \dot{E}_{35})$
HE and electrolyzer	$\dot{Q}_{\mathrm{HE}} = \dot{m}_{11}(h_{11} - h_{34})$ $\dot{Q}_{\mathrm{HE}} = \dot{m}_{23}(h_{24} - h_{23})$	$\dot{E}_{\mathrm{D}}^{\mathrm{HE}} = (\dot{E}_{11} - \dot{E}_{34}) - (\dot{E}_{24} - \dot{E}_{23})$ $\dot{E}_{\mathrm{D}}^{\mathrm{HE}} = \dot{W}_{\mathrm{PEM}} - (\dot{E}_{26} + \dot{E}_{27})$
Pump 1	$\dot{W}_{\mathrm{pu1}} = \dot{m}_4(h_5 - h_4)$ $\eta_{\mathrm{is,pu1}} = \frac{h_{5s} - h_4}{h_5 - h_4}$	$\dot{E}_{\mathrm{D}}^{\mathrm{pu1}} = \dot{W}_{\mathrm{pu1}} - (\dot{E}_5 - \dot{E}_4)$
Pump 2	$\dot{W}_{\mathrm{pu2}} = \dot{m}_{18}(h_{19} - h_{18})$ $\eta_{\mathrm{is,pu2}} = \frac{h_{19s} - h_{18}}{h_{19} - h_{18}}$	$\dot{E}_{\mathrm{D}}^{\mathrm{pu2}} = \dot{W}_{\mathrm{pu2}} - (\dot{E}_{19} - \dot{E}_{18})$
High-pressure pump (HPP)	$\dot{W}_{\mathrm{HPP}} = \dot{m}_{29}(h_{30} - h_{29})$ $\eta_{\mathrm{is,HPP}} = \frac{h_{30s} - h_{29}}{h_{30} - h_{29}}$	$\dot{E}_{\mathrm{D}}^{\mathrm{HPP}} = \dot{W}_{\mathrm{HPP}} - (\dot{E}_{30} - \dot{E}_{29})$
RO unit	See equations	$\dot{E}_{\mathrm{D}}^{\mathrm{RO}} = (\dot{E}_{30} - \dot{E}_{31})$
Intercooler	$\dot{Q}_{\mathrm{int}} = \dot{m}_{13}(h_{13} - h_{14})$ $\dot{Q}_{\mathrm{int}} = {}_{21}(h_{22} - h_{21})$	$\dot{E}_{\mathrm{D}}^{\mathrm{int}} = (\dot{E}_{21} - \dot{E}_{22}) - (\dot{E}_{13} - \dot{E}_{14})$
Turbine 1	$\dot{W}_{\mathrm{t1}} = \dot{m}_1(h_1 - h_2)$ $\eta_{\mathrm{is,t1}} = \frac{h_1 - h_2}{h_1 - h_{2s}}$	$\dot{E}_{\mathrm{D}}^{\mathrm{t1}} = (\dot{E}_1 - \dot{E}_2) - \dot{W}_{\mathrm{t1}}$
Turbine 2	$\dot{W}_{\mathrm{t2}} = \dot{m}_{20}(h_{20} - h_{21})$ $\eta_{\mathrm{is,t2}} = \frac{h_{20} - h_{21}}{h_{20} - h_{21s}}$	$\dot{E}_{\mathrm{D}}^{\mathrm{t2}} = (\dot{E}_{20} - \dot{E}_{21}) - \dot{W}_{\mathrm{t2}}$
Turbine 3	$\dot{W}_{\mathrm{t3}} = \dot{m}_{32}(h_{32} - h_{33})$ $\eta_{\mathrm{is,t3}} = \frac{h_{32} - h_{33}}{h_{32} - h_{33s}}$	$\dot{E}_{\mathrm{D}}^{\mathrm{t3}} = (\dot{E}_{32} - \dot{E}_{33}) - \dot{W}_{\mathrm{t3}}$
Expansion valve 1	$h_8 = h_9$	$\dot{E}_{\mathrm{D}}^{\mathrm{EV1}} = (\dot{E}_8 - \dot{E}_9)$
Expansion valve 2	$h_{16} = h_{17}$	$\dot{E}_{\mathrm{D}}^{\mathrm{EV2}} = (\dot{E}_{16} - \dot{E}_{17})$
Compressor 1	$\dot{W}_{\mathrm{comp1}} = \dot{m}_{13}(h_{13} - h_{12})$ $\eta_{\mathrm{is,comp1}} = \frac{h_{13s} - h_{12}}{h_{13} - h_{12}}$	$\dot{E}_{\mathrm{D}}^{\mathrm{comp1}} = \dot{W}_{\mathrm{comp1}} - (\dot{E}_{13} - \dot{E}_{12})$
Compressor 2	$\dot{W}_{\mathrm{comp2}} = \dot{m}_{14}(h_{15} - h_{14})$ $\eta_{\mathrm{is,comp2}} = \frac{h_{15s} - h_{14}}{h_{15} - h_{14}}$	$\dot{E}_{\mathrm{D}}^{\mathrm{comp2}} = \dot{W}_{\mathrm{comp1}} - (\dot{E}_{15} - \dot{E}_{14})$
Total system	$\eta_{\mathrm{PEM}} = 0.1$ $\dot{W}_{\mathrm{PEM}} = 0.2\dot{W}_{\mathrm{t2}}$ $\dot{W}_{\mathrm{HPP}} = 0.2(1 - \eta_{\mathrm{power}})\dot{W}_{\mathrm{t2}}$ $\dot{W}_{\mathrm{net}} = \dot{W}_{\mathrm{t1}} + 0.8(1 - \eta_{\mathrm{PEM}})\dot{W}_{\mathrm{t2}}$ $+\dot{W}_{\mathrm{t3}} - \dot{W}_{\mathrm{p1}}$ $-\dot{W}_{\mathrm{p2}} - \dot{W}_{\mathrm{comp1}} - \dot{W}_{\mathrm{comp2}}$ $\eta_{\mathrm{tri}} = \frac{\dot{Q}_{\mathrm{h}} + \dot{W}_{\mathrm{net}} + \dot{N}.LHV_{\mathrm{H2}}}{\dot{Q}_{\mathrm{g}} + \dot{Q}_{\mathrm{HE}}}$	$\dot{E}_{\mathrm{D}}^{\mathrm{tot}} = \sum_{i=1}^{n} \dot{E}_{\mathrm{D}}^{i}$ $\eta_{\mathrm{ex,tot}} = \frac{\dot{E}_{\mathrm{P},h} + \dot{E}_{31} + \dot{E}_{26} + \dot{W}_{\mathrm{net}}}{\dot{E}_{\mathrm{F,g}} + \dot{E}_{\mathrm{F,HE}} + (\dot{E}_{18} - \dot{E}_{22})}$

3 directly supply the electricity of the user, not to mention that some percentage of turbine 2 power is transferred to PEM electrolyzer and HPP, and the rest power of turbine 2 is directed to the users.

7.5 Results and Discussion

In this section, the proposed system evaluation outcomes are presented and discussed in two main subsections: energy and exergy evaluation results and parametric study outcomes. In the first subsection, the important results of thermodynamic assessment are explained in format of tables. In parametric study subsection, some significant parameters of the system have been chosen to study the effects of them on the system performance. To drive the developed EES code, some input parameters are needed that are listed in Table 7.2.

7.5.1 Energy and Exergy Analysis Results

The results of energy and exergy evaluations have been presented in Tables 7.3 and 7.4, respectively. In proposed cycle, the geothermal heat is considered as main heat source of cycle in which the geothermal inlet temperature is 438 K and inlet pressure is 7 bar. The results indicate that the net power amount of the system is 3319 kW and heating output is 157.4 kW. In addition, the hydrogen production rate and pure water production rate are 5.796 kg/h and 26.7 kg/s, respectively. Also, the trigeneration efficiency is obtained as 25.36%, as listed in Table 7.3.

Table 7.4 consists of exergy rate of product, exergy rate of fuel, exergy destruction rate, exergy destruction ratio, and exergy efficiency of each component. From the exergy assessment results, it can be figured out that the absorber with 76.96% of exergy destruction has the highest exergy destruction as denoted in Table 7.4. However, other component exergy destruction ratio does not exceed 5%. Also, the exergy efficiency of the whole system is 21.04%.

7.5.2 Parametric Study

In this section, the impacts of some significant inputs on the trigeneration efficiency and exergy efficiency of the whole system have been investigated. The pressure of generator, heater temperature, expansion ratio of turbine 2, ammonia water concentration, and the PEM temperature are the chosen parameters.

Table 7.2 Input parameters for simulation of the proposed system

Parameter	Value
Ambient temperature, T_0(K)	298
Ambient pressure, P_0(bar)	1.01
Geothermal inlet temperature, $T_{\text{in, Gth}}$(K)	438
Geothermal inlet pressure, $P_{\text{in, Gth}}$(bar)	7
Hot terminal temperature difference of generator, $\text{TTD}_{\text{g, hot}}$(K)	15
Cold terminal temperature difference of generator, $\text{TTD}_{\text{g, cold}}$(K)	10
Terminal temperature difference of absorber, TTD_{abs}(K)	5
Terminal temperature difference of recovery heat exchanger, TTD_{RHE}(K)	5
Heater temperature, T_{heat}(K)	348
Absorber temperature, T_{abs}(K)	313
Mass flow rate of geothermal $\dot{m}_{Gth}(\text{kg.s}^{-1})$	53
Turbine 1 isentropic efficiency, $\eta_{\text{is, t1}}$(%)	90
Turbine 1 isentropic efficiency, $\eta_{\text{is, t2}}$(%)	70
Turbine 2 efficiency ratio, TER2	6
Basic ammonia concentration, *YB*	0.5
Generator pressure, P_{g}(bar)	20
Pumps isentropic efficiency, $\eta_{\text{is, pu}}$(%)	95
Pump 2 ratio, *PR2*	12
Solution heat exchanger effectiveness, $\varepsilon_{\text{is, SHE}}$	0.82
Inlet water temperature, $T_{\text{w, in}}$(K)	298
Inlet water pressure, $P_{\text{w, in}}$(MPa)	0.101
LNG inlet temperature, T_{18}(K)	111.5
Oxygen pressure, P_{O2} (bar)	1.01
Hydrogen pressure, P_{H2} (bar)	1.01
Electrolyzer temperature, $T_{\text{Electrolyzer}}$(K)	353
Activation energy in cathode, $E_{\text{act, c}}$(kJ/mol)	76
Activation energy in cathode, $E_{\text{act, c}}$(kJ/mol)	18
Water content at the anode-membrane interface, $\lambda_{\text{a}}(\Omega^{-1})$	14
Water content at the cathode-membrane interface, $\lambda_{\text{c}}(\Omega^{-1})$	10
Membrane thickness, D(μm)	100
Pre-exponential factor of anode, $J_{\text{a}}^{\text{ref}}$	1.7×10^5
Pre-exponential factor of cathode, $J_{\text{c}}^{\text{ref}}$	4.6×10^3
Faraday constant, F (*C/mol*)	96,486
Recovery ratio of RO unit, RR	0.3
Salt rejection percentage, SR	0.9944
Element area, $A_{\text{e}}(\text{m}^2)$	35.4
Number of pressure vessels, n_{V}	42
Number of pressure membrane elements, n_{e}	7

Table 7.3 Thermodynamic assessment outcomes obtained from the simulation

Performance parameters	Amount
Turbine 1 power, $\dot{W}_{t1}$(kW)	1042
Turbine 2 power, $\dot{W}_{t2}$(kW)	2850
Turbine 3 power, $\dot{W}_{t3}$(kW)	313.3
Pump 1 power, $\dot{W}_{pu1}$(kW)	36.42
Pump 2 power, $\dot{W}_{pu2}$(kW)	36.22
High-pressure pump power, $\dot{W}_{HPP}$(kW)	447.7
PEM electrolyzer power, $\dot{W}_{PEM}$(kW)	285
Compressor 1 power, $\dot{W}_{comp1}$(kW)	7.45
Compressor 2 power, $\dot{W}_{comp2}$(kW)	7.351
Net power, $\dot{W}_{net}$(kW)	3319
Heating output, $\dot{Q}_{h}$(kW)	157.4
Generator duty, $\dot{Q}_{g}$(kW)	13,701
Absorber duty, $\dot{Q}_{abs}$(kW)	12,545
Recovery heat exchanger duty, $\dot{Q}_{RHE}$(kW)	150.5
Heat exchanger duty, $\dot{Q}_{HE}$(kW)	7.387
Intercooler duty, $\dot{Q}_{int}$(kW)	7.899
Trigeneration efficiency, η_{tri}(%)	25.36
Exergy efficiency, η_{ex}(%)	21.04
Hydrogen production rate, $\dot{m}_{hydrogen}$(kg/h)	5.796
Produced pure water rate, $\dot{m}_{p,water}$(kg/s)	26.7

7.5.2.1 The Impact of Generator Pressure on the System

According to the energy conservation relation, the produced heat in generator is decreased when generator pressure increases. The reduction of generated heat leads to a minor reduction in power production of turbine 1 and a sensible reduction in power production of turbine 2. Moreover, the mass flow rate of produced hydrogen will decrease. In spite of decrease in products of the system, the trigeneration efficiency increases because the quantity of heat generation reduction due to pressure increment is more than product reduction. The behavior of exergy efficiency of the system is the same as trigeneration efficiency. Thus, the exergy efficiency increases with generator pressure augmentation (Fig. 7.2).

7.5.2.2 The Impact of Heater Temperature on the System

Increasing the heater temperature leads to an increase in the heating load needed for the users. Accordingly, the compressors input work will increase due to this temperature augmentation which leads to net power reduction. Considering that the thermal energy input of the system in generator does not change, the trigeneration efficiency will decrease. The exergy efficiency of the whole system decreases, while

Table 7.4 Exergy analysis of components

Component	$\dot{E}_{P}^{i}$(kW)	$\dot{E}_{F}^{i}$(kW)	$\dot{E}_{D}^{i}$(kW)	y_{D}^{i}(%)	η_{ex}^{i} (%)
Absorber	1779	9162	7384	76.96	19.41
Compressor 1	6.325	7.45	1.125	0.006	84.9
Compressor 2	6.278	7.351	1.073	0.006	85.4
Expansion valve 1	960.8	979.5	18.77	0.19	98.08
Expansion valve 2	55.07	56.16	1.092	0.006	98.06
Generator	3644	3674	30.65	0.31	99.17
HE	0.61	129.4	128.7	1.13	0.047
Heater	10.81	22.73	11.92	0.073	47.56
HPP	487.9	512.9	95.36	0.026	95.12
Intercooler	1.009	2.722	1.713	0.017	37.06
Pump 1	34.69	36.42	1.7333	0.018	95.24
Pump 2	31.39	36.22	4.827	0.051	86.67
PEM electrolyzer	1.937	285	283.06	2.95	0.067
RHE	12.23	16.36	4.129	0.043	74.76
RO unit	83.07	487.9	404.83	4.29	17.03
SHE	640	1052	412.1	4.29	60.83
Turbine 1	1042	1452	410.3	4.27	71.75
Turbine 2	2850	3287	437.3	4.55	86.69
Turbine 3	313.1	343.5	30.4	0.33	90.67
Total of system	3414	16,224	9594	100	21.04

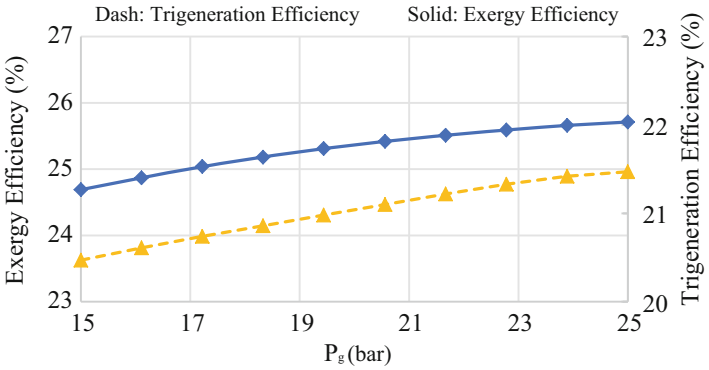

Fig. 7.2 The impact of generator pressure on the trigeneration energy efficiency and total exergy efficiency

heater temperature increases. It can be expressed that the exergy of products declines sensibly due to net power output reduction, and accordingly, the exergy efficiency raises in spite of minor fuel exergy increment (Fig. 7.3).

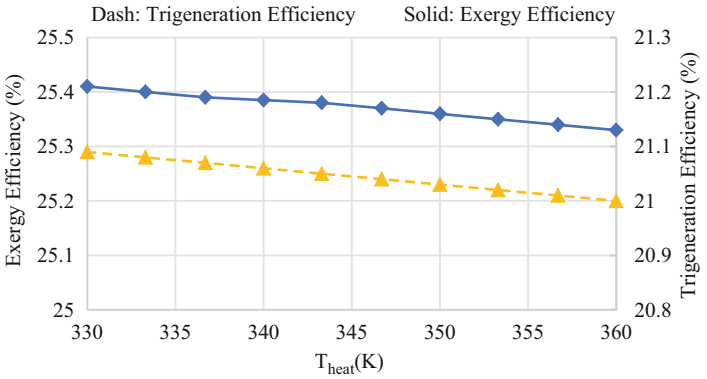

Fig. 7.3 The impact of heater temperature on the trigeneration energy efficiency and total exergy efficiency

7.5.2.3 The Impact of Turbine 2 Expansion Ratio on the System

The heat transfer in generator and PEM heat exchanger do not change with TER2 variation, but the amount of the produced net power will increase due to the increment in power production of turbine 2, and accordingly, the hydrogen production increases. The effects of these two parameters cause the increase in trigeneration efficiency. The exergy efficiency of the whole system shows increasing behavior with increment in expansion ratio of turbine 2, which is predictable. Because of the produced pure water, the produced hydrogen and net power production have increased, while the exergy of fuel has not changed sensibly. So, the exergy efficiency of the whole system has been raised (Fig. 7.4).

7.5.2.4 The Impact of Ammonia Density on the System

Increasing the density of ammonia raises the generated heat. So, the produced power in turbines increase, which leads to net power production augmentation. Moreover, the produced heating and amount of hydrogen production increases. Both products and consumption parameters increase with ammonia density increment, but this raising in product parameters is more than the consumption parameters of up to YB = 0.4. After that, the ratio reverses and augmentation of the consumption parameters becomes more. Thus, the trigeneration efficiency will follow this trend and will be enhanced by ammonia density increment up to 0.4; then, this amount will decline as shown in Fig. 7.5. The exergy efficiency follows the same trend until YB = 0.33 increase with ammonia density increment and then start to decrease, while the product augmentation is overwhelmed by the product raising.

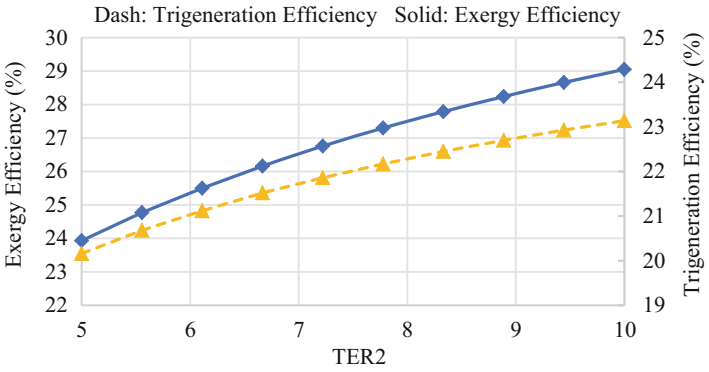

Fig. 7.4 The impact of turbine 2 expansion ratio on the trigeneration energy efficiency and total exergy efficiency

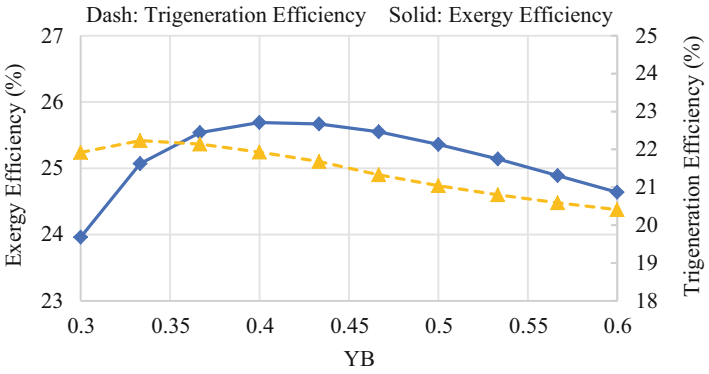

Fig. 7.5 The impact of ammonia water density on the trigeneration energy efficiency and exergy efficiency

7.5.2.5 The Impact of PEM Temperature of the System

The PEM temperature increment leads to change the heat transfer in PEM heat exchanger, and other energy consumption or product parameters in the system are constant. Thus, the trigeneration efficiency has been remained, which is depicted in Fig. 7.6. The exergy of fuel of the system increases because fuel exergy of the PEM heat exchanger raises and fuel exergy of generator and LNG remain constant. So, the exergy efficiency of the whole system is declined.

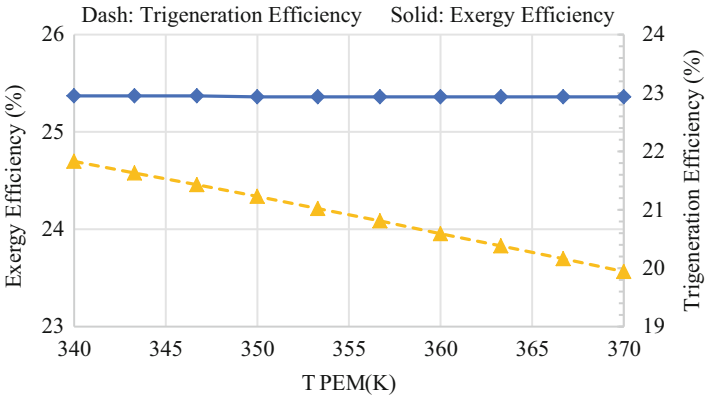

Fig. 7.6 The impact of PEM temperature on the trigeneration energy efficiency and exergy efficiency

7.6 Conclusion

In this chapter, a novel multi-generation system has been advanced and evaluated. The main products of the system are power, heating, hydrogen, pure water, and NG. The needed input power of both PEM and RO sub-cycles is supplied by net power production of system. The proposed cycle has been assessed from energy and exergy standpoints. Furthermore, a parametric study has been conducted on the important parameters of the system. The significant results can be expressed as follows:

- The net power production is 3319 kW, and the produced heating for the user is 157.4 kW. In addition, the mass flow rate of the produced hydrogen and pure water are 5.796 kg/h and 26.7 kg/s respectively.
- The high-pressure pump of RO sub-cycle is the highest power consumption component of the system with more than 400 kW of power consumption.
- The exergy evaluation outcomes showed that the absorber has the highest exergy destruction rate with more than 76 percentage of exergy destruction.
- The trigeneration efficiency and exergy efficiency of the system are 25.36% and 21.04% respectively.
- Both generator pressure and turbine 2 expansion ratio increment improves the trigeneration and exergy efficiency of the system, while heater temperature augmentation has reverse effect on both efficiencies.

References

1. Ghaebi, H., Namin, A. S., & Rostamzadeh, H. (2018). Performance assessment and optimization of a novel multi-generation system from thermodynamic and thermoeconomic viewpoints. *Energy Conversion and Management, 165*, 419–439.
2. Kanoglu, M., & Bolatturk, A. (2008). Performance and parametric investigation of a binary geothermal power plant by exergy. *Renewable Energy, 33*(11), 2366–2374.
3. Ratlamwala, T., & Dincer, I. (2014). Energetic and exergetic investigation of novel multi-flash geothermal systems integrated with electrolyzers. *Journal of Power Sources, 254*, 306–315.
4. Ghaebi, H., Parikhani, T., & Rostamzadeh, H. (2018). A novel trigeneration system using geothermal heat source and liquefied natural gas cold energy recovery: Energy, exergy and exergoeconomic analysis. *Renewable Energy, 119*, 513–527.
5. Rostamzadeh, H., et al. (2018). A novel multigeneration system driven by a hybrid biogas-geothermal heat source, part I: Thermodynamic modeling. *Energy Conversion and Management, 177*, 535–562.
6. Rostamzadeh, H., et al. (2019). A novel multigeneration system driven by a hybrid biogas-geothermal heat source, part II: Multi-criteria optimization. *Energy Conversion and Management, 180*, 859–888.
7. Ebadollahi, M., et al. (2019). Proposal and assessment of a new geothermal-based multigeneration system for cooling, heating, power, and hydrogen production, using LNG cold energy recovery. *Renewable Energy, 135*, 66–87.
8. Ghaebi, H., Parikhani, T., & Rostamzadeh, H. (2017). Energy, exergy and thermoeconomic analysis of a novel combined cooling and power system using low-temperature heat source and LNG cold energy recovery. *Energy Conversion and Management, 150*, 678–692.
9. Ebadollahi, M., et al. (2019). Proposal and multi-criteria optimization of two new combined heating and power systems for the Sabalan geothermal source. *Journal of Cleaner Production, 229*, 1065–1081.
10. Ebadollahi, M., et al. (2019). Exergoeconomic analysis and optimization of innovative cascade bi-evaporator electricity/cooling cycles with two adjustable cooling temperatures. *Applied Thermal Engineering, 152*, 890–906.
11. Rostamzadeh, H., et al. (2019). Comparative study of two novel micro-CCHP systems based on organic Rankine cycle and Kalina cycle. *Energy Conversion and Management, 183*, 210–229.
12. Rostamzadeh, H., et al. (2018). Exergoeconomic optimisation of basic and regenerative triple-evaporator combined power and refrigeration cycles. *International Journal of Exergy, 26*(1–2), 186–225.
13. Nafey, A. S., & Sharaf, M. A. (2010). Combined solar organic Rankine cycle with reverse osmosis desalination process: Energy, exergy, and cost evaluations. *Renewable Energy, 35*(11), 2571–2580.
14. Cengel, Y. A., & Boles, M. A. (2002). Thermodynamics: An engineering approach. *Sea, 1000*, 8862.
15. Bejan, A., & Tsatsaronis, G. (1996). *Thermal design and optimization*. Elsevier Inc., USA.
16. Rostamzadeh, H., et al. (2017). Energy and exergy analysis of novel combined cooling and power (CCP) cycles. *Applied Thermal Engineering, 124*, 152–169.

Chapter 8
Performance and Cost Optimization of Integrated Absorption Power Cycle and Liquefied Natural Gas for the Sabalan Geothermal Heat Source

Hadi Rostamzadeh, Towhid Parikhani, and Hadi Ghaebi

8.1 Introduction

The thermal energy of the earth, known as geothermal energy, can be extracted through natural rocks or boreholes as a reliable heat flow for a plethora of commercial, industrial, or residential applications. Typically, a geothermal heat is categorized based on their temperature in three classifications of below 100 °C (low temperature), between 100 and 180 °C (medium temperature), and above 180 °C (high temperature) [1]. Based upon this classification, the extracted water (or geofluid) can be used directly or indirectly for different applications. For instance, in the case of low-temperature geothermal heat (LTGH), the exploited water can directly be used for heat extractions to heat a building. In the case of extracting medium- or high-temperature geothermal heat (MTGH or HTGH) , however, more high-efficient applications or suggestions can be recommended to produce more valuable products like electricity. That is, MTGH can be utilized in small-scale applications to supply electrical power of a factory or a large mall, while in the case of HTGH, the scale of electricity production can profusely be large enough to provide a specific portion of the power network of a city.

Galloping consumption of energy around the world has captivated attention of many scholars to design more efficacious energy conversion systems. While many sectors in industry convert the available energy from one form to another more

H. Rostamzadeh
Energy and Environment Research Center, Niroo Research Institute (NRI), Tehran, Iran

T. Parikhani · H. Ghaebi (✉)
Department of Mechanical Engineering, Faculty of Engineering, University of Mohaghegh Ardabili, Ardabil, Iran
e-mail: hghaebi@uma.ac.ir

F. Jabari et al. (eds.), *Integration of Clean and Sustainable Energy Resources and Storage in Multi-Generation Systems*,
https://doi.org/10.1007/978-3-030-42420-6_8

useful form, the conversion of energy in power plants is highly crucial in the developed civilization today. Numerous schemes are devised to further increase power plants' efficiency with considering cost aspect of the procedure, where among all using renewable energy has received a well agreement benefit [2, 3].

Among all renewable energies introduced as prime mover for power plants, geothermal energy provides more reliable and sustainable solution where its availability is promised. Geothermal energy is mainly stored in form of heat within the underground fluids and rocks of the earth. The stored heat can be extracted and used directly for heating of a place or be converted into another form of energy by an appropriate energy system [4]. Even though high content of non-condensable gases (NCG) in geothermal wells may affect its sustainability, various methods are devised recently to abate the emission rate via water absorption process and reinjection of NCG back to the reservoir [5]. As a general classification, geothermal sources can be arranged into three following categories [6, 7]: low-temperature sources (below 90 °C), moderate-temperature sources (between 90 °C and 150 °C), and high-temperature sources (above 150 °C). Low-temperature geothermal sources are more appropriate for direct heating, medium-temperature geothermal sources are highly commendable for different commodity production (i.e., power, heating, cooling, etc.) and for small-scale applications, and high-temperature geothermal sources are very appealing for large-scale energy networks [7].

In recent years, absorption power cycle (APC) is spotlighted in research-based projects due to its several merits in terms of thermal conversion process as well as its exergy loss. Broadly speaking, APC has high thermal efficiency due to the use of zeotropic mixture. Also, its cost of components is low due to their small volume. More consequentially, APC has a great merit at low environment temperature. The use of low-grade geothermal energy for APC as a heat source can hence be an adequate arrangement, especially when internally improved APC is accounted for this utility. As an example, in a study by Parikhani et al. [8], APC is integrated with a conventional cooling cycle for cogeneration of electricity and cooling by cutting high heating capacity of lean solution for the sake of cooling production. In another study by Ghaebi et al. [9], a comparative study between two power/hydrogen cogeneration systems constructed based upon a Rankine cycle (RC) and an APC ran by waste heat of a city gate station of a pipeline transmission station is carried out. They clearly delineated competitiveness of APC for this aim by comparing its revealed performance with RC. Ahmadi et al. [10] put the APC into use for power augmentation of a fuel cell (FC) and underlined the main characteristics of the integrated system by investigating impact of chief APC's constant parameters on the new defined thermal efficiency. They found a meaningful increment in thermal and exergy efficiencies of the composed setup. Based upon the exhibited literature review in this paragraph regarding performance enhancement of APC, it can be discerned that augmenting efficiency of this system can be an encouraging topic which is accounted in this system. For this aim, LNG, which stands for liquefied natural gas, is used, and the accountability of the idea is inspected based on thermodynamic concept. However, before we can proceed further, it is valuable to talk about LNG and its application in energy systems.

More recently, Ghaebi et al. [11] used LNG to recover cold energy from an innovative refrigeration/electricity cogeneration setup. They analyzed the performance of the devised unit based on exergoeconomic viewpoint, showing that the thermal and exergetic performance parameters may yield 43.25% and 22.51%, respectively. The scholars showed that as LNG-turbine inlet pressure increases, the net electricity, thermal performance, and exergetic performance increase, while unit cost (UC) decreases. In another study conducted by this group [12], LNG (as a thermal sink) and geothermal source (as thermal source) are used to drive a novel trigeneration setup by accounting an absorption refrigeration system (ARS) and a heat pump system (HPS). They used high-concentrated ammonia at condenser outlet of ARS to produce heat, while latent thermal energy of the main solution from condenser is set to practice of power production. Conducting exergoeconomic inspection of the devised trigeneration plant, the results demonstrated that the devised plant can produce 405.1 kW net power. They also made a conclusion that a surfeit of exergy loses occurs through regasification process in the corresponding heat exchanger.

In light of the authors' background, evaluation of the combined absorption power cycle with LNG power system ran by geothermal source is not performed up to yet. For this sake, efficiency of the APC is ameliorated by hybridizing APC and LNG in an adequate form, using Sabalan geothermal heat source in Iran. The main objectives of the ongoing report are multitudes and are itemized below:

- To uphold the integration of APC and LNG in a single platform accounting low-temperature thermal heat of Sabalan geothermal heat source for power and natural gas extraction
- To assess performance of the devised setup using thermodynamic balance relations
- To present optimization of the devised unit by implementing GA approach
- To inspect impact of some chief parameters on performance of the devised plant

8.2 Cycle Description

The overall layout of a simple APC is shown in Fig. 8.1. The cycle encompasses a turbine, a generator, a solution heat exchanger (SHX), an absorber, an expansion device, and a pump. Geothermal heat is used to supply required heating load of a generator. As the saturated ammonia is rotated through the turbine, the extracted power is stored, and the expanded flow is directed to the absorber. The rich solution at the outlet of a generator is cooled down via the SHX and then is throttled to the down pressure of the unit. At the same time, the weak solution is pumped to the upper-head pressure of the unit and is heated up via an SHX before entering the generator.

To augment power of the described APC, cold exergy of LNG is used to recover condensation heat sink load. The description of the integrated APC/LNG system is

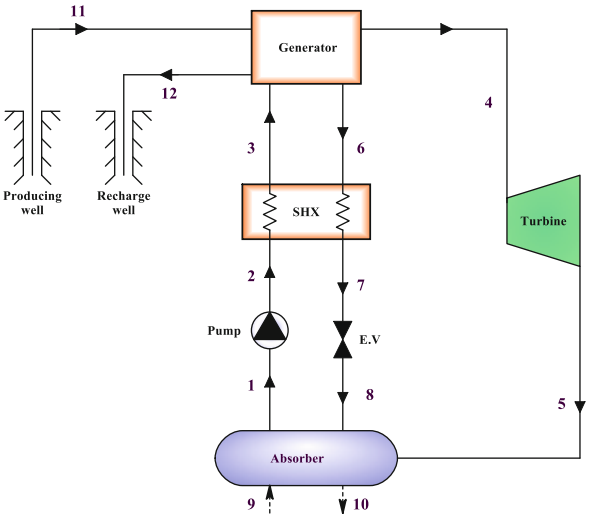

Fig. 8.1 Layout of an APC driven by the Sabalan geothermal heat source

depicted in Fig. 8.2. In the LNG sub-cycle, the liquid gas at sub-zero temperature is supplied to the LNG sub-cycle via pressurizing through a pump and then recovering part of its energy via absorber of APC. Subsequently, this NG is warmed up to a higher temperature (saturated vapor) by HX (state 15) and then is rotated through a turbine for further electricity production as the output gas is supplying the Sabalan district for direct uses (state 16).

8.3 Mathematical Model

8.3.1 Energy Analysis

Some presumptions are pondered in order to effectuate an intensive thermodynamic assessment of the devised integrated power system as follows [13, 14]:

- Steady-state condition is governed.
- Isentropic efficiency relations are used to deal with turbines and pumps.
- Isenthalpic condition is assumed before and after the expansion valve.
- Only physical and chemical exergies are pondered through exergy assessment [15].
- The Sabalan geothermal temperature, pressure, and flow rate are assumed 165 °C, 700 kPa, and 53 kg/s, respectively [16].

In the meantime, some major input data, prerequisite of simulation of the devised APC/LNG setup, are given in Table 8.1.

The inclusive format of governing equations at steady state (SS) for thermodynamic evaluation of a unit is articulated as follows:

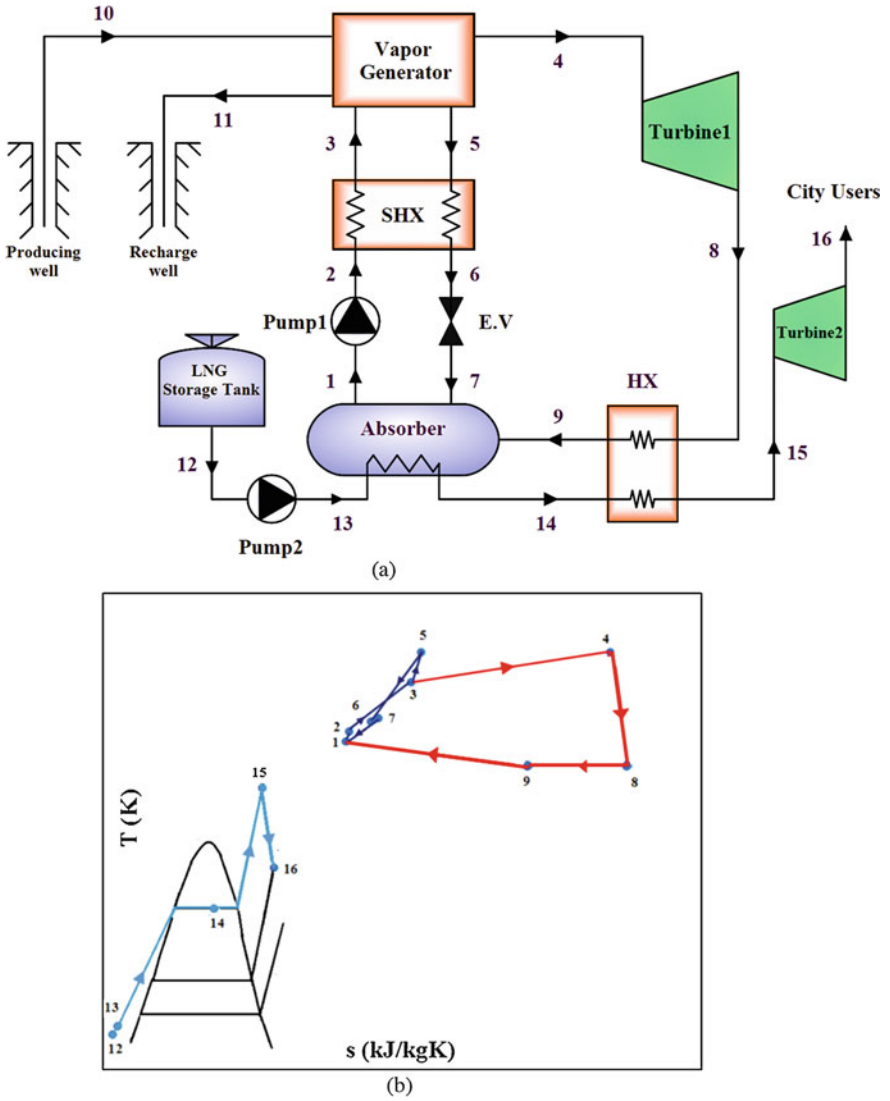

Fig. 8.2 Layout of the (**a**) APC utilizing geothermal heat source and LNG and (**b**) its related T-s sketch

$$\sum \dot{m}_{\text{in}} - \sum \dot{m}_{\text{out}} = 0 \tag{8.1}$$

$$\sum (\dot{m}X)_{\text{in}} = \sum (\dot{m}X)_{\text{out}} \tag{8.2}$$

Table 8.1 Main and necessary input data for the base case

Parameter	Unit	Value
Dead-state temperature, T_0	°C	25
Dead-state pressure, P_0	kPa	101.3
Geothermal inlet pressure, $P_{\text{in, Geo}}$	kPa	700
Geothermal inlet temperature, $T_{\text{in, Geo}}$	°C	165
Mass flow rate of geothermal source, $\dot{m}_{\text{Geo}}$	kg. s^{-1}	53
Turbine 1 inlet pressure, P_4	kPa	106.4
Turbine 2 inlet pressure, P_{15}	kPa	3000
Absorber outlet temperature, T_1	C	50
LiBr mass fraction, X_1	%	45
Minimum temperature difference of heat exchanger, $\Delta T_{\text{min, HX}}$	°C	8
Minimum temperature difference of solution heat exchanger, $\Delta T_{\text{min, SHX}}$	°C	16
Generator hot pinch point temperature difference, $\Delta T_{\text{hot, gen}}$	°C	25
Generator cold pinch point temperature difference, $\Delta T_{\text{cold, gen}}$	°C	3
Pump isentropic efficiency, $\eta_{\text{is, pu}}$	%	85
Turbine isentropic efficiency, $\eta_{\text{is, tur}}$	%	90
Cost of LNG, c_{12}	$/GJ	0
Cost of geothermal source, $c_{\text{in, Geo}}$	$/GJ	15.24
Effectiveness of solution heat exchanger, ε_{SHX}	%	82

$$\sum (\dot{m}h)_{\text{in}} - \sum (\dot{m}h)_{\text{out}} + \sum \dot{Q}_{\text{in}} - \sum \dot{Q}_{\text{out}} + \dot{W} = 0 \tag{8.3}$$

Some energy- and mass-based balance relations to each constituent of the reckoned setup are enumerated in Table 8.2.

8.3.2 Exergy Analysis

In terms of exergy, the balance relation of a unit may be articulated as follows:

$$\dot{\text{E}}\text{x}_{\text{D},k} = \sum_{i=1}^{k} \dot{\text{E}}\text{x}_{\text{in},i} - \sum_{i=1}^{k} \dot{\text{E}}\text{x}_{\text{out},i} \tag{8.4}$$

The overall exergy of the kth state at a unit is declared as follows:

$$\dot{\text{E}}\text{x}_k = \dot{\text{E}}\text{x}_{\text{ph},k} + \dot{\text{E}}\text{x}_{\text{ch},k} \tag{8.5}$$

where

Table 8.2 Mathematical relations to satisfy energy balance concept for different elements

Element	Equation
Vapor generator	$\dot{m}_5 + \dot{m}_4 = \dot{m}_3$, $\dot{m}_3 X_3 = \dot{m}_5 X_5$, $\dot{Q}_{\text{gen}} = \dot{m}_{\text{in,Geo}}(h_{\text{in,Geo}} - h_{\text{out,Geo}})$, $\dot{Q}_{\text{gen}} = \dot{m}_4 h_4 + \dot{m}_5 h_5 - \dot{m}_3 h_3$, $\Delta T_{\text{hot, gen}} = T_{10} - T_4$, $\Delta T_{\text{cold, gen}} = T_{11} - T_3$
Absorber	$\dot{Q}_{\text{abs}} = \dot{m}_9 h_9 + \dot{m}_7 h_7 - \dot{m}_1 h_1$, $\dot{Q}_{\text{abs}} = \dot{m}_{\text{LNG}}(h_{14} - h_{13})$
Solution heat exchanger	$\dot{Q}_{\text{SHX}} = \dot{m}_5(h_5 - h_6)$, $\dot{Q}_{\text{SHX}} = \dot{m}_2(h_2 - h_3)$ $\varepsilon_{\text{SHX}} = (T_5 - T_6)/(T_5 - T_2)$
Heat exchanger	$\dot{Q}_{\text{HX}} = \dot{m}_8(h_8 - h_9)$, $\dot{Q}_{\text{HX}} = \dot{m}_{\text{LNG}}(h_{15} - h_{14})$
Pump 1	$\dot{W}_{\text{pu1}} = \dot{m}_1(h_2 - h_1)$, $\eta_{\text{is, pu1}} = (h_{2s} - h_1)/(h_2 - h_1)$
Pump 2	$\dot{W}_{\text{pu2}} = \dot{m}_{\text{LNG}}(h_{13} - h_{12})$, $\eta_{\text{is, pu2}} = (h_{13s} - h_{12})/(h_{13} - h_{12})$
Turbine 1	$\dot{W}_{\text{tur1}} = \dot{m}_4(h_4 - h_8)$, $\eta_{\text{is, tur1}} = (h_4 - h_8)/(h_4 - h_{8s})$
Turbine 2	$\dot{W}_{\text{tur1}} = \dot{m}_{\text{LNG}}(h_{15} - h_{16})$, $\eta_{\text{is, tur2}} = (h_{15} - h_{16})/(h_{15} - h_{16s})$

$$\dot{\text{E}}\text{x}_{\text{ph},k} = \dot{m}(h - h_0 - T_0(s - s_0))_k \tag{8.6}$$

$$\dot{\text{E}}\text{x}_{\text{ch},k} = \dot{n}_k \left(\sum_k y_i \overline{\text{ex}}_i^{\text{ch},0} + \overline{R} T_0 \sum_i y_i \ln y_i \right) \tag{8.7}$$

where, $\overline{\text{ex}}_i^{\text{ch},0}$ is known as the standard chemical exergy found in Ref. [15] and y_i is concentration of the ith constituent.

The exergetic efficiency of the kth element is declared as follows:

$$\eta_{\text{ex},k} = \frac{\dot{\text{E}}\text{x}_{\text{out}}}{\dot{\text{E}}\text{x}_{\text{in}}} = \frac{\dot{\text{E}}\text{x}_{\text{P},k}}{\dot{\text{E}}\text{x}_{\text{F},k}} \tag{8.8}$$

Some exergy-based balance relations enrolled to each constituent of the reckoned system are enumerated in Table 8.3.

8.3.3 Exergoeconomic Analysis

The balance equation based on cost of the kth element of a unit is pinpointed as follows [15]:

Table 8.3 Mathematical relations to satisfy exergy balance concept for different elements

Element	$\dot{E}x_F^i$	$\dot{E}x_P^i$	$\dot{E}x_D^i$
Vapor generator	$\dot{E}x_{10} - \dot{E}x_{11}$	$\dot{E}x_4 + \dot{E}x_5 - \dot{E}x_3$	$(\dot{E}x_{10} - \dot{E}x_{11}) - (\dot{E}x_4 + \dot{E}x_5 - \dot{E}x_3)$
Absorber	$\dot{E}x_9 + \dot{E}x_7 - \dot{E}x_1$	$\dot{E}x_{14} - \dot{E}x_{13}$	$(\dot{E}x_9 + \dot{E}x_7 - \dot{E}x_1) - (\dot{E}x_{14} - \dot{E}x_{13})$
Solution heat exchanger	$\dot{E}x_5 - \dot{E}x_6$	$\dot{E}x_3 - \dot{E}x_2$	$(\dot{E}x_5 - \dot{E}x_6) - (\dot{E}x_3 - \dot{E}x_2)$
Heat exchanger	$\dot{E}x_8 - \dot{E}x_9$	$\dot{E}x_{15} - \dot{E}x_{14}$	$(\dot{E}x_8 - \dot{E}x_9) - (\dot{E}x_{15} - \dot{E}x_{14})$
Pump 1	$\dot{W}_{pu1}$	$\dot{E}x_2 - \dot{E}x_1$	$\dot{W}_{pu1} - (\dot{E}x_2 - \dot{E}x_1)$
Pump 2	$\dot{W}_{pu2}$	$\dot{E}x_{12} - \dot{E}x_{13}$	$\dot{W}_{pu2} - (\dot{E}x_{12} - \dot{E}x_{13})$
Turbine 1	$\dot{E}x_4 - \dot{E}x_8$	$\dot{W}_{tur1}$	$(\dot{E}x_4 - \dot{E}x_8) - \dot{W}_{tur1}$
Turbine 2	$\dot{E}x_{15} - \dot{E}x_{16}$	$\dot{W}_{tur2}$	$(\dot{E}x_{15} - \dot{E}x_{16}) - \dot{W}_{tur2}$

$$\dot{C}_{q,k} + \sum \dot{C}_{in,k} + \dot{Z}_k = \dot{C}_{w,k} + \sum \dot{C}_{out,k} \tag{8.9}$$

where

$\dot{C}_{out,k}$: refers to the outflowing stream cost rate of the kth element,
$\dot{C}_{in,k}$: refers to the inflowing stream cost rate of the kth element,
$\dot{C}_{w,k}$: refers to the cost rate connected to work generated by the unit,
$\dot{C}_{q,k}$: refers to the cost rate of heat done on the unit.
Exergy, unit cost, and cost rate are related to each other [15]:

$$\dot{C}_k = c_k \dot{E}x_k \tag{8.10}$$

The overall input cost rate of the kth element of a unit can be pinpointed as follows [15]:

$$\dot{Z}_k = \dot{Z}_k^{CI} + \dot{Z}_k^{OM} = CRF \times \frac{\phi_r \times 365 \times 24}{N} \times Z_k \tag{8.11}$$

where

$\dot{Z}_k^{CI}$: refers to the capital investment (CI) cost of the kth element,
$\dot{Z}_k^{OM}$: refers to the operating and maintenance (OM) cost of the kth element,
N: is the annual operational hour of the unit,
ϕ_r: is the maintenance coefficient,
Z_k: refers to the kth element overall cost,
CRF: is the capital recovery factor and is pinpointed as follows [15]:

$$CRF = \frac{k(1+k)^{n_r}}{(1+k)^{n_r} - 1} \tag{8.12}$$

where

n_r: is known as the total period of operation of the unit,

k: is known as the interest rate.

The cost rate connected to the exergy destruction of the kth element is pinpointed as follows [15]:

$$\dot{C}_{D,k} = c_{Fu,k}\dot{E}x_{D,k} \quad \left(\text{If} \quad \dot{E}x_{Pr,k} = \text{constant}\right) \tag{8.13}$$

The detailed cost balance relations and purchase equipment cost (PEC) for each constituent of the devised system are presented in Table 8.4.

The relation between logarithmic mean temperature difference (LMTD) with heat exchanger area and coefficient can be articulated as follows:

$$A_k = \frac{\dot{Q}_k}{U_k \Delta T_{LMTD}} \tag{8.14}$$

The total heat transfer coefficients for each heat exchanger are tabulated in Table 8.5. The attained cost rate at the end of calculation can be updated as follows:

$$\text{Original cost} = \text{Cost at reference year} \times \frac{\text{Cost index for the original year}}{\text{Cost index for the reference year}} \tag{8.15}$$

8.4 Optimization

To augment performance of an energy system, it is highly important to design the devised setup around an optimum condition since the best performance of the system can be obtained and any deliberation and changes can be carried out after that. Normally, optimization based on thermodynamic equations can be achieved by defining energy and exergy efficiency as objective functions. Later on, the best performance of the setup can be attained by maximizing these two parameters as "objective functions." However, in exergoeconomic optimization, the cost index is also added to be minimized. This duty is reckoned in this study by employing genetic algorithm (GA) scheme in a single way or by aggrandizing each parameter into a single operator. The proficiency of each proposal is demonstrated in our previous works [17–20]. Regarding that, Table 8.6 has listed some important parameters employed through the optimization process.

Energy and exergy efficiencies as well as sum unit cost of production (SUCP)of the plant are accounted as objective functions, while the turbine 1 inlet pressure, turbine 2 inlet pressure, generator hot pinch point temperature difference, absorber temperature, HX minimum temperature difference, and LiBr fraction are accounted

Table 8.4 Mathematical relations associated with the cost balance, auxiliary, and purchase equipment cost equations for each element of the devised plant

Component	Cost balance equation	Auxiliary equation	Cost equation
Vapor generator	$\dot{C}_{10} + \dot{C}_3 + \dot{Z}_{gen} = \dot{C}_4 + \dot{C}_5 + \dot{C}_1$	$c_{10} = c_{11}$, $c_{10} = 15.24$ \$/G	$Z_{gen} = 130\left(\frac{A_{gen}}{0.093}\right)^{0.78}$
Absorber	$\dot{C}_7 + \dot{C}_9 + \dot{C}_{13} + \dot{Z}_{abs} = \dot{C}_{14} + \dot{C}_1$	$\left(\dot{C}_7 + \dot{C}_9\right)/\left(\dot{E}x_9 + \dot{E}x_7\right) = \dot{C}_1/\left(\dot{E}x_1\right.$	$Z_{abs} = 130\left(\frac{A_{abs}}{0.093}\right)^{0.78}$
Solution heat exchanger	$\dot{C}_5 + \dot{C}_2 + \dot{Z}_{SHE} = \dot{C}_3 + \dot{C}_6$	$c_5 = c_6$	$Z_{SHX} = 130\left(\frac{A_{SHX}}{0.093}\right)^{0.78}$
Heat exchanger	$\dot{C}_8 + \dot{C}_{14} + \dot{Z}_{HX} = \dot{C}_9 + \dot{C}_{15}$	$c_9 = c_8$	$Z_{HX} = 130\left(\frac{A_{HX}}{0.093}\right)^{0.78}$
Pump 1	$\dot{C}_2 = \dot{C}_{W,pu1} + \dot{C}_1 + \dot{Z}_{pu1}$	$c_{w,\ pu1} = c_{w,\ tur1}$	$Z_{pu1} = 3540\dot{W}_{pu1}^{0.71}$
Pump 2	$\dot{C}_{13} = \dot{C}_{W,pu2} + \dot{C}_{12} + \dot{Z}_{pu2}$	$c_{w,\ pu2} = c_{w,\ tur2}$, $c_{12} = 0$	$Z_{pu2} = 3540\dot{W}_{pu2}^{0.71}$
Turbine 1	$\dot{C}_8 + \dot{C}_{W,tur1} = \dot{C}_4 + \dot{Z}_{tur1}$	$c_4 = c_8$	$Z_{tur1} = \left(\frac{1536\dot{m}_4}{0.92-\eta_{is,tur1}}\right)\ln\left(\frac{P_4}{P_8}\right)\left(1 + e^{(0.036T_4 - 54.4)}\right)$
Turbine 2	$\dot{C}_{16} + \dot{C}_{W,tur2} = \dot{C}_{15} + \dot{Z}_{tur2}$	$c_{15} = c_{16}$	$Z_{tur2} = \left(\frac{1536\dot{m}_{15}}{0.92-\eta_{is,tur2}}\right)\ln\left(\frac{P_{15}}{P_{16}}\right)\left(1 + e^{(0.036T_{15} - 54.4)}\right)$

Table 8.5 Overall heat transfer coefficients associated to heat exchangers [12]

Component	U (kW/m^{2}K)
Generator	1.6
Solution heat exchanger	1
Heat exchanger	1.1
Absorber	0.6

Table 8.6 Main parameters adjusted through the optimization process [21–23]

Parameter	Value
Initial mutation rate	0.25
Crossover probability	0.85
Population individuals number	32
Maximum mutation rate	0.25
Number of generations	64
Minimum mutation rate	0.0005

as the decision variables due to their significance. Next, a multi-objective operator (MOO) is described by counting energy and exergy efficiencies and SUCP in this operator. Now, the chief principle is maximization of the reckoned operator instead of individual parameters. MOO may mathematically be articulated as follows:

$$\mathrm{Max}(\mathrm{MOO} = w_1 \times \eta_{\mathrm{th}} + w_2 \times \eta_{\mathrm{ex}} + w_3 \times (1 - \mathrm{SUCP}_{\mathrm{TOT}}/c_{10})) \tag{8.16}$$

$$w_1 + w_2 + w_3 = 1, \quad 0 \le w_1, w_2, w_3 \le 1 \tag{8.17}$$

where w_1 to w_3 are energy and exergy efficiencies' and SUCP's weight coefficients, respectively. The range of reckoned decision variables are given hereunder:

$$\begin{gathered} 90 \le P_{\mathrm{in,tur1}}(\mathrm{kPa}) \le 120 \\ 2500 \le P_{\mathrm{in,tur2}}(\mathrm{kPa}) \le 3500 \\ 15 \le \Delta T_{\mathrm{hot,gen}}(^{\circ}\mathrm{C}) \le 30 \\ 45 \le T_{\mathrm{abs}}(^{\circ}\mathrm{C}) \le 55 \\ 8 \le \Delta T_{\mathrm{min,HX}}(^{\circ}\mathrm{C}) \le 12 \\ 40 \le X_{\mathrm{B}}(\%) \le 48 \end{gathered} \tag{8.18}$$

For the single-objective optimization (SOO) method, we have the following:
Optimize:

$$\begin{gathered} \eta_{\mathrm{th}} \ \text{ or } \ \eta_{\mathrm{ex}} \ \text{ or} \\ \mathrm{SUCP}_{\mathrm{sys}}\left(P_{\mathrm{in,tur1}}, P_{\mathrm{in,tur2}}, \Delta T_{\mathrm{hot,gen}}, T_{\mathrm{abs}}, \Delta T_{\mathrm{min,HX}}, X_{\mathrm{B}}\right) \end{gathered} \tag{8.19}$$

8.5 Results and Discussions

8.5.1 Parametric Study

8.5.1.1 Generator Hot Pinch Point Temperature Difference's Varying Impact

Figure 8.3 exhibits varying impact of the net electricity, thermal efficiency, exergetic efficiency, and total SUCP with a specific range of generator hot pinch point (PP) temperature differences. As sketch portrays, a rise in the generator hot PP temperature difference leads to the decrease of the net electricity, which can be elaborated by deliberating the fact that a rise in the generator hot PP temperature difference gives a rise to the flow rate of LiBr through turbine 1 while leading to the decrease of the enthalpy difference through it. Since the drops of enthalpy difference are higher than the surge of LiBr flow rate, thus, the turbine 1 electrical power will drop with the rise of generator hot PP temperature difference. In contrary, turbine 2 electricity is moved up as generator hot PP temperature difference rises up, since the natural gas flow rate is moved upward. In the aggregated form, the electrical power of turbines is dropped, since the drop rate of turbine 1 electricity is considerable. Also, the power consumption by both pumps is slightly increased as the generator hot PP temperature difference augments, whereas the augmentation rate of electricity consumed through the processes is lower than the drop rate of attained electricity. Therefore, the net electricity of the combined APC/LNG setup will drop

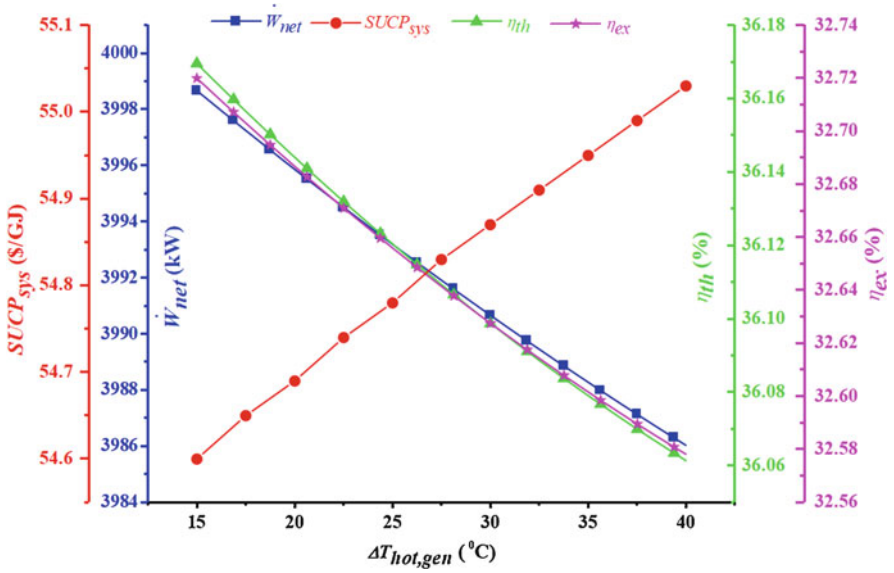

Fig. 8.3 Varying impact of generator hot PP temperature difference on the net electricity, thermal and exergy efficiencies, and total SUCP of the plant

as the generator hot PP temperature difference moves forward. The variation of thermal efficiency resembles variation of the net electricity, and hence, it will drop as the generator hot PP temperature difference goes up. Similarly, the exergetic efficiency is also decreased as generator hot PP temperature difference rises up. Increasing the generator hot PP temperature difference increases exergy of supplied natural gas while decreases net electricity of the unit (as mentioned before). Further, the SUCP goes up as generator hot PP temperature difference increases, which is primarily due to the net electricity augmentation.

8.5.1.2 Turbine 1 Inlet Pressure's Varying Impact

Influence of turbine 1 inlet pressure on the thermal efficiency, net electricity, exergy efficiency, and total SUCP of the plant is exhibited in Fig. 8.4. For relatively high turbine 1 inlet pressures, the flow rates of LiBr and NG are decreased; thus, the aggregated turbine output power (turbine 1 and 2 electricity) will drop. Additionally, pump 1 and 2 consumed electricity is raised up and dropped with the rise of the turbine 1 inlet pressure, respectively. However, the augmentation rate of pump 1 consumed power is lower than the drop of pump 2 consumed electricity; hence, the aggregated pump consumed electricity will drop throughout this variation. Since the drop of the aggregated turbine electricity is profusely appreciable than the drop

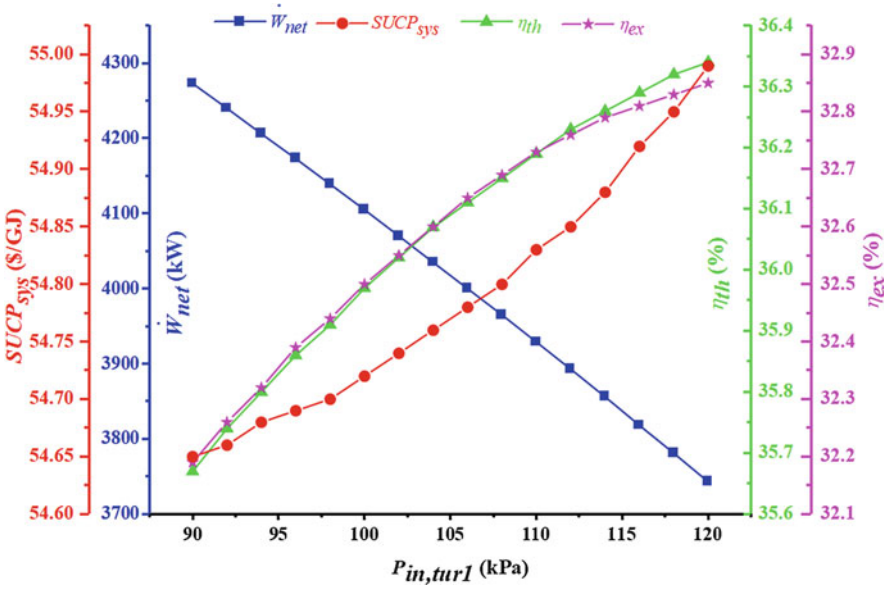

Fig. 8.4 Varying effect of turbine 1 inlet pressure on the thermal efficiency, net electricity, exergy efficiency, and total SUCP of plant

of the aggregated pump consumed electricity, thus, the net electricity will drop with the rise of turbine 1 inlet pressure.

Meanwhile, the geothermal outlet energy increases as turbine 1 inlet pressure goes up, and hence, less heat supply is required. Since the reduction rate of this heat supply from the geothermal source is considerably higher than the drop of net electricity, hence, the thermal performance will improve as turbine 1 inlet pressure goes up. Based upon Fig. 8.4, exergy efficiency is lifted up as turbine 1 inlet pressure goes up since the overall supplied exergy (supplied exergy rates of generator and LNG) is dropped considerably as turbine 1 inlet pressure moves upward, which is sensible than the drop of net electricity. Since raising the turbine 1 inlet pressure leads to production of less electricity, thus, the SUCP will move upward as turbine 1 inlet pressure augments.

8.5.1.3 Turbine 2 Inlet Pressure's Varying Impact

Impact of turbine 2 inlet pressure on the thermal performance, exergy performance, net electricity, and total SUCP of plant is depicted in Fig. 8.5. Since at higher turbine 2 inlet pressures the flow rate of NG and enthalpy drop through the pump 2 and turbine 2 increase, thus, the turbine 2 electricity and pump 2 consumed electricity will drop. However, turbine 1 generated electricity and pump 1 consumed electricity remained unvaried throughout this alteration. Since the augmentation rate of turbine

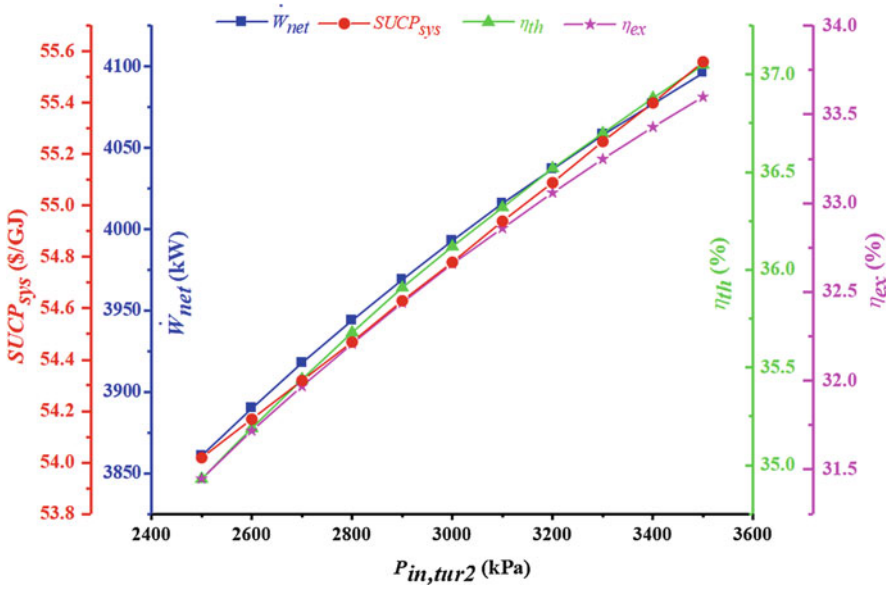

Fig. 8.5 Varying effect of turbine 2 inlet pressure on the thermal efficiency, net electricity, exergy efficiency, and total SUCP of the plant

2 generated electricity is considerably sensible than the augmentation rate of pump 2 consumed electricity, hence, the net electricity will rise up as turbine 2 inlet pressure goes up.

Meanwhile, the geothermal outlet energy remained unchanged with any variations in the turbine 2 inlet pressure, and hence, less heat will be supplied. Since the net electricity goes up with the rise of turbine 2 inlet pressure, hence, the thermal efficiency will rise up. Exergy performance has gone up as turbine 2 inlet pressure moves upward since the supplied exergy rates of LNG are decreased considerably as turbine 2 inlet pressure rises, while net electricity is increased throughout this alteration (as pointed out). Since increment of the turbine 2 inlet pressure increases cost of net electricity more dramatically, thus, the SUCP of the plant will be increased as turbine 2 inlet pressure goes up.

8.5.1.4 Absorber Temperature's Varying Impact

Figure 8.6 outlines varying effect of the absorber temperature on the thermal efficiency, net electricity, exergy efficiency, and total SUCP of the plant for the devised combined APC/LNG cycle. Accordingly, a rise in the absorber temperature has led to the decrease of enthalpy drop through turbine 1, and hence, turbine 1 output power will drop. Also, the flow rate of NG is dropped considerably with the rise of absorber temperature, and hence, pump 2 and turbine 2 powers decrease.

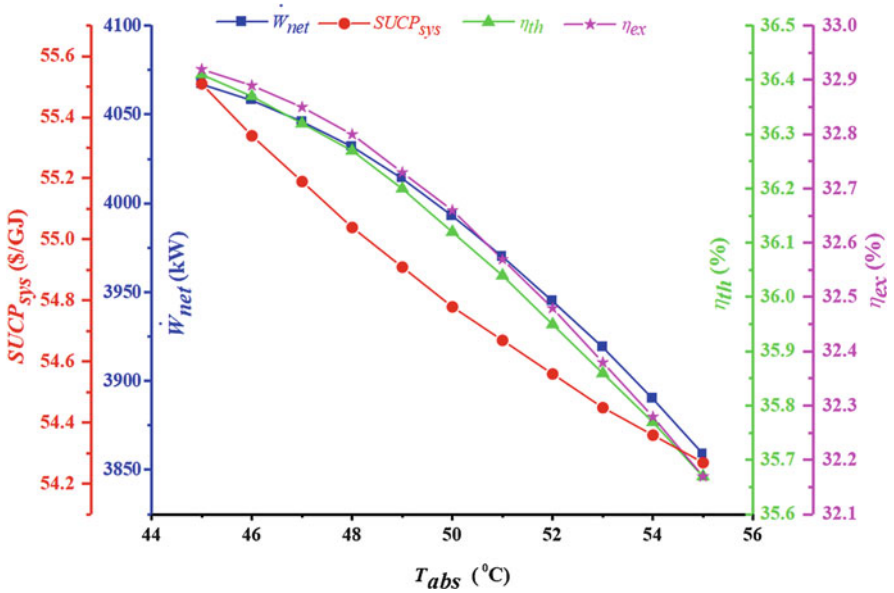

Fig. 8.6 Varying effect of absorber temperature on the thermal efficiency, net electricity, exergy efficiency, and total SUCP of the plant

Moreover, the pump 1 consumed electricity is reduced as absorber temperature rises up since the mass flow rate through this element is dropped. All in all, since the drop of the aggregated turbine electricity outweighs the aggregated pump consumed electricity, thus, the net electricity of the devised combined APC/LNG system will be decreased. Also, increasing absorber temperature decreases the vapor generator duty since the outlet energy of the supplied geofluid goes up through this alteration. Through this analysis, it is discerned that the drop of net electricity is considerably higher than that of the vapor generator duty, and hence, the thermal efficiency of the system will drop with a rise in the absorber temperature. From exergy evaluation perspective, it is concluded that the supplied exergy rates of LNG and geothermal source are dropped as the absorber temperature increases, where their reduction rate is lower than that of the net electricity; hence, exergy efficiency will drop.

The outcomes of parametric study from economics viewpoint showed that the SUCP of the plant is decreased as absorber temperature goes up since the cost of net electricity is dramatically dropped with the rise of absorber temperature which is more sensible than the drop of net electricity.

8.5.1.5 Geothermal Inlet Temperature's Varying Impact

Figure 8.7 exhibits alteration of the thermal efficiency, net electricity, exergy efficiency, and total SUCP of the plant with various geothermal inlet temperatures. Raising the geothermal inlet temperature leads to the rise of the fluid flow rate

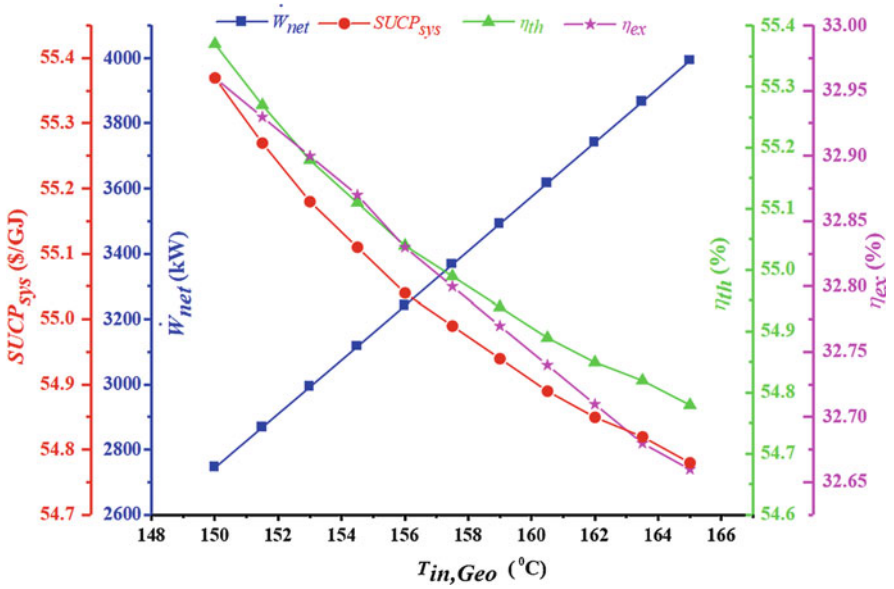

Fig. 8.7 Varying effect of geothermal inlet temperature on the thermal efficiency, net electricity, exergy efficiency, and total SUCP of the plant

through turbines and pumps, and hence, the aggregated turbine electricity and pump consumed electricity will rise up. Since the increment of the aggregated turbine electricity is higher than that of the aggregated pump consumed electricity, thus, the net electricity of the combined APC/LNG plant will rise up as geothermal inlet temperature goes up. Raising the geothermal inlet temperature leads to the rise of the enthalpy difference of geofluid through the generator, resulting in the rise of the generator duty. As the augmentation rate of generator duty is sensibly higher than that of the net electricity, thus, the thermal efficiency will drop as geothermal inlet temperature moves up. Similarly, exergy efficiency of the plant is dropped as geothermal inlet temperature goes up for the reason that as geothermal inlet temperature moves upward, the supplied exergy rates of a generator and LNG will be increased, where its augmentation rate is higher than that of the net electricity.

8.5.1.6 LiBr Fraction's Varying Impact

Figure 8.8 exhibits varying effect of the basic LiBr fraction on the thermal efficiency, net electricity, exergy efficiency, and total SUCP of the plant. Accordingly, the net electricity of the system is decreased as the basic LiBr fraction rises up. As basic LiBr fraction goes up, the LiBr flow rate drops, whereas the enthalpy drop through turbine 1 rises up. Since the augmentation rate of enthalpy drop through turbine 1 is dominated by drop of LiBr flow rate, thus, the turbine 1 electricity will be dropped.

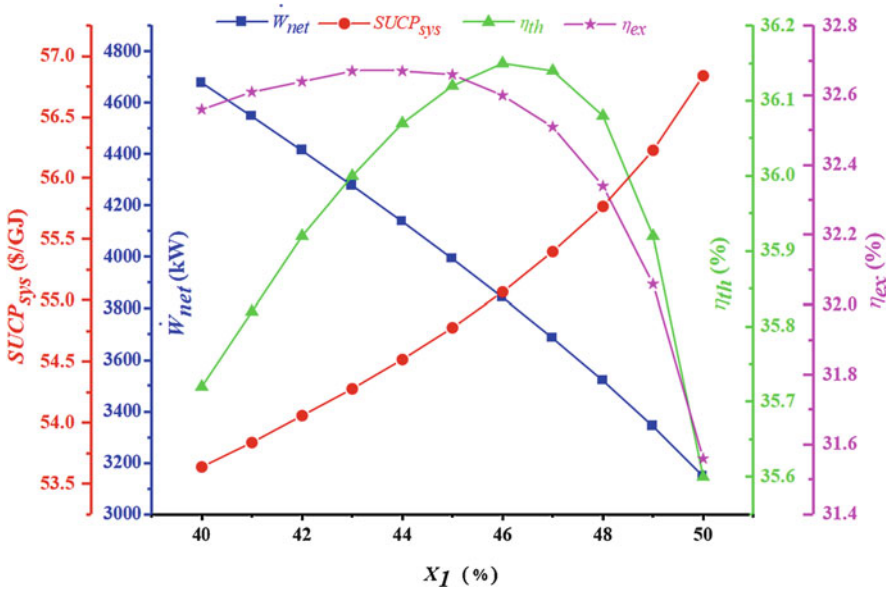

Fig. 8.8 Varying effect of lithium bromide concentration on the thermal efficiency, net electricity, exergy efficiency, and total SUCP of the plant

Also, increasing the basic LiBr fraction decreases enthalpy drop and mass flow rate through turbine 2, and hence, its net electricity will drop. On the other hand, as basic lithium bromide fraction increases, the mass flow rate through pumps 1 and 2 is raised up and decreased, respectively. Since the drop of pump 2 consumed electricity is considerably higher than the augmentation rate of pump 1 consumed power, thus, the aggregated consumed power will drop down. Consequently, the net electricity of the unit will drop as the basic lithium bromide fraction increases.

As Fig. 8.8 indicates, the performance of the devised combined APC/LNG plant can be optimized with basic LiBr fraction based on the 1st and 2nd laws of thermodynamics. As basic lithium bromide fraction increases, the geothermal discharge energy increases, and hence, generator duty decreases. Through this analysis, it was discerned that the net electricity drop is dominated by that of the generator load at low basic LiBr fractions, while the trend will be reversed at high LiBr fractions. Therefore, a peak point for thermal efficiency will be observed. Similar trend is observed for exergy efficiency. Finally, the SUCP of the plant is dropped as LiBr fraction rises up since the net electricity is decreased through this alteration.

8.5.2 Optimization Results

Table 8.7 presents chief thermodynamic properties and unit cost at each stream of the devised APC/LNG plant for the base case.

Table 8.8 outlines attribution of different elements of the devised plant to cost of exergy destruction rate ($\dot{C}_{D,k}$), exergy destruction rate ($\dot{E}x_{D,k}$), and investment cost ($\dot{Z}$) for the base, thermal optimal mode (TOM), exergy optimal mode (EOM), cost optimal mode (COM), and multi-objective optimal mode (MOOM). According to the calculated results, absorber accounts for the largest attribute to exergy destruction for all five modes, followed by the heat exchanger (HX). This is mainly due to the fact that these components have a huge temperature difference that leads to a huge loss of exergy. This is the main thermodynamic price that is paid in the recovery of LNG cold energy for power plants. As expected, among all elements, turbines own the highest investment cost, followed by the vapor generator. Additionally, the highest attribute to the cost of exergy destruction is corresponded to the absorber, followed by turbine 2 (for all optimal modes). The investment cost of expansion device in all optimization scenarios is low enough as the drop in its pressure aside is low. The lowest overall exergy destruction and cost rate related to this parameter were computed 6115 kW and 319,324 $/yr, respectively (for base case).

Figure 8.9 outlines simulated outcomes of the SOO and MOO procedures implemented to the devised APC/LNG plant for different weight coefficients. Juxtaposing data of TOM and base mode, it is fathomed out that the thermal and exergy efficiencies may improve up to 4.09% and 5.35%, respectively, while the total SUCP of the system is degraded by 0.98%, quite small for this optimal case. Thus, TOM is appropriate from the 1st and 2nd laws of thermodynamics viewpoints

Table 8.7 Cost rates and thermodynamic properties corresponded to each stream point for the devised APC/LNG plant for the base case

State	T (°C)	P (kPa)	h (kJ. kg^{-1})	X (%)	s (kJ. kg^{-1}. K^{-1})	$\dot{m}$ (kg.s^{-1})	Ėx (kW)	$\dot{C}$ ($. yr^{-1})	c ($. GJ^{-1})
1	50	5.437	102.8	45	0.403	25.15	52.02	1115	21.43
2	50.04	106.4	102.9	45	0.4032	25.15	52.16	1602	30.72
3	106.4	106.4	234.5	45	0.7833	25.15	511.8	19,404	37.91
4	140	106.4	2756	–	7.536	3.844	1974	38,062	19.29
5	138.9	106.4	298.5	53.12	0.8495	21.31	1378	33,918	24.62
6	66.04	106.4	143.2	53.12	0.4267	21.31	753.4	18,551	24.62
7	63.6	5.437	143.2	53.12	0.4114	21.31	850.8	18,551	21.8
8	34.38	5.437	2353	0.9133	7.681	3.844	261	5034	19.29
9	34.38	5.437	1381	0.5112	4.518	3.844	147	2834	19.29
10	165	710	697.4	–	1.993	53	5717	87,127	15.24
11	116.4	710	488.8	–	1.488	53	2634	40,135	15.24
12	−161.5	101.3	−911	–	−6.677	10.85	11,722	0	0
13	−160.4	3000	−902.9	–	−6.667	10.85	11,775	9914	0.842
14	−95.88	3000	−371	–	−3.339	10.85	6779	30,881	4.555
15	26.38	3000	−26.5	–	−1.818	10.85	5599	34,358	6.137
16	−93.68	300	−260.2	–	−1.668	10.85	2577	15,816	6.137

Table 8.8 Exergoeconomic parameters for the devised APC/LNG plant for base and optimal cases

	Base case			TOM			EOM			COM			MOOM		
Component	$\dot{E}x_{D,k}$ (kW)	$\dot{C}_{D,k}$ (/yr)	$\dot{Z}_k$ (/yr)	$\dot{E}x_{D,k}$ (kW)	$\dot{C}_{D,k}$ (/yr)	$\dot{Z}_k$ (/yr)	$Ex_{D,k}$ (kW)	$\dot{C}_{D,k}$ (/yr)	$\dot{Z}_k$ (/yr)	$\dot{E}x_{D,k}$ (kW)	$\dot{C}_{D,k}$ (/yr)	$\dot{Z}_k$ (/yr)	$\dot{E}x_{D,k}$ (kW)	$\dot{C}_{D,k}$ (/yr)	$\dot{Z}_k$ (/yr)
Vapor generator	244.2	4521	5584	313.3	5860	5444	335.3	6278	5729	297.3	5598	6864	335.3	6278	5738
Absorber	4050	89,776	696.4	4145	82,877	748.7	4563	99,700	782.2	5087	134,521	737.6	4571	100,283	782.4
SHX	164.5	6370	2434	208.8	9438	2851	186.8	8330	2370	106.5	3975	1306	185.9	8270	2354
HX	1067	20,573	1277	1151	22,592	1392	1196	23,411	1469	1075	20,892	1407	1197	23,414	1470
Pump 1	1.96	6642	369.1	2.632	11,462	448.9	2.331	10,540	411.6	1.272	4069	273.8	2.313	10,444	409.4
Pump 2	34.74	6534	5206	43.58	7968	6121	46.38	8357	6398	32.71	6058	4983	46.43	8364	6403
Turbine 1	166.5	9374	53,992	189	10,671	60,781	198.6	11,156	63,882	161.7	8870	51,925	198.5	11,149	63,854
Turbine 2	484.7	26,093	118,022	561.4	30,646	134,947	598	32,286	143,622	499.9	25,460	123,420	598.6	32,317	143,771
Total	6115	319,324	187,581	6349	333,469	212,733	6987	364,016	224,663	7447	373,447	190,916	7000	364,636	224,781

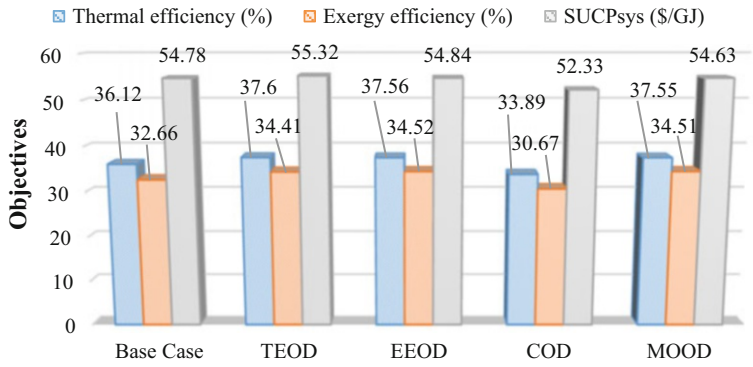

Fig. 8.9 Comparison of the base case with the single- and multi-objective optimizations cases

while would not be proper exergoeconomically. The comparison also reveals that TOM increases the net electricity value by 11.57%.

In the EOM, the optimization results indicate that the thermal and exergy efficiencies are improved by 3.98% and 5.69%, respectively, while the total SUCP of the system is degraded by 0.1% (quit negligible). Thus, EOM case is appropriate from both laws of thermodynamics viewpoints while would not be proper exergoeconomically. The comparison also reveals that the EOM also leads to the rise of the net electricity by 19.08%.

In the 3rd mode, the SUCP is enhanced by 4.47%, presenting attractive outcomes economically. However, since the thermal and exergy efficacies are dropped by 6.17% and 6.09%, respectively, hence, COM is not recommended from both laws of thermodynamics viewpoints. The net electricity rises up near 8.28% through this mode, seemingly considerable.

Finally, for the MOOM, the thermal efficiency and exergy efficiency are improved by 3.95% and 5.66%, respectively. In addition, the net produced power and total SUCP of system are also improved by 19.15% and 0.27%, respectively. Thus, the MOOM appears so appropriate from thermodynamics and thermoeconomics viewpoints.

8.6 Conclusion

3E (energy, exergy, and exergoeconomic) analysis of an APC coupled with an LNG unit using the Sabalan geothermal energy was carried out in this chapter. The main purpose was supply of simultaneous power and NG to the Sabalan district users. The simulation was conducted under steady-state condition, using Engineering Equation Solver (EES). In order to have an in-depth understanding from the devised plant, parametric study was conducted. Single- and multi-objective optimizations of the devised plant were carried out by considering some chief parameters as decision

variables, including turbine 1 inlet pressure, turbine 2 inlet pressure, generator hot pinch point temperature difference, absorber temperature, heat exchanger minimum temperature difference, and LiBr fraction, using GA. Following the purpose of maximization of thermal and exergy efficiencies and minimization of total SUCP of the plant as objective functions, the optimum values of key thermodynamic properties and performance characteristics were obtained and presented. Some main findings of this study are as follows:

- The optimum net electricity, thermal performance, exergy performance, and SUCP of unit were attained 4758 kW, 37.55%, 34.51%, and 54.63 $/GJ, respectively, considering MOOD case.
- The optimum decision variables of turbine 1 inlet pressure, turbine 2 inlet pressure, generator hot PP temperature difference, absorber temperature, heat exchanger minimum temperature difference, and LiBr fraction were corresponded to 119.7 kPa, 3500 kPa, 15 °C, 45.06 °C, 8.004 °C, and 40%, respectively, when MOOD case was used.
- Among all components, absorber was accounted as an irreversible component in the whole system followed by heat exchanger.
- The thermal and exergy efficiencies of the devised APC/LNG plant can be optimized based on the LiBr fraction.
- A higher thermal efficiency could be obtained at higher turbine 1 inlet pressures and turbine 2 inlet pressures or lower generator hot PP temperature differences, absorber temperatures, and geothermal inlet temperatures.
- A higher exergy efficiency could be obtained at higher turbine 1 inlet pressures and turbine 2 inlet pressures or lower generator hot pinch point temperature differences, absorber temperatures, and geothermal inlet temperatures.
- A lower unit cost of product could be obtained at higher absorber temperatures and geothermal inlet temperatures or lower generator hot pinch point temperature differences, turbine 1 inlet pressures, turbine 2 inlet pressures, and basic LiBr fractions.

References

1. Sigfusson, B., & Uihlein, A. (2015). *JRC geothermal energy status report*. Publications Office of the European Union. Netherlands.
2. Dincer, I., & Rosen, M. A. (2012). *Exergy: energy, environment and sustainable development*. Newnes. Elsevier Inc., USA.
3. Kalogirou, S. A. (2013). *Solar energy engineering: processes and systems*. Academic Press. Elsevier Inc., USA.
4. Ghaebi, H., Namin, A. S., & Rostamzadeh, H. (2018). Performance assessment and optimization of a novel multi-generation system from thermodynamic and thermoeconomic viewpoints. *Energy Conversion and Management, 165*, 419–439.
5. Manente, G., Bardi, A., Lazzaretto, A., & Paci, M. (2019). Low emission flash-binary and two-phase binary geothermal power plants with water absorption and reinjection of non-condensable gases. *Geothermics, 80*, 155–169.

6. Kanoglu, M., & Bolatturk, A. (2008). Performance and parametric investigation of a binary geothermal power plant by exergy. *Renewable Energy, 33*(11), 2366–2374.
7. Ratlamwala, T., & Dincer, I. (2014). Energetic and exergetic investigation of novel multi-flash geothermal systems integrated with electrolyzers. *Journal of Power Sources, 254*, 306–315.
8. Parikhani, T., Ghaebi, H., & Rostamzadeh, H. (2018). *A novel geothermal combined cooling and power cycle based on the absorption power cycle: Energy, exergy and exergoeconomic analysis*. Energy.
9. Ghaebi, H., Farhang, B., Rostamzadeh, H., & Parikhani, T. (2018). Energy, exergy, economic and environmental (4E) analysis of using city gate station (CGS) heater waste for power and hydrogen production: A comparative study. *International Journal of Hydrogen Energy, 43*(3), 1855–1874.
10. Ahmadi, S., Ghaebi, H., & Shokri, A. (2019). A comprehensive thermodynamic analysis of a novel CHP system based on SOFC and APC cycles. *Energy*, 115899.
11. Ghaebi, H., Parikhani, T., & Rostamzadeh, H. (2017). Energy, exergy and thermoeconomic analysis of a novel combined cooling and power system using low-temperature heat source and LNG cold energy recovery. *Energy Conversion and Management, 150*, 678–692.
12. Ghaebi, H., Parikhani, T., & Rostamzadeh, H. (2018). A novel trigeneration system using geothermal heat source and liquefied natural gas cold energy recovery: Energy, exergy and exergoeconomic analysis. *Renewable Energy, 119*, 513–527.
13. Rostamzadeh, H., Namin, A. S., Ghaebi, H., & Amidpour, M. (2018). Performance assessment and optimization of a humidification dehumidification (HDH) system driven by absorption-compression heat pump cycle. *Desalination, 447*, 84–101.
14. Nemati, A., Mohseni, R., & Yari, M. (2018). A comprehensive comparison between CO2 and ethane as a refrigerant in a two-stage ejector-expansion transcritical refrigeration cycle integrated with an organic Rankine cycle (ORC). *The Journal of Supercritical Fluids, 133*, 494–502.
15. Bejan, A., & Tsatsaronis, G. (1996). *Thermal design and optimization*. Wiley.
16. Aali, A., Pourmahmoud, N., & Zare, V. (2017). Exergoeconomic analysis and multi-objective optimization of a novel combined flash-binary cycle for Sabalan geothermal power plant in Iran. *Energy Conversion and Management, 143*, 377–390.
17. Ghaebi, H., Parikhani, T., Rostamzadeh, H., & Farhang, B. (2017). Thermodynamic and thermoeconomic analysis and optimization of a novel combined cooling and power (CCP) cycle by integrating of ejector refrigeration and Kalina cycles. *Energy, 139*, 262–276.
18. Ghaebi, H., Parikhani, T., Rostamzadeh, H., & Farhang, B. (2017). *Proposal and assessment of a novel geothermal combined cooling and power cycle based on Kalina and ejector refrigeration cycles*. Applied Thermal Engineering.
19. Rostamzadeh, H., Ebadollahi, M., Ghaebi, H., Mostoufi, K., & Amidpour, M. (2017). Thermodynamic and thermoeconomic analyses and optimization of basic and regenerative triple-evaporator combined power and refrigeration cycles for different applications. In *9 th International Exergy, Energy and Environment Symposium (IEEES-9), Split, Croatia May 14-17*.
20. Zare, V., Mahmoudi, S. S., Yari, M., & Amidpour, M. (2012). Thermoeconomic analysis and optimization of an ammonia–water power/cooling cogeneration cycle. *Energy, 47*(1), 271–283.
21. Ghaebi, H., Yari, M., Gargari, S. G., & Rostamzadeh, H. (2019). Thermodynamic modeling and optimization of a combined biogas steam reforming system and organic Rankine cycle for coproduction of power and hydrogen. *Renewable Energy, 130*, 87–102.
22. Rostamzadeh, H., & Nourani, P. (2019). Investigating potential benefits of a salinity gradient solar pond for ejector refrigeration cycle coupled with a thermoelectric generator. *Energy, 172*, 675–690.
23. Rostamzadeh, H., Ghaebi, H., Vosoughi, S., & Jannatkhah, J. (2018). Thermodynamic and thermoeconomic analysis and optimization of a novel dual-loop power/refrigeration cycle. *Applied Thermal Engineering, 138*, 1–17.

Chapter 9
A Novel Framework for Robust Scheduling of Hydro-Driven Combined Drinking Water and Electricity Generation Systems

Hossein Saber, Hesam Mazaheri, and Moein Moeini-Aghtaie

Nomenclature

Sets

T Operating time interval (h)

Variables

λ_t	Electricity market price at operating time period t ($/kWh)
$P_{\text{in},\,t}$	Imported energy from upstream network at operating time period t (kW)
$P_{\text{out},\,t}$	Exported energy to upstream network at operating time period t (kW)
P_t^{dis}	Discharging power of BESS at operating time period t (kW)
P_t^{ch}	Charging power of BESS at operating time period t (kW)
PD_t	Active power demand at operating time period t (kW)
PG_t	Active power generation of in-pipe hydropower at operating time period t (kW)
u_t	Binary variable denoting the direction of power exchange with upstream network at operating time period t
z_t	Binary variable denoting the charging status of BESS at operating time period t
eSOC_t	State of charge of BESS at operating time period t (kWh)

H. Saber · H. Mazaheri
Electrical Engineering Department, Sharif University of Technology, Tehran, Iran

M. Moeini-Aghtaie (✉)
Faculty of Energy Engineering, Sharif University of Technology, Tehran, Iran
e-mail: moeini@sharif.edu

F. Jabari et al. (eds.), *Integration of Clean and Sustainable Energy Resources and Storage in Multi-Generation Systems*,
https://doi.org/10.1007/978-3-030-42420-6_9

Parameters

FIT_t	Feed-in-tariff rate at operating time period t (\$/kWh)
$P^{\max}$	Power rating of BESS (kW)
M	Sufficiently large positive number
η_{ch}, η_{dis}	Charge and discharge efficiency of BESS
$\mathrm{eSOC}^{\max}$	Maximum capacity of BESS (kWh)
$\mathrm{eSOC}_{\mathrm{initial}}$	Initial state of charge of BESS (kWh)
$\overline{\mathrm{PD}_t}$	Expected value of demand at operating time period t (kW)
$\overline{\mathrm{PG}_t}$	Expected value of in-pipe hydropower generation at operating time period t (kW)
$\overline{\lambda_t}$	Expected value of electricity market price at operating time period t (\$/kWh)
β_{D}, β_{G}, β_{λ}	Degree of MG demand uncertainty, hydropower generation uncertainty, and electricity market prices uncertainty, respectively
Λ_{D}, Λ_{G}, Λ_{λ}	Uncertainty budget of MG demand, generation, and electricity market price, respectively

9.1 Introduction

In recent years, rising growth consumption of power electricity in industrial and other sectors imposes ongoing issues on generation sector of power systems. Therefore, experts in power system area are always trying to find new resources to effectively handle this issue. One of these new resources that knowingly progress is hydropower renewable energy resources. Hydropower resources can help the system operators in dealing with their issues such as high energy cost, energy efficiency problems, and the shortage of fuel resources; in addition, they can produce clean and consistent energy in power systems. In order to better understand the importance of hydropower renewable resources, global hydroelectric power consumption until 2016 is presented in Fig. 9.1 [1].

Hydropower has the leading role of the renewable energy resources with great flexibility as well as consistency in output. Moreover, these resources are capable to equip with energy storage system to satisfy the peak load in critical hours. The availability of hydropower potential worldwide is approximately ten million GWh/year, but there are few countries throughout the world that are trying to produce power electricity form hydropower, such as China, the United States, Brazil, Canada, India, and Russia [2]. Due to the possibility of installing these systems around the world, there is hope that they can be appropriate alternative energy resources in comparison with other resources of power technologies in the near future. According to the advantages of hydropower systems, countries should increase the investments on these systems to generate an environmentally friendly energy, so they can improve their country's strategic positions in many aspects like economic and environment.

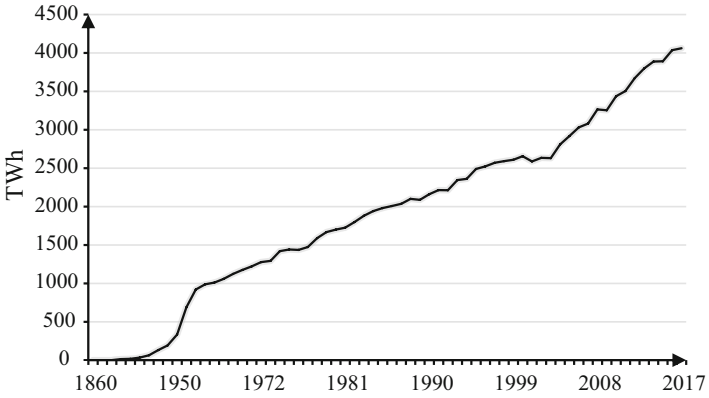

Fig. 9.1 Global hydroelectric power consumption over the long term [1]

To estimate the abilities of hydropower in power systems, some criteria are presented in the literature. The "Gross Theoretical Capacity" is defined as all natural water flows, which are accessible with 100 percent efficient turbines. On the contrary, this capacity is not practical, so "Technically Exploitable Capacity" and "Economically Exploitable Capacity" are defined to satisfy the limits of current technology and local economic conditions, respectively. Hydropower technology can supply 71 percent of all renewable electricity; furthermore, they can generate 16.4 percent of the world's electricity from all sources with 1,064,000 MW installed capacity in 2016 [2].

Hydropower plants can be classified into five major ranges in size from less than 100 kW to greater than 22 GW [2]. Considering this classification, micro hydropower plants are introduced for less than 100 kW capacity, and mini hydropower plants are introduced for 100 kW to 1 MW capacity; small hydropower plants are introduced for 1 MW to 10 MW capacity. Moreover, medium hydropower plants are introduced for 10 MW to 300 MW capacity, and large hydropower plants are introduced for greater than 300 MW capacity [3, 4]. Total renewable energy consumption until 2016 around the world is presented in Fig. 9.2. According to this figure, the usage of hydropower has been growing in comparison with other technologies in recent years [1].

Hydropower plants can operate in isolated areas as well as in grid-connected modes. In this vein, these systems are categorized in three schemes [2, 5], and a comparison between these types of hydropower systems is presented in Table 9.1:

- Run-of-river: Power electricity is generated by enough water from river or stream without any water storage capability.
- Reservoir or powerhouse located at the base of a dam: Power electricity is generated by the release of stored water.
- In-pipe hydropower system: Power electricity is generated by turbines installed in drinking water or sewage pipelines.

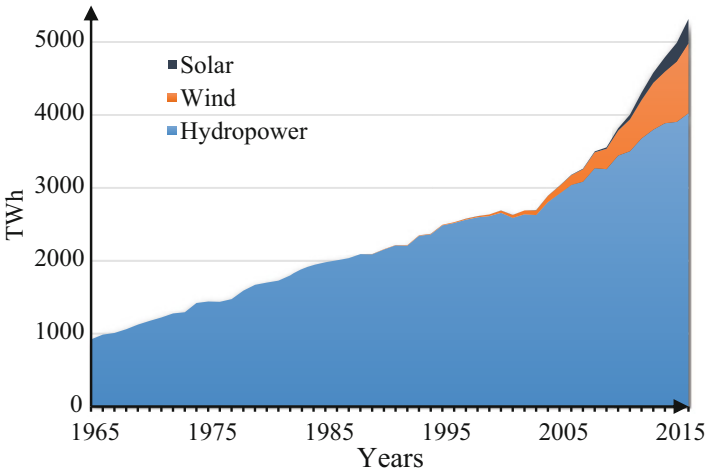

Fig. 9.2 Total renewable energy consumption until 2016 [1]

Table 9.1 A comparison between the types of hydropower systems

Types	Advantages	Disadvantages
Conventional	Clean fuel source Huge power electricity production Controlling flood and irrigation Storing water supply	Costly construction like dams, pumps Unpredictable and weather-dependent production Impacts on water delivery and quality Damage ecosystems and animal habitats Environmental problems Impacted by drought Serious geological damage Changing the natural water table level
In-pipe	Environmentally friendly Approximately constant water flow in each day Without effects on water delivery and quality Without changing wildlife and ecosystems Consistent and predictable power electricity Economic construction without pumps or dams	Small power electricity production Demands of water or sewage pipelines

As a stream of literature, some papers are presented to consider the application of hydropower in power systems. In this regard, paper [6] presents a hydropower scheduling problem to calculate a reservoir management strategy for maximum revenues of the produced electricity by attending a trade-off between releasing the water now or saving the water for future release. In this paper, market prices and reservoir inflows are considered as uncertainties that are implemented on four

Norwegian hydropower plants in a 10-year time horizon. Authors in [7] present a coordinated model predictive control scheme for the Mid-Columbia hydropower system including seven hydropower plants on the Columbia River in the United States. In this regard, the hydropower generation depends on turbine discharge and hydraulic head. In [8], a compact mixed-integer linear programming is presented to consider unit commitment problem. In this case, each unit discharge is defined including the water head, the total plant downstream flow, the variable discharge upper limit, the unit efficiency curves, and the restricted operating zones to maximize power efficiency on Brazilian hydropower plants. In [9], a mixed-integer linear programming model is investigated to consider hydropower unit commitment with a head-sensitive reservoir and multiple vibration zones, varying with net head. This model is solved by branch and bound algorithm. The authors in [10] present a day-ahead coordinated scheduling method of hydro and wind power generation systems. In this paper, the effects of uncertain wind power, water inflow, and electricity load are considered on a real test system in a western area of China. In [11], the impact of wind generation and small hydropower plants (SHPs) is presented to improve power system reliability, and the variable energy sources such as wind as well as river inflows and variable load are considered by sequential Monte Carlo simulation. In detail, an analysis is investigated to evaluate system planning by considering the uncertainty of wind energy production and the reduction of reservoirs capacity. Reference [12] proposes a mixed-integer linear stochastic model for bid optimization and short-term production allocation. This analysis is implemented on a complex real-life river system by considering market prices and inflow to the reservoirs as uncertainties. Authors in [13] present a stochastic bi-level program for strategic bidding of a hydropower producer by considering wind power generation, variation of inflows for the hydropower producer, and demand variability as uncertainties. This model is solved by a modified Benders decomposition algorithm (MBDA).

Although there are several studies on the hydropower applications in the viewpoint of reservoirs and run-of-river turbines, the application of in-pipe hydropower generation has been neglected in the literature. In-pipe hydropower generation could be an appropriate source for supplying the local demand of many rural areas in mountain range. Moreover, the uncertainty associated with the flow rate of drinking water in pipelines is an effective parameter in in-pipe hydropower generation studies. In this regard, this study aims to propose an appropriate model to determine the battery energy storage system (BESS) charge/discharge schedule by using an appropriate uncertainty modeling method. Hence, a min-max optimization problem that is modeled as a bi-level optimization problem is developed, and the proposed model is solved using a two iterative steps algorithm. Finally, the concept of uncertainty budget is developed for the described problem.

The rest of the current chapter is presented as follows: In Sect. 9.2, in-pipe hydropower systems is introduced. The proposed model for managing the BESS in the microgrid (MG) by considering the associated uncertainties is explained in Sect. 9.3. Afterward, the proposed solution methodology and case study are described in Sects. 9.4 and 9.5, respectively. Finally, conclusion is presented in Sect. 9.6.

9.2 In-pipe Hydropower Systems

According to in-pipe hydropower systems, the source of water must be gravity-fed not pumped. Therefore, because the water pressure will be lessen after turbines, the extra pressure should be available in order to prevent a drop in water pressure for customers [14]. Moreover, in-pipe hydropower systems are effective in cities, which are placed in the mountains above the city with mountain reservoirs or high-elevation storage tanks because gravity can pull the water down the pipelines and, as a result, it does not require any electricity to pump the water [15]. Due to the existence of million miles of gravity-fed drinking water pipelines around the world, these systems have significant opportunities to produce huge power electricity. For example, there are 1.2 million miles of drinking water pipelines in the United States [16]. In this structure, turbines can be installed in drinking water pipelines in order to produce the required power electricity for villages as well as small cities, which do not have access to generated power electricity from distribution grids. Also, this system can be used in metropolises in order to help power distribution companies to manage the peak load. Internal scheme of in-pipe hydropower systems is presented in Fig. 9.3 [3].

The most advantages of in-pipe hydropower systems include being environmentally friendly, the possibility of using energy storage systems, no impact on water delivery, constant water flow, and non-intermittent power output. Also, these systems avoid killing fish and other marine life, or altering aquatic habitats unlike other hydropower systems [15]. In in-pipe hydropower systems, the vertical distance between turbines and end point of the pipelines on the ground is named "Head"; therefore, the head for in-pipe hydropower systems is classified into three major ranges. In this vein, low head is introduced for 2–30 m, medium head is introduced for 30–100 m, and high head is defined for greater than 100 m [5]. Although water

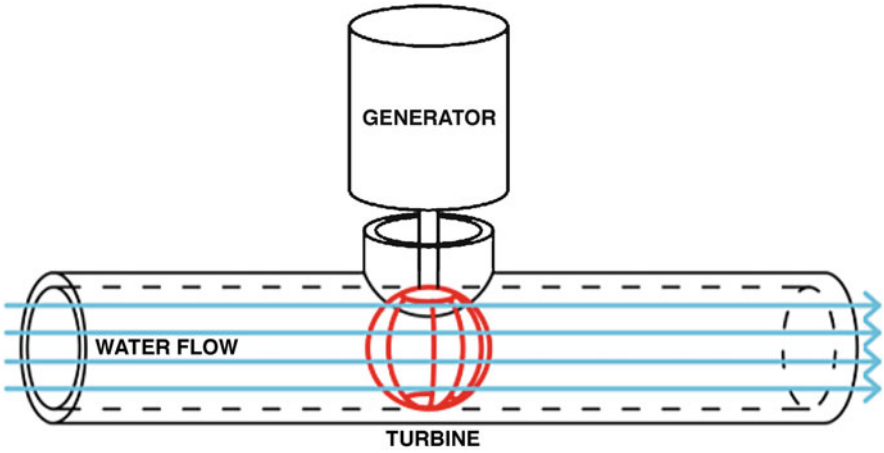

Fig. 9.3 In-pipe hydropower systems [3]

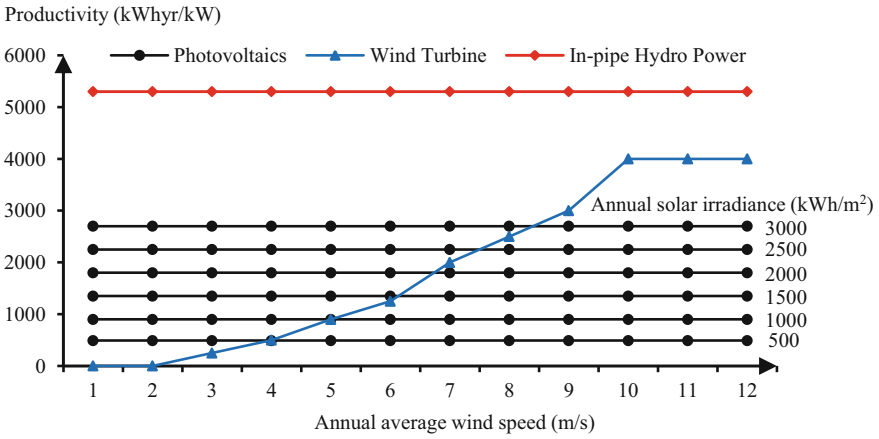

Fig. 9.4 Comparison between the productions of renewable energy resources

flow changes in daily hours, in-pipe hydropower systems can generate consistent as well as predictable energy in particular hours during a year. The consistent nature of in-pipe hydropower production in a year in comparison with other renewable technologies such as wind turbines and photovoltaics is presented in Fig. 9.4 [3].

Selecting turbine is a main point in in-pipe hydropower systems in order to satisfy the requirements of the water pipeline conditions. These requirements are as follows [17]:

- The average water velocity in pipelines is 1.5 m/s.
- The water turbine should not use a lot of water.
- The pathway of water flow should not be changed.
- The drinking water quality should not be lessened.

Conventional water turbines are named Francis, Kaplan, bulb, and Pelton turbines, and their efficiencies are ranged from 75 to 95 percent. Kaplan turbine has an advantage to work on low flow rate and low water head condition, but they will change water flow pathway. In contrast, bulb turbine will not change water flow pathway, but improper waterproofing of this system will pollute drinking water. Turbines can be selected in different work conditions. For instance, Kaplan turbines work in low and medium head, while Francis and Pelton work in high head [17]. Finally, Lucid Energy company constructs a lift-type vertical axis water turbine in order to utilize in large water pipelines (24″ to 60″ diameter) presented in Fig. 9.5. These turbines are installed for large-diameter gravity-fed water transmission pipelines that can operate in a wide range of flow conditions, volumes, and velocities. They do not have any impact on water delivery and can be installed in series in order to maximize energy output [18]. Also, Lucid Energy's system is not affected by the sort of external conditions like weather conditions in comparison with other renewable technologies [19], and Lucid turbines are designed for water utilities with gravity-fed water delivery pipelines [20].

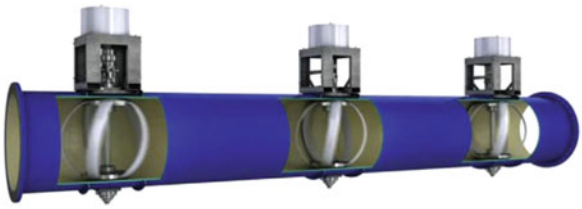

Fig. 9.5 Lucid Energy life-type turbine

The first-generation 42 inch Lucid Energy's system is operated by two water utilities in the United States. In this regard, a four-turbine system in a Portland Water Bureau pipeline in Portland, Oregon, and a single-turbine system at Riverside Public Utilities are operated. The project presented in city of Portland in Oregon in 2015 has approximately invested $1.7 M and is anticipated to earn $2 M over a 20-year contract. This project can generate 1100 MWh/year that is enough renewable energy to power about 150 homes [15].

The output generation power of these in-pipe hydropower turbines is dependent on water flow and head, and water flow is related to water velocity. Therefore, head produces pressure at end point of the pipeline on the ground, and therefore, pressurized drinking water in the pipeline can spin turbines, so water flow and head have direct impacts on generating energy; actually, the difference in elevation is a major factor in power generation. In a particular Lucid Energy company life-type turbine, the range of water velocity is 0.9 m/s for cut-in speed and 3.57 m/s for cut-out speed, and the maximum flow rate is equal to 2.7 m^3/s that happened in cut-in speed [3]. The relation between flow rate and water velocity is presented in (9.1). Also, the output generation power of in-pipe hydropower turbine is presented in (13.2) [21]:

$$V = \frac{4Q}{\pi d^2} \tag{9.1}$$

where "V" is water velocity in m/s, "Q" is flow rate in m^3/s, and "d" is internal pipeline diameter in m.

$$P = Q\rho g H\eta \tag{9.2}$$

where "P" is output generation power in W, "ρ" is density of water in kg/m^3, "g" is gravity acceleration in m/s^2, "H" is head in m, and "η" is efficiency ratio (usually between 0.7 and 0.9).

9.3 Problem Identification

In this section at first, a deterministic optimization problem for a hydro-driven combined drinking water and electricity generation system (hydropower generator) is developed. After that, the robust model of described problem is addressed. For this

purpose, a grid-connected MG is considered. This MG consists of one in-pipe hydropower generator, one BESS, and several local loads. Moreover, the MG can exchange power with the upstream network under the market rules and has a centralized control system. Thus, it is assumed that the MG operator tries to meet the local loads in the lowest cost. Figure 9.6 demonstrates the schematic of the aforementioned MG.

As stated earlier, first, a deterministic problem is developed, and the objective function of this deterministic problem is considered as minimizing the net value cost of purchasing energy from upstream network. The mathematical formulation of the proposed problem including the objective function and constraints can be written as follows:

$$\min_{V} \quad \text{obj} = \sum_{t \in T} (\lambda_t P_{\text{in},t} - \text{FIT}_t P_{\text{out},t}) \tag{9.3}$$

Subject to:

$$P_{\text{in},t} - P_{\text{out},t} + \left(P_t^{\text{dis}} - P_t^{\text{ch}}\right) = \text{PD}_t - \text{PG}_t \tag{9.4}$$

$$\text{PG}_t = Q_t \rho g H \eta \tag{9.5}$$

$$0 \le P_{\text{in},t} \le (1 - u_t) M \tag{9.6}$$

$$0 \le P_{\text{out},t} \le u_t M \tag{9.7}$$

$$0 \le P_t^{\text{ch}} \le (1 - z_t) P^{\max} \tag{9.8}$$

$$0 \le P_t^{\text{dis}} \le z_t P^{\max} \tag{9.9}$$

$$\text{eSOC}_t = \text{eSOC}_{t-1} + \eta_{\text{ch}} P_t^{\text{ch}} - \frac{1}{\eta_{\text{dis}}} P_t^{\text{dis}} \tag{9.10}$$

$$0 \le \text{eSOC}_t \le \text{eSOC}^{\max} \tag{9.11}$$

$$\text{eSOC}_0 = \text{eSOC}_T = \text{eSOC}_{\text{initial}} \tag{9.12}$$

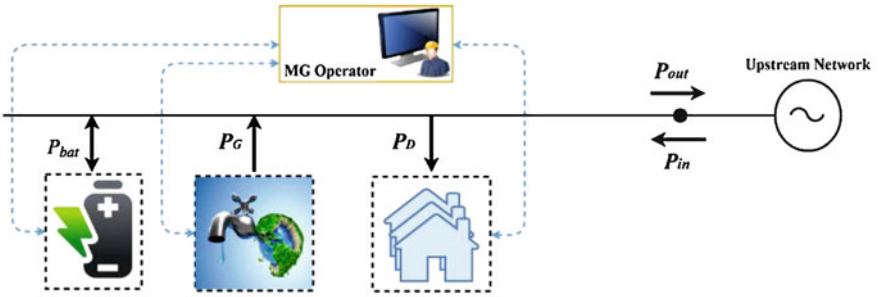

Fig. 9.6 Schematic of described MG

Decision variables of the problem are $V = \left\{P_{\text{in},t}, P_{\text{out},t}, P_t^{\text{dis}}, P_t^{\text{ch}}, \text{eSOC}_t\right\}$. Equation (9.3) represents the objective function, which minimizes the net value cost of purchasing energy from upstream network (cost minus revenue). In (9.3), λ_t and FIT_t are related to hourly electricity market price and feed-in-tariff price, respectively. Moreover, $P_{\text{in},\ t}$ and $P_{\text{out},\ t}$ are the hourly imported and exported energy from/to upstream network. Thus, the first term of (9.3) is related to cost, and the second term is related to revenue. Equation (9.4) shows the power balance between the MG and the upstream network. In this equation, P_t^{ch} and P_t^{dis} are battery charging and discharging power, respectively. Moreover, PD_t and PG_t are the hourly MG demand and hydropower generation, respectively. Equation (9.5) presents the output generation power of in-pipe hydropower. Equations (9.6) and (9.7) show that during each time interval, at least one of two variables of $P_{\text{in},t}$ and $P_{\text{out},t}$ is zero. Similarly, Eqs. (9.8) and (9.9) present that during each time interval, at least one of two variables of P_t^{ch} and P_t^{dis} is zero. Equations (9.10) and (9.11) refer to hourly energy balance and limitation of energy capacity of BESS, respectively. In (9.10), eSOC_t shows the state of charge of BESS during time interval t, and η_{ch} and η_{dis} represent charging and discharging efficiencies of BESS. Finally, (9.12) refers to the initial and final values of state of charge of BESS that are equal.

In the second step, the aforementioned optimization problem is modified by considering the uncertain parameters. The uncertainties decrease the attractiveness of the energy management model of MG. In recent decades, several methods were developed to model the uncertainties in the optimization problem to reduce the effect of uncertainties on the attractive factor. Each of these methods has their advantages and drawbacks and is suitable for different types of optimization problems. Probabilistic methods are dependent on historical data of uncertain parameters and the associated probability density function (PDF). Thus, in the problems that the data are unavailable, these methods are not suitable. Moreover, for the probabilistic methods, increasing the number of scenarios increases the computational complexity of the problem. In addition, the fuzzy optimization methods suffer from the similar challenges and have to solve the problem for different α-cuts [22].

The non-probabilistic and non-fuzzy optimization methods, unlike probabilistic optimization and fuzzy methods, respectively, do not require the PDF and membership function, which is one of the advantages of these methods. Therefore, these methods are the best choices for cases where the information of uncertain parameters are very poor. Information-gap decision theory (IGDT) and robust optimization are the most popular methods of non-probabilistic and non-fuzzy uncertainty modeling. The IGDT, which was developed by Ben Haim [23], models the gap between what is known and what may happen in realization of uncertainty. This method guarantees a specified amount of objective when the uncertain parameter falls into a symmetrical bounded centered at the predicted value [24]. In other words, IGDT specifies how much uncertain variable can deviate from predicted values while the performance of system stays acceptable. One of the most important drawbacks of this approach is related to the uncertainty space of the problem. If the optimal determined space becomes much larger than the real horizon of uncertainty, the results can differ from the estimated values [22].

The robust optimization (RO) technique, which was first introduced by Sosyster in 1973 [25], is another non-probabilistic and non-fuzzy uncertainty modeling method that does not require the accurate PDF and membership function of uncertain variables and only requires the upper and lower bounds of uncertainty [26]. Therefore, the RO approach assumes stochastic variables take values within an uncertainty set. Then, a robust decision is determined as the solution to an optimization problem that must be feasible for any realization of the uncertainty in a given set and optimal in the worst-case choice of the stochastic parameters in the aforementioned set [27]. Hence, this optimization approach aims at optimizing the objective function in the worst-case realization of the uncertainty. The main motivation for RO approach is twofold. First, the model of set-based uncertainty is interesting in its own right and in many applications is an appropriate notion of parameter uncertainty. Second, computational tractability is also a primary motivation and goal [28].

As mentioned earlier, the RO approach does not need so much information about the uncertain parameter. Thus, this method easily models the uncertainty by defining parametric sets using little information like the lower and upper bounds of uncertain parameter which are much easier to derive than probability distribution function in probabilistic programming approach. After that, the optimization problem can be solved using RO technique, and the best decision related to worst-case condition of uncertainty in predefined bounded interval is determined. In other words, this method takes into account the worst-case condition, and the obtained solution will be firstly feasible for any values of uncertain parameters; secondly, the solution is optimal for the worst-case amount of the uncertain parameters [29].

As a stream of literature, we review some papers to consider robust optimization approach to consider uncertainties in power system optimization, particularly MG scheduling problem optimization. In this vein, authors in [30] present a comprehensive review on the application of robust optimization method in order to solve power system optimization problems, resulted from different series of uncertainties including market price, renewable energy sources generation, and load demand. This review is investigated on an economic dispatch problem with uncertainty of market price. Furthermore, reference [31] aims to propose chance-constrained scheduling model of grid-connected MG. In this paper, both probabilistic optimization and robust optimization are applied to consider the uncertainty of renewable energy generation and loads. In [32], a novel approach is presented to consider MG optimal operation in both grid-connected and grid-isolated modes, which consider renewable energy resources as uncertainties. In this paper, the variety of uncertainties can be considered by robust optimization for optimal scheduling of MG in deregulated environment. Moreover, paper [33] presents a scenario-based robust energy management method for grid-connected MG to consider the worst-case amount of renewable energy resources generation and load in order to maximize the total exchange cost while getting the minimum social benefits cost. Moreover, authors in [29] investigate a scenario-based robust energy management with upper and lower bounds to control the uncertainties. In this paper, robust optimization method can handle market price as an uncertainty to consider maximum total cost as worst-case scenario; also, demand response program is presented to robustly operate MG with a

lower cost in the presence of the uncertainties. Finally, in [34], an optimal short-term scheduling of MG is presented that is included hydrothermal systems and energy storage systems. In addition, robust optimization method is applied to consider the uncertainties of market price.

In our problem, it is assumed that the hourly MG demand, the hourly hydropower generation, and the hourly electricity market prices are considered as uncertain parameters such that their hourly expected values are denoted by $\overline{PD_t}$, $\overline{PG_t}$, and $\overline{\lambda_t}$, respectively. Without loss of generality, suppose that variation ranges of uncertain parameters are symmetrically bounded as follows:

$$PD_t \in \left[(1-\beta_{\mathrm{D}})\overline{\mathrm{PD}_t}, (1+\beta_{\mathrm{D}})\overline{\mathrm{PD}_t}\right] \tag{9.13}$$

$$PG_t \in \left[(1-\beta_{\mathrm{G}})\overline{\mathrm{PG}_t}, (1+\beta_{\mathrm{G}})\overline{\mathrm{PG}_t}\right] \tag{9.14}$$

$$\lambda_t \in \left[(1-\beta_{\lambda})\overline{\lambda_t}, (1+\beta_{\lambda})\overline{\lambda_t}\right] \tag{9.15}$$

where β_{D}, β_{G}, and β_{λ} are degree of MG demand uncertainty, hydropower generation uncertainty, and electricity market prices uncertainty, respectively. Consequently, the abovementioned deterministic problem is transformed to the robust formulation as follows:

$$\min_{V} \ \max_{\Delta} \ \mathrm{obj} = \sum_{t\in T}(\lambda_t P_{\mathrm{in},t} - \mathrm{FIT}_t P_{\mathrm{out},t}) \tag{9.16}$$

$$(1-\beta_{\mathrm{D}})\overline{\mathrm{PD}_t} \le \mathrm{PD}_t \le (1+\beta_{\mathrm{D}})\overline{\mathrm{PD}_t} \tag{9.17}$$

$$(1-\beta_{\mathrm{G}})\overline{\mathrm{PG}_t} \le \mathrm{PG}_t \le (1+\beta_{\mathrm{G}})\overline{\mathrm{PG}_t} \tag{9.18}$$

$$(1-\beta_{\lambda})\overline{\lambda_t} \le \lambda_t \le (1+\beta_{\lambda})\overline{\lambda_t} \tag{9.19}$$

$$\mathrm{Eqs.}(9.4)--(9.12) \tag{9.20}$$

It can be seen that the proposed model is a bi-level optimization problem that in the lower-level problem (maximization subproblem), the decision variables are related to uncertainties ($\Delta = \{\lambda_t, PD_t, PG_t\}$), while the decision variables of the upper-level problem (minimization subproblem) are equal to decision variables of deterministic problem $\left(V = \left\{P_{\mathrm{in},t}, P_{\mathrm{out},t}, P_t^{\mathrm{dis}}, P_t^{\mathrm{ch}}, \mathrm{eSOC}_t\right\}\right)$. Therefore, it is important to choose an appropriate methodology to solve it.

9.4 Solution Methodology

The aforementioned optimization problem is categorized as bi-level optimization problem. It is also a non-convex optimization problem due to non-convexities in the objective function and binary variables. Thus, because of their nonlinearity and integer variables (mixed-integer nonlinear bi-level optimization problem), the

problem could not be solved using analytical methods. In addition, in this formulation, there are same uncertainties in both objective function and constraints, which cannot be reformulated and solved using commercial solvers. For this purpose, in this study, an iterative two-step method is developed to solve the aforementioned bi-level optimization problem using a genetic algorithm (GA) and mixed-integer linear programming (MILP). In this method, the GA is utilized to determine the worst case of uncertainties. GA has a powerful global search in the domain of possible solutions. Then, (9.3)–(9.12) are solved by receiving the worst case of uncertain parameters from the GA. Figure 9.7 demonstrates the flowchart of the solution methodology.

As can be traced from the flowchart, at first, an initial population (related to uncertainties) as initial condition is defined. Then, for each individual of this population, the hourly scheduling of BESS is determined considering the minimization of net value cost of purchasing energy from upstream network. Then, the obtained results are sent to the second step, and the fitness evaluations of all individuals are determined. After that, the crossover, mutation, and selection operators are utilized to generate the population of the next iteration. Finally, the previous steps are repeated for new population until arriving to the termination criterion of GA. and the final optimal scheduling of BESS (minimum procurement cost in the worst case of uncertainties) is determined.

9.5 Illustrative Example and Discussions

In this section, the proposed robust model is applied to a typical low-voltage MG as shown in Fig. 9.6. As described earlier, this MG consists of one in-pipe hydropower generator, one BESS, and several local loads. The hourly forecasted water velocity in a typical day is depicted in Fig. 9.8 [35]. Moreover, it is supposed that the type of in-pipe hydropower generator is Lucid Energy company life-type turbine, which its range of water velocity is 0.9 m/s for cut-in speed and 3.57 m/s for cut-out speed. Therefore, the in-pipe hydropower generator has output power in the aforementioned range of speed, and considering internal pipeline diameter, head, and efficiency ratio are, respectively, equal to 1 m, 35 m, and 85%, the hourly forecasted output power of in-pipe hydropower generator in the typical day can be depicted in Fig. 9.9.

The BESS has a power rating and capacity, respectively, equal to 500 kW and 3000 kWh, and charging and discharging efficiencies are 0.9 and 0.85, respectively. Moreover, the initial state of the BESS at midnight (00:00) is 500 kWh. The hourly forecasted demand is shown in Fig. 9.10 [36], and the hourly forecasted electricity market price [37] and the feed-in-tariff (FIT) rate, which is considered as time-of-use (TOU) scheme, are shown in Figs. 9.11 and 9.12, respectively.

After explanations of the case study, the described deterministic scheduling problem is solved using the forecasted values of uncertain parameters. For this purpose, the optimization problems (9.3)–(9.12) are solved using CPLEX solver in GAMS software environment. The expected minimum cost of purchasing energy

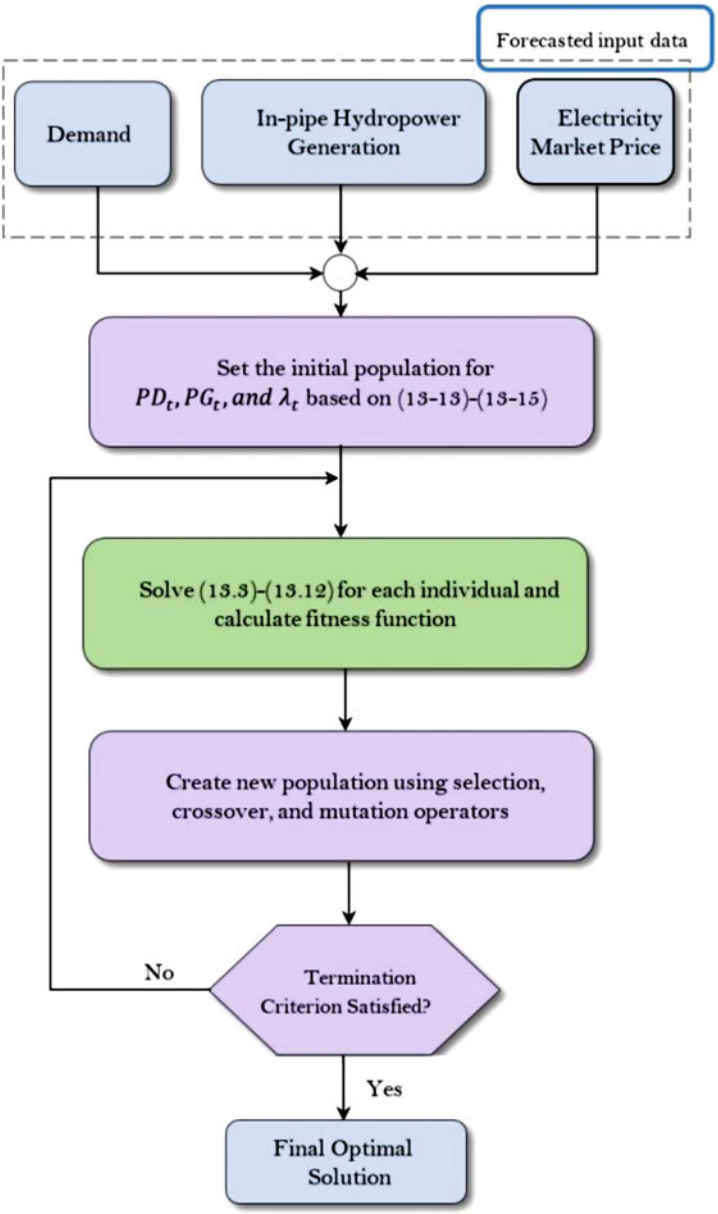

Fig. 9.7 Flowchart of the proposed solution methodology

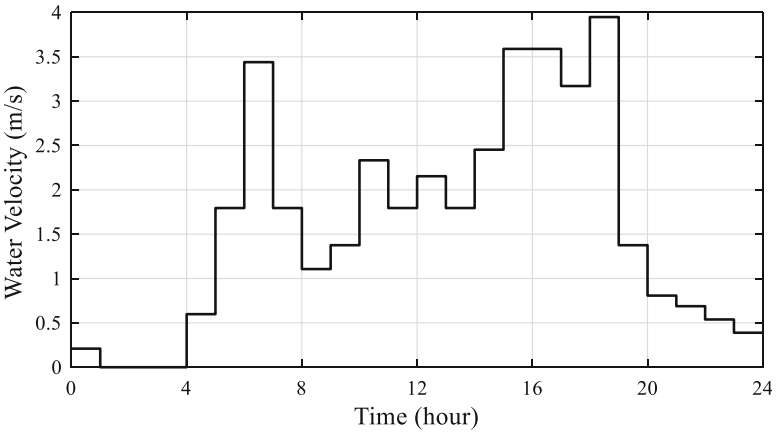

Fig. 9.8 The hourly forecasted water velocity in drinking water pipeline

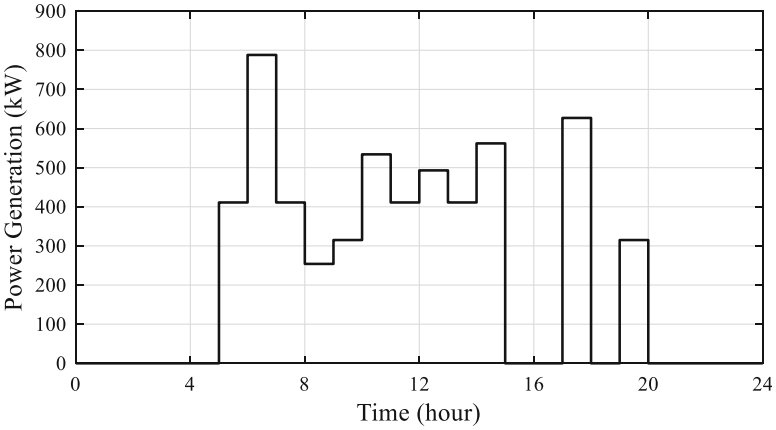

Fig. 9.9 The hourly forecasted output power of in-pipe hydropower generator

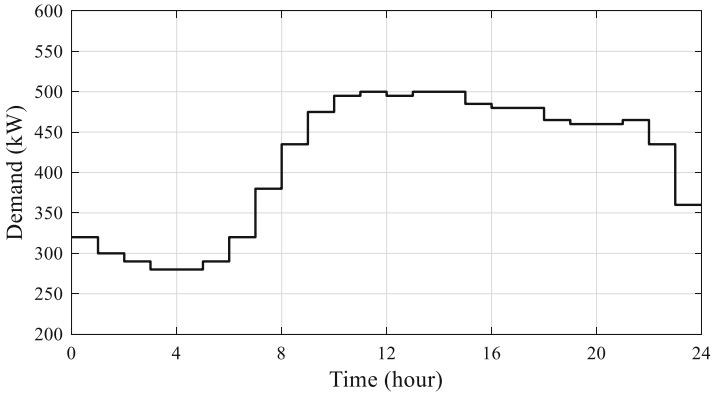

Fig. 9.10 The hourly forecasted demand

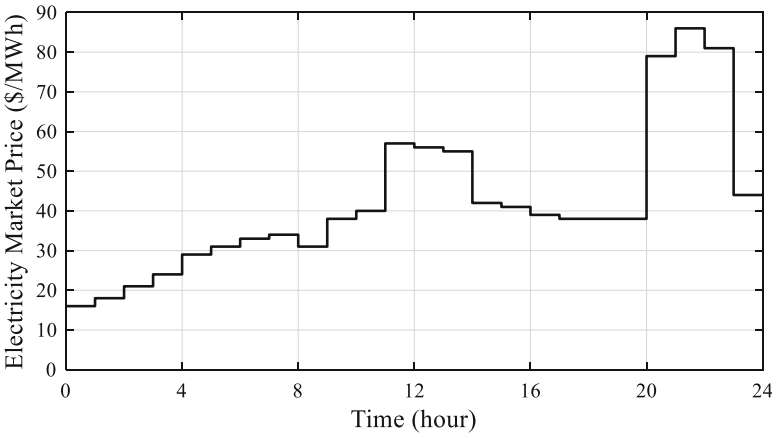

Fig. 9.11 The hourly forecasted electricity market price

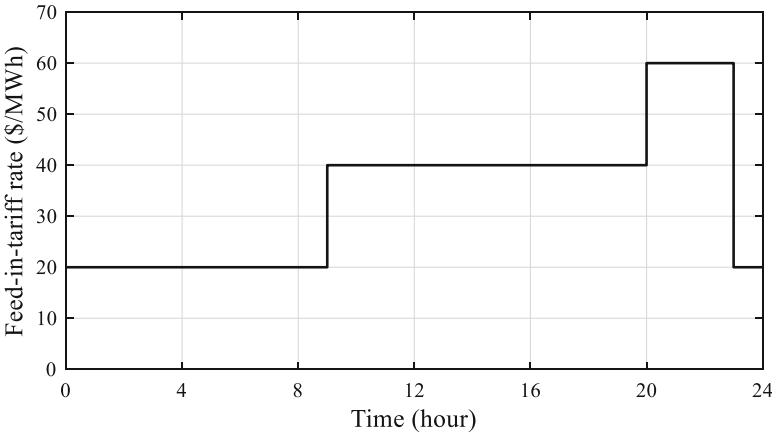

Fig. 9.12 Feed-in-tariff (FIT) rate

from upstream network in the typical day based on the forecasted values is equal to $123. Figure 9.13 shows the optimal charging/discharging schedule of BESS. As shown in this figure, BESS would be charged (negative output power) during hours of lower market prices (hours 1–8), and they would be discharged (positive output power) in hours with higher feed-in-tariff rates (hours 20–24). Moreover, Fig. 9.14 depicts the hourly exchange of energy with upstream network. In this figure, negative and positive values, respectively, show the imported and exported energy from/to upstream network. As can be seen in this figure, during hours 11, 15, 18, and 23, the MG exported energy to upstream network, because in these hours the output generation power of in-pipe turbine is high and feed-in-tariff rates are relatively high. Moreover, during hours 1–5, 9, 17–18, and 19–20, the MG imported energy from

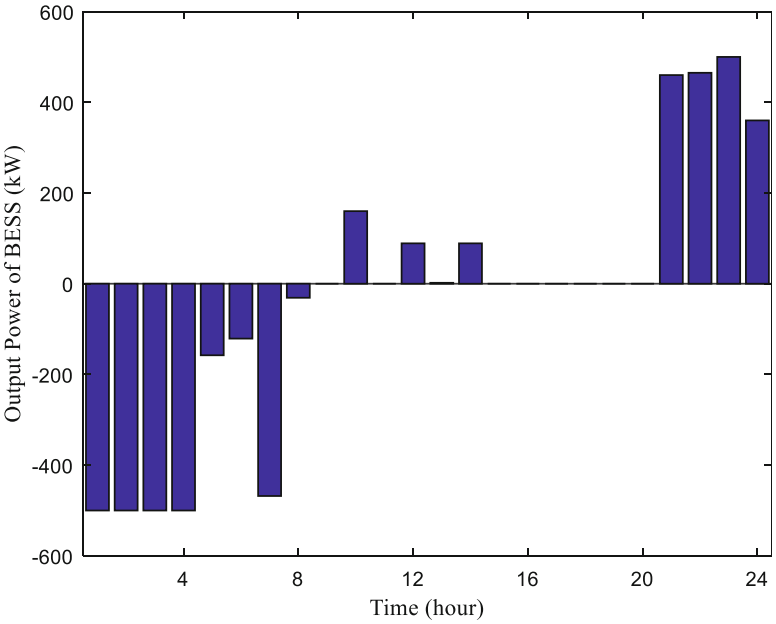

Fig. 9.13 The hourly BESS scheduling (for deterministic problem)

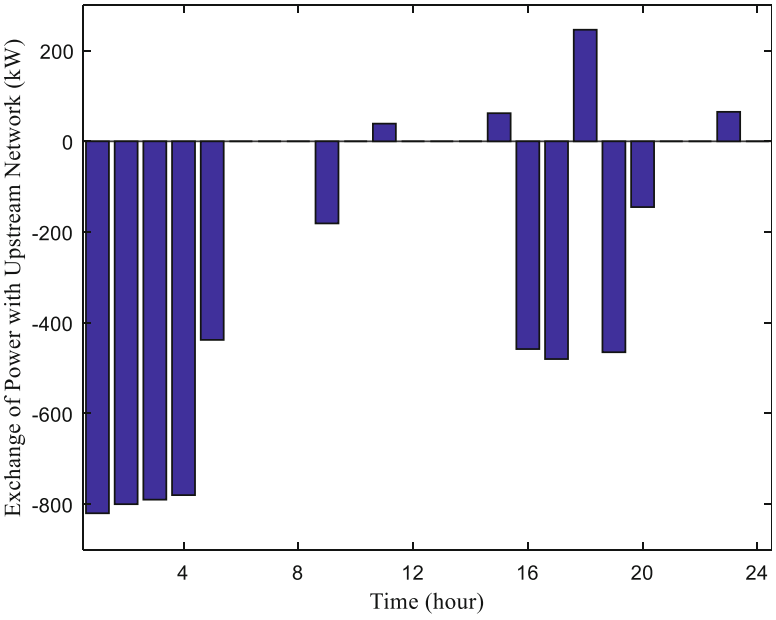

Fig. 9.14 The exchange of power with upstream network (for deterministic problem)

upstream network, because in these hours, either electricity market prices are lower than feed-in-tariff rates or the output generation power of in-pipe turbine is low.

After solving the deterministic scheduling problem, the robust scheduling optimization problems (9.16)–(9.20) considering the input parameter data and uncertainties are solved using the proposed two-step solution methodology by a link between GAMS and MATLAB software. The allowable changing ranges for uncertain parameters of λ_t and PD_t are considered identical and equal to 20% and for PG_t is 10%. As can be understood from the optimization, the worst case occurs when the in-pipe hydropower generation is in its lower bound and the demand and electricity market prices are in their upper bound. Figures 9.15 and 9.16 demonstrate the optimal charging/discharging schedule of BESS and the optimal exchange of energy with upstream network, respectively. As shown in Fig. 9.16, during all hours of the typical day, the MG imported energy from upstream network, and the exported energy to upstream network is zero. The reason is that in the worst situation of uncertainties, the local demand is at its upper bound and in-pipe turbine generation is at its lower bound. Therefore, in order for MG to meet the local demand, the MG must import energy from upstream network.

In addition, the results show that the maximum net value cost of purchasing energy from upstream network in the typical day for the robust model (in the worst case) is \$271. Moreover, by comparing the results of deterministic and robust problems, the cost of the robust problem is higher than that of the deterministic one. The reason is that due to uncertainties, the production of in-pipe hydropower

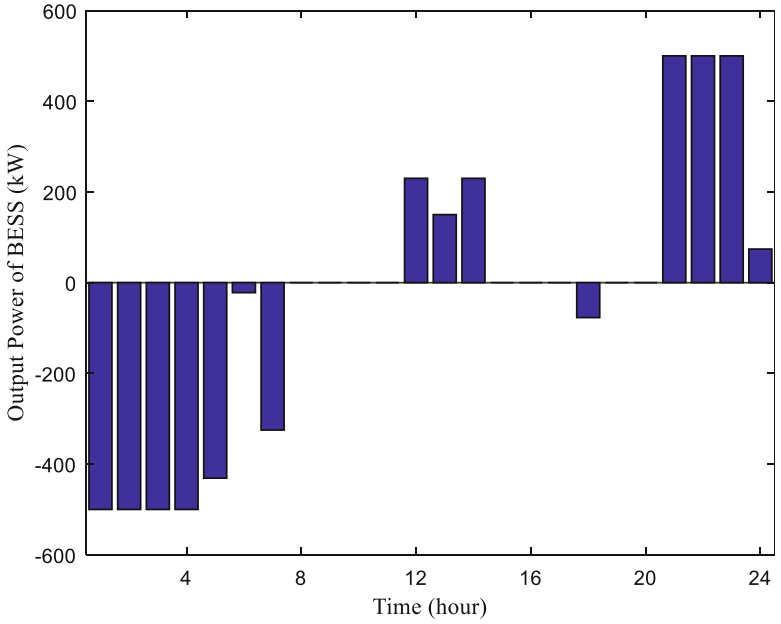

Fig. 9.15 The hourly BESS scheduling (for robust problem)

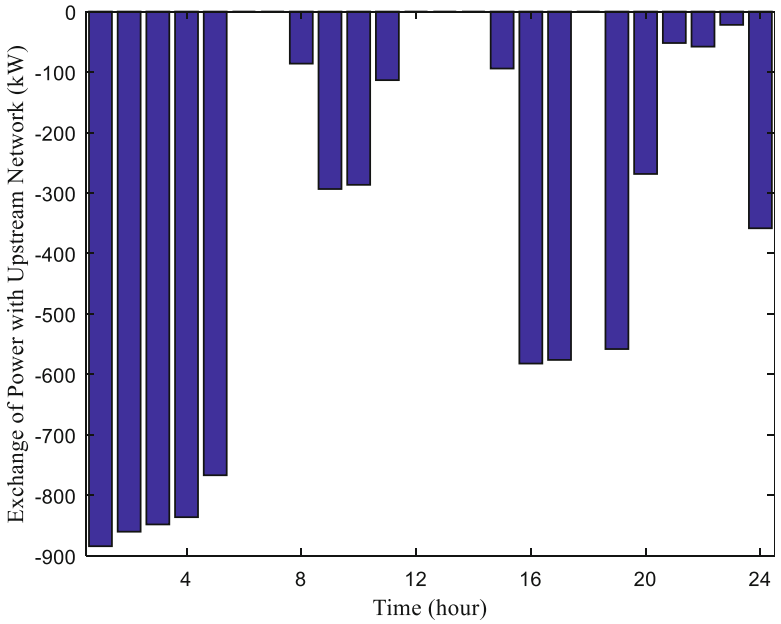

Fig. 9.16 The exchange of power with upstream network (for robust problem)

turbine in the robust model is decreased, and the electricity market price and local demand are increased. This result indicates that having a level of robustness in BESS scheduling increases costs of the MG in the worst situation.

In the next step, we decide to consider the concept of uncertainty budget in the aforementioned robust optimization problem. In this regard, constraints (9.21)–(9.23) limit the variability of uncertain variables. In these equations, Λ_{D}, Λ_{G}, and Λ_{λ} represent the corresponding uncertainty budget, respectively, for demand, generation, and electricity market price. These uncertainty budgets can take values between zero and one. If the value of uncertainty budget is chosen equal to zero, the uncertainty is not considered, and the robust problem is converted to a deterministic problem. On the other hand, if the value of uncertainty budget is chosen equal to one, the uncertainty parameter can take any values between lower and upper bounds. This can be seen as the case of maximum uncertainty. Thus, by choosing different values for uncertainty budget, we can analyze the impact of different levels of uncertainty on scheduling problem decisions [38]:

$$\frac{\sum_{t=1}^{T}(\mathrm{PD}_t - \mathrm{PD}_{t,\min})}{\sum_{t=1}^{T}(\mathrm{PD}_{t,\max} - \mathrm{PD}_{t,\min})} = \frac{\sum_{t=1}^{T}\left(\mathrm{PD}_t - (1-\beta_{\mathrm{D}})\overline{\mathrm{PD}_t}\right)}{\sum_{t=1}^{T}\left((1+\beta_{\mathrm{D}})\overline{\mathrm{PD}_t} - (1-\beta_{\mathrm{D}})\overline{\mathrm{PD}_t}\right)} \leq \Lambda_{\mathrm{D}} \quad (9.21)$$

$$\frac{\sum_{t=1}^{T}(\mathrm{PG}_{t,\max}-\mathrm{PG}_t)}{\sum_{t=1}^{T}(\mathrm{PD}_{t,\max}-\mathrm{PG}_{t,\min})}=\frac{\sum_{t=1}^{T}\left((1+\beta_{\mathrm{G}})\overline{\mathrm{PG}_t}-\mathrm{PG}_t\right)}{\sum_{t=1}^{T}\left((1+\beta_G)\overline{\mathrm{PG}_t}-(1-\beta_{\mathrm{G}})\overline{\mathrm{PG}_t}\right)}\le\beta_{\mathrm{G}} \quad (9.22)$$

$$\frac{\sum_{t=1}^{T}(\lambda_t-\lambda_{t,\min})}{\sum_{t=1}^{T}(\lambda_{t,\max}-\lambda_{t,\min})}=\frac{\sum_{t=1}^{T}\left(\lambda_t-(1-\beta_\lambda)\overline{\lambda_t}\right)}{\sum_{t=1}^{T}\left((1+\beta_\lambda)\overline{\lambda_t}-(1-\beta_\lambda)\overline{\lambda_t}\right)}\le\Lambda_\lambda \quad (9.23)$$

To analyze the impact of uncertainty on scheduling problem decision, we consider four categories of uncertainty budgets. In three categories of them, the uncertainty budgets for demand, generation, and electricity market price are identical, and their values are 0.2, 0.5, and 0.8, respectively, for first, second, and third group. Moreover, the abovementioned robust scheduling problem can be considered as fourth category with uncertainty budget equal to one. Table 9.2 demonstrates the optimal BESS scheduling (B.S.), the exchange of power with upstream network (P.E.), and the objective function values of these four categories of uncertainty

Table 9.2 Hourly BESS scheduling and power exchange in different categories of uncertainty budget

	Category 1		Category 2		Category 3		Category 4	
	Objective = $81.6		Objective = $147.3		Objective = $226.4		Objective = $270.6	
Hour	B.S.	P.E.	B.S.	P.E.	B.S.	P.E.	B.S.	P.E.
1	−500	766	−500	842	−500	884	−500	884
2	−500	771	−500	798	−500	860	−500	860
3	−500	732	−500	828	−500	801	−500	848
4	0	224	0	224	−500	801	−500	836
5	0	224	0	226	0	288	−431	767
6	−190	0	−500	280	−102	0	−22	0
7	−500	−98	−391	0	−393	0	−325	0
8	−147	0	−386	320	0	77	0	86
9	−441	524	0	175	0	211	0	293
10	0	40	0	34	0	276	0	287
11	0	−75	0	−111	−284	368	0	113
12	51	0	177	0	213	0	230	0
13	14	0	74	0	111	0	150	0
14	166	0	0	148	148	0	230	0
15	0	−18	−329	376	0	78	0	94
16	395	6	0	501	0	582	0	582
17	0	400	386	0	0	576	0	576
18	0	−281	0	−95	−136	0	−77	0
19	0	374	0	555	0	498	0	558
20	0	24	0	56	0	154	0	269
21	500	14	500	−30	500	31	500	52
22	500	−54	500	−31	500	57	500	58
23	500	−89	500	9	500	−6	500	22
24	0	291	239	129	258	174	74	358

budget. Moreover, the optimum values of uncertainty parameters in four categories of uncertainty budget, which are determined using the optimization problems (9.16)-(9.23), are depicted in Fig. 9.17.

9.6 Conclusion

In this chapter, a robust BESS scheduling problem was comprehensively presented to determine the best schedule of BESS for the worst case of uncertainties. In the described problem, it is assumed that an MG consists of an in-pipe hydropower, BESS, and local loads, and the MG operator aims to find the optimal BESS scheduling considering the uncertainties of in-pipe hydropower generation, demand, and electricity market price. The objective of MG operator is minimizing the energy procurement cost in the worst situation of aforementioned uncertainties. The operation constraints of BESS such as hourly energy balance, limitation of energy capacity, and equality of initial and final values of state of charge are considered as BESS constraints. Moreover, the power balance between MG and upstream network and the constraints related to uncertainties include the other constraints of the described robust BESS scheduling problem. The robust problem is solved using an iterative two-step algorithm, genetic algorithm, and mixed-integer linear programming. The results reveal that the worst case of uncertainties happens wherein the uncertainties of demand and electricity market price are in their upper bound and the generation is in its lower bound. Moreover, the concept of uncertainty budget has been added to the robust problem, and the worst situation of uncertainties for different values of uncertainty budgets is presented. As a result, it was found that in all cases of uncertainty budgets, generally, BESS charges in early hours of the day, with lower values of electricity price and demand, and discharges in late hours of the day, with higher values of electricity price and demand. In addition, the results show that BESS has a mitigation of 31% in energy procurement cost of MG in the worst situation of uncertainty. In other words, as stated earlier, the objective value of robust problem considering BESS is \$271, while the similar value without considering BESS is equal to \$391. As the future trends, the scheduling problem of MG with in-pipe hydropower generation can be enhanced by considering the demand response program and plug-in electric vehicle technology. Furthermore, the co-planning of BESS and in-pipe hydropower turbine (sizing and siting) in a distribution system (or rural area) can be proposed as the future work.

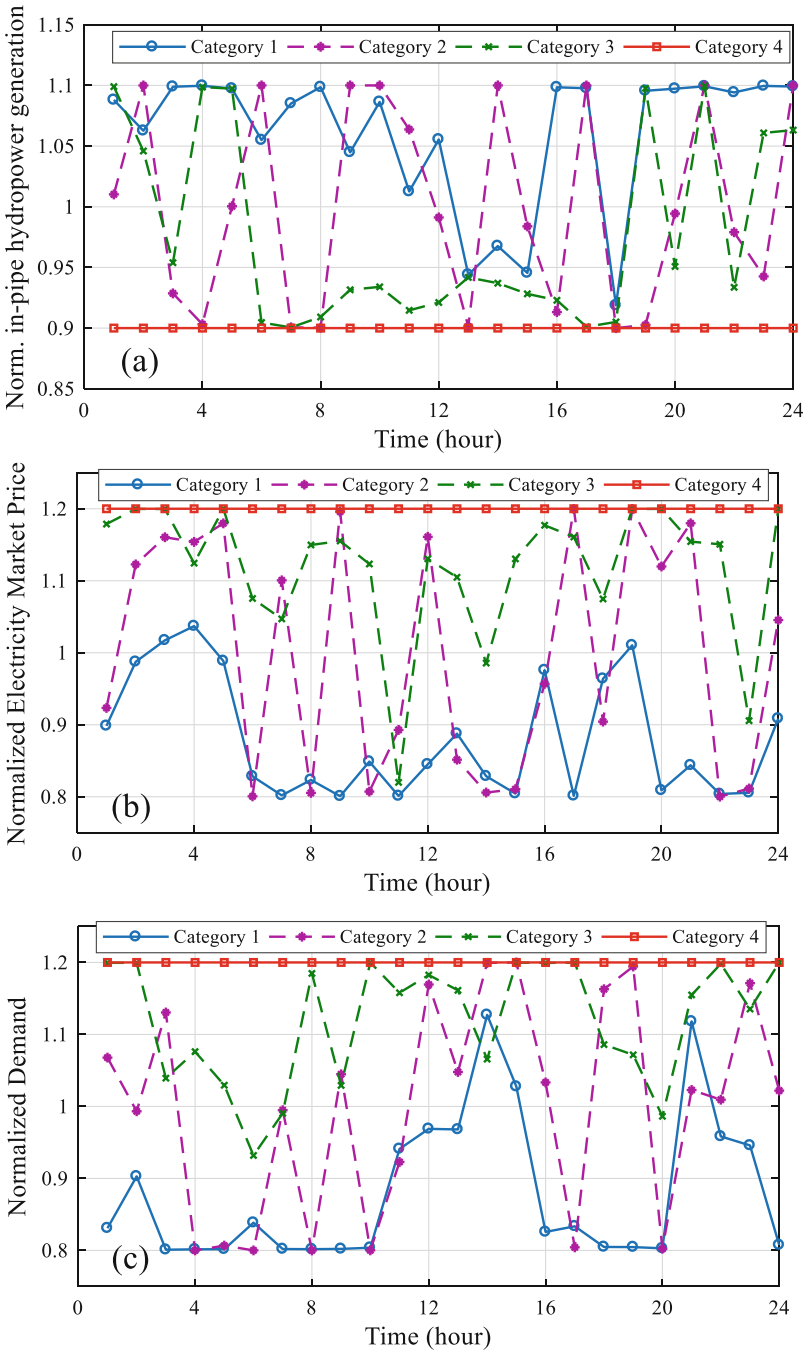

Fig. 9.17 The optimum values of uncertainty parameters for different uncertainty budgets (**a**: in-pipe hydropower generation uncertainty, **b**: electricity market price uncertainty, and **c**: demand uncertainty)

References

1. Ritchie, H., and Roser, M. (2019). *Renewable energy*. Published online at OurWorldInData.org. Retrieved from: https://ourworldindata.org/ renewable-energy [Online Resource].
2. Energy Resources*: Hydropower*. (2016). Published online at WorldEnergy.org. Retrieved from: https://www.worldenergy.org/data/resources/resource/hydropower/ [Online Resource].
3. Kunwor, A. (2012). *Technical specifications of micro hydropower system design and its implementation feasibility analysis and design of Lamaya Khola Micro Hydro Power Plant*. Bachelor's Degree Thesis Industrial Management.
4. Casini, M. (2015). Harvesting energy from in-pipe hydro systems at urban and building scale. *International Journal of Smart Grid and Clean Energy, 4*, 316–327.
5. Gatte, M. T., & Kadhim, R. A. (2012). Hydro power. *Energy Conservation, 9*(51000), 95–124.
6. Egging, R., Fleten, S. E., Grønvik, I., Hadziomerovic, A., & Ingvoldstad, N. (2016). Linear decision rules for hydropower scheduling under uncertainty. *IEEE Transactions on Power Systems, 32*(1), 103–113.
7. Hamann, A., Hug, G., & Rosinski, S. (2016). Real-time optimization of the mid-columbia hydropower system. *IEEE Transactions on Power Systems, 32*(1), 157–165.
8. Guedes, L. S., de Mendonça Maia, P., Lisboa, A. C., Vieira, D. A. G., & Saldanha, R. R. (2016). A unit commitment algorithm and a compact MILP model for short-term hydro-power generation scheduling. *IEEE Transactions on Power Systems, 32*(5), 3381–3390.
9. Cheng, C., Wang, J., & Wu, X. (2016). Hydro unit commitment with a head-sensitive reservoir and multiple vibration zones using MILP. *IEEE Transactions on Power Systems, 31*(6), 4842–4852.
10. Li, Y., Zhao, T., Liu, C., Zhao, Y., Yu, Z., Li, K., & Wu, L. (2019). Day-ahead coordinated scheduling of hydro and wind power generation system considering uncertainties. *IEEE Transactions on Industry Applications, 55*(3), 2368–2377.
11. Lopes, V. S., & Borges, C. L. (2014). Impact of the combined integration of wind generation and small hydropower plants on the system reliability. *IEEE Transactions on Sustainable Energy, 6*(3), 1169–1177.
12. Aasgård, E. K., Andersen, G. S., Fleten, S. E., & Haugstvedt, D. (2014). Evaluating a stochastic-programming-based bidding model for a multireservoir system. *IEEE Transactions on Power Systems, 29*(4), 1748–1757.
13. Moiseeva, E., & Hesamzadeh, M. R. (2017). Strategic bidding of a hydropower producer under uncertainty: Modified benders approach. *IEEE Transactions on Power Systems, 33*(1), 861–873.
14. Calderone, L. (2016). *What is hydropower in a pipe?*. Published online at AltEnergyMag.com. Retrieved from: https://www.altenergymag.com/article/2016/04/what-is-hydropower-in-a-pipe/23404/ [Online Resource].
15. Boone, A. (2018) *How portland is sourcing hydropower from its drinking water.*. Published online at CityLab.com. Retrieved from: https://www.citylab.com/environment/2018/01/portlands-drinking-water-is-powering-the-grid/550721/ [Online Resource].
16. *Can a city's water infrastructure produce hydropower?*. (2018). Published online at PowerTechnology.com. Retrieved from: https://www.power-technology.com/features/city-water-infrastructure-hydropower/ [Online Resource].
17. Chen, J., Yang, H. X., Liu, C. P., Lau, C. H., & Lo, M. (2013). A novel vertical axis water turbine for power generation from water pipelines. *Energy, 54*, 184–193.
18. Published online at LucidEnergy.com. Retrieved from: http://lucidenergy.com/how-it-works/ [Online Resource].
19. Schwartz, R. (2017). *Portland now generates electricity from turbines installed in city water pipes*. Published online at Money.Good.Is. Retrieved from: https://money.good.is/articles/portland-pipeline-water-turbine-power [Online Resource].
20. *Water – WEF flags up in-pipeline turbine tech to generate electricity*. (2018). Published online at WaterBriefing.org. Retrieved from: https://www.waterbriefing.org/home/technology-focus/

item/15384-wef-flags-up-turbine-tech-to-generate-electricity-from-inside-gravity-fed-water-pipelines [Online Resource].
21. *Calculation of hydroelectric power and energy.* Published online at Power-Calculation.com. Retrieved from: https://power-calculation.com/hydroelectricity-energy-calculator.php [Online Resource].
22. Mohammadi-ivatloo, B., Nazari-Heris, M. & Editors (2019). Robust optimal planning and operation of electrical energy systems. *Springer*.
23. Ben-Haim, Y. (2006). *Info-gap decision theory: Decisions under severe uncertainty,* 2nd ed. Oxford, UK: Academic Press.
24. Ranjbar, H., & Hosseini, S. H. (2016). IGDT-based robust decision making applied to merchant-based transmission expansion planning. *International Transactions on Electrical Energy Systems, 26*(12), 2713–2726.
25. Sosyster, A. L. (1973). Technical note—Convex programming with set-inclusive constraints and applications to inexact linear programming. *Operations Research, 21*, 1154–1157.
26. Ranjbar, H., Hosseini, S. H., & Kasebahadi, M. (2016). Robust transmission expansion planning considering private investments maximization. *2016 IEEE International Conference on Power System Technology (POWERCON),* 1–6.
27. Zugno, M., & Conejo, A. J. (2015). A robust optimization approach to energy and reserve dispatch in electricity markets. *European Journal of Operational Research, 247*(2), 659–671.
28. Bertsimas, D., Brown, D. B., & Caramanis, C. (2011). Theory and applications of robust optimization. *SIAM Review, 53*(3), 464–501.
29. Zeinal-Kheiri, S., Mohammadpour Shotorbani, A., & Mohammadi-Ivatloo, B. (2019). Robust energy management of a microgrid with uncertain price, renewable generation, and load using Taguchi's orthogonal array method. *Journal of Energy Management and Technology, 3*(3), 1–13.
30. Nazari-Heris, M., & Mohammadi-Ivatloo, B. (2018). Application of robust optimization method to power system problems. *Classical and recent aspects of power system optimization: Elsevier,* 19–32.
31. Liu, C., Wang, X., Guo, J., Huang, M., & Wu, X. (2018). Chance-constrained scheduling model of grid-connected microgrid based on probabilistic and robust optimisation. *IET Generation, Transmission & Distribution, 12*(11), 2499–2509.
32. Gupta, R. A., & Gupta, N. (2014). Robust microgrid operation considering renewable power uncertainties. *2014 Eighteenth National Power Systems Conference (NPSC),* Guwahati, 1–6.
33. Xiang, Y., Liu, J., & Liu, Y. (2015). Robust energy management of microgrid with uncertain renewable generation and load. *IEEE Transactions on Smart Grid, 7*(2), 1034–1043.
34. Nazari-Heris, M., Madadi, S., & Mohammadi-Ivatloo, B. (2018). Optimal management of hydrothermal-based micro-grids employing robust optimization method. *Classical and recent aspects of power system optimization: Elsevier,* 407–420.
35. Design, sizing, construction and maintenance of gravity-fed system in rural areas, MODULE 2: principles and sizing of a gravity fed system. (2008).
36. Grigg, C., et al. (1999). The IEEE reliability test system-1996. A report prepared by the reliability test system task force of the application of probability methods subcommittee. *IEEE Transactions on Power Systems, 14*(3), 1010–1020.
37. Shafiee, S., Zareipour, H., Knight, A. M., Amjady, N., & Mohammadi-Ivatloo, B. (2017). Risk-constrained bidding and offering strategy for a merchant compressed air energy storage plant. *IEEE Transactions on Power Apparatus and Systems, 32*, 946–957.
38. Conejo, A. J., et al. (2016). *Investment in electricity generation and transmission*. Cham Zug: Springer International Publishing.

Chapter 10
Game Theory Application for Finding Optimal Operating Point of Multi-production System Under Fluctuations of Renewable and Various Load Levels

Hossein Nezamabadi, Vahid Vahidinasab, Saeed Salarkheili, Vahid Hosseinnezhad, and Hamidreza Arasteh

10.1 Introduction and Motivations

Game theory (GT) is a popular tool to solve a problem consisting of different decision-makers with conflicting goals [1]. Through a GT, the interactions among multiple rational players should mathematically be modeled [2, 3]. The application of the GT includes a wide area of knowledge, such as social science, logic, and computer science, as well as power systems. In fact, GT addressed a zero-sum game, where the gain enhancement of a player will impose gain decrement for other players. Nowadays, GT has been applied to a huge number of decision-making problems and is an umbrella term for the science of logical decision-makings in the wide fields of knowledge [3].

H. Nezamabadi · V. Vahidinasab
Department of Electrical Engineering, Abbaspour School of Engineering, Shahid Beheshti University, Tehran, Iran
e-mail: h_nezamabadi@sbu.ac.ir; v_vahidinasab@sbu.ac.ir

S. Salarkheili (✉)
Department of Electrical Engineering, Abbaspour School of Engineering, Shahid Beheshti University, Tehran, Iran

Tehran Regional Electric Company (TREC), Tehran, Iran
e-mail: s_salarkheil@sbu.ac.ir

V. Hosseinnezhad
University of Salerno, Salerno, Italy
e-mail: v_hosseinnezhad@sbu.ac.ir

H. Arasteh
Niroo Research Institute (NRI), Tehran, Iran
e-mail: harasteh@nri.ac.ir

F. Jabari et al. (eds.), *Integration of Clean and Sustainable Energy Resources and Storage in Multi-Generation Systems*,
https://doi.org/10.1007/978-3-030-42420-6_10

Under the GT umbrella, the players are decision-makers who are aware that their strategies will affect the decisions of other players. A game includes a number of participants who are trying to achieve their own objective functions, and they will react to the actions of other players [4].

Generally, there are two types of games in GT [4]:

- Noncooperative game: where each player determines its strategy without collaborating with other participants. A strategy profile includes all the strategies of all the decision-makers.
- Cooperative game: where the participants try to reach an agreement or consensus through cooperating with other players. In this type of game, decision-makers could have negotiation with other players in order to maximize their possible benefits.

In both types, the equilibrium solution points will be determined according to the strategies of the players who want to achieve their maximum benefits. Nash equilibriums are solution points in which no player could enhance its profit by unilaterally changing only its own behavior. If a player has made its decision and other players cannot enhance their gains by changing their decisions, then the current strategies and their relevant gains constitute a Nash equilibrium [4].

The modern power electrical system consists of various stakeholders (such as distribution companies, generation companies, system operators, and auxiliary service providers) with contrary optimization goals. Therefore, for the implementation of sustainable and efficient energy generation, transmission, and distribution, solid mathematical tools are needed to determine a proper strategy at different levels of planning and operation. Considering all the points alongside the heterogeneous and uncertain nature of modern power systems inspires the examination of game theory to solve technical problems at various levels.

10.2 Application of Game Theory in Power System Analyzing

This section presents a survey of game theory applications in power system issues. This overview discusses the success and possible challenges of adopting game theoretical approaches in different aspects of future systems. The goal of this section is to study several power system problems that have been solved by using the GT concept. The investigated studies prove that game theoretic approaches are useful tools, which could be employed to find the Nash equilibrium point and achieve different optimization aims [4].

GT has been used in many researches in order to find the solution of many decision-making problems in a wide area of studies, e.g., distributed load management and micro storage management in smart grid. Therefore, several objectives have been presented in different studies that are solved by using GT. GT deals with a

situation of conflict and cooperation (where the aim of each decision-maker is to maximize its objective function) to find the Nash equilibrium solution point of such decision-making problems [4].

Murphy et al. [5] shown that GT is useful for the optimization procedure, because it can imitate the auction process. On the basis of the payoff values of the power plants, the optimum power plant compositions are determined. The best solution is the composition with the highest payoff value.

Kaymaz et al. [6] have considered the transmission line and investment cost competition and used the GT to solve a generation expansion planning (GEP) problem. The uncertainty factors are not considered in this paper, and a static model is used here. Reference [7] has taken into account the demand uncertainties to introduce a probabilistic dynamic programming model for solving its proposed problem [7].

Reference [8] integrates the GT and a bi-level model. The objective of the upper level is the maximization of the profit of a long-term planning problem, while the lower level is developed to apply some modifications on the basis of the real demand. Also, there are other studies that combine a bi-level model and GT with a different research focus. Ruiz et al. [9] focused on demand uncertainties. Kazempour et al. [10] focused on uncertainties of rival offerings and rival investments. The uncertainties of rival producer decisions and market offerings as well as load levels have been considered in [11].

The Cournot game is used in [12], where an expansion planning problem is addressed and a hybrid dynamic programming/game framework is utilized to find the optimum solution. Sarjiya et al. [13] combined the bi-level optimization technique and a multi-period framework into GT. The economical and reliability aspects have been considered as the objectives of [13].

There are many researches that investigated the GT under noncooperative game models (e.g., the Bertrand, Stackelberg, Cournot, and SFE models) in order to simulate power markets [14–18]. SFE and Cournot models have been utilized by a large number of studies in order to analyze the market power in oligopoly power markets [14]. According to [14, 19], the outcomes of the Cournot models have shown high accuracies compared to the actual markets. Baldick et al. [20] investigated the utilization of SFE model in the real-world power markets. References [21–24] have developed the transmission restrictions in the Cournot and SFE. A large-scale Cournot model of the US wholesale electricity markets is evaluated in [21]. Yu et al. [22] employed the SFE model and investigate how strategic forward contracts could affect the market power of generation companies. Cunningham et al. [23] analyzed an empirical evaluation in a transmission-constrained Cournot power market to assess the existence of a pure strategy equilibrium. Yang et al. [24] presented a solution technique on the basis of polynomial equations and payoff matrix, to calculate the Nash equilibrium that utilizes Cournot and SFE models for multiplayer games.

In the following sections, the GT applications in power systems are studied in more detail, where the review is outlined in two general categories: planning and operation.

10.2.1 Planning of Power Systems

Power system planning is one of the main issues in electrical engineering studies. The main topics of this subject are to locate and determine the size of generation/storage equipment, as well as to expand the network components and grid versus the possible load growth [25–27]. In fact, this is more about investing in the network. Meanwhile, if multiple investors are involved, the power system planning is turned into a decision-making problem with multi-agent and multi-objective players. In this regard, GT can play an important role in determining the proper solutions.

In [28], the Cournot model is utilized to model competitive generation planning, in which each company maximizes its profits according to the decisions of other companies. According to the Cournot model of [29], planning of transmission and generation expansion is considered simultaneously. In [30], a noncooperative game for the planning of a grid-connected system consisted of wind turbines, photovoltaic panels, and storage equipment is introduced. In [31], planning of static reserve capacity in a system with high penetration of wind power is modeled in the form of a zero-sum game.

10.2.2 Operation of Power Systems

The application of GT is also welcomed because participants in modern power systems can quickly respond to changing operational conditions. In this regard, various research directions to apply the GT have attracted widespread attention. Power market, dynamic control of the power system, demand response (DR), power dispatch, and energy management are the most important topics that have already been addressed.

Owning the ability to estimate the interactions between dependent decision-making problems, GT is the main paradigm adopted in energy market researches. In [32], the Bertrand model is used to predict market prices. The Stackelberg model is introduced in [33] to simulate the restructured electricity markets. In [15], the Stackelberg model is applied to an AC network to analyze the role of various companies in optimizing profit. In [34, 35], the Cournot model is applied to model the electricity market. The Cournot model is used to simulate the California electricity crisis in [36]. In [23], the Cournot equilibrium is investigated about a network subject to the transmission constraints. In [37], determining the equilibrium point in a two-settlement market is formulated based on the Cournot model as an equilibrium problem with equilibrium constraints (EPEC). In this case, each generation company solves a mathematical problem with equilibrium constraints (MPEC). This work has continued in [38] with regard to future strategic contracts. In [20, 39], the supply function equilibrium (SFE) model is used to simulate the UK and Wales power markets. In [40], the influence of strategies that increase competition in the electricity market of the United Kingdom and Wales is also investigated based on the SFE

model. The conjectural variation (CV) model is first proposed in [41] to simulate the Spanish electricity market. Then, this method is used in [42] to simulate the UK and Wales electricity markets.

Power systems may experience different perturbations during operation such as load disturbances and the outages related to transmission and generation sections. Robust control is the most representative use of differential GT. In [43], based on the principle of the saddle point, a robust excitation controller plan is presented for large generators. In [44], a cooperative control method based on the differential game is proposed to provide a coordinated scheme among load frequency control and tie-line scheduling.

Pricing schemes play an important role in demand-response programs since they can be used to encourage load deformation. In [45], a Stackelberg-based pricing method is suggested for retailers in a demand-response market. In [46], a similar technique is used to regulate the optimum contract price of the distributed generators (DGs).

The main purpose of the power system dispatch and proper energy management is to preserve stable, reliable, and economical operating conditions. The gaming reflection on the power dispatch is discussed in [47], where a zero-sum two-stage dynamic game model is proposed to dispatch electric power with electric vehicles. In [48–50], in order to model both preventive and corrective actions, a three-stage dynamic game is modeled to solve a unit commitment problem. In [51, 52], for a multi-objective dispatch problem, Nash equilibrium concept is used to compromise conflicting goals of generation cost and emission. In [53], a distributed energy management model is proposed based on GT. In this study, a solution methodology is implemented to determine the Nash equilibrium while fairness and privacy are being secured. The solution of the problem is extended with the features of load prediction and real-time adjustment in [54] as a Nash equilibrium problem. In [55], a Stackelberg game is introduced between the utility and consumers. In this research, a distributed algorithm is presented to obtain a unique equilibrium based on local information.

10.3 Integrating Distributed Energy Resources into the Power Grid

After the 1970s energy crisis, renewable energy sources (RESs) have been selected by many countries as an alternative to fossil fuel. As an important step, environmental pollution and emission has been reduced by Kyoto protocol, and thus, penetration of RESs has been accelerated. Next, in respect to promoting energy efficiency, supportive policies have been issued to increase demand response (DR) programs. Therefore, in order to increase security of energy supply, decrease environmental pollution, and promote energy efficiency, people worldwide turned to using distributed energy resources (DERs).

Past limitations in structure of distribution system, technology, and controls caused the electric grid to stop at the meter. Therefore, there are some regulatory barriers and operational limits, which don't allow the DERs seen by the market and system operators. In other words, DERs have been invisible in the management of power system, although they have been designed and installed in the grid with appropriate engineering methods. Large investment will be done in the grid in the future. Under these conditions, the cost of investment and operation will rise. By increasing DERs, distribution systems have been faced with some problems such as load forecast uncertainties, voltage fluctuations, unbalanced phase, increasing energy losses, and distribution line congestion. On the other hand, energy not served has been increased by occurrence of natural disasters and malicious attacks, and the necessity of a more resilient grid has been felt to supply the emergency loads during such time.

Two major complementary developments are achieving to help address the challenges associated with the emerging challenges and integrate the DERs into the grid: micro grids (MGs) and virtual power plants (VPPs). MGs and VPPs expands a full utilization of demand-side resources and DERs.

10.3.1 MG and VPP Components

By the capabilities of the components, energy and ancillary services can be provided by the MGs and VPPs. Generally, the components can be categorized into five groups: producers (including power, heat, and combined heat and power (CHP)), storages (including thermal and electrical), and flexible and fix demands (consist of thermal and electrical). Producers have been classified by their main resources into fuel-based and renewable-based.

In [56–74, 84, 85, 88–91, 93–96], MGs and VPPs consist of a set of fuel-based distributed generation (DG) units, including micro turbines (MTs) and fuel cells (FCs), and in [56–66, 75, 77, 79–84, 88, 90, 91, 93–95], MGs and VPPs consist of a set of RESs, including photovoltaic (PV) panels and wind turbine (WT). By considering thermal demand, MGs and VPPs can supply heat demand in addition to electrical one by CHP units in [69, 78, 81, 85, 86]. ESSs and their constraints have been considered in [56, 57, 59–61, 63, 65, 66, 72–74, 77–82]. As DR programs, flexible demands have been investigated in [57–59, 62, 63, 65–68, 70–74, 77, 79, 80–84]. For the sake of comparison, the considered components by the papers have been given in Table 10.1.

Some characteristics of components have been ignored by the authors in some papers, while they have been investigated by the others. Therefore, the MG loads have been considered as heat ventilation air conditioner (HVAC) and non-HVAC loads in [58]. It have been assumed that MG can sign load curtailment and load shifting contracts with its customers in Ref. [59]. In [61], a detail model of the energy storage system (ESS) model is proposed which considers ESS cost and enables it to be employed in a unit commitment problem. In order to make the operation of MG

Table 10.1 MG and VPP components

	Concepts		Producers						Energy storage system			Flexible demands		Fix demands	
			Power						Electrical						
			fuel-based		Renewable-based										
Ref. no.	VPP	MG	MT	FC	WT	PV	Heat	CHP	Battery	EV	Thermal	Electrical	Thermal	Electrical	Thermal
[56]		✓	✓	✓	✓				✓					✓	
[57]		✓	✓		✓	✓			✓			✓			
[58]		✓	✓	✓	✓	✓						✓	✓	✓	✓
[59]		✓	✓		✓				✓			✓		✓	
[60]		✓	✓	✓	✓	✓			✓						
[61]		✓	✓		✓	✓			✓						✓
[62]	✓		✓		✓	✓						✓		✓	
[63]	✓		✓		✓	✓			✓			✓		✓	
[64]	✓		✓		✓	✓								✓	
[65]	✓		✓		✓	✓			✓			✓			
[66]	✓		✓		✓				✓			✓	✓	✓	
[67]		✓	✓									✓		✓	
[68]	✓		✓									✓		✓	
[69]	✓		✓					✓						✓	✓
[70]	✓		✓									✓		✓	
[71]	✓		✓									✓		✓	
[72, 73]	✓		✓						✓			✓		✓	
[74]	✓		✓						✓			✓		✓	
[75]		✓			✓					✓				✓	
[76]		✓				✓									
[77]		✓			✓				✓			✓		✓	
[78]		✓				✓		✓	✓						

(continued)

Table 10.1 (continued)

	Concepts		Producers						Energy storage system			Flexible demands		Fix demands	
			Power												
			fuel-based		Renewable-based				Electrical						
Ref. no.	VPP	MG	MT	FC	WT	PV	Heat	CHP	Battery	EV	Thermal	Electrical	Thermal	Electrical	Thermal
[79]	✓				✓				✓			✓		✓	
[80]	✓				✓				✓			✓		✓	
[81]	✓				✓	✓	✓	✓	✓		✓	✓		✓	✓
[82]	✓				✓				✓			✓			
[83]	✓				✓									✓	
[84]		✓	✓		✓	✓			✓			✓		✓	
[85]		✓						✓						✓	✓
[86]	✓						✓	✓						✓	✓
[87]	✓											✓	✓	✓	✓
[88]		✓	✓	✓	✓	✓			✓					✓	
[89]		✓				✓		✓	✓					✓	
[90]		✓			✓	✓	✓	✓	✓		✓	✓	✓	✓	✓
[91]		✓	✓		✓				✓			✓			✓
[92]	✓					✓						✓			
[93]		✓	✓		✓	✓			✓					✓	
[94]		✓	✓	✓	✓	✓			✓					✓	
[95]		✓			✓	✓				✓		✓		✓	
[96]		✓		✓		✓						✓		✓	

more resilient, thermal and electrical demands are served by the interdependent electricity and natural gas supplies in Ref. [85]. Coordination of the WT and electric vehicles (EV) has been exploited in [75]. In Ref. [87], an optimization algorithm is provided to manage thermostatically loads in a VPP.

10.3.2 Optimal Operation of DERs via MGs and VPPs

The origin of MG expression was proposed for the first time by Lasseter in [97]. The author has mentioned that an MG is a community of DERs as a single entity that can respond to central control signals. By the definition, an MG is a group of interconnected loads and DERs within clearly defined electrical boundaries that acts as a single controllable entity with respect to the grid (see Fig. 10.1). An MG can connect and disconnect from the grid to enable it to operate in both grid-connected or island mode.

On the other hand, VPP is a group of aggregated loads and DERs which can be participated in the electricity markets as an entity with dual role including producer

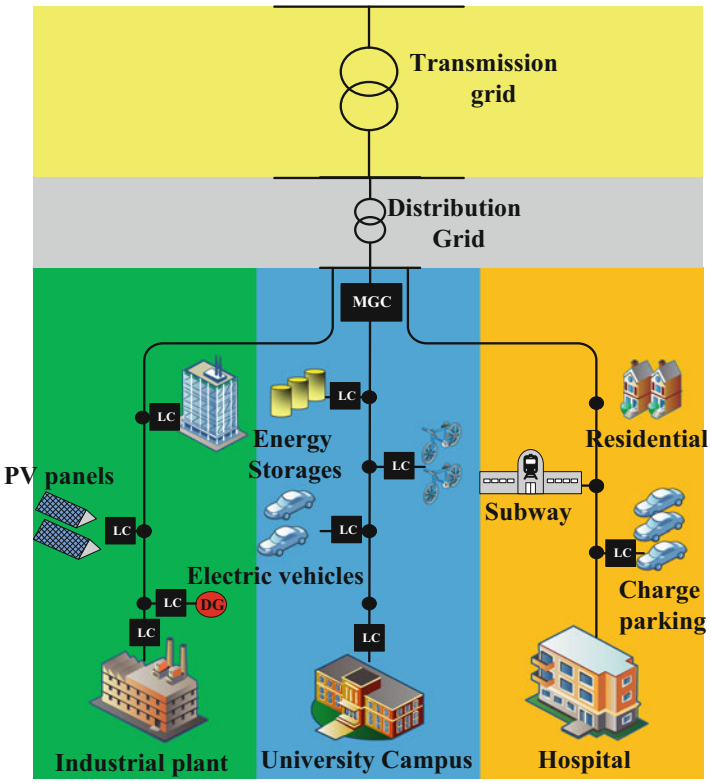

Fig. 10.1 MG definition (LC local controller, MGC MG controller)

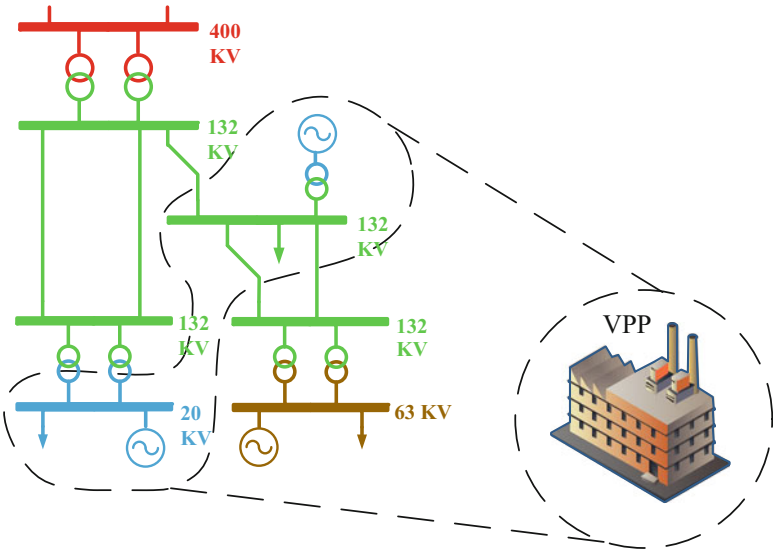

Fig. 10.2 VPP definition

and consumer (see Fig. 10.2). It should be noted that VPP is an aggregator, which can consider grid topology or not. The origin of VPP expression was proposed for the first time by the "virtual utility" definition in [98]. The author has been mentioned that the virtual utility is a flexible collaboration of independent, market-driven entities that provide efficient energy service demanded by consumers without necessarily owning the corresponding assets. In order to achieve a market-based entity which can provide efficient energy service, using decentralized power plants, which is called VPP, was introduced as a suitable solution. For optimal operation of the DERs, MG and VPP face with optimal bidding strategy in the electricity markets. In the following text, this challenge has been investigated.

10.3.3 Bidding Strategy of MG and VPP in the Electricity Markets Considering the Intermittent Nature of the Renewables and the Load Variation

Generally, bidding strategy of MG and VPP in the electricity markets can be categorized into equilibrium and nonequilibrium models. Nonequilibrium models are based on forecasting market clearing price (MCP) and using price-based unit commitment (PBUC) approaches. Equilibrium models are subject to Nash equilibrium and game theoretic approaches. In equilibrium models, it is assumed that the model of competition between market players is imperfect, so VPP and MG have been considered as a price maker in these models. As mentioned before, the

competition models have been classified into Bertrand, Stackelberg, SFE, and Cournot. To the best of our knowledge, the bidding strategies of MG and VPP have been investigated by the Bertrand, Stackelberg, and SFE models. In Bertrand model, the VPP bidding strategy have been proposed based on repeated games in which multiple VPPs compete each other by the price of their production [62]. Based on Stackelberg model, a bi-level approach has been presented in [66, 67], in order to determine the optimal offering strategy of VPPs and MGs. And finally, in the SFE model, the strategic behavior of VPP is presented by a supply function (SF) [71]. On the other hand, to cope with the uncertain nature of the RESs, the MG's bidding strategy has been investigated in two categories: the deterministic and the stochastic manner. In the deterministic one, the uncertainty is modeled by a single parameter. In this approach, the uncertain variable is substituted by its expected value in the problem. Stochastic programming (SP) is another solution to model the uncertain process. In the SP approach, the decisions are made by the expectation of scenario realization [66]. Therefore, the main requirement of the SP is scenario generation for the uncertain variables and the existence of precise probability distributions. In the SP approach, the expected value of the cost function has been minimized over the realization of all scenarios.

10.3.4 Optimal Operation of Multi-production System as a VPP Under Fluctuations of RESs and Load Variability

Considering the commitments of a multi-production system (i.e., VPP) in the electricity market, the intermittent nature of RESs, and unknown consumption pattern of load causes the VPP faced with deficiencies or excesses in the energy balance. Therefore, the fluctuation in the production of RESs (e.g., wind and photovoltaic) makes the optimal operation problem of the VPP challenging. Generally, there are two major problems, which affect the optimal operation of VPP. The first one is the uncertainties of the net load (i.e., consumption of the loads minus production of the RESs), and the second one is the effectiveness of VPP on the market prices as a price maker player in the electricity market. In order to deal with the problems, deterministic and stochastic approaches have been proposed in the following text.

10.3.4.1 Deterministic Approach

In the deterministic approach, the fluctuations of RESs and load variability have been modeled by the expected values. In other words, the RESs' production and the loads' consumption have been considered by applying their expected values. Therefore, the intermittency of the RESs and variability of the loads are modeled by the

most expected value of the net load (i.e., expected value of the loads' consumption minus expected value of the RESs' production). By the following, the optimal bidding of a VPP has been investigated in an intraday electricity market via Nash-SFE equilibrium. The strategic behavior of the market participants has been modeled by the SFE model. In the SFE model, market participants represent their bidding strategy by the both quantity and price. In the first step, VPP needs to extract its cost function to represent in the electricity market. For this purpose, the SF of the VPP has been determined by a nonlinear programming (NLP). In this step, the constraints of DGs and interruptible loads (ILs) have been considered. On the other hand, the loading rate of the electrical lines and the bus voltage limits are considered by the AC power flows in this step. After determining the SF, the VPP can strategically compete with the other market participants in the intraday market by the Nash-SFE equilibrium.

(a) *1st Step: Determining SF of VPP*

In order to determine the SF of VPP, an iterative process has been proposed in Fig. 10.3. In this algorithm, first, the cost function of the VPP can be determined by the problem 10.1, 10.2, 10.3, 10.4, 10.5, 10.6, 10.7, and 10.8, and then, the SF of the VPP can result from the derivation of the cost function:

$$\text{Minimize cost}_{\text{VPP},k} = \sum_{i \in S_{\text{DG}}} F(P_{\text{DG}_i}) + \sum_{j \in S_{\text{int}}} F\left(P_{\text{LC}_j}\right). \tag{10.1}$$

Subject to the following:

$$\sum_{i \in S_{\text{DG}}} P_{\text{DG}_i} - \sum_{j \in S_{\text{int}}} P_{\text{LC}_j} = P_{\text{VPP},k} + P_{\text{loss}} + P_{\text{load}} \tag{10.2}$$

$$P_{\text{DG}_i}^{\min} \le P_{\text{DG}_i} \le P_{\text{DG}_i}^{\max} \tag{10.3}$$

$$P_{\text{LC}_j}^{\min} \le P_{\text{LC}_j} \le P_{\text{LC}_j}^{\max} \tag{10.4}$$

$$P_{mn}(V,\theta) = G_{mn}\left(V_m^2 - V_m V_n \cos\left(\theta_m - \theta_n\right)\right) - B_{mn}(V_m V_n \sin\left(\theta_m - \theta_n\right)) \tag{10.5}$$

$$\begin{aligned} Q_{mn}(V,\theta) = &-B_{mn}\left(V_m^2 - V_m V_n \cos\left(\theta_m - \theta_n\right)\right) \\ &- G_{mn}(V_m V_n \sin\left(\theta_m - \theta_n\right)) \end{aligned} \tag{10.6}$$

$$S_{mn}(V,\theta) \le S_{mn}^{\max} \tag{10.7}$$

$$V_m^{\min} \le V_m \le V_m^{\max} \tag{10.8}$$

The operation cost of VPP including the DGs and IL cost is given in (10.1). The $F(P_{\text{DG}_i})$ and $F\left(P_{\text{LC}_j}\right)$ are the operation cost of the DGs and ILs, respectively. The balance of supply and demand is enforced by (10.2). The DER limitations are enforced by (10.3) and (10.4). Equations (10.5) and (10.6) consider the AC power flow. The transmission line loading limits are enforced by (10.7). Finally, the bus

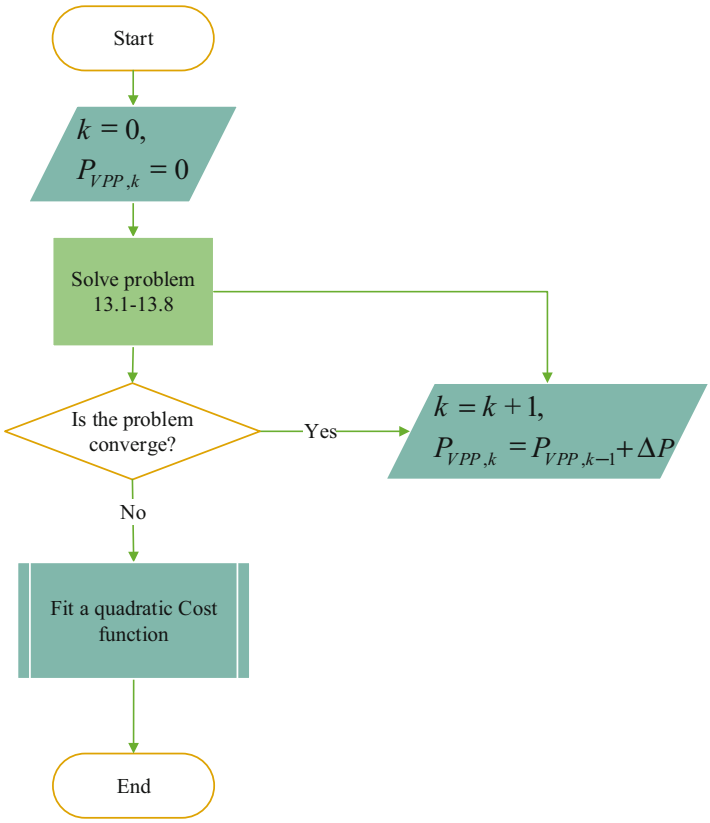

Fig. 10.3 Determining SF of VPP

voltage limits are constrained by (10.8). Therefore, by an iterative manner, the SF of the VPP can result from the derivation of the cost function.

(b) *2nd Step: Strategic Bidding of VPP*

It should be noted that the Nash equilibrium is in a point in which the profits of market players are simultaneously maximum and any player has no changes in its bidding strategy. Therefore, it is considered that

$$\text{Cost}_i = \frac{1}{2} a_i p_i^2 + b_i p_i + c_i. \tag{10.9}$$

$$\text{Marginal cost}_i = a_i p_i + b_i. \tag{10.10}$$

$$\text{SF}_i = \alpha_i p_i + \beta_i \tag{10.11}$$

In an imperfect competitive market, instead of representing marginal cost to the market, the market participants represent its SF to the market where SF_i shows the

SF of the producers. For simplicity's sake, one degree of freedom has been considered in the problem. Therefore, the only decision variable is equal to β_i (i.e., α_i is equal to a_i). Regarding uniform pricing, all suppliers are paid by MCP. Therefore, the profit of each supplier is written by the following:

$$\pi_i = p_i \text{MCP} - \text{Cost}_i \tag{10.12}$$

By considering supply-demand balance, the MCP can be written by the following:

$$\text{MCP} = \frac{\text{Demand} + \sum_i \frac{\beta}{a_i}}{\sum_i \frac{1}{a_i}} \tag{10.13}$$

Therefore, the profit can be written as

$$\pi_i(\beta_i) = \frac{1}{2a_i}\left[\frac{\text{Demand} + \sum_i \frac{\beta}{a_i}}{\sum_i \frac{1}{a_i}}\right]^2 - \frac{b_i}{a_i}\left[\frac{\text{Demand} + \sum_i \frac{\beta}{a_i}}{\sum_i \frac{1}{a_i}}\right] - \frac{\beta_i}{2a_i} + \frac{b_i\beta_i}{a_i} - c_{i.} \tag{10.14}$$

As mentioned before, the Nash equilibrium is in a point in which players' profits are simultaneously maximum, and any market player has no changes in its bidding strategy. In this purpose, the first-order differential conditions are needed:

$$\begin{bmatrix} \frac{\partial \pi_1(\beta_1)}{\partial \beta_1} \\ \vdots \\ \frac{\partial \pi_i(\beta_i)}{\partial \beta_i} \end{bmatrix} = \begin{bmatrix} 0 \\ \vdots \\ 0 \end{bmatrix} \Rightarrow \begin{bmatrix} \beta_1^* \\ \vdots \\ \beta_i^* \end{bmatrix} \tag{10.15}$$

By this way, the VPP's bidding strategy in the electricity market has been proposed.

(c) *Numerical Study*

In Fig. 10.4, the VPP model is studied on a distribution network as a VPP.

The characteristics of DGs and ILs are in Table 10.2. The VPP forecasts the net, so the forecasted loads are given in Table 10.3. The cost function of the VPP rivals are given in Table 10.4. The strategic behavior of VPP is investigated for the 260 MWh demand load.

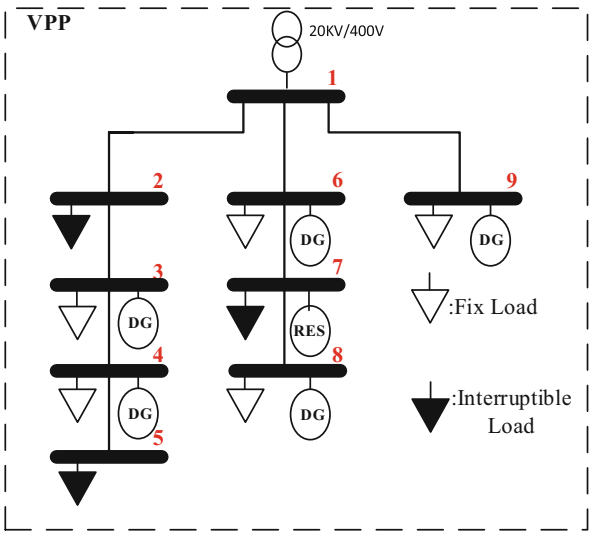

Fig. 10.4 VPP network model

Table 10.2 VPP component characteristics

Unit	a_i ($/MWh^2)	b_i ($/MWh)	c_i ($)	P_{min} (MW)	P_{max} (MW)
DG_3	0.03	16.5	0	0	10
DG_4	0.0177	16.35	0	0	10
DG_6	0.0235	17.5	0	0	3
DG_8	0.0635	16.5	0	0	3
DG_9	0.022	17.6	0	0	3
LC_2	0.03	18	0	0	2
LC_5	0.0177	17.85	0	0	2
LC_7	0.022	19.1	0	0	1

Table 10.3 Forecasted loads of VPP

Unit	Load(MWh)
L3	2
L4	2
L6	0
L8	0
L9	1

Table 10.4 SF of market players

Unit	Bus	a_i ($/MWh^2)	b_i ($/MWh)	P_{min} (MW)	P_{max} (MW)
1	1	0.02	15	15	80
2	27	0.0175	14.75	15	80
3	13	0.025	16	5	40
4	22	0.0625	14	5	50
5	23	0.025	16.1	5	30

Table 10.5 First step output

A (\$/MWh^2)	B (\$/MWh)	C (\$)	P_{min} (MW)	P_{max} (MW)
0.0292	15.863	1.9083	0	33.3

Table 10.6 Nash-SFE equilibrium point characteristics

	β_i^* (\$/MWh)	Quantity (MWh)
G1	16.27	60.03
G2	17.47	70.35
G3	14.34	35.33
G4	16.45	30.99
G5	15.75	30
VPP	15.81	33.3
MCP	18.22	

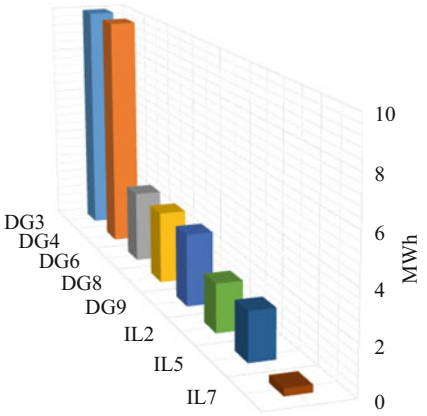

Fig. 10.5 VPP component schedule

The outputs of the first step are given in Table 10.5. It should be noted that the maximum production of VPP is equal to 33.3 MW in reason of losses and voltage drop, while the total capacity of DGs and ILs is equal to 34 MW.

The characteristics of Nash-SFE equilibrium point are given in Table 10.6. It is shown that the VPP can compete with rivals (i.e., other power plants).

Regarding Nash-SFE equilibrium point, the VPP can schedule their components in an optimal way. In Fig. 10.5, the optimal operation of DERs has been shown. Since the DGs' operation costs are below the equilibrium point of the market (i.e., MCP = 18.22 \$/MWh), all of DGs produce maximum capability (i.e., 10, 10, 3, 3, and 3 MWh) to export their energy into the upstream network. Moreover, the operation costs of IL2 and IL5 are below the equilibrium point of the market (i.e., MCP = 18.22 \$/MWh), these ILs curtail their maximum capability (i.e., 2 and 2 MWh) to export their energy into the upstream network. However, the operation costs of IL7 is higher than the equilibrium point of the market (i.e., MCP = 18.22 \$/MWh), it curtails part of its capability (i.e., 0.295 MWh).

10.3.4.2 Stochastic Approach

In this section, it is assumed that VPP offering strategy can influence the market price (i.e., it's a price maker) but considers the other market participants' offers/bids, which can be known by the historical data. In Stackelberg model, the VPP can act as a "leader," and the rivals' behavior (i.e., "followers") can be obtained by the aggregation of the rivals' demand declarations and their supply offers. Regarding Stackelberg model, the VPP optimal offering strategy problem is formulated as a bi-level optimization problem. Moreover, the fluctuation of the RESs and variation of the loads are modeled by the stochastic process. In the upper-level problem, VPP runs PBUC selects the best stepwise supply curve to maximize its profit subject to the market clearing conditions included within the lower-level problem. Therefore, the VPP optimal offering strategy problem is formulated as a stochastic bi-level optimization problem, which is converted to a mathematical program with equilibrium constraints (MPEC). To reformulate the bi-level problem of VPP bidding strategy, the lower-level problem is replaced by its Karush-Kuhn-Tucker (KKT) condition as an MPEC.

(a) *Bi-level Model*

The considered bi-level model for strategic bidding of VPP is explained below. The bi-level structure of the model is shown in Fig. 10.6. The upper-level problem represents the profit maximization of the VPP subject to DER constraints and to the

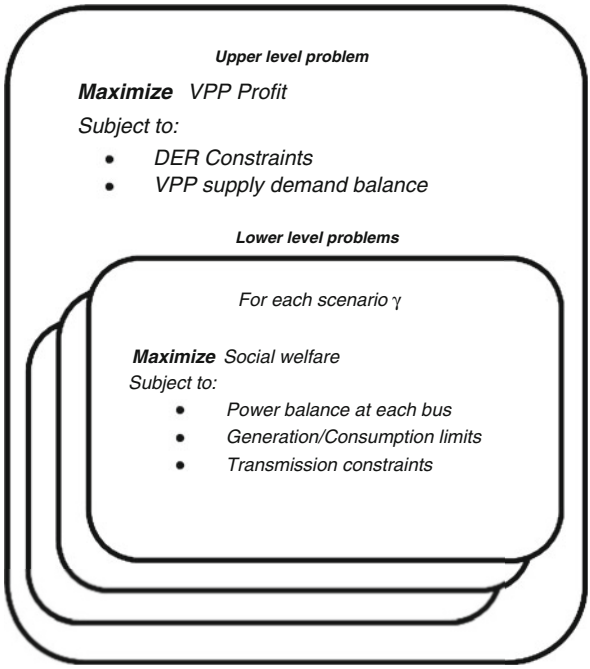

Fig. 10.6 Bi-level structure of VPP offering strategy

lower-level problems. The market clearing problem is modeled by the lower-level problem. The lower-level problem maximizes the social welfare subject to the supply-demand balance at each bus, the production and consumption limits, and also transmission constraints.

The problem formulation can be casted by the following:

$$\begin{aligned}
&\text{Maximizing} \sum_{t\epsilon \mathrm{T}} \sum_{i\in S_{\mathrm{GSP}}} (\lambda_{it} \times P_{it}) \\
&-\sum_{\gamma\epsilon\Omega} \pi_{\gamma} \left\{ \sum_{t\epsilon \mathrm{T}} \left(\sum_{i\in S_{dg}} C^{dg}_{i\gamma t}\left(P^{dg}_{i\gamma t}\right) + \mathrm{SUC}^{dg}_{i\gamma t} + \mathrm{SHC}^{\mathrm{DG}}_{i\gamma t} \right.\right. \\
&+ \sum_{i\in S_{\mathrm{int}}} C^{\mathrm{int}}_{i\gamma t}\left(P^{\mathrm{int}}_{i\gamma t}\right) + \sum_{i\in S_{\mathrm{str}}} C^{\mathrm{str}}_{i\gamma t}\left(P^{\mathrm{str}}_{i\gamma t}\right) \\
&\left.\left. -\sum_{i\in S_L} \rho_{i\gamma t} \times \left(\mathrm{LOAD}_{i\gamma t} - P^{\mathrm{int}}_{i\gamma t}\right)\right)\right\}
\end{aligned} \tag{10.16}$$

Subject to the following:

$$P^{G}_{it} + \sum_{i\in S_{dg}} P^{dg}_{i\gamma t} - \eta_{\mathrm{str}} \sum_{i\in S_{\mathrm{str}}} P^{\mathrm{str}}_{i\gamma t} = \mathrm{LOAD}_{i|(i\epsilon S_n)\gamma t} - \sum_{i\in S_{\mathrm{int}}} P^{\mathrm{int}}_{i\gamma t} + \sum_{m\in\theta_n} B_{nm}(\theta_{tn} - \theta_{tm}) \quad \forall n.\gamma.t \tag{10.17}$$

$$P^{dg\,\min}_{i} I^{dg}_{i\gamma t} \le P^{dg}_{i\gamma t} \le P^{dg\,\max}_{i} I^{dg}_{i\gamma t} \quad \forall \gamma.i \mid i\epsilon S_{dg}.t \tag{10.18}$$

$$P^{dg}_{i\gamma(t+1)} - P^{dg}_{i\gamma t} \ge RU^{dg}_{i} \quad \forall \gamma.i \mid i\epsilon S_{dg}.t \tag{10.19}$$

$$P^{dg}_{i\gamma t} - P^{dg}_{i\gamma(t+1)} \ge RD^{dg}_{i} \quad \forall \gamma.i \mid i\epsilon S_{dg}.t \tag{10.20}$$

$$\begin{cases} I^{dg}_{i\gamma t} - I^{dg}_{i\gamma(t-1)} \le J^{dg}_{i\gamma t} \\ I^{dg}_{i\gamma(t-1)} - I^{dg}_{i\gamma t} \le K^{dg}_{i\gamma t} \quad \forall \gamma.i \mid i\epsilon S_{dg}.t \\ I^{dg}_{i\gamma t} - I^{dg}_{i\gamma(t-1)} \le J^{dg}_{i\gamma t} - K^{dg}_{i\gamma t} \end{cases} \tag{10.21}$$

$$\sum_{l=1}^{\mathrm{MUT}} I^{dg}_{i\gamma(t+l)} - 1 \ge \mathrm{MUT} \quad \forall J^{dg}_{i\gamma t} = 1 \quad \forall \gamma.i \mid i\epsilon S_{dg}.t \tag{10.22}$$

$$\sum_{l=1}^{\mathrm{MDT}} 1 - I^{dg}_{i\gamma(t+l)} \ge \mathrm{MDT} \quad \forall K^{dg}_{i\gamma t} = 1 \quad \forall \gamma.i \mid i\epsilon S_{dg}.t \tag{10.23}$$

$$-\left(\text{cap}_{0.i\gamma} - P_{i\gamma}^{\text{strmin}}\right) \leq \sum_{k=1}^{t} P_{ik}^{\text{str}} \leq P_{i\gamma}^{\max} - \text{cap}_{0.i\gamma} \quad \forall \gamma.i \mid i \epsilon S_{\text{str}}.t \tag{10.24}$$

$$P_{i\gamma t}^{\text{str}} \leq R_i^{\text{str-ch}} \text{ in charging mode} \quad \forall \gamma.i \mid i \epsilon S_{\text{str}}.t \tag{10.25}$$

$$-P_{i\gamma t}^{\text{str}} \leq R_i^{\text{str-dch}} \text{ in discharging mode} \quad \forall \gamma.i \mid i \epsilon S_{\text{str}}.t \tag{10.26}$$

$$0 \leq P_{i\gamma t}^{\text{int}} \leq P_i^{\text{intmax}} I_{i\gamma t}^{\text{int}} \quad \forall \gamma.i \mid i \epsilon S_{\text{int}}.t \tag{10.27}$$

$$\sum_{t} P_{i\gamma t}^{\text{int}} \leq E_i^{\text{intmax}} \quad \forall \gamma.i \mid i \epsilon S_{\text{int}} \tag{10.28}$$

$$-F_{nm}^{\text{vpp}} \leq B_{nm}^{\text{vpp}} \left(\theta_{tn\gamma}^{\text{vpp}} - \theta_{tm\gamma}^{\text{vpp}}\right) \leq F_{nm}^{\text{vpp}} \quad \forall \gamma.n.m.t \tag{10.29}$$

$$-\pi \leq \theta_{tn\gamma}^{\text{vpp}} \leq \pi \quad \forall \gamma.n.m.t \tag{10.30}$$

$$\theta_{tn\gamma}^{\text{vpp}} = \theta_{tn} \quad \forall \gamma.n \mid n = \text{GSP}.t \tag{10.31}$$

$$\lambda_{it}.P_{it}^{G} \in \arg\{\text{Minimizing} \sum_{t} \left(\sum_{i \in S_{\text{VPP}}} \alpha_{it} P_{it}^{G} + \sum_{i \in S_R} \lambda_{it}^{R} P_{it}^{\text{GR}} - \sum_{i \in S_D} \lambda_{it}^{D} P_{it}^{D} \right) \tag{10.32}$$

$$P_{i|(i \in S_{n'})t}^{G} + P_{i|(i \in S_{n'})t}^{GR} - P_{i|(i \in S_{n'})t}^{D} = \sum_{m' \in \theta_{n'}} B_{n'm'}(\theta_{tn'} - \theta_{tm'}) \quad : \lambda_{it} \quad \forall n'.t \tag{10.33}$$

$$0 \leq P_{it}^{G} \leq P_{it}^{G\max} \quad : \mu_{it}^{G\max}, \mu_{it}^{G\min} \quad \forall i \mid i \epsilon S_{\text{VPP}}.t \tag{10.34}$$

$$0 \leq P_{it}^{\text{GR}} \leq P_{it}^{\text{GRmax}} \quad : \mu_{it}^{\text{GRmax}}, \mu_{it}^{\text{GRmin}} \quad \forall i \mid i \epsilon S_R.t \tag{10.35}$$

$$0 \leq P_{it}^{D} \leq P_{it}^{D\max} \quad : \mu_{it}^{D\max}, \mu_{it}^{D\min} \quad \forall i \mid i \epsilon S_D.t \tag{10.36}$$

$$-F_{n'm'} \leq B_{n'm'}(\theta_{tn'} - \theta_{tm'}) \leq F_{n'm'} : \nu_{n'm't}^{\max}, \nu_{n'm't}^{\max} \quad \forall n'.m'.t \tag{10.37}$$

$$-\pi \leq \theta_{tn'} \leq \pi \quad : \nu_{n'm't}^{\max}, \nu_{n'm't}^{\max} \quad \forall n'.t \tag{10.38}$$

$$\theta_{tn'|(n'=1)} = 0 \quad : \xi_t^1 \quad \forall n' = 1.t \tag{10.39}$$

It should be noted that the variable after colon shows the dual variable of the constraints.

(b) *Recasting Bi-level to MPEC Model*

The MPEC corresponding to problems (10.16, 10.17, 10.18, 10.19, 10.20, 10.21, 10.22, 10.23, 10.24, 10.25, 10.26, 10.27, 10.28, 10.29, 10.30, 10.31, 10.32, 10.33, 10.34, 10.35, 10.36, 10.37, 10.38, and 10.39) is reformulated below. The lower-level problems (10.32, 10.33, 10.34, 10.35, 10.36, 10.37, 10.38, and 10.39) are replaced by their KKT condition. In [99], the KKT optimality condition is described in detailed (10.16, 10.17, 10.18, 10.19, 10.20, 10.21, 10.22, 10.23, 10.24, 10.25, 10.26, 10.27, 10.28, 10.29, 10.30, and 10.31).

$$\alpha_{it} - \lambda_{it} + \mu_{it}^{G\max} - \mu_{it}^{G\min} = 0 \quad \forall i \mid i\epsilon S_{\mathrm{VPP}}.t \tag{10.40}$$

$$\lambda_{it}^{R} - \lambda_{it} + \mu_{it}^{\mathrm{GRmax}} - \mu_{it}^{\mathrm{GRmin}} = 0 \quad \forall i \mid i\epsilon S_{R}.t \tag{10.41}$$

$$-\lambda_{it}^{D} + \lambda_{it} + \mu_{it}^{D\max} - \mu_{it}^{D\min} = 0 \quad \forall i \mid i\epsilon S_{D}.t \tag{10.42}$$

$$\begin{aligned}&\sum_{m'\in\theta_{n'}} B_{n'm'}(\lambda_{n't} - \lambda_{m't}) + \sum_{m'\in\theta_{n'}} B_{n'm'}\left(\nu_{n'm't}^{\max} - \nu_{n'm't}^{\max}\right)\\ &\quad + \sum_{m'\in\theta_{n'}} B_{n'm'}\left(\nu_{n'm't}^{\min} - \nu_{n'm't}^{\min}\right) + \xi_{tn'}^{\max} - \xi_{tn'}^{\min} + \left(\xi_{t}^{1}\right)_{n'=1}\\ &\quad = 0 \quad \forall n'.t\end{aligned} \tag{10.43}$$

$$P_{i|(i\in S_{n'})t}^{G} + P_{i|(i\in S_{n'})t}^{\mathrm{GR}} - P_{i|(i\in S_{n'})t}^{D} = \sum_{m'\in\theta_{n'}} B_{n'm'}(\theta_{tn'} - \theta_{tm'}) \quad \forall n'.t \tag{10.44}$$

$$0 \le P_{it}^{G} \perp \mu_{it}^{G\min} \ge 0 \quad \forall i \mid i\epsilon S_{\mathrm{VPP}}.t \tag{10.45}$$

$$0 \le P_{it}^{\mathrm{GR}} \perp \mu_{it}^{\mathrm{GRmin}} \ge 0 \quad \forall i \mid i\epsilon S_{R}.t \tag{10.46}$$

$$0 \le P_{it}^{D} \perp \mu_{it}^{D\min} \ge 0 \quad \forall i \mid i\epsilon S_{D}.t \tag{10.47}$$

$$0 \le P_{it}^{G\max} - P_{it}^{G} \perp \mu_{it}^{G\max} \ge 0 \quad \forall i \mid i\epsilon S_{\mathrm{VPP}}.t \tag{10.48}$$

$$0 \le P_{it}^{\mathrm{GRmax}} - P_{it}^{\mathrm{GR}} \perp \mu_{it}^{\mathrm{GRmax}} \ge 0 \quad \forall i \mid i\epsilon S_{R}.t \tag{10.49}$$

$$0 \le P_{it}^{D\max} - P_{it}^{D} \perp \mu_{it}^{D\max} \ge 0 \quad \forall i \mid i\epsilon S_{D}.t \tag{10.50}$$

$$0 \le F_{n'm'} + B_{n'm'}(\theta_{tn'} - \theta_{tm'}) \perp \nu_{n'm't}^{\min} \ge 0 \quad \forall n'.m'.t \tag{10.51}$$

$$0 \le F_{n'm'} - B_{n'm'}(\theta_{tn'} - \theta_{tm'}) \perp \nu_{n'm't}^{\max} \ge 0 \quad \forall n'.m'.t \tag{10.52}$$

$$0 \le \pi + \theta_{tn'} \perp \xi_{tn'}^{\min} \ge 0 \quad \forall n'.t \tag{10.53}$$

$$0 \le \pi - \theta_{tn'} \perp \xi_{tn'}^{\max} \ge 0 \quad \forall n'.t \tag{10.54}$$

$$\theta_{tn'|(n'=1)} = 0 \quad \forall n' = 1.t \tag{10.55}$$

It should be noted that this MPEC model can be linearized and converted to a mixed integer linear problem (MILP). There are two kinds of nonlinearity in the problem. First, the multiplication of the λ_{it} and P_{it} in the objective function, which can be linearized by the strong duality theorem. In a convex problem, the primal and dual problems are equal to each other at the optimum point by the strong duality theorem [8]. Second, the complementarity condition is given in Eqs. 10.45, 10.46, 10.47, 10.48, 10.49, 10.50, 10.51, 10.52, 10.53, and 10.54. Such a condition can be linearized by replacing $a, b \ge 0$, $\theta \in \{0, 1\}$, $a \le \theta M_a$, $b \le (1 - \theta)M_b$ instead of $0 \le a \perp b \ge 0$. Noteworthy, M_a and M_b should be tuned large enough to reach the optimal value [9]. Therefore, the MILP problem can be solved by the existing CPLEX commercial solver [10].

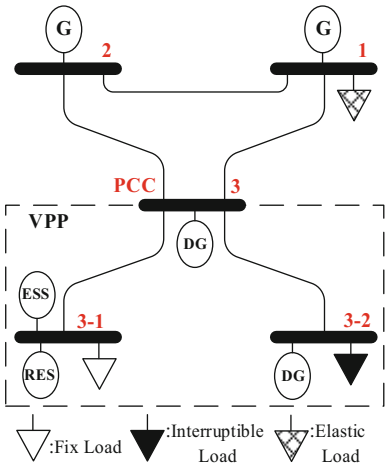

Fig. 10.7 Upstream and VPP grids

Table 10.7 Cost function of DGs

Unit	Bus	Cost ($/MWh)			Step width (MWh)			P_{min} (MW)	P_{max} (MW)
		Step 1	Step 2	Step 3	Step 1	Step 2	Step 3		
DG_1	3	70	75	80	2	6	4	0	12
DG_2	3–2	61	65	70	1	7	6	0	14

Table 10.8 Cost function of ILs

Unit	Bus	Variable cost ($/MWh)	Fix cost ($)	P_{min} (MW)	P_{max} (MW)	E_{max} (MWh)
IL_1	3–2	25	5	0	2	8

Table 10.9 Cost function of ESS

Unit	Bus	Variable cost ($/MWh)	Fix cost ($)	P_{min} (MW)	P_{max} (MW)	η (%)	E_{max} (MWh)
ESS_1	3–1	2	5	0	2	90	4

(c) *Numerical Study*

For the sake of simplicity, the proposed model tests on a three-bus test system as a VPP. The VPP system is connected to the upstream network at the PCC. The upstream network is a three-bus test system (see Fig. 10.7).

The operation costs of the VPP's components (i.e., DGs, IL, and ESS) are in Tables 10.7, 10.8, and 10.9. The VPP's net load (i.e., load's consumption minus RES's productions) can be forecasted based on historical data, so the intervals of the net loads are given in Fig. 10.8. It should be noted that the net load scenarios are determined in the grey shade intervals.

For numerical analysis of electricity market, a three-bus test system is considered. It is assumed that the market players can offer its cost function by the three pairs of

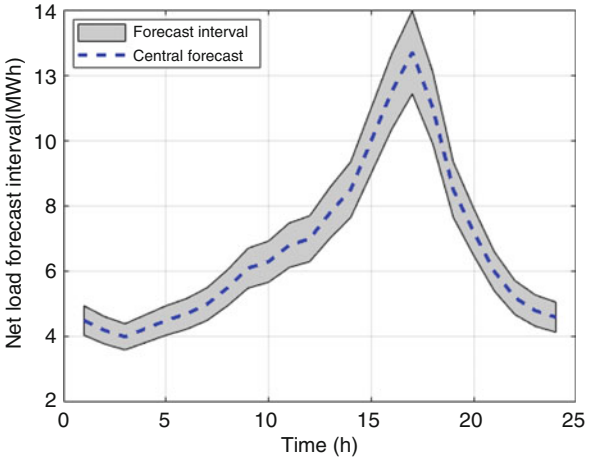

Fig. 10.8 VPP net load forecast interval

Table 10.10 Price offer of market participants

Unit	Bus	Cost and step width pairs ($/MWh, MWh)			P_{min} (MW)	P_{max} (MW)
		Step 1	Step 2	Step 3		
G_1	1	(100, 2)	(120, 4)	(130, 4)	0	10
G_2	2	(73.5, 2)	(75.2, 3)	(100, 3)	0	8

the cost and step width. The rival's offering strategies, which compete with VPP in the market, are in Table 10.10.

Table 10.11 shows the net demand block for each period of time for the wholesale energy market. In order to consider the net load fluctuations, the proposed model has been studied for the two cases. In the first case, the fluctuation of the RESs' production and load consumption have been considered by the only one scenario (i.e., central forecast in Fig. 10.8). In the second case, the net load uncertainty has been considered by the scenarios in the forecasted interval, which is shown in Fig. 10.8.

In Fig. 10.9, the total productions of the DERs, including DGs, IL, and ESS, have been shown by the two cases. The expected value and the standard deviation are illustrated by the marks and vertical bars, respectively. Regarding central forecast in the first case, the VPP is not faced with the net load uncertainty. Therefore, the standard deviation of the total productions in each hour is equal to zero. However, the VPP can operate its DERs in a certain manner. Since the standard deviation value indicates the minimum and maximum of the total production of DERs, it is evident that VPP operates its DERs to cover the net load uncertainty by regarding net load scenarios in the second case.

In Fig. 10.10, the production shares of each market participants, including G1, G2, and VPP, have been shown in two case studies. By considering net load uncertainty, the market shares of G1 and G2 in the electricity market have no changes in cases 1 and 2. However, the market shares of VPP in the electricity

Table 10.11 Net demand block for each period of time

$/MWh Hours	110	105	98	95	85	80	78	76	74	73	70	65
1									16	2	2	2
2									16	2	2	2
3									16	2	2	2
4									16	2	2	2
5									16	2	2	2
6									16	2	2	2
7					16	2	2	2				
8					16	2	2	2				
9					16	2	2	2				
10					16	2	2	2				
11					16	2	2	2				
12					16	2	2	2				
13					16	2	2	2				
14	16	2	2	2								
15	16	2	2	2								
16	16	2	2	2								
17	16	2	2	2								
18	16	2	2	2								
19	16	2	2	2								
20	16	2	2	2								
21					16	2	2	2				
22					16	2	2	2				
23									16	2	2	2
24									16	2	2	2

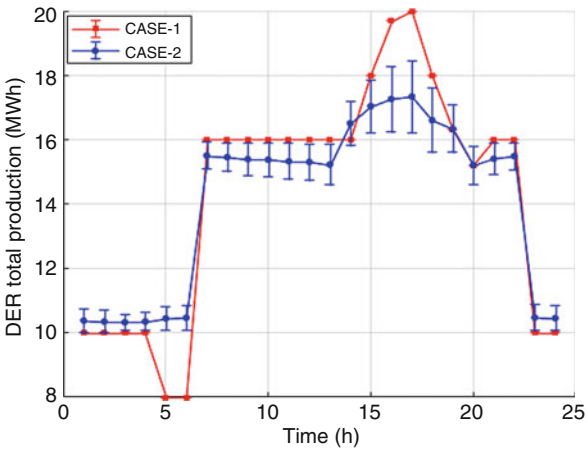

Fig. 10.9 DERs' total production

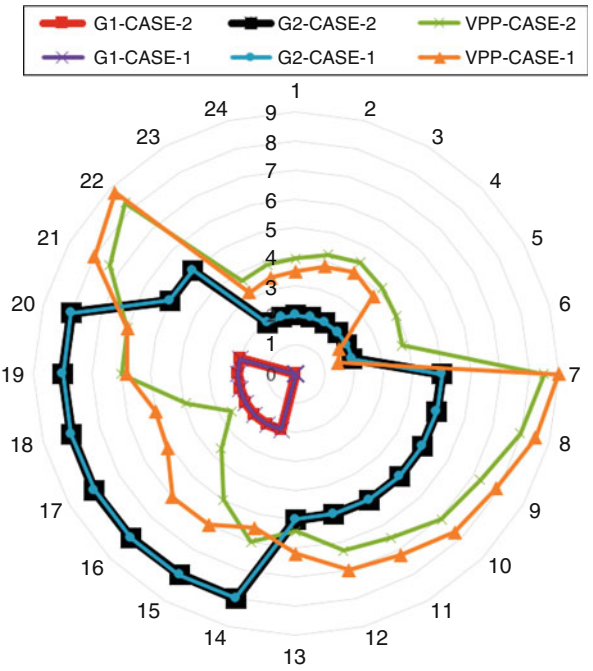

Fig. 10.10 Production shares of market participants

market have been affected by considering net load uncertainty. During hours 1–6, 14, and 19, the market shares of the VPP have been increased in case 2. It should be noted that the VPP's DER total productions have been increased in case 2 in comparison to case 1 during hours 1–6, 14, and 19; (see Fig. 10.9). During hours 7–13, 15–18, and 21–24, the market shares of the VPP have been decreased in case 2. Noteworthy, the VPP's DER total productions have been decreased in case 2 in comparison to case 1 during hours 7–13, 15–18, and 21–24; (see Fig. 10.9). Finally, the market shares of the VPP have no changes in case 2 during hour 20, when the total productions of DERs have no changes in two cases (see Fig. 10.10).

References

1. Singh, H. (1999). Introduction to game theory and its application in electric power markets. *IEEE Computer Applications in Power, 12*, 18–20.
2. Myerson, R. B. (1991). *Game theory: Analysis of conflict* (p. 1). Cambridge, Massachusetts; London, England: Harvard University Press. Chapter-preview links, pp. vii–xi.
3. https://en.wikipedia.org/wiki/Game_theory#cite_note-Myerson-1.
4. Fadlullah, M. D., et al. (2011). *A survey of game theoretic approaches in smart grid*, International Conference on Wireless Communications and Signal Processing, Nanjing, China.
5. Murphy, F. H., et al. (2005). Generation capacity expansion in imperfectly competitive restructured electricity markets. *Operation Research, 53*, 646–661.

6. Kaymaz, P., et al. (2007). Transmission congestion and competition on power generation expansion. *IEEE Transactions on Power Systems, 22*, 156–163.
7. Botterrud, A., et al. (2005). Optimal investments in power generation under centralized and decentralized decision making. *IEEE Transactions on Power Systems, 20*, 254–263.
8. Kazempour, S. J., et al. (2013). Generation investment equilibria with strategic producers-part I: Formulation. *IEEE Transactions on Power Systems, 28*, 2613–2622.
9. Ruiz, C., et al. (2009). Pool strategy of a producer with endogenous formation of locational marginal prices. *IEEE Transactions on Power Systems, 24*, 1855–1866.
10. Kazempour, S. J., et al. (2011). Strategic generation investment using a complementarity approach. *IEEE Transactions on Power Systems, 26*, 940–948.
11. Kazempour, S. J., et al. (2012). Strategic generation investment under uncertainty via benders decomposition. *IEEE Transactions on Power Systems, 27*, 424–432.
12. Barforoushi, T., et al. (2010). Evaluation of regulatory impacts on dynamic behavior of investments in electricity markets: A new hybrid DP/GAME framework. *IEEE Transactions on Power Systems, 25*, 1978–1986.
13. Sarjiya, et al. (2019). Game theory for multi-objective and multi-period framework generation expansion planning in deregulated markets. *Energy, 174*, 323–330.
14. Salarkheili, S., et al. (2016). Capacity withholding analysis in transmission-constrained electricity markets. *IET Generation, Transmission & Distribution, 10*, 487–495.
15. Latorre, M. D. L., et al. (2003). The Stackelberg equilibrium applied to AC power systems-a non-interior point algorithm. *IEEE Transactions on Power Systems, 18*, 611–618.
16. Chen, H., et al. (2006). A coevolutionary approach to analyzing supply function equilibrium model. *IEEE Transactions on Power Systems, 21*, 1019–1028.
17. Hasan, E., et al. (2008). Electricity markets cleared by merit order – Part II: Strategic offer and market power. *IEEE Transactions on Power Systems, 23*, 372–379.
18. Ruiz, C., et al. (2008). Some analytical results pertaining to Cournot models for short-term electricity markets. *Electric Power Systems Research, 78*, 1672–1678.
19. Bushnell, J. B. (2003). *Looking for trouble competition policy in the US electricity industry*. Center for the Study of Energy Markets: Univ. California Energy Institute.
20. Baldick, R., et al. (2004). Theory and application of linear supply function equilibrium in electricity markets. *Journal of Regulatory Economics, 25*, 143–167.
21. Helman, U., et al. (2010). Large-scale market power modeling: Analyzing of the U. S. eastern interconnection and regulatory applications. *IEEE Transactions on Power Systems, 25*, 1434–1448.
22. Yu, C. W., et al. (2010). Modeling and analysis of strategic forward contracting in transmission constrained power markets. *Electric Power Systems Research, 80*, 354–361.
23. Cunningham, L. B., et al. (2002). An empirical study of applied game theory: Transmission constrained Cournot behavior. *IEEE Transactions on Power Systems, 17*, 166–172.
24. Yang, Y., et al. (2012). Computing all Nash equilibria of multiplayer games in electricity markets by solving polynomial equations. *IEEE Transactions on Power Systems, 27*, 81–91.
25. Arasteh, H., et al. (2019). Stochastic system of systems architecture for adaptive expansion of smart distribution grids. *IEEE Transactions on Industrial Informatics, 15*, 377–389.
26. Arasteh, H., et al. (2016). SoS-based multiobjective distribution system expansion planning. *Electric Power Systems Research, 141*, 392–406.
27. Arasteh, H., et al. (2016). An aggregated model for coordinated planning and reconfiguration of electric distribution networks. *Energy, 94*, 786–798.
28. Chuang, A. S., et al. (2001). A game-theoretic model for generation expansion planning: Problem formulation and numerical comparisons. *IEEE Transactions on Power Systems, 16*, 885–891.
29. Jenabi, M., et al. (2013). Bi-level game approaches for coordination of generation and transmission expansion planning within a market environment. *IEEE Transactions on Power Systems, 28*, 2639–2650.

30. Mei, S., et al. (2012). Game approaches for hybrid power system planning. *IEEE Transactions on Sustainable Energy, 3*, 506–517.
31. Mei, S., et al. (2014). Robust optimization of static reserve planning with large-scale integration of wind power: A game theoretic approach. *IEEE Transactions on Sustainable Energy, 5*, 535–545.
32. Green, R. (1991). Reshaping the CEGB: Electricity privatization in the UK. *Utilities Policy, 1*, 245–254.
33. Yu, Z., et al. (2000). *A Stackelberg price leadership model with application to deregulated electricity markets,* IEEE Power Engineering Society Winter Meeting, Conference Proceedings (Cat. No. 00CH37077).
34. Hogan, W. W. (1997). A market power model with strategic interaction in electricity networks. *The Energy Journal, 19*, 107–141.
35. Cardell, J. B., et al. (1997). Market power and strategic interaction in electricity networks. *Resource and Energy Economics, 19*, 109–137.
36. Borenstein, S., et al. (1999). An empirical analysis of the potential for market power in California's electricity industry. *The Journal of Industrial Economics, 47*, 285–323.
37. Yao, J., et al. (2008). Modeling and computing two-settlement oligopolistic equilibrium in a congested electricity network. *Operations Research, 56*, 34–47.
38. Zhang, S., et al. (2009). Analyzing two-settlement electricity market equilibrium by coevolutionary computation approach. *IEEE Transactions on Power Systems, 24*, 1155–1164.
39. Green, R. J., et al. (1992). Competition in the British electricity spot market. *Journal of Political Economy, 100*, 929–953.
40. Green, R. (1996). Increasing competition in the British electricity spot market. *The Journal of Industrial Economics, 44*, 205–216.
41. García-Alcalde, A., et al. *Fitting electricity market models: A conjectural variations approach*. Proc. 14th PSCC 2002.
42. Day, C. J., et al. (2002). Oligopolistic competition in power networks: A conjectured supply function approach. *IEEE Transactions on Power Systems, 17*, 597–607.
43. Mei, S.-W., et al. (Eds.). (2011). Development of an industrial non-linear robust power system stabiliser and its improved frequency-domain testing method. *IET Generation, Transmission & Distribution, 5*, 1201–1210.
44. Chen, H., et al. (2014). Cooperative control of power system load and frequency by using differential games. *IEEE Transactions on Control Systems Technology, 23*, 882–897.
45. Zugno, M., et al. (2013). A Bilevel model for electricity retailers' participation in a demand response market environment. *Energy Economics, 36*, 182–197.
46. López-Lezama, J. M., et al. (2010). Optimal contract pricing of distributed generation in distribution networks. *IEEE Transactions on Power Systems, 26*, 128–136.
47. Mei, S., et al. (2013). A game model for robust optimization of power systems and its application. *Proceedings of the CSEE, 33*, 47–56.
48. Zhao, L., et al. (2012). Robust unit commitment problem with demand response and wind energy. *IEEE Power and Energy Society General Meeting, San Diego, CA, USA*.
49. Jiang, R., et al. (2011). Robust unit commitment with wind power and pumped storage hydro. *IEEE Transactions on Power Systems, 27*, 800–810.
50. Bertsimas, D., et al. (2012). Adaptive robust optimization for the security constrained unit commitment problem. *IEEE Transactions on Power Systems, 28*, 52–63.
51. Wei, W., et al. (2016). Convexification of the Nash bargaining based environmental-economic dispatch. *IEEE Transactions on Power Systems, 31*, 5208–5209.
52. Wei, W., et al. (2014). Nash bargain and complementarity approach based environmental/economic dispatch. *IEEE Transactions on Power Systems, 30*, 1548–1549.
53. Mohsenian-Rad, A.-H., et al. (2010). Autonomous demand-side management based on game-theoretic energy consumption scheduling for the future smart grid. *IEEE Transactions on Smart Grid, 1*, 320–331.
54. Atzeni, I., et al. (2014). Noncooperative day-ahead bidding strategies for demand-side expected cost minimization with real-time adjustments: A GNEP approach. *IEEE Transactions on Signal Processing, 62*, 2397–2412.

55. Maharjan, S., et al. (2013). Dependable demand response management in the smart grid: A Stackelberg game approach. *IEEE Transactions on Smart Grid, 4*, 120–132.
56. Zhao, B., et al. (2014). Short-term operation scheduling in renewable-powered microgrids: A duality-based approach. *IEEE Transactions on Sustainable Energy, 5*, 209–217.
57. Palma-Behnke, R., et al. (2013). A microgrid energy management system based on the rolling horizon strategy. *IEEE Transactions on Smart Grid, 4*, 996–1006.
58. Nguyen, D. T., et al. (2014). Optimal bidding strategy for microgrids considering renewable energy and building thermal dynamics. *IEEE Transactions on Smart Grid, 5*, 1608–1620.
59. Nguyen, D. T., et al. (2015). Risk-constrained profit maximization for microgrid aggregators with demand response. *IEEE Transactions on Smart Grid, 6*, 135–146.
60. Liu, G., et al. (2016). Bidding strategy for microgrid in day-ahead market based on hybrid stochastic/robust optimization. *IEEE Transactions on Smart Grid, 7*, 227–237.
61. Nguyen, T. A., et al. (2016). Stochastic optimization of renewable-based microgrid operation incorporating battery operating cost. *IEEE Transactions on Power Systems, 31*, 2289–2296.
62. Wang, Y., et al. (2016). Interactive dispatch modes and bidding strategy of multiple virtual power plants based on demand response and game theory. *IEEE Transactions on Smart Grid, 7*, 510–519.
63. Peik-Herfeh, M., et al. (2013). Decision making of a virtual power plant under uncertainties for bidding in a day-ahead market using point estimate method. *International Journal of Electrical Power & Energy Systems, 44*, 88–98.
64. Peik-herfeh, M., et al. (2014). Two-stage approach for optimal dispatch of distributed energy resources in distribution networks considering virtual power plant concept. *International Transactions on Electrical Energy Systems, 24*, 43–63.
65. Pandžić, H., et al. (2013). Offering model for a virtual power plant based on stochastic programming. *Applied Energy, 105*, 282–292.
66. Kardakos, E. G., et al. (2016). Optimal offering strategy of a virtual power plant: A stochastic bi-level approach. *IEEE Transactions on Smart Grid, 7*, 794–806.
67. Asimakopoulou, G. E., et al. (2013). Leader-follower strategies for energy management of multi-microgrids. *IEEE Transactions on Smart Grid, 4*, 1909–1916.
68. Dielmann, K., et al. (2003). *Virtual power plants (Vpp)-A new perspective for energy generation?*. In Proceedings of the 9th international scientific and practical conference of students, post-graduates and young scientists. Italy.
69. Caldon, R., et al. (2004). *Optimal control of a distribution system with a virtual power plant*. In Bulk power system dynamics and control. Italy.
70. Nezamabadi, H., et al. (2011). *Participation of virtual power plants in energy market with optimal bidding based on Nash-SFE equilibrium strategy and considering interruptible load*. In Proceedings of the 3rd conference on thermal power plants (CTPP). Iran.
71. Nezamabadi, H. et al. (2015). *Two stage decision making of technical virtual power plants in electricity market via Nash-SFE equilibrium*. In 3rd International Istanbul smart grid congress and fair (ICSG). Turkey.
72. Mashhour, E., et al. (2011). Bidding strategy of virtual power plant for participating in energy and spinning reserve markets—Part I: Problem formulation. *IEEE Transactions on Power Systems, 26*, 949–956.
73. Mashhour, E., et al. (2011). Bidding strategy of virtual power plant for participating in energy and spinning reserve markets—Part II: Numerical analysis. *IEEE Transactions on Power Systems, 26*, 957–964.
74. Nezamabadi, H., et al. (2016). Arbitrage strategy of virtual power plants in energy, spinning reserve and reactive power markets. *IET Generation, Transmission & Distribution, 10*, 750–763.
75. Wu, T., et al. (2013). Coordinated energy dispatching in microgrid with wind power generation and plug-in electric vehicles. *IEEE Transactions on Smart Grid, 4*, 1453–1463.
76. Kekatos, V., et al. (2015). Stochastic reactive power management in microgrids with renewables. *IEEE Transactions on Power Systems, 30*, 3386–3395.
77. Rahimiyan, M., et al. (2014). Energy management of a cluster of interconnected price-responsive demands. *IEEE Transactions on Power Systems, 29*, 645–655.

78. Guan, X., et al. (2010). Energy-efficient buildings facilitated by microgrid. *IEEE Transactions on Smart Grid, 1*, 243–252.
79. Rahimiyan, M., et al. (2015). Strategic bidding for a virtual power plant in the day-ahead and real-time markets: A price-taker robust optimization approach. *IEEE Transactions on Power Systems, 31*, 2676–2687.
80. Dabbagh, S. R., et al. (2015). Risk assessment of virtual power plants offering in energy and reserve markets. *IEEE Transactions on Power Systems, 31*, 3572–3582.
81. Giuntoli, M., et al. (2013). Optimized thermal and electrical scheduling of a large scale virtual power plant in the presence of energy storages. *IEEE Transactions on Smart Grid, 4*, 942–955.
82. Mohammadi, J., et al. (2011). Aggregated wind power and flexible load offering strategy. *IET Renewable Power Generation, 5*, 439–447.
83. Zhao, Q., et al. (2016). Control and bidding strategy for virtual power plants with renewable generation and inelastic demand in electricity markets. *IEEE Transactions on Sustainable Energy, 7*, 562–575.
84. Nezamabadi, H., et al. (2019). Market bidding strategy of the microgrids considering demand response and energy storage potential flexibilities. *IET Generation, Transmission & Distribution, 13*, 1346–1357.
85. Manshadi, S. D., et al. (2015). Resilient operation of multiple energy carrier microgrids. *IEEE Transactions on Smart Grid, 6*, 2283–2292.
86. You, S., et al. (2009). *A market-based virtual power plant*. In International conference on clean electrical power Capri. Italy.
87. Ruiz, N., et al. (2009). A direct load control model for virtual power plant management. *IEEE Transactions on Power Systems, 24*, 959–966.
88. Shi, L., et al. (2014). Bidding strategy of microgrid with consideration of uncertainty for participating in power market. *International Journal of Electrical Power & Energy Systems, 59*, 1–13.
89. Derakhshandeh, S. Y., et al. (2013). Coordination of generation scheduling with PEVs charging in industrial microgrids. *IEEE Transactions on Power Systems, 28*, 3451–3461.
90. Hawkes, A., et al. (2009). Modelling high level system design and unit commitment for a microgrid. *Applied Energy, 86*, 1253–1265.
91. Khodaei, A. (2014). Microgrid optimal scheduling with multi-period islanding constraints. *IEEE Transactions on Power Systems, 29*, 1383–1392.
92. Liu, Y., et al. (2015). Control of virtual power plant in microgrids: A coordinated approach based on photovoltaic systems and controllable loads. *IET Generation, Transmission & Distribution, 9*, 921–928.
93. Logenthiran, T., et al. (2011). Multi-agent system for energy resource scheduling of integrated microgrids in a distributed system. *Electric Power Systems Research, 81*, 138–148.
94. Mohammadi, S., et al. (2014). Scenario-based stochastic operation management of microgrid including wind, photovoltaic, micro-turbine, fuel cell and energy storage devices. *International Journal of Electrical Power & Energy Systems, 54*, 525–535.
95. Rabiee, A., et al. (2016). Optimal operation of microgrids through simultaneous scheduling of electrical vehicles and responsive loads considering wind and PV units uncertainties. *Renewable and Sustainable Energy Reviews, 57*, 721–739.
96. Zhang, L., et al. (2014). Energy management in a microgrid with distributed energy resources. *Energy Conversion and Management, 78*, 297–305.
97. Lasseter, B. (2001). *Microgrids [distributed power generation]*, Power Engineering Society Winter Meeting, USA.
98. Awerbuch, S., et al. (1997). *The virtual utility: Accounting, technology & competitive aspects of the emerging industry*. New York: Springer Science & Business Media.
99. Boyd, S., et al. (2004). *Convex optimization*. New York, Cambridge University Press.

Chapter 11
4E Analysis of Subcooled-Compressed Air Energy Storage System, a Smart Tool for Trigeneration and Integration of Cold, Heat and Power Sectors

Ahmad Arabkoohsar

11.1 Introduction

Moving towards an energy system in which all the energy supply chains are supported fully by renewable technologies has been the energy planning strategy of many countries. This, especially, has been more serious in developed lands including EU countries [1]. This transition from fossil-fuel-based energy supply systems towards the fully renewable-energy-based systems is, however, extremely challenging due to the technical and economic restrictions for employing renewable energy technologies [2]. One of the most serious challenges in this regard is that solar irradiation and wind energy as the two most important renewable sources are extremely fluctuating and there is not a precise long-term forecast method for them yet [3]. Among the different solutions proposed so far for addressing this gap, using energy storage technologies, i.e. electricity storage and thermal energy storage, is one of the topics of interest [4].

Unlike thermal energy storage solutions which mostly have well-developed state-of-practice, electricity storage technologies are still being developed in different categories. The possible categories of electricity storage include chemical, electro-chemical, electrical and mechanical technologies [5]. Regardless of the categories, batteries are the most widespread electricity storage systems which are well-developed and broadly used from very small scale to medium scales [6]. The problems of batteries, however, are being too expensive per kilowatt-hour of capacity and offering very low energy density. These problems make batteries not being appropriate for large-scale renewable power plants [7]. Among other electricity

A. Arabkoohsar (✉)
Department of Energy Technology, Aalborg University, Aalborg, Denmark
e-mail: ahm@et.aau.dk

F. Jabari et al. (eds.), *Integration of Clean and Sustainable Energy Resources and Storage in Multi-Generation Systems*,
https://doi.org/10.1007/978-3-030-42420-6_11

storage solutions, pumped hydroelectric storage, after batteries, is probably one of the most popular and most widely used systems for large-scale energy storage. This technology has a very good round-trip efficiency (about 75–85%) and can be sized from medium scales to super large scales, though the large investment cost of constructing huge water dams is a serious disadvantage of that. Besides this, special geographical needs for building up this system restrict its deployment in many locations [8].

Besides pumped hydroelectric storage, gravitational storage, flywheel storage, pumped heat electricity storage, hydrogen storage, high-temperature heat and power storage and, of course, compressed air energy storage (CAES) are the other possible methods of electricity storage technologies. Each of the aforementioned technologies has its own advantages and limitations. For example, gravitational energy storage is a simple electricity storage that has very recently been introduced and is still in the development stage. The primary observations show that it can result in an interesting efficiency of above 90% while its cost-effectiveness looks quite interesting too [9]. This system, however, should be proved first via thorough research, development and pilot-scale demonstration to be considered as a serious storage role maker of energy systems. Flywheel storage which might be as efficient as gravitational storage, i.e. round-trip efficiency of about 90%, has a more advanced state-of-the-art and even state-of-practice and could be found in operation in some energy systems. But the low energy density, the high self-discharge rate and large cost of the system are the main reasons of restricting the widespread use of this technology on a large scale [10].

Pumped heat electricity storage, just the same as gravitational electricity storage, is another new concept of electricity storage which looks so much promising but needs more research and development behind. This technology is claimed to offer a round-trip efficiency of 70–80% and a great energy density. In addition, the use of packed beds of rocks as the heat storage method of the system makes the technology cheap and cost-effective. However, not-developed state-of-the-art, especially for the special air expander and compressor technologies it needs to operate, is its main restrictor for being used at the moment [11]. High-temperature heat and power storage, based on the same principle as that of pumped heat electricity storage, i.e. storing excess electricity as thermal energy, is another new type of electricity storage receiving attention from the market players and researchers [12]. The main differences of this technology from pumped heat electricity storage is that, however, a simple electrical coil is used for converting electricity to high-temperature heat and the stored heat is reclaimed to drive a conventional power cycle, e.g. gas turbine or steam cycle [13, 14]. This technology is a cogeneration system offering heat and electricity production in discharging mode at the electricity-to-heat and electricity-to-electricity efficiencies in the ranges of 50–65% and 25–35%, respectively [15].

As mentioned before, CAES is also one of the most important electricity storage technologies in the category of mechanical energy storage systems [16]. A CAES system might be seen in different configurations depending on where and based on which aim it is to be implemented [17]. The best electricity-to-electricity efficiency that one could expect from a CAES configuration is claimed to be about 80%, while

for simpler configurations, it can be as low as 30% or even lower [18]. The configuration that leads to the best electricity efficiency is multistage adiabatic CAES in which multistage compressors and multistage expanders are used and the heat generated during the expansion process is collected for preheating the airflow before the air expands in the discharging mode [19]. One level simpler design of this system might be an adiabatic CAES which takes advantage of the heat generation due to the air compression process but has a single-stage expander and compressor [20]. The oldest design of CAES, however, is diabatic CAES which neither uses multistage turbomachinery nor utilizes the heat of compressors and, as a result, has a lower efficiency than the other configurations [21].

Besides these three older configurations of CAES technology, there are two newer configurations proposed for that which are appropriate for specific energy system conditions. The first one is a low-temperature CAES system which is mostly similar to a multistage adiabatic CAES but does not go for high temperatures before expansion [22]. Thus, this configuration does not need any fossil-fuel-based high-temperature heater for compressed air heating and is most suitable for locations with medium-temperature excess heat flows or strict restriction of fossil fuel use. The most recent configuration of CAES, however, is the electricity storage yet trigeneration concept of subcooled-CAES [23]. This design not only does not need any fossil-fuel-based heaters for air preheating process, just like the low-temperature CAES system, but also it does not spend the collected heat of the compression phase for preheating the airflow of the expanders. Therefore, the airflow through the air turbines goes to very low temperatures (in the range of -50 to -100 °C), and this is why the concept is called subcooled-CAES [24]. The low-temperature air discharged from each turbine stage is used for cold production. This technology presents an electricity-to-heat efficiency of about 80–90% in the charging mode and the electricity-to-electricity and electricity-to-cold efficiencies of about 20–30% [25]. Having said all these, one could sum up that this innovative design of CAES is most appropriate for locations with widespread cold, heat and electricity grids, e.g. Scandinavian countries [26]. Such a trigeneration system can be a source of synergies between the three different energy sectors as a very important characteristic of future energy systems [27].

The primary thermodynamic model of subcooled-CAES technology has been presented in the literature [24, 25]. Its off-design performance investigation in terms of energy efficiency has also been carried out [28]. This work presents very detailed energy, exergy, economic and environmental analyses of the subcooled-CAES system in a double-stage configuration when operating in a real energy market of Scandinavia. This would give a much bigger picture of the technology in terms of technical performance and expected economic benefits when coming to real-life operation.

11.2 Concept Introduction

Figure 11.1 shows a schematic of a double-stage compression-expansion subcooled-CAES system. According to the figure, in the charging part, the system comprises a double-stage compressor in which after each of the stages, there is a heat exchanger letting the heat generated through the compressors be utilized for heating objectives. Here, the proposition is using this heat flow to go directly for district heating supply with an inlet temperature of 40 °C and the target temperature of 80 °C [29]. Then, the compressed air is collected in an air storage space which can be a multi-tank chamber, an underground-storage or similar depending on the design capacity and pressure of the system.

In the discharging part, there are two turbine stages: after each, there is a heat exchanger. In other configurations of the CAES, these heat exchangers (and an auxiliary heater) are located before the expansion processes, but here, there is no need to any preheating heat exchanger (or heater), and the air enters into the turbines

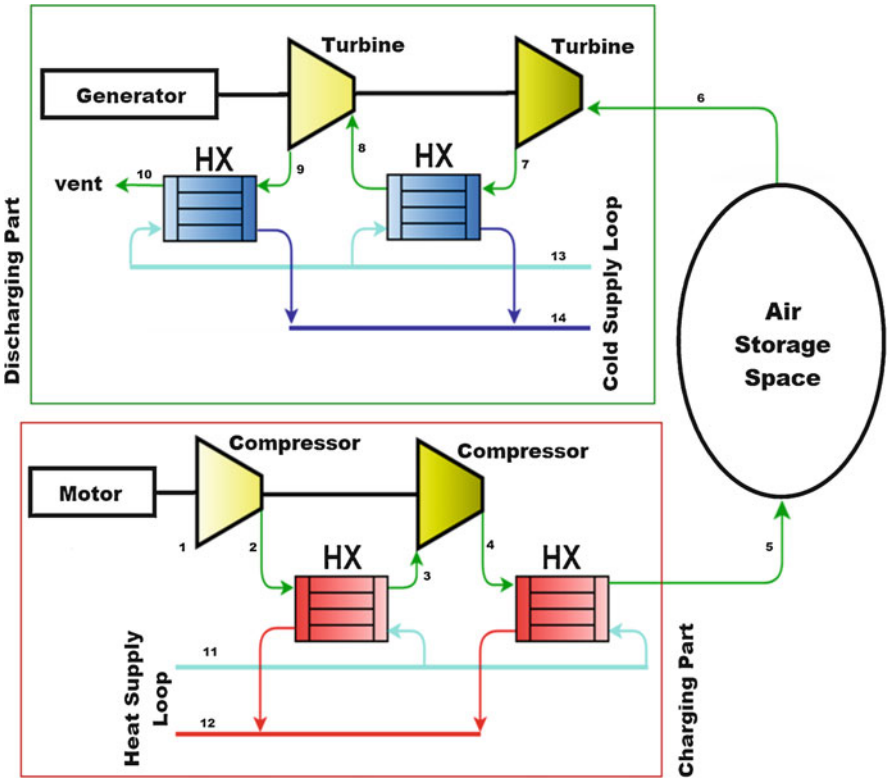

Fig. 11.1 Subcooled-CAES system diagram; HX: heat exchanger, green lines: air stream, light-blue lines: medium-temperature water stream, red-lines: high-temperature water, dark-blue line: low-temperature water stream

Table 11.1 Characteristics considered for the subcooled-CAES system in this study

Parameter	Information
System nominal capacity	10 MWp
Expansion/compression stages	2
Expansion/compression ratio of each stage	8
Charging/discharging time	10 hours
Maximum pressure of the system	64 bar
Air storage space temperature	298 K
Effectiveness factor of heat exchangers	0.95 [31]
Isentropic efficiency of compressors	0.85 [32]
Isentropic efficiency of turbines	0.65 [33]

at the same temperature as that in the air storage. Instead, the heat exchangers are located after the turbines to let the air temperature drop to very low levels and then, the cold air stream is used for cooling applications. Here, it is supposed to use the cold supply potential for district cooling support in which the inlet temperature is 15 °C and the target temperature is 8 °C [30]. Clearly, in addition to the cold supply potential, the system will also generate electricity when discharging.

Naturally, the number of stages of the system could be larger, but this is a matter of cost and effectiveness which needs a comprehensive cost analysis with real components' costs and other economic factors which is out of the scope of this work. Here, as an example, a double-stage configuration is analysed.

The maximum pressure of the system is also a matter of capacity of the system. For larger plant capacities, higher pressures are required. The literature shows air pressures even up to 150 bar. Here, however, the capacity is to be limited to 10 MW as maximum charging and discharging rates. Thus, a medium peak pressure of 64 bar is considered for the system. In this case, no underground cavern would be needed for the plant either.

Table 11.1 gives general information about the system design and features which is going to be used for the modelling in this work.

Note that the turbine stages (and also compressor stages) may work in parallel or in series with each other depending on the instantaneous pressure of the air storage chamber. If the pressure of the chamber is below 8 bar, the stages are in parallel, and if the pressure is above 8, they come in series.

11.3 Mathematical Model

The mathematical model of the system is presented in the four subsections: the energy model, exergy model, economic model and environmental model.

11.3.1 Energy Model

For the analysis of the system performance in terms of energy, the energy balance equations governing all of its components are required. For the charging part, one has the following:

$$\mathrm{C}P_{\mathrm{surplus}} = \dot{W}_{\mathrm{C}} = \dot{m}_{\mathrm{a,c1}} w_{\mathrm{c1}} + \dot{m}_{\mathrm{a,c2}} w_{\mathrm{c2}}. \tag{11.1}$$

$$T_{\mathrm{a,ce}} = T_{\mathrm{a,ci}} \left(1 + \frac{r_{\mathrm{c}}^{\left(\frac{k-1}{k}\right)} - 1}{\eta_{\mathrm{is,c}}} \right) \tag{11.2}$$

$$\dot{Q}_{\mathrm{hx}} = \varepsilon_{\mathrm{hx}} \dot{m}_{\mathrm{a}} c_{\mathrm{p,i}} (T_{\mathrm{a,i}} - T_{\mathrm{dhw,i}}) = \dot{m}_{\mathrm{a}} \left(c_{\mathrm{p,i}} T_{\mathrm{a,i}} - c_{\mathrm{p,e}} T_{\mathrm{a,e}} \right). \tag{11.3}$$

$$\mathrm{C}p_{\mathrm{ass}}^{t} = \frac{\left(M_{\mathrm{ass}}^{t-1} + \dot{m}_{\mathrm{a}}^{t} dt \right) R T_{\mathrm{ass}}}{V_{\mathrm{ass}}^{t}}. \tag{11.4}$$

Here, Eq. (11.1), neglecting mechanical losses of the compressors, calculates the total electricity consumption of the compressors for producing compressed air in which P_{surplus} is the surplus electricity of the renewable power plant coupled to the energy storage unit, $\dot{m}_{\mathrm{a}}$ is the air flow rate, and w_{c} is the specific work consumption of each of the compressor stages. Equation (11.2).) calculates the outlet temperature of the air after each compression stage where subscripts ci and ce refer to the compressor inlet and outlet conditions, r_{c} is the compression ratio, k is air specific heat ratio (1.4), and and $\eta_{\mathrm{is,\ c}}$ is the compressor isentropic efficiency. In Eq. (11.3), which calculates how much heat is transferred from the airflow to district heating, $\varepsilon_{\mathrm{hx}}$ is the effectiveness factor of the heat exchangers (0.95), $c_{\mathrm{p,\ i}}$ is the specific heat of airflow at inlet condition, and $T_{\mathrm{dhw,\ i}}$ is the inlet temperature of district heating water (40 °C). Finally, Eq. (11.4) calculates the changes of the air storage space pressure over the charging period in which M_{ass} is the mass of the air in the storage, V_{ass} is the storage volume, and T_{ass} is its temperature. R is the air gas constant, and the superscript t counts the time steps.

Similarly, for the discharging part, one has the following:

$$\dot{W}_{\mathrm{T}} = \frac{P_{\mathrm{required}}}{\eta_{\mathrm{g}}} = \dot{m}_{\mathrm{a,t1}} w_{\mathrm{t1}} + \dot{m}_{\mathrm{a,t2}} w_{\mathrm{t2}}. \tag{11.5}$$

$$w_{\mathrm{t}} = R T_{\mathrm{t,i}} \frac{k}{k-1} \left(\frac{1 - r_{\mathrm{t}}^{\left(\frac{k-1}{k}\right)}}{\eta_{\mathrm{is,t}}} \right). \tag{11.6}$$

$$p_{\text{ass}}^{t} = \frac{\left(M_{\text{ass}}^{t-1} - \dot{m}_{\text{a}}^{t} dt\right) RT_{\text{ass}}}{V_{\text{ass}}^{t}}. \tag{11.7}$$

Here, Eq. (11.5) calculates the work product of the turbines in which P_{required} is the power needed to be produced by the system and η_{g} is the efficiency of the electricity generator (0.95). Also, w_{t} is the specific work of turbine stages which could be calculated by Eq. (11.6) in which r_{t} is the expansion ratio (1/8) and $\eta_{\text{is, t}}$ is the turbine isentropic efficiency. Finally, Eq. (11.7) calculates how the pressure of the air storage changes as the system discharges. Note that the cold supplied to the district cooling via the heat exchangers between the turbines could be calculated by the same equation as Eq. (11.3) where $T_{\text{dcw, i}}$ (the inlet district cooling water) sits instead of $T_{\text{dhw, i}}$.

Then, one could calculate the round-trip electricity-to-heat, electricity-to-cold and electricity-to-electricity efficiencies of the subcooled-CAES as below:

$$\eta_{\text{el-to-h}} = \frac{\sum_{t=1}^{tt} \dot{Q}_{\text{h}}^{t}}{\sum_{t=1}^{tt} P_{\text{surplus}}^{t}}. \tag{11.8}$$

$$\eta_{\text{el-to-c}} = \frac{\sum_{t=1}^{tt} \dot{Q}_{\text{c}}^{t}}{\sum_{t=1}^{tc} P_{\text{surplus}}^{\lambda}}. \tag{11.9}$$

$$\eta_{\text{el-to-el}} = \frac{\sum_{\lambda=1}^{tt} P_{\text{generated}}^{t}}{\sum_{t=1}^{tt} P_{\text{surplus}}^{t}}. \tag{11.10}$$

where the parameters $\dot{Q}_{\text{h}}^{t}$, $\dot{Q}_{\text{c}}^{t}$ and $P_{\text{generated}}^{t}$ are the rates of heat, cold and electricity production of the subcooled-CAES system at any time step of t. tt is the number of the time steps for a full round-trip operation of the storage system.

11.3.2 Exergy Model

By the same approach as that presented for the energy analysis, the exergy model of the subcooled-CAES is presented as follows. For the charging part, the exergy balance of each of the compressor stages, each of the heat exchangers, and the air storage space could be given by the following correlations, respectively:

$$\dot{m}_{\mathrm{a,c}}\dot{w}_{\mathrm{C}} + \dot{m}_{\mathrm{a,c}}\left[(h_{\mathrm{i,c}} - h_{\mathrm{e,c}}) - T_{\mathrm{o}}\left(\overline{c}_{\mathrm{p}}\ln\left(\frac{T_{\mathrm{i,c}}}{T_{\mathrm{e,c}}}\right) + R\ln\left(r_{\mathrm{c}}\right)\right)\right] = T_{\mathrm{o}}\dot{S}_{\mathrm{gen,c}} \quad (11.11)$$

$$\dot{m}_{\mathrm{a,hx}}\left[(h_{\mathrm{i,a}} - h_{\mathrm{e,a}}) - T_{\mathrm{o}}\overline{c}_{\mathrm{p}}\ln\left(\frac{T_{\mathrm{i,a}}}{T_{\mathrm{e,a}}}\right)\right] + \overbrace{\dot{m}_{\mathrm{dhw}}\left[(h_{\mathrm{i,dhw}} - h_{\mathrm{e,dhw}}) - T_{\mathrm{o}}c_{\mathrm{w}}\ln\left(\frac{T_{\mathrm{i,dhw}}}{T_{\mathrm{e,dhw}}}\right)\right]}^{\dot{\psi}_{\mathrm{dhw}}} = T_{\mathrm{o}}\dot{S}_{\mathrm{gen,hx}} \quad (11.12)$$

$$\frac{d\dot{\psi}_{\mathrm{ass}}}{dt} = \dot{m}_{\mathrm{a}}\left[(h_{\mathrm{i,a}} - h_{\mathrm{o}}) - T_{\mathrm{o}}\left(\overline{c}_{\mathrm{p}}\ln\left(\frac{T_{\mathrm{i,a}}}{T_{\mathrm{o}}}\right) - R\ln\left(\frac{p_{\mathrm{i,a}}}{p_{\mathrm{o}}}\right)\right)\right] - T_{\mathrm{o}}\dot{S}_{\mathrm{gen,ass}} \quad (11.13)$$

where h is the specific enthalpy, T_{o} and p_{o} are the ambient temperature and pressure, $\overline{c}_{\mathrm{p}}$ is the average heat capacity of the fluid on the two sides of the control volume, and c_{w} is water specific heat. Also, $\dot{\psi}$ is the exergy rate, and $\dot{S}_{\mathrm{gen}}$ refers to the rate of entropy generation of each process.

Having similar parameters, in the discharging part, the same exergy balance equations apply to the heat exchangers and the air storage, while the exergy balance of each of the turbine stages could be defined as below:

$$\dot{m}_{\mathrm{a,t}}\left[(h_{\mathrm{i,t}} - h_{\mathrm{e,t}}) - T_{\mathrm{o}}\left(\overline{c}_{\mathrm{p}}\ln\left(\frac{T_{\mathrm{i,t}}}{T_{\mathrm{e,t}}}\right) + R\ln\left(r_{\mathrm{t}}\right)\right)\right] = \dot{m}_{\mathrm{a,t}}\dot{w}_{\mathrm{t}} + T_{\mathrm{o}}\dot{S}_{\mathrm{gen,t}}. \quad (11.14)$$

By applying these exergy balance equations, the exergetic electricity efficiency, exergetic heat efficiency and exergetic cold efficiency of the subcooled-CAES are found as follows: storage space could be given by the following correlations, respectively:

$$\eta_{\mathrm{II,el-to-h}} = \frac{\sum_{t=1}^{tt}\dot{\psi}^{t}_{\mathrm{dhw}}}{\sum_{t=1}^{tt}\mathrm{P}^{t}_{\mathrm{sur}}}. \quad (11.15)$$

$$\eta_{\mathrm{II,el-to-c}} = \frac{\sum_{t=1}^{tt}\dot{\psi}^{t}_{\mathrm{dcw}}}{\sum_{t=1}^{tt}\mathrm{P}^{t}_{\mathrm{sur}}}. \quad (11.16)$$

$$\eta_{\mathrm{II,el-to-el}} = \frac{\sum_{t=1}^{tt}\mathrm{P}^{t}_{\mathrm{generated}}}{\sum_{t=1}^{tt}\mathrm{P}^{t}_{\mathrm{sur}}} \quad (11.17)$$

where $\dot{\psi}^{f}_{\mathrm{dhw}}$ and $\dot{\psi}^{f}_{\mathrm{dcw}}$ are the rates of exergy supplied to the district heating and cooling grids at any time steps.

11.3.3 Environmental Analysis

Generally, since an energy storage unit is to stabilize the energy output of renewable power plants, it is absolutely environmentally friendly. But in order to quantify how impressive the subcooled-CAES performs for emission reduction, a certain energy system and certain operating conditions are considered in this work, and calculations are done for that. Here, the case study is the Danish energy system which has widespread district heating and cooling networks besides the electricity grids. In the Danish energy system, there is a high penetration of waste-fired CHP plants. Thus, here, it is assumed that all the energy supplied by the subcooled-CAES would be provided by waste-fired CCHP plants if the energy storage unit is not employed. Generally, in a CHP plant, about 30% of the supplied energy as fuel is given back in the form of electricity, and around 55% is extracted as heat. Supposing that the CCHP plant is to provide the same amount of cold and heat, and considering the reasonable COP of 0.7 for the absorption chiller driven by the heat output of the CHP plant, 59% of the net produced heat goes for cold supply (resulting in 22.5% fuel-to-cold efficiency, i.e. $59\% \times 55\% \times 0.7 = 22.5\%$), and 22.5% of the energy released via combustion of the solid waste remains for heat supply. Thus, in a CCHP plant, 30% is the fuel-to-electricity efficiency, and 22.5% is the fuel-to-cold and fuel-to-heat efficiencies.

According to Ref. [34], an average of 415 kg of equivalent CO_2 might be released when incinerating one tonne of municipal solid waste. The heating value of municipal solid waste is considered as 8500 kJ/kg [35].

Thus, having the performance indices of the waste-fired CCHP plant, and just calculating the amount of waste to be incinerated to cover the same amount of energy as that provided by the subcooled-CAES, one could simply calculate how much pollution would be released otherwise.

11.3.4 Economic Analysis

In order to assess the effectiveness of a subcooled-CAES system in the Danish energy matrix, a net present value (NPV) analysis is carried out on the system for certain numbers of full charging-discharging operating rounds of the system during each year. For this, the standard electricity, heat and cold spot prices of 30 €/MWh, 21 €/MWh and 28 €/MWh are taken into account [36]. The NPV of a system is calculated as follows:

$$\mathbf{NPV} = \sum_{j=1}^{N} \frac{(\boldsymbol{B_j} - \boldsymbol{C_j})}{(1+\boldsymbol{r})^{\boldsymbol{j}}}. \tag{11.18}$$

where B is the system benefits including the heat, cold and electricity supply benefits; C is the initial cost of the system as well as the running, operating and maintenance costs; r is the interest rate considered for such projects, 4% here; and j counts the years of operation of the system [37].

11.4 Performance Analysis Results

As mentioned, in this study, the performance of a double-stage subcooled-CAES system is to be investigated when employed in a renewable power plant with an excess power rate of 10 MW for a continuous period of 10 hours. Figure 11.2 shows the required size of the air storage to achieve the maximum pressure of 64 bar exactly at the end of the 10-hour charging period. According to the figure, the maximum pressure of 64 bar is achieved as the air storage vessel volume is set at 7740 m^3.

Having set this storage volume for the storage, one could follow the variation of the storage pressure over the 10 hours of charging process followed by a 10-hour discharging period. This is shown in Fig. 11.3. As seen in the figure, the pressure first increases to 8 bar, and then, due to the change of the arrangement of the compressors from parallel to series, with a sharper inclination, its pressure hits the peak value of 64 bar at the end of the charging process. Then, over the discharging process, while the turbines work in series, the pressure decreases to 8 bar, and then, the turbines change to parallel operation to totally empty the storage vessel. This, however, does not take 10 hours because of the inefficiencies of the system.

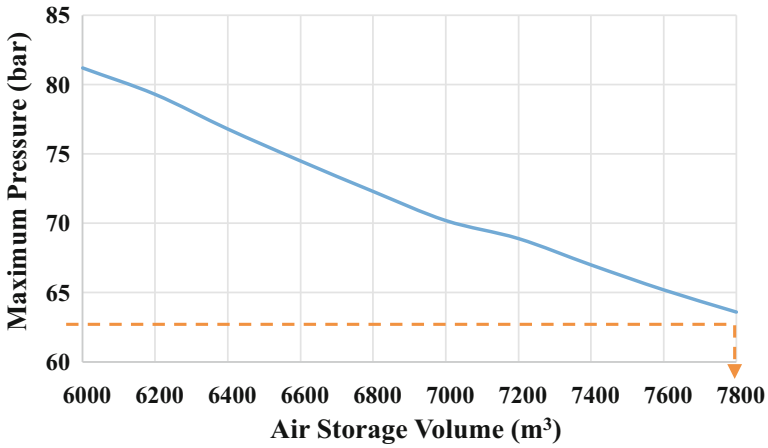

Fig. 11.2 Maximum pressure of the system for different air storage volumes

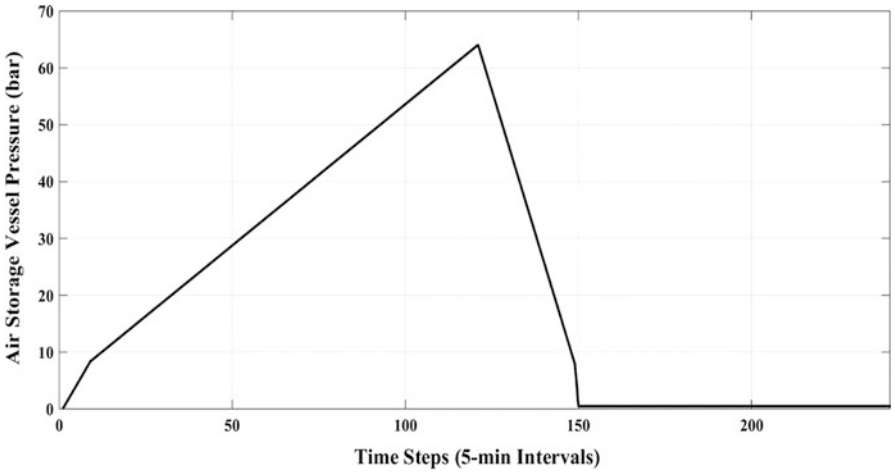

Fig. 11.3 Air storage pressure over the 20-hour charging-discharging operation period

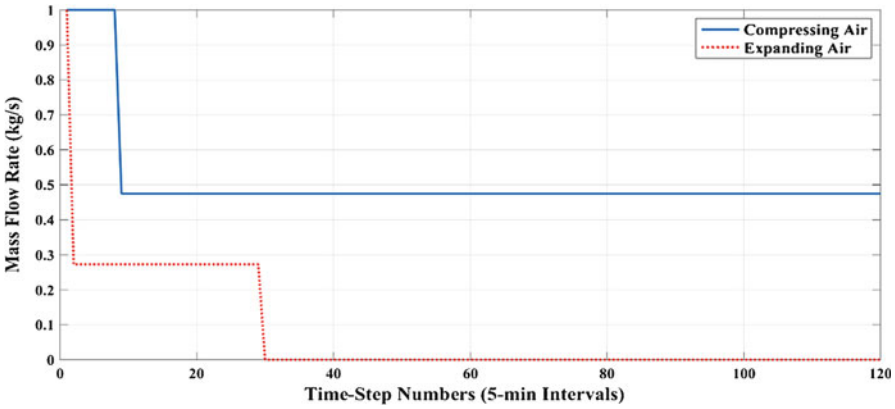

Fig. 11.4 Non-dimensional mass flow rate of expanding/compressing air during the charging and discharging periods

Figure 11.4 presents information about the mass flow rate of air being compressed in the charging mode and being expanded during the discharging mode. The data is sorted from large to small values and in a non-dimensional format (divided by the maximum compression/expansion flow rates). The maximum compression flow rate is 32.6 kg/s, and the maximum value of expanding air flow rate is 229.3 kg/s. The maximum flow rates are both associated with the modes that turbomachinery work in parallel. This figure shows how many time steps and in what ranges the compressors and the expanders operate to cover their assigned tasks.

Table 11.2 details the properties of the system working fluids (air and district heating/cooling water) at different points of the cycle when working at full load. These points are marked on the schematic of the system in Fig. 11.1.

Table 11.2 System thermodynamic properties at different points

No.	Fluid	Temperature (K)	Pressure (kPa)	Enthalpy (kJ/kg)	Entropy (kJ/kg. K)
1	Air	298	100	298.4	5.699
2	Air	582	800	588.5	5.784
3	Air	323	800	323.6	5.183
4	Air	582	6400	588.5	5.187
5	Air	323	6400	323.6	4.586
6	Air	298	6400	298.4	4.505
7	Air	211	800	211.1	4.756
8	Air	278	800	278.4	5.032
9	Air	197	100	197.1	5.284
10	Air	278	100	278.4	5.629
11	Pressurized Water	313	1200	168	0.5699
12	Pressurized Water	353	1200	335.3	0.5699
13	Pressurized Water	288	1200	63.5	0.2221
14	Pressurized Water	281	1200	34.18	0.119

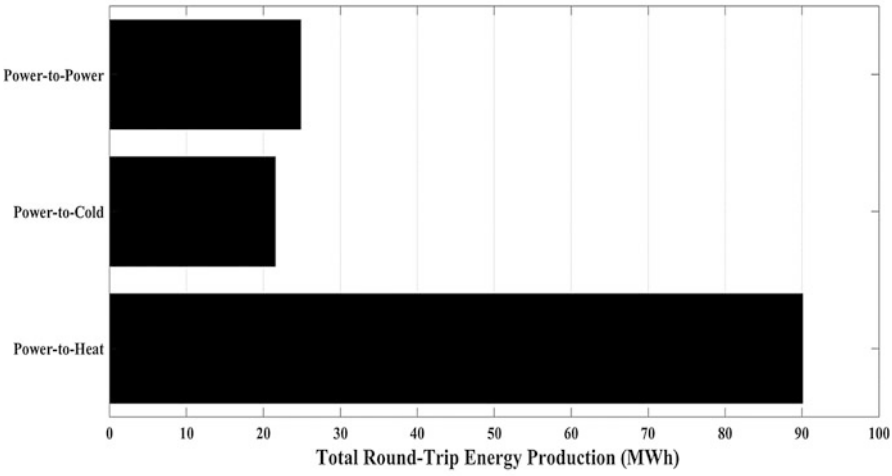

Fig. 11.5 Rates of heat, cold and electricity supply of the subcooled-CAES over a round-trip operation

Figure 11.5 shows the rate of heat, cold and power supplies when the system charges/discharges. Naturally, as the excess power for charging and the delivered power when discharging are considered constant, the rates of cold, heat and power

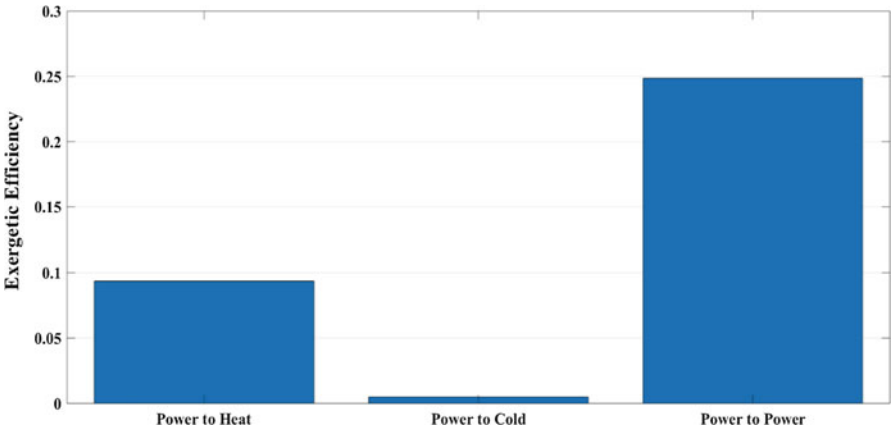

Fig. 11.6 Exergetic efficiencies of the subcooled-CAES system over a round-trip full-load operation

supplies of the system are constant over time. It should be noted that the heat supply continuous for exactly 10 hours, while the cold and power supplies will stop as the cavern is fully discharged of the compressed air, which is at the 150th time step according to Fig. 11.3. Thus, the total delivered heat, cold and power over a complete charging/discharging cycle will be 90.1 MWh, 21.5 MWh and 24.9 MWh, respectively.

Having this information, and considering the total excess electricity of 100 MWh supplied to the storage system, one could simply calculate the electricity-to-electricity, electricity-to-heat, electricity-to-cold and overall efficiencies of a double-stage subcooled-CAES as 24.9%, 90.1%, 21.5% and 136.5%, respectively. Since efficiency above 100% is not logically defined, for the subcooled-CAES system, the overall coefficient of performance is defined, which will be 1.36.

In a similar manner, having information about the enthalpy and entropy values of the working fluids in different points of the cycle, one can quantify the efficiencies of the system over a full load charging-discharging process. Figure 11.6 gives information about the exergetic efficiency of a double-stage subcooled-CAES system working based on the configuration and specifications considered in this work.

According to the figure, the heat exergy efficiency of the system is about 9%, the cold production exergy efficiency is below 1%, and the electricity exergy efficiency is 24.9%. The noteworthy point is that the heat and cold exergetic efficiencies are too low, especially for the cold production process, because the temperature variation in the working fluids are so low that the rates of irreversibilities remain too high. The exergy and energy efficiency indices for electricity should be the same because an electrical flow is 100% net exergy.

Considering the information given for the environmental impact analysis and the performance assessment report presented above for the subcooled-CAES unit, one could calculate how much emission is prevented by using this energy storage system over a round-trip full-load charging-discharging operation. Figure 11.7 gives

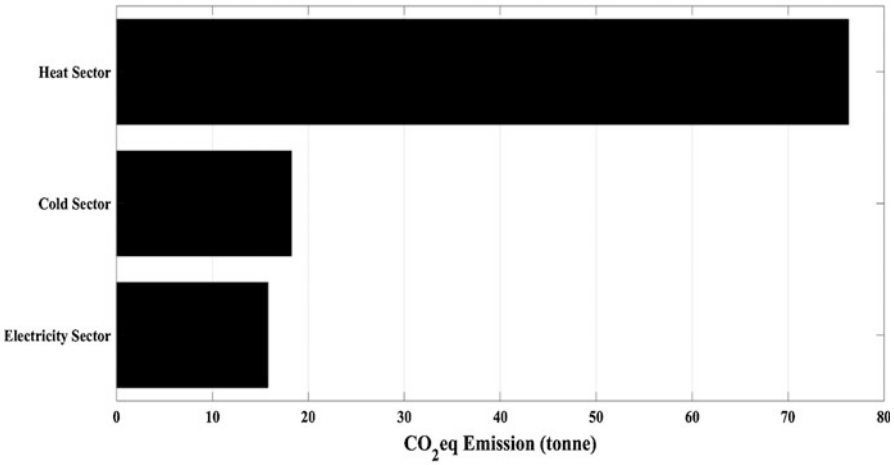

Fig. 11.7 Level of emission prevention of the system in each energy sector over a round cycle operation

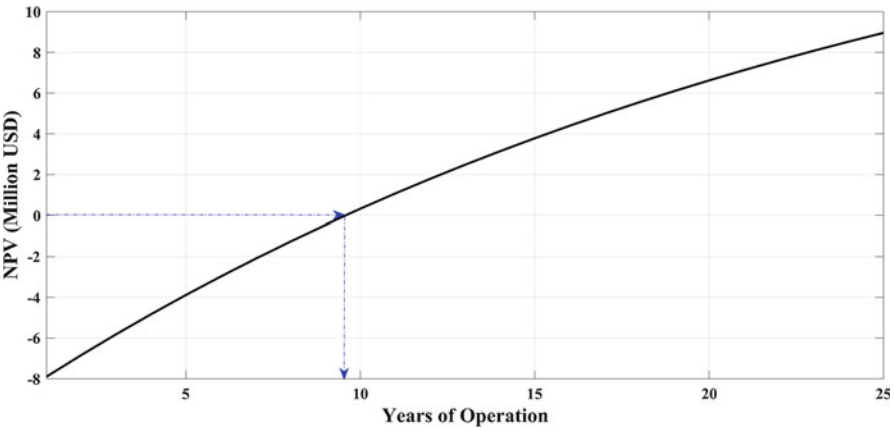

Fig. 11.8 NPV analysis of the system

information about this matter categorizing the emission prevention values in different sectors. According to the figure, a round-trip operation of the energy storage system would prevent the emission of about 76 tonnes of equivalent CO_2, while this prevention for the cold and electricity sectors is about 16 and 18 tonnes of CO_2eq, respectively.

Figure 11.8 presents the trend of variation of the NPV value of the system over the years of operation. For plotting this figure, the capital investment of 900 USD/kW, including the installation costs, for the subcooled-CAES is considered. As mentioned before, the interest rate is considered as 4%, and the annual

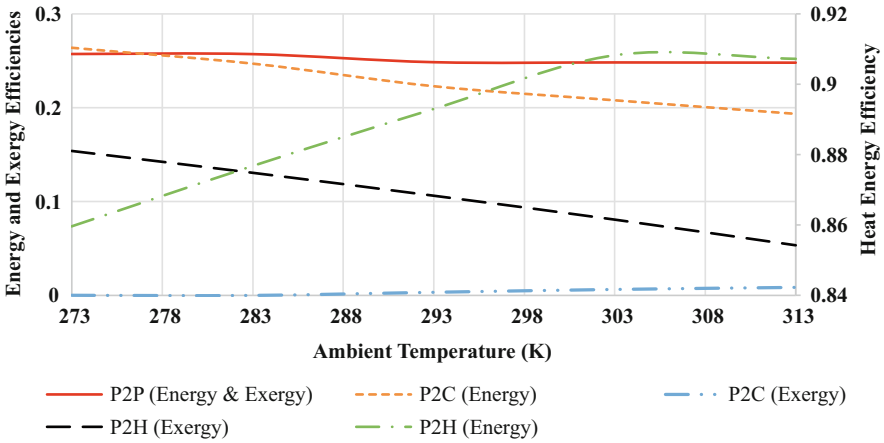

Fig. 11.9 Sensitivity analysis of the system energetic and exergetic indices to the ambient temperature

operating and maintenance costs are 3% of initial investment [23]. The plot is based on a continuous charging-discharging operation of the system over the entire year (meaning 438 cycles). As seen, by such economic assessment values and the energy pricing strategies considered, the payback period of the system will be about 9 years.

The results presented so far are all based on certain operation/analysis considerations. Thus, a sensitivity analysis of the results to some key parameters should be carried out to get a better insight into the system's techno-economic performance criteria. These parameters are the ambient temperature, isentropic efficiencies of turbines and compressors, the pinch temperature of the heat exchangers and the number of operating cycles over the year.

Figure 11.9 shows how the exergetic and energetic efficiencies would vary for different ambient temperature ranges. As seen, increasing the temperature of ambient slightly reduces the energetic and exergetic performance indices but the cold production exergy efficiency which improves mildly and the heat production energy efficiency which first increases and then reduces. The heat energy efficiency is optimal at ambient temperature of 303 K.

Figure 11.10 shows the effect of isentropic efficiency of the turbines on the overall cold and power energetic and exergetic efficiencies. Naturally, the heat production efficiencies are independent of the turbine performance. As seen, the cold and electricity production energy efficiencies linearly and significantly improve as the turbine isentropic efficiency improves. The best power (energy and exergy) efficiency with a turbine as good as having the isentropic efficiency of 95% can be about 37%. The cold production exergetic efficiency does not show much sensitivity to this parameter.

Figure 11.11 investigates and the effect of compressor isentropic efficiency on the overall energy and exergy performances of the system. Unlike the turbine efficiency which only has impacts on the discharging mode performance, compressor

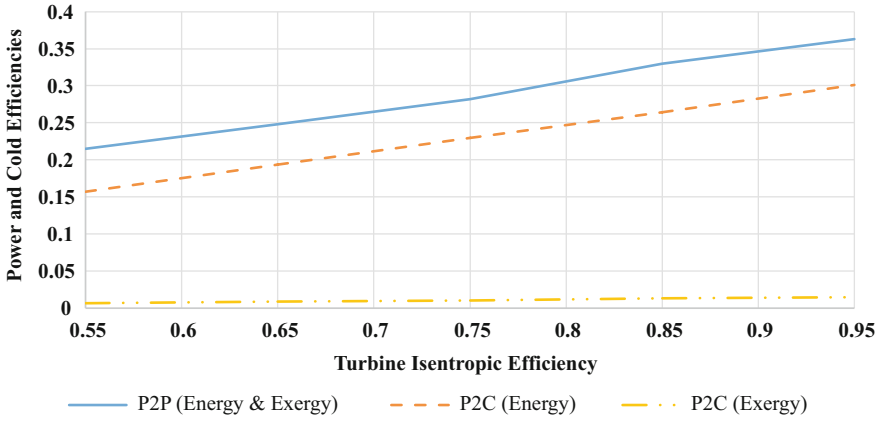

Fig. 11.10 Turbine efficiency effects of the cold and power production efficiencies

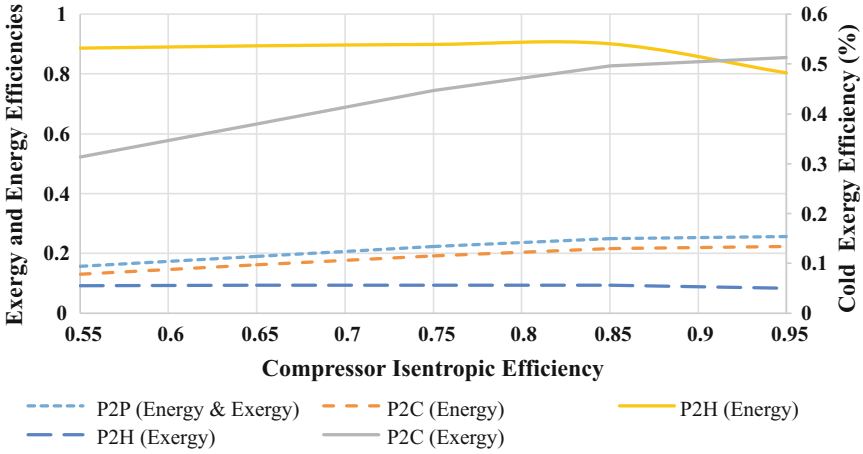

Fig. 11.11 Compressor efficiency effects of the heat, cold and power production efficiencies

isentropic efficiency affects both charging and discharging modes because a smaller compressor efficiency means less compressed air generation and, consequently, less net power and cold efficiencies. This can be seen from the figure too where all the parameters improve as the isentropic efficiency of the turbine enhances but the heat energy and exergy efficiencies which do not change up to the critical isentropic efficiency of 0.85 and, thereafter, decrease gradually.

The pinch temperature for the cold and heat supply heat exchangers was considered 10 K during the simulations so far. Figure 11.12 shows how changing the pinch temperature of the heat exchangers after the compressors and the turbines on the heat, cold and electricity production energy/exergy efficiencies. The pinch temperature 0 K means that the heat exchangers are so efficient and large enough that the

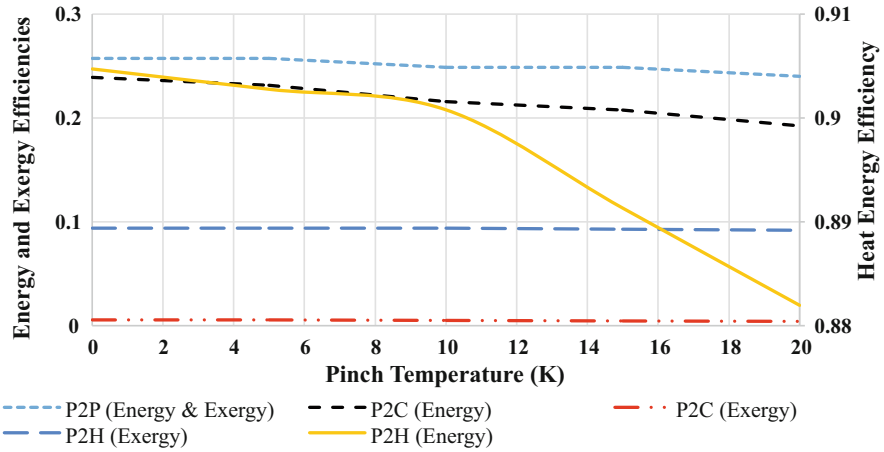

Fig. 11.12 Effects of heat exchangers pinch temperature on the heat, cold and power production efficiencies

airflow reaches the temperature of water flows entering the heat exchangers. Naturally, this is the best possible case, and as the pinch temperature increases, the efficiencies drop accordingly. Although a pinch point of 0 K is not impossible, it is most often not economically feasible, and therefore, heat exchangers are so designed that an acceptable effectiveness factor is obtained yet the costs of the system are kept as low as possible.

Naturally, an energy storage system cannot be in operation all the time. There are occasions that the system needs to stay on standby mode and neither receives any excess electricity nor generates energy. Therefore, the number of full charging-discharging rounds in a year is an important factor that affects the economic feasibility of the system and the level of its environmental effectiveness. Figure 11.13 investigates the impacts of the number of round-trip operation of the subcooled-CAES system on its payback period and the total annual emission reduction. As seen, the payback period of the system destroys as the number of operating cycles drop. For example, at the operation cycles of 250, the payback period of the technology will be about 27 years, while for 400 cycles a year, the payback period will be only 10 years which is an acceptable term. The environmental benefit, on the other hand, linearly improves as the number of cycles increases. For 400 cycles of operation a year, a total amount of 44 million kg of CO_2eq is prevented to be wasted.

11.5 Future Prospective

This work presents a detailed energy, exergy, economic and environmental analysis of a double-stage subcooled-CAES system. The subcooled-CAES is a new mechanical energy storage technology that offers the trigeneration of cold, heat and

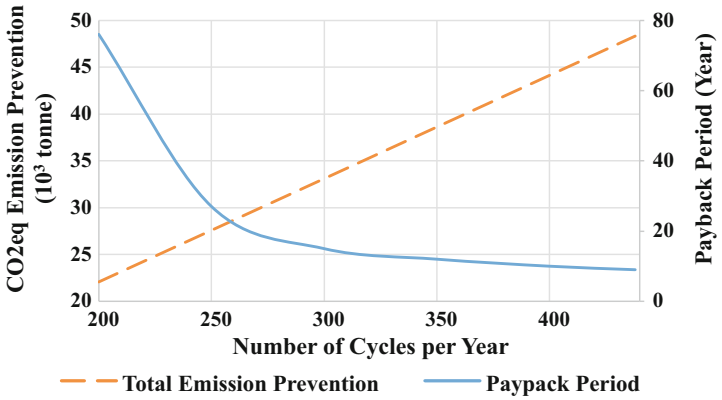

Fig. 11.13 Effects of operating cycle numbers of the storage system on its economic feasibility and environmental benefit

electricity at a pretty high overall efficiency and can facilitate the integration of three energy sectors. For carrying out the analyses, the system is assumed to be employed in the energy system of Denmark with its certain energy pricing and supply specifications. The results show that for a double-stage subcooled-CAES with the maximum pressure of 64 bar, a storage vessel with the volume of 7740 m^3 would be needed. The analyses show that for an ambient temperature of 298 K, pinch temperature of 10 K for the heat exchangers and isentropic efficiencies of 0.85 and 0.65 for the compressor and expanders, this system will result in the electricity-to-heat, electricity-to-cold and electricity-to-electricity efficiencies of about 90%, 21% and 24%. Thus, the overall performance coefficient of the system will be about 1.3. The exergetic performance indices of the system, however, will not be that impressive where the heat production exergy efficiency will be around only 9% while the cold production exergy efficiency remains as low as below 1%. The sensitivity analysis carried out shows that the performance could be enhanced by improving the isentropic efficiencies of turbines and compressors. In addition, lowering the ambient temperature could increase the electricity efficiency and overall performance of the storage technology. It was shown that increasing the effectiveness factor of the heat exchangers, in the form of a smaller pinch temperature, could help in getting better electricity, cold and heat energy/exergy production efficiencies. The economic analysis showed that, in case of continuous operation of the system at full-load all over the year, a payback period of below 9 years could be achieved. This, however, will not be practically possible. The sensitivity analysis shows that if the number of operating cycles drops to 300 rounds per year, the payback period will be 15 years. For 200 cycles, the payback period will be 76 years. The analyses also show that the subcooled-CAES can be extremely helpful for a cleaner production chain where with 300 cycles of full-load operation a year, it can prevent a total of 33 million kg of CO_2eq from being emitted. In case of full-time operation, this figure even increases to 48 million kg CO_2eq/year.

References

1. Sadi, M., & Arabkoohsar, A. (2019). Modelling and analysis of a hybrid solar concentrating-waste incineration power plant. *Journal of Cleaner Production, 216*, 570–584. https://doi.org/10.1016/j.jclepro.2018.12.055.
2. O'Dwyer, E., Pan, I., Acha, S., & Shah, N. (2019). Smart energy systems for sustainable smart cities: Current developments, trends and future directions. *Applied Energy, 237*, 581–597. https://doi.org/10.1016/j.apenergy.2019.01.024.
3. Alnaser, W. E., & Alnaser, N. W. (2011). The status of renewable energy in the GCC countries. *Renewable and Sustainable Energy Reviews, 15*, 3074–3098. https://doi.org/10.1016/j.rser.2011.03.021.
4. Paiho, S., Saastamoinen, H., Hakkarainen, E., Similä, L., Pasonen, R., Ikäheimo, J., Rämä, M., Tuovinen, M., & Horsmanheimo, S. (2018). Increasing flexibility of Finnish energy systems—A review of potential technologies and means. *Sustainable Cities and Society, 43*, 509–523. https://doi.org/10.1016/j.scs.2018.09.015.
5. Zakeri, B., & Syri, S. (2015). Electrical energy storage systems: A comparative life cycle cost analysis. *Renewable and Sustainable Energy Reviews, 42*, 569–596. https://doi.org/10.1016/j.rser.2014.10.011.
6. Yang, Y., Bremner, S., Menictas, C., & Kay, M. (2018). Battery energy storage system size determination in renewable energy systems: A review. *Renewable and Sustainable Energy Reviews, 91*, 109–125. https://doi.org/10.1016/j.rser.2018.03.047.
7. Salim, H. K., Stewart, R. A., Sahin, O., & Dudley, M. (2019). Drivers, barriers and enablers to end-of-life management of solar photovoltaic and battery energy storage systems: A systematic literature review. *Journal of Cleaner Production, 211*, 537–554. https://doi.org/10.1016/j.jclepro.2018.11.229.
8. Yang, C.-J. (2016). In T. M. B. T.-S. E. Letcher (Ed.), *Chapter 2 - pumped hydroelectric storage* (pp. 25–38). Oxford: Elsevier. https://doi.org/10.1016/B978-0-12-803440-8.00002-6.
9. Berrada, A., Loudiyi, K., & Zorkani, I. (2017). System design and economic performance of gravity energy storage. *Journal of Cleaner Production, 156*, 317–326. https://doi.org/10.1016/j.jclepro.2017.04.043.
10. Mousavi G, S. M., Faraji, F., Majazi, A., & Al-Haddad, K. (2017). A comprehensive review of Flywheel Energy Storage System technology. *Renewable and Sustainable Energy Reviews, 67*, 477–490. https://doi.org/10.1016/j.rser.2016.09.060.
11. Benato, A., & Stoppato, A. (2018). Pumped thermal electricity storage: A technology overview. *Thermal Science and Engineering Progress, 6*, 301–315. https://doi.org/10.1016/j.tsep.2018.01.017.
12. Siemens high temeprature heat and power storage project (2016). https://www.siemens.com/press/en/pressrelease/?press=/en/pressrelease/2016/windpower-renewables/pr2016090419wpen.htm&content[]=WP.
13. Arabkoohsar, A., & Andresen, G. B. (2017). Design and analysis of the novel concept of high temperature heat and power storage. *Energy, 126*, 21–33. https://doi.org/10.1016/j.energy.2017.03.001 .
14. Arabkoohsar, A., & Andresen, G. B. (2017). Dynamic energy, exergy and market modeling of a high temperature heat and power storage system. *Energy, 126*. https://doi.org/10.1016/j.energy.2017.03.065.
15. Arabkoohsar, A., & Andresen, G. B. (2017). Thermodynamics and economic performance comparison of three high-temperature hot rock cavern based energy storage concepts. *Energy, 132*. https://doi.org/10.1016/j.energy.2017.05.071.
16. Arabkoohsar, A., Machado, L., Koury, R. N. N., & Ismail, K. A. R. (2016). Energy consumption minimization in an innovative hybrid power production station by employing PV and evacuated tube collector solar thermal systems. *Renewable Energy, 93*, 424–441. https://doi.org/10.1016/j.renene.2016.03.003.

17. Arabkoohsar, A., Machado, L., Farzaneh-Gord, M., & Koury, R. N. N. (2015). Thermo-economic analysis and sizing of a PV plant equipped with a compressed air energy storage system. *Renewable Energy, 83*. https://doi.org/10.1016/j.renene.2015.05.005.
18. Arabkoohsar, A., Machado, L., Farzaneh-Gord, M., & Koury, R. N. N. (2015). The first and second law analysis of a grid connected photovoltaic plant equipped with a compressed air energy storage unit. *Energy, 87*, 520–539. https://doi.org/10.1016/j.energy.2015.05.008 .
19. Odukomaiya, A., Abu-Heiba, A., Gluesenkamp, K. R., Abdelaziz, O., Jackson, R. K., Daniel, C., Graham, S., & Momen, A. M. (2016). Thermal analysis of near-isothermal compressed gas energy storage system. *Applied Energy, 179*, 948–960. https://doi.org/10.1016/j.apenergy.2016.07.059.
20. Peng, H., Yang, Y., Li, R., & Ling, X. (2016). Thermodynamic analysis of an improved adiabatic compressed air energy storage system. *Applied Energy, 183*, 1361–1373. https://doi.org/10.1016/j.apenergy.2016.09.102.
21. Elmegaard, B., & Brix, W. (2011). Efficiency of compressed air energy storage, *Proc 24th Int Conf Effic Cost, Optim Simul Environ Impact Energy Syst ECOS*. (pp. 2512–2523).
22. Wolf, D., & Budt, M. (2014). LTA-CAES – A low-temperature approach to adiabatic compressed air energy storage. *Applied Energy, 125*, 158–164. https://doi.org/10.1016/j.apenergy.2014.03.013.
23. Arabkoohsar, A., Dremark-Larsen, M., Lorentzen, R., & Andresen, G. B. (2017). Subcooled compressed air energy storage system for coproduction of heat, cooling and electricity. *Applied Energy, 205*, 602–614. https://doi.org/10.1016/j.apenergy.2017.08.006.
24. Arabkoohsar, A., & Andresen, G. B. (2019). Design and optimization of a novel system for trigeneration. *Energy, 168*, 247–260. https://doi.org/10.1016/j.energy.2018.11.086.
25. Arabkoohsar, A. (2018). An integrated subcooled-CAES and absorption chiller system for cogeneration of cold and power, in: IEEE Xplore. *Proceeding SEST, 2018*, 1–5.
26. Sadi, M., Arabkoohsar, A. (2018). Modelling and analysis of a hybrid solar concentrating-waste incineration power plant. *Journal of Cleanear Production*. https://doi.org/10.1016/j.jclepro.2018.12.055.
27. Lund, H., Østergaard, P. A., Connolly, D., & Mathiesen, B. V. (2017). Smart energy and smart energy systems. *Energy, 137*, 556–565. https://doi.org/10.1016/J.ENERGY.2017.05.123.
28. Alsagri, A. S., Arabkoohsar, A., Rahbari, H. R., & Alrobaian, A. A. (2019). Partial load operation analysis of Trigeneration subcooled compressed air energy storage system. *Journal of Cleaner Production*, 117948. https://doi.org/10.1016/j.jclepro.2019.117948.
29. Arabkoohsar, A. (2019). Non-uniform temperature district heating system with decentralized heat pumps and standalone storage tanks. *Energy, 170*, 931–941. https://doi.org/10.1016/j.energy.2018.12.209.
30. Arabkoohsar, A., & Andresen, G. B. (2017). Supporting district heating and cooling networks with a bifunctional solar assisted absorption chiller. *Energy Conversion and Management, 148*, 184–196. https://doi.org/10.1016/j.enconman.2017.06.004.
31. Guo, H., Xu, Y., Zhang, Y., Liang, Q., Tang, H., Zhang, X., Zuo, Z., & Chen, H. (2019). Off-design performance and an optimal operation strategy for the multistage compression process in adiabatic compressed air energy storage systems. *Applied Thermal Engineering, 149*, 262–274. https://doi.org/10.1016/j.applthermaleng.2018.12.035.
32. Li, Y., Miao, S., Yin, B., Yang, W., Zhang, S., Luo, X., & Wang, J. (2019). A real-time dispatch model of CAES with considering the part-load characteristics and the power regulation uncertainty. *International Journal of Electrical Power & Energy Systems, 105*, 179–190. https://doi.org/10.1016/j.ijepes.2018.08.024.
33. He, W., Wu, Y., Peng, Y., Zhang, Y., Ma, C., & Ma, G. (2013). Influence of intake pressure on the performance of single screw expander working with compressed air. *Applied Thermal Engineering, 51*, 662–669. https://doi.org/10.1016/j.applthermaleng.2012.10.013.
34. US Environmental Protection Agency (USEPA), (n.d.). https://www.epa.gov/.

35. Arabkoohsar, A., & Nami, H. (2019). Thermodynamic and economic analyses of a hybrid waste-driven CHP–ORC plant with exhaust heat recovery. *Energy Conversion and Management, 187*, 512–522. https://doi.org/10.1016/j.enconman.2019.03.027.
36. Sadi, M., & Arabkoohsar, A. (2019). Exergoeconomic analysis of a combined solar-waste driven power plant. *Renewable Energy, 141*, 883–893. https://doi.org/10.1016/j.renene.2019.04.070.
37. Arabkoohsar, A., Gharahchomaghloo, Z., Farzaneh-Gord, M., Koury, R. N. N., & Deymi-Dashtebayaz, M. (2017). An energetic and economic analysis of power productive gas expansion stations for employing combined heat and power. *Energy, 133*. https://doi.org/10.1016/j.energy.2017.05.163.

Chapter 12
3E Analysis of Hybrid Solar-Waste Driving CHP Plant with Flue Gas Recovery Unit, a Smart Solution Toward Sustainable Energy Systems

Meisam Sadi and Ahmad Arabkoohsar

12.1 Introduction

Due to population increase and extensive material (food, etc.) consumption growth, the global volume of municipal solid waste (MSW) is increasing every day. Besides this, as nations and cities urbanize and further develop economically, it is estimated that waste generation capacity augments from just about 2 billion tons to around 3.5 billion tons from 2016 to 2050 [1]. Efficient MSW treatment is, therefore, extremely important for the world to not let the increasing waste production lead to serious challenges. Apart from recycling which is, of course, the smartest method of waste treatment, the nonrecyclable part of MSW could be either landfilled or incinerated [2]. Among the two alternative methods of waste recycling mentioned above, MSW incineration with the aim of energy production, of course, is by far the preferred method [3]. Waste-incineration plants are usually erected to supply heat and power or co-supply heat and power (waste-fired CHP plants) [4]. Even trigeneration (CCHP plants) mainly driven by waste energy is considered as a competitive solution wherever there are an efficient waste treatment system and simultaneous demand of cold, heat, and power [5].

Although a waste-incineration plant has negative environmental impacts due to the pollutions it makes, compared to the alternative method of landfilling, its pollution is almost half. Therefore, it is considered as an environmentally friendly solution [6]. There are a large number of articles investigating waste-fired energy plants for various purposes. Rydén et al. [7] estimated the usefulness of CHP plants in combination with waste-fired systems. Tobiasen and Kamuk [8] investigated

M. Sadi (✉) · A. Arabkoohsar
Department of Energy Technology, Aalborg University, Aalborg, Denmark
e-mail: mesa@et.aau.dk; ahm@et.aau.dk

F. Jabari et al. (eds.), *Integration of Clean and Sustainable Energy Resources and Storage in Multi-Generation Systems*,
https://doi.org/10.1007/978-3-030-42420-6_12

waste-incineration CHP plants with the main aim of enhancing the operation of the plant by increasing the power generation of the system. Tomić et al. [9] evaluated the performance of CHP systems integrated with waste incineration when working in the EU countries with new legislation and energy pricing standards. Erikson et al. [10] investigated the use of waste-firing systems already used in the power sector of Denmark for district heating networks. Touš et al. [11] recommended a day-ahead pattern of a heat-power production for waste-firing CHP plants, resulting in overall higher efficiency. Munster and Meibom [12] investigated the most effective strategies of using waste resources and recommended creative waste-firing plants with distinguished layouts of heat-power production systems for this. Khoshnevisan et al. [13] carried out an investigation on different methods of energy recovery from specific waste resources and recommended a number of technologies as the most appropriate ones for heat-power production from such wastes. Chacartegui et al. [14] investigated the feasibility of biogas generation from waste resources considering energy legislations of the past and the present and showed that even with much more strict actions, acceptable techno-economic outcomes of such plants could be expected. Yang et al. [15] carried out an extensive techno-economic investigation of a specific waste-firing plant configuration and found not only an acceptable efficiency but also an interesting levelized cost of energy for that.

As a waste-fired plant energy output is, in an agile manner, controllable according to the instantaneous demand of the energy systems connected to that, it is also an interesting measure to use a waste incinerator as the backup for fluctuating renewable source energy plants, e.g., solar power plants. Sadi and Arabkoohsar [16] recently proposed accompanying a solar parabolic trough CHP plant with a waste incinerator for the sake of making a dispatchable energy output profile of the plant for the power and heat grids. An exergoeconomic analysis of this solution was later presented in Ref. [17] to get a deep insight into the economic and exergetic performance of such a combined system. This system, however, suffers from the very high rate of losses from the chimney of the waste-incineration unit, resulting in lower overall efficiency of the plant than that expected from such a smart hybrid configuration. Flue gas condensation is a measure that provides the bed for exploiting the higher heating value (HHV) of the burnt fuel, increasing the efficiency of the plant. Therefore, exhaust waste heat recovery (so-called flue gas condensation) can be a smart approach to enhance the energy efficiency of any power plant, including waste-firing CHP plants. Based on the information coming from Ref. [18], more than 12% of the total district heating demand of Denmark is supplied by waste-incineration heat production plants equipped with flue gas condensation units. Samer et al. [19] investigated two different waste heat recovery processes in an organic Rankine cycle, i.e., direct and indirect contact water vapor condensation recovery, and compared the results and highlighted the advantages and disadvantages of each of the approaches. Murer et al. [20] investigated the effect of adding a steam reheater in a waste-firing plant in the Netherlands taking advantage of the flue gas of the boiler. Eboh et al. [21] studied the effect of flue gas condensation on the cost and profitability of a waste-to-energy plant and compared this with a sort of more proposed modifications (including air heater arrangement modification, adding a reheater, etc.) and found the flue gas heat recovery proposal most effective on

lowering the cost of energy production of the plant. Nami and Arabkoohsar [22] proposed the use of a flue gas condensation section to a combined waste-firing CHP with an organic Rankine cycle and found the added unit extremely beneficial to increase the heat and power supply rates of the hybrid plant.

Therefore, strengthening the hybrid yet flexible heat-power generator solar-waste system proposed in Ref. [16] with a flue gas condensation unit is proposed in this work, and the proposed solution is thoroughly analyzed from energy, exergy, and environmental impacts' points of view. The results are compared to the conventional design of the plant, i.e., hybrid solar-waste CHP plant without a flue gas condensation unit, and the outcomes are discussed.

12.2 Conventional Systems and the Proposed Design

The waste is delivered via a waste collection system and collected in a place where it is mixed. The mixing is required to blend the waste to ensure that the energy input to the combustion chamber is as consistent as possible. The incineration of MSW can be directed on either combustion of the raw residual waste or of pretreated MSW. Plant configuration will change according to the feedstock. When MSW receives air and attains the necessary ignition temperature, a combustion reaction occurs. The combustion process occurs in the gas and solid phase. This process releases a large amount of heat energy. A minimum required autothermic combustion of the waste is required to enable spontaneous combustion in which no extra fuel is required. During combustion, exhaust gases are allowed to exit to the atmosphere via the stack of the incinerator. This flue gas flow carries much energy as it still has a high temperature. The heat generated in the incinerator can be used for any energy supply purposes including direct heat supply, electricity generation via adding a power block, cold supply via adding an absorption chiller, or a combination of these all.

The proposed system of this study is a waste incinerator which is hybridized with a Rankine cycle solar power plant. The arrangement of the Rankine power plant integrated with the waste incinerator and the solar collector field is presented in Fig. 12.1. According to the schematic, in the Rankine cycle, the system consists of a three-stage turbine. After the first expansion stage, the steam is reheated in the boiler and then goes through the second and third expansion processes. In addition, two withdrawal streams are considered for preheating the water flow before entering the boiler. In the open feedwater heater, the extracted steam is allowed to mix with the feedwater. Unlike the open feedwater heater, the streams exchanging heat in the closed feedwater heater do not mix. In such kind of systems, the solar field provides the primary source of energy. Due to the variable amount of solar energy, the solar working fluid (at the outlet of the solar collectors' field, i.e., parabolic trough collectors, PTCs) has variable temperature, and consequently, the main working fluid will have a variable temperature after the boiler, while the steam temperature at the turbine inlet should reach the desired specific value. Thus, the rest of the heat required to push the working fluid to the desired temperature is provided by the

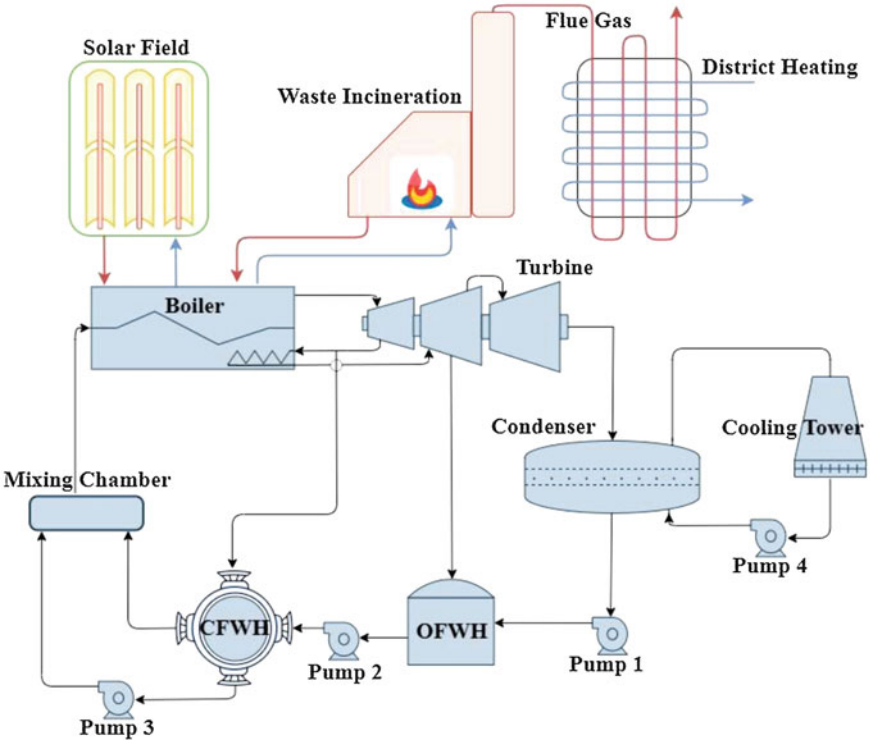

Fig. 12.1 Schematic of the proposed system

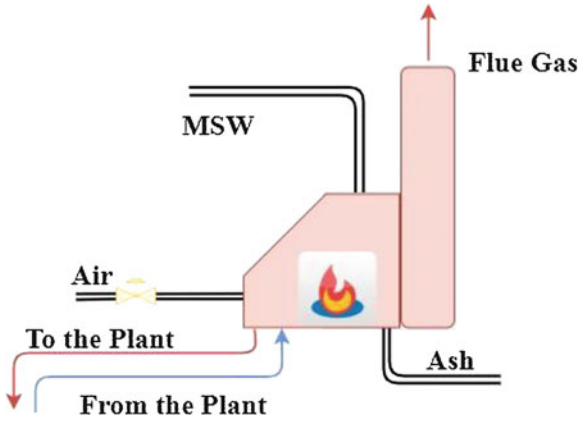

Fig. 12.2 Schematic of the waste incinerator

waste incinerator. The reheat line also gets the required energy from the energy supplied by the waste incinerator.

The conventional configuration of a waste-fired boiler is given in Fig. 12.2. In waste-incineration plants, MSW with an adequate amount of air is burned and the

hot fluid stream goes through the boiler. The ash and flue gas are the product of the combustion process in the incinerator. At the outlet of the stack, flue gas exits to the atmosphere through a channel from the furnace. In the proposed system, for the sake of enhancing the efficiency of the combined solar-waste CHP plant, the flue gas heating potential is utilized. For this, a process which is called the flue gas condensation is implemented via which the exhaust gas is cooled down below the water content dew point temperature. Here, the heat provided via the flue gas condensation process is to be utilized for district heating. The working fluid in the district heating system has a low temperature; thus, it will be possible to get a large amount of energy from the flue gas, and that might make possible the higher usage of the availability of the primary energy sources.

As mentioned, solar energy is the primary source of energy for the combined plant. Here, PTCs, as the most common type of collectors for concentrating solar power systems, are used. Among PTCs, LS-2 collector is one of the generations which is used in many power plants. The mirror aperture is 5 m and the length is 7.8 m. A complete LS-2 solar collector assembly consists of six collector modules and is 49 m long. In this type of PTCs, two different receiver selective coatings – black chrome and cermet – are utilized. The solar receiver gets solar radiation from the reflector. Reflectors have a parabolic configuration, which concentrates solar radiation over the solar receiver. The trough is positioned such that its aperture plane is perpendicular to the sun's beams. It tracks the sun in a single axis to transfer energy to fluid circulating through the receiver pipe. Detailed information on substantial specifications of the LS-2 PTC is seen in Table 12.1.

Figure 12.3 presents a cross-sectional view of the central receiver of the collector and the way solar irradiation components are distributed. Figure 12.4 presents the thermal resistance of the solar collector which will be required for modeling the collector.

12.3 Mathematical Model

The mathematical modeling of the different parts of the hybrid cycle is presented in this section. The proposed hybrid cycle has three main parts in each of which, there are a few components that should be considered and the governing equations should be explained. The main part of the hybrid section is the Rankine cycle. This cycle comprises a three-stage turbine, a condenser, an open and a closed feedwater heater, three pumps, a mixer, and finally a boiler in which the required heat of the cycle is provided from the other source of energy.

The target of the Rankine cycle is electricity production which is produced by electricity generators with conversion efficiency η_{gen}. $\dot{E}_{gen}$ is the product of η_{gen} in the net mechanical power output of the three-stage turbine. It can be presented as below:

Table 12.1 The characteristics of the PTCs [16]

Parameter	Symbol	Value
Width of the PTC	W	5 m
Length of the PTC	L	7.8 m
Focal distance of the PTC	F	1.71 m
Aperture of the PTC	A_a	39.0 m^2
Concentration ratio of the PTC	C	22.74
Receiver inner diameter	D_{ri}	66 × 10
Receiver outer diameter	D_{ro}	70 × 10
Cover inner diameter	D_{ci}	109 × 10
Cover outer diameter	D_{co}	115 × 10
Receiver inner surface	A_{ri}	1.617 m^2
Receiver outer surface	A_{ro}	1.715 m^2
Cover inner surface	A_{ci}	2.671 m^2
Cover outer surface	A_{co}	2.818 m^2
Receiver emittance	ε_r	0.2
Cover emittance	ε_c	0.9
Absorber absorbance	α_{abs}	0.96
Cover transmittance	T	0.95
Concentrator reflectance	r_{conc}	0.83
Incident angle modifier	IAM	1

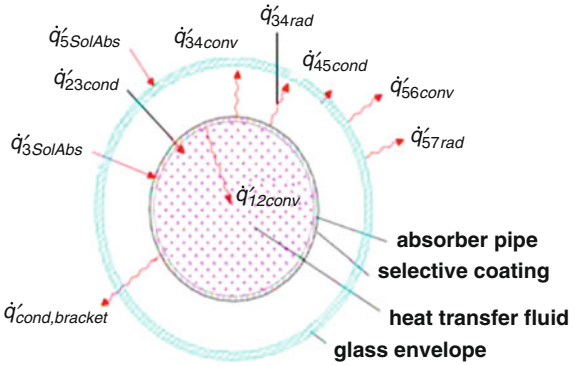

Fig. 12.3 Cross section of the receiver, components of heat transfer [16]

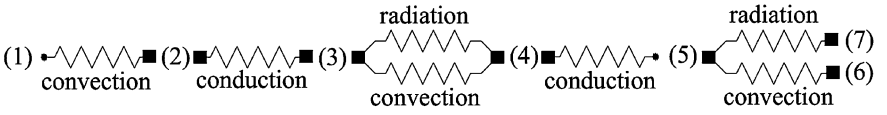

Fig. 12.4 Thermal resistance model for heat transfer components. (1) Heat transfer fluid. (2) Absorber inner surface. (3) Absorber outer surface. (4) Glass envelope inner surface. (5) Glass envelope outer surface. (6) Surrounding air. (7) Sky

$$\dot{W}_{\text{net}} = \frac{\dot{E}_{\text{gen}}}{\eta_{\text{gen}}}; \quad \text{where} : \dot{W}_{\text{net}} = \dot{W}_{\text{hp}} + \dot{W}_{\text{mp}} + \dot{W}_{\text{lp}} - \sum \dot{W}_{\text{pump}} \tag{12.1}$$

In this equation, $\dot{W}$ is the rate of work production of the turbine stages, where hp, mp, and lp are, respectively, the high-pressure, medium-pressure, and low-pressure stages. Some of the produced work in the turbine should be spent on the pumps. $\sum \dot{W}_{\text{pump}}$ is the total work of the pumps. Thus, considering the efficiency of the turbine, the inlet and outlet conditions, etc., one has:

$$\dot{W}_{\text{net}} = \dot{m}_{\text{s}} w_{\text{hp}} + (\dot{m}_{\text{s}} - \dot{m}_{\text{L1}}) w_{\text{mp}} + (\dot{m}_{\text{s}} - \dot{m}_{\text{L1}} - \dot{m}_{\text{L2}})\left(w_{\text{mp}} + w_{\text{lp}}\right) - \dot{m}_{\text{s}} \sum w_{\text{pump}} \tag{12.2}$$

where, $\dot{m}_{\text{s}}$, w, $\dot{m}_{\text{L1}}$, and $\dot{m}_{\text{L2}}$ are, respectively, steam flow rate, specific work rate of turbomachinary, the first steam withdrawal flow rate (for the open feedwater heater), and the second withdrawal flow rate (for the closed feedwater heater).

Low-pressure steam leaves the low-pressure turbine and becomes cooled to a liquid state in the condenser. The rejected heat is presented as:

$$\dot{Q}_{\text{cond}} = \dot{m}_6 (h_6 - h_7) \tag{12.3}$$

in which h_6 is the steam enthalpy at the low-pressure turbine exit and h_7 is the enthalpy at the condenser exit.

For the open and closed feedwater heaters as well as the mixing tank, one has:

$$\dot{m}_2 (h_2 - h_{12}) = \dot{m}_{10} (h_{11} - h_{10}) \tag{12.4}$$

$$\dot{m}_4 h_4 + \dot{m}_8 h_8 = \dot{m}_9 h_9 \tag{12.5}$$

$$\dot{m}_{14} h_{14} = \dot{m}_{11} h_{11} + \dot{m}_{13} h_{13} \tag{12.6}$$

For the energy balance on the boiler, the energy equations gives:

$$\dot{Q}_{\text{in}} = \dot{m}_{\text{solar}} . \Delta h_{\text{solar}} + \dot{m}_{\text{WIP}} . \Delta h_{\text{WIP}} = \dot{m}_{\text{s}} (h_1 - h_{13}) \tag{12.7}$$

The energy balance for the whole Rankine cycle is then can be expressed as follows:

$$\left(\dot{Q}_{\text{in}} - \dot{Q}_{\text{out}}\right) - \left(\dot{W}_{\text{Turbine}} - \dot{W}_{\text{pump}}\right) = 0 \tag{12.8}$$

The net work done by the system is $W_{\text{turbine}} - W_{\text{pump}}$. Therefore, the thermal efficiency of this Rankine cycle can be presented as follows:

$$\eta = \frac{\dot{W}_{\text{Turbine}} - \dot{W}_{\text{pump}}}{\dot{Q}_{\text{in}}} \tag{12.9}$$

By considering the first law of thermodynamics for this incinerator, one would write the following energy equation as follows:

$$\dot{m}_{\text{MSW}}\text{LHV}_{\text{MSW}} + \dot{m}_{\text{air}}h_{\text{air}} + \dot{H}_{\text{f,in}} = \dot{m}_{\text{ash}}h_{\text{ash}} + \dot{m}_{\text{flue}}h_{\text{flue}} + \dot{H}_{\text{f,out}} \tag{12.10}$$

For the heat exchanger that utilizes the heat recovered from the flue gas condensation unit, one could write:

$$\dot{m}_{\text{dh,in}}h_{\text{dh,out}} + \dot{m}_{\text{fg,in}}h_{\text{fg,in}} = \dot{m}_{\text{dh,out}}h_{\text{dh,out}} + \dot{m}_{\text{fg,out}}h_{\text{fg,out}} \tag{12.11}$$

For the solar collectors, using heat transfer components in Fig. 12.3, the first law of thermodynamics could be written at each surface of the receiver. Heat transfers occur between surfaces through different heat transfer mechanisms: conduction, convection, and radiation. These heat transfer equations are presented as follows: Heat transfer between heat transfer fluid and absorber inner surface occurs by convection. This heat passes through absorber by conduction mechanism.

$$\dot{Q}_{12\text{Conv}} = \dot{Q}_{23\text{Cond}} \tag{12.12}$$

$\dot{Q}_{12\text{Conv}}$ is the convection heat transfer rate between the heat transfer fluid and inside wall of the absorber pipe, and $\dot{Q}_{23\text{Cond}}$ is the conduction heat transfer rate through the absorber pipe wall. For absorber surface, glass envelope, and surrounding air and sky, we have:

$$\dot{Q}_{3\text{SolAbs}} = \dot{Q}_{34\text{Conv}} + \dot{Q}_{34\text{Rad}} + \dot{Q}_{34\text{Cond}} + \dot{Q}_{\text{Cond,bracket}} \tag{12.13}$$

$$\dot{Q}_{34\text{Conv}} + \dot{Q}_{34\text{Rad}} = \dot{Q}_{45\text{Cond}} \tag{12.14}$$

$$\dot{Q}_{45\text{Cond}} + \dot{Q}_{5\text{SolAbs}} = \dot{Q}_{56\text{Conv}} + \dot{Q}_{57\text{Rad}} \tag{12.15}$$

$$\dot{Q}_{\text{HeatLoss}} = \dot{Q}_{56\text{Conv}} + \dot{Q}_{57\text{Rad}} + \dot{Q}_{\text{Cond,bracket}} \tag{12.16}$$

$\dot{Q}_{3\text{SolAbs}}$ is the solar irradiation absorption rate into the absorber pipe. $\dot{Q}_{34\text{Conv}}, \dot{Q}_{34\text{Rad}}$, and $\dot{Q}_{34\text{Cond}}$ are the convection, radiation, and conduction heat transfer rate between the outer surface of the absorber pipe to the inner surface of the glass envelope. $\dot{Q}_{45\text{Cond}}$ is the conduction heat transfer rate through the glass envelope. $\dot{Q}_{5\text{SolAbs}}$ is the solar irradiation absorption rate into the absorber pipe. $\dot{Q}_{56\text{Conv}}$ is the convection heat transfer rate between the outer surface of the glass envelope to the atmosphere. $\dot{Q}_{57\text{Rad}}$ is the radiation heat transfer rate between the outer surface of the glass envelope to the sky. $\dot{Q}_{\text{Cond,bracket}}$ is the total conductive heat losses through all receiver support brackets, and $\dot{Q}_{\text{HeatLoss}}$ is the total heat loss rate

from the heat collecting element to the surroundings. Note that each parameter is written per unit receiver length. These heat transfer terms are discussed hereunder.

($q'_{12\text{Conv}}$): This convective term could be presented as:

$$q'_{12\text{Conv}} = h_{c1} D_2 \pi (T_2 - T_1) \tag{12.17}$$

where h_{c1}, D_2, T_1, and T_2 are the internal convective heat transfer coefficient at T_1, the internal diameter of the absorber pipe, the bulk temperature of the working fluid, and the internal surface temperature of absorber pipe, respectively. h_{c1} may also be given by:

$$h_{c1} = \frac{k_1 \text{Nu}_{D2}}{D_2} \tag{12.18}$$

Nu_{D2} is the Nusselt numbers of the working fluid at T_1. Generally, the receiver length is very long and the flow in the receiver pipe is turbulent. For turbulent flow, Nu number may be given by:

$$\text{Nu}_{D2} = \frac{f_2/8(\text{Re}_{D2} - 1000)\text{Pr}_1}{1 + 12.7\sqrt{f_2/8}\left(\text{Pr}_1^{\frac{2}{3}} - 1\right)} \left(\frac{\text{Pr}_1}{\text{Pr}_2}\right)^{0.11} \tag{12.19}$$

$$f_2 = (1.82 \log_{10}(\text{Re}_{D2}) - 1.64)^{-2} \tag{12.20}$$

where f_2, Pr_1, and Pr_2 are the friction factor for the inner surface of the absorber pipe, Prandtl number at the working fluid temperature, and Prandtl number at the absorber inner surface temperature, respectively.

($q'_{23\text{Cond}}$): This conductive term could be presented as:

$$q'_{23\text{Cond}} = 2\,\pi k_{23}(T_2 - T_3)/\ln(D_3 - D_2) \tag{12.21}$$

where k_{23}, T_2, T_3, D_2, and D_3 are the absorber thermal conductance at the average absorber temperature, the absorber internal surface temperature (K), the absorber external surface temperature (K), the absorber internal and external diameters, respectively.

($q'_{34\text{Rad}}$): This space is to be fully vacuumed and the only heat transfer mechanism will be radiation. The radiative heat transfer between the absorber and the glass envelope is estimated as [16]:

$$q'_{34\text{Rad}} = \frac{\sigma \pi D_3 \left(T_3^4 - T_4^4\right)}{(1/\varepsilon_3 + (1 - \varepsilon_4)D_3/(\varepsilon_4 D_4))} \tag{12.22}$$

σ, D_4, T_4, ε_3, and ε_4 are Stefan-Boltzmann constant, the inner glass envelope diameter, the inner envelope surface temperature (K), the absorber selective coating, and the glass emissivity factors, respectively.

($q'_{45\text{Cond}}$): The envelope is made of Pyrex glass. Here, according to [16], this term is assumed as a constant value of 1.04 W/m^2.

($q'_{56\text{Conv}}$ and $q'_{56\text{Rad}}$): The heat transfer between the glass envelope and the ambient and sky will occur through two different mechanisms, convection and radiation mechanisms. For convective terms, we have:

$$q'_{56\text{Conv}} = h_{c56} D_5 \pi (T_5 - T_6) \tag{12.23}$$

$$h_{c56} = \frac{k_{56}\text{Nu}_{D5}}{D_5} \tag{12.24}$$

$$\text{Nu}_{D5} = C\,\text{Re}_{D5}^{m}\text{Pr}_6^{n}\left(\frac{\text{Pr}_6}{\text{Pr}_5}\right)^{1/4} \tag{12.25}$$

where T_5, T_6, H_{56}, k_{56}, and Nu_{D5} are the glass envelope outer surface temperature, the ambient temperature, convective heat transfer coefficient of air, air thermal conductance, the glass envelope outer diameter, and the average Nusselt number based on the glass envelope outer diameter given by the Zukauskas' correlation, respectively. In the Nusselt number correlation, the values of the constant coefficients of C and M depend on the Reynolds number of the airflow around the envelope surface. For a different range of Reynolds numbers, C and M are variable parameters and they would be found in [16]. Also, the value of n will be 0.37 if $\text{Pr} \leq 10$; otherwise, $n = 0.36$. As such, the net radiative heat transfer rate will be calculated by the same correlation as that of the absorber envelope. The equation for solar absorption in the glass envelope is:

$$q'_{5\text{SolAbs}} = q'_{si}\varepsilon'_1\varepsilon'_2\varepsilon'_3\varepsilon'_4\varepsilon'_5\varepsilon'_6\rho_{cl}.\text{IAM}.\alpha_{env} \tag{12.26}$$

in which q'_{si}, α_{env}, and IAM are solar irradiation per receiver length, the absorptance of the envelope, and the incidence angle modifier, respectively.

Finally, the rate of solar energy absorbed by the absorber is given by:

$$q'_{3\text{SolAbs}} = q'_{si}\eta_{env}\tau_{env}\alpha_{abs} \tag{12.27}$$

where α_{abs} and τ_{env} are the absorptance of the absorber and the transmittance of the envelope, respectively.

To assess the performance of the hybrid cycle, two energy parameters are defined, the coefficient of performance of the hybrid cycle, COP_{hyb}, and the heating efficiency of the hybrid cycle, hef_{hyb}:

$$\text{COP}_{hyb} = \frac{\dot{W}_{\text{Rankine}} + \dot{Q}_{dh}}{\dot{Q}_{solar} + \dot{m}_{MSW}\text{LHV}} \tag{12.28}$$

Table 12.2 Exergy balance equations for each component

Components	Exergy balance equations
Waste incinerator	$\left(\dot{E}X_{\mathrm{MSW}} + \dot{E}X_{\mathrm{air}} + \dot{E}X_{\mathrm{wf,in}}\right) - \left(\dot{E}X_{\mathrm{flue,out}} + \dot{E}X_{\mathrm{wf,out}} + \dot{E}X_{\mathrm{ash}}\right)$
Solar site	$\left(\dot{E}X_{\mathrm{sun}} + \dot{E}X_{\mathrm{htf,in}}\right) - \left(\dot{E}X_{\mathrm{htf,out}}\right)$
DH	$\left(\dot{E}X_{\mathrm{flue,in}} + \dot{E}X_{\mathrm{dh,in}}\right) - \left(\dot{E}X_{\mathrm{flue,out}} + \dot{E}X_{\mathrm{dh,out}}\right)$
Boiler	$\left(\dot{E}X_{13} + \dot{E}X_{2} + \dot{E}X_{\mathrm{SF,in}} + \dot{E}X_{\mathrm{WI,in}}\right) - \left(\dot{E}X_{1} + \dot{E}X_{3} + \dot{E}X_{\mathrm{SF,out}} + \dot{E}X_{\mathrm{WI,out}}\right)$
Turbine	$\left(\dot{E}X_{1} + \dot{E}X_{3}\right) - \left(\dot{E}X_{2} + \dot{E}X_{4} + \dot{E}X_{5}\right) - \dot{W}_{\mathrm{ST}}$
Condenser	$\left(\dot{E}X_{\mathrm{in}} - \dot{E}X_{\mathrm{out}}\right)_{S} - \left(\dot{E}X_{\mathrm{out}} - \dot{E}X_{\mathrm{in}}\right)_{\mathrm{CT}}$
Pump 1	$\dot{E}X_{\mathrm{in}} - \dot{E}X_{\mathrm{out}} + \dot{W}_{\mathrm{P}}$
Pump 2	$\dot{E}X_{\mathrm{in}} - \dot{E}X_{\mathrm{out}} + \dot{W}_{\mathrm{P}}$
Pump 3	$\dot{E}X_{\mathrm{in}} - \dot{E}X_{\mathrm{out}} + \dot{W}_{\mathrm{P}}$
OFWH	$\dot{E}X_{4} + \dot{E}X_{7} - \dot{E}X_{8}$
CFWH	$\dot{E}X_{2} + \dot{E}X_{9} - \dot{E}X_{10} - \dot{E}X_{11}$
Chamber	$\dot{E}X_{10} + \dot{E}X_{12} - \dot{E}X_{13}$

$$\mathrm{hef}_{\mathrm{hyb}} = \frac{\dot{Q}_{\mathrm{dh}}}{\dot{Q}_{\mathrm{solar}} + \dot{m}_{\mathrm{MSW}}\mathrm{LHV}} \tag{12.29}$$

By the same general approach as that presented for the energy balance of the plant, one could fulfill an exergy modeling of the combined cycle. Table 12.2 gives information about the exergy balance equations for each component of the hybrid system.

12.4 Case Study

The case study is located at Aarhus, the second largest city in Denmark. It is located on the east coast of the Jutland peninsula, in the geographical center of Denmark, with an altitude of 56°. Aarhus has a temperate oceanic climate, and the weather is constantly influenced by major weather systems from all four ordinal directions, resulting in unstable conditions throughout the year. Temperature varies a great deal across the seasons with a mild spring in April and May, warmer summer months from June to August, frequently rainy and windy autumn months in October and September, and cooler winter months. Yearly solar irradiation available on a horizontal surface is presented in Fig. 12.5. This figure shows that the maximum radiation is about 1100 W/m^2 which is available during the summer, while the irradiation during the winter is rather small.

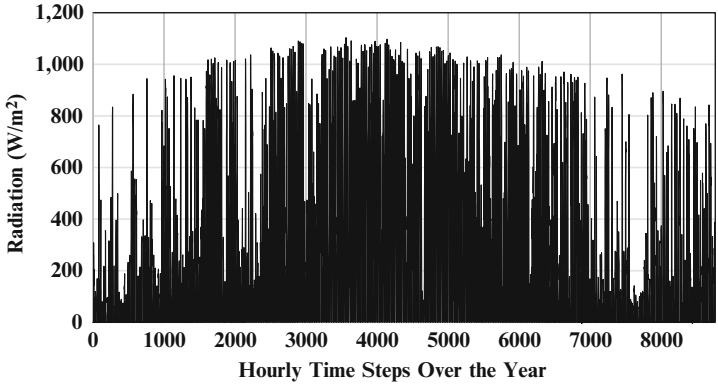

Fig. 12.5 Solar irradiation on a horizontal surface in Aarhus

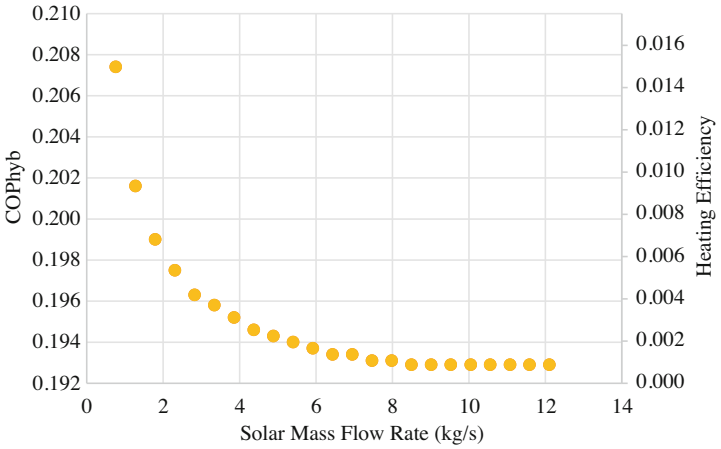

Fig. 12.6 Effect of the solar mass flow rate on the COP of hybrid plant

12.5 Simulation Results

In this section, the results of simulation of the hybrid cycle will be presented for discussion about the effect of this hybridization. When one would like to consider energy recovery in a power plant, energy analysis, exergy analysis, and economic and environmental issues need to be thoroughly considered.

In Fig. 12.6, the effect of the mass flow rate of the solar heat transfer fluid on the coefficient of performance and the heating efficiency of the hybrid system is presented. This figure is produced for a constant value of the solar irradiation, 800 W/m^2. By increasing the mass flow rate, the share of solar energy in power production increases, and vice versa, the waste incinerator share in power production decreases. Thus, due to the lower efficiency of solar thermal plants in comparison with the efficiency of waste-incineration plants, an increase in mass flow rate causes

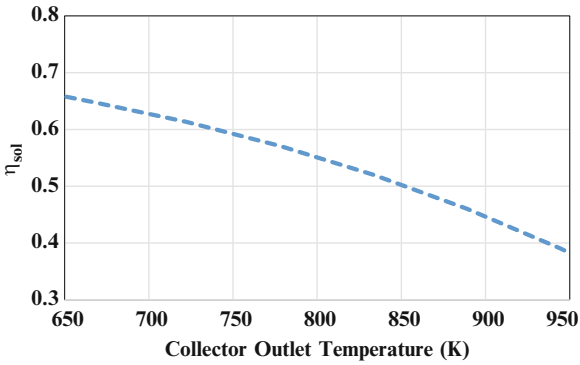

Fig. 12.7 Effect of the collector outlet temperature on the heating efficiency of the collector

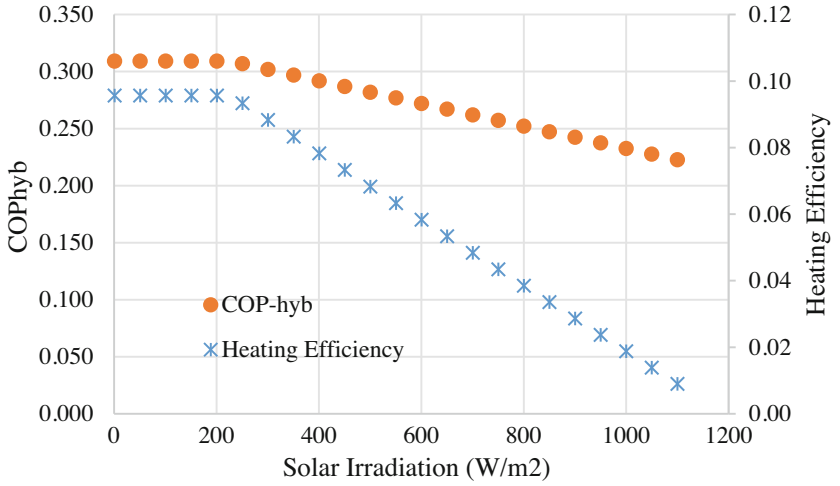

Fig. 12.8 Effect of the solar irradiation on the COP of the hybrid plant

the COP to decrease. The efficiency of the PTC for different values of the collector outlet temperature is seen in Fig. 12.7. An increase in this temperature causes the decrease in efficiency of PTC to the lower values. This figure shows that in the specified range of the collector outlet temperature, the efficiency never reaches 0.65 or over. Even for higher collector outlet temperature, the efficiency of 0.38 will be also experienced. However, the heating efficiency of waste incineration is always higher than 0.65, and in this regard, whenever the share of waste-incineration increases compared to the share of solar PTC field, we can expect higher overall efficiency for the hybrid cycle.

Figure 12.8 shows the effect of solar irradiation on the coefficient of performance and the heating efficiency of the hybrid system. For low values of the solar radiation in the range of 0–200 W/m^2, both COP_{hyb} and heating efficiency are almost constant. This is because, in the specified range, the PTCs do not perform efficiently and have almost very little heat production. In this regard, the heat supply of the system is on the waste-incineration neck. With an increase in solar irradiation, both COP_{hyb} and

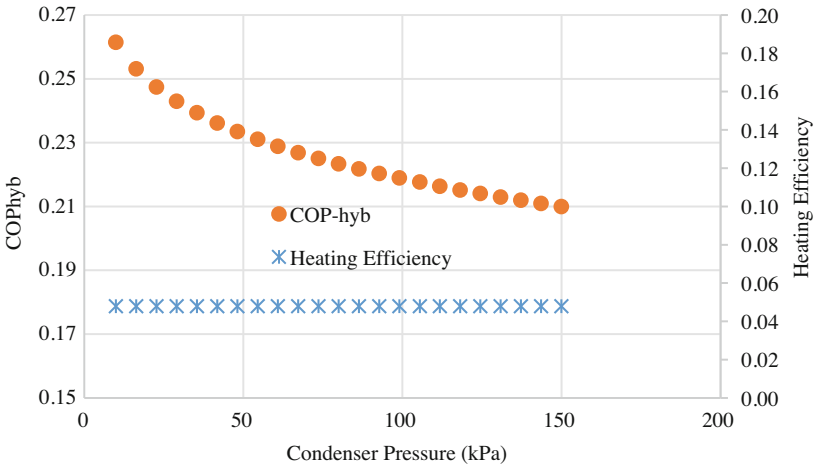

Fig. 12.9 Effect of the condenser pressure on the COP of the hybrid plant

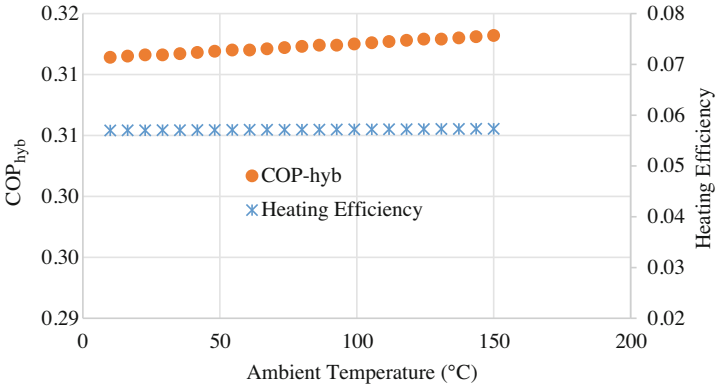

Fig. 12.10 Effect of the ambient temperature on the COP of the hybrid plant

heating efficiency start decreasing. An increase in solar irradiation causes a decrease in waste-incineration share, and this can result in a lower amount of exhaust gas which is provided for the district heating.

Figure 12.9 shows the effect of condenser pressure on the coefficient of performance and the heating efficiency of the hybrid system. For low values of condenser pressure, heating efficiency is constant. It means that the variation of the condenser pressure does not affect the waste-incineration performance. While an increase in the condenser pressure results in a decrease in COP_{hyb}. In this situation, the produced work of the turbine decreases, and this is a technical reason for the reduction in the coefficient of performance of the hybrid system.

Figure 12.10 shows the effect of ambient temperature on the coefficient of performance and the heating efficiency of the hybrid system. From the figure, it is

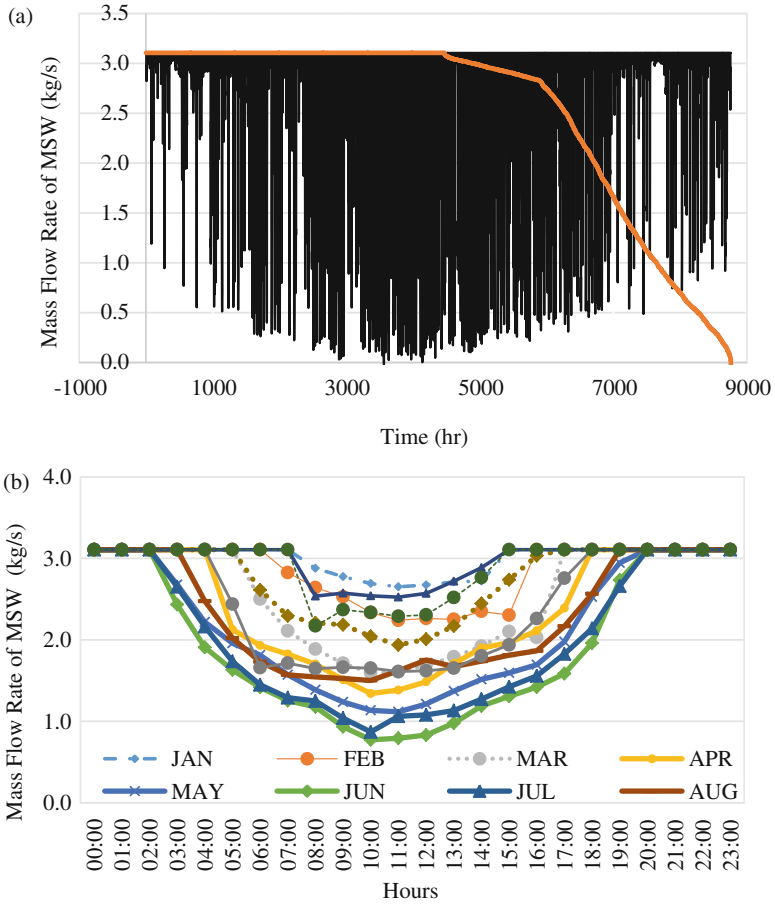

Fig. 12.11 Variation of the mass flow rate of MSW (**a**) during the year with duration curve and (**b**) for each month of the year

evident that the heating efficiency is constant. It means that the variation of the ambient temperature does not affect the waste-incineration performance. While an increase in the ambient temperature results in COP_{hyb} increase, however, this increase is very small. When ambient temperature increases, the produced heat of the solar field slightly increases for a constant value of solar irradiation. Thus, for constant solar irradiation in the denominator of the COP_{hyb} term, a slight increase in the solar share causes a reduction in the mass flow rate of the MSW and consequently smaller share of the waste-incineration plant.

Figure 12.11a shows the mass flow rate of MSW is required to be burnt in the waste incinerator to provide the remaining required heat of the boiler before the steam turbine during the year. The fluctuations in the mass flow rate of MSW seen in the figure are due to the fluctuations of the solar irradiation. In addition, the duration curve of the mass flow rate of MSW is represented. In 48% of the cases, a maximum

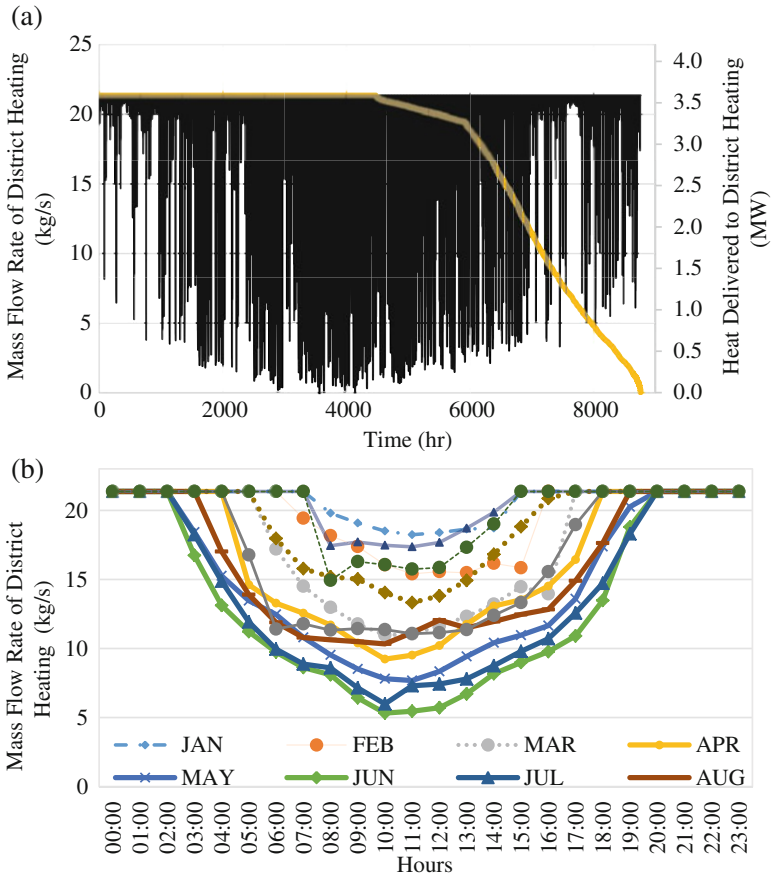

Fig. 12.12 Variation of the mass flow rate of district heating (**a**) during the year with duration curve and (**b**) for each month of the year

mass flow rate of MSW which is 3.1 kg/s is required. This maximum value occurs when no solar irradiation exists and depends on the condition of full cloudiness of the weather. Then for the other 52% of the cases, the mass flow rate of MSW decreases from 3.1 kg/s to 0. Figure 12.11b shows the average of the mass flow rate of MSW for each month of the year during 24 hours of a day. For cold months like December and January, the required mass flow rate is at the maximum level for about 17 hours, while in the remaining hours of the day, the MSW mass flow rate does not fall below the 2.5 kg/s. As the months become warmer, the hour in which the maximum mass flow rate of MSW is required reduces.

Figure 12.12a shows the mass flow rate of district heating which is provided by the waste energy of the flue gas. The fluctuations in the mass flow rate of district heating are also seen in this figure. Similar to Fig. 12.11, these fluctuations are due to the variations of solar irradiation. In addition, the duration curve of the mass flow

rate of district heating is represented. In 48% of the cases, the maximum mass flow rate of district heating which is produced will be 21.1 kg/s. This maximum value occurs when no solar irradiation exists. Then for the other 52% of the cases, the provided mass flow rate of district heating decreases from 21.1 kg/s to 0. In addition, this figure shows the value of delivered heat to the district heating from the flue. In 48% of the cases, maximum delivered heat to district heating will be 35.4 MW, and it is when waste incineration provides all required heat of the plant. As a result of the decrease in the share of WI, the provided heat for the heat exchanger of district heating decreases from 35.4 kg/s to 0. In Fig. 12.12b, the average of district heating mass flow rate is illustrated for each month of the year for 24 hours of a day. For cold months, for about 17 hours, the provided mass flow rate is at the maximum level, while in the remaining hours of the day, the value falls. As the months become warmer, the number of hours, in which the maximum mass flow rate of district heating is provided, and the amount of heat will be both reduced.

Table 12.3 presents the exergy destruction rate of the components when the total energy of the hybrid cycle is provided by both sources with an equal share. The table also presents information about the obtained exergy efficiency and total exergy efficiency ratio of the components. About 44% of exergy destruction occurs at the solar PTC collection. After the solar field, WI, boiler, and closed feedwater heater present the highest exergy destruction in the cycle.

The combustion of MSW results in the release of CO_2. Figure 12.13 shows the values of the CO_2 emission reduction, if one would consider that the required heat of district heating is going to be directly provided by the waste-incineration plant with the heating efficiency of 0.8, i.e., compared with the conventional system with no flue gas condensation. It is seen that in the cold months of the year, a higher reduction in the amount of CO_2 emission occurs compared to the hot seasons. In the cold season, the lower amount of solar irradiation and also sunny hours of days

Table 12.3 Exergy performance audit of the Rankine cycle components

Components	Exergy destruction (kW)	Exergy efficiency (%)	Total exergy destruction ratio (%)
Waste incinerator	8388	43	14.7
Solar site	24,853	37	43.7
DH	195	53	0.3
Boiler	8462	64	14.9
Turbine	4892	67	8.6
Condenser	1244	86	2.2
Pump 1	0.6	77	0.00
Pump 2	23	81	0.04
Pump 3	2.9	86	0.01
OFWH	297.4	65	0.5
CFWH	8417	12	14.8
Chamber	162	93	0.3

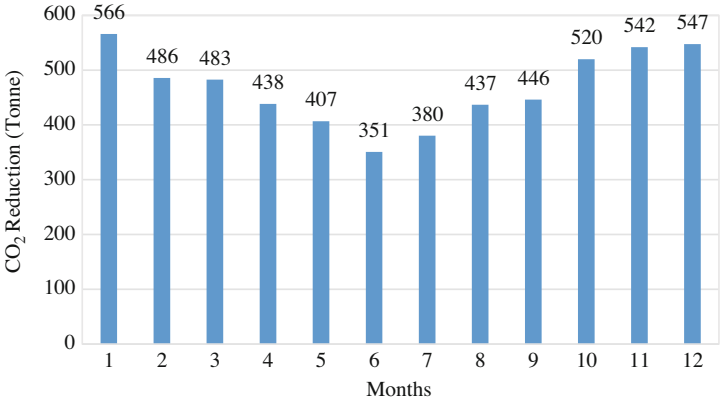

Fig. 12.13 CO_2 emission reduction for each month compared with the conventional system

make the waste-incineration plant to be more on baseload or non-baseload operation to provide the nominal load of the power plant. With this respect, a higher amount of flue gas provides a higher heating potential for district heating, and consequently if one would directly provide this heating by the waste-incineration plant, more CO_2 emission will be generated.

12.6 Conclusion

In this study, the hybridization of waste-incineration power plants with solar parabolic trough collectors was proposed to provide reliable growth of solar power plants into the existing energy matrices. The hybrid power plant is proposed to have a flue gas condensation unit to maximize the net efficiency. The proposed hybrid system is thoroughly analyzed via energy, exergy, and economic and environmental analysis, and the results are compared with the conventional system. The results have been developed to analyze the sensitivity of solar mass flow rate, solar irradiation, condenser pressure, and the ambient temperature on the COP of hybrid plants. The effect of the collector outlet temperature on the heating efficiency of the collector is also studied. By increasing the mass flow rate, the share of solar energy in power production increases, and vice versa, the waste-incineration share in power production decreases. Thus, due to the lower efficiency of solar thermal plants in comparison with the efficiency of waste-incineration plants, an increase in mass flow rate causes the COP to decrease. With an increase in solar irradiation, both COP_{hyb} and heating efficiency decrease. An increase in solar irradiation causes a decrease in waste-incineration share, and this can result in the lower amount of exhaust gas which is provided for the district heating. The condenser pressure and ambient temperature have no great effects on the performance of the cycle. However, an increase in the condenser pressure results in a very slight decrease in COP_{hyb}. The

mass flow rate of MSW which is required to be burnt in the waste incinerator is calculated. This amount of MSW provides the required heat of the boiler. In 48% of the cases, a maximum mass flow rate of MSW occurs when no solar irradiation exists. For cold months like December and January, the required mass flow rate is at the maximum level for about 17 hours. Energy recovery from the flue gas condensation process made an excellent chance to heat the district heating system. The mass flow rate of district heating, which is provided by this preparation, was calculated and presented in an hourly format. The fluctuations in the mass flow rate are due to the variations of solar irradiation. In 48% of the cases when no solar irradiation exists, the maximum mass flow rate of district heating is produced. Then for the other 52% of the cases, the provided mass flow rate of district heating decreases from 21.1 kg/s to 0. For any energy production unit, it could be said that the more efficient the energy, the lower the CO_2 emission and the greater the energy benefits. The application of the flue gas condensation process leads to a decrease in CO_2 emission compared with the conventional system for different seasons of the year. It was observed that in the cold months of the year, a higher reduction in the amount of CO_2 emission occurs compared with the hot seasons.

References

1. *Municipal solid waste incineration, a decision-makers guide*. Available from: http://documents.worldbank.org/curated/en/206371468740203078/Municipal-solid-waste-incineration-a-decision-makers-guide.
2. Hassan, G. K., Massanet-Nicolau, J., Dinsdale, R., Jones, R. J., Abo-Aly, M. M., El-Gohary, F. A., et al. (2019). A novel method for increasing biohydrogen production from food waste using electrodialysis. *International Journal of Hydrogen Energy Pergamon, 44*, 14715–14720.
3. Pei, Z. (2019). Roles of neighborhood ties, community attachment and local identity in residents' household waste recycling intention. *Journal of Cleaner Production Elsevier, 241*, 118217.
4. Nami, H., & Arabkoohsar, A. (2019). Improving the power share of waste-driven CHP plants via parallelization with a small-scale Rankine cycle, a thermodynamic analysis. *Energy, 171*, 27–36.
5. Nami, H., Arabkoohsar, A., & Anvari-Moghaddam, A. (2019). Thermodynamic and sustainability analysis of a municipal waste-driven combined cooling, heating and power (CCHP) plant. *Energy Conversion and Management Pergamon, 201*, 112158.
6. Assamoi, B., & Lawryshyn, Y. (2012). The environmental comparison of landfilling vs. incineration of MSW accounting for waste diversion. *Waste Management Pergamon, 32*, 1019–1030.
7. Rydén, B., Johnsson, J., & Wene, C.-O. (1993). CHP production in integrated energy systems examples from five Swedish communities [Internet]. *Energy Policy, 21*, 176–190. Available from: http://www.sciencedirect.com/science/article/pii/0301421593901397.
8. Tobiasen, L., & Kamuk, B. (2013). 8 - Waste to energy (WTE) systems for district heating. In N. B. Klinghoffer & M. J. Castaldi (Eds.), *Waste to energy conversion technology: Woodhead Publishing Series in Energy [Internet]* (pp. 120–145). Woodhead Publishing. Available from: http://www.sciencedirect.com/science/article/pii/B9780857090119500089.
9. Tomić, T., Dominković, D. F., Pfeifer, A., Schneider, D. R., Pedersen, A. S., & Duić, N. (2017). Waste to energy plant operation under the influence of market and legislation conditioned

changes [Internet]. *Energy, 137*, 1119–1129. Available from: http://www.sciencedirect.com/science/article/pii/S0360544217306461.
10. Eriksson, O., Finnveden, G., Ekvall, T., & Björklund, A. (2007). Life cycle assessment of fuels for district heating: A comparison of waste incineration, biomass- and natural gas combustion [Internet]. *Energy Policy, 35*, 1346–1362. Available from: http://www.sciencedirect.com/science/article/pii/S0301421506001820.
11. Touš, M., Pavlas, M., Putna, O., Stehlík, P., & Crha, L. (2015). Combined heat and power production planning in a waste-to-energy plant on a short-term basis [Internet]. *Energy, 90*, 137–147. Available from: http://www.sciencedirect.com/science/article/pii/S0360544215006581.
12. Münster, M., & Meibom, P. (2011). Optimization of use of waste in the future energy system [Internet]. *Energy, 36*, 1612–1622. Available from: http://www.sciencedirect.com/science/article/pii/S0360544210007760.
13. Khoshnevisan, B., Tsapekos, P., Alvarado-Morales, M., Rafiee, S., Tabatabaei, M., & Angelidaki, I. (2018). Life cycle assessment of different strategies for energy and nutrient recovery from source sorted organic fraction of household waste [Internet]. *Journal of Cleaner Production, 180*, 360–374. Available from: http://www.sciencedirect.com/science/article/pii/S0959652618302269.
14. Chacartegui, R., Carvalho, M., Abrahão, R., & Becerra, J. (2015). Analysis of a CHP plant in a municipal solid waste landfill in the South of Spain. *Applied Thermal Engineering Pergamon, 91*, 706–717.
15. Yang, Y., Wang, J., Chong, K., & Bridgwater, A. V. (2018). A techno-economic analysis of energy recovery from organic fraction of municipal solid waste (MSW) by an integrated intermediate pyrolysis and combined heat and power (CHP) plant. *Energy Conversion and Management Pergamon, 174*, 406–416.
16. Sadi, M., & Arabkoohsar, A. (2019). Modelling and analysis of a hybrid solar concentrating-waste incineration power plant. *Journal of Cleaner Production, 216*, 570–584.
17. Sadi, M., & Arabkoohsar, A. (2019). Exergoeconomic analysis of a combined solar-waste driven power plant [Internet]. *Renewable Energy, 141*, 883–893. Available from: http://www.sciencedirect.com/science/article/pii/S0960148119305543.
18. State of Green [Internet]. Available from: https://stateofgreen.com/en/sectors/district-energy/district-heating/waste-to-energy/.
19. Maalouf, S., Boulawz Ksayer, E., & Clodic, D. (2016). Investigation of direct contact condensation for wet flue-gas waste heat recovery using Organic Rankine Cycle. *Energy Conversion and Management Pergamon, 107*, 96–102.
20. Murer, M. J., Spliethoff, H., de Waal, C. M. W., Wilpshaar, S., Berkhout, B., van Berlo, M. A. J., et al. (2011). High efficient waste-to-energy in Amsterdam: Getting ready for the next steps. *Waste Management & Research SAGE Publications Ltd STM, 29*, S20–S29.
21. Eboh, F. C., Andersson, B.-Å., & Richards, T. (2019). Economic evaluation of improvements in a waste-to-energy combined heat and power plant. *Waste Management Pergamon, 100*, 75–83.
22. Arabkoohsar, A., & Nami, H. (2019). Thermodynamic and economic analyses of a hybrid waste-driven CHP–ORC plant with exhaust heat recovery [Internet]. *Energy Conversion and Management, 187*, 512–522. Available from: http://www.sciencedirect.com/science/article/pii/S0196890419303115.

Chapter 13
Stochastic Analysis of Gas-Electricity Hybrid Grid Using Nataf Transformation Combined with Point Estimation Method

Salar Balaei-sani, Farkhondeh Jabari, and Behnam Mohammadi-Ivatloo

Nomenclature

Indices

Ω_{G}^{i}	Set of all thermal generating units connected to bus i
Ω_{ℓ}^{i}	Set of all buses connected to bus i
i,j	Index of network buses
in	Cut-in
k	Number of the points for each random variable
m	Number of input variables
n	Number of blocks considered for piecewise linear fuel cost function
out	Cutout
r	Rated
g	Index of thermal generating units

Parameters

σ_i	Standard deviation of x_i
Φ/Φ^{-1}	CDF/inverse CDF of the standard normal distribution

S. Balaei-sani (✉)
Faculty of Electrical and Computer Engineering, University of Tabriz, Tabriz, Iran

F. Jabari
Department of Power System Operation and Planning, Niroo Research Institute (NRI), Tehran, Iran
e-mail: f.jabari@tabrizu.ac.ir

B. Mohammadi-Ivatloo
Faculty of Electrical and Computer Engineering, University of Tabriz, Tabriz, Iran

Department of Energy Technology, Aalborg University, Aalborg, Denmark
e-mail: bmohammadi@tabrizu.ac.ir

F. Jabari et al. (eds.), *Integration of Clean and Sustainable Energy Resources and Storage in Multi-Generation Systems*,
https://doi.org/10.1007/978-3-030-42420-6_13

c	Scale parameter
cov (x_i, x_j)	Covariance of x_i and x_j
f_i	PDF of x_i
h	Shape parameter
$Pr_n^{\max / \min}$	Maximum/minimum limits of gas pressure at the *nth* node (bar)
$P_{d,\,i}$	Load demand (MW)
$P_g^{\max / \min}$	Maximum/minimum limits of power generation of thermal unit i
P_i^{w}	Active power generation by wind turbine connected to bus i
$P_{ij}^{\max}$	Maximum power flow limits of branch connecting bus i to j
$P_{r,\,i}$	Rated power of wind turbine
$\mathrm{RU}_g/\mathrm{RD}_g$	Ramp-up/ramp-down limit of generation unit i (MW/h)
$Sg_n^{\max / \min}$	Maximum/minimum limits of gas generation of unit n (Scm)
w_i	Availability of wind turbine connected to bus i

Variables

OF	Total cost ($)
P_{ij}	Active power flow from bus i to j (MW)
P_g	Active power generated by thermal unit g (MW)
Pr_n	Rate of pressure in the nth node (bar)
Sg_n	Rate of gas generation of unit n (Scm)
Sd_n	Rate of gas consumption in the nth node
v_i	Wind speed of wind turbine connected at bus i
$v_{\mathrm{in},\,i}$	Cut-in speed of wind turbine
$v_{\mathrm{out},\,i}$	Cutout speed of wind turbine

Greek symbols

ξ_{ik}	Coefficient representing the kth location on its probability distribution
δ_i	Voltage angle of bus i (rad)
λ_i	Locational marginal price in bus i ($/MW h)
ρ_{ij}	Correlation coefficient of x_i and x_j
μ	Mean
σ	Standard deviation
Λ_i^w	Capacity of wind turbine connected to bus i

13.1 Introduction

In summer days, on-peak energy consumption usually occurs as a result of simultaneous operation of air-conditioners. Therefore, the load-generation mismatch may occur in the interconnected power networks. The probability of voltage collapse, uncontrolled islanding, and the catastrophic wide area blackouts will increase. Additionally, the gas-fired generation stations utilize more natural gas. Meanwhile, the gas suppliers should produce the large volume of gas to fuel the thermal units. Hence, the gas pipelines may be overloaded. For these reasons, the probabilistic

co-optimization of the gas-energy hubs is an important challenge to consider the uncertainties of loads and wind products; find the critical gas nodes and the crucial electrical buses, stressed pipelines, and transmission branches; and minimize the gas extraction cost and the fuel cost of the thermal power plants.

In recent years, several scholars focused on probabilistic investigation of power systems. A new fortuitous optimal power flow (OPF) which has considered the security constraints is proposed in [1]. It was named new multi-period security-constrained OPF. The uncertainties of wind power and load are considered in this method. Compared with Latin hypercube sampling, it might get lower costs. In [2], the enhanced binary black hole algorithm is integrated with the point estimation method (PEM)-based Newton-Raphson power flow for finding the optimum generation schedules of the thermal units, boilers, and the combined heat and power generation units under variable wind speed, solar irradiations, and uncertain demand. This approach is able to improve the bus voltage magnitude and reduce the fuel cost and the greenhouse gas emissions. In [3], the OPF issue is formulated with intermittent renewable energy (IRE) sources and line temperature limits. The impact of IRE uncertainty cost on the OPF is also incorporated into the optimization process. A primal-dual interior point solver is used to solve the nonlinear optimization issue. It is found that the rate of IRE source generation can be higher or lower than the envisaged values due to the IRE stochastic behavior. In [4], the P-OPF that considers the uncertainties of wind power, plug-in electric vehicles, and the photovoltaic is solved for hybrid power systems. In this approach, the Monte Carlo simulation (MCS) and the antithetic variates method (AVM) are applied to specify the probability distribution function (PDF) of the power generation. It is proven that the proposed method has high accuracy than other optimization algorithms. In [5], the correlation between the stochastic loads in transmission grid is considered. The load correlation is modeled by the unscented transformation method and copula approach. Almost both of them reach the similar results, but it is perceived that the copula strategy is more time-consuming. Fang et al. [6] has utilized a sparse correlation matrix to model the spatial-temporal correlation of the wind power forecast. Also, distributional robust chance-constrained OPF model has been considered to receive a reliable economic solution. It has high efficiency within a short time. In [7], an adaptive robust AC-OPF model which includes wind power is suggested. The introduced model is strong against any uncertain input variables. The proposed method cannot be solved by an off-the-shelf optimization package. So, a decomposition strategy depending on basic and binary cuts is suggested to solve the problem. In [8], a new optimization model for economic dispatch of renewable sources within a micro grid environment is proposed. In this method the uncertainty of solar photovoltaic outputs and loads is considered. In [9], a three-step methodology is suggested to solve the chance-constrained optimal power flow problems, which are named formulation, parameterization, and optimization, in order to ensure power balance while retaining economic and secure operation. The results are confirmed for transmission grids under dc power flow suppositions. In [10], a new approach for long-term designing of wind energy regarding its natural uncertainty is proposed. The uncertainty of wind energy is coped through information gap decision theory (IGDT) method. The voltage stability is considered in this algorithm. The

gained results are compared with MCS. In [11], a new method is presented to specify the CDF of output variables in P-OPF. In order to cope with uncertainties of inputs and correlation among them, the ninth-order polynomial normal transformation (NPNT) method is used. Also, the quasi-MCS is applied to obtain the statistical data from the outputs. Results show a high accuracy for CDF with low computational range. In [12], a method to solve OPF considering wind and solar power uncertainties is proposed. To cope with different restrictions, the algorithm is merged with the superiority of feasible (SF) method. Without this method, the limitations of parameters might be disaffirmed. Moreover, this method is predicting wind and solar power outputs. Xia et al. [13] suggest a probabilistic transient stability-constrained optimal power flow (P-TSCOPF) to regard stochastic behavior of load, wind and fault clearing time, and transient stability in power system. To solve this algorithm's problem, PEM and group search optimization (GSO) methods are applied. This method is compared with MCS and the results show the precision of proposed method. In [14], the generalized dynamic factor model (GDFM) to regard correlation among different wind farms is suggested. Meanwhile, artificial bee colony (ABC) method is applied to deal with static optimization problem. The main advantage of this algorithm is a low computational range and minimization of total fuel cost. In [15], a probabilistic multi-objective optimal power flow (MO-OPF) which considers the correlation between wind farms and loads is proposed. For dealing with wind and load uncertainties, PEM based on Nataf transformation is applied. This method is compared with MCS. The results demonstrate a high accuracy of this method. In [16], a multi-objective reactive power dispatch (MO-RPD) problem is discussed using the 2PEM to minimize the real power losses and voltage deviations considering the load uncertainties. Due to load uncertainty, a 2PEM is utilized. This method is compared with MCS. The results show the competence of this method. In [17], an OPF with considering wind-solar power (with their storage) and load uncertainties is discussed. For dealing with these uncertainties, genetic algorithm (GA) and 2PEM methods are employed. The results of comparing proposed method with MSC demonstrate high efficiency of proposed method.

Aien et al. [18] perform a review on probabilistic techniques which are utilized for P-OPF. Then a new method is proposed which is accurate enough to deal with P-OPF problem. This method is called the unscented transformation (UT) method. The basic purpose of this method is to decrease the sampling points. In other words, this method is trying to solve P-OPF issue with low sample points of uncertain input variables but, at the same time, having high accuracy with minor computational range. The introduced method is compared with MCS and 2PEM. The results show the efficiency of proposed method. In [19], OPF considering wind power uncertainty which is modeled by employing two-parameter Weibull probability density function is discussed. For solving optimization problem, Gbest-guided artificial bee colony optimization algorithm (GABC) is utilized. The proposed method is compared with bacteria foraging algorithm and genetic algorithm. It is definite that alteration of voltage profile under probability analysis for proposed method is minor. In [20], P-OPF considering wind power with correlated loads is discussed. It is presumed that wind speed chases Weibull distribution. For correlation among loads, Cholesky

decomposition is used. Then $2m$ and $2m + 1$ PEMs are applied to solve P-OPF issue. The results demonstrate that $2m + 1$ point estimate method is more precise for P-OPF issue. Chen et al. [21] introduces a method to solve P-OPF for power system which includes wind farm. Also, uncertainty of load is considered. For solving P-OPF problem, it has merged cumulants and Gram-Charlier expansion. The suggested algorithm is compared with MCS. The results demonstrate that offered method can solve P-OPF issue quickly. Moreover, the error of this method is admissible. In [22], OPF issue is discussed considering renewable sources which causes grid to go to uncertainty conditions. In this paper, polynomial chaos expansion (PCE) is utilized to revise the input RVs which are infinite-dimensional to finite-dimensional second-order cone program. The main contribution of this algorithm is that it can solve the problem with a single numerical run without needing MCS. So, it has less computational burden. Meanwhile, this method furnishes a feedback policy in terms of the fluctuations. Rahmani et al. [23] introduces a multi-objective information gap decision theory (IGDT) to solve AC OPF issue regarding the wind power and load uncertainties. To solve IGDT problem, directed search domain (DSD) is applied. The results demonstrate the competence of this method. In [24], the quasi-Monte Carlo simulation (QMCS) is proposed for P-OPF problem considering the correlation between wind farms. To model the correlation among wind farms, the copula functions are utilized. This algorithm is employed in PLF, too. In addition to this, QMCS causes decrease of computational range. This method is compared with analytical method and PEM. It is specified that proposed method has high computational speed.

In [25], P-OPF problem considering correlation between various wind farms is discussed. The PDF of wind speed in different wind farms is guessed by Kernel density estimate method which doesn't need to count on assumed probability distribution of variables. Then, pair-copula method is applied to obtain a joint PDF of wind speed between wind farms. Also, it considers the correlation among wind farms. After that, MCS is utilized to solve P-OPF issue. This method's mean comparative error is smaller than copula function. In [26], a new method is suggested to solve OPF problem considering the wind power and different factors of uncertainties. To cope with these uncertainties, evidence theory and affine arithmetic which are merged together are applied. In order to deal with correlation between variables, copula theory and affine arithmetic are utilized. Meanwhile, the uncertainty of wind farm active power and reactive power are modeled and combined with the power flow computation. The results show the precision of this method. Kazemdehdashti et al. [27] introduces a new robust density estimator for P-OPF issue. The generalized cross-entropy (GCE) method is used to describe the approximate density functions of wind power, solar power, and load. Comparing with diffusion method and two-point estimate method, proposed method has less computational range with high precision. Moreover, it considers the correlation among wind and solar farms and loads. Also, this method is more meticulous than MCS. In [28], a new method based on the multivariate Gaussian mixture model (GMM) and the Markov chain Monte Carlo (MCMC) sampling technique is proposed for P-OPF issue. It can deal with different wind speed distributions and consider the correlation

between wind farms. The GMM is utilized to estimate wind speed distribution of various wind farms. Then MCMC sampling method is applied to solve P-OPF issue. Meanwhile, the Sobol-based quasi-Monte Carlo (QMC) technique is combined with MCMC sampling method to gain a quick isotropy speed. Rouhani et al. [29] propose a numerical method to solve P-OPF issue. Parzen window density estimator is utilized to guess the probability of OPF outputs. In proposed algorithm, the uncertainty of wind, load, and plug-in hybrid electric vehicle (PHEV) and the correlation among them are considered. This method is very utilizable when the accessible information is finite. This algorithm is compared with point estimate method and diffusion method. The results demonstrate that proposed method is precise for some variables. In [30], the unscented transformation (UT) is employed to solve P-OPF problem regarding wind and load uncertainties and correlation among them. Also, this method guesses the mean and variance of locational marginal prices. This method is compared with MCS in which the results show the efficiency of proposed method.

As reviewed, many researchers have studied P-OPF of transmission and distribution power systems. But, uncertainties of renewables such as wind and variable nature of demands in coupled natural gas and energy networks have not been discussed, yet. Hence, this chapter aims to present a novel framework for stochastic analysis of gas-power nexus while considering the fluctuations of the wind products, the electrical demand, and gas load of the hybrid systems using Nataf transformation-based $2m + 1$ PEM. In each stochastic scenario, stressed transmission lines and gas pipelines, critical electrical buses and gas nodes, optimal power generation schedules of thermal power plants, and gas extraction pattern of gas suppliers are found under uncertain operating conditions.

Other sections of this chapter are organized as follows: Section 13.2 presents a comprehensive problem formulation on Nataf transformation-based point estimation method. Simulations and discussions are provided in Sect. 13.3. Finally, concluding remarks appear in Sect. 13.4.

13.2 Proposed Methodology

In all alternatives to provide generator's fuel in electrical systems, natural gas gets more attention as power systems' primary fuel because of its lower pollutant emission, economic prospective, environment effects in comparison with fossil fuels, and other advantages. Nowadays, natural gas is a substantial section of the total fuel of generators in so many countries. It forms 40% of generators' fuel in Britain, 39.4% of generators' fuel in America, more than 30% of generators' fuel in Europe, and 29% of generators' fuel in Japan [31]. Hence, the integration of natural gas and electricity systems has increased in the last few decades. So, natural gas is playing an important part in power systems. Among gas and electricity systems, there is a high interdependency. Interdependency among coupled gas-electric systems is studied in [32]. In the past, gas system and electrical system's design and

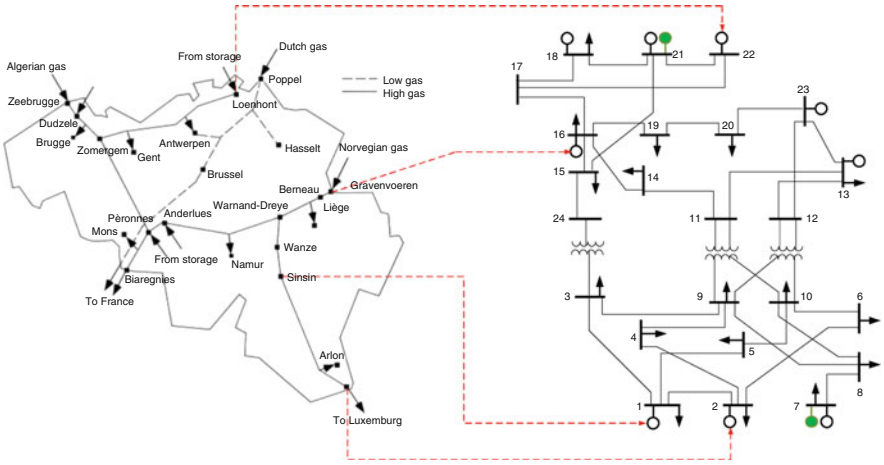

Fig. 13.1 The natural gas- and electricity-coupled networks

operation have performed separately. However, the loads and renewable energy's fluctuations in electrical systems and pressure losses and gas transmission congestion in gas systems can impact the security and stability of power systems. In other words, design of gas and electricity systems separately causes potential challenges of energy storages. To protect the power systems' stability and reliable operation of gas system and electrical system, it is important to analyze both of the systems collectively. On the other hand, wind power penetration makes more challenges in power system operation. Its uncertainty impacts stability of power systems, too. Therefore, it must be considered in power system operation. The effect of wind power is modeled using Weibull distribution which is elaborated in Sect. 13.2.1.

In this chapter, we propose an integrated P-OPF of natural gas and electrical systems under wind power penetration. The electric network is IEEE 24-bus system which is a transmission grid with the voltage levels of 138 kV, 230 kV, and Sbase = 100MVA. The slack bus is bus 13 in this grid. The gas system is Belgium gas network which has 20 gas nodes and 24 pipelines. The mentioned system is shown in Fig. 13.1. In this method, load (gas and electrical) and wind speed are modeled as uncertain variables which are described in the following section. The wind turbines have been added to the 7th and 21th buses. Each wind farm includes four wind turbines. The integrated gas-electricity P-OPF issue is solved using $2m + 1$ PEM based on Nataf transformation. The levels of proposed method are explained in the following sections. The proposed method is robust against wind power, gas, and electrical load uncertainties.

The formulas of gas grid are described in Eqs. (13.1, 13.2, 13.3, 13.4, 13.5, and 13.6):

$$\mathrm{GC} = \sum\nolimits_n c_n Sg_n \tag{13.1}$$

$$\sum\nolimits_m f_{n,m} = \sum\nolimits_m f_{m,n} + Sg_n - \zeta_g Sd_n - Se_n \tag{13.2}$$

$$f_{m,n} = c_{m,n}\sqrt{Pr_m^2 - Pr_n^2} \qquad \text{Passive arcs} \tag{13.3}$$

$$f_{m,n} \geq c_{mn}\sqrt{Pr_m^2 - Pr_n^2} \qquad \text{Active arcs} \tag{13.4}$$

$$Sg_n^{\min} \leq Sg_n \leq Sg_n^{\max} \tag{13.5}$$

$$Pr_n^{\min} \leq Pr_n \leq Pr_n^{\max} \tag{13.6}$$

The electrical network equations are described in Eqs. (13.7, 13.8, 13.9, 13.10, 13.11, 13.12, 13.13, 13.14, and 13.15):

$$\mathrm{EC} = \sum\nolimits_g a_g \left(P_g\right)^2 + b_g P_g + c_g + \sum\nolimits_i \mathrm{VOLL} \times \mathrm{LS}_i \tag{13.7}$$

$$\sum\nolimits_{g \in \Omega_G^i} P_g + \mathrm{LS}_i + P_i^{\mathrm{w}} - P_{d,i} = \sum\nolimits_{j \in \Omega_t^i} P_{ij} : \lambda_i \tag{13.8}$$

$$P_{ij} = \frac{\delta_i - \delta_j}{X_{ij}} \tag{13.9}$$

$$-P_{ij}^{\max} \leq P_{ij} \leq P_{ij}^{\max} \tag{13.10}$$

$$P_g^{\min} \leq P_g \leq P_g^{\max} \tag{13.11}$$

$$P_{g,t} - P_{g,t-1} \leq \mathrm{RU}_g \tag{13.12}$$

$$P_{g,t-1} - P_{g,t} \leq \mathrm{RD}_g \tag{13.13}$$

$$0 \leq \mathrm{LS}_i \leq P_{d,i} \tag{13.14}$$

$$0 \leq P_i^{\mathrm{w}} \leq w_i \Lambda_i^{\mathrm{w}} \tag{13.15}$$

The main objective function and the decision variables are specified as follows:

$$\text{Min OF} = \mathrm{EC} + \mathrm{GC} \tag{13.16}$$

$$\mathrm{DV} = \left\{ \begin{matrix} \delta_i, P_g, P_c, W_c, W_w \\ Sg_n, f_{n,m}, Pr_n \end{matrix} \right\} \tag{13.17}$$

13.2.1 Modeling of Load and Wind Speed Uncertainties

Active demand, either gas or electrical, is generally modeled with normal distribution [33]. The analogous PDF is formulated as follow:

$$f(P_{d,i}) = \frac{1}{\sqrt{(2\pi)\sigma}} \exp\left(-\frac{(P_{d,i}-\mu)^2}{2\sigma^2}\right) \tag{13.18}$$

Wind speed cannot chase normal distribution; however, it approximately follows Weibull distribution. Many researches demonstrate that wind speed can be modeled as two-parameter Weibull distribution either for short-term or long-term period [34, 35]. Weibull distribution is formulated as follows:

$$f(v) = \frac{\mathrm{h}}{c}\left(\frac{v}{c}\right)^{(h-1)} \exp\left(-\left(\frac{v}{c}\right)^{h}\right) \tag{13.19}$$

Output power of wind turbine counts on the wind speed which can be calculated as follows:

$$P_i^{\mathrm{w}}(v_i) = \begin{cases} 0, & 0 \le v_i \le v_{\mathrm{in},i} \\ P_{r,i}\dfrac{v_i - v_{\mathrm{in},i}}{v_{r,i} - v_{\mathrm{in},i}}, & v_{\mathrm{in},i} \le v_i \le v_{r,i} \\ P_{r,i}, & v_r \le v_i \le v_{\mathrm{out},i} \\ 0, & v_{\mathrm{out},i} \le v_i \end{cases} \tag{13.20}$$

13.2.2 Nataf Transformation

As we mentioned in the previous sections, the input RVs of power systems are correlated. In this case, PEM is not useful to solve P-OPF. So, for using PEM to solve P-OPF problem, it is necessary to make these RVs independent. In this way, there are several methods to solve this issue such as polynomial normal transformation (PNT), Rosenblatt transformation, and Nataf transformation. In this chapter, we utilize Nataf transformation due to its high accuracy with low computational burden. Nataf transformation utilizes Copula function to obtain joint PDF of input RVs by applying marginal PDF of RVs and correlation matrix to get relative correlation

matrix in standard normal space. Nataf transformation is explained in detail in [36]. Suppose that the arbitrary input vector $X = (x_1, x_2, \ldots x_n)$ and marginal PDFs $F_i(x_i)$ with correlation matrix C_x are available pursuant to historical information which is gained from numerical studies:

$$C_x = \begin{bmatrix} 1 & \rho_{12} & \cdots & \rho_{1n} \\ \rho_{21} & 1 & \cdots & \rho_{2n} \\ \vdots & \vdots & \ddots & \vdots \\ \rho_{n1} & \rho_{n2} & \cdots & 1 \end{bmatrix}, \qquad \rho_{ij} = \frac{\operatorname{cov}\left(x_i, x_j\right)}{\sigma_i \sigma_j} \tag{13.21}$$

The standard normal vector $Y = (y_1, y_2, \ldots y_n)$ can be obtained as follows:

$$\begin{cases} \Phi(y_i) = F_i(x_i) \\ \\ y_i = \Phi^{-1}(F_i(x_i)) \end{cases} \tag{13.22}$$

By using the above equation, the input RVs are transformed to standard normal space; however, the RVs still correlated with correlation matrix of C_y. In order to calculate C_y , below empirical expression which is proposed in [37] is employed:

$$\rho_{ij} = T\rho_{0ij} \tag{13.23}$$

For two-parameter Weibull distribution, T has the following formulation:

$$\begin{aligned} T = {} & 1.063 - 0.004\rho_{0ij} - 0.2\left(\frac{\sigma_i}{\mu_i} + \frac{\sigma_j}{\mu_j}\right) - 0.001\rho_{0ij}^2 + 0.337\left(\frac{\sigma_i^2}{\mu_i^2} + \frac{\sigma_j^2}{\mu_j^2}\right) \\ & + 0.007\rho_{0ij}\left(\frac{\sigma_i}{\mu_i} + \frac{\sigma_j}{\mu_j}\right) - 0.007\frac{\sigma_i\sigma_j}{\mu_i\mu_j} \end{aligned} \tag{13.24}$$

For normal distribution, $T = 1$. In [37, 38], 49 empirical formulas are introduced to compute T for ten various probability distributions. After computing correlation matrix in standard normal space, Cholesky decomposition is applied to C_y:

$$C_y = L_O L_0^{\mathrm{T}} \tag{13.25}$$

L_O is a lower triangular matrix which can be employed to gain vector $U = (u_1, u_2, \ldots u_n)$ using the following equation:

$$U = L_0^{-1} Y \tag{13.26}$$

U is the independent vector in standard normal space. Hence, utilizing Nataf transformation-independent vector U is obtained from correlated vector X. Then PEM can be used to get samples of input variables. After that, the inverse Nataf transformation is applied to transform these samples from standard normal space to original spaces. For load demand, it doesn't need to transform to normal space. As we said in the previous section, load demand is modeled with normal distribution. It needs to transform to normal space just for wind speed which is modeled with Weibull distribution.

13.2.3 2m + 1 Point Estimation Method

The aim of PEM is to compute the raw moments of output variables. In this chapter, we apply $2m + 1$ PEM to solve P-OPF issue. The $2m + 1$ PEM computes $2m + 1$ points for each input uncertain variable in standard normal space. Then these points are transformed from standard normal space to their original space using inverse Nataf transformation. $2m + 1$ PEM specifies three samples and their weights which are determined as follows for each RV:

$$u_{ik} = \mu_i + \xi_{ik}\sigma_i \qquad (i = 1, 2, 3, \ldots, m;\ \ k = 1, 2, 3) \tag{13.27}$$

The locations ξ_{ik} for each RV are computed as follows:

$$\xi_{ik} = \frac{\lambda_{i3}}{2} + (-1)^{3-k}\sqrt{\lambda_{i4} - \frac{3}{4}\lambda_{i3}^2} \qquad (k = 1, 2);\ \ \xi_{i3} = 0 \tag{13.28}$$

λ_{i3} and λ_{i4} are the skewness and kurtosis of the input RVs, respectively, which are computed in Eqs. (13.29) and (13.30):

$$\lambda_{i3} = \frac{\int_{-\infty}^{\infty}(x_i - \mu_i)^3 f_i dx_i}{\sigma_i^3} \tag{13.29}$$

$$\lambda_{i4} = \frac{\int_{-\infty}^{\infty}(x_i - \mu_i)^4 f_i dx_i}{\sigma_i^4} \tag{13.30}$$

Weighting factors of each sample u_{ik} are computed in following equations:

$$W_{ik} = \frac{(-1)^{3-k}}{\xi_{ik}(\xi_{i1} - \xi_{i2})} \qquad (k = 1, 2) \tag{13.31}$$

$$W_{i3} = \frac{1}{m} - \frac{1}{\lambda_{i4} - \lambda_{i3}^2} \tag{13.32}$$

When the three locations of each input RV are obtained, the deterministic OPF can be solved using each of three samples while other input variables are determined as their mean value. It is obvious that only $2m + 1$ OPF computations need to be executed since $\xi_{i3} = 0$ is correct for all input RVs. Ultimately, the raw moments and standard deviation of output random variable R (total generation cost (gas and electricity), node pressure, power losses, etc.) can be obtained in Eqs. (13.33, 13.34, and 13.35):

$$\mu_n = E[R_n(i,k)] = \sum_{i=1}^{m} \sum_{K=1}^{3} W_{ik}(R_n(i,k)) \tag{13.33}$$

$$E\left[R_n(i,k)^2\right] = \sum_{i=1}^{m} \sum_{k=1}^{3} W_{ik}\left(R_n(i,k)^2\right) \tag{13.34}$$

$$\sigma_n = \sqrt{E\left[R_n(i,k)^2\right] - \mu_n} \tag{13.35}$$

13.3 Simulation Results and Discussions

In this section, we want to apply the proposed method on integrated gas and electric system, which is described in Sect. 13.2. The electric grid is the IEEE 24-bus test system, and the gas grid is Belgian high-calorific 20 node natural gas system. The gas network has 24 pipelines. All information of test system is given in [39]. In this system, we have two wind farms with 317.12 MW rated power, which are connected to the electricity network at bus 7 and 21. The scale parameters are 8.4546 and 3.3125 and shape factors are 1.4925 and 1.3237, respectively. The information of wind turbines is given in Table 13.1. The used wind speed data is the output of weather parameter measurement station. These data are related to 4 months which are measured per hour. The graphs of wind speed data in two different areas are shown in Figs. 13.2 and 13.3.

The gas and electric loads are supposed to confirm to a normal distribution with mean value of nominal load and standard deviation equal to 5% of mean values. Also, wind speed is assumed to follow a two-parameter Weibull distribution [40]. The schematic of the mentioned system is given in Fig. 13.1. Also, three

Table 13.1 The wind turbine parameters

Parameters	Rated power (m/s)	Cut-in speed (m/s)	Cutout speed (m/s)	Rated speed (m/s)
Value	79.28	3	65	37

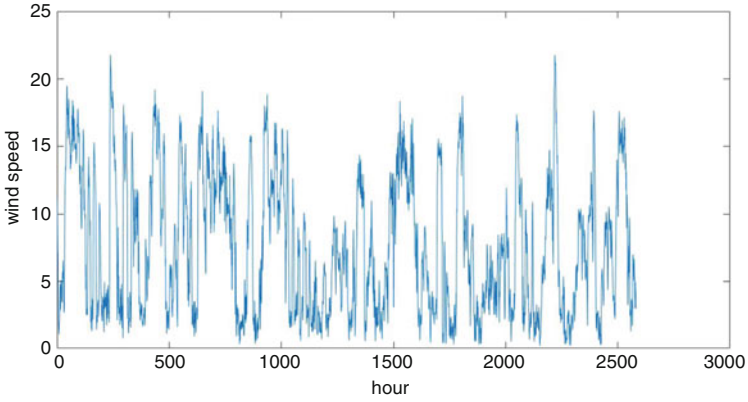

Fig. 13.2 The graph of the wind speed in wind farm A

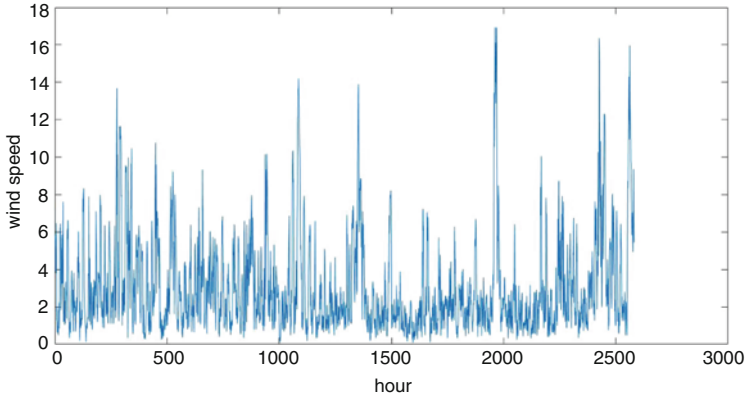

Fig. 13.3 The graph of the wind speed in wind farm B

samples of each electrical and gas demands and wind speeds are given in Tables 13.2, 13.3, and 13.4, respectively.

The proposed model is a nonlinear programming (NLP) problem, which is administered on GAMS (General Algebraic Modeling System) environment using the LP solver in electric network and NLP tool in gas network.

From iteration 1 to 34, the electrical load uncertainties are considered. From iteration 35 up to 52, the gas load uncertainties are considered, and from iteration 53 to 56, the wind speed uncertainty is considered. In iteration 57, all the input variables are specified as their means. Figure 13.4 shows that cost of the electrical grid might be 33.33% more than base state (iteration 57) cost. So, it must be considered in scheduling generation units in order to get an optimal schedule. During iterations 1–52, the two wind farms' produced powers are set in their mean values. In iteration 53, the rate of produced power by wind farm A is high, and because of that the electrical cost has been minimized. In iteration 54, since the rate of produced

Table 13.2 The samples of the electrical demand in different buses

Bus no.	$K = 1$	$K = 2$	$K = 3$
1	117.29	98.6	108
2	105.27	88.5	97
3	195.63	164.45	180
4	80.34	67.54	74
5	77.23	64.92	71
6	147.78	124.23	136
7	135.76	114.12	125
8	185.83	156.22	171
9	190.21	159.9	175
10	211.88	178.1	195
13	288	242.1	265
14	210.86	177.26	194
15	344.52	289.61	317
16	108. 7	91.37	100
18	361.9876	304.2121	333
19	196.74	165.39	181
20	139.1	116.93	128

Table 13.3 The samples of the gas demand

Gas consumer	$K = 1$	$K = 2$	$K = 3$
Antwerpen	4.383	3.684	4.034
Arlon	0.241	0.202	0.222
Blaregnies	16.967	14.262	15.616
Brugge	4.257	3.578	3.918
Gent	5.712	4.802	5.256
Liege	6.936	5.83	6.385
Mons	7.443	6.257	6.848
Namur	2.302	1.935	2.12
Petange	2.086	1.754	1.919

Table 13.4 The samples of the wind speed

Wind speed	$K = 1$	$K = 2$	$K = 3$
A	18.1742	1.0635	6.5694
B	7.6437	0.3347	2.5381

power by both wind farms are zero, generating units must compensate the additional load. So, in this case the cost of electrical network has been maximized. The cost of gas grid during scenarios of $2m + 1$ PEM is shown in Fig. 13.5. According to this figure, rate of gas load in Blaregnies determines the maximum and minimum cost of gas network. And Fig. 13.6 shows the total cost of test system, which is obtained by summing electrical and gas costs together. Due to the existing conditions in the system and optimization problem, most of the generating units are producing maximum limit of their capacity during all the scenarios. Figure 13.7 indicates the produced power of the thermal unit 10 during scenarios of $2m + 1$ PEM. Pursuant to

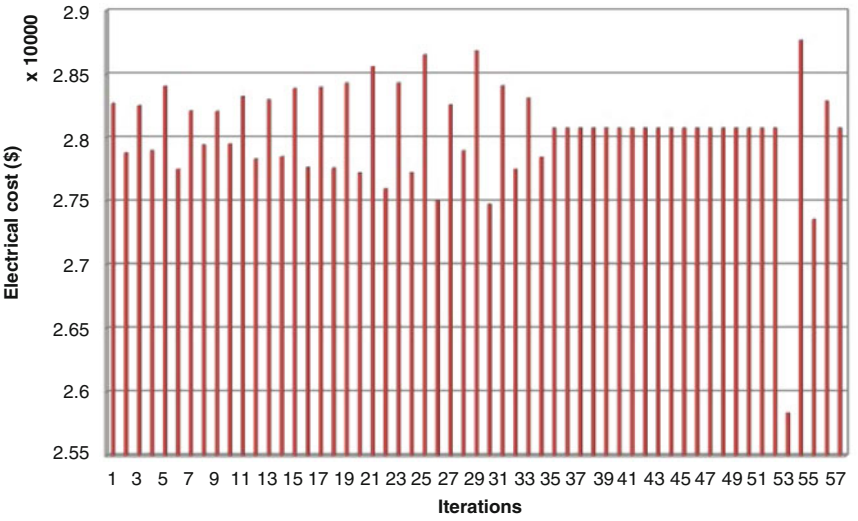

Fig. 13.4 The electrical cost

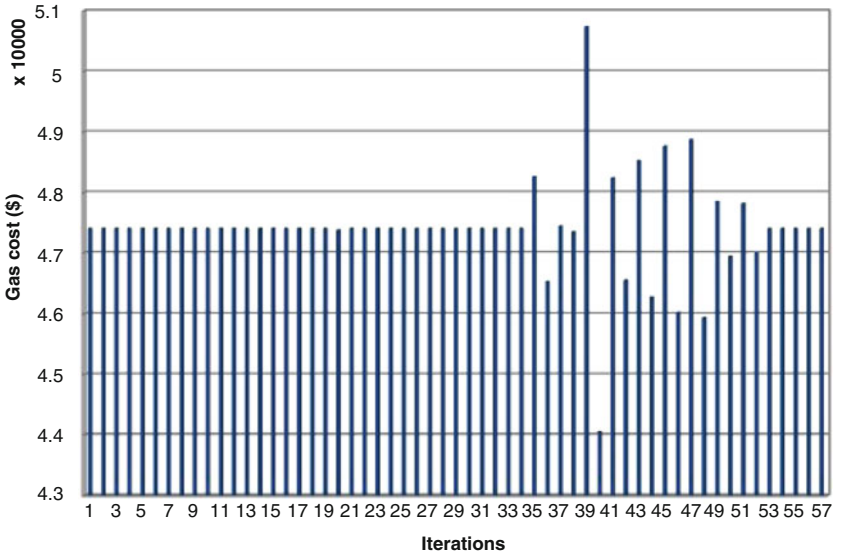

Fig. 13.5 The gas cost

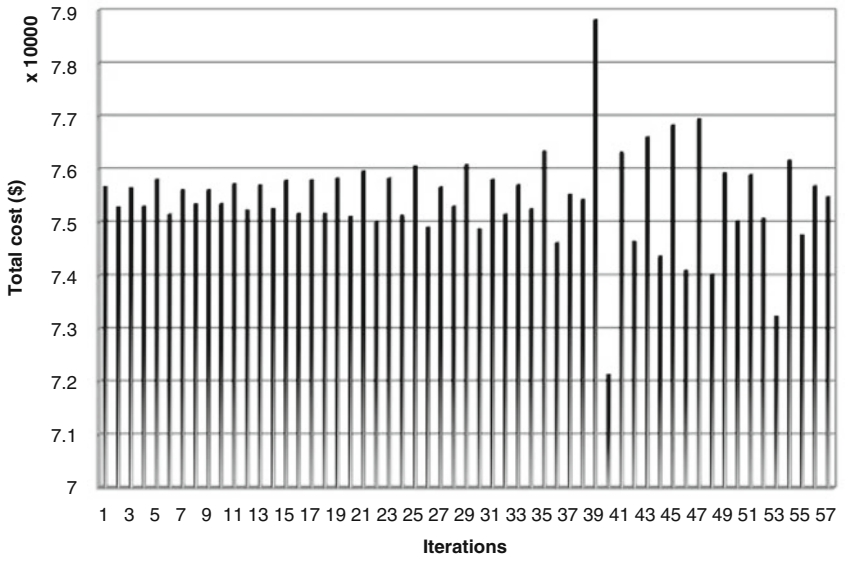

Fig. 13.6 The total cost

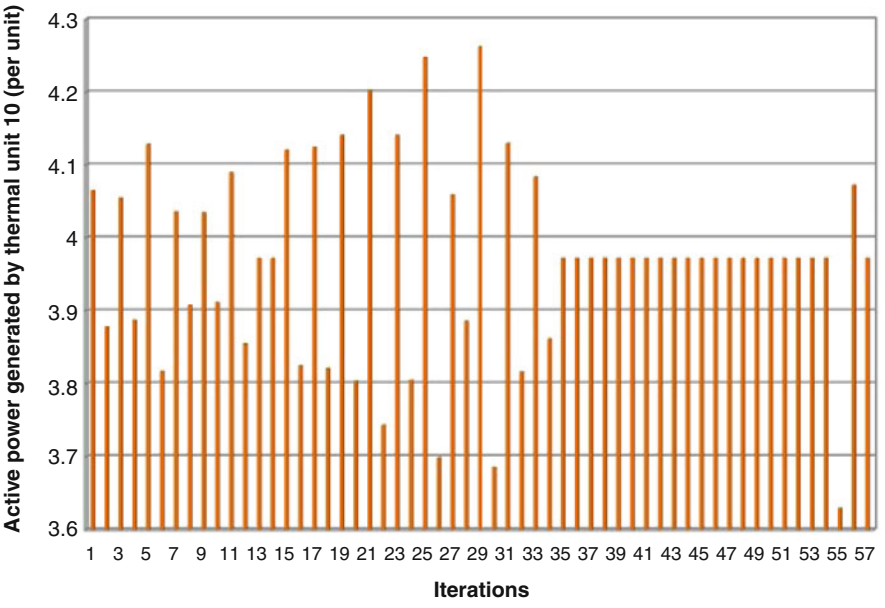

Fig. 13.7 The optimum generation schedules of thermal unit 10

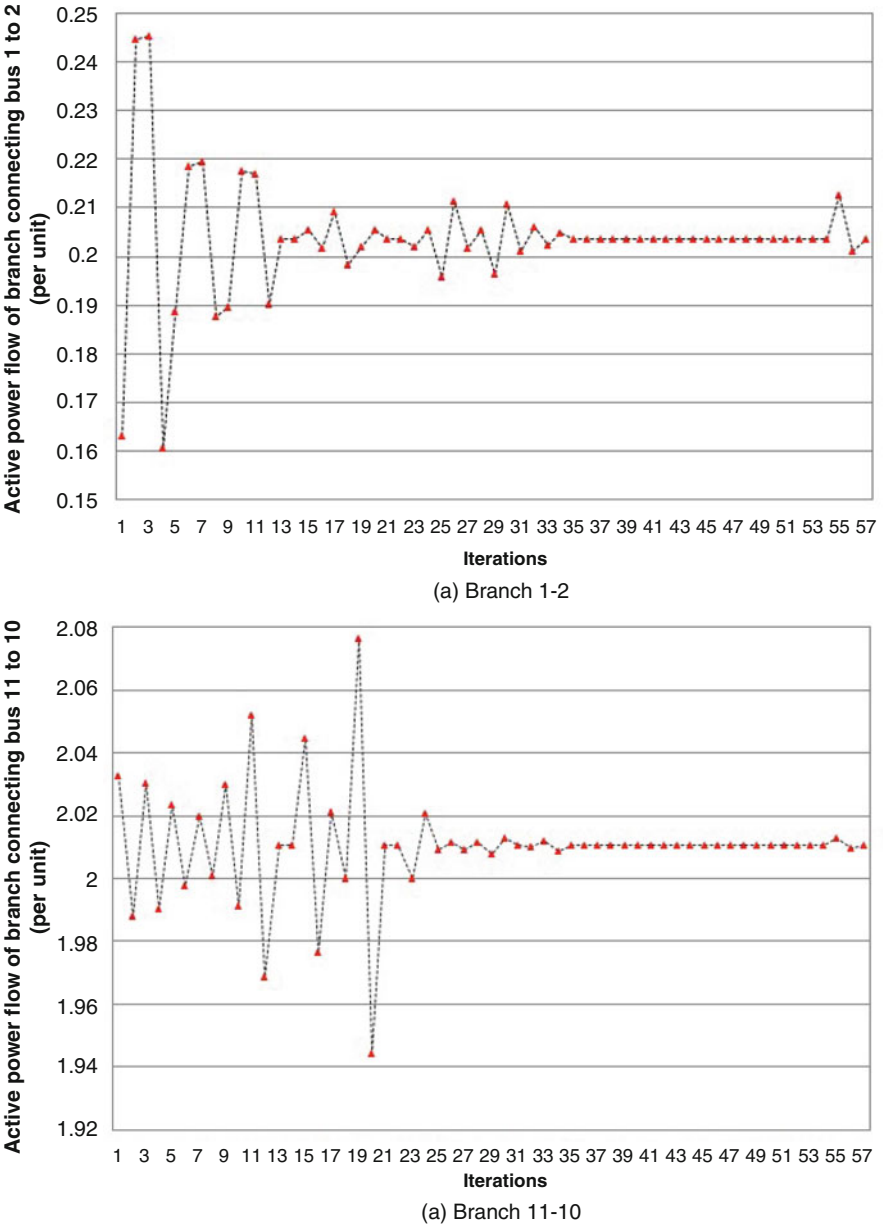

Fig. 13.8 The active power flow of the transmission lines 1–2 and 11–10. (**a**) Branch 1–2. (**b**) Branch 11–10

the situation, we can compensate the additional load system by setting this thermal unit in each scenario. The maximum and minimum value of produced power by this unit occurred in iterations 29 and 55, respectively. Figure 13.8 *(sections a and b)*

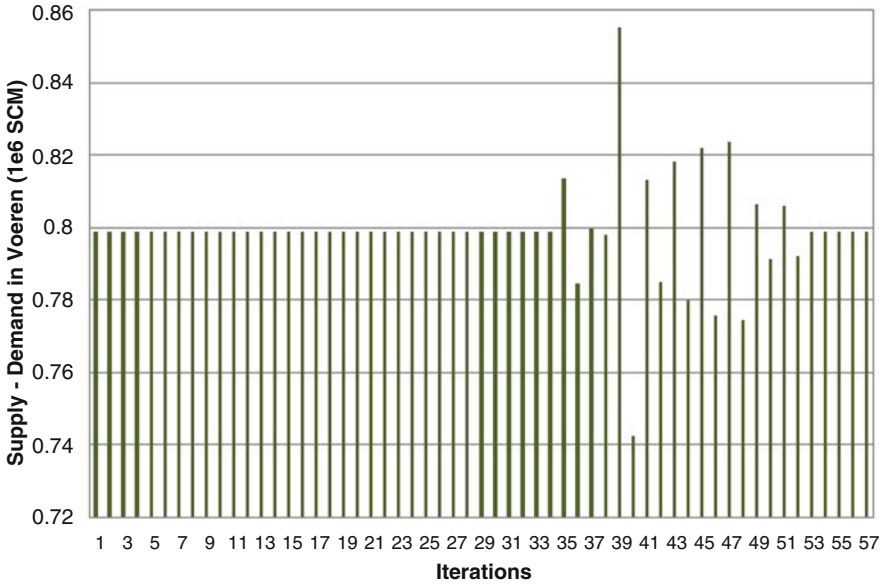

Fig. 13.9 The produced gas at Voeren

shows the active power flow's *fluctuations* from bus 1 to 2 and 11 to 10, respectively. We can see the impact of the stochastic behavior of electrical load demands and wind speed in *the rate of* active power flow in branches. The maximum limit of active power, which can be transmitted through branches 1–2 and 11–10, is 1.75 and 4 per unit, respectively. According these figures, it is concluded that the branches have enough capacity to tolerate extra transmitted power and not become overloaded. The rate of gas supply at Voeren in each scenario is illustrated in Fig. 13.9. It can be observed that the gas demand of Blaregnies specifies the maximum and minimum gas supply in Voeren. Figure 13.10 *(sections a and b)* demonstrates the gas pressure in Antwerpen and Sinsin, respectively. Maximum and minimum value of gas pressure in Antwerpen is 80 and 30 and in Sinsin is 63 and 0. Also, we can see the fluctuations of gas pressure in these two gas supplies between iterations 35 and 52, which are related to gas demand uncertainties. Figure 13.11 shows the pipe flow variations in Voeren to Berneau node. It can be noticed that stochastic behavior of gas demands during 35–52 iterations highly impacts the power flows in gas nodes. And finally Fig. 13.12a, b demonstrates the voltage angle in bus 2 and 18, respectively. Maximum and minimum value of voltage angle in each bus must be limited between $-\pi/2$ and $\pi/2$ radian. Regarding this figure, maximum and minimum value of voltage angle at bus 2 is -0.36873 and -0.35191 radian and at bus 18 is 0.214612 and 0.258696 radian. It is comprehended that during simulation phases, we don't have a critical condition in voltage angle.

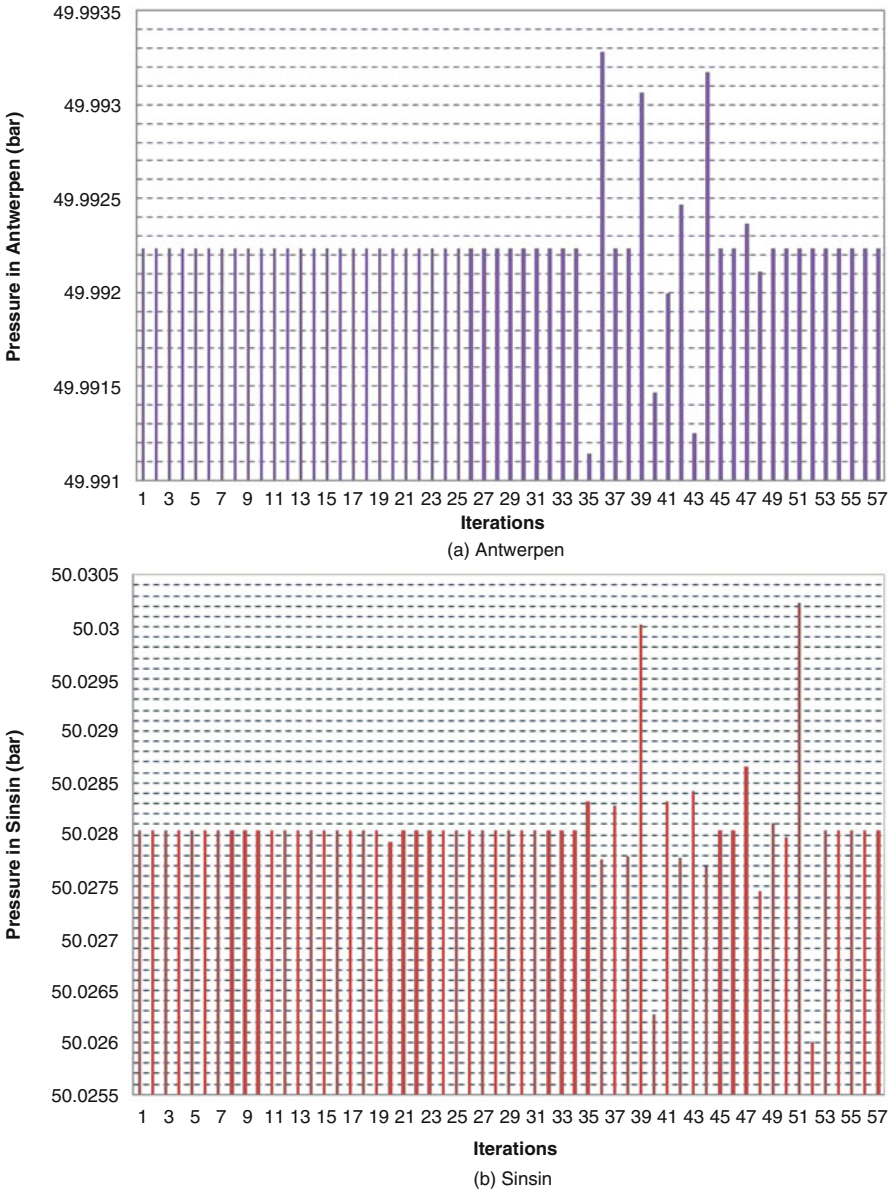

Fig. 13.10 The gas pressure at Antwerpen and Sinsin. (**a**) Antwerpen (**b**) Sinsin

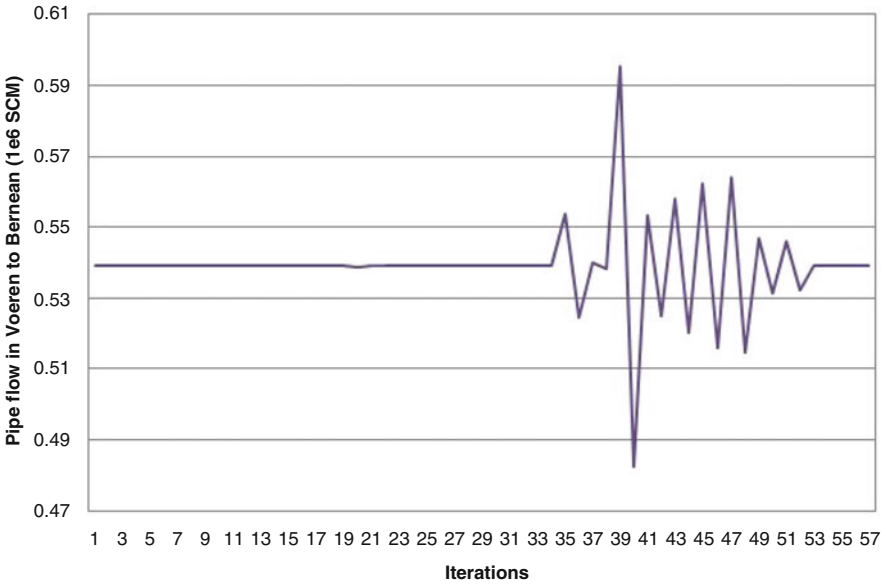

Fig. 13.11 The pipe flow in Voeren to Berneau

13.4 Conclusion and Future Trend

This chapter presents a $2m + 1$ PEM based on Nataf transformation to solve P-OPF issue. The stochastic behavior of electrical demand, gas demand, and wind speed is considered. The main contribution of employing Nataf transformation is to make the input RVs uncorrelated. Hence, PEM can be employed to solve P-OPF issue. The Nataf transformation applies the normal Copula function to build the joint PDFs of the input RVs with information of the marginal distributions and their correlation coefficients. Therefore, this method is more appropriate than conventional methods. Then, a nonlinear programming problem was solved under generalized algebraic mathematical modeling system to detect the best operating point of the system under different gas and electricity load levels and various wind speed. The effectiveness of proposed method was indicated by applying to integrated gas power system. All operational limits of P-OPF and power balance criterion were satisfied in optimization process. Minimization of thermal generating units' cost was accomplished as single objective function. It is demonstrated that the output of the discussed optimization problem, which is gained by the GAMS optimization software using CPLEX and CONOPT solvers, is highly effected by electrical and gas demands and wind speed uncertainties which must be regarded in designing and operating system. In

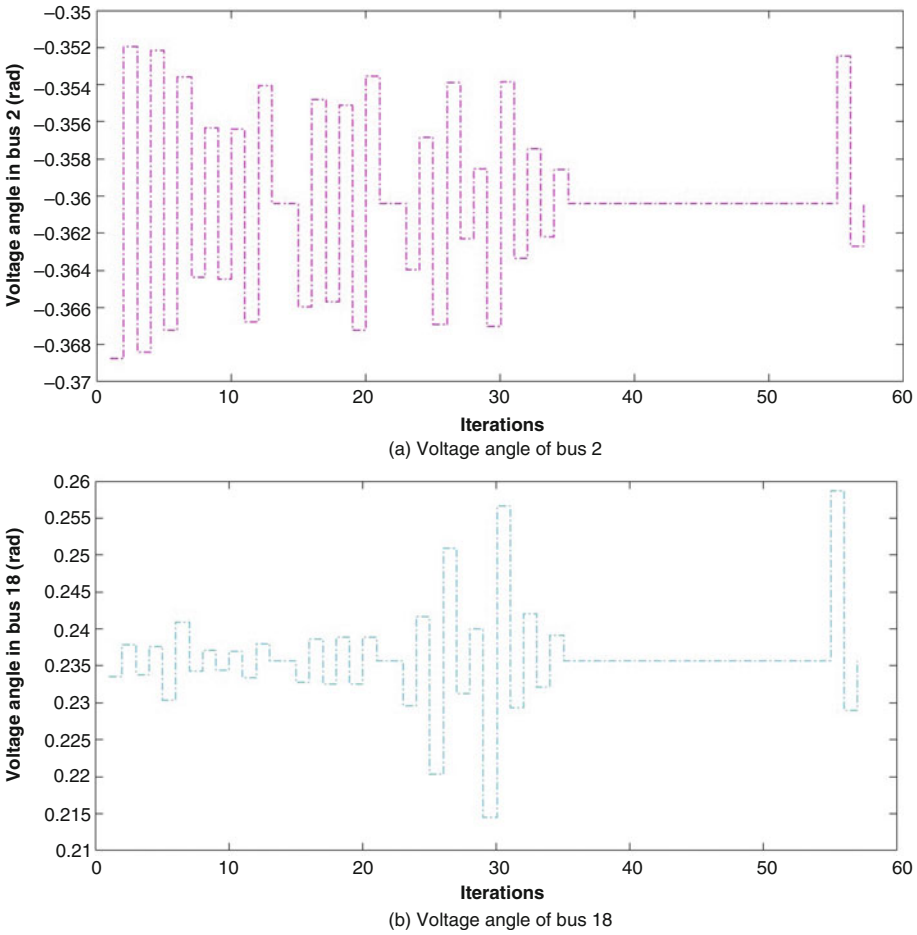

Fig. 13.12 The voltage angle at buses 2 and 18. (**a**) Voltage angle of bus 2. (**b**) Voltage angle of bus 18

future work, we will perform this method on integrated water, gas, and electricity system. Moreover, we can regard the demand response in our discussed problem.

References

1. Sharifzadeh, H., Amjady, N., & Zareipour, H. (2017). Multi-period stochastic security-constrained OPF considering the uncertainty sources of wind power, load demand and equipment unavailability. *Electric Power Systems Research, 146*, 33–42.

2. Azizipanah-Abarghooee, R., et al. (2015). Optimal power flow based TU/CHP/PV/WPP coordination in view of wind speed, solar irradiance and load correlations. *Energy Conversion and Management, 96*, 131–145.
3. Ngoko, B. O., Sugihara, H., & Funaki, T. (2018). Optimal power flow considering line-conductor temperature limits under high penetration of intermittent renewable energy sources. *International Journal of Electrical Power & Energy Systems, 101*, 255–267.
4. Morshed, M. J., Hmida, J. B., & Fekih, A. (2018). A probabilistic multi-objective approach for power flow optimization in hybrid wind-PV-PEV systems. *Applied Energy, 211*, 1136–1149.
5. Abbasi, S., et al. (2018). Transmission network expansion planning considering load correlation using unscented transformation. *International Journal of Electrical Power & Energy Systems, 103*, 12–20.
6. Fang, X., et al. (2018). Modelling wind power spatial-temporal correlation in multi-interval optimal power flow: A sparse correlation matrix approach. *Applied Energy, 230*, 531–539.
7. Attarha, A., Amjady, N., & Conejo, A. J. (2018). Adaptive robust AC optimal power flow considering load and wind power uncertainties. *International Journal of Electrical Power & Energy Systems, 96*, 132–142.
8. Grover-Silva, E., et al. (2018). A stochastic optimal power flow for scheduling flexible resources in microgrids operation. *Applied Energy, 229*, 201–208.
9. Mühlpfordt, T., Faulwasser, T., & Hagenmeyer, V. (2018). A generalized framework for chance-constrained optimal power flow. *Sustainable Energy, Grids and Networks, 16*, 231–242.
10. Rabiee, A., Nikkhah, S., & Soroudi, A. (2018). Information gap decision theory to deal with long-term wind energy planning considering voltage stability. *Energy, 147*, 451–463.
11. Zou, B., & Xiao, Q. (2014). Solving probabilistic optimal power flow problem using quasi Monte Carlo method and ninth-order polynomial normal transformation. *IEEE Transactions on Power Systems, 29*(1), 300–306.
12. Biswas, P. P., Suganthan, P. N., & Amaratunga, G. A. J. (2017). Optimal power flow solutions incorporating stochastic wind and solar power. *Energy Conversion and Management, 148*, 1194–1207.
13. Xia, S., et al. (2016). Probabilistic transient stability constrained optimal power flow for power systems with multiple correlated uncertain wind generations. *IEEE Transactions on Sustainable Energy, 7*(3), 1133–1144.
14. Bai, W., Lee, D., & Lee, K. (2016). Stochastic dynamic optimal power flow integrated with wind energy using generalized dynamic factor model. *IFAC-PapersOnLine, 49*(27), 129–134.
15. Shargh, S., et al. (2016). Probabilistic multi-objective optimal power flow considering correlated wind power and load uncertainties. *Renewable Energy, 94*, 10–21.
16. Mohseni-Bonab, S. M., et al. (2016). A two-point estimate method for uncertainty modeling in multi-objective optimal reactive power dispatch problem. *International Journal of Electrical Power & Energy Systems, 75*, 194–204.
17. Reddy, S. S. (2017). Optimal power flow with renewable energy resources including storage. *Electrical Engineering, 99*(2), 685–695.
18. Aien, M., Rashidinejad, M., & Firuz-Abad, M. F. (2015). Probabilistic optimal power flow in correlated hybrid wind-PV power systems: A review and a new approach. *Renewable and Sustainable Energy Reviews, 41*, 1437–1446.
19. Roy, R., & Jadhav, H. T. (2015). Optimal power flow solution of power system incorporating stochastic wind power using Gbest guided artificial bee colony algorithm. *International Journal of Electrical Power & Energy Systems, 64*, 562–578.
20. Li, X., Cao, J., & Du, D. (2015). Probabilistic optimal power flow for power systems considering wind uncertainty and load correlation. *Neurocomputing, 148*, 240–247.
21. Chen, M. J., Chen, Y. Q., Dong, W. C., & Wu B. (2015). Containing wind farm power system probabilistic optimal power flow calculation using the method of combined cumulants and Gram-Charlier expansion. In *Advanced materials research*, *Trans Tech Publ*, *1071*, 193–199.

22. Mühlpfordt, T., et al. (2017). Solving optimal power flow with non-Gaussian uncertainties via polynomial chaos expansion. In *Decision and Control (CDC), 2017 IEEE 56th Annual Conference on*. IEEE.
23. Rahmani, S., & Amjady, N. (2018). Non-deterministic optimal power flow considering the uncertainties of wind power and load demand by multi-objective information gap decision theory and directed search domain method. *IET Renewable Power Generation, 12*(12), 1354–1365.
24. Xie, Z. Q., et al. (2018). Quasi-Monte Carlo based probabilistic optimal power flow considering the correlation of wind speeds using copula function. *IEEE Transactions on Power Systems, 33* (2), 2239–2247.
25. Cao, J., & Yan, Z. (2017). Probabilistic optimal power flow considering dependences of wind speed among wind farms by pair-copula method. *International Journal of Electrical Power & Energy Systems, 84*, 296–307.
26. Luo, J., Shi, L., & Ni, Y. (2018). A solution of optimal power flow incorporating wind generation and power grid uncertainties. *IEEE Access, 6*, 19681–19690.
27. Kazemdehdashti, A., Mohammadi, M., & Seifi, A. R. (2018). The generalized cross-entropy method in probabilistic optimal power flow. *IEEE Transactions on Power Systems, 33*(5), 5738–5748.
28. Sun, W., et al. (2018). *Probabilistic optimal power flow considering correlation of wind farms via Markov Chain Quasi-Monte Carlo sampling.* arXiv preprint arXiv:1809.05228.
29. Rouhani, M., Mohammadi, M., & Kargarian, A. (2016). Parzen window density estimator-based probabilistic power flow with correlated uncertainties. *IEEE Transactions on Sustainable Energy, 7*(3), 1170–1181.
30. Qiao, C., Livani, H., & Fadali, M. S. (2015). *Probabilistic optimal power flow using unscented transformation*. In *North American Power Symposium (NAPS),* 2015. IEEE.
31. Du, D., & Huang, H. (2013). Experience and enlightenment of gas generation abroad. *Shanghai Gas, 2*, 23–26.
32. Li, T., Eremia, M., & Shahidehpour, M. (2008). Interdependency of natural gas network and power system security. *IEEE Transactions on Power Systems, 23*(4), 1817–1824.
33. Villanueva, D., Feijóo, A. E., & Pazos, J. L. (2014). An analytical method to solve the probabilistic load flow considering load demand correlation using the DC load flow. *Electric Power Systems Research, 110*, 1–8.
34. Garcia, A., et al. (1998). Fitting wind speed distributions: A case study. *Solar Energy, 62*(2), 139–144.
35. Lalas, D., Tselepidaki, H., & Theoharatos, G. (1983). An analysis of wind power potential in Greece. *Solar Energy, 30*(6), 497–505.
36. Li, H., Lü, Z., & Yuan, X. (2008). Nataf transformation based point estimate method. *Chinese Science Bulletin, 53*(17), 2586.
37. Liu, P.-L., & Der Kiureghian, A. (1986). Multivariate distribution models with prescribed marginals and covariances. *Probabilistic Engineering Mechanics, 1*(2), 105–112.
38. Der Kiureghian, A., & Liu, P.-L. (1986). Structural reliability under incomplete probability information. *Journal of Engineering Mechanics, 112*(1), 85–104.
39. De Wolf, D., & Smeers, Y. (2000). The gas transmission problem solved by an extension of the simplex algorithm. *Management Science, 46*(11), 1454–1465.
40. Li, Y., et al. (2014). Probabilistic optimal power flow considering correlations of wind speeds following different distributions. *IEEE Transactions on Power Systems, 29*(4), 1847–1854.

Chapter 14
A Review on the Technical and Economic Prospects of Biofuel Production from Integrated Biomass Gasification and Fischer-Tropsch Processes

Karittha Im-orb and Amornchai Arpornwichanop

Nomenclature

Sets

i	Chemical species
j	Reactions
n	The length of hydrocarbon chain

Variables

a, b	Reaction constant
$\mathrm{COST}_{\mathrm{size1}}$	Cost of a base scale
$\mathrm{COST}_{\mathrm{size2}}$	Cost of a required scale
M_n	Mole fraction of hydrocarbon with chain length n
n_i	Number of moles of component i per mole of biomass
P_i	Partial pressure of component i
a_i	Mole fraction of component i
γ_i	Mole fraction of component i
sf	Power scaling factor
$S_{\mathrm{C5+}}$	Selectivity of hydrocarbon with a chain length longer than five

K. Im-orb
Faculty of Food-Industry, King Mongkut's Institute of Technology Ladkrabang, Bangkok, Thailand
e-mail: karittha.im@kmitl.ac.th

A. Arpornwichanop (✉)
Center of Excellence in Process and Energy Systems Engineering, Department of Chemical Engineering, Faculty of Engineering, Chulalongkorn University, Bangkok, Thailand
e-mail: Amornchai.A@chula.ac.th

F. Jabari et al. (eds.), *Integration of Clean and Sustainable Energy Resources and Storage in Multi-Generation Systems*,
https://doi.org/10.1007/978-3-030-42420-6_14

$SIZE_1$	Size of a base scale
$SIZE_2$	Size of a required scale
[CO]	CO concentration in the FT-feed gas
$[H_2]$	H_2 concentration in the FT-feed gas
R_{CO}	Reaction rate of carbon monoxide (mol s^{-1} kg_{cat}^{-1})
α	Chain growth probability
W_n	Weight fraction of hydrocarbon with chain length n
P_{Total}	Operating pressure of FT reactor (bar)
k_j	Rate constant of reaction j
$E_{A,\,j}$	Activation energy of reaction j (kJ mol^{-1})
ΔH_{ads}	Heat of adsorption
T	Operating Temperature (K)

14.1 Introduction

The world consumption rate of fossil fuel is increasing rapidly due to strong economic growth. The gases released from energy production units result in air pollution and global warming problems. All industrialized and some developing countries have therefore enacted rigorous environmental laws to control the emissions of pollutant gases. The transportation sector which utilizes a large amount of fossil-derived transportation fuels such as diesel and gasoline is responsible for a substantial percentage of total carbon dioxide (CO_2) emissions. Concerns about energy shortage and the environment impact motivate the expanded consumption of nonfossil fuel sources in the transportation sector. By year 2050, the market share of advanced biofuels in the transportation sector of the European Union (EU) is expected to be in the range of 10–30% [1].

Biomass is an alternative energy resource that recently performs a crucial role in the energy generation industry, as it is environmentally friendly and CO_2 neutral. Several biomass sources have been introduced for use, including several tree species, agro-crops, and crop residue. In 2014, the global energy supply from biomass was 10.3% of total energy [2]. The production of biodiesel and bioethanol uses only certain parts of a plant, such as sugar, oil, cellulose, or starch, while the entire plant can be gasified in the gasification process. One promising technology used to produce green liquid transportation fuels from biomass is the biomass gasification (BG) and Fischer-Tropsch (FT) process [3]. The ultraclean liquid fuel from the FT process has low aromatic content and is free of sulfur, resulting in low emission of CO_2 and NO_x and zero emission of particulate matter compared to fuels derived from crude distillation when used in combustion units. Moreover, the specifications of FT fuel can be adjusted to meet customer requirements during the distillation or hydro-treatment processes. Additionally, FT transportation fuel can be integrated into existing infrastructure and automotive technology very well.

Integrated gasification and FT synthesis are not a new process. This process has been commercialized; however, its application has mainly been limited to coal feedstocks. SASOL Synfuels operates two coal-to-liquid (CTL) plants that supply 28% of South Africa's diesel demand [4]. Inner Mongolia Yitai CTO Company Limited has produced 160,000 tons of oil products per year since 2009 and plans to launch four CTL plants to increase its oil production to 20 million tons per year [5]. However, a few BG-FT plants utilize different gasification technologies on a commercial scale. In 2007, CHOREN Industries established the BG-FT demonstration plant in Freiberg, Germany, which produces 15,000 tons of biofuel per year. However, it was stopped in 2012 because of financial difficulties [6]. British Airways has signed a 10-year agreement to take 60 million liters a year of bio-jet fuel produced from London's municipal waste by Solena Fuels Corporation [7]. Table 14.1 summarizes the established BG-FT plants.

Although several commercial BG-FT plants are in operation, process studies are still carried out to enhance the process performance in technical, environmental, and economic points of view to compete with fossil-based fuels. The subsequent section describes the current status of the BG-FT process, the basic background of the BG-FT process including the BG, gas cleaning, and FT processes, and the research and development efforts in the three major units of the BG-FT process (i.e., the BG, gas cleaning and conditioning, and FT processes) to improve its overall performance efficiency and to increase its competitiveness with fossil-derived oil. In gas cleaning section, the review related to tar removal processes to produce synthesis gas (syngas) satisfying the FT specification has been quite limited; therefore, the work related to this topic is also included in this review. Simultaneously, the technical and economic potential of the BG-FT process for transportation fuel production is also discussed. Finally, future trends in the BG-FT process are described.

14.2 The Integrated Biomass Gasification and Fischer-Tropsch Synthesis Process

The BG-FT is an interesting process utilized to generate green liquid transportation fuels [10]. As illustrated in Fig. 14.1, the BG-FT process involves three main subprocesses: the BG, gas cleaning and conditioning, and FT processes. Firstly, the biomass is converted to a raw syngas in the gasifier, which normally uses oxygen (O_2) as a gasifying agent. Subsequently, impurities are removed from the produced gas, and its hydrogen-to-carbon monoxide (H_2/CO) ratio is tuned during the gas cleaning and gas conditioning processes, respectively. Then, the cleaned syngas that meets the FT specifications is compressed to the expected pressure prior to entering the FT process, where the desired hydrocarbon products are synthesized.

Table 14.1 Established BG-FT plants [8, 9]

Organization (location)	Year	Gasifier technology	Scale and reactor details
Frontline BioEnergy, LLC (Pasadena Texas, USA)	2013	TarFreeGas® gasification	Pilot plant 1575 tpd feed (wood, agricultural residue) SGC Energia's FT Co catalyst 1 bpd light and heavy FT intermediates
Solena Fuels, Green Sky (Essex, UK)	2015	Solena plasma gasification	Commercial 1575 tpd feed (commercial waste and municipal) Velocys microchannel FT reactor Co catalyst 1157 bpd jet fuel
SYNDIESE, CEA (Nevada, USA)	2015	Entrained flow, O_2 blown, high-pressure gasifier	Commercial 205 tpd feed (forest and agricultural waste) 530 bpd liquid fuel
Sierra Biofuels, Fulkrum Bio-energy (Nevada, USA)	2016	TRI steam reformer	Commercial 400 tpd biomass feed (municipal solid waste) Velocys FT reactor Co catalyst 657 bpd liquid fuel
Red Rock Biofuels (Oregon, USA)	2017	TRI steam reformer	Commercial 460 tpd feed (forest and saw mill waste) Velocys FT reactor Co catalyst 1100 bpd liquid fuel
Velocys (Gussing, Austria)	2010	Dual fluidized bed gasifier	Pilot plant 150 tpd dry biomass feed Microchannel FT reactor Co catalyst 1 bpd FT products
CUTEC (Germany)	2010	CFB, steam-O_2 gasification	Laboratory 2.7 tpd dry biomass feed Fixed-bed FT reactor Co catalyst 150 mlpd FT products

14.2.1 Gasification

A gasification process involved the partial oxidation of a carbonaceous substance. This process can be achieved by supplying oxygen less than that needed for the complete combustion at temperature range of 600–1500 °C. This process is an

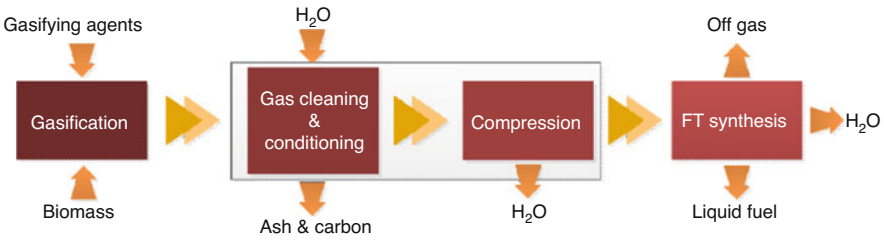

Fig. 14.1 Schematic of the BG-FT process. (Adapted from [11])

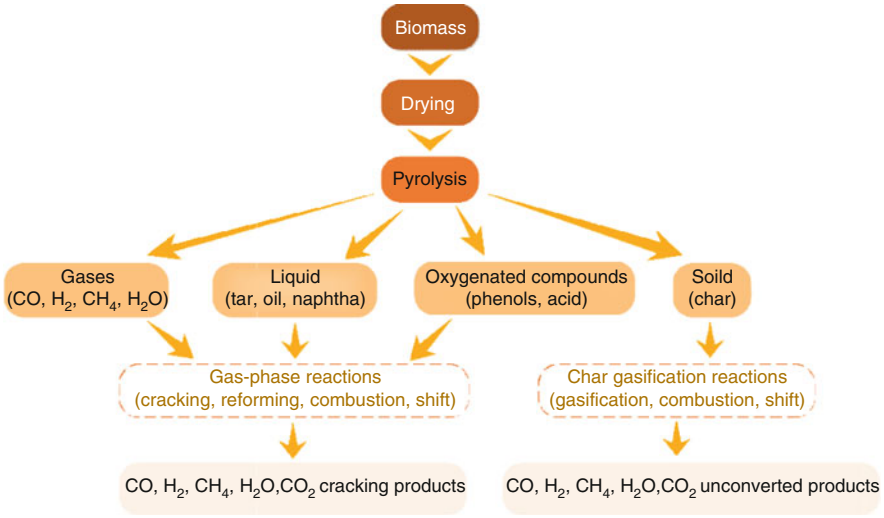

Fig. 14.2 Basic chemistry involves the gasification of biomass. (Adapted from [12])

intermediate process between combustion and pyrolysis. The calorific value of the produced gas, which consists of combustible and noncombustible gases, depends on the type of the process and operation parameters. During biomass gasification, the gasifying agents react with the solid biomass to produce a synthesis gas (syngas), char, and heavy hydrocarbons (tar). Figure 14.2 illustrates the complex series of chemical reactions within biomass gasification.

Some experiments and theoretical studies based on thermodynamic and kinetic models have been done to investigate the gasification process by considering the influence of the feedstock characteristics (i.e., particle size, density, and moisture content), operating parameters (i.e., gasifying pressure and temperature), and type of gasifying agents on its performance.

14.2.1.1 Influence of the Feedstock Characteristics

Various chemical and physical characteristics of the biomass, such as its moisture content and particle size, may affect the gasification behavior. The equilibrium model of a downdraft gasifier was proposed by Zainal et al. [13] and used to examine the influence of the change in the initial moisture content and gasifying temperature in wood on the syngas heating value. They found that the syngas heating value decreased when the moisture content increased. Tinaut et al. [14] studied the influence of the biomass particle size on the performance of a downdraft fixed-bed gasifier. Their result showed that the maximum efficiency was achieved when a smaller particle size was used. The effect of using different types of biomass was also studied. The gasification of palm oil fronds was examined by Atnaw et al. [15]. The results indicated that the syngas heating value, the cold gas efficiencies, and the derived carbon conversion were comparable to those of woody biomass. The syngas heating value was found to decrease when the moisture content of wood or the gasifying temperature increased. Mavukwana et al. [16] developed a thermodynamic gasification model of the sugarcane bagasse. Their model underpredicted the concentration of methane (CH_4), whereas the concentration of H_2 was slightly overpredicted. Nevertheless, the overall predictions agreed well with the reported experimental results. Ramzan et al. [17] investigated the impact of moisture content in solid waste feedstock generated from both households and the industrial sector, including poultry waste, food waste, and municipal solid waste, on the performance of gasification process. The energy production from low-density nonwoody biomass via gasification process has also received increased attention because it is abundant and widely available. However, some fluidization problems and high energy input requirement have been encountered. Widjaya et al. [18] reported that the upgrading of nonwoody biomass into a good-quality solid fuel might be the best alternative options before it was fed to the gasifier.

14.2.1.2 Parametric Study of Gasification

Gasifying agents

Utilization of different types of gasifying agent (i.e., O_2, steam, CO_2, air, or a mixture thereof) results in the production of gases with different heating values because of their different compositions. The energy demand of the systems using different gasifying agents has also been studied. Several works have investigated the effect of using different types and amounts of gasifying agents on the composition and calorific value of the produced syngas and the total energy consumption of the system. Previous works showed that the steam gasification could increase the calorific value of the syngas to 10–18 MJ Nm^{-3} compared to the 4–7 MJ Nm^{-3} of the air gasification [19, 20]. Bhattacharya et al. [21] examined the impact of the percentage of O_2 in the gasifying agent (between 85 and 99%) and the equivalence ratio (ER) (between 2 and 4) on the exergy efficiency of the system. In their work,

the concentration of H_2 in the produced syngas was found to increase with an increase of ER; therefore, the cold gas and exergy efficiencies were also increased. On the other hand, these efficiencies were relatively unaffected by the purity of O_2 containing in the gasifying agent. Shayan et al. [22] investigated and compared the gasification performance with different gasifying agents (i.e., steam, air, O_2, and O_2-enriched air) using their developed thermodynamic model. The results indicated that the highest yield of H_2 was achieved in the steam system, followed by O_2, O_2-enriched air, and air systems, respectively. Moreover, the highest sensible energy efficiency was achieved in air gasification, while the maximum exergy efficiency was achieved in steam gasification. The influence of gasifying agent on the content of inorganic substance in the produced gas was also studied. Effect of the steam-to-biomass ratio (SB) and the ER on the gaseous chloride distribution in the gasification process was studied by Gai et al. [23]. The results indicated that these parameters had a strong effect on gaseous chloride distribution. In addition to air, steam, and O_2, CO_2 is used as a gasifying agent and offers several benefits, i.e., not requiring energy for vaporization, allowing a wide range of H_2/CO ratios in the syngas, and resulting in more volatiles being obtained during devolatilization due to the crucial role of the Boudouard reaction, resulting in efficient gasification. Moreover, CO_2 recycling could offer environmental benefits [24]. Chaiwatanodom et al. [25] investigated the biomass gasification with the CO_2 recirculation. They found that the recycled CO_2 improved the production rate of syngas. However, only the condition of low temperature and high pressure was beneficial when using recycled CO_2 in terms of energy demand. The gasification of aquatic biomass using CO_2 and O_2 in helium (He) atmosphere was studied by Hanaoka et al. [26]. The results indicated that the use of CO_2 and O_2 raised the conversion to syngas (CO and H_2). The concentration of CO in the produced syngas was found to increase as the CO_2 feed rate increased, whereas that of H_2 decreased. However, the concentrations of both H_2 and CO were found to increase when O_2 feed rate increased. The conversion to gas of 94.0 C-mol % and the maximum yield of syngas of 69.7 vol.% were achieved at CO_2/O_2 of 45/55 vol.%. Moreover, it was found that the conversion to gas of the system with CO_2/O_2 was higher than that with He/O_2 due to the strong effect of Boudouard and tar decomposition reactions. Sadhwani et al. [27] found that the use of steam and CO_2 as gasifying agents offered benefits over the traditional biomass gasification process economically, socially, and environmentally. Im-orb et al. [28] investigated the effect of gasifying agents (air-steam and CO_2-steam) on the performance of the gasification process using rice straw feedstock. They found that one-step syngas production that satisfied H_2/CO ratio for FT synthesis could be achieved in the gasifier under thermal self-sufficient conditions at the air-to-biomass ratio of 0.57, steam-to-biomass ratio of 1.17, and a gasifying temperature of 700 °C.

Operating Conditions

The influence of operating parameters, i.e., flow rate of feed, gasifying pressure, and temperature, on the calorific value and composition of the produced syngas and the total energy consumption of the system has been extensively investigated in

previous studies. Typically, an equilibrium model is used to perform the parametric analysis during the preliminarily design of a gasifier, because thermodynamic models do not rely on the gasifier design and require less data; only the feed elemental composition data and the chemical reaction data are needed. Li et al. [29] studied the sawdust gasification in a demonstration plant. They found that air ratio, temperature, steam injection, suspension density, and fly ash reinjection influenced the composition and heating value of the produced gas. Their experimental data were compared with the results derived from an equilibrium model which were calculated using the Gibbs free energy minimization approach; the predictions were found to deviate from the experimental results due to the slow reaction rate of the char gasification. Therefore, the model was modified to account for the unconverted carbon and CH_4 observed in the experiment as nonequilibrium factors to improve the model accuracy. Renganathan et al. [30] examined the influences of varying gasifying agents (steam, O_2, CO_2, or a mixture thereof), gasifying temperature, pressure on syngas composition, amount of released CO_2, and cold gas efficiency (CGE). The results indicated that CO and H_2 concentration increased, whereas the CO_2 concentration decreased when the gasifying temperature increased. Pressure had negative effect on CO_2 gasification. The concentration of CO decreased with increasing pressure, while that of H_2 was almost independent of pressure. Loha et al. [31] experimentally tested and developed an equilibrium model for a fluidized bed steam gasification of rice husk. The effect of the steam-to-biomass ratio and gasifying temperature on the syngas composition was studied, and a correlation between the yield of H_2 from the rice husk at different temperatures and steam-to-biomass ratios was presented. The results indicated that the production rates of CO_2 and CH_4 decreased whereas those of CO and H_2 increased. The increase of supplied steam caused CO_2, CH_4 and H_2 to increase and CO to decrease. The sugarcane bagasse gasification in a circulating fluidized bed gasifier was studied by Ardila et al. [32]. The effect of operating parameters on the conversion efficiency, heating value, and product gas composition was reported. A thermodynamic based-gasification model using poultry waste, food waste, and municipal solid waste as feedstock was established by Ramzan et al. [17]. The effect of ER, steam injection, moisture content, and gasifying temperature on the cold gas efficiency, heating value, and produced gas composition was investigated. They found that the production rate of H_2 and CO decreased when the ER increased. The moisture content influenced the calorific value of syngas and the steam injection could enhance the H_2 production. Moreover, the production rates of H_2 and CO were found to decrease as gasifying temperature increased. Xiong et al. [33] found that the increase of gasifying temperature could enhance rice husk gasification efficiency in the bubbling fluidized bed gasifier but the increase of inlet velocity of gasifying agent and biomass humidity showed inverse effect.

Although extensive experimental data is required in order to generate a kinetic model to derive the reaction kinetics of the main reactions, such models can present a clear picture of the complex phenomena occurring in each section of the gasifier and offer high accuracy. Several works have focused on the development of kinetic models. Kojima et al. [34] determined the kinetic data for gasification of sawdust

char by performing an experimental fluidized bed gasifier containing inert particles under stable and differential conditions. Nikoo and Mahinpey [35] included the reaction kinetic data of char gasification and hydrodynamic parameters in the gasification model by using embedded external FORTRAN user subroutines. Their model predictions matched well with the experimental results from a lab-scale fluidized bed gasifier using pine feedstock. The effect of average particle size of the biomass, ER, gasifying temperature, and steam-to-biomass ratio on the carbon conversion efficiency and composition of syngas was investigated. Yaghoubi et al. [36] developed the model of a dual bubbling fluidized bed gasifier for the hydrogen production. Their developed model consisted of a set of several differential equations that considered the influence of chemical reactions, convection, diffusion, and flow hydrodynamics on the allocation of gaseous species in the gasifier and final composition of produced gas. The model was utilized to study the impact of humidity, particle size, reactor size, gasifying agent flow rate, and gasifying temperature on the generation of hydrogen. The results showed that steam was more suitable gasifying agent for H_2-rich syngas production than air, and the most suitable operating condition was found at the steam-to-biomass ratio of almost equal to 1.3 and the gasifying temperature ranging between 800 and 820 °C. Gao and Li [37] investigated the behavior of a biomass gasification in fixed-bed reactor by developing a mathematical model of the combined pyrolysis and reduction section which embedded the kinetic rates of reactions occurring in the latter zone. The volatiles leaving the pyrolysis section were used as original concentrations of the reduction section. The temperature profile along the height of the reduction zone at various times and the concentration of each component in the syngas were found to be comparable with the published experimental result. The mathematical model of steam gasification, using char as a feedstock, based on the gas transportation and the reaction kinetics of the produced gas was developed by Xu et al. [38]. Three types of char (i.e., coal char, biomass char, and a blend of coal and biomass char) were considered. The developed model was used to examine the influence of the char structure on the gasification characteristics. They found that the different structures of char (biomass char and coal char) were the major factor influencing the gasification characteristics. The biomass char had more amorphous structure; hence, the intrinsic reaction rate was improved while the coal char had high transportation rate of gasifying agent into char particle. Kaushal et al. [39] proposed a biomass gasification model of bubbling fluidized bed reactor. Two zones (upper freeboard and bottom dense bed) and two phases (emulsion and bubble) were considered in the model development. The model predictions showed good agreement with other bubbling fluidized bed gasification model, and the model could predict the bed temperature and tar yield, as well as the production rate, composition, and heating value of the produced syngas. A biomass gasification model of circulating fluidized bed including the hydrodynamics and reaction kinetics was developed by Miao et al. [40]. Two regions, such as the dense and dilute regions, were considered in the model. The developed model was used to investigate the temperature and product gas distributions along the gasifier length, and the syngas production rate, heating value, carbon conversion, and the gasification efficiency are compared with the

published data. Sharma [41] developed a biomass gasification model of a downdraft gasifier based on experimental results of the pyrolysis zone and reaction kinetic of the reduction zone. The model consisted of the fluid flow, the heat transfer, and the thermochemical process modules. The model predictions matched well with the reported experimental data. Sharma [42] performed the comparison between kinetic and equilibrium models for the char reactions in a downdraft gasifier and studied the effects of the reaction temperature on the unconverted char, the composition of dry gas, and the rate of endothermic heat absorption in the reduction zone. The critical char bed height of 25 cm at a gas flow rate of 10 g s^{-1} and critical reaction temperature of 950 K in the reduction zone were derived from the kinetic and equilibrium models.

14.2.1.3 Design of Plant Configuration

To obtain efficient syngas production process which offers the high-quality syngas and consumes less energy, improvement of the gasification performance is needed. Several attempts have been made to enhance the gasification performance such as optimization of the operating conditions and process modifications (i.e., installation of a stream preheater and implementation of syngas cleaning and tar reforming processes). The Aspen Plus model of the H_2 generation from biomass gasification in the interconnected fluidized beds with two separate zones of combustion and gasification was developed by Shen et al. [43]. The parametric analysis was performed, and the results showed that a high H_2 yield and relatively high H_2 content were achieved via this process, and the most favorable condition was obtained at the combustion temperature of 920 °C, the gasifying temperature range of 750–800 °C, and the steam-to-biomass ratio range of 0.6–0.7. Arpornwichanop et al. [44] analyzed the biomass gasification under a supercritical water operation for H_2 production by examining the influence of key operating parameters on its performance. The suitable condition for H_2 production was obtained by using the inlet feed concentration of 20–25 wt.% and the gasifying temperature of 600 °C. Doherty et al. [45] developed an Aspen Plus model of the biomass gasification in an atmospheric circulating fluidized bed (CFB) based on the Gibbs free energy minimization method to investigate the influences of the air preheating. It was found that the production rates of H_2 and CO increased with increasing air preheating rate; as a result, the syngas calorific value and the CGE of the gasifier increased. The three biomass gasification models with CO_2 recirculation – (1) direct heating, (2) indirect heating using syngas, and (3) indirect heating using biomass as a fuel – were developed and compared by Chaiwatanodom et al. [25]. Their results indicated that CO_2 recycling was beneficial to syngas production. The indirect heating gasification using biomass as a fuel offered the maximum gasification efficiency with the minimum CO_2 emissions.

Biomass gasification has been combined with other downstream processes, i.e., fuel cells, power plants, or FT synthesis, to increase the overall process performance. A model of the wood gasification for cogeneration of power and heat developed in

Aspen Plus was presented by Francois et al. [46]. Their result indicated that the overall thermal efficiency of the gasification plant of 76% was achieved. The performance evaluation of the biomass gasification combined with proton exchange membrane fuel cell (PEMFC) system was performed by Chutichai et al. [47]. Based on an electrical load of 5 kW, the electrical and total energy efficiency of 22% and 51%, respectively, was achieved. The maximum efficiency of 40–45% on higher heating value (HHV) basis of the combined biomass gasification and FT process was presented by Hamelinck et al. [48].

Although the gasification is a favorable process used to generate synthesis gas from the biomass, it utilizes large amount of energy, notably at air separation unit (ASU) that occupied the largest part of total electricity consumption [49]. Moreover, the formation of tar which causes fouling of piping and downstream equipment are another concerned problem. The IBPG process, in which the produced charcoal from the pyrolysis process is subsequently gasified, is therefore studied. The simplified diagram of the IBPG is illustrated in Fig. 14.3. Im-orb et al. [50] described that the IBPG provided not only syngas with the required H_2/CO ratio for FT process but also additional bio-oil as a valuable by-product. Regarding the energy performance, the IBPG offered higher thermal efficiency and released less waste heat compared with the conventional gasification when the same amount of syngas was produced. The installation of CO_2 capture technology and the utilization of captured CO_2 in the pyrolysis-gasification process were later investigated. It was found that the process with CO_2 capture offered better environmental benefit; however, the larger amount of energy was required. The use of captured CO_2 as a gasifying agent could increase

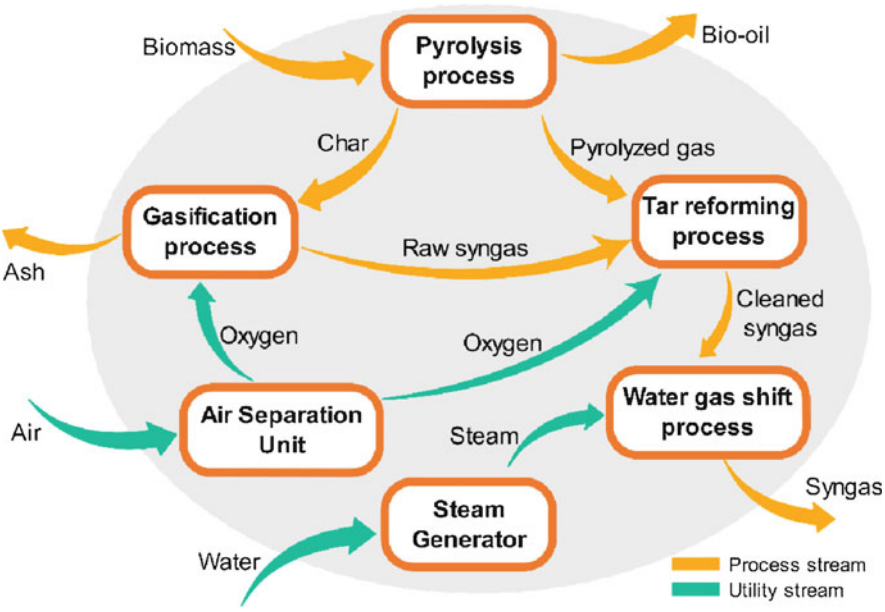

Fig. 14.3 Simplified diagram of the integrated biomass pyrolysis and gasification process

the production rate of syngas and CO_2, whereas that of bio-oil did not change [51]. The syngas production via chemical looping pyrolysis-gasification (CLPG) of biomass was studied by Zeng et al. [52]. The result indicated that the optimum condition offering the H_2/CO ratio of 2.45 and CGE of 61.87% was achieved at the steam-to-biomass ratio of 1 kg kg^{-1} and the fuel reactor temperature of 820 °C.

14.2.2 Gas Cleaning

Typically, the syngas generated from gasification consists of various types of impurities, i.e., inorganic impurities (hydrogen sulfide (H_2S), hydrochloric acid (HCI), ammonia (NH_3), hydrogen cyanide (HCN), and carbonyl sulfide (COS)), organic impurities (tars), and volatile metals, dust, and soot. As the FT process involves an FT catalyst that can be poisoned by various impurities, the raw syngas must be cleaned prior to transfer to the FT plant. Table 14.2 presents the syngas specifications for the conventional FT process.

14.2.2.1 Conventional Gas Cleaning Process

The syngas cleaning technologies used for commercial processes are illustrated in Fig. 14.4. Typically, the temperature of raw syngas is decreased in the quench tower by direct contact with water, and then volatile alkaline metals and solid particles are eliminated. Halides (HF, HBr, and HCl) and NH_3 are simultaneously eliminated in a water washer, and H_2S is converted to elementary sulfur or is removed in an absorber. Because of the lower price of sulfur, absorption process is selected when H_2S are slightly present. Finally, the active carbon filters as downstream guard beds are applied to remove impurities, COS, and HCN.

Table 14.2 Syngas specifications for the FT process [48, 53]

Impurity	Specification
NH_3 + HCN	<1 ppmv
H_2S + COS + CS_2	<1 ppmv
Hetero-organic components (S, N, O)	<1 ppmv
Alkali metals (Na + K)	<1 ppbv
HCl + HBr + HF	<1 ppbv
Particles (soot, ash)	Almost completely removed
Tar	Catalyst poisoning compounds <1 ppmv
Benzene, toluene, and xylene (BTX)	Below dew point at FT pressure

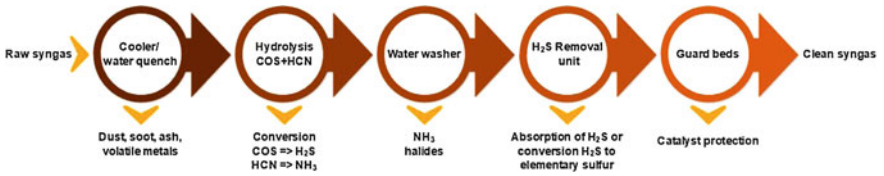

Fig. 14.4 Schematic of well-known and commercially available cleaning technologies for raw syngas. (Adapted from [53])

14.2.2.2 Tar Removal

The major technical challenge for implementing the integrated biomass gasification process is an elimination of tar from the produced gas. The tar contained in syngas is another important contaminant that can cause deactivation of the FT catalyst and fouling of downstream equipment, leading to a decrease of process performance. Hence, an understanding of the formation of tar and attempts at decreasing tar formation, as well as the tar-eliminating methods, are interesting topics. Basu [54] reported that the produced gas leaving a downdraft gasifier contains approximately 2 wt.% of tar. Qin et al. [55] analyzed the impact of the biomass composition on tar generation. The lignin-rich forest residue sawdust and cellulose-rich agricultural waste cornstalks were gasified in a spout-fluidized bed gasifier during 700–900 °C. The cornstalk tar and sawdust tar were polyaromatic substance, but tar from cornstalk contained higher aliphatic compounds than that from sawdust.

In general, the tar removal method can be classified in two groups: (1) primary method (or in situ method) and (2) secondary method (or post gasification method).

Primary Method

For primary method, tar is converted to light gases within the gasifier by selecting suitable operating conditions [56] and also by using appropriate catalysts and additives within the gasification process. Several studies have investigated the impact of operating condition and gasifying agent on the amount of tar contained in produced syngas. Tar formation in sawdust gasification pilot test was examined by Li et al. [29]. Their results indicated that the tar yield decreased exponentially when temperature increased. The influence of changes in gasifying pressure on the activity of tar decomposing on different materials i.e., magnesium oxide (MgO), dolomite, olivine A, sand, and a mixture of kaolin and olivine B (50/50 wt.%), was studied by Tuomi et al. [57]. MgO and dolomite were found to be the most active bed materials when the gasification process was operated at 1 atm, while the activity of dolomite and MgO decreased as operating pressure increased. However, elevated operating pressure increased the thermal decomposition reactions of tar over olivine A and sand. The type of gasifying agents also affects tar concentration in the produced gas. The high tar content was found when steam was utilized as a gasifying agent due to a

decrease in gasifying temperatures [58]. However, the use of oxygen provides better performance. Galindo et al. [59] reported that the two-stage air supply in the gasification can decrease the tar concentration in the produced syngas. Lui et al. [60] conducted an experiment on a two-stage fluidized bed reactor for the gasification of rice straw and examined the consequence of secondary O_2 injection on the tar formation. The result showed that the concentration of tar decreased from 15.78 g Nm^{-3} to 10.24 g Nm^{-3} when the secondary O_2 ratio increased from 0 to 6.5%.

Secondary Method

In the secondary method, secondary equipment is installed to eliminate tar through physical processes or chemical reactions. Tar elimination using physical method is widely used in commercial gasification process because it is easy to maintain and its operating cost is lower than the catalytic process. Physical cleaning methods can be separated into wet and dry gas cleaning. For the wet gas cleaning, a water scrubber is utilized to remove tar, but the removal efficiency is low because of the fact that tar consists of many organic compounds having low water solubility. Therefore, searching for more efficient absorbents is required. Phuphuakrat et al. [61] examined the performance of tar elimination using different scrubbing liquids (i.e., water, biodiesel fuel, diesel fuel, engine oil, and vegetable oil). When the polyhydroxyalkanoates (PAHs) were considered a tar, the diesel fuel offered the highest tar elimination efficiency followed by vegetable oil, biodiesel fuel, engine oil, and water, respectively. Nakamura et al. [62] presented the biomass gasification using a char bed and bio-oil scrubber to remove tar. The result showed that 98% of tar could be removed without using any primary method.

Regarding the dry gas cleaning, there are several types of cleaning equipment such as cyclone separator, electrostatic precipitator, bag filter, ceramic filter, fabric filter, sand bed filter, adsorbents, activated carbon adsorbents, and catalytic filter. Generally, the operating temperature of wet gas and dry gas cleaning is in a range of 20–60 °C and 200–500 °C, respectively; hence, the dry gas cleaning seems to be more suitable for the FT plant than the wet cleaning due to the energy benefit. Leibold et al. [63] proposed the optimized dry high-temperature high-pressure (HTHP) syngas cleaning process consisting of high-temperature (HT) particulate filtration, suitable sorption, and catalysis processes which offer syngas satisfying FT synthesis. The particulate filter was the main component in this process. In the clean gas side of the particulate filter, the filter was integrated with a porous tar reforming catalyst layer and an entrained flow sorption process upstream, as illustrated in Fig. 14.5. The flow rate of the particle-free syngas was controlled by the filtration velocity of the filter element; therefore, the resident time within the catalyst layer was long enough to ensure the complete tar conversion.

The conversion of tar to syngas through chemical reactions, i.e., partial oxidation (POX), autothermal reforming (ATR), and steam reforming, was also investigated. This method could increase the amount of syngas and also of downstream products

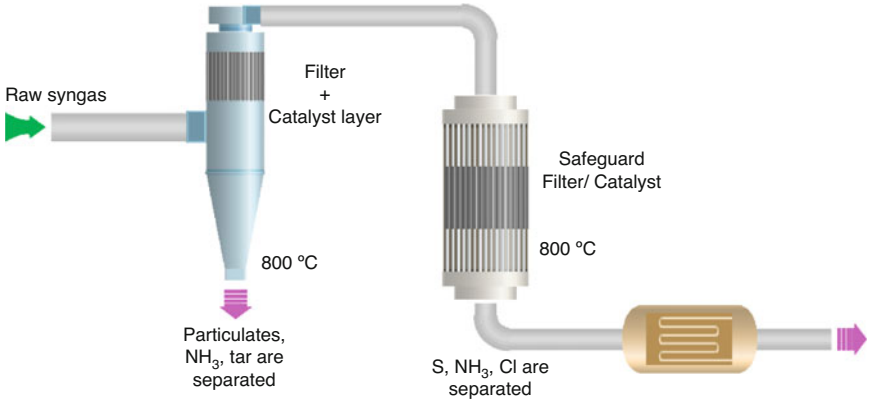

Fig. 14.5 Optimized HTHP syngas cleaning process. (Adapted from [63])

that use syngas as a feedstock. The catalytic tar elimination has been one of the interesting topics. Zhang et al. [64] found that benzene and toluene were completely decomposed at the temperature higher than 1200 °C. Regarding the hot gas conditioning process, steam reforming and catalytic cracking of tar offer the advantages in terms of high tar conversion and thermal integration. A model of the combined biomass gasification and tar steam reforming process for hydrogen generation was suggested by Vivanpatarakij and Assabumrungrat [65]. The simulation results indicated that the integrated unit could completely eliminate tar and increase syngas yield under thermally self-sufficient conditions. In general, nickel (Ni)-based catalysts, dolomite, olivine, and novel developed catalysts including ceramic and nano-Ni-based catalysts are widely used for tar catalytic elimination [66]. Josuinkas et al. [67] presented that CH_4 and benzene (a biomass tar model compound) could be entirely transformed to CO and H_2 through steam reforming using a Ni-based catalyst at operating conditions of 1 atm and 780 °C. The activity of K_2CO_3 catalyst during the steam gasification of lignin was investigated by Kuchonthara et al. [68]. The potassium carbonate (K_2CO_3) offered a good catalytic activity for tar decomposition during steam gasification and pyrolysis. Davi et al. [69] studied and compared the tar removal efficiency of pre-calcined dolomite, olivine, and pure sand, which were placed in the secondary reactor of the gasification process. The highest tar elimination efficiency of 90% was reached when the 17% pre-calcined dolomite in pure sand was used as catalyst, followed by the 17% olivine in sand and pure sand which offered 48% and 71% of tar removal efficiency.

The Energy Research Center of Netherland (ECN) proposed the OLGA tar elimination technology based on gas scrubbing with oil. During the OLGA process, the product gas temperature is decreased and the heavy tar is removed by condensation while the lighter tar is absorbed in the scrubbing liquid. Figure 14.6 shows that the tar collection and tar absorption processes occurred in a collector and an absorber, and the tar-dissolved scrubbing liquid is then regenerated at the stripper column where the tar is stripped by air. Moreover, the heavy tar- and light tar-loaded

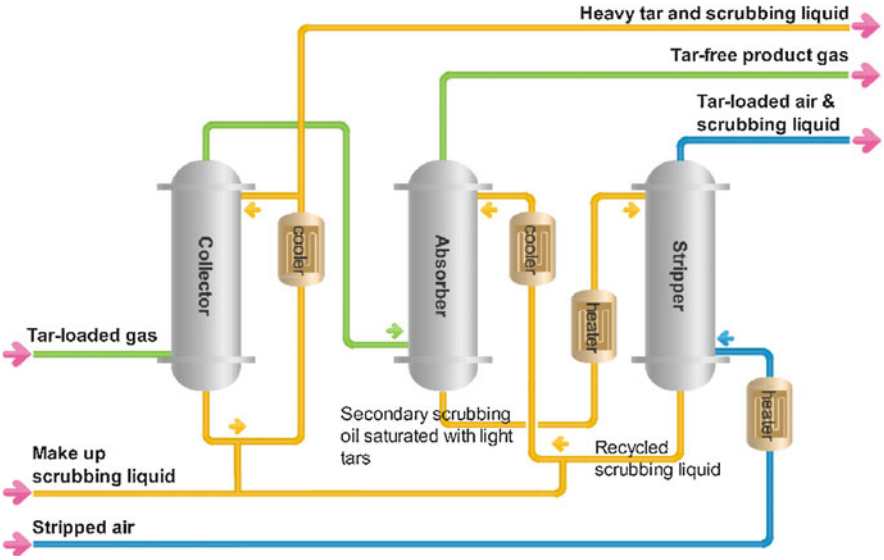

Fig. 14.6 Simplified diagram of the OLGA tar removal process. (Adapted from [70])

stripped gas is recycled to the gasifier and then cracked to provide higher syngas yield. The economy of the OLGA technology was reported at plant scales above approximately 4000 $m^3\ h^{-1}$ (corresponding to 10 MW biomass input) [70].

The developed OLGA tar removal process was implemented in the BG-FT demonstration plant. The result showed that the OLGA process not only totally removed the heavy and light tars but also removed the BTX to produce the syngas satisfying the FT specification [53].

14.2.3 Fischer-Tropsch Synthesis

The syngas containing mainly H_2 and CO is converted to strength-chain hydrocarbons through the FT process. The FT process is a highly exothermic polymerization reaction over cobalt- or iron-based catalysts in which CO is reacted with H_2 to form the intermediate $-CH_2-$, which later grows to form hydrocarbons of variable lengths; this reaction is presented in (14.1).

$$nCO + 2nH_2 \rightarrow (-CH_2-)_n + nH_2O \tag{14.1}$$

There are two types of FT reactor operating conditions: (1) low-temperature FT synthesis (LTFT) and (2) high-temperature FT synthesis (HTFT). Generally, the FT operating pressure is in the range of 20–60 bar. Table 14.3 shows a comparison of operation characteristics and the reactor types for HTFT and LTFT processes.

Table 14.3 Operating condition of HTFT and LTFT processes [71]

	LTFT	HTFT
Reactor types	Three-phase, multitubular, fixed bed,	Two-phase
Catalysts	Cobalt or iron	Iron
Temperature	220–250 °C	300–350 °C
Products	Waxes and diesel	Gasoline and olefins

In the past, many studies on FT synthesis focused on an improvement of the catalyst performance to increase the yield of the required product. Parametric analysis has been done to examine the influence of operating pressure and temperature on the distribution of product and energy consumption. Additionally, design of the reactor to decrease its configuration complexity improves the heat transfer performance, and increase in the production capacity has also been investigated.

14.2.3.1 Fischer-Tropsch Product Distribution

FT products contain saturated long-chain hydrocarbons from CH_4 up to olefins, heavy waxes, and oxygenate compounds that are obtained from the polymerization of the -CH_2- monomers. The hydrocarbon products were interpreted by the Anderson-Schulz-Flory (ASF) distribution due to the stepwise growth mechanism; the molar (M_n) and mass (W_n) variants of the distribution are presented in (14.2) and (14.3), respectively.

$$M_n = \alpha^{n-1}(1-\alpha) \tag{14.2}$$

$$W_n = \alpha^{n-1}(1-\alpha)^2 n \tag{14.3}$$

Figure 14.7 shows a diagram of the ASF distribution. The chain growth probability (α) is used to characterize a distribution of FT product. A high value of α represents a higher content of long-chain hydrocarbons and less CH_4 in the final product. The selectivity for C_5^+ indicates the selectivity of a catalyst for long-chain hydrocarbons. Higher values of α are obtained at lower temperatures, higher pressures, and lower H_2/CO ratio of feed gas. The value of α relies on the catalyst characteristics such as pore size, pellet size, and promoters. To obtain the maximum yield of diesel, the production of wax is firstly focused because it is later hydrocracked into the lighter molecule of diesel fraction (C_9–C_{25}). Therefore, the FT studies are presently concentrated on how to synthesize the catalysts that give a high value of α. A typical value of α around 0.9 is used for a wax-producing FT process. Table 14.4 indicates the value of α of the commercial FT plants. The synthesized FT liquid fuel is an ultraclean product due to its sulfur-free nature, and it contains a greater percentage of the valuable fraction compared to fuel derived from crude distillation. A comparison between the products obtained from crude distillation and conventional FT process is presented in Fig. 14.8.

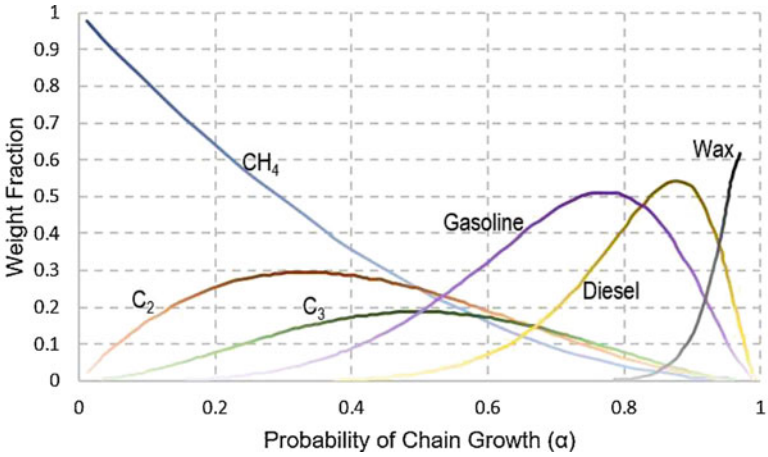

Fig. 14.7 Graphic showing the ASF distribution. (Adapted from [72])

Table 14.4 The value of α for the commercial FT plants [73, 74]

Plants	Reactor	Operating condition	Catalyst	α
Sasol 1 – Kellogg Synthol process	Circulating fluidized bed (CFB)	$P = 22$ bar $T = 290–340$ °C	Fused Fe	<0.7
American Hydrocol facility	Fixed fluidized bed	$P = 27$ bar $T = 305–340$ °C	Fused Fe	<0.7
Arge LTFT synthesis	Multitubular fixed bed	$P = 25–27$ bar $T = 200–250$ °C	Precipitated Fe	0.9
Sasol slurry bed process (SSBP)	Slurry bed (catalyst suspended in liquid wax)	$P = 21$ bar $T = 245$ °C	Precipitated Fe	0.95
Mossgass facility	Sasol synthol CFB	$P = 25$ bar $T = 330–360$ °C	Fused Fe	0.7–0.8
Sasol advanced synthol (SAS)	Fixed fluidized bed	$P = 25$ bar $T = 310–350$ °C	Fused Fe	0.7–0.8
Shell middle distillate synthesis (SMDS)	Multitubular fixed bed	$P = 25$ bar $T = 220$ °C	Co based	0.90–0.92
Oryx-GTL facility	Sasol slurry phase distillate	$P = 20–25$ bar $T = 230$ °C	Co/Pt/Al_2O_3	0.90–0.92

14.2.3.2 Improvement of the Catalyst Performance

The improvement of catalyst performance to obtain the maximum yield of the desired product is key to the success of the FT synthesis process. Lohitharn et al. [76] founded that the addition of manganese, chromium, molybdenum, vanadium, tantalum, or zirconium into the iron-based catalyst could enhance the activity for

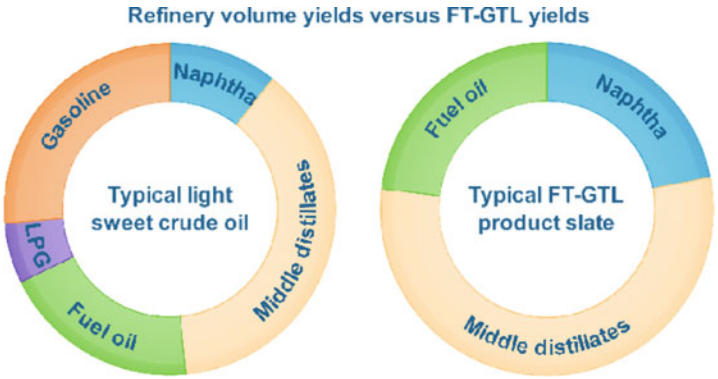

Fig. 14.8 Products derived from FT and from crude distillation. (Adapted from [75])

hydrogenation of CO and water gas shift reactions due to a higher iron dispersion. Ma et al. [77] analyzed the influence of noble metal promoters on the selectivity and activity of cobalt-based catalysts. They found that the catalyst promotors could enhance the rate of CO hydrogenation. Additionally, the addition of Ni and ruthenium (Ru) could enhance the catalytic activity to produce hydrocarbon products in a gasoline range [78]. The FT synthesis process entails complex reactions and requires a suitable H_2/CO ratio in the synthesis gas; hence, the effect of H_2/CO ratio on the distribution of hydrocarbon products over different types of FT catalysts was investigated. Lu and Lee [79] found that the highest yield of FT diesel was achieved as the H_2/CO ratio was closed to 2.0 for the FT reaction carried out over cobalt-based catalysts; however, this ratio should be set in the range of 1.1–1.7 when iron-based catalysts were used. Tristantini et al. [80] studied the influence of the feed gas composition over the catalysts CO-Re/γ-Al_2O_3 and CO/γ-Al_2O_3. In their work, the conversion of CO and selectivity of CH_4 were found to decrease, whereas the olefin-to-paraffin ratio for C_2-C_4 and the selectivity of $C5^+$ hydrocarbon slightly increased. Rahmati et al. [81] examined the influence of different alumina supports on the performance of cobalt FT catalyst. The results demonstrated that the Al-Si-based catalyst support was the best active catalyst, with a rate of 49 mmol CO g_{cat}^{-1} h^{-1} at temperature and pressure of 220 °C and 20 atm, respectively.

14.2.3.3 Parametric Study of the Fischer-Tropsch Synthesis Process

Many parametric studies of the effect of feed gas composition, operating pressure, and temperature on FT process performance have been performed via experimental and modeling approaches. Many attempts have been made to create a process model to explain the behavior of the catalyst and the hydrodynamic and aerodynamic of the fluids inside different FT reactors as well as to predict the FT product distributions. The FT synthesis through the microchannel reactor including an iron-based catalyst

was studied in terms of catalyst deactivation, CO conversion, gas hourly space velocity, and pressure drop [82]. The outstanding heat and mass transfer was achieved in the microchannel reactor. A fixed-bed reactor two-dimensional model, which included the reaction rate and transport equations, was developed by Rafiq et al. [83]. Their model predictions matched well with the experimental results, and the model was applied to study the conversion of H_2 and CO, the temperature of fluid along the reactor axis, and the hydrocarbon production. A model of a fixed-bed reactor, based on kinetic data and the fact that the liquid wax was filled in the catalyst pores under actual conditions, was proposed by Wang et al. [84]. The equilibrium between the wax in the catalyst pores and the gases in the bulk was calculated using Soave-Redlich-Kwong (SRK) equations. The effect of the process variables on the reaction behavior of the recycling process was also examined. Furthermore, bubble column slurry reactors have been widely studied. A model of this reactor was presented by de Swart and Krishna [85]. The mixing behavior of the catalyst particle and liquid phases inside a commercial-scale reactor was also investigated. Kwack et al. [86] studied a slurry continuous stirred tank reactor (CSTR) containing Co/P-Al_2O_3 catalyst for FT synthesis by using the mathematical model. The prediction of their developed model agreed well with the experimental result. The 3D-CFD model including the chemical kinetics of the FT reaction in the fluidized bed reactor was presented by Zhang et al. [87]. The bed height, the particle diameter, the reaction temperature, and the superficial gas velocity influenced the selectivity and the effective reaction rate. Iliuta and Larachi [88] employed a complex three-dimensional, transient, multiphase model of FT synthesis in trickle bed reactors for offshore floating applications. The model was based on the volume averaged mass, species and momentum balance equations in the gas and liquid phases combined with the simultaneous chemical reactions, and diffusion inside the catalyst.

14.2.3.4 Empirical Correlation of Chain Growth Probability

Chain growth probability (α) is an important factor applied to predict the distribution of FT product; however, it is difficult to measure. The development of empirical correlations for α with the operating temperature, pressure, and H_2/CO ratio has been extensively studied. A correlation for a cobalt-based catalyst was derived from experimental research. Yermakova and Anikeev [89] developed a correlation based on several experiments over an alumina-supported cobalt catalyst promoted with zirconium at 20 atm and 533 K, which is given in (14.4).

$$\alpha = A\frac{a_{CO}}{a_{CO} + a_{H_2}} + B \tag{14.4}$$

The values of the constants A and B were 0.2332 ± 0.0740 and 0.6330 ± 0.042, respectively. Equation (14.5) presents a correlation between α and the operating temperature in Kelvin, which was developed by Song et al. [90].

$$\alpha = \left(A\frac{\gamma_{CO}}{\gamma_{CO}+\gamma_{H_2}} + B\right)[1 - 0.0039(T - 533)] \tag{14.5}$$

Moreover, the relation of α on the operating pressure (bar), the operating temperature (K), and the H_2/CO ratio was reported by Hamelinck et al. [48]. The selectivity of hydrocarbons with a chain length longer than 5 (S_{C5+}) was also proposed in (14.6) and (14.7).

$$\alpha = 0.75 - 0.373\sqrt{-\log\left(S_{C5+}\right)} + 0.25S_{C5+} \tag{14.6}$$

$$S_{C5+} = 1.7 - 0.0024T - 0.088\frac{[H_2]}{[CO]} + 0.18([H_2] + [CO]) + 0.0079P_{Total} \tag{14.7}$$

Kinetic expressions for the FT synthesis process using various types of FT catalysts have also been studied. Pondini and Ebert [91] proposed kinetic expressions for the FT reaction over a cobalt- and iron-based catalysts as shown in (14.8) and (14.9), respectively.

$$-R_{CO} = \frac{k_{FT}P_{CO}P_{H_2}}{P_{CO} + aP_{H_2O}} \tag{14.8}$$

$$-R_{CO} = \frac{k_{FT}P_{CO}P_{H_2}}{(1 + bP_{CO})^2} \tag{14.9}$$

where R_{CO} is the CO consumption rate (mol s^{-1} $kg^{-1}{}_{cat}$) and P_{CO} and P_{H_2} are the partial pressures of CO and H_2 (bar), respectively. Equation (14.9) can be rewritten in terms of kinetic parameters (a and b) as shown in (14.10).

$$-R_{CO} = \frac{aP_{CO}P_{H_2}}{(1 + bP_{CO})^2} \tag{14.10}$$

Equations for the a and b kinetic parameters were also reported in earlier works. Hamelinck et al. [48] defined these parameters as shown in (14.11) and (14.12); the values of the related constants are different when different types of FT reactors are used, as summarized in Table 14.5.

$$a = k_0 \times \exp\left(\frac{E_{A,reaction}}{RT}\right) \text{ mol } s^{-1}\ kg_{cat}^{-1}\ bar^{-2} \tag{14.11}$$

$$b = k_1 \times \exp\left(\frac{-\Delta H_{ads}}{RT}\right) \text{ bar}^{-1} \tag{14.12}$$

Krishna and Sie [92] proposed the expressions for a and b shown in (14.13) and (14.14).

Table 14.5 Kinetic parameters for solid bed and slurry reactors [48]

	E_A (kJ mol^{-1})	k_0 (mol s^{-1} kg$_{cat}^{-1}$ bar^{-2})	ΔH_{ads} (kJ mol^{-1})	k_1 (bar^{-1})	ρ (kg$_{cat}$m^{-3})
Solid bed	68	1.5×10^5	192	3.5×10^{-23}	1200
Slurry bed	115	1.0×10^{10}	192	3.5×10^{-23}	600

$$a = 8.8533 \times 10^{-3} \times \exp\left[4494.41\left(\frac{1}{493.15} - \frac{1}{T}\right)\right] \text{ mol s}^{-1} \text{ kg}_{cat}^{-1} \text{ bar}^{-2} \quad (14.13)$$

$$b = 2.226 \times \exp\left[-8236\left(\frac{1}{493.15} - \frac{1}{T}\right)\right] \text{ bar}^{-1} \quad (14.14)$$

Another expression for a and b was reported by Panahi et al. [93] and is expressed as follows:

$$a = 8.01368 \times \exp\left(\frac{-37,326}{RT}\right) \text{ kmol s}^{-1} \text{ kg}_{cat}^{-1} \text{ MPa}^{-2} \quad (14.15)$$

$$b = 1.248 \times 10^{-6} \times \exp\left(\frac{68,402}{RT}\right) \text{ MPa}^{-1} \quad (14.16)$$

14.3 Technical and Economic Feasibility of the BG-FT Process

The techno-economic study of the BG-FT process has attracted wide interest because of the increased concern regarding the decrease in global reserves of fossil fuels and the increase in global warming problems. Presently, most BG-FT processes are still in the research and development phases. Although the BG-FT process is less economically feasible, its environmental advantages compared to natural gas or coal-based FT plants are obvious. As a result, continuous improvement of this technology in order to produce synthesis fuel that can compete with fossil-based fuels is an interesting topic. The economic and technical feasibility of the process seems to be the most important issue to justify an investment effectiveness of a proposed BG-FT process. Therefore, the complete studies of the combined technical and economic performance of the BG-FT process should be performed.

Several parameters affect the economic performance indicator, such as the gasification efficiency, the energy requirements of syngas cleaning and conditioning unit, effectiveness of FT catalyst, and FT crude upgrading efficiency, as well as feed and product prices. Vogel et al. [94] reported that the cost of wood chip and forest residue feedstock ranged from 2 to 5 euros per gigajoule. Additionally, the

availability of a steady source of biomass and government regulations regarding green energy production also affects the performance of BG-FT process. The total cost of BG-FT process consists of (1) the price of the biomass transferred to the plant, (2) capital costs including investment costs, and (3) other variable costs, including operation, manpower, and electricity costs. The biomass price accounted for 40–60% of the total cost, and the capital and other variable costs are in the range of 17–40% and 10–40%, respectively [95]. Normally, the fixed capital investment consists of electric appliances, instruments, pipes, production equipment, process plants design, and construction, and some invisible cost can be determined from the factored estimation method as shown in (14.17).

$$\frac{\mathrm{COST}_{\mathrm{size2}}}{\mathrm{COST}_{\mathrm{size1}}} = \left(\frac{\mathrm{SIZE}_2}{\mathrm{SIZE}_1}\right)^{\mathrm{sf}} \tag{14.17}$$

where SIZE_1 and SIZE_2 are the size of the base scale and the required scale, respectively; sf is the power scaling factor; $\mathrm{COST}_{\mathrm{size1}}$ is the cost of the base scale; and $\mathrm{COST}_{\mathrm{size2}}$ is the cost of the required scale. Additionally, the chemical engineering plant cost index (CEPCI) is used to determine the capital cost of chemical plant at the present time as shown in (14.18).

$$\text{Present cost} = \text{Original cost} \times \left(\frac{\text{Index at present}}{\text{Index when original cost was obtained}}\right) \tag{14.18}$$

The conventional cost structure of a total capital investment of the gasification process is shown in Table 14.6.

The technical performance of a BG-FT process was demonstrated by continuous run for 500 h under steady conditions in lab scale [97]. Muradov et al. [98] found that the integration of O_2/steam biomass gasification and FT synthesis processes using charred pinewood pellets (CPP) yielded primarily C_7–C_{28} long-chain hydrocarbons. Leibbrandt et al. [99] reported that the process showed an energy efficiency of 51%, which related to 40% efficiency of gasification and 75% of FT process. Exergy analysis of the BG-FT process using different types of biowaste feedstock was performed to investigate the efficiency of energy utilization, and the highest exergy efficiency of 42% was reported by Sues et al. [100]. Im-orb et al. [101] evaluated the performance of the BG-FT process with and without tar elimination process based on steam reforming and ATR. The BG-FT process coupled with ATR is the most practical configuration, offering the minimum external utility requirement and maximum internal heat recovery. Moreover, the techno-economic comparison of the BG-FT process and the integration of fast pyrolysis and hydroprocessing (FP-H) process were examined based on energy and exergy analyses and on risk and financial analyses. The evaluation outcome indicated that the BG-FT was a more efficient option to produce hydrocarbon fuels [102]. Im-orb et al. [103] reported that the production rates of FT diesel, syngas, FT off gas, and electricity could be

Table 14.6 Cost structure of the total capital investment [96]

Component	Range (%)
(1) Direct investment	
Installation	6–14
Equipment	15–40
Piping	3–20
Instruments and controls	2–8
Buildings (including services)	3–18
Land	1–2
Electrical	2–10
(2) Indirect investment	
Construction expenses	4–16
Engineering and supervision	4–21
Contingency	5–15
Constructor's fee	2–6
(3) Fixed capital investment	(1) + (2)
(4) Working capital	10–20
(5) Total capital investment	(3) + (4)

maximized via the optimization of the FT off gas recirculation and FT reactor volume. Excluding the secondary equipment installation, the reuse of the FT off gas was less economically feasible than the once-through operation. The price of FT diesel from the once-through process was lower than that of fossil diesel when only the reaction section, including gasification, water-gas shift, and FT reactors, was considered in the economic analysis. Tock et al. [104] developed the detailed thermo-economic model to assess the performance of the BG-FT process. The proposed process yielded the overall thermal efficiency range of 50–60% (crude FT fuel). The production cost of FT fuel was found in the range of 56–106 Euro MWh^{-1} which was still higher than the fuel market price and the corresponding biomass breakeven cost in the range of 46–64 Euro MWh^{-1}. Bridgwater [105] concluded that the yield was the most sensitive factor and had a major effect on the production cost. Additionally, the investment cost was also found to decrease as the production plant size increased. Hunpinyo et al. [106] studied a conceptual techno-economic analysis using their developed BG-FT model. The thermal efficiency of 28.84%, 36.02%, and 36.92%, consistent with the production scales of 1 MW, 2 MW, and 3 MW, could be achieved, respectively. Although the production scale of 3 MW had high economic potential, its final product price of 1.768 USD per LDE (liter diesel equivalent) was still not competitive with the fossil-derived diesel. The cumulative FT fuel production costs decreased when the plant capacity was increased [104, 107], as shown in Fig. 14.9. They found that the production cost decreased from 30 euros per gigajoule for a 50 MW_{th} FT plant to approximately 15 euros per gigajoule at a plant scale of 8500 MW_{th}. Mustafa et al. [108] evaluated the techno-economic performance of liquid fuel production from biomass to reach the public transport demand in Narvik, Norway. The main sources of considered biomass come normally from municipal solid waste (MSW) and forests. The results showed that the maximum possible capacity of biofuel was three times higher than the demand of fuel for public transport, which meant that surplus biofuel supplied

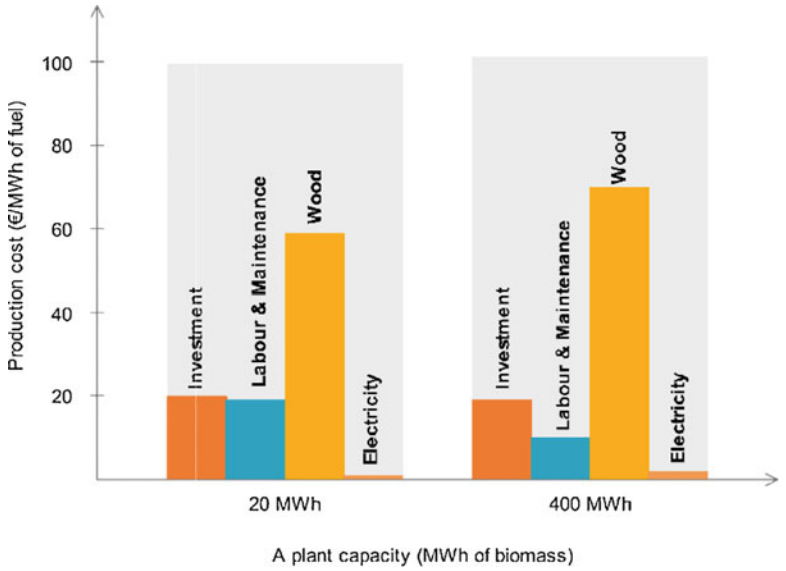

Fig. 14.9 The buildup of total production cost for different plant capacities

could be used in other applications, e.g., heating, etc. Moreover, the economic analysis indicated that the project payback period is about 4 years.

Performance enhancement of the BG-FT process by developing an efficient combined heat and power (CHP) network and heat integration and the improvement of its economic viability by employing a complete conversion configuration of bio-oil were also examined [109]. Cruz et al. [110] studied and compared two alternative configurations of the integrated BG, FT synthesis, and combined cycle process. The first configuration was an autothermal reforming of a fraction of FT gas product to enhance the yield of fuel, and the second one was the oxidation of a part of the conditioned bio-syngas to produce additional electricity. They found that the former process offered an improved yield of biofuel; however, its electricity production decreases. Moreover, this design could enhance the exergy efficiency and the thermodynamic performance. Trippe et al. [111] determined the key process parameters which affect the effectiveness of BTL process. They reported that the increase in gasification pressure significantly decreased the production cost, however; the reverse effect was found when the steam was introduced as a gasifying agent. Wang et al. [112] performed a multi-objective optimization problem based on the global warming potential (GWP) and the net present value (NPV) using a mixed-integer nonlinear programming (MINPL) model. The optimal solution offering the maximum environmental and economic performances was proposed. Additionally, the generated electricity could be sold as a by-product to decrease the cost of FT liquid fuel. Larson et al. [113] found that a 50% reduction in liquid fuel price could be achieved when the selling price of the generated electricity was increased 75% from the base price. Ali and Dasappa [8] studied and compared the techno-economic

Table 14.7 Techno-economic comparison of the BG-FT processes [8, 114]

Fuel	Gasification process	Production capacity (bpd)	Liquid fuel cost (USD l^{-1}) and FT reactor type
Switch grass	Pressurized O_2 blown fluidized bed gasifier, 4545 tpd feed	4630	0.52 Slurry bed FT reactor
Residual wood straw	Pressurized O_2 blown entrained flow gasifier, 5000 tpd feed	5500	1.57 Fixed-bed FT reactor
Corn stover	Pressurized oxy-steam fluidized bed gasifier, 1200 tpd feed	2362	1.39 Fixed-bed FT reactor
Woody biomass	Pressurized O_2 blown fluidized bed gasifier, 1000 tpd feed	1700	0.81 Slurry bed FT reactor
Woody biomass	Entrained flow gasifier, 2000 tpd feed	2180	0.4 Fluidized bed FT reactor
Wood chip	Entrained flow gasifier, 2016 tpd feed	407	0.77 N/A
Wood chip	Circulating fluidized bed gasifier, 2016 tpd feed	430	0.65 N/A

performance of various BG-FT processes in which liquid fuel was produced as the main product and the generated electricity was sold as a by-product at a reasonable high price and biomass cost was low, and the production cost of the produced liquid fuel could compete with the petroleum fuel when the oil price less than 60 USD bbl^{-1}. Their comparison results are shown in Table 14.7.

14.4 Future Trends

Liquid transportation fuel derived from the BG-FT process using second-generation biomass represents an attractive alternative energy source to replace fuels derived from crude distillation, as it offers benefits in terms of energy security and environmental friendliness. Although commercial-scale BG-FT processing facilities are in operation, several major obstacles to the economically feasible production of biofuels by the BG-FT process remain, such as low energy density of biomass, the high investment cost, limitation on the productivity of photosynthesis, lack of infrastructure, and availability of cultivable land areas for the bioenergy crop production, which compete with food production. Therefore, continuous study of the BG-FT process aims at improving its performance, for the large-scale replacement of fossil-based fuels is still being carried out.

As technical limitations affect the economic performance of BG-FT, the development of new technologies or the performance improvement of existing plants to

produce green transportation fuel that can compete with fossil-based fuels is a motivating topic. Studies of the main subprocesses are ongoing, with the purpose of improving the overall efficiency as well as achieving cost reduction. The design of an efficient gasifier to enhance the efficiency of syngas conversion is the main focus in terms of the syngas production subprocess. The reduction of thermal energy demand for the syngas cleaning and conditioning section is mostly studied. Regarding the FT process, the preparation of advanced-performance FT catalysts that can efficiently convert syngas to liquid fuel and the design of an FT reactor that offers good heat transfer performance are the key research themes. Exergy and energy analyses and the design of heat integration system are also being studied to develop a BG-FT process with high energy efficiency and low capital costs. Additionally, to achieve better process efficiency, the integration of the BG-FT process with other processes, such as chemical production units, power plants, or fuel cells, is being investigated.

Taking into account the implementation viewpoint, expected production capacity, fuel production economy, and biomass logistics, the optimal operational capacity lies in the range of 2000 to 4000 MW_{th} or 16,000–32,000 bpd [109]. This implies that several amounts of biomass feedstock are needed, which in turn results in high transportation costs. Biomass pretreatments, such as torrefication and fast pyrolysis, have been studied to overcome this problem. Torrefication is a thermal pretreatment process which is operated during 200–320 °C in the lack of oxygen. In the process, volatiles and water are removed, and the derived product is the biochar or torrefied biomass. In fast pyrolysis, biomass is thermally decomposed to char, gases, and bio-oil, during 450–550 °C under an inert atmosphere. After undergoing a suitable pretreatment process, the biomass volume is decreased while its energy density is increased, resulting in a decrease in transportation costs. Fluctuating oil prices is another concern issue for the liquid fuel production, as low oil prices influence large-scale BG-FT processes. Hence, small-scale BG-FT processes producing a spectrum of products that include a broad range of chemicals can be developed to minimize the impact of variations in oil prices.

The BG-FT process is a green fuel production method because of the CO_2 neutrality of the cycle and the renewable nature of biomass feedstocks. The environmental benefits of the BG-FT process can therefore be analyzed and compared to the conventional fossil-based process by performing life cycle analysis (LCA). CO_2 sequestration processes can be integrated with the BG-FT process to obtain negative carbon emissions. One future research area in the BG-FT process focuses on the usage of CO_2 from carbon capture and storage (CCS) in the FT process for the transportation fuel production via CO_2 hydrogenation over an FT catalyst [115].

Acknowledgment Support from the Thailand Science Research and Innovation (Global Partnership Program) and Chulalongkorn University is gratefully acknowledged.

References

1. Grahn, M., Azar, C., & Lindgren, K. (2009). The role of biofuels for transportation in CO_2 emission reduction scenarios with global versus regenal carbon caps. *Biomass and Bioenergy, 33*, 360–370.
2. http://worldbioenergy.org/uploads/WBA%20GBS%202017.
3. Omer, A. M. (2008). Green energies and the environment. *Renewable and Sustainable Energy Reviews, 12*(7), 1789–1821.
4. Steynberg, A.P., & M.E. Dry. Fischer-Tropsch technology A. P. Steynberg and M.E. Dry 1. 152. The Netherland: Elsevier E.V.
5. https://www.masterbuilder.co.in/chinas-yitai-receives-green-light-4-2-bln-coal-liquids-project/.
6. Paris, R. S., et al. (2015). Catalytic conversion of biomass-derived synthesis gas to fuels. *Catalysis, 27*, 33–61.
7. Lang, A., & Elhaj, H.F.A. (2014). The worldwide production of bio-jet fuels- The current developments regarding technologies and feedstocks, and innovative new R&D developments. Technical report.
8. Ali, S. S., & Dasappa, S. (2016). Biomass to liquid transportation fuel via Fischer Tropsch synthesis – Technology review and current scenario. *Renewable and Sustainable Energy Reviews, 28*, 267–286.
9. Smeenk, J. *Innovative gasification to produce Fischer Tropsch jet and diesel fuel.* DOE Bioenergy Technologies Office *(*BETO*)* Project Peer Review*,* (March 23 2015). Frontline BioEnergy, LLC.
10. Hu, J., Yu, F., & Lu, Y. (2018). Application of Fischer-Tropsch synthesis in biomass to liquid conversion. *Catalysts, 2*(2), 303–326.
11. Im-orb, K., Simasatitkul, L., & Arpornwichanop, A. (2015). Performance analysis and optimization of the biomass gasification and Fischer-Tropsch integrated process for green fuel productions. *Computer Aided Chemical Engineering, 37*, 275–280.
12. Yang, H., & Chen, H. (2015). Biomass gasification for synthetic liquid fuel production. In *Gasification for synthetic fuel production*. Cambridge. Woodhead Publishing.
13. Zainal, Z. A., et al. (2001). Prediction of performance of a downdraft gasifier using equilibrium modeling for different biomass materials. *Energy Conversion and Management, 42*(12), 1499–1515.
14. Tinaut, F. V., et al. (2008). *Effect of biomass particle size and air superficial velocity on the gasification process in a downdraft fixed bed gasifier.* An experimental and modelling study. *Fuel Processing Technology, 89*(11), 1076–1089.
15. Atnaw, S. M., Sulaiman, S. A., & Yusup, S. (2013). Syngas production from downdraft gasification of oil palm fronds. *Energy, 61*, 491–501.
16. Mavukwana, A., et al. *Simulation of sugarcane bagasse gasification using Aspen plus*. (April 15–13, 2013) Paper presented at the International conference on chemical and environmental engineering (ICCEE 2013), Johannesburg, South Africa.
17. Ramzan, N., et al. (2011). Simulation of hybrid biomass gasification using Aspen plus: A comparative performance analysis for food, municipal solid and poultry waste. *Biomass and Bioenergy, 35*(9), 3962–3969.
18. Widjaya, E. R., et al. (2018). Gasification of non-woody biomass: A literature review. *Renewable and Sustainable Energy Reviews, 89*, 184–193.
19. Basu, P. (2010). Chapter 5 – Gasification theory and modeling of gasifier.In *Biomass gasification and pyrolysis: Practical design and theory*. Oxford. Academic Press.
20. Higman, C., & van der Burgt, M. (2008). Chapter 5 – Gasification processes. In *Gasification (2nd ed.)*. Oxford. Gulf Professional Publishing.
21. Bhattacharya, A., Das, A., & Datta, A. (2014). Exergy based performance analysis of hydrogen production from rice straw using oxygen blown gasification. *Energy, 69*, 525–533.

22. Shayan, E., Zare, V., & Mirzaee, I. (2018). Hydrogen production from biomass gasification; a theoretical comparison of using different gasification agents. *Energy Conversion and Management, 159*, 30–41.
23. Gai, C., Dong, Y., & Zhang, T. (2014). Downdraft gasification of corn straw as a non-woody biomass: Effects of operating conditions on chlorides distribution. *Energy, 71*, 638–644.
24. Irfan, M. F., Usman, M. R., & Kusakabe, K. (2011). Coal gasification in CO_2 atmosphere and its kinetics since 1948: A brief review. *Energy, 36*(1), 12–40.
25. Chaiwatanodom, P., Vivanpatarakij, S., & Assabumrungrat, S. (2014). Thermodynamic analysis of biomass gasification with CO_2 recycle for synthesis gas production. *Applied Energy, 114*, 10–17.
26. Hanaoka, T., Hiasa, S., & Edashige, Y. (2013). Syngas production by CO_2/O_2 gasification of aquatic biomass. *Fuel Processing Technology, 116*, 9–15.
27. Sadhwani, N., et al. (2013). Simulation, analysis, and assessment of CO_2 enhanced biomass gasification. *Computer Aided Chemical Engineering, 32*, 421–426.
28. Im-orb, K., Simasatitkul, L., & Arpornwichanop, A. (2016). Analysis of synthesis gas production with a flexible H_2/CO ratio from rice straw gasification. *Fuel, 164*, 361–373.
29. Li, X. T., et al. (2004). Biomass gasification in a circulating fluidized bed. *Biomass and Bioenergy, 26*(2), 171–193.
30. Renganathan, T., et al. (2012). CO_2 utilization for gasification of carbonaceous feedstocks: A thermodynamic analysis. *Chemical Engineering Science, 83*, 159–170.
31. Loha, C., Chatterjee, P. K., & Chattopadhyay, H. (2011). Performance of fluidized bed steam gasification of biomass – Modeling and experiment. *Energy Conversion and Management, 52* (3), 1583–1588.
32. Ardila, Y. C., et al. (2012). Syngas production from sugar cane bagasse in a circulating fluidized bed gasifier using Aspen plus™: Modelling and simulation. *Computer Aided Chemical Engineering, 30*, 1093–1097.
33. Xiong, Q., et al. (2018). Parametric investigation on biomass gasification in a fluidized bed gasifier and conceptual design of gasifier. *Chemical Engineering & Processing – Process Intensification, 127*, 271–291.
34. Kojima, T., Assavadakorn, P., & Furusawa, T. (1993). Third international Rolduc symposium on coal science and technology and related processes measurement and evaluation of gasification kinetics of sawdust char with steam in an experimental fluidized bed. *Fuel Processing Technology, 36*(1), 201–207.
35. Nikoo, M. B., & Mahinpey, N. (2008). Simulation of biomass gasification in fluidized bed reactor using ASPEN PLUS. *Biomass and Bioenergy, 32*(12), 1245–1254.
36. Yaghoubi, E., et al. (2018). The effect of different operational parameters on hydrogen rich syngas production from biomass gasification in a dual fluidized bed gasifier. *Chemical Engineering & Processing – Process Intensification, 126*, 210–221.
37. Gao, N., & Li, A. (2008). Modeling and simulation of combined pyrolysis and reduction zone for a downdraft biomass gasifier. *Energy Conversion and Management, 49*(12), 3483–3490.
38. Xu, Q., Pang, S., & Levi, T. (2011). Reaction kinetics and producer gas compositions of steam gasification of coal and biomass blend chars, part 2: Mathematical modelling and model validation. *Chemical Engineering Science, 66*(10), 2232–2240.
39. Kaushal, P., Abedi, J., & Mahinpey, N. (2010). A comprehensive mathematical model or biomass gasification in a bubbling fluidized bed reactor. *Fuel, 89*(12), 3650–3661.
40. Miao, Q., et al. (2013). Modeling biomass gasification in circulating fluidized beds. *Renewable Energy, 50*, 655–661.
41. Sharma, A. K. (2011). Modeling and simulation of a downdraft biomass gasifier 1. Model development and validation. *Energy Conversion and Management, 52*(2), 1386–1396.
42. Sharma, A. K. (2008). Equilibrium and kinetic modeling of char reduction reactions in a downdraft biomass gasifier: A comparison. *Solar Energy, 82*(10), 918–928.
43. Shen, L., Gao, Y., & Xiao, J. (2008). Simulation of hydrogen production from biomass gasification in interconnected fluidized beds. *I Biomass and Bioenergy, 32*(2), 120–127.

44. Arpornwichanop, A., et al. (2014). Performance analysis of a biomass supercritical water gasification process under energy self-sufficient condition. *Computer Aided Chemical Engineering, 33*, 1699–1704.
45. Doherty, W., Reynolds, A., & Kennedy, D. (2009). The effect of air preheating in a biomass CFB gasifier using ASPEN plus simulation. *Biomass and Bioenergy, 33*(9), 1158–1167.
46. Francois, J., et al. (2008). Modeling and simulation of combined pyrolysis and reduction zone for a downdraft biomass gasifier. *Energy Conversion and Management, 40*, 3483–3490.
47. Chutichai, B., et al. (2013). Performance analysis of an integrated biomass gasification and PEMFC (proton exchange membrane fuel cell) system: Hydrogen and power generation. *Energy, 55*, 98–106.
48. Hamelinck, C. N., et al. (2004). Production of FT transportation fuels from biomass; technical options, process analysis and optimisation, and development potential. *Energy, 29*(11), 1743–1771.
49. Yu, G., et al. (2010). Process analysis for polygeneration of Fischer–Tropsch liquids and power with CO_2 capture based on coal gasification. *Energy, 89*, 1070–1076.
50. Im-orb, I., Wiyaratn, W., & Arpornwichanop, A. (2018). Technical and economic assessment of the pyrolysis and gasification integrated process for biomass conversion. *Energy, 153*, 592–603.
51. Im-orb, I., & Arpornwichanop, A. (2018, June 3–6). *Process analysis and environmental assessment of the pyrolysis-gasification process with CO_2capture.* Paper presented at the 6th international congress on green process engineering (GPE 2018), Toulouse, France.
52. Zeng, J., et al. (2017). Chemical looping pyrolysis-gasification of biomass for high H_2/CO syngas production. *Fuel Processing Technology. Energy, 168*, 116–122.
53. Boerrigter, H., et al. (2004). *Gas cleaning for integrated Biomass Gasification (BG) and Fischer-Tropsch (FT) systems; experimental demonstration of two BG-FT systems*. Petten: Energy research Centre of the Netherlands (ECN).
54. Basu, P. (2010). Chapter 9 – Production of synthetic fuels and chemicals from biomass. In *Biomass gasification and pyrolysis: Practical design and theory*. Oxford. Academic Press.
55. Qin, Y., et al. (2015). The influence of different chemical compositions in biomass on gasification tar formation. *Biomass and Bioenergy, 83*, 77–84.
56. Pereira, E. G., et al. (2012). Sustainable energy: A review of gasification technologies. *Renewable and Sustainable Energy Reviews, 16*(7), 4753–4762.
57. Tuomi, S., et al. (2015). Effect of pressure on tar decomposition activity of different bed materials in biomass gasification conditions. *Fuel, 158*, 293–305.
58. Couto, N., et al. (2013). Influence of the biomass gasification processes on the final product gas. *Energy Procedia, 36*, 596–606.
59. Galindo, A. L., et al. (2014). Biomass gasification in a downdraft gasifier with a two-stage air supply: Effect of operating conditions on gas quality. *Biomass and Bioenergy, 61*, 236–244.
60. Liu, L., et al. (2018). Experimental study of biomass gasification with oxygen-enriched air in fluidized bed gasifier. *Science of the Total Environment, 626*, 423–433.
61. Phuphuakrat, T., Namioka, T., & Yoshikawa, K. (2011). Absorptive removal of biomass tar using water and oily materials. *Bioresource Technology, 102*, 543–549.
62. Nakamura, S., Kitano, S., & Yoshikawa, K. (2016). Biomass gasification process with the tar removal technologies utilizing bio-oil scrubber and char bed. *Applied Energy, 170*, 186–192.
63. Leibold, H., Hornung, A., & Seifert, H. (2008). HTHP syngas cleaning concept of two stage biomass gasification for FT synthesis. *Powder Tecnology, 180*, 265–270.
64. Zhang, L., Xu (Chales), C., & P. Champagnes. (2010). Overview of recent advances in thermo-chemical conversion of biomass. *Energy Conversion and Management, 51*, 969–982.
65. Vivanpatarakij, S., & Assabumrungrat, S. (2013). Thermodynamic analysis of combined unit of biomass gasifier and tar steam reformer for hydrogen production and tar removal. *International Journal of Hydrogen Energy, 38*(10), 3930–3936.

66. Shen, Y., & Yoshikawa, K. (2013). Recent progresses in catalytic tar elimination during biomass gasification or pyrolysis – a review. *Renewable and Sustainable Energy Reviews, 21*, 371–392.
67. Josuinkas, F. M., et al. (2014). Steam reforming of model gasification tar compounds over nickel catalysts prepared from hydrotalcite precursors. *Fuel Processing Technology, 121*, 76–82.
68. Kuchonthara, P., Vitidsant, T., & Tsutsumi, A. (2008). Catalytic effects of potassium on lignin steam gasification with γ-Al_2O_3 as a bed material. *Korean Journal of Chemical Engineering, 25*, 656–662.
69. Devi, L., et al. (2005). Catalytic decomposition of biomass tars: Use of dolomite and untreated olivine. *Renewable Energy, 30*, 565–587.
70. Boerrigter, H. et al. *Tar removal from biomass produced gas: Development and optimization of the OLGA tar removal technology*. Paper presented at the 14th European Biomass Conference and exhibition, Paris, France.
71. Dry, M. E. (2002). The Fischer–Tropsch process: 1950–2000. *Catalysis Today, 71*(3–4), 227–241.
72. Steynberg, A. P., et al. (2004). Chapter 2 – Fischer-Tropsch reactors. *Studies in Surface Science and Catalysis, 152*, 64–195.
73. Khodakov, A. Y., Chu, W. F., & Fongarland, P. (2007). Advances in the development of novel cobalt Fischer-Tropsch catalysts for synthesis of long-chain hydrocarbons and clean fuels. *Chemical Reviews, 107*(5), 1692–1744.
74. de Klerk, A. (2011). Chapter 1 – Fischer-Tropsch facilities at a glance. In *Fischer–Tropsch Refining (5ed.).* Singapore. Wiley-VCH.
75. Wood, D. A., Nwaoha, C., & Towler, B. F. (2012). Gas-to-liquids (GTL): A review of an industry offering several routes for monetizing natural gas. *Journal of Natural Gas Science and Engineering, 9*, 196–208.
76. Lohitharn, N., Goodwin, J. G., Jr., & Lotero, E. (2008). Fe-based Fischer–Tropsch synthesis catalysts containing carbide-forming transition metal promoters. *Journal of Catalysis, 255*(1), 104–113.
77. Ma, L., et al. (2012). A review of thermal–chemical conversion of lignocellulosic biomass in China. *Biotechnology Advances, 30*(4), 859–873.
78. Wang, B., Gebreslassie, B. H., & You, F. (2013). Sustainable design and synthesis of hydrocarbon biorefinery via gasification pathway: Integrated life cycle assessment and technoeconomic analysis with multiobjective superstructure optimization. *Computers & Chemical Engineering, 52*, 55–76.
79. Lu, Y., & Lee, T. (2007). Influence of the feed gas composition on the Fischer-Tropsch synthesis in comercial operation. *Journal of Natural Gas Chemistry, 16*, 329–341.
80. Tristantini, D., et al. (2007). The effect of synthesis gas composition on the Fischer–Tropsch synthesis over Co/γ-Al_2O_3 and Co–Re/γ-Al_2O_3 catalysts. *Fuel Processing Technology, 88*(7), 643–649.
81. Rahmati, M., et al. (2018). Effect of different alumina supports on performance of cobalt Fischer-Tropsch catalysts. *Journal of Catalysis, 359*, 92–100.
82. Sun, Y., et al. (2017). Fischer-Tropsch synthesis using iron based catalyst in a microchannel reactor: Performance evaluation and kinetic modeling. *International Journal of Hydrogen Energy, 42*, 29222–29235.
83. Rafiq, M. H., et al. (2011). Experimental studies and modeling of a fixed bed reactor for Fischer–Tropsch synthesis using biosyngas. *Fuel Processing Technology, 92*(5), 893–907.
84. Wang, Y., et al. (2003). Heterogeneous modeling for fixed-bed Fischer–Tropsch synthesis: Reactor model and its applications. *Chemical Engineering Science, 58*(3–6), 867–875.
85. de Swart, J. W. A., & Krishna, R. (2002). Simulation of the transient and steady state behaviour of a bubble column slurry reactor for Fischer–Tropsch synthesis. *Chemical Engineering and Processing: Process Intensification, 41*(1), 35–47.

86. Kwack, S. H., et al. (2011). Modeling a slurry CSTR with Co/P–Al2O3 catalyst for Fischer–Tropsch synthesis. *Fuel Processing Technology, 92*(12), 2264–2271.
87. Zhang, X., et al. (2018). Effect of the operation parameters on the Fischer–Tropsch synthesis in fluidized bed reactors. *Chinese Journal of Chemical Engineering, 26*, 245–251.
88. Iliuta, I., & Larachi, F. (2018). Fischer-Tropsch synthesis in vertical, inclined and oscillating trickle-bed reactors for offshore floating applications. *Chemical Engineering Science, 177*, 509–522.
89. Yermakova, A., & Anikeev, V. (2000). Thermodynamic calculations in the modeling of multiphase processes and reactors. *Industrial and Engineering Chemistry Research, 39*(5), 1453–1472.
90. Song, H. S., et al. (2004). Operating strategies for Fischer-Tropsch reactors: A model-directed study. *Korean Journal of Chemical Engineering, 21*(2), 308–317.
91. Pondini, M., & Ebert, M. (2013). *Process synthesis and design of low temperature Fischer-Tropsch crude production from biomass derived syngas*. Göteborg: Chalmers University of Technology.
92. Krishna, R., & Sie, S. T. (2000). Design and scale-up of the Fischer-Tropsh bubble column slurry reactor. *Fuel Processing Technology, 64*, 73–105.
93. Panahi, M., Skogestad, S., & Yelchuru R. (2010, January 10–14) *Steady state simulation for optimal design and operation of GTL process.* Proceedings of the 2nd annual gas processing symposium. p. 275–285.
94. Vogel, A., Mueller-Langer, F., & Kaltschmitt, M. (2008). Analysis and evaluation of technical and economic potentials of BTL-fuels. *Chemical Engineering & Technology, 31*(5), 755–764.
95. Sunde, K., Brekke, A., & Solberg, B. (2011). Environmental impacts and costs of woody biomass-to-liquid (BTL) production and use- a review. *Forest Policy and Economics, 13*, 591–602.
96. Xiang, D., et al. (2014). Techno-economic analysis of the coal-to-olefins process in comparison with the oil-to-olefins process. *Applied Energy, 113*, 639–647.
97. Kim, K., et al. (2013). Long-term operation of biomass-to-liquid systems coupled to gasification and Fischer–Tropsch processes for biofuel production. *Bioresource Technology, 127*, 391–399.
98. Muradov, N., et al. (2015). Production of Fischer-Tropsch hydrocarbons via oxygen-blown gasification of charred pinewood pellets. *Fuel Processing Technology, 140*, 236–244.
99. Leibbrandt, N. H., et al. (2013). Process efficiency of biofuel production via gasification and Fischer–Tropsch synthesis. *Fuel, 109*, 484–492.
100. Sues, A., Jurascık, M., & Ptasinsk, K. (2010). Exergetic evaluation of 5 biowastes-to-biofuels routes via gasification. *Energy, 35*, 996–1007.
101. Im-orb, K., Simasatitkul, L., & Arpornwichanop, A. (2006). Techno-economic analysis of the biomass gasification and Fischer-Tropsch integrated process with off-gas recirculation. *Energy, 94*, 483–496.
102. Michailos, S., Parker, D., & Webb, C. (2017). A techno-economic comparison of Fischer-Tropsch and fast pyrolysis as ways of utilizing sugarcane bagasse in transportation fuel production. *Chemical Engineering Research and Design, 118*, 206–214.
103. Im-orb, K., & Arpornwichanop, A. (2016). Techno-environmental analysis of the biomass gasification and Fischer-Tropsch integrated process for the co-production of bio-fuel and power. *Energy, 112*, 121–132.
104. Tock, L., Gassner, M., & Marechal, F. (2010). Thermochemical production of liquid fuels from biomass: Thermo-economic modeling, process design and process integration analysis. *Biomass and Bioenergy, 34*, 1838–1854.
105. Bridgwater, A. *Technical and economic assessment of thermal processes for biofuels.* Technical report, COPE Ltd., UK.
106. Hunpinyo, P., et al. (2014). Alternative route of process modification for biofuel production by embedding the Fischer–Tropsch plant in existing stand-alone power plant (10 MW) based on

biomass gasification – Part I: A conceptual modeling and simulation approach (a case study in Thailand). *Energy Conversion and Management, 88*, 1179–1192.
107. Swain, P. K., Das, L. M., & Naik, S. N. (2011). Biomass to liquid: A prospective challenge to research and development in 21st century. *Renewable and Sustainable Energy Reviews, 15*(9), 4917–4933.
108. Mustafa, A., Calay, R. K., & Mustafa, M. Y. (2017). A techno-economic study of a biomass gasification plant for the production of transport biofuel for small communities. *Energy Procedia, 112*, 529–536.
109. Ng, K. S., & Sadhukhan, J. (2011). Techno-economic performance analysis of bio-oil based Fischer-Tropsch and CHP synthesis platform. *Biomass and Bioenergy, 35*(7), 3218–3234.
110. Cruz, P. L., Iribarren, D., & Dufour, J. (2017). Exergy analysis of alternative configurations of a system coproducing synthetic fuel and electricity via biomass gasification, Fischer-Tropsch synthesis and a combined cycle scheme. *Fuel, 194*, 375–394.
111. Trippe, F., et al. (2011). Techno-economic assessment of gasification as a process step within biomass-to-liquid (BtL) fuel and chemicals production. *Fuel Processing Technology, 92*, 2169–2184.
112. Wang, S., et al. (2013). Improved Fischer–Tropsch synthesis for gasoline over Ru, Ni promoted co/HZSM-5 catalysts. *Fuel, 108*, 597–603.
113. Larson, E., Jin, H., & Celik, F. (2009). Large-scale gasification-based coproduction of fuels and electricity from swichgrass. *Biofuels Bioproducts Biorefining, 3*(2), 174–194.
114. Dimitriou, I., Goldingay, H., & Bridgwater, A. V. (2018). Techno-economic and uncertainty analysis of biomass to liquid (BTL) systems for transportation fuel production. *Renewable and Sustainable Energy Reviews, 88*, 160–175.
115. Yao, Y., et al. (2010). Fischer-Tropsch synthesis using $H_2/CO/CO_2$ syngas mixtures over a cobalt catalyst. *Industrial & Engineering Chemistry Research, 49*(21), 11061–11066.

Chapter 15
Integration of Clean and Sustainable Energy Resources and Storage in Multigeneration Systems: Design, Modeling, and Robust Optimization

Fatih Yilmaz, Yunus Emre Yuksel, and Murat Ozturk

Nomenclature

Greek letters

λ	Membrane water content
n	Energy efficiency
ψ	Exergy efficiency

Subscripts

Abs	Absorber
A_{hTES}	Energy loss area
ch	Chemical
comp	Compressor
cond	Condenser
Dr	Dryer
DWH	Domestic water heater
e	Output
ejc	Ejector
en	Energy
Eva	Evaporator
ex	Exergy

F. Yilmaz · M. Ozturk (✉)
Faculty of Technology, Isparta University of Applied Science, Isparta, Turkey
e-mail: fatihyilmaz@isparta.edu.tr; muratozturk@isparta.edu.tr

Y. E. Yuksel
Faculty of Education, Afyon Kocatepe University, Afyonkarahisar, Turkey
e-mail: yeyuksel@aku.edu.tr

F. Jabari et al. (eds.), *Integration of Clean and Sustainable Energy Resources and Storage in Multi-Generation Systems*,
https://doi.org/10.1007/978-3-030-42420-6_15

ht, loss	Thermal energy loss
hTES	Stored heat in TES
HW	Hot water
i	Input
O & M	Operating and maintenance
p	Pump
ph	Physical
ref	Reflector field
RT	Rankine turbine
ST	Solar tower
StT	Storage tank
Vl	Valve

Acronyms

AP	Ammonia process
$\dot{C}$	Cost rate
COP	Coefficient of performance
CRF	Capital recovery factor
DC	Drying cycle
EES	Engineering Equation Solver
$\dot{E}x$	Exergy flow rate
h	Specific enthalpy
HEX	Heat exchanger
HPLP	Hydrogen production and liquefaction process
HWP	Hot water production
I_{DSI}	Direct solar irradiance
LCOH	Levelized cost of hydrogen
$\dot{m}$	Mass flow rate
N	Annual number of working hours
ORC	Organic Rankine cycle
P_o	Dead reference pressure
$\dot{Q}$	Heat flow rate
PEM	Proton exchange membrane
PVT	Photovoltaic thermal
RC	Rankine cycle
s	Specific entropy
SEACE	Single-effect absorption cycle with ejector
SPTC	Solar power tower cycle
T_o	Dead reference temperature
TES	Thermal energy storage
V	Net voltage
$\dot{W}$	Workflow rate
Z	Purchase cost

15.1 Introduction

Energy demands have been on a steady upward trend, over the last decade, due to an increase in the various factors such as world population and industrialization. According to the International Energy Agency (IEA) report, it is claimed that worldwide energy demand will increase by 50% from 2016 to 2030 [1, 2]. In the present day, about 80% of the global energy needed is obtained from fossil-based fuels, and thus this situation gives rise to environmental complications, for example global warming, acid rain, and climate change [3]. It is a well-known fact that renewable energy sources are an important solution to combat these environmental problems caused by the burning of fossil fuels. In addition, in parallel with renewable energy sources, the efficient use of energy resources is also very important to overcome environmental problems, and in this context, multigeneration systems especially renewable energy-supported plants will become a very important topic for an environmentally friendly future.

A multigeneration plant can be defined as the integration of different thermal plants for various useful products. In these systems, it is possible to obtain various energy outputs with a single energy input and essentially utilize the same energy source. In this book chapter, the solar energy is selected as an energy source of system. Multigeneration systems have various advantages, for example, efficient plant operation, minimum energy and exergy losses, less material waste and operating and maintenance costs, lower greenhouse gas emissions, and higher performance [4–6]. Moreover, it is advantageous to design these systems with renewable energy sources, because renewable energy sources do not release harmful gases. Solar energy is the source of energy that is converted into thermal or electrical energy from the sun and is expressed as the cleanest and most abundant renewable energy source available [7].

There are many studies done by various authors about solar-based multigeneration systems for different purposes in literature research. Ozlu and Dincer [8] have performed a performance evaluation of the multigeneration plant driven by solar energy. The plant modeled by them includes a solar collector cycle, two-stage steam cycle, a two-stage Rankine cycle, a PEM electrolyzer, and desalination process. The computed maximum total energy and exergy efficiency of the plant are 36% and 44%, respectively. Behzadi et al. [9] have investigated and optimized a multigeneration system assisted by solar and geothermal energy in terms of energy, exergy, and exergoeconomic analyses. The suggested plant consists of a concentrated PVT, a double-effect absorption cooling cycle, and a geothermal unit. The results of the study indicate that the maximum exergy destruction rate is seen in PVT system with 29.6 kW. The study performed by Al-Zareer [10] presents the development and investigation of the novel solar energy-based system with thermochemical cycle and hydrogen compression. The overall energy and exergy efficiency of the plant are calculated as 12.6% and 20.7%, respectively, according to their analyses results.

Yilmaz et al. [11] have studied a thermodynamic performance evaluation of combined plant integrated with solar energy and the high-temperature steam electrolyzer. They have modeled the work, which supported solar energy, for hydrogen, power, heating-cooling, drying, and liquefaction of hydrogen, and also found the total energy and exergy efficiency of the plant to be 20% and 30%, respectively. Shahid et al. [12] have carried out comprehensive thermodynamic analyses of multigeneration plant driven by renewable energy for the generation of ammonia synthesis, power, heating-cooling, and desalinated water. In their study, they have proposed a phase change material as energy storage to provide uninterrupted energy. They have calculated the energy efficiency of the whole system as 18.9% and the exergy efficiency as 28.0%.

Khalid et al. [13] have evaluated a thermodynamic and economic assessment of renewable energy-based integrated plant for green constructions. The key aim of their paper is to generate useful products such as heating, cooling, power, and hot water with solar and wind energy. The suggested plant includes a wind turbine, a solar collector, an ORC, and a heat pump system, and the overall energy and exergy efficiency are found as 46.1% and 7.3%, respectively. Bamisile et al. [14] have proposed a performance examination of a new solar-driven integrated combined plant for multipurpose generation. They have developed the energy plant in order to generate power, hydrogen, hot water, and cooling. The performance of the modeled system is found as 71.6% and 24.5%, respectively, in terms of energy and exergy efficiency.

Zafar and Dincer [15] have examined comprehensive thermodynamic and exergoeconomic analyses of a renewable energy-assisted integrated plant for buildings. The renewable energy-based system includes a PV panel and wind turbine for power generation and also electrolyzer for hydrogen production. According to their analysis results, when fuel cell temperature is used as an output, the system energetic performance is increased from 12% to 28%. Atiz et al. [16] have conducted an evaluation of evacuated solar tube collector-based hydrogen and electricity generation performance. The suggested unified system comprises of a solar-evacuated collector, solar pond, an ORC, and electrolyzer. The overall energy and exergy efficiency of the system are computed as 5.92% and 18.21% respectively. Ishaq et al. [17] have presented a renewable energy-based combined trigeneration system, based on thermodynamic analyses. The system includes a solar heliostat field, Cu-Cl thermochemical cycle, wind turbine, and hydrogen compression system. The results of their determined study show that general energy and exergy efficiency are computed as 49% and 48.2%, respectively.

The key aim of this book chapter is to investigate comprehensive thermodynamic and economic analyses of a solar energy-based combined plant for hydrogen, power, heating-cooling, hot water, drying, and ammonia production. Also, the effects of the dead state temperature, solar radiation, pump and turbine isentropic efficiency, and number of heliostats on the system's performance and useful outputs are investigated and modeled. For this thermodynamic calculation, Engineering Equation Solver (EES) software is used. Energy and exergy efficiency of the proposed system and subsystems are determined and presented in graphs.

15.2 System Design

In this chapter, a solar energy-assisted multigeneration plant is proposed for multiple purposes such as hydrogen, power, heating-cooling, drying, and ammonia generation using the clean and sustainable way. A detailed flow diagram including the state points of the modeled plant is plotted in Fig. 15.1. As clearly seen from this figure, the suggested plant consists mainly of eight subsystems: a solar tower cycle, a Rankine cycle, a hydrogen generation and liquefaction cycle, an ammonia process, an ORC, a single-effect absorption cycle with ejector, a drying cycle, and hot water production. This system is designed for the production of hydrogen, ammonia, heating-cooling, power, and hot water by providing the thermal energy required from the solar tower system.

At first, the working fluid of the solar tower cycle enters the solar receiver at point 10 and rises to a temperature of about 875 ° C and then enters the hot thermal energy storage tank (TES) at point 1. This working fluid enters the HEX1, generator, generator 2, dryer, hot water storage tank, and cold TES tank (between points 1 and 10), respectively, to transfer thermal energy on it. Then, in HEX1, the solar tower working fluid transfers some of its thermal energy to the working fluid of Rankine cycle. The Rankine cycle includes three turbines, a condenser 1, and pump 3 and produces power for PEM electrolyzer. The inlet pressure of the turbine 1 of the Rankine cycle at point 11 is assumed as 9000 kPa. Subsequently, another energy generation cycle is the ORC operating with R123 working fluid (between point 45 and 50). The solar tower working fluid is transferred of heat energy to ORC

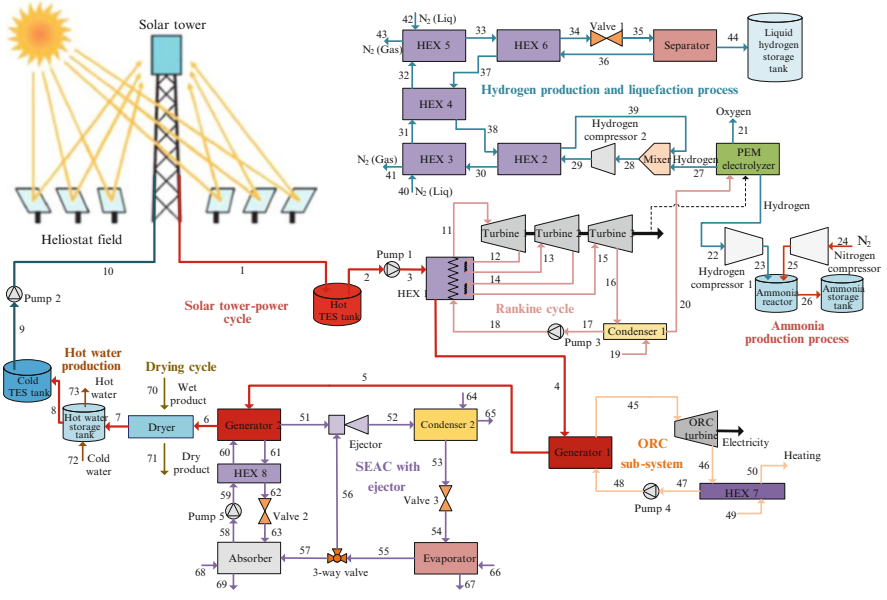

Fig. 15.1 Flow diagram of the multigeneration plant for hydrogen production and liquefaction

Table 15.1 Working parameters of solar tower-based multigeneration plant

Dead reference temperature, T_o	25 °C
Dead reference pressure, P_o	101.3 kPa
Direct solar irradiance, I_{DSI}	760 W/m^2
Outlet temperature of solar tower, T_1	875 °C
Heliostat number, $n_{heliostat}$	4350
Heliostat surface area, $A_{heliostat}$	2.3 m^2
Reflector field performance, η_{ref}	0.74
Solar tower performance, η_{ST}	0.14
Output pressure of pump 1, P_3	1344 kPa
Output pressure of pump 2, P_{10}	2010 kPa
Pump isentropic performance, η_p	0.80
Output temperature of hot TES tank, T_2	825 °C
Isentropic efficiency of Rankine turbine, η_{RT}	0.80
Turbine 1 inlet pressure, P_{11}	9000 kPa
Turbine 2 inlet pressure, P_{13}	5000 kPa
Turbine 3 inlet pressure, P_{15}	2000 kPa
COP_{en} for cooling plant	1.069
COP_{ex} for cooling plant	0.284
Isentropic efficiency of ORC turbine, η_{ORC_T}	0.78
ORC turbine inlet temperature, T_{45}	132 °C
ORC turbine inlet pressure, P_{45}	700 kPa
Working fluid of ORC subsystem	R123

generator 1 at point 4. The working fluid of ORC then enters the ORC turbine at point 45 as superheated steam and then where power is generated.

Another important subsystem of this study is the single-effect absorption cooling system with ejector (SEACE) (between point 51 and 69), where heating and cooling applications take place. The solar tower working fluid, which still has high thermal energy, enters generator 2 at point 5 point and then provides the thermal energy required for the operation of the SEACE system with ejector. Then, it is used for drying the product by using the thermal energy of the fluid entering the dryer at point 6. The solar tower working fluid then enters the cold TES tank and offers continuous operation if the system requires energy. In addition, working parameters of the suggested plant are given in Table 15.1.

Some of the electricity generated by the Rankine cycle is sent to the PEM electrolyzer for hydrogen production, where hydrogen and oxygen are produced from water. The problem of hydrogen storage is a known fact, and, in this study, it is proposed to store hydrogen by liquefying it (between point 27 and 44). As shown in Fig. 15.1, the hydrogen produced in the form of gas is liquefied through various compressor and heat exchanger processes and sent to the storage unit. A portion of the produced hydrogen gas reacts with nitrogen at the ammonia rector and ammonia is produced.

15.3 First and Second Law Analyses

The first and second law performance of the combined multigeneration plant is evaluated by conducting quantitative energetic and exergetic analyses. The economic estimation of the combined plant is performed according to the exergoeconomic assessment. In this part, the basic assumptions, opinions, methods, and equalities utilized to evaluate plant performance are defined and explained. The primary assumptions for the assessment can be defined as:

- Cycles take place at steady-state and steady-flow conditions.
- Potential and kinetic energy and also exergy changes can be negligible.
- Environment and ambient condition at $T_o = 25\ ^\circ\text{C}$ and $P_o = 1$ atm.
- All flows and parts are always at the working temperature and pressure levels.

At the steady-state status, the mass balance equation is [18–20]:

$$\sum \dot{m}_i = \sum \dot{m}_e \tag{15.1}$$

where $\dot{m}$ is mass flow rate and the subscripts "i" and "e" specify the input and output of control volume. Based on the first law of thermodynamic, the energy balance equality is:

$$\sum \dot{m}_i h_i + \sum \dot{Q}_i + \sum \dot{W}_i = \sum \dot{m}_e h_e + \sum \dot{Q}_e + \sum \dot{W}_e \tag{15.2}$$

where $\dot{Q}$ and $\dot{W}$ show the rates of heat and power flows and h stands for specific enthalpy. General entropy balance equality is:

$$\sum \dot{m}_i s_i + \sum \left(\frac{\dot{Q}}{T}\right)_i + \dot{S}_{gen} = \sum \dot{m}_e s_e + \sum \left(\frac{\dot{Q}}{T}\right)_e \tag{15.3}$$

where s and $\dot{S}_{gen}$ give the specific entropy and rate of entropy generation. According to the second law of thermodynamic, the exergetic balance equation can be described as:

$$\sum \dot{m}_i \text{ex}_i + \sum \dot{\text{Ex}}_i^Q + \sum \dot{\text{Ex}}_i^W = \sum \dot{m}_e \text{ex}_e + \sum \dot{\text{Ex}}_e^Q + \sum \dot{\text{Ex}}_e^W + \dot{\text{Ex}}_D \tag{15.4}$$

where $\dot{\text{Ex}}^Q$ and $\dot{\text{Ex}}^W$ give the exergetic flows associated with heat, boundary, or shaft work. In Eq. (15.4), different thermodynamic variables can be defined as given below:

$$\dot{\mathrm{E}}\mathrm{x}^{Q} = \dot{Q}\left(1 - \frac{T_{\mathrm{o}}}{T}\right) \tag{15.5}$$

$$\dot{\mathrm{E}}\mathrm{x}^{W} = \dot{W} \tag{15.6}$$

$$\dot{\mathrm{E}}\mathrm{x}_{d} = \dot{S}_{\mathrm{gen}} T_{\mathrm{o}} \tag{15.7}$$

In the end, the specific exergetic variable can be defined as:

$$\mathrm{ex} = \mathrm{ex}_{\mathrm{ph}} + \mathrm{ex}_{\mathrm{ch}} \tag{15.8}$$

In Eq. (15.8), the physical and chemical specific exergetic variables can be described as:

$$\mathrm{ex}_{\mathrm{ph}} = h - h_{\mathrm{o}} - T_{\mathrm{o}}(s - s_{\mathrm{o}}) \tag{15.9}$$

$$\mathrm{ex}_{\mathrm{mix}}^{\mathrm{ch}} = \sum y_i \mathrm{ex}_{\mathrm{ch}}^{\mathrm{o}} + RT_{\mathrm{o}} \sum y_{\mathrm{i}} \ln y_{\mathrm{i}} \tag{15.10}$$

Based on these standpoints, the energetic and exergetic balance equalities are given in Tables 15.2 and 15.3, respectively.

15.3.1 Solar Power Tower

The solar-powered reflection area of 524 heliostats is utilized to the investigated plant, and achieved solar power inlet is used to the multigeneration aim for hydrogen production and compression. The net heliostat performance of 82% is considered during the assessment. Some parametric works analyzing the heliostat design indicators' impact on plant efficiency are conducted. The statement utilized to calculate the solar energy inlet is as given below:

$$\dot{Q}_{\mathrm{solar}} = \eta_{\mathrm{rf}} I_{\mathrm{si}} A_{\mathrm{a}} n_{\mathrm{r}} \tag{15.11}$$

where η_{rf} shows the reflector performance, I_{si} is the solar irradiance, A_{a} indicates the aperture area, and n_{r} implies the number of reflectors.

15.3.2 PEM Electrolyzer

A part of the produced electricity from Rankine process is used by the PEM plant for hydrogen generation. Thermodynamic analysis of the PEM plant needs the definition of activation, ohmic, and concentration overpotential changes. The activation losses produce the additional voltage changes that are necessary for the migration of

Table 15.2 First law balance and efficiency equations

Components	Energy balance equation	Energy efficiency equation
Solar tower	$\dot{m}_{10}h_{10} + \dot{Q}_{\text{solar}} = \dot{m}_1 h_1$	$\eta_{\text{st}} = \frac{\dot{m}_1 h_1 - \dot{m}_{10} h_{10}}{\dot{Q}_{\text{solar}}}$
Hot TES tank	$\dot{m}_1 h_1 = \dot{m}_2 h_2 + \dot{Q}_L^{\text{hTES}}$	$\eta_{\text{hTES}} = \frac{\dot{m}_2 h_2}{\dot{m}_1 h_1}$
Pump 1	$\dot{m}_2 h_2 + \dot{W}_{P1} = \dot{m}_3 h_3$	$\eta_{\text{P1}} = \frac{\dot{m}_3 h_3 - \dot{m}_2 h_2}{\dot{W}_{P1}}$
Cold TES tank	$\dot{m}_8 h_8 = \dot{m}_9 h_9 + \dot{Q}_L^{\text{cTES}}$	$\eta_{\text{cTES}} = \frac{\dot{m}_9 h_9}{\dot{m}_8 h_8}$
Pump 2	$\dot{m}_9 h_9 + \dot{W}_{P2} = \dot{m}_{10} h_{10}$	$\eta_{\text{P2}} = \frac{\dot{m}_{10} h_{10} - \dot{m}_9 h_9}{\dot{W}_{P2}}$
HEX 1	$\dot{m}_3 h_3 + \dot{m}_{12} h_{12} + \dot{m}_{14} h_{14} + \dot{m}_{18} h_{18} = \dot{m}_4 h_4 + \dot{m}_{11} h_{11} + \dot{m}_{13} h_{13} + \dot{m}_{15} h_{15}$	$\eta_{\text{Con1}} = \frac{\dot{m}_{11}(h_{11} + h_{13} + h_{15} - h_{18} - h_{12} - h_{14})}{\dot{m}_3 h_3 - \dot{m}_4 h_4}$
Turbine 1	$\dot{m}_{11} h_{11} = \dot{m}_{12} h_{12} + \dot{W}_{T1}$	$\eta_{\text{T1}} = \frac{\dot{W}_{T1}}{\dot{m}_{11} h_{11} - \dot{m}_{12} h_{12}}$
Turbine 2	$\dot{m}_{13} h_{13} = \dot{m}_{14} h_{14} + \dot{W}_{T2}$	$\eta_{\text{T2}} = \frac{\dot{W}_{T2}}{\dot{m}_{13} h_{13} - \dot{m}_{14} h_{14}}$
Turbine 3	$\dot{m}_{15} h_{15} = \dot{m}_{16} h_{16} + \dot{W}_{T3}$	$\eta_{\text{T3}} = \frac{\dot{W}_{T3}}{\dot{m}_{15} h_{15} - \dot{m}_{16} h_{16}}$
Condenser 1	$\dot{m}_{16} h_{16} + \dot{m}_{19} h_{19} = \dot{m}_{17} h_{17} + \dot{m}_{20} h_{20}$	$\eta_{\text{Con1}} = \frac{\dot{m}_{20} h_{20} - \dot{m}_{19} h_{19}}{\dot{m}_{16} h_{16} - \dot{m}_{17} h_{17}}$
Pump 3	$\dot{m}_{17} h_{17} + \dot{W}_{P3} = \dot{m}_{18} h_{18}$	$\eta_{\text{P3}} = \frac{\dot{m}_{18} h_{18} - \dot{m}_{17} h_{17}}{\dot{W}_{P3}}$
PEM electrolyzer	$\dot{m}_{20} h_{20} + \dot{W}_{\text{PEM}} = \dot{m}_{21} h_{21} + \dot{m}_{22} h_{22} + \dot{m}_{27} h_{27}$	$\eta_{\text{PEM}} = \frac{\dot{m}_{22} h_{22} + \dot{m}_{27} h_{27}}{\dot{m}_{20} h_{20} + \dot{W}_{\text{PEM}}}$
Hydrogen compressor 1	$\dot{m}_{22} h_{22} + \dot{W}_{\text{HC1}} = \dot{m}_{23} h_{23}$	$\eta_{\text{HC1}} = \frac{\dot{m}_{23} h_{23} - \dot{m}_{22} h_{22}}{\dot{W}_{\text{HC1}}}$
Nitrogen compressor	$\dot{m}_{24} h_{24} + \dot{W}_{\text{NC}} = \dot{m}_{25} h_{25}$	$\eta_{\text{NC}} = \frac{\dot{m}_{25} h_{25} - \dot{m}_{24} h_{24}}{\dot{W}_{\text{NC}}}$
Ammonia reactor	$\dot{m}_{23} h_{23} + \dot{m}_{25} h_{25} = \dot{m}_{26} h_{26}$	$\eta_{\text{ar}} = \frac{\dot{m}_{26} h_{26}}{\dot{m}_{23} h_{23} + \dot{m}_{25} h_{25}}$
Mixer	$\dot{m}_{27} h_{27} + \dot{m}_{39} h_{39} = \dot{m}_{28} h_{28}$	$\eta_{\text{mix}} = \frac{\dot{m}_{28} h_{28}}{\dot{m}_{27} h_{27} + \dot{m}_{39} h_{39}}$
Hydrogen compressor 2	$\dot{m}_{28} h_{28} + \dot{W}_{HC2} = \dot{m}_{29} h_{29}$	$\eta_{\text{HC2}} = \frac{\dot{m}_{29} h_{29} - \dot{m}_{28} h_{28}}{\dot{W}_{HC2}}$

(continued)

Table 15.2 (continued)

Components	Energy balance equation	Energy efficiency equation
HEX 2	$\dot{m}_{29}h_{29} + \dot{m}_{38}h_{38} = \dot{m}_{30}h_{30} + \dot{m}_{39}h_{39}$	$\eta_{HEX2} = \frac{\dot{m}_{38}h_{38} - \dot{m}_{39}h_{39}}{\dot{m}_{30}h_{30} - \dot{m}_{29}h_{29}}$
HEX 3	$\dot{m}_{30}h_{30} + \dot{m}_{40}h_{40} = \dot{m}_{31}h_{31} + \dot{m}_{41}h_{41}$	$\eta_{HEX3} = \frac{\dot{m}_{31}h_{31} - \dot{m}_{30}h_{30}}{\dot{m}_{40}h_{40} - \dot{m}_{41}h_{41}}$
HEX 4	$\dot{m}_{31}h_{31} + \dot{m}_{37}h_{37} = \dot{m}_{32}h_{32} + \dot{m}_{38}h_{38}$	$\eta_{HEX4} = \frac{\dot{m}_{32}h_{32} - \dot{m}_{31}h_{31}}{\dot{m}_{37}h_{37} - \dot{m}_{38}h_{38}}$
HEX 5	$\dot{m}_{32}h_{32} + \dot{m}_{42}h_{42} = \dot{m}_{33}h_{33} + \dot{m}_{43}h_{43}$	$\eta_{HEX5} = \frac{\dot{m}_{33}h_{33} - \dot{m}_{32}h_{32}}{\dot{m}_{42}h_{42} - \dot{m}_{43}h_{43}}$
HEX 6	$\dot{m}_{33}h_{33} + \dot{m}_{36}h_{36} = \dot{m}_{34}h_{34} + \dot{m}_{37}h_{37}$	$\eta_{HEX6} = \frac{\dot{m}_{34}h_{34} - \dot{m}_{33}h_{33}}{\dot{m}_{36}h_{36} - \dot{m}_{37}h_{37}}$
Valve 1	$\dot{m}_{34}h_{34} = \dot{m}_{35}h_{35}$	$\eta_{v1} = \frac{\dot{m}_{35}h_{35}}{\dot{m}_{34}h_{34}}$
Separator	$\dot{m}_{35}h_{35} = \dot{m}_{36}h_{36} + \dot{m}_{40}h_{40}$	$\eta_{Sep} = \frac{\dot{m}_{36}h_{36} + \dot{m}_{44}h_{44}}{\dot{m}_{35}h_{35}}$
Generator 1	$\dot{m}_4h_4 + \dot{m}_{48}h_{48} = \dot{m}_5h_5 + \dot{m}_{45}h_{45}$	$\eta_{Gen1} = \frac{\dot{m}_{45}h_{45} - \dot{m}_{48}h_{48}}{\dot{m}_4h_4 - \dot{m}_5h_5}$
ORC Turbine	$\dot{m}_{45}h_{45} = \dot{m}_{46}h_{46} + \dot{W}_{ORC\_T}$	$\eta_{ORC\_T} = \frac{\dot{W}_{ORC\_T}}{\dot{m}_{45}h_{45} - \dot{m}_{46}h_{46}}$
HEX 7	$\dot{m}_{46}h_{46} + \dot{m}_{49}h_{49} = \dot{m}_{47}h_{47} + \dot{m}_{50}h_{50}$	$\eta_{HEX7} = \frac{\dot{m}_{50}h_{50} - \dot{m}_{49}h_{49}}{\dot{m}_{46}h_{46} - \dot{m}_{47}h_{47}}$
Pump 4	$\dot{m}_{47}h_{47} + \dot{W}_{P4} = \dot{m}_{48}h_{48}$	$\eta_{P4} = \frac{\dot{m}_{48}h_{48} - \dot{m}_{47}h_{47}}{\dot{W}_{P4}}$
Generator 2	$\dot{m}_5h_5 + \dot{m}_{60}h_{60} = \dot{m}_6h_6 + \dot{m}_{51}h_{51} + \dot{m}_{61}h_{61}$	$\eta_{Gen2} = \frac{\dot{m}_{51}h_{51} + \dot{m}_{61}h_{61} - \dot{m}_{60}h_{60}}{\dot{m}_5h_5 - \dot{m}_6h_6}$
HEX 8	$\dot{m}_{59}h_{59} + \dot{m}_{61}h_{61} = \dot{m}_{60}h_{60} + \dot{m}_{62}h_{62}$	$\eta_{HEX8} = \frac{\dot{m}_{60}h_{60} - \dot{m}_{59}h_{59}}{\dot{m}_{61}h_{61} - \dot{m}_{62}h_{62}}$
Pump 5	$\dot{m}_{58}h_{58} + \dot{W}_{P5} = \dot{m}_{59}h_{59}$	$\eta_{P5} = \frac{\dot{m}_{59}h_{59} - \dot{m}_{58}h_{58}}{\dot{W}_{P5}}$
Valve 2	$\dot{m}_{62}h_{62} = \dot{m}_{63}h_{63}$	$\eta_{v2} = \frac{\dot{m}_{63}h_{63}}{\dot{m}_{62}h_{62}}$
Absorber	$\dot{m}_{57}h_{57} + \dot{m}_{63}h_{63} + \dot{m}_{68}h_{68} = \dot{m}_{58}h_{58} + \dot{m}_{69}h_{69}$	$\eta_{Abs} = \frac{\dot{m}_{69}h_{69} - \dot{m}_{68}h_{68}}{\dot{m}_{58}h_{58} - \dot{m}_{57}h_{57} - \dot{m}_{63}h_{63}}$
3-Way valve	$\dot{m}_{55}h_{55} = \dot{m}_{56}h_{56} + \dot{m}_{57}h_{57}$	$\eta_{3WV} = \frac{\dot{m}_{56}h_{56} + \dot{m}_{57}h_{57}}{\dot{m}_{55}h_{55}}$
Evaporator	$\dot{m}_{54}h_{54} + \dot{m}_{66}h_{66} = \dot{m}_{55}h_{55} + \dot{m}_{67}h_{67}$	$\eta_{Eva} = \frac{\dot{m}_{67}h_{67} - \dot{m}_{66}h_{66}}{\dot{m}_{54}h_{54} - \dot{m}_{55}h_{55}}$

Valve 3	$\dot{m}_{53}h_{53} = \dot{m}_{54}h_{54}$	$\eta_{v3} = \frac{\dot{m}_{54}h_{54}}{\dot{m}_{53}h_{53}}$
Condenser 2	$\dot{m}_{52}h_{52} + \dot{m}_{64}h_{64} = \dot{m}_{53}h_{53} + \dot{m}_{65}h_{65}$	$\eta_{\text{Con2}} = \frac{\dot{m}_{65}h_{65} - \dot{m}_{64}h_{64}}{\dot{m}_{52}h_{52} - \dot{m}_{53}h_{53}}$
Ejector	$\dot{m}_{51}h_{51} + \dot{m}_{56}h_{56} = \dot{m}_{52}h_{52}$	$\eta_{\text{Ejc}} = \frac{\dot{m}_{52}h_{52}}{\dot{m}_{51}h_{51} + \dot{m}_{56}h_{56}}$
Dryer	$\dot{m}_6h_6 + \dot{m}_{70}h_{70} = \dot{m}_7h_7 + \dot{m}_{71}h_{71}$	$\eta_{\text{Dr}} = \frac{\dot{m}_{71}h_{71} - \dot{m}_{70}h_{70}}{\dot{m}_6h_6 - \dot{m}_7h_7}$
Hot water storage tank	$\dot{m}_7h_7 + \dot{m}_{72}h_{72} = \dot{m}_8h_8 + \dot{m}_{73}h_{73}$	$\eta_{\text{HWST}} = \frac{\dot{m}_{73}h_{73} - \dot{m}_{72}h_{72}}{\dot{m}_7h_7 - \dot{m}_8h_8}$

Table 15.3 Second law balance and efficiency equations

Components	Exergy balance equation	Exergy efficiency equation
Solar tower	$\dot{m}_{10}\mathrm{ex}_{10} + \dot{\mathrm{E}}\mathrm{x}^{Q}_{\mathrm{solar}} = \dot{m}_{1}\mathrm{ex}_{1} + \dot{\mathrm{E}}\mathrm{x}^{\mathrm{st}}_{D}$	$\psi_{\mathrm{st}} = \frac{\dot{m}_{1}\mathrm{ex}_{1} - \dot{m}_{10}\mathrm{ex}_{10}}{\dot{\mathrm{E}}\mathrm{x}^{Q}_{\mathrm{solar}}}$
Hot TES tank	$\dot{m}_{1}\mathrm{ex}_{1} = \dot{m}_{2}\mathrm{ex}_{2} + \dot{\mathrm{E}}\mathrm{x}^{Q}_{L,\mathrm{hTES}} + \dot{\mathrm{E}}\mathrm{x}^{\mathrm{hTES}}_{D}$	$\psi_{\mathrm{hTES}} = \frac{\dot{m}_{2}\mathrm{ex}_{2}}{\dot{m}_{1}\mathrm{ex}_{1}}$
Pump 1	$\dot{m}_{2}\mathrm{ex}_{2} + \dot{\mathrm{E}}\mathrm{x}^{W}_{P1} = \dot{m}_{3}\mathrm{ex}_{3} + \dot{\mathrm{E}}\mathrm{x}^{P1}_{D}$	$\psi_{P1} = \frac{\dot{m}_{3}\mathrm{ex}_{3} - \dot{m}_{2}\mathrm{ex}_{2}}{\dot{\mathrm{E}}\mathrm{x}^{W}_{P1}}$
Cold TES tank	$\dot{m}_{8}\mathrm{ex}_{8} = \dot{m}_{9}\mathrm{ex}_{9} + \dot{\mathrm{E}}\mathrm{x}^{Q}_{L,\mathrm{cTES}} + \dot{\mathrm{E}}\mathrm{x}^{\mathrm{cTES}}_{D}$	$\psi_{\mathrm{cTES}} = \frac{\dot{m}_{9}\mathrm{ex}_{9}}{\dot{m}_{8}\mathrm{ex}_{8}}$
Pump 2	$\dot{m}_{9}\mathrm{ex}_{9} + \dot{\mathrm{E}}\mathrm{x}^{W}_{P2} = \dot{m}_{10}\mathrm{ex}_{10} + \dot{\mathrm{E}}\mathrm{x}^{\mathrm{P2}}_{D}$	$\psi_{\mathrm{P2}} = \frac{\dot{m}_{10}\mathrm{ex}_{10} - \dot{m}_{9}\mathrm{ex}_{9}}{\dot{\mathrm{E}}\mathrm{x}^{W}_{P2}}$
HEX 1	$\dot{m}_{3}\mathrm{ex}_{3} + \dot{m}_{12}\mathrm{ex}_{12} + \dot{m}_{14}\mathrm{ex}_{14} + \dot{m}_{18}\mathrm{ex}_{18} = \dot{m}_{4}\mathrm{ex}_{4} + \dot{m}_{11}\mathrm{ex}_{11} + \dot{m}_{13}\mathrm{ex}_{13} + \dot{m}_{15}\mathrm{ex}_{15} + \dot{\mathrm{E}}\mathrm{x}^{\mathrm{HEX1}}_{D}$	$\psi_{\mathrm{Con1}} = \frac{\dot{m}_{11}(\mathrm{ex}_{11} + \mathrm{ex}_{13} + \mathrm{ex}_{15} - \mathrm{ex}_{18} - \mathrm{ex}_{12} - \mathrm{ex}_{14})}{\dot{m}_{3}\mathrm{ex}_{3} - \dot{m}_{4}\mathrm{ex}_{4}}$
Turbine 1	$\dot{m}_{11}\mathrm{ex}_{11} = \dot{m}_{12}\mathrm{ex}_{12} + \dot{\mathrm{E}}\mathrm{x}^{W}_{T1} + \dot{\mathrm{E}}\mathrm{x}^{\mathrm{T1}}_{D}$	$\psi_{\mathrm{T1}} = \frac{\dot{\mathrm{E}}\mathrm{x}^{W}_{\mathrm{T1}}}{\dot{m}_{11}\mathrm{ex}_{11} - \dot{m}_{12}\mathrm{ex}_{12}}$
Turbine 2	$\dot{m}_{13}\mathrm{ex}_{13} = \dot{m}_{14}\mathrm{ex}_{14} + \dot{\mathrm{E}}\mathrm{x}^{W}_{T2} + \dot{\mathrm{E}}\mathrm{x}^{T2}_{D}$	$\psi_{T2} = \frac{\dot{\mathrm{E}}\mathrm{x}^{W}_{T2}}{\dot{m}_{13}\mathrm{ex}_{13} - \dot{m}_{14}\mathrm{ex}_{14}}$
Turbine 3	$\dot{m}_{15}\mathrm{ex}_{15} = \dot{m}_{16}\mathrm{ex}_{16} + \dot{\mathrm{E}}\mathrm{x}^{W}_{T3} + \dot{\mathrm{E}}\mathrm{x}^{T3}_{D}$	$\psi_{T3} = \frac{\dot{\mathrm{E}}\mathrm{x}^{W}_{T3}}{\dot{m}_{15}\mathrm{ex}_{15} - \dot{m}_{16}\mathrm{ex}_{16}}$
Condenser 1	$\dot{m}_{16}\mathrm{ex}_{16} + \dot{m}_{19}\mathrm{ex}_{19} = \dot{m}_{17}\mathrm{ex}_{17} + \dot{m}_{20}\mathrm{ex}_{20} + \dot{\mathrm{E}}\mathrm{x}^{\mathrm{Con1}}_{D}$	$\psi_{\mathrm{Con1}} = \frac{\dot{m}_{20}\mathrm{ex}_{20} - \dot{m}_{19}\mathrm{ex}_{19}}{\dot{m}_{16}\mathrm{ex}_{16} - \dot{m}_{17}\mathrm{ex}_{17}}$
Pump 3	$\dot{m}_{17}\mathrm{ex}_{17} + \dot{\mathrm{E}}\mathrm{x}^{W}_{P3} = \dot{m}_{18}\mathrm{ex}_{18} + \dot{\mathrm{E}}\mathrm{x}^{P3}_{D}$	$\psi_{P3} = \frac{\dot{m}_{18}\mathrm{ex}_{18} - \dot{m}_{17}\mathrm{ex}_{17}}{\dot{\mathrm{E}}\mathrm{x}^{W}_{P3}}$
PEM electrolyzer	$\dot{m}_{20}\mathrm{ex}_{20} + \dot{\mathrm{E}}\mathrm{x}^{W}_{\mathrm{PEM}} = \dot{m}_{21}\mathrm{ex}_{21} + \dot{m}_{22}\mathrm{ex}_{22} + \dot{m}_{27}\mathrm{ex}_{27} + \dot{\mathrm{E}}\mathrm{x}^{\mathrm{PEM}}_{D}$	$\psi_{\mathrm{PEM}} = \frac{\dot{m}_{22}\mathrm{ex}_{22} + \dot{m}_{27}\mathrm{ex}_{27}}{\dot{m}_{20}\mathrm{ex}_{20} + \dot{\mathrm{E}}\mathrm{x}^{W}_{\mathrm{PEM}}}$
Hydrogen compressor 1	$\dot{m}_{22}\mathrm{ex}_{22} + \dot{\mathrm{E}}\mathrm{x}^{W}_{\mathrm{HC1}} = \dot{m}_{23}\mathrm{ex}_{23} + \dot{\mathrm{E}}\mathrm{x}^{\mathrm{HC1}}_{D}$	$\psi_{\mathrm{HC1}} = \frac{\dot{m}_{23}\mathrm{ex}_{23} - \dot{m}_{22}\mathrm{ex}_{22}}{\dot{\mathrm{E}}\mathrm{x}^{W}_{\mathrm{HC1}}}$
Nitrogen compressor	$\dot{m}_{24}\mathrm{ex}_{24} + \dot{\mathrm{E}}\mathrm{x}^{W}_{NC} = \dot{m}_{25}\mathrm{ex}_{25} + \dot{\mathrm{E}}\mathrm{x}^{NC}_{D}$	$\psi_{\mathrm{NC}} = \frac{\dot{m}_{25}\mathrm{ex}_{25} - \dot{m}_{24}\mathrm{ex}_{24}}{\dot{\mathrm{E}}\mathrm{x}^{W}_{NC}}$
Ammonia reactor	$\dot{m}_{23}\mathrm{ex}_{23} + \dot{m}_{25}\mathrm{ex}_{25} = \dot{m}_{26}\mathrm{ex}_{26} + \dot{\mathrm{E}}\mathrm{x}^{ar}_{D}$	$\psi_{\mathrm{ar}} = \frac{\dot{m}_{26}\mathrm{ex}_{26}}{\dot{m}_{23}\mathrm{ex}_{23} + \dot{m}_{25}\mathrm{ex}_{25}}$
Mixer	$\dot{m}_{27}\mathrm{ex}_{27} + \dot{m}_{39}\mathrm{ex}_{39} = \dot{m}_{28}\mathrm{ex}_{28} + \dot{\mathrm{E}}\mathrm{x}^{\mathrm{mix}}_{D}$	$\psi_{\mathrm{mix}} = \frac{\dot{m}_{28}\mathrm{ex}_{28}}{\dot{m}_{27}\mathrm{ex}_{27} + \dot{m}_{39}\mathrm{ex}_{39}}$

Hydrogen compressor 2	$\dot{m}_{28}ex_{28} + \dot{E}x^{W}_{HC2} = \dot{m}_{29}ex_{29} + \dot{E}x^{HC2}_{D}$	$\psi_{HC2} = \frac{\dot{m}_{29}ex_{29} - \dot{m}_{28}ex_{28}}{\dot{E}x^{W}_{HC2}}$
HEX 2	$\dot{m}_{29}ex_{29} + \dot{m}_{38}ex_{38} = \dot{m}_{30}ex_{30} + \dot{m}_{39}ex_{39} + \dot{E}x^{HEX2}_{D}$	$\psi_{HEX2} = \frac{\dot{m}_{38}ex_{38} - \dot{m}_{39}ex_{39}}{\dot{m}_{30}ex_{30} - \dot{m}_{29}ex_{29}}$
HEX 3	$\dot{m}_{30}ex_{30} + \dot{m}_{40}ex_{40} = \dot{m}_{31}ex_{31} + \dot{m}_{41}ex_{41} + \dot{E}x^{HEX3}_{D}$	$\psi_{HEX3} = \frac{\dot{m}_{31}ex_{31} - \dot{m}_{30}ex_{30}}{\dot{m}_{40}ex_{40} - \dot{m}_{41}ex_{41}}$
HEX 4	$\dot{m}_{31}ex_{31} + \dot{m}_{37}ex_{37} = \dot{m}_{32}ex_{32} + \dot{m}_{38}ex_{38} + \dot{E}x^{HEX4}_{D}$	$\psi_{HEX4} = \frac{\dot{m}_{32}ex_{32} - \dot{m}_{31}ex_{31}}{\dot{m}_{37}ex_{37} - \dot{m}_{38}ex_{38}}$
HEX 5	$\dot{m}_{32}ex_{32} + \dot{m}_{42}ex_{42} = \dot{m}_{33}ex_{33} + \dot{m}_{43}ex_{43} + \dot{E}x^{HEX5}_{D}$	$\psi_{HEX5} = \frac{\dot{m}_{33}ex_{33} - \dot{m}_{32}ex_{32}}{\dot{m}_{42}ex_{42} - \dot{m}_{43}ex_{43}}$
HEX 6	$\dot{m}_{33}ex_{33} + \dot{m}_{36}ex_{36} = \dot{m}_{34}ex_{34} + \dot{m}_{37}ex_{37} + \dot{E}x^{HEX6}_{D}$	$\psi_{HEX6} = \frac{\dot{m}_{34}ex_{34} - \dot{m}_{33}ex_{33}}{\dot{m}_{36}ex_{36} - \dot{m}_{37}ex_{37}}$
Valve 1	$\dot{m}_{34}ex_{34} = \dot{m}_{35}ex_{35} + \dot{E}x^{v1}_{D}$	$\psi_{v1} = \frac{\dot{m}_{35}ex_{35}}{\dot{m}_{34}ex_{34}}$
Separator	$\dot{m}_{35}ex_{35} = \dot{m}_{36}ex_{36} + \dot{m}_{40}ex_{40} + \dot{E}x^{Sep}_{D}$	$\psi_{Sep} = \frac{\dot{m}_{36}ex_{36} + \dot{m}_{44}ex_{44}}{\dot{m}_{35}ex_{35}}$
Generator 1	$\dot{m}_{4}ex_{4} + \dot{m}_{48}ex_{48} = \dot{m}_{5}ex_{5} + \dot{m}_{45}ex_{45} + \dot{E}x^{Gen1}_{D}$	$\psi_{Gen1} = \frac{\dot{m}_{45}ex_{45} - \dot{m}_{48}ex_{48}}{\dot{m}_{4}ex_{4} - \dot{m}_{5}ex_{5}}$
ORC turbine	$\dot{m}_{45}ex_{45} = \dot{m}_{46}ex_{46} + \dot{E}x^{W}_{ORC\_T} + \dot{E}x^{ORC\_T}_{D}$	$\psi_{ORC\_T} = \frac{\dot{E}x^{W}_{ORC\_T}}{\dot{m}_{45}ex_{45} - \dot{m}_{46}ex_{46}}$
HEX 7	$\dot{m}_{46}ex_{46} + \dot{m}_{49}ex_{49} = \dot{m}_{47}ex_{47} + \dot{m}_{50}ex_{50} + \dot{E}x^{HEX7}_{D}$	$\psi_{HEX7} = \frac{\dot{m}_{50}ex_{50} - \dot{m}_{49}ex_{49}}{\dot{m}_{46}ex_{46} - \dot{m}_{47}ex_{47}}$
Pump 4	$\dot{m}_{47}ex_{47} + \dot{E}x^{W}_{P4} = \dot{m}_{48}ex_{48} + \dot{E}x^{P4}_{D}$	$\psi_{P4} = \frac{\dot{m}_{48}ex_{48} - \dot{m}_{47}ex_{47}}{\dot{E}x^{W}_{P4}}$
Generator 2	$\dot{m}_{5}ex_{5} + \dot{m}_{60}ex_{60} = \dot{m}_{6}ex_{6} + \dot{m}_{51}ex_{51} + \dot{m}_{61}ex_{61} + \dot{E}x^{Gen2}_{D}$	$\psi_{Gen2} = \frac{\dot{m}_{51}ex_{51} + \dot{m}_{61}ex_{61} - \dot{m}_{60}ex_{60}}{\dot{m}_{5}ex_{5} - \dot{m}_{6}ex_{6}}$
HEX 8	$\dot{m}_{59}ex_{59} + \dot{m}_{61}ex_{61} = \dot{m}_{60}ex_{60} + \dot{m}_{62}ex_{62} + \dot{E}x^{HEX8}_{D}$	$\psi_{HEX8} = \frac{\dot{m}_{60}ex_{60} - \dot{m}_{59}ex_{59}}{\dot{m}_{61}ex_{61} - \dot{m}_{62}ex_{62}}$
Pump 5	$\dot{m}_{58}ex_{58} + \dot{E}x^{W}_{P5} = \dot{m}_{59}ex_{59} + \dot{E}x^{P5}_{D}$	$\psi_{P5} = \frac{\dot{m}_{59}ex_{59} - \dot{m}_{58}ex_{58}}{\dot{E}x^{W}_{P5}}$
Valve 2	$\dot{m}_{62}ex_{62} = \dot{m}_{63}ex_{63} + \dot{E}x^{v2}_{D}$	$\psi_{v2} = \frac{\dot{m}_{63}ex_{63}}{\dot{m}_{62}ex_{62}}$
Absorber	$\dot{m}_{57}ex_{57} + \dot{m}_{63}ex_{63} + \dot{m}_{68}ex_{68} = \dot{m}_{58}ex_{58} + \dot{m}_{69}ex_{69} + \dot{E}x^{Abs}_{D}$	$\psi_{Abs} = \frac{\dot{m}_{69}ex_{69} - \dot{m}_{68}ex_{68}}{\dot{m}_{58}ex_{58} - \dot{m}_{57}ex_{57} - \dot{m}_{63}ex_{63}}$
3-Way valve	$\dot{m}_{55}ex_{55} = \dot{m}_{56}ex_{56} + \dot{m}_{57}ex_{57} + \dot{E}x^{3WV}_{D}$	$\psi_{3WV} = \frac{\dot{m}_{56}ex_{56} + \dot{m}_{57}ex_{57}}{\dot{m}_{55}ex_{55}}$

(continued)

Table 15.3 (continued)

Components	Exergy balance equation	Exergy efficiency equation
Evaporator	$\dot{m}_{54}ex_{54} + \dot{m}_{66}ex_{66} = \dot{m}_{55}ex_{55} + \dot{m}_{67}ex_{67} + \dot{E}x_D^{Eva}$	$\psi_{Eva} = \frac{\dot{m}_{67}ex_{67} - \dot{m}_{66}ex_{66}}{\dot{m}_{54}ex_{54} - \dot{m}_{55}ex_{55}}$
Valve 3	$\dot{m}_{53}ex_{53} = \dot{m}_{54}ex_{54} + \dot{E}x_D^{v3}$	$\psi_{v3} = \frac{\dot{m}_{54}ex_{54}}{\dot{m}_{53}ex_{53}}$
Condenser 2	$\dot{m}_{52}ex_{52} + \dot{m}_{64}ex_{64} = \dot{m}_{53}ex_{53} + \dot{m}_{65}ex_{65} + \dot{E}x_D^{Con2}$	$\psi_{Con2} = \frac{\dot{m}_{65}ex_{65} - \dot{m}_{64}ex_{64}}{\dot{m}_{52}ex_{52} - \dot{m}_{53}ex_{53}}$
Ejector	$\dot{m}_{51}ex_{51} + \dot{m}_{56}ex_{56} = \dot{m}_{52}ex_{52} + \dot{E}x_D^{Ejc}$	$\psi_{Ejc} = \frac{\dot{m}_{52}ex_{52}}{\dot{m}_{51}ex_{51} + \dot{m}_{56}ex_{56}}$
Dryer	$\dot{m}_6ex_6 + \dot{m}_{70}ex_{70} = \dot{m}_7ex_7 + \dot{m}_{71}ex_{71} + \dot{E}x_D^{Dr}$	$\psi_{Dr} = \frac{\dot{m}_{71}ex_{71} - \dot{m}_{70}ex_{70}}{\dot{m}_6ex_6 - \dot{m}_7ex_7}$
Hot water storage tank	$\dot{m}_7ex_7 + \dot{m}_{72}ex_{72} = \dot{m}_8ex_8 + \dot{m}_{73}ex_{73} + \dot{E}x_D^{HWST}$	$\psi_{HWST} = \frac{\dot{m}_{73}ex_{73} - \dot{m}_{72}ex_{72}}{\dot{m}_7ex_7 - \dot{m}_8ex_8}$

Table 15.4 Defined governing equations of PEM plant

PEM plant	Equalities
Net voltage	$V = V_o + V_{\text{act}}^a + V_{\text{act}}^c + V_{\text{ohm}} + V_{\text{con}}^a + V_{\text{con}}^c$
Reversible potential	$V_o = 1.229 - 8.5 \times 10^{-4}(T_{\text{PEM}} - 298)$
Activation overpotential	$V_{\text{act}}^i = \frac{RT}{F} \sin h^{-1}\left(\frac{J}{2\,J_o^i}\right), \quad i =$ cathode or anode
Ohmic overpotential	$V_{\text{ohm}} = JR_{\text{PEM}}$
Total ohmic resistance	$R_{\text{PEM}} = \int_0^D \frac{dx}{\sigma[\lambda(x)]}$
Membrane water content	$\lambda(x) = \frac{\lambda_a - \lambda_c}{D} x + \lambda_c$
Concentration overpotential for anode	$V_{\text{con}}^a = \frac{RT}{4F} \ln \frac{C_{O_2}^{\text{mem}}}{C_{O_2,0}^{\text{mem}}}$
Concentration overpotential for cathode	$V_{\text{con}}^c = \frac{RT}{4F} \ln \frac{C_{H_2}^{\text{mem}}}{C_{H_2,0}^{\text{mem}}}$
Required energy for PEM plant	$E_{\text{stack}}^{\text{PEM}} = n_{\text{cell}} V_{\text{PEM}} I_{\text{PEM}}$

e^- and H_2 ions through the membrane and e^-, respectively. Furthermore, the resistance of bipolar structure, membrane, and electrode is used to analyze the ohmic overpotential. Additionally, the concentration losses are performed owing to modifications of reactant concentration at the electrode material along the electrochemical cycle. The thermodynamic equalities for first and second law analyses of PEM plant are defined in Table 15.4.

15.3.3 Storage Tank

The TES sub-plant has the molten salt-type tanks with hot temperature and cold temperature, and they are integrated with two molten salt pumps (see in Fig. 15.1, pump 1 and 2). At the start of a new day, the working fluid of the solar process should be stored in the cold TES tank. When the reflector area starts to run, the solar radiation receiver area is effectively warmed, and the working fluid is pumped by using the pump 2 to the solar radiation receiver to absorb thermal power. After the warming process, the working fluid enters the hot TES tank and, after that, is available to be utilized to produce steam at hot temperature in the HEX-1. Alternatively, the mass and energetic balance equations for the hot TES tank can be defined as follows:

$$m_{\text{hTES}} = m_{\text{p}} + (\dot{m}_{\text{ms,i}} - \dot{m}_{\text{ms,o}})\Delta t \tag{15.12}$$

$$Q_{\text{hTES}} = Q_{\text{p}} + \left(q_{\text{i}} - q_{\text{o}} - q_{\text{ht,loss}}\right)\Delta t/3600 \tag{15.13}$$

$$q_{\text{ht,loss}} = U_{\text{hTES}} A_{\text{hTES}} (T_{\text{hTES}} - T_{\text{o}}) \tag{15.14}$$

Here, m_{hTES} shows the mass of working fluid in the hot TES tank, m_p is the primary mass of working fluid in the hot TES tank, and $\dot{m}_{\mathrm{ms},i}$ and $\dot{m}_{\mathrm{ms,o}}$ show the mass flow rates of working fluid inlet and outlet of the hot TES tank, respectively, Δt is the time interval in the storage plant, Q_{hTES} gives the stored heat in the hot TES tank, Q_{p} gives the primary power stored in the hot TES tank, q_{i} and q_{o} show the thermal energy inlet and outlet of the hot TES tank, respectively, $q_{\mathrm{ht,\ loss}}$ gives the thermal energy loss, U_{hTES} shows the general energy loss parameter, A_{hTES} gives the energy loss area, and T_{hTES} shows the hot TES tank temperature. Similar equations can be defined for the cold TES tank.

15.3.4 Efficiencies

In the evaluation of power-related impact, the power performance of a cycle or plant should be described as the ratio of beneficial exit of the plant to the power input to the plant:

$$\eta = \frac{\sum \text{Useful output energy}}{\sum \text{Input energy}} = 1 - \frac{\sum \text{Energy loss}}{\sum \text{Input energy}} \tag{15.15}$$

The energetic efficiency of solar tower-based integrated plant for hydrogen production and liquefaction plant is defined as given below:

$$\eta_{\mathrm{WS}} = \frac{\dot{W}_{\mathrm{Net}} + \dot{Q}_{\mathrm{Cooling}} + \dot{Q}_{\mathrm{Heating}} + \dot{Q}_{\mathrm{Hot\_water}} + \dot{Q}_{\mathrm{Dryer}} + \dot{m}_{\mathrm{NH_3}}\mathrm{LHV}_{\mathrm{NH_3}} + \dot{m}_{\mathrm{H_2}}\mathrm{LHV}_{\mathrm{H_2}}}{\dot{Q}_{\mathrm{solar}}} \tag{15.16}$$

$$\dot{W}_{\mathrm{Net}} = \dot{W}_{\mathrm{T1}} + \dot{W}_{\mathrm{T2}} + \dot{W}_{\mathrm{T3}} + \dot{W}_{\mathrm{ORC}} - \sum \dot{W}_{\mathrm{HyC}} - \sum \dot{W}_{\mathrm{P}} - \dot{W}_{\mathrm{NiC}} \tag{15.17}$$

Here, $\dot{W}_{\mathrm{HyC}}$ and $\dot{W}_{\mathrm{NiC}}$ are the power needs for the hydrogen and nitrogen compressor, respectively. The energetic performance equations for combined plant parts are given in Table 15.2.

According to the exergetic analysis viewpoints, exergetic efficiency should be described based on the exergetic content of the plant inlets and outlets, which presents a better understanding of the plant efficiency. The exergetic performance opinion diversifies irreversibilities from exergy transfers; this supplies details concerning the potential plant developments by reducing the losses. Based on these definitions, the exergetic performance of a cycle or plant should be defined as:

$$\psi = \frac{\sum \text{useful output exergy}}{\sum \text{input exergy}} = 1 - \frac{\sum \text{exergy loss}}{\sum \text{input exergy}} \tag{15.18}$$

The exergetic efficiency of integrated plant can be defined as:

Table 15.5 Energetic performance equations for integrated plant subsystems

Subsystems	Energy efficiency equation
Solar power tower cycle	$\eta_{\mathrm{SPTC}} = \frac{\dot{Q}_{\mathrm{HEX1}}+\dot{Q}_{\mathrm{Gen1}}+\dot{Q}_{\mathrm{Gen2}}+\dot{Q}_{\mathrm{Dryer}}+\dot{Q}_{\mathrm{Hot\_water}}}{\dot{Q}_{\mathrm{solar}}}$
Rankine cycle	$\eta_{\mathrm{RC}} = \frac{\dot{W}_{T1}+\dot{W}_{T2}+\dot{W}_{T3}-\dot{W}_{P3}-\dot{W}_{\mathrm{PEM}}}{\dot{m}_3 h_3-\dot{m}_4 h_4}$
Hydrogen production and liquefaction process	$\eta_{\mathrm{HPLP}} = \frac{\dot{m}_{21}h_{21}+\dot{m}_{22}h_{22}+\dot{m}_{44}h_{44}}{\dot{m}_{20}h_{20}+\dot{W}_{\mathrm{PEM}}+\dot{W}_{\mathrm{HyC2}}}$
Ammonia process	$\eta_{\mathrm{AP}} = \frac{\dot{m}_{26}h_{26}}{\dot{m}_{22}h_{22}+\dot{m}_{24}h_{24}+\dot{W}_{\mathrm{NiC}}+\dot{W}_{\mathrm{HyC1}}}$
ORC cycle	$\eta_{\mathrm{ORC}} = \frac{\dot{W}_{\mathrm{ORC}}+\dot{Q}_{\mathrm{Heating}}}{(\dot{m}_4 h_4-\dot{m}_5 h_5)+\dot{W}_{P4}}$
Single-effect absorption cooling with ejector	$\eta_{\mathrm{SEACE}} = \frac{\dot{Q}_{\mathrm{Cooling}}}{(\dot{m}_5 h_5-\dot{m}_6 h_6)+\dot{W}_{P5}}$
Drying cycle	$\eta_{\mathrm{DC}} = \frac{\dot{Q}_{\mathrm{Drying}}}{(\dot{m}_6 h_6-\dot{m}_7 h_7)}$
Hot water production	$\eta_{\mathrm{HWP}} = \frac{\dot{Q}_{\mathrm{Hot\_water}}}{(\dot{m}_7 h_7-\dot{m}_8 h_8)}$

$$\psi_{\mathrm{WS}} = \frac{\dot{\mathrm{E}}\mathrm{x}^{W}_{\mathrm{Net}} + \dot{\mathrm{E}}\mathrm{x}^{Q}_{\mathrm{Cooling}} + \dot{\mathrm{E}}\mathrm{x}^{Q}_{\mathrm{Heating}} + \dot{\mathrm{E}}\mathrm{x}^{Q}_{\mathrm{Hot\_water}} + \dot{\mathrm{E}}\mathrm{x}^{Q}_{\mathrm{Dryer}} + \dot{m}_{\mathrm{NH_3}}\mathrm{ex}_{\mathrm{NH_3}} + \dot{m}_{\mathrm{H_2}}\mathrm{ex}_{\mathrm{H_2}}}{\dot{\mathrm{E}}\mathrm{x}^{Q}_{\mathrm{Solar}}} \tag{15.19}$$

The exergetic performance equalities for combined plant parts are written in Table 15.3. In addition to that, the energetic and exergetic performance equations for sub-plants, which are defined in system description title, are written in Tables 15.5 and 15.6, respectively.

Finally, the energetic and exergetic performance coefficient of cooling system are evaluated as:

$$\mathrm{COP}_{\mathrm{en}} = \frac{\dot{Q}_{\mathrm{Eva}}}{\dot{Q}_{\mathrm{Gen}} + \dot{W}_{\mathrm{P5}}} \tag{15.20}$$

$$\mathrm{COP}_{\mathrm{ex}} = \frac{\dot{\mathrm{E}}\mathrm{x}^{Q}_{\mathrm{Eva}}}{\dot{\mathrm{E}}\mathrm{x}^{Q}_{\mathrm{Gen}} + \dot{\mathrm{E}}\mathrm{x}^{W}_{\mathrm{P5}}} \tag{15.21}$$

15.3.5 Thermoeconomic Assessment

Thermoeconomic assessments are the category of engineering that favorably integrates, at the level of plant parts, thermodynamic estimations based on the exergetic assessment and economic viewpoints, in order to supply knowledge that is beneficial to the project and mechanism of the cost-effective plant, but not derivable by

Table 15.6 Exergetic efficiency equations for integrated plant subsystems

Subsystems	Exergy efficiency equation
Solar power tower cycle	$\psi_{\mathrm{SPTC}} = \frac{\dot{\mathrm{E}}\mathrm{x}^{Q}_{\mathrm{HEX1}} + \dot{\mathrm{E}}\mathrm{x}^{Q}_{\mathrm{Gen1}} + \dot{\mathrm{E}}\mathrm{x}^{Q}_{\mathrm{Gen2}} + \dot{\mathrm{E}}\mathrm{x}^{Q}_{\mathrm{Dryer}} + + \dot{\mathrm{E}}\mathrm{x}^{Q}_{\mathrm{Hot\_water}}}{\dot{\mathrm{E}}\mathrm{x}^{Q}_{\mathrm{Solar}}}$
Rankine cycle	$\psi_{\mathrm{RC}} = \frac{\dot{\mathrm{E}}\mathrm{x}^{W}_{T1} + \dot{\mathrm{E}}\mathrm{x}^{W}_{T2} + \dot{\mathrm{E}}\mathrm{x}^{W}_{T3} - \dot{\mathrm{E}}\mathrm{x}^{W}_{P3} - \dot{\mathrm{E}}\mathrm{x}^{W}_{\mathrm{PEM}}}{\dot{m}_3 \mathrm{ex}_3 - \dot{m}_4 \mathrm{ex}_4}$
Hydrogen production and liquefaction process	$\psi_{\mathrm{HPLP}} = \frac{\dot{m}_{21}\mathrm{ex}_{21} + \dot{m}_{22}\mathrm{ex}_{22} + \dot{m}_{44}\mathrm{ex}_{44}}{\dot{m}_{20}\mathrm{ex}_{20} + \dot{\mathrm{E}}\mathrm{x}^{W}_{\mathrm{PEM}} + \dot{\mathrm{E}}\mathrm{x}^{W}_{\mathrm{HyC2}}}$
Ammonia process	$\psi_{\mathrm{AP}} = \frac{\dot{m}_{26}\mathrm{ex}_{26}}{\dot{m}_{22}\mathrm{ex}_{22} + \dot{m}_{24}\mathrm{ex}_{24} + \dot{\mathrm{E}}\mathrm{x}^{W}_{\mathrm{NiC}} + \dot{\mathrm{E}}\mathrm{x}^{W}_{\mathrm{HyC1}}}$
ORC cycle	$\psi_{\mathrm{ORC}} = \frac{\dot{\mathrm{E}}\mathrm{x}^{W}_{ORC} + \dot{\mathrm{E}}\mathrm{x}^{Q}_{\mathrm{Heating}}}{(\dot{m}_4 \mathrm{ex}_4 - \dot{m}_5 \mathrm{ex}_5) + \dot{\mathrm{E}}\mathrm{x}^{W}_{\mathrm{P4}}}$
Single-effect absorption cooling with ejector	$\psi_{\mathrm{SEACE}} = \frac{\dot{\mathrm{E}}\mathrm{x}^{Q}_{\mathrm{Cooling}}}{(\dot{m}_5 \mathrm{ex}_5 - \dot{m}_6 \mathrm{ex}_6) + \dot{\mathrm{E}}\mathrm{x}^{W}_{\mathrm{P5}}}$
Drying cycle	$\psi_{\mathrm{DC}} = \frac{\dot{\mathrm{E}}\mathrm{x}^{Q}_{\mathrm{Drying}}}{(\dot{m}_6 \mathrm{ex}_6 - \dot{m}_7 \mathrm{ex}_7)}$
Hot water production	$\psi_{\mathrm{HWP}} = \frac{\dot{\mathrm{E}}\mathrm{x}^{Q}_{\mathrm{Hot\_water}}}{(\dot{m}_7 \mathrm{ex}_7 - \dot{m}_8 \mathrm{ex}_8)}$

traditional energetic and exergetic assessments and economic assessment [21]. Different works proffer that, when the exergetic costing assessments are not performed, the common statements of thermoeconomic analyses are more suitable as it defines any integration of thermodynamically and economical assessments.

15.3.5.1 Cost Balance Equality

For each current in the considered solar plant, an indicator called the flow cost rate $\dot{C}$ ($/h) can be described, and any cost balance equation can be defined for each part as given below:

$$\dot{C}_{q,k} + \sum\nolimits_i \dot{C}_{i,k} + \dot{Z}_k = \sum\nolimits_e \dot{C}_{e,k} + \dot{C}_{w,k} \tag{15.22}$$

The cost balance equations are usually defined so that all conditions are positive. Utilizing Eq. (15.20), one should be defined as [22]:

$$\sum \left(c_e \dot{\mathrm{E}}\mathrm{x}_e\right)_k + c_{w,k}\dot{W}_k = c_{q,k}\dot{\mathrm{E}}\mathrm{x}_{q,k} + \sum \left(c_i \dot{\mathrm{E}}\mathrm{x}_i\right)_k + \dot{Z}_k \tag{15.23}$$

$$\dot{C}_j = c_j \dot{\mathrm{E}}\mathrm{x}_j \tag{15.24}$$

$$\dot{Z} = \frac{Z_k \mathrm{CRF}\phi}{N \times 3600} \tag{15.25}$$

Here, Z_k shows the purchase cost of the kth part, and purchase cost of integrated plant components are given in Table 15.7, and CRF gives the capital recovery factor and can be defined as:

Table 15.7 Purchase cost functions of the system components

Components	Purchase cost functions
Heliostat	$Z_{\mathrm{Hel}} = 150 A_{Hel} N$
Receiver	$Z_{\mathrm{Rec}} = A_{\mathrm{Rec}}(79 R_{\mathrm{Rec}} - 42000)$
TES tank	$Z_{\mathrm{TES\_t}} = 4.8509 - 03973 \log_{10}(V) + 0.1445[\log_{10}(V)]^2$
Material	$Z_{\mathrm{PCM}} = 247 \times M_{\mathrm{PCM}}$
Rankine turbine	$Z_{\mathrm{RT}} = 4405 \times \left(\dot{W}_{\mathrm{RT}}\right)^{0.89}$
Heat exchanger	$Z_{\mathrm{HEX}} = 1010 \times (A_{\mathrm{HEX}})^{0.8}$
Condenser	$Z_{\mathrm{cond}} = 280.74 \frac{\dot{Q}_{\mathrm{cond}}}{k \Delta T} + 746 \dot{m}_{wf}$
Valve	$Z_{\mathrm{Vl}} = 37 \left(\frac{P_{34}}{P_{35}}\right)^{0.68}$
Storage tank	$Z_{\mathrm{StT}} = 4042 V_{\mathrm{ST}}^{0.506}$
Heating system unit	$Z_{\mathrm{Heating}} = 5714 \dot{m}_{49}$
Pump	$Z_{\mathrm{P}} = 1120 \times \left(\dot{W}_{\mathrm{Pump}}\right)^{0.8}$
Compressor	$Z_{\mathrm{comp}} = (71.1 \dot{m}_{22}) / \left\{ \left(0.9 - \eta_{\mathrm{comp}}\right) \times (P_{23}/P_{22}) \, ln \, (P_{23}/P_{22}) \right\}$
PEM electrolyzer	$Z_{\mathrm{PEM}} = 1000 \dot{W}_{\mathrm{PEM}}$
Absorber	$Z_{\mathrm{Abs}} = 309.14 \times (A_{\mathrm{Abs}})^{0.85}$
Ejector	$Z_{\mathrm{ejc}} = 1000 \times 15.96 \dot{m}_{51} \left(\frac{T_{51}+273.15}{\frac{P}{1000}}\right)^{0.05} \left(\frac{P_{516}}{1000}\right)^{-0.75}$
Evaporator	$Z_{\mathrm{Eva}} = 1144.3 \times \left(\dot{Q}_{\mathrm{Evp}}\right)^{0.67}$
Dryer	$Z_{\mathrm{Dr}} = 1000 \times (A_{\mathrm{Dr}})^{0.65}$
Domestic water heater	$Z_{\mathrm{DWH}} = 0.3 m_{\mathrm{DWH}}$

$$\mathrm{CRF} = \frac{ix(1+i)^n}{(1+i)^n - 1} \tag{15.26}$$

where i is the interest rate and n is the total working time of plant in years. In addition, N shows the annual number of working hours for component, and ϕ gives the maintenance indicator, which is generally 1.06 [22].

The economic assessment of the solar-powered plant can be performed to compute the cost of generated hydrogen as given below:

$$\mathrm{LCOH} = \frac{\dot{Z} + \dot{Z}_{\mathrm{O\&M}}}{M_{\mathrm{annual,H_2}}} \tag{15.27}$$

where LCOH is the levelized cost of hydrogen ($/kg), $\dot{Z}_{O\&M}$ is the annual cost for operating and maintenance, and M_{annual,H_2} shows the annual hydrogen production (kg/year).

15.4 Results and Discussion

In this part of the study, results of the thermodynamic analyses, parametric analyses, and economic analysis are presented. Firstly, in Table 15.8 thermodynamic analyses results which are energy and exergy efficiency and also exergy destruction rate in the second, third, and fourth column of the table are presented, respectively. The thermodynamic analysis which is very crucial in order to see the inefficiencies in the system can be used as a guide for the improvement of the system performance. For instance, these results presented in Table 15.7 indicate that the lowest energy and exergy efficiencies occurred in SEACE subsystem and ORC cycle, respectively. Hence it can be concluded that if the efficiencies of those subsystems increase, the performance of the system increases. However, this decision should of course be supported by economic and environmental data.

Table 15.9 presents the main outputs of the solar energy-based multigeneration system of which products are power, hydrogen, ammonia, cooling, heating, and hot water. Power in this multigeneration system is produced from both Rankine cycle and organic Rankine cycle, and the amount of overall produced power is 16,811 kW. Cooling and heating production rate are 2643 kW and 1941 kW, respectively. Hydrogen which is one of the main products for the multigeneration system is produced 0.026 kg per second (Table 15.9).

Coefficient of performance (COP) is a useful tool to evaluate the cooling systems. Figure 15.2 provides how energetic and exergetic coefficient of performance and exergy destruction rate of cooling system change with varying evaporator exit

Table 15.8 Thermodynamic assessment results of solar-powered plant

	Energy efficiency η (%)	Exergy efficiency ψ (%)	Exergy destruction rate $\dot{E}x_D$ (kW)
Solar power tower cycle	54.26	50.14	12,982
Rankine cycle	47.03	43.64	6143
Hydrogen production and liq-uefaction process	61.26	56.52	2427
Ammonia process	64.67	60.93	1423
ORC cycle	24.54	21.18	2984
Single-effect absorption cooling with ejector	20.93	17.67	2516
Drying cycle	78.96	75.61	1867
Hot water production	69.21	65.34	1058
Whole plant	56.17	52.83	31,400

Table 15.9 Main achieved outputs for the solar energy-based combined plant

Plant outputs	Values
Gross power generation from Rankine cycle, $\dot{W}_{RC}$	14,625 kW
Power generation from ORC, $\dot{W}_{ORC}$	2186 kW
Cooling generation, $\dot{Q}_{Cooling}$	2643 kW
Heating producing, $\dot{Q}_{Heating}$	1941 kW
Hydrogen production, $\dot{m}_{Hydrogen}$	0.026 kg/s
Ammonia production, $\dot{m}_{Ammonia}$	0.1012 kg/s
Hot water production, $\dot{m}_{HW}$	3.94 kg/s

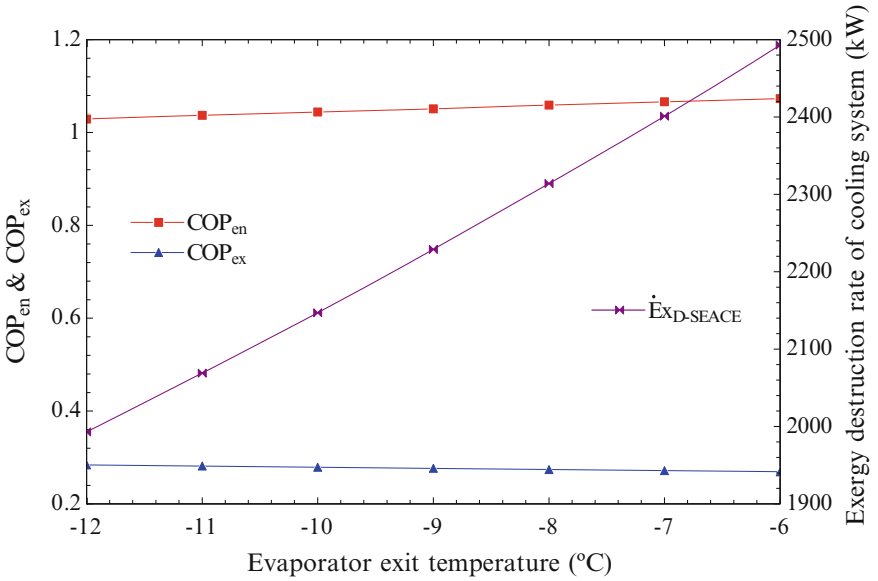

Fig. 15.2 Effect of evaporator exit temperature on the COPen, COPex, and exergy destruction rate of cooling system

temperature from −12 °C to −6 °C. As evaporator exit temperature increases from −12 °C to −6 °C, exergy destruction rate of single-effect absorption cooling system with ejector (SEACE) goes up to 2500 kW from about 2000 kW. On the other hand, energetic COP and exergetic COP of SEACE nearly stay the same with increasing evaporator exit temperature.

Figure 15.3 illustrates how dead state temperature affects energy efficiencies of subsystems of multigeneration system and whole system itself. Dead state temperature is of interest because changes in dead state temperature affect how subsystems work. Looking at Fig. 15.3, it is apparent that all subsystems and whole system perform better in terms of energy efficiency while dead state temperature increases. However, in SEACE subsystems not only an increment is seen, but also little decrease occurs due to increasing load of the SEACE subsystem.

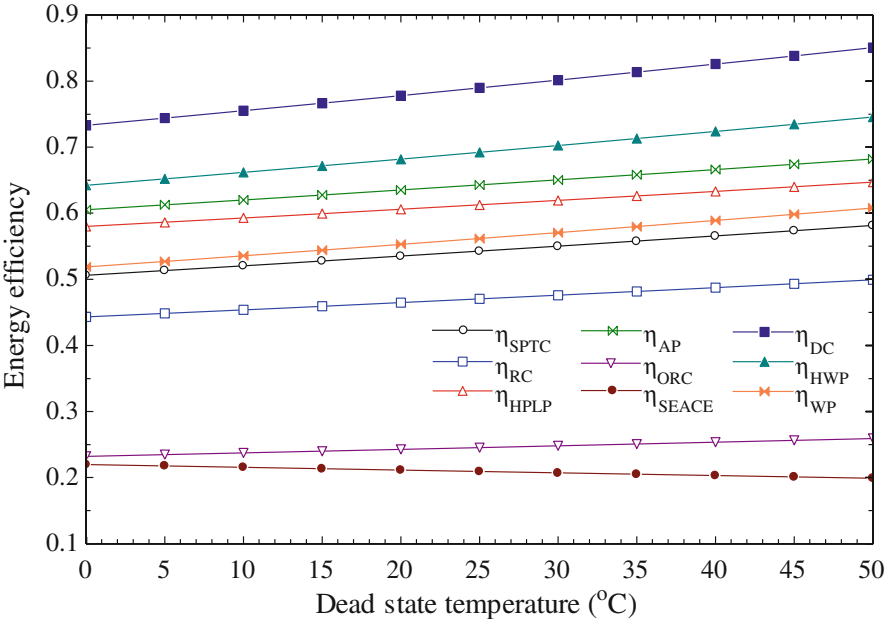

Fig. 15.3 Variation of energy efficiencies of the whole plant and its subsystems with increasing dead state temperature

Figure 15.4 provides the results obtained from the exergy analysis for all subsystems and whole system. Similar to the energy analysis results, exergy efficiencies of all subsystems and whole system except for SEACE increase with rising dead state temperature from 0 °C to 50 °C. The reason of those increments in subsystems and whole system lies in the exergy efficiency equations and exergy definition itself. As dead state temperature goes up, the difference between the environment temperature and working temperature of subsystems decreases; therefore, losses caused by those temperature differences are minimized. What is striking in the figure is that while exergy efficiency of whole plant is 48% at 0 °C, it will rise to 58% at 50 °C.

The results of the effect of dead state temperature on system outputs and hydrogen and ammonia production are displayed in Fig. 15.5. From the figure, a clear trend of increase can be seen for hydrogen and ammonia production rate and work produced by Rankine cycle. As displayed out from the figure, ammonia production rate rises up to 0.112 kg/s from 0.086 kg/s for the range of dead state temperature change from 0 °C to 50 °C. For the same range, hydrogen production range increases from 0.024 kg/s to above 0.028 kg/s value. The same reason with exergy efficiency increments is valid for these increasing product rates. There is a very slow increasing rate on ORC, cooling and heating product rates (Fig. 15.6).

One of the most important parameters for this multigeneration system is solar radiation because it is the only energy source of this integrated energy system. What stands out in this figure is the growth of energy efficiencies of subsystems and whole

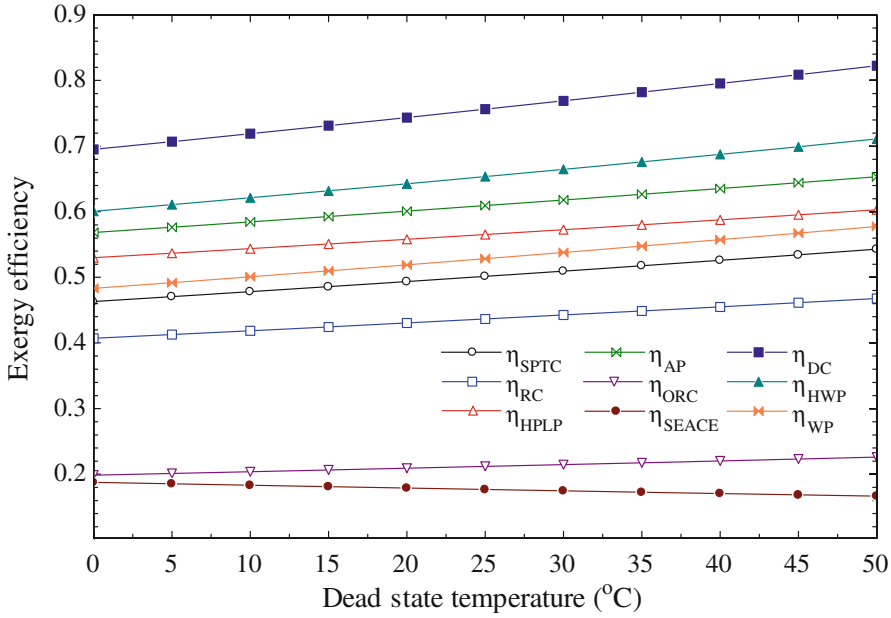

Fig. 15.4 Variation of exergy efficiencies of the whole plant and its subsystems with increasing dead state temperature

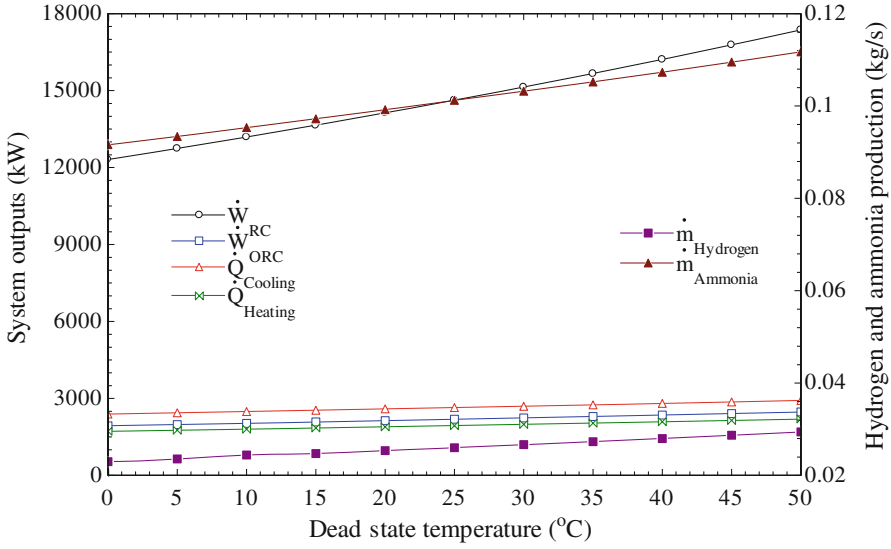

Fig. 15.5 Impact of dead state temperature on the system useful outputs

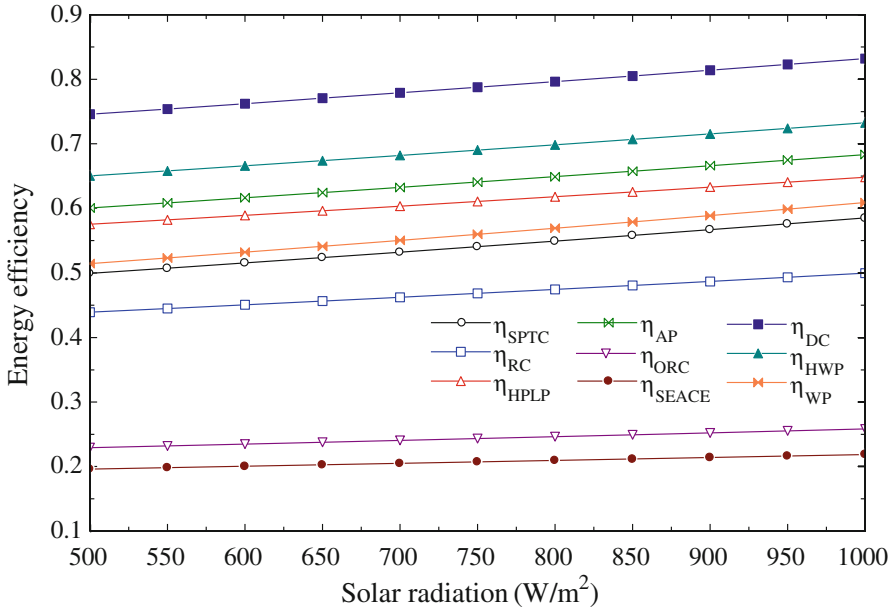

Fig. 15.6 Variation of energy efficiencies of the whole plant and its subsystems with increasing solar radiation

plant with varying solar radiation from 500 W/m^2 to 1000 W/m^2. For given range of solar radiation, energy efficiency of whole plant increases from 52% to 61%. The highest energy efficiency occurs in drying cycle, and it varies 75% to 83% as solar radiation changes from 500 W/m^2 to 1000 W/m^2. From the thermodynamic viewpoint, it can be concluded that any increase in solar radiation surely up to a certain point makes system perform better because of higher enthalpy input to the subsystems.

The result of how exergy efficiencies of subsystems and whole plant change with increasing solar radiation is presented in Fig. 15.7. The positive correlation among exergy efficiencies of all subsystems and whole plant with solar radiation is found. The reason of this rise in exergy efficiencies is the same with the reason of increase in energy efficiency which is clarified above. Figure 15.7 reveals that if solar radiation boosts up to 1000 W/m^2 from 500 W/m^2, exergy efficiency of whole plant rises from 48% to 56%.

Figure 15.8 reveals that there has been a slight growth in the values of system outputs and hydrogen and ammonia production rates. Especially ammonia production rate reaches its peak value which is 0.0116 when solar radiation is 1000 W/m^2. The highest power production which occurred in Rankine cycle varies from 11,500 kW to 17,200 kW as solar radiation changes from 500 W/m^2 to 1000 W/m^2. By considering the effect of solar radiation on energy and exergy efficiency and useful outputs of multigeneration system, it can be said that higher solar radiation up

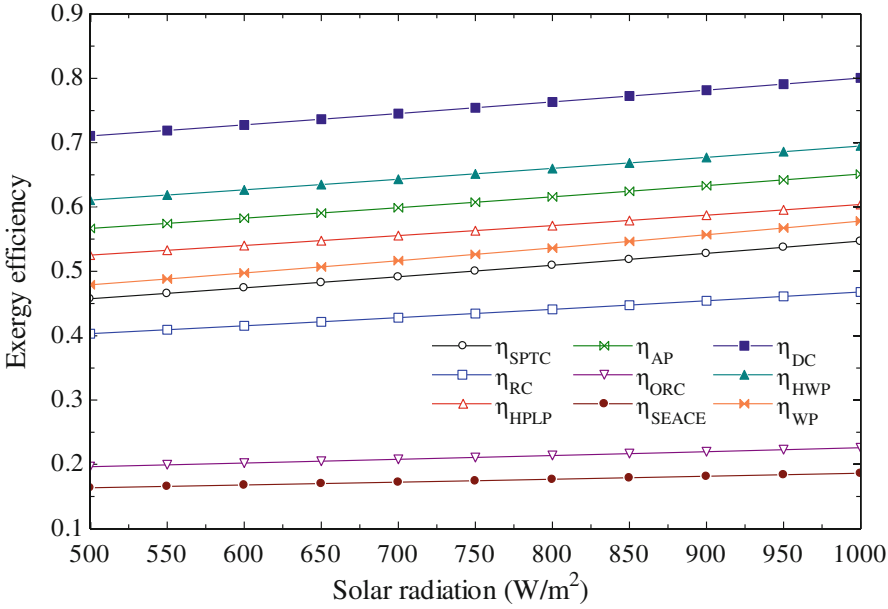

Fig. 15.7 Variation of exergy efficiencies of the whole plant and its subsystems with increasing solar radiation

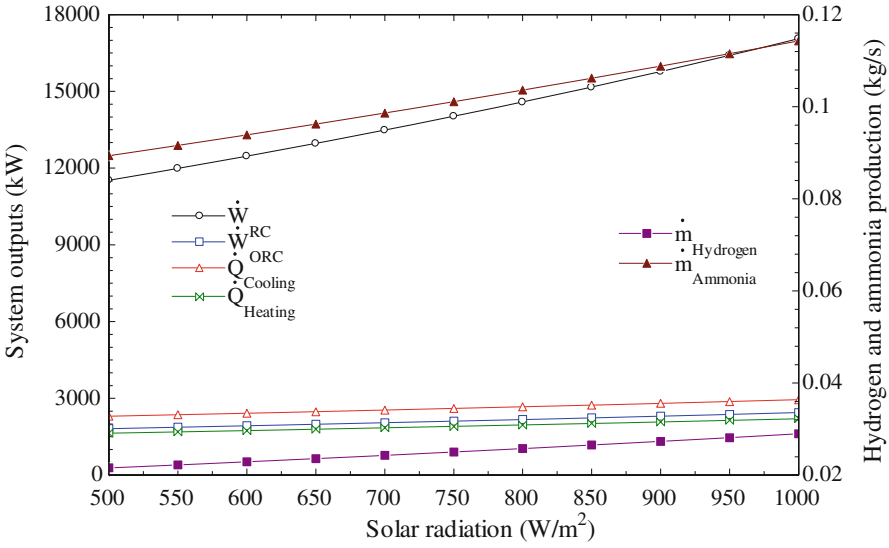

Fig. 15.8 Impact of solar radiation on the system useful outputs

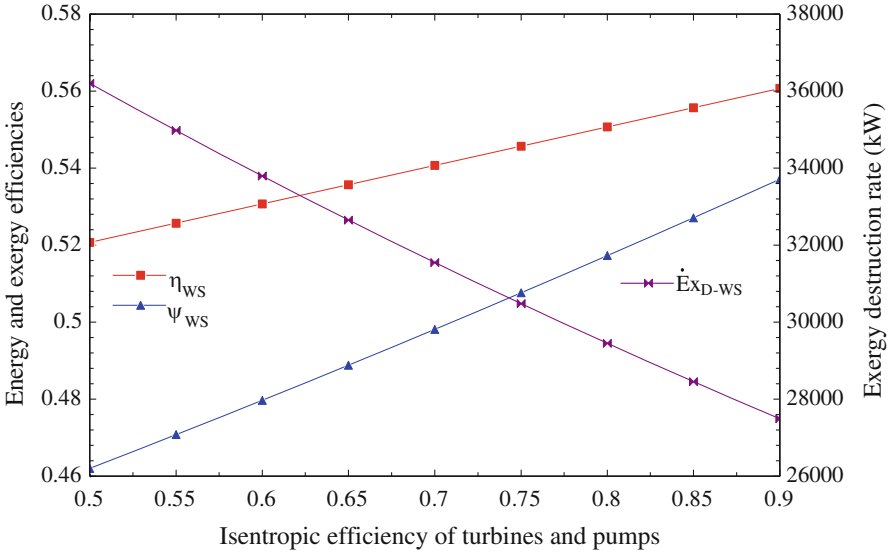

Fig. 15.9 Impact of isentropic efficiency of turbines and pumps on the performances and exergy destruction rate of whole system

to a certain point which is one of the most important parameters means higher efficiency of the system.

Another parameter investigated in this study to reveal the effect on the system performances which are energy and exergy efficiency is isentropic efficiency of turbines and pumps. For this multigeneration system design, isentropic efficiency of turbines and pumps are assumed to be 0.78 and 0.80. What is clarified in Fig. 15.9 is that as isentropic efficiencies of turbines and pumps increase, both energy and exergy efficiencies rise. For instance, for the range of 0.50–0.90 of isentropic efficiencies of turbines and pumps, energy and exergy efficiencies of whole plant increase from 52% and 46% to 56% and 53.6%, respectively. The reason for those improvements in efficiencies can be explained by looking at the right side of the figure which points out that as efficiencies of turbines and pumps increase, the amount of exergy destruction rates in subsystems decreases. Hence, the amount of energy and exergy efficiency values is likely to grow for this range.

Turbine 1 which is found in Rankine cycle, the first subsystem using thermal energy coming from solar tower, has surely effect on system performance when considering its inlet pressure. What is striking about this result given in Fig. 15.10 is the sharp fall of exergy destruction rate from about 34,000 kW to 26,400 kW as turbine 1 inlet pressure varies from 6000 kPa to 11,000 kPa. As mentioned above, when exergy destruction rate falls, energy and exergy efficiency values of whole system rise from 51% to 59% and from 47% and 55%, respectively.

Levelized cost of hydrogen is found by dividing the purchase cost and operating and maintenance cost by annual hydrogen production; therefore, unit for levelized cost is $/kg for hydrogen. Figure 15.11 reveals the effect of turbine 1 inlet pressure

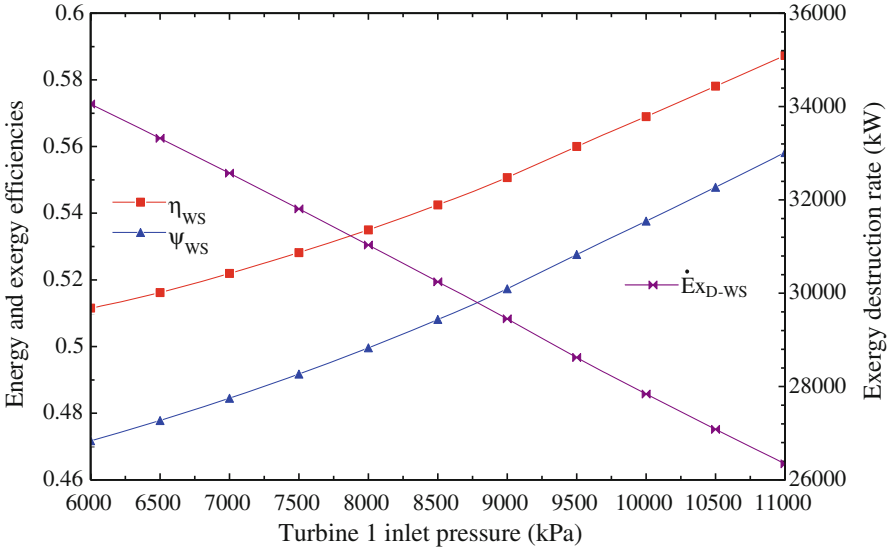

Fig. 15.10 Impact of turbine 1 inlet pressure on the performances and exergy destruction rate of whole system

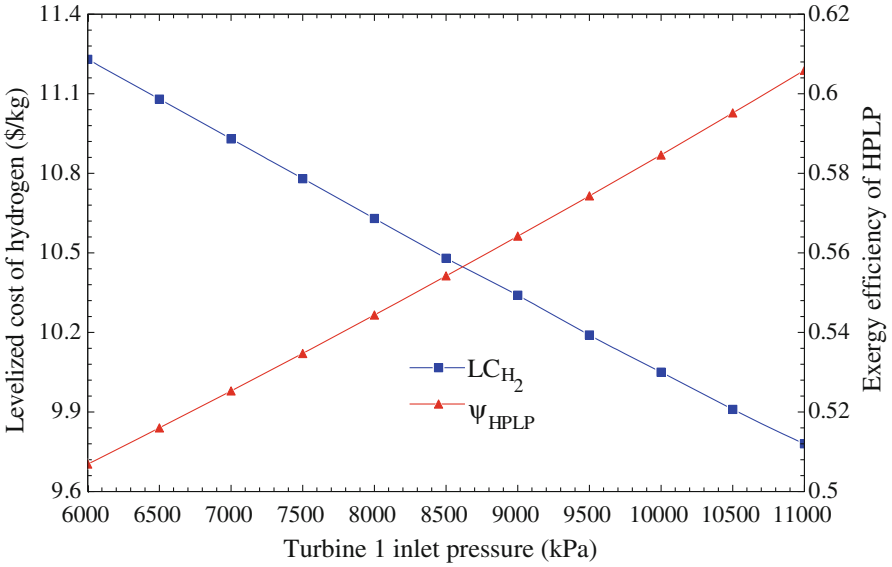

Fig. 15.11 Impact of turbine 1 inlet pressure on the levelized cost of hydrogen and exergy efficiency of HPLP

on levelized cost of hydrogen production and exergy efficiency of hydrogen production and liquefaction process. As turbine 1 inlet pressure grows from 6000 kPa to 110,000 kPa, levelized cost of hydrogen falls down to the 9.78 from 11.22 $/kg, while exergy efficiency of HPLP goes up from 51% to approximately 61%. As understood from Fig. 15.10, turbine 1 inlet pressure has positive effect on system performance, so it is expected that levelized cost decreases and exergy efficiency of HPLP rises.

In this multigeneration system, solar energy is used as the only driving source, and solar tower is used for utilizing solar energy supported by heliostats. Then as another parameter, the number of heliostats is selected, and its effect on energy and exergy efficiencies and exergy destruction rate of whole system is investigated. As the number of heliostats increases from 3000 to 5500, both efficiencies and exergy destruction rate of whole system go up. Because there has been exergy destruction in every single element of the multigeneration system, heliostats have also exergy destruction rate. So, when the number of heliostats increases, exergy destruction rate increases. However, this increment in exergy destruction rate that occurred in heliostats is not directly proportional with its number. Even if exergy destruction rate goes up, energy and exergy efficiencies of whole system can advance slightly, too. For the given range of number of heliostats, energy efficiency of whole system goes up to 57% from 54.6%, and exergy efficiency of whole system rises from 50.3% to 53%.

As seen from Fig. 15.12, the increase in number of heliostats has positive effect on system performance. Accordingly, it is expected that levelized cost will be decreased and exergy efficiency of HPLP increases as seen in Fig. 15.13. For the

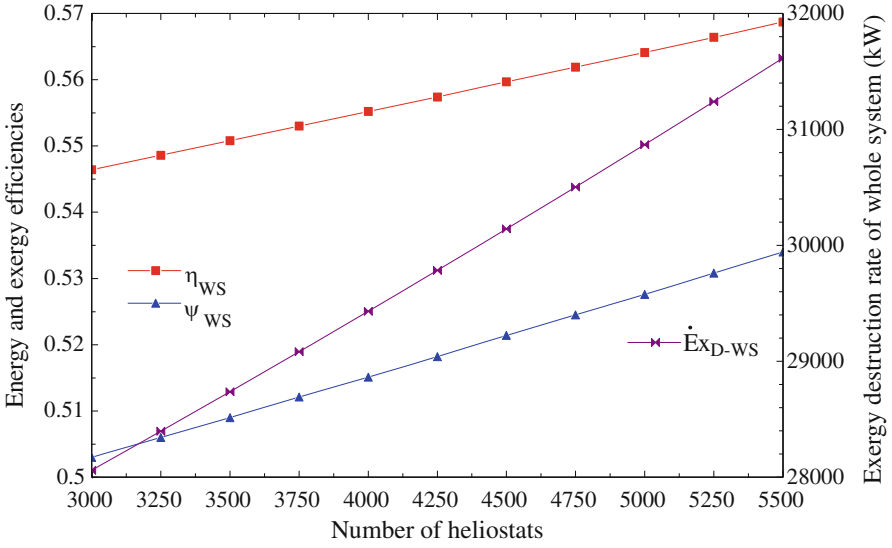

Fig. 15.12 Impact of number of heliostats on the performance and exergy destruction of whole system

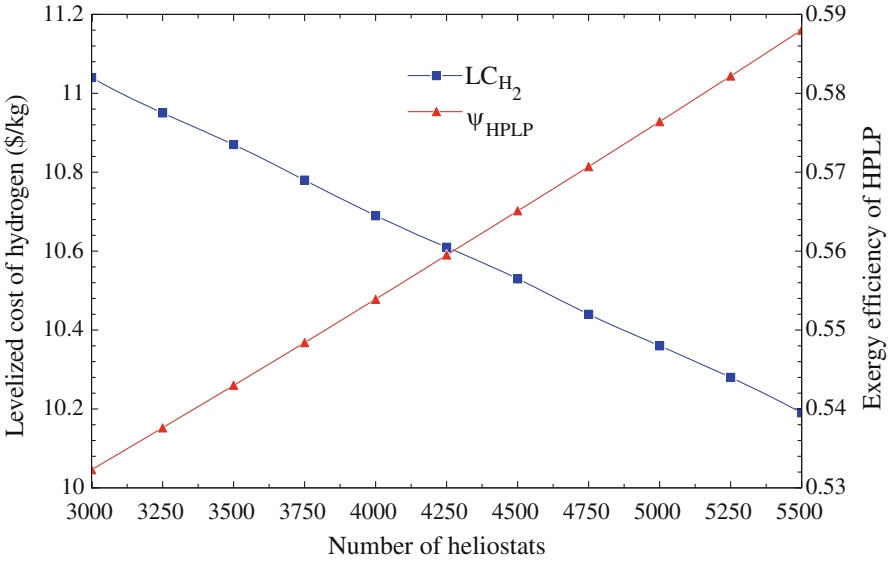

Fig. 15.13 Impact of number of heliostats on the levelized cost of hydrogen and exergy efficiency of HPLP

given number of heliostats, levelized cost of hydrogen production decreases from 11.04 $/kg to 10.2 $/kg, and exergy efficiency of HPLP boosts from 53.2% to 58.8%.

Figure 15.14 reveals how total cost and exergy efficiency of whole system vary with respect to increasing total power production. As total power production is increased from 12,000 kW to 22,000 kW, total cost of the multigeneration system rises from 33 M$ to 44 M$, and exergy efficiency of whole system increases from 51% to 60% (Fig. 15.15).

The last parameter investigated for this study is the hydrogen production rate which is varied from 0.007 kg/s to 0.097 kg/s. For the given range, total cost of the multigeneration system advances from 36.8 M$ to 40.6 M$. On the other hand, exergy efficiency of whole system increases from 50.5% to 56.2% for the same range.

15.5 Conclusion

In this study, a novel solar-based multigeneration energy system is designed and analyzed thermodynamically, parametrically, and economically. The multigeneration system is designed according to useful outputs such as compressed and liquefied hydrogen, power, heating and cooling, hot water, drying, and ammonia production. Thermodynamic analysis results reveal that for working parameters

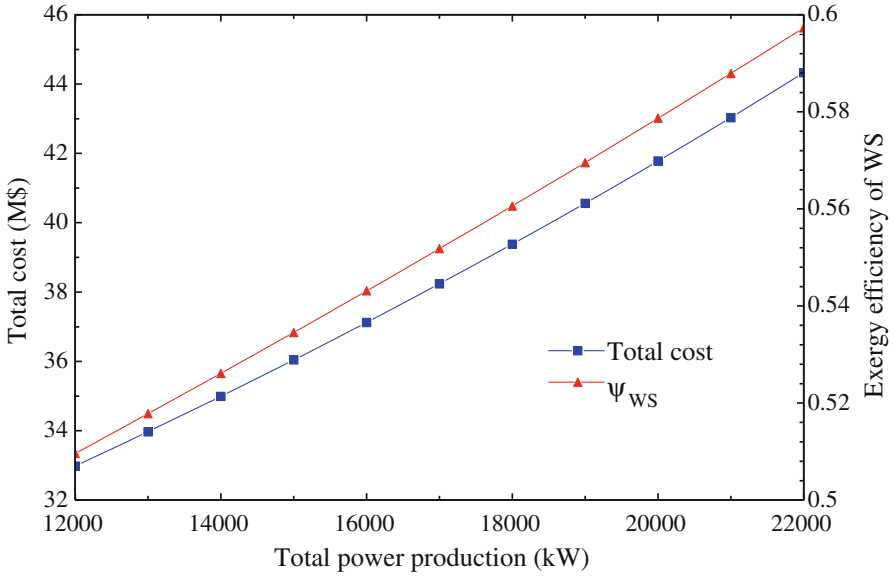

Fig. 15.14 Impact of total power production on the total cost and exergy efficiency of whole system

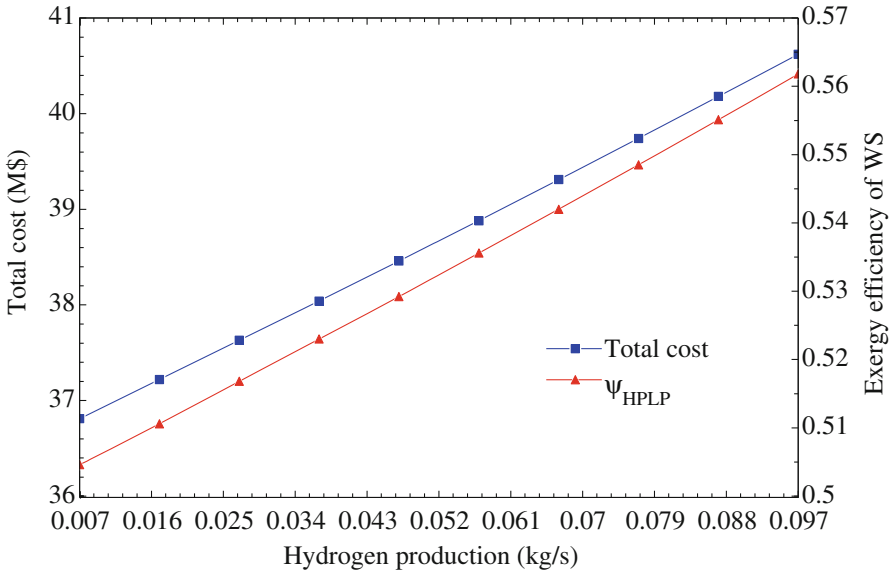

Fig. 15.15 Impact of hydrogen production on the total cost and exergy efficiency of whole system

given in Table 15.1, energy and exergy efficiencies of whole system are found to be 56.17% and 52.83%, respectively. Other striking results gained from the analyses can be listed as follows:

- The multigeneration plant proposed can provide power production up to 16,811 kW from Rankine and organic Rankine cycles together, by considering working parameters given in Table 15.1.
- Hydrogen and ammonia production rates of multigeneration system are found as 0.026 kg/s and 0.1012 kg/s, respectively.
- Evaporator exit temperature affects slightly the COP of cooling system of multigeneration system proposed.
- As dead state temperature increases, both energy and exergy efficiencies of whole system increase. System outputs are also affected positively with increasing dead state temperature.
- Solar radiation is an important parameter making energy and exergy efficiencies higher as it advances. When solar radiation is 1100 W/m^2, exergy efficiency of whole system is 56%.
- Isentropic efficiencies of turbines and pumps are directly proportional to energy and exergy efficiencies of whole system.
- If turbine 1 inlet pressure peaks at 11000 kPa, levelized cost of hydrogen production will be 9.78 $/kg.
- Number of heliostats is directly proportional to both energy and exergy efficiencies of whole system. While the number of heliostats rises to 5500, levelized cost of hydrogen production falls down to 10.2 $/kg.

If total power production is targeted to be 22,000 kW, the total cost of multigeneration system will reach 44 M$.

References

1. EIA – Annual Energy Outlook. (2019). https://www.eia.gov/outlooks/aeo/index.php. Accessed 8 Dec 2019.
2. Siddiqui, O., & Dincer, I. (2018). Examination of a new solar-based integrated system for desalination, electricity generation and hydrogen production. *Solar Energy, 163*, 224–234. https://doi.org/10.1016/J.SOLENER.2018.01.077.
3. World Banka Data. (n.d.). International Energy Agency, (IEA) *Fossil fuel energy consumption (% of total).* Data. https://data.worldbank.org/indicator/eg.use.comm.fo.zs. Accessed 28 Sep 2019.
4. Dincer, I., & Zamfirescu, C. (2012). Renewable-energy-based multigeneration systems. https://doi.org/10.1002/er.2882.
5. Ozturk, M., & Dincer, I. (2013). Thermodynamic analysis of a solar-based multi-generation system with hydrogen production. *Applied Thermal Engineering, 51*, 1235–1244. https://doi.org/10.1016/j.applthermaleng.2012.11.042.
6. Yilmaz, F., Ozturk, M., & Selbas, R. (2019). Energy and exergy performance assessment of a novel solar-based integrated system with hydrogen production. *International Journal of Hydrogen Energy, 44*, 18732–18743. https://doi.org/10.1016/j.ijhydene.2018.10.118.

7. Renewable energy target (RET) & alternate energy sources. (n.d.). https://www.energymatters.com.au/components/renewable-energy/. Accessed 8 Dec 2019.
8. Ozlu, S., & Dincer, I. (2016). Performance assessment of a new solar energy-based multigeneration system. https://doi.org/10.1016/j.energy.2016.06.040.
9. Behzadi, A., Gholamian, E., Ahmadi, P., Habibollahzade, A., & Ashjaee, M. (2018). Energy, exergy and exergoeconomic (3E) analyses and multi-objective optimization of a solar and geothermal based integrated energy system. *Applied Thermal Engineering, 143*, 1011–1022. https://doi.org/10.1016/j.applthermaleng.2018.08.034.
10. Al-Zareer, M., Dincer, I., & Rosen, M. A. (2017). Development and assessment of a new solar heliostat field based system using a thermochemical water decomposition cycle integrated with hydrogen compression. *Solar Energy, 151*, 186–201. https://doi.org/10.1016/J.SOLENER.2017.04.045.
11. Yilmaz, F., Ozturk, M., & Selbas, R. (2019). Development and performance analysis of a new solar tower and high temperature steam electrolyzer hybrid integrated plant. *International Journal of Hydrogen Energy*. https://doi.org/10.1016/j.ijhydene.2019.03.061.
12. Bin, S. U., Bicer, Y., Ahzi, S., & Abdala, A. (2019). Thermodynamic assessment of an integrated renewable energy multigeneration system including ammonia as hydrogen carrier and phase change material energy storage. *Energy Conversion and Management, 198*, 111809. https://doi.org/10.1016/j.enconman.2019.111809.
13. Khalid, F., Dincer, I., & Rosen, M. A. (2016). Techno-economic assessment of a renewable energy based integrated multigeneration system for green buildings. https://doi.org/10.1016/j.applthermaleng.2016.01.055.
14. Bamisile, O., Huang, Q., Hu, W., Dagbasi, M., & Kemena, A. D. (n.d.). Performance analysis of a novel solar PTC integrated system for multi-generation with hydrogen production. https://doi.org/10.1016/j.ijhydene.2019.10.234.
15. Zafar, S., & Dincer, I. (2014). Energy, exergy and exergoeconomic analyses of a combined renewable energy system for residential applications. *Energy and Buildings, 71*, 68–79. https://doi.org/10.1016/J.ENBUILD.2013.12.006.
16. Atiz, A., Karakilcik, H., Erden, M., & Karakilcik, M. (2019). Assessment of electricity and hydrogen production performance of evacuated tube solar collectors. *International Journal of Hydrogen Energy, 44*, 14137–14144. https://doi.org/10.1016/j.ijhydene.2018.09.100.
17. Ishaq, H., Dincer, I., & Naterer, G. F. (2018). Development and assessment of a solar, wind and hydrogen hybrid trigeneration system. *International Journal of Hydrogen Energy, 43*, 23148–23160. https://doi.org/10.1016/j.ijhydene.2018.10.172.
18. Çengel, Y. A., & Boles, M. A. (2015). *Thermodynamics : An engineering approach* (8th ed.). New York, McGraw-Hil
19. Kotas, T. J. (1985). *The exergy method of thermal plant analysis* (1st ed.). London, Butterworth-Heinemann
20. Dincer, I., & Rosen, M. (2012). *EXERGY : Energy, environment and sustainable development*. Elsevier Science Oxford, UK.
21. Haseli, Y., Dincer, I., & Naterer, G. F. (2008). Thermodynamic modeling of a gas turbine cycle combined with a solid oxide fuel cell. *International Journal of Hydrogen Energy, 33*, 5811–5822. https://doi.org/10.1016/j.ijhydene.2008.05.036.
22. Bejan, A., George, T., & Moran, M. J. (1996). *Thermal design and optimization*. John Wiley & Sons, New York

Index

F. Jabari et al. (eds.), *Integration of Clean and Sustainable Energy Resources and Storage in Multi-Generation Systems*,
https://doi.org/10.1007/978-3-030-42420-6